Modeling of Diesel HCCI combustion and its impact on pollutant emissions applied to global engine system simulation

Alessio Dulbecco

To cite this version:

Alessio Dulbecco. Modeling of Diesel HCCI combustion and its impact on pollutant emissions applied to global engine system simulation. Fluids mechanics [physics.class-ph]. Institut National Polytechnique de Toulouse - INPT, 2010. English. NNT : 2010INPT0015 . tel-04272194

HAL Id: tel-04272194
https://theses.hal.science/tel-04272194
Submitted on 6 Nov 2023

THÈSE

En vue de l'obtention du

DOCTORAT DE L'UNIVERSITÉ DE TOULOUSE

Délivré par :
Institut National Polytechnique de Toulouse (INP Toulouse)

Discipline ou spécialité :

Énergétique et Mécanique des Fluides

Présentée et soutenue par :
Alessio DULBECCO
le : mardi 2 février 2010

Titre :

MODELING OF DIESEL HCCI COMBUSTION AND ITS IMPACT ON POLLUTANT EMISSIONS APPLIED TO GLOBAL ENGINE SYSTEM SIMULATION

JURY

Olivier COLIN (Encadrant), François-Xavier DEMOULIN (Examinateur),
Jean-François HETET (Examinateur), Pascal HIGELIN (Rapporteur),
François-Alexandre LAFOSSAS (Examinateur), Angelo ONORATI (Rapporteur),
Thierry POINSOT (Directeur de thèse), Vincent TALON (Examinateur)

Ecole doctorale :
Mécanique, Energétique, Génie civil et Procédés (MEGeP)
Unité de recherche :
IFP, CERFACS
Directeur(s) de Thèse :
Thierry POINSOT
Olivier COLIN
Rapporteurs :
Pascal HIGELIN
Angelo ONORATI

.

Numéro d'ordre : ????

THÈSE

En vue de l'obtention du

DOCTORAT DE L'UNIVERSITÉ DE TOULOUSE

Délivré par : ***Institut National Polytechnique de Toulouse (INP Toulouse)***
Discipline : ***Énergétique et Mécanique des Fluides***

Présentée et soutenue par Alessio DULBECCO
le mardi 2 février 2010

TITRE

MODELING OF DIESEL HCCI COMBUSTION AND ITS IMPACT ON POLLUTANT EMISSIONS APPLIED TO GLOBAL ENGINE SYSTEM SIMULATION

JURY

Olivier COLIN	Chargé de Recherche, IFP	Encadrant IFP
François-Xavier DEMOULIN	Maitre de Conférences, Université de Rouen	Examinateur
Jean-François HETET	Professeur, Centrale Nantes	Examinateur
Pascal HIGELIN	Professeur, Université d'Orléans	Rapporteur
François-Alexandre LAFOSSAS	Ingénieur de Recherche, Toyota	Examinateur
Angelo ONORATI	Professeur, Politecnico di Milano	Rapporteur
Thierry POINSOT	Directeur de Recherche, IMFT/CNRS	Directeur de thèse
Vincent TALON	Ingénieur de Recherche, Renault	Examinateur

École Doctorale : ***Mécanique, Énergétique, Génie civil et Procédés (MEGeP)***
Unités de recherche : ***IFP, CERFACS***
Directeur de thèse : Thierry POINSOT
Rapporteurs : Pascal HIGELIN **et** Angelo ONORATI

Ai miei genitori Walter e Ornella
e ai miei nonni Edo, Anna, Angelo e Maria

Abstract

More and more stringent restrictions concerning the pollutant emissions of Internal Combustion Engines ($ICEs$) constitute a major challenge for the automotive industry. New combustion strategies such as Homogeneous Charge Compression Ignition ($HCCI$) and the implementation of complex injection strategies are promising solutions for achieving the imposed emission standards as they permit low $\mathrm{NO_x}$ and soot emissions, via lean and highly diluted combustions, thus assuring low combustion temperatures. This requires the creation of numerical tools adapted to these new challenges. This Ph.D presents the development of a new 0D Diesel HCCI combustion model : the dual Combustion Model ($dual-CM$). The dual-CM is based on the PCM-FPI approach used in 3D CFD, which allows to predict the characteristics of Auto-Ignition and Heat Release for all Diesel combustion modes. In order to adapt the PCM-FPI approach to a 0D formalism, a good description of the in-cylinder mixture is fundamental. Consequently, adapted models for liquid fuel evaporation, mixing zone formation and mixture fraction variance, which allow to have a detailed description of the local thermochemical properties of the mixture even in configurations adopting multiple injection strategies, are proposed. The results of the 0D model are compared in an initial step to the 3D CFD results. Then, the dual-CM is validated against a large experimental database; considering the good agreement with the experiments and low CPU costs, the presented approach is shown to be promising for global engine system simulations. Finally, the limits of the hypotheses made in the dual-CM are investigated and perspectives for future developments are proposed.

Key words : Diesel HCCI Combustion, Fuel Evaporation, Probability Density Functions, Tabulated Complex Chemistry, 0D Model, Multiple Injection Sprays.

Résumé

La législation sur les émissions de polluants des Moteurs à Combustion Interne (*ICEs*) est de plus en plus contraignante et représente un gros défi pour les constructeurs automobiles.

De nouvelles stratégies de combustion telles que la Combustion à Allumage par Compression Homogène (*HCCI*) et l'exploitation de stratégies d'injections multiples sont des voies prometteuses qui permettent de respecter les normes sur les émissions de $\mathrm{NO_x}$ et de suies, du fait que la combustion a lieu dans un mélange très dilué et par conséquent à basse température.

Ces aspects demandent la création d'outils numériques adaptés à ces nouveaux défis.

Cette thèse présente le développement d'un nouveau modèle 0D de combustion Diesel HCCI : le dual Combustion Model ($dual - CM$). Le modèle dual-CM a été basé sur l'approche PCM-FPI utilisée en Mécanique des Fluides Numérique (*CFD*) 3D, qui permet de prédire les caractéristiques de l'auto-allumage et du dégagement de chaleur de tous les modes de combustion Diesel. Afin d'adapter l'approche PCM-FPI à un formalisme 0D, il est fondamental de décrire précisément le mélange à l'intérieur du cylindre. Par consequent, des modèles d'évaporation du carburant liquide, de formation de la zone de mélange et de variance de la fraction de mélange, qui permettent d'avoir une description détaillée des proprietés thermochimiques locales du mélange y compris pour des configurations adoptant des stratégies d'injections multiples, sont proposés.

Dans une première phase, les résultats du modèle ont été comparés aux résultats du modèle 3D. Ensuite, le modèle dual-CM a été validé sur une grande base de données expérimentales; compte tenu du bon accord avec l'expérience et du temps de calcul réduit, l'approche présentée s'est montrée prometteuse pour des applications de type simulation système. Pour conclure, les limites des hypothèses utilisées dans dual-CM ont été investiguées et des perspectives pour les dévélopements futurs ont été proposées.

Mots Clés : Combustion Diesel HCCI, Évaporation de Carburant, Fonctions de Densité de Probabilité, Tabulation de la Chimie Complexe, Modèle 0D, Jets d'Injections Multiples.

Contents

Nomenclature

Acronyms

0D	Zero Dimensional
1D	One Dimensional
2D	Two Dimensional
3D	Three Dimensional
ACEA	Automotive European Manufacturers' Association
ADF-PCM	Approximated Diffusion Flame - PCM
AI	Auto-Ignition
ALE	Arbitrary Lagrangian Eulerian
ATDC	After TDC
BDC	Bottom Dead Center
BG	Burned Gas
BTDC	Before TDC
CFD	Computational Fluid Dynamics
CI	Compression Ignition
CMC	Conditional Moment Closure
CR	Common Rail
CRS	Common Rail System
DPF	Diesel Particulate Filter
dual-CM	dual Combustion Model
ECFM3Z	Three Zones Extended Coherent Flame Model
ECU	Electronic Control Unit
EGR	Exhaust Gas Recirculation
EU	European Union
EVC	Exhaust Valve Closing
EVO	Exhaust Valve Opening
FIAT	Fabbrica Italiana Automobili Torino
FPI	Flame Prolongation of ILDM
HCCI	Homogeneous Charge Compression Ignition
HR	Heat Release
HRR	Heat Release Rate

ICE	Internal Combustion Engine
ILDM	Intrinsic Low-Dimensional Manifolds
IVC	Inlet Valve Closing
IVO	Inlet Valve Opening
LAS	Laser Absorption Spectrometry
LIF	Laser Induced Fluorescence
LTC	Low Temperature Combustion
NADI	Narrow Angle Direct Injection
NTC	Negative Temperature Coefficient
PCCI	Premixed Controlled Compression Ignition
PCM	Presumed Conditional Moment
PDF	Probability Density Function
PIV	Particle Image Velocimetry
TDC	Top Dead Center
VVA	Variable Valve Actuator

Latin abbreviations

$\boldsymbol{a}$	[m]	crank radius
A	[-]	pure ambient air zone
$A(x)$	[m^2]	spray cross section area
AVI	[CAD]	Injection Advance
$\boldsymbol{b}$	[m]	connecting rod length
B	[-]	transfer number at steady-state
$\boldsymbol{B}$	[m]	bore
B_M	[-]	mass transfer number
B_T	[-]	thermal transfer number
c	[-]	normalized progress variable
$\mathcal{C}$	[mol/m^3]	molar concentration
C_a	[-]	orifice area contraction coefficient
C_d	[-]	orifice discharge coefficient
c_v	[J/kg/K]	specific heat capacity at constant volume
C_v	[-]	orifice velocity coefficient
c_p	[J/kg/K]	specific heat capacity at constant pressure
$\mathcal{D}$	[m^2/s]	laminar diffusion coefficient
D_d	[m]	drop diameter

d_h	[m]	injector orifice diameter
d_{vc}	[m]	vena contracta diameter
$Dissip$	[J/m^3/s]	sensible enthalpy dissipation term
DT	[s]	Dwell Time
$\boldsymbol{e}$	[m]	squish height
$\dot{E}$	[1/s]	mass transfer rate between zones
E_c	[J]	kinetic energy
EOC	[CAD]	End Of Combustion
EOI	[CAD]	End Of Injection
ET	[s]	Energizing time
F	[-]	pure fuel zone
F_i	[N/m^3]	volumetric force
h	[J/kg]	specific enthalpy
h^0	[J/kg]	formation enthalpy (computed at the temperature T_0)
h_c	[W/m^2/K]	convective heat transfer coefficient
h_s	[J/kg]	sensible enthalpy (referred to the temperature T_0)
$IMEP$	[bar]	Indicated Mean Effective Pressure
$\mathcal{J}$	[mol/m^2/s]	diffusion flux
J_i^h	[J/m^2/s]	enthalpy flow rate
k	[J/m/s/K]	thermal conductivity
K	[J/kg]	mean specific kinetic energy
l	[J/kg]	fuel latent heat of vaporization
L	[m]	fuel liquid penetration length
$\widetilde{L}$	[-]	non-dimensional spray liquid penetration
Le	[-]	Lewis' number
m	[kg]	mass
$\dot{\mathbf{m}}$	[kg/s]	mass flow rate through a spray cross section
$\dot{\widehat{m}}$	[kg/s/m^2]	mass flow rate per surface unit
M	[-]	mixing zone
$\mathcal{M}$	[kg/mol]	molecular weight
$\dot{M}_{F_l}$	[N]	spray momentum
m_{tot}	[kg]	total gaseous mass within the cylinder
n	[mol]	number of moles
n_{cyl}	[-]	number of cylinders

n_h	[-]	number of injector orifices
p	[Pa]	pressure
$\mathcal{P}$	[-]	single variable PDF
$\mathcal{P}_{co}$	[-]	coupled PDF
p_{vp}	[Pa]	saturation pressure of the fuel
p_x	[Pa]	partial pressure of the species x
Pr	[-]	Prandtl's number
$\dot{Q}^{cb}$	[J/s]	combustion Heat Release Rate
$\dot{Q}_{ev}$	[J/s]	fuel evaporation heat flow rate
$\dot{Q}_{hu}$	[J/s]	heat up heat flow rate
$\dot{Q}_{th}$	[J/s]	thermal losses
$\dot{Q}_{tot}$	[J/s]	total heat flow rate
r	[m]	drop radius
R	[J/kg/K]	gas constant of the mixture
$\mathcal{R}$	[J/mol/K]	universal gas constant
s	[-]	mass stoichiometric coefficient
$\boldsymbol{s}$	[m]	stroke
S	[m]	spray gaseous penetration
$\dot{S}$	[1/s]	mass source term
$\widetilde{S}$	[-]	non-dimensional spray gaseous penetration
$\dot{S}_{h_s}$	[J/kg/s]	sensible enthalpy source term
$\bar{S}_p$	[m/s]	mean piston velocity
S_w	[m^2]	wall surface
Sc	[-]	Schmidt's number
Sc_t	[-]	turbulent Schmidt's number
SMD	[m]	Sauter's Mean Diameter
SOC	[CAD]	Start Of Combustion
SOI	[CAD]	Start Of Injection
t	[s]	time
T	[K]	temperature
$\widetilde{t}$	[-]	non-dimensional time
t^+	[s]	temporal length scale
t_{nod}	[s]	needle opening delay
T_w	[K]	wall temperature

u	[m/s]	absolute velocity
u_B	[m/s]	Bernoulli's velocity
u_r	[m/s]	radial convective velocity
v	[-]	fuel mixture fraction variance
V	[m^3]	cylinder volume
V_b	[m^3]	piston bowl volume
V_d	[m^3]	dead volume
V_{displ}	[m^3]	piston displacement
v_r	[m/s]	radial diffusion velocity
W	[J/m^3/s]	sensible enthalpy production term
x	[m]	spray penetration length coordinate
$\boldsymbol{x}$	[m]	piston position coordinate
X	[-]	molar fraction
$\widetilde{x}$	[-]	non-dimensional penetration length
x^+	[m]	penetration length scale
Y	[-]	mass fraction
Y_c	[-]	progress variable
Z	[-]	fuel mixture fraction

Greek abbreviations

α	[rad]	theoretical spray spreading angle
β	[rad]	opening solid angle containing the injection spray axes
γ	[-]	isentropic evolution coefficient
δ	[-]	segregation factor
Δp	[Pa]	fuel pressure drop through the injector nozzle
ϵ	[J/kg/s]	specific turbulent kinetic energy dissipation rate
ζ	[-]	Pitzer's acentric factor
η	[debyes]	dipole momentum
θ	[rad]	measured spray spreading angle
$\boldsymbol{\theta}$	[CAD]	crank angle
κ	[J/kg]	specific turbulent kinetic energy
λ	[m^2/s]	evaporation constant
μ	[kg/m/s]	dynamic viscosity
μ_t	[kg/m/s]	turbulent dynamic viscosity
ν	[-]	molar coefficient

Π	[N/m^3]	diphasic coupling term
ρ	[kg/m^3]	density
τ	[s]	relaxation time
τ_{chem}	[s]	chemical characteristic time
τ_{ij}	[Pa]	shear stress tensor
τ_{ev}	[s]	evaporation characteristic time
τ_m	[s]	mixing characteristic time
τ_t	[s]	turbulent characteristic time
ϕ	[-]	Schwab-Zeldovitch variable
Φ	[-]	equivalence ratio
$\hat{\Phi}$	[-]	apparent equivalence ratio
χ	[1/s]	scalar dissipation rate
$\dot{\omega}$	[1/s]	mass reaction rate
Ω_{eng}	[rpm]	engine speed
Ω_v	[-]	collision integral for fluid viscosity
$\dot{\omega}_{Y_c}$	[1/s]	progress variable reaction rate

Subscripts

0	initial/reference value
a	ambient-air
a_w	withdrawn ambient air
bn	normal boiling point
cr	critical conditions
D	combustion duluent (Burned Gases)
eq	chemical equilibrium
exp	experimental variable
F	gaseous fuel
F_{inj}	injected liquid-fuel
F_l	liquid fuel
g	gaseous mixture
h	injector orifice
i	injection number
I	liquid-gas interface
in	incoming flow rate
ini	initial value

inj	relative to liquid-fuel injection
max	maximum value
ms	mass boundary layer
out	outgoing flow rate
pa	pure air
r	reference conditions
s	saturated conditions
S	spray
st	steady-state
t	thermal boundary layer
x	species x
$\beta - PDF$	PDF parameter
τ	tracer variable
∞	variable at infinite distance

Superscripts

A	pure ambient air zone
b	burned gas region
cb	associated to combustion
$COMP$	computed variable
F	pure fuel zone
$IFP - C3D$	IFP-C3D variable
i/o	input/output flow rates
M	mixing zone
PCM	variable computed using the PCM approach
ref	reference value
st	steady-state
TAB	tabulated variable
u	unburned gas region
∞	variable at infinite distance

Chapter 1

Introduction

This ending decade is clearly marked by a worldwide general understanding of the implications that the pollutant and carbon dioxide (CO_2) emissions generated by human activities have on the quality of life. Relatively to the major atmospheric pollutants, the road transportation sector represents one of the major contributors. For instance, in the 2008 european pollutant emission panorama, the road transportation contributes for almost 40% to the global emissions of nitrogen oxides (NO_x), for about 36% to the global emissions of carbon monoxide (CO) and for around 17% to the global emissions of Particulate Matter (PM), figure 1.1.

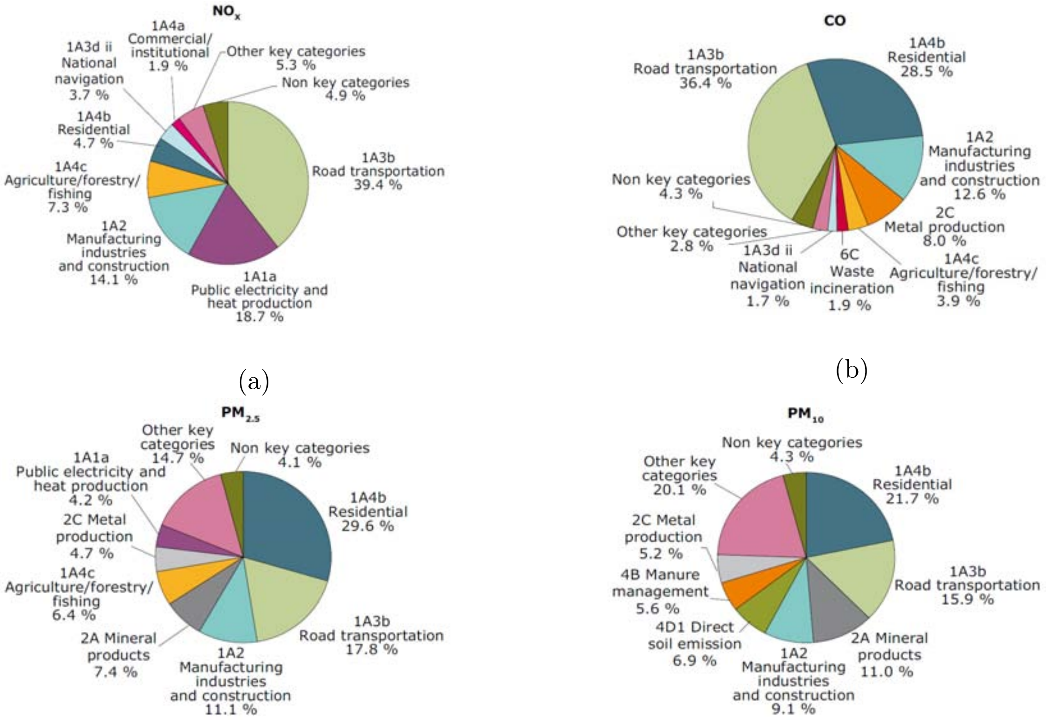

(a) (b)

(c) (d)

Figure 1.1: Emissions of $\mathrm{NO_x}$ (a), CO (b), $\mathrm{PM_{2.5}}$ (c), and $\mathrm{PM_{10}}$ (d) in Europe per activity sector [96].

Accordingly, standards concerning the road transportation pollutant emissions were established by the European Union (EU), and imposed on car manufacturers. Figure 1.2 (top) shows the evolution of the main pollutant specific emission limits (expressed in g/km) associated with the Diesel car european standards, from 1992 to 2014. The data concerning the PM and $\mathrm{NO_x}$ emissions are also plotted in figure 1.2 (bottom) in a diagram. Looking at figure 1.2, it is clear that there is a willingness from the institutions to reduce the pollutant emissions, and to do that in a relatively short period of time. On the other hand, the introduction of increasingly stringent pollutant emission standards has obliged car manufacturers to invest in research and development in order to improve the performance of their products.

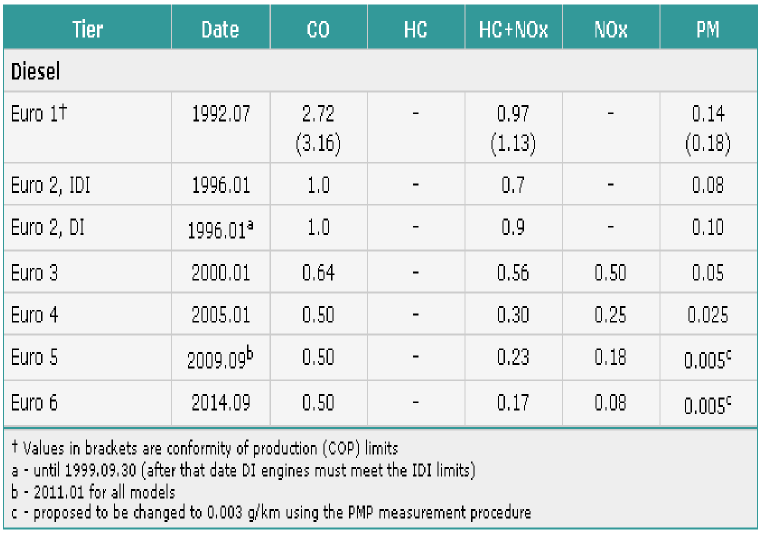

Tier	Date	CO	HC	HC+NOx	NOx	PM
Diesel						
Euro 1†	1992.07	2.72 (3.16)	-	0.97 (1.13)	-	0.14 (0.18)
Euro 2, IDI	1996.01	1.0	-	0.7	-	0.08
Euro 2, DI	1996.01[a]	1.0	-	0.9	-	0.10
Euro 3	2000.01	0.64	-	0.56	0.50	0.05
Euro 4	2005.01	0.50	-	0.30	0.25	0.025
Euro 5	2009.09[b]	0.50	-	0.23	0.18	0.005[c]
Euro 6	2014.09	0.50	-	0.17	0.08	0.005[c]

† Values in brackets are conformity of production (COP) limits
a - until 1999.09.30 (after that date DI engines must meet the IDI limits)
b - 2011.01 for all models
c - proposed to be changed to 0.003 g/km using the PMP measurement procedure

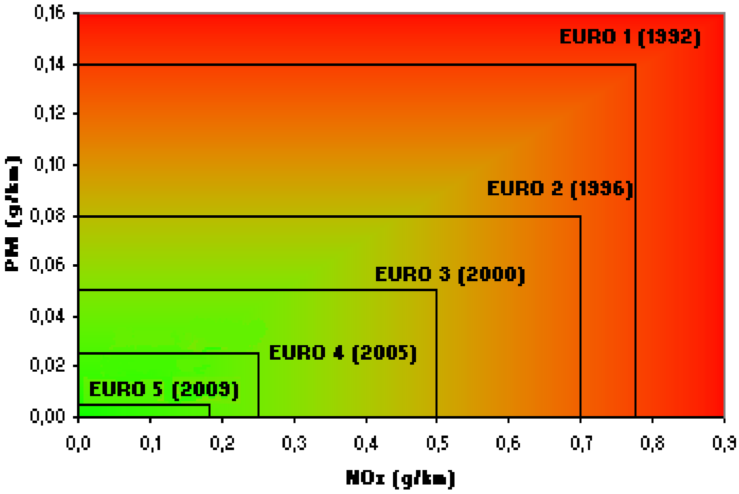

Figure 1.2: European Union emission standards for light duty Diesel vehicles [97].

Figure 1.3 shows the trends relative to the absolute emissions of NO_x, figure 1.3 (top), and CO, figure 1.3 (bottom), plotted per activity sectors, and relative to the period of time going from 2000 to 2006. Looking at figure 1.3, two important aspects must be kept in mind :

- the effect of the introduction of new standards is not immediate : in fact several years are necessary in order to significantly renew the existing car park,
- the number of cars is constantly growing.

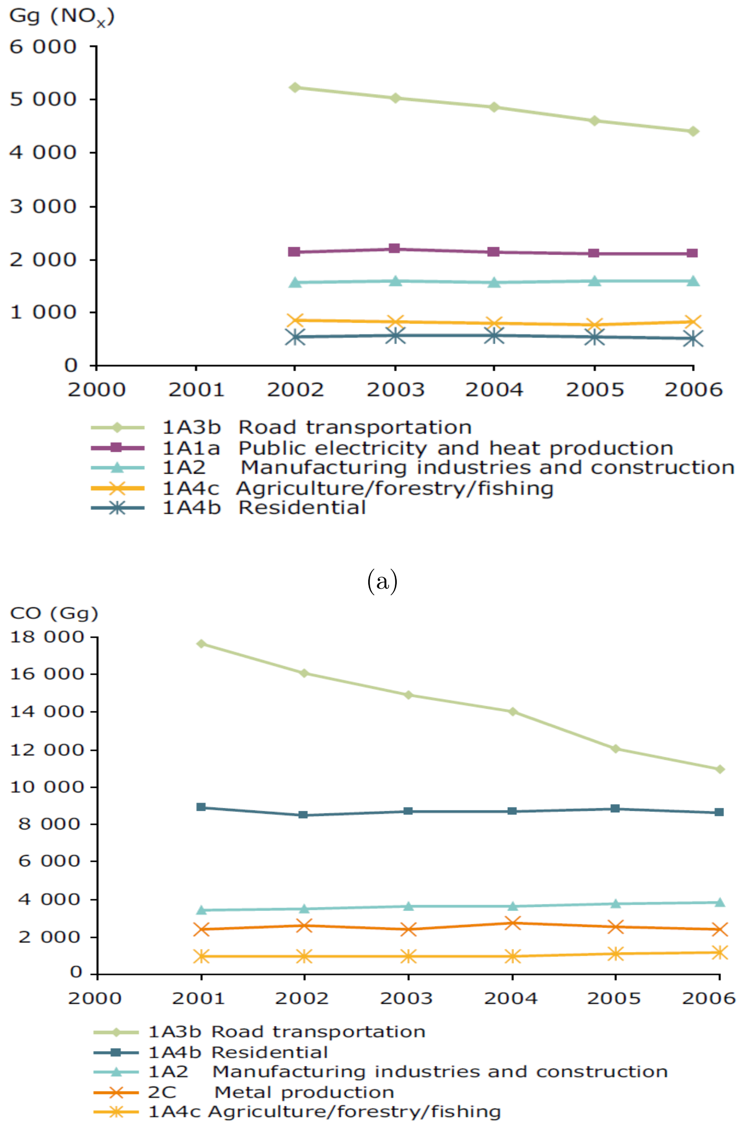

(a)

(b)

Figure 1.3: Trends in NO$_x$ (top) and CO (bottom) emissions from the five most important activity sectors on the period from 2000 to 2006 [96].

As seen in figure 1.3, in the last years the tendencies are clearly positive : even if the number of cars continues to increase, the NO$_x$ and CO emissions associated with the road transportation are in constant decrease. Moreover, the trends shown in figure 1.3 are due to the introduction of the Euro 1 to Euro 4 standards. Consequently, it is reasonable to expect further pollutant emission reductions in the following years. At the present time, the chemical species recognized as pollutant species for Internal Combustion Engines ($ICEs$) are nitrogen oxides (NO_x), carbon mono-oxide (CO), Particulate Matter (PM) and unburned hydrocarbons (HC). These species are responsible for local atmospheric pollution, often localized around urban sites or along the main connection axes. However, the road transportation contributes up to 20% to the carbon dioxide (CO_2) emissions.

Even if presently CO_2 is not considered as a pollutant species, it is in part responsible for global warming. Unlike the ICE pollutant species, which can be reduced by optimizing the combustion, CO_2 is a product of combustion. Consequently, it can only be reduced by reducing fuel consumption, that is by improving engine efficiency.

Even if a law limiting the CO_2 emissions still does not exist, in response to the Kyoto protocol of 1997, the Automotive European Manufacturers' Association (*ACEA*) commits itself to reduce the specific CO_2 emissions to 140 g/km before 2008, and to 120 g/km before 2012[1].

In the following of this chapter, first a brief description of a standard recent commercial Diesel Internal Combustion Engine (*ICE*) is given, section 1.1. In particular, the principle of the Diesel engine and the main technologies integrated in the engine architecture influencing the combustion process are presented. Then, a comparison between conventional Diesel and Diesel Homogeneous Charge Compression Ignition (*HCCI*) combustion regimes is detailed. In section 1.2, an overview of experimental and numerical devices used to study the global engine systems is given. Finally at the end of this chapter, the context of this dissertation is defined and the methodology used to develop and validate the dual Combustion Model (*dual-CM*), which is the central element of this Ph.D, is detailed.

1.1 The Diesel engine

In recent years, technological improvements allowed the development of new devices which strongly improve the quality of the combustion process in ICEs. The integration in the engine architecture of devices such as Common Rail System (*CRS*) and Exhaust Gas Recirculation (*EGR*) loop represented a real breakthrough that marked the beginning of a worldwide diffusion of Diesel engines.

Figure 1.4 shows the FIAT 1.3 JTD multijet engine, the symbol of the new generation of Diesel engines. The engine architecture shown in figure 1.4, conceived for respecting the Euro 4 standards, is a turbo-charged inline four cylinders with four valves per cylinder equipped with an EGR loop and a second generation high pressure Direct Injection (*DI*) CRS, able to perform up to five fuel injections per engine cycle.

At the present in Europe, almost 50% of passenger cars are equipped with Diesel engines.

---

[1] The values of 140 and 120 g/km are mean values of specific CO_2 emissions computed on the whole range of car production.

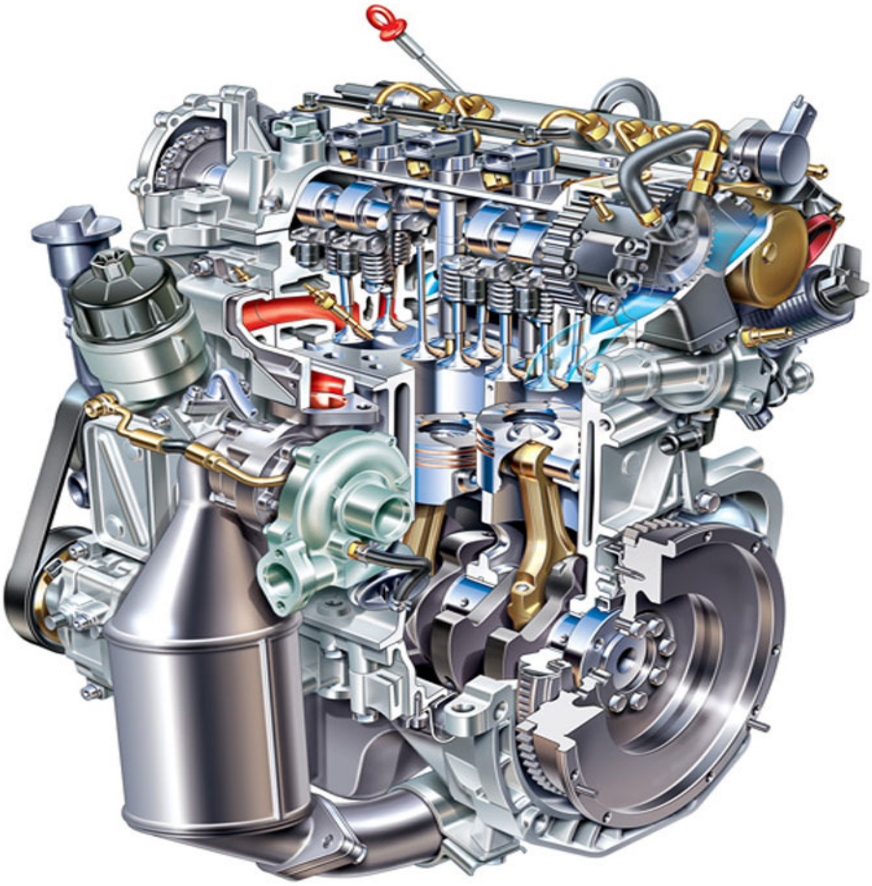

Figure 1.4: FIAT 1.3 JTD 16v multijet engine architecture [99]. This engine, developed for respecting the Euro 4 standards, has a maximum power of 55 kW (75 HP) at 4000 rpm and a maximum torque of 145 Nm at 1500 rpm.

1.1.1 Principle of the four stroke Diesel engine

In this section, the principle of the four stroke compression ignition engine is briefly presented. Figures 1.5 to 1.7 show the different phases of a classical four stroke Diesel engine cycle. In particular, figure 1.5 represents the physical phenomena associated with each stroke, figure 1.6 shows the angular extents of the different phases of the four stroke engine cycle and figure 1.7 represents on the pressure/volume ($p - V$) thermodynamic diagram the evolutions of the thermodynamic conditions within the cylinder, during a complete engine cycle. In the following, the different Diesel engine cycle phases are discussed more in detail.

Stroke n° 1 : intake

The piston is moving from Top Dead Center (TDC) towards Bottom Dead Center (BDC), figure 1.5. In this first phase, the intake valves are opened and allow the fresh ambient air mixture, composed in the most general case of pure air and Exhaust Gas

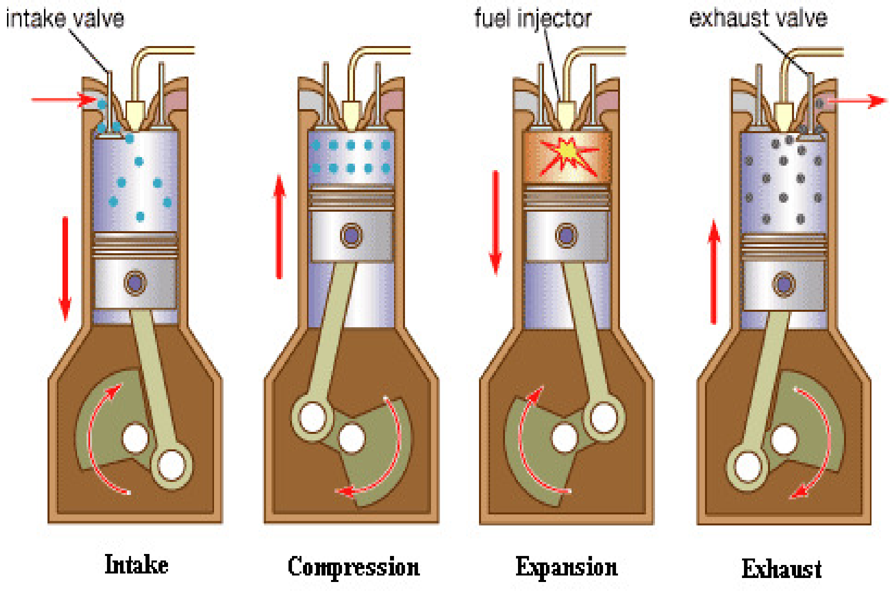

Figure 1.5: The Diesel four-stroke operating cycle.

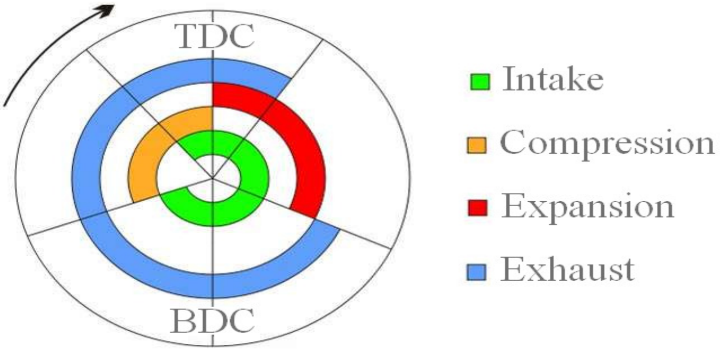

Figure 1.6: Angular extents of the engine cycle phases for a Diesel four-stroke engine.

Recirculation (EGR) gases, to fill the combustion chamber. As the Intake Valve Opening/Closing (IVO/IVC) times are finite, in order to optimize the volumetric efficiency, the intake valve opening interval begins before TDC and ends after BDC, figure 1.6. The intake phase on the pressure/volume thermodynamic diagram, figure 1.7, corresponds to the evolution $\overrightarrow{AB}$ which, because of the pressure drop of the gases crossing the intake valve seats, lies at a pressure level lower than the atmospheric pressure[2].

Stroke n° 2 : compression

The piston is moving from BDC towards TDC, figure 1.5. In this second phase, the cylinder is filled with fresh ambient-air gases, the intake and exhaust valves are closed, and the piston compresses the gases within the combustion chamber. The compression

---

[2] The pressure/volume thermodynamic diagram shown in figure 1.7 refers to a naturally aspirated Diesel engine.

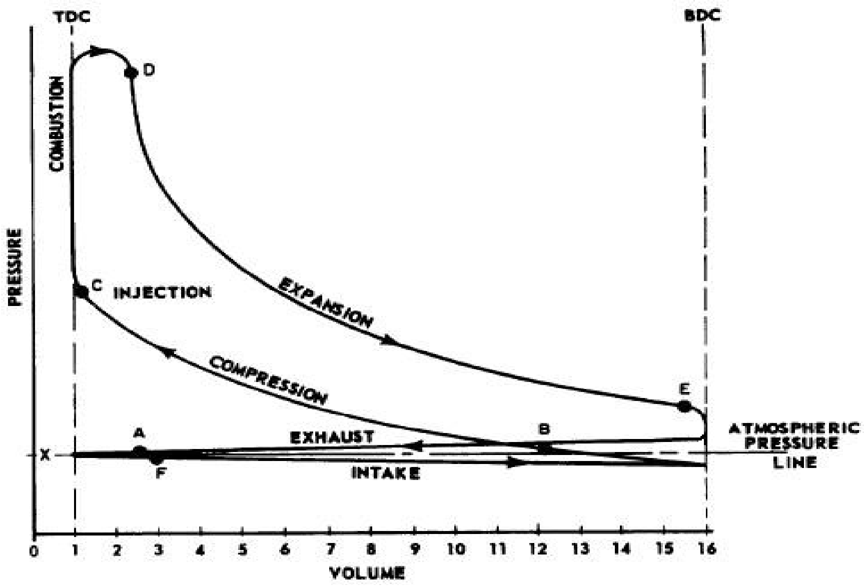

Figure 1.7: Pressure-volume thermodynamic diagram for a Diesel four-stroke operating cycle.

phase begins after BDC and ends at TDC, figure 1.6. During this phase, the ambient-air gases heat up and exchange heat with the cylinder walls. Consequently, the compression phase on the pressure/volume thermodynamic diagram, figure 1.7, is represented as a polytropic evolution, $\overrightarrow{BC}$. Usually, the liquid fuel injection within the cylinder starts just before the piston reaches TDC. In fact, at this time, the thermodynamic conditions of the gases within the combustion chamber favor the liquid fuel evaporation and the formation of radicals which permits the auto-ignition of the reactive mixture (mixture of fuel and ambient-air).

Stroke n° 3 : expansion

The piston is moving from TDC towards BDC, figure 1.5. In this third phase, both the intake and exhaust valves are closed, and the reactive mixture burns and expands within the combustion chamber. The expansion phase is the major work contribution to the engine cycle. The expansion phase begins at TDC and ends before BDC, figure 1.6. On the pressure/volume thermodynamic diagram, figure 1.7, the expansion phase is represented by $\overrightarrow{CDE}$. In the evolution indicated as $\overrightarrow{CD}$, representing the reactive mixture combustion, two combustion regimes can be distinguished. The first starting around TDC, point C in figure 1.7, and taking place at a constant volume, which corresponds to the auto-ignition of the reactive mixture; the second going up to point D in figure 1.7, which corresponds to the combustion of fuel burning as a diffusion flame[3]. Then, during the evolution indicated as $\overrightarrow{DE}$, the burned gases expand within the cylinder and, at the

---

[3] In a diffusion flame the fuel consumption rate is limited by the mixing process between gaseous fuel and oxidizer [91].

same time, exchange heat with the cylinder walls (heat loss). In figure 1.7 the expansion phase is represented as a polytropic evolution.

Stroke n° 4 : exhaust

The piston is moving from BDC towards TDC, figure 1.5. In this fourth phase, the exhaust valves are opened and the piston movement pushes out the burned gases from the cylinder. As the Exhaust Valve Opening/Closing (EVO/EVC) times are finite, in order to optimize the engine efficiency, the exhaust valve opening interval begins before BDC and ends after TDC, figure 1.6. The intake phase on the pressure/volume thermodynamic diagram, figure 1.7, corresponds to the evolution $\overrightarrow{EF}$ which, because of the pressure drop of the gases crossing the exhaust valve seats, lies at a pressure level higher than the atmospheric pressure.

Diesel operating cycle analysis

Figure 1.8 shows the operation of a typical naturally aspirated Compression Ignition (CI) engine [6]. The represented Diesel engine has a compression ratio, defined as the ratio between the maximum and the minimum cylinder volumes equal to 16[4]. The figure shows four plots; in the following the different plots will be indicated using the letters from (a) to (d) as going from the top to the bottom of the figure.

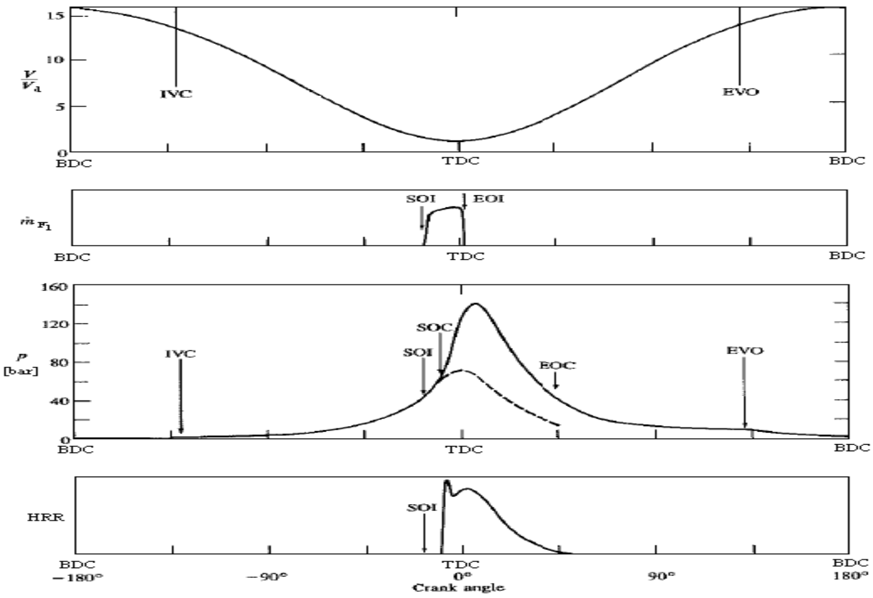

Figure 1.8: Sequence of events during compression, combustion, and expansion processes of a naturally aspirated compression-ignition engine operating cycle [6]. Cylinder volume/dead volume (V/V_d), liquid fuel injection rate ($\dot{m}_{F_l}$), in-cylinder pressure (p) (solid line, firing cycle; dashed line, motored cycle), and Heat Release Rate (HRR) are plotted against crank angle.

---

[4] Classical values of Diesel engine compression ratios vary between 12 to 24, depending on the type of engine and whether the engine is naturally aspirated or turbo-charged.

Figure 1.8 (a) shows the evolution of the cylinder volume, V, normalized with respect to the dead volume, V_d, as a function of the crank angle. In figure 1.8 (b), the profile of the liquid fuel injection rate is shown, $\dot{m}_{F_l}$; the Start Of Injection (SOI) and the End Of Injection (EOI) crank angle values are put in evidence. As seen, the fuel is injected about 20 CAD before TDC. The liquid fuel atomizes, evaporates and mixes with ambient air. After a short delay, the gaseous mixture of fuel and ambient air auto-ignites. The auto-ignition represents the Start Of Combustion (SOC), figure 1.8 (c). Hence, the cylinder pressure (solid line in figure 1.8 (c)) rises above the motored engine level (dashed line). At the SOC, part of the injected fuel which has already mixed with sufficient air to burn, reacts very fast, figure 1.8 (d). As the expansion process proceeds, mixing between fuel and ambient air continues, accompanied by further combustion in which fuel burns in a diffusion flame regime.

1.1.2 The Common Rail system

The Common Rail (CR) system is one of the key devices that have allowed the strong diffusion of Diesel engines all over the world. In particular the CR system allows higher injection pressures[5], faster switching times and greater adaptability of the injection pattern to engine operating conditions. All these characteristics are necessary for making the Diesel engine more efficient, cleaner and more powerful. The major advantage of the CR system is its ability to vary injection pressure and timing over a broad scale. This is made possible by separating the functions of pressure generation and fuel injection. Figure 1.9 shows a typical CR system integrated in a modern engine architecture.

The CR fuel injection system is made from three subsystems :

- the low pressure circuit charged of supplying the fuel to the high pressure circuit,
- the high pressure circuit consisting of the high pressure pump, high pressure accumulator ($rail$) and injectors,
- the electronic control system made from the sensors, control unit and actuators.

All the injectors, one for each cylinder, are fed by the common fuel rail. The injectors are the most important component of the CR system. They incorporate fast-switching solenoid valves by means of which the nozzle is opened and closed. This enables the injection pattern to be individually controlled for each cylinder.

A continuously operating high pressure pump, driven by the engine, produces the desired injection pressure. Pressure is controlled by a pressure limiter positioned on the rail, figure 1.9. As the pressure is stored in the rail, it is largely independent of

---

[5] In the next generation of CR injection systems, the injection pressure can rise up to 2000 bar.

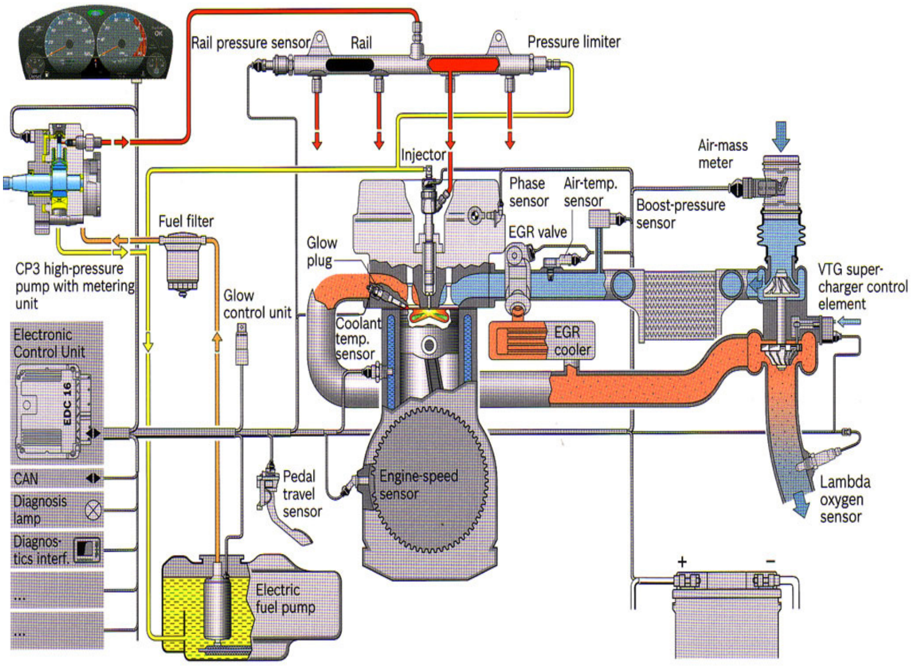

Figure 1.9: Common Rail injection system [100].

the engine speed and injected fuel quantity. The injectors inject fuel directly into the combustion chamber. The fuel injection is controlled by the Electronic Control Unit (ECU), figure 1.9.

Schematics of the injector and injector tip are shown in figure 1.10.

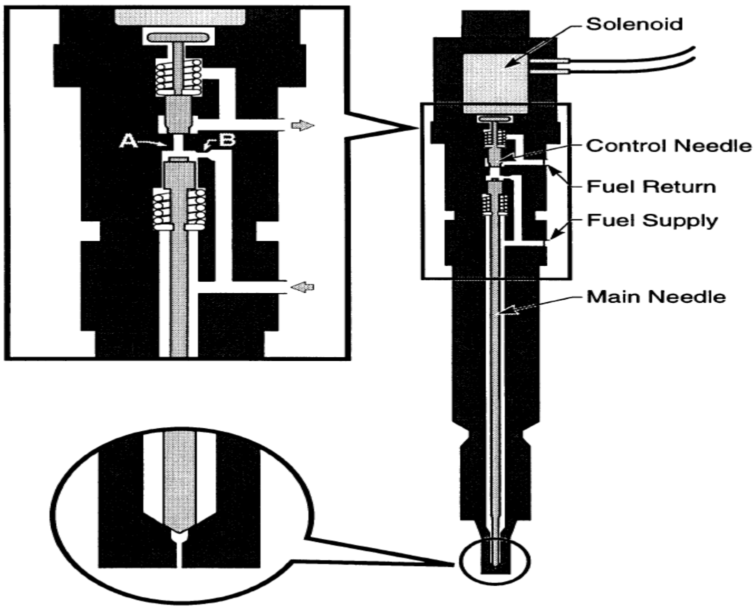

Figure 1.10: Common Rail injector [52].

The main features of the injector are the solenoid, the control needle, the main needle, and the fuel supply and return lines. The enlargement on the top left in figure 1.10 can be used to describe the operation of the injector. Activation of the solenoid lifts the control needle, opening orifice A directly above the main needle. This action allows fuel flow from the supply line through orifice B into the small chamber above the main needle, then through orifice A to the return line. Since orifice B is smaller than A, the pressure in the small chamber is much less than the fuel line pressure, creating a force imbalance that unseats the main needle and starts the injection. When the solenoid is deactivated a closure spring reseats the control needle. The pressure in the chamber above the control needle then returns to the fuel supply pressure causing the main needle to reseat, ending the injection.

1.1.2.1 The multiple injection strategies

Multiple injection strategies, that is the introduction in the cylinder of liquid fuel mass split into several injections, have permitted a strong improvement in the combustion process in Diesel engines, in terms of performance and pollutant emissions.

Figure 1.11 shows a double injection pattern : on the top of the figure, is represented the injection command, while on the bottom is represented the corresponding injection rate. The engine operating conditions as well as the injection parameters are given in table 1.1.

	Injection$_1$	Injection$_2$
Injected liquid fuel mass [mg]	5	15
Injection advance [CAD BTDC]	35	55
Engine speed [rpm]	3000	
Injector opening delay [μs]	350	
Injection pressure [bar]	800	

Table 1.1: Engine operating conditions and injection pattern variables. The values given in the table refer to the injection pattern shown in figure 1.11.

As shown in figure 1.11 (top), the variables commonly used for defining the injection command of the i^{th} fuel injection are :

- the Injection Advance (AVI_i), defining the crank angle at which the injection command starts,
- the Energizing Time (ET_i), giving the length of time of the injection command and
- the Dwell Time, ($DT_{i-(i+1)}$), giving the time interval between the end of the i^{th} injection command and the start of the $(i+1)^{th}$ injection command.

Looking at figure 1.11 (bottom), it is interesting to note that, for the i^{th} injection, the AVI_i does not correspond to the Start of Injection (SOI_i) of the liquid fuel. This is due

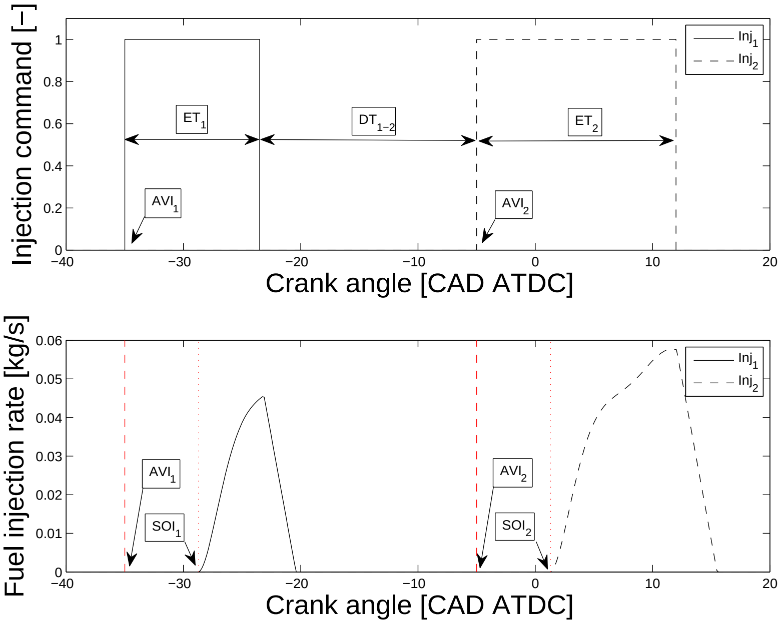

Figure 1.11: Multiple injection pattern. The values of the variables defining the injection pattern shown in the figure are given in table 1.1.

to the injector opening delay, associated with hydraulic and mechanical inertias, which depends on the injection system.

Figure 1.12 schematically represents the difference between single and multiple injection strategies in terms of fuel injection rates and Heat Release Rates. As shown in

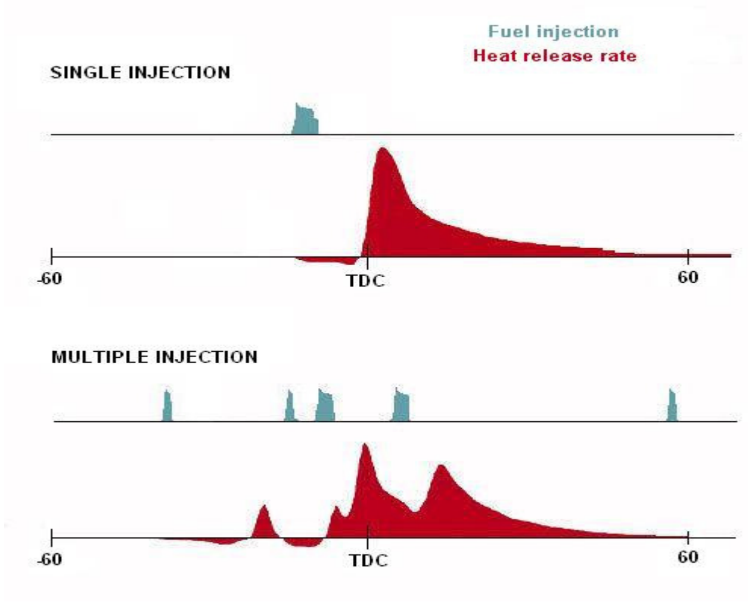

Figure 1.12: Comparison of the fuel injection rates and Heat Release Rates associated with single and multiple injection strategies.

figure 1.12, the injection strategy pattern strongly influences the Heat Release Rate of the engine cycle.

The injection pattern shown in figure 1.12 contains five injections[6] (from the left to the right) :

- *pilot injection* : usually performed very early respect to the SOI of the main injection, it reduces the combustion noise during cold-start and idle regimes. Moreover it contributes to the reduction of soot emissions, and increases the engine volumetric efficiency[7],

- *pre injection* : usually performed very close to the main injection, it controls the premixed combustion process which has a strong impact on the combustion noise, and on soot and $\mathrm{NO_x}$ formation,

- *main injection* : it involves most of the injected fuel mass $(70 \div 80\%)$. Its role is to generate the performance in terms of torque/power demanded by the driver. The SOI associated to the main injection has strong effects on the $\mathrm{NO_x}$ formation,

- *after injection* : usually performed very close to the main injection, it has an impact on the end of the combustion and favors the completion of the soot oxidation process for mainly two reasons :
  - it increases the gaseous mixture temperature favoring the oxidation reactions,
  - the kinetic energy associated to the injected mass of fuel generates turbulence in the cylinder, that favors mixing motion increasing oxygen concentration where necessary for soot oxidation,

- *post injection* : usually performed very late in the engine cycle, it considerably increases the exhaust gas temperature. Generally, the post injection is adopted in injection strategies performed periodically for improving the aftertreatment device performance :
  - quick warm-up of the catalyst,
  - regeneration of the Diesel Particulate Filter (DPF),
  - improvement of lean-$\mathrm{NO_x}$ trap efficiency.

---

[6] Up to present, the injection strategies adopted for commercial vehicles, never exceed five injections per cycle.

[7] This effect, commonly observed in gasoline engines, can be encountered in Diesel engines when very early injections are performed in order to obtain homogeneous mixtures burning in HCCI combustion regime. The evaporation of the liquid fuel cools the gaseous mixture in the cylinder. The intake pressure being imposed, a temperature decrease implies a volume decrease and consequently the possibility of introducing more fresh air.

1.1.3 The combustion process

In the last decades, in order to reduce the engine pollutant emissions, many efforts were made in the research domain for understanding the pollutant species formation mechanisms.

It was found that a promising way for reducing the pollutant emissions consists in acting directly on the combustion process.

In fact, the pollutant species formation is strongly related to the local thermochemical properties of the mixture within the cylinder. Accordingly, establishing the right in-cylinder thermochemical conditions would allow a reduction of pollutant emissions. These studies brought to the introduction of non-conventional combustion regimes, such as Premixed Controlled Compression Ignition ($PCCI$), Low Temperature Combustion (LTC) and HCCI combustion processes, figure 1.13.

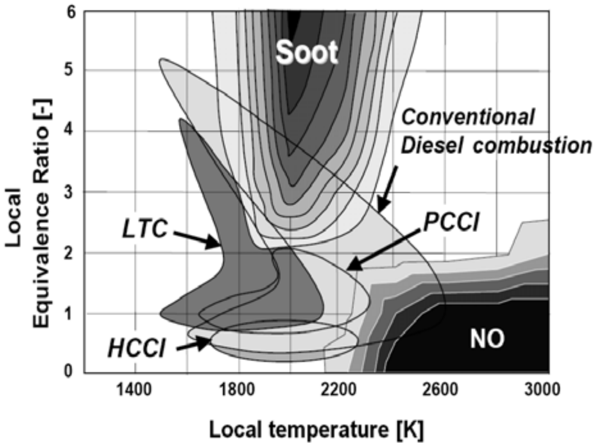

Figure 1.13: PCCI, LTC and HCCI concept on a $\Phi - T$ map [62].

As shown in figure 1.13, the tendency is to obtain a combustion process characterized by lower temperatures and a higher level of local air-excess ratio, in order to get out of the region relative to NO_x and soot emissions. Nowadays, to reduce the combustion temperatures, it is usual to dilute the fuel-air mixture with EGR because of its high specific heat-capacity and immediate availability.

In the following, in order to put in evidence the major differences between conventional and non conventional combustion processes, attention will be focused on the differences between conventional Diesel and Diesel HCCI combustions.

Conventional Diesel and HCCI combustion modes are governed by different physical mechanisms.

In conventional Diesel combustion, the mixture inside the cylinder is characterized by a high fuel mass fraction stratification. The first site of auto-ignition appears inside the spray, where chemical and thermodynamic conditions are the most favourable. Heat released by combustion at the first site, subsequently favors the multiplication of auto-ignition sites. This chain reaction leads to the sharp heat release process typical of the premixed Diesel combustion phase. The remaining fuel burns in a diffusion flame and the heat release is governed by the mixing process. In this phase, turbulence plays the most important role. The dynamics of a convention Diesel combustion are shown in figure 1.14. In figure 1.14 are clearly distinguished the six injection cones coming out of the injector nozzle, which is positioned at the center of the combustion chamber. The injected fuel penetrates within the cylinder and mixes with ambient-air. As seen, the gaseous mixture within the cylinder is strongly heterogeneous, hence, the local thermochemical properties of the gases strongly vary in terms of temperature and equivalence ratio. In the conventional Diesel regime, combustion is essentially controlled by mixing.

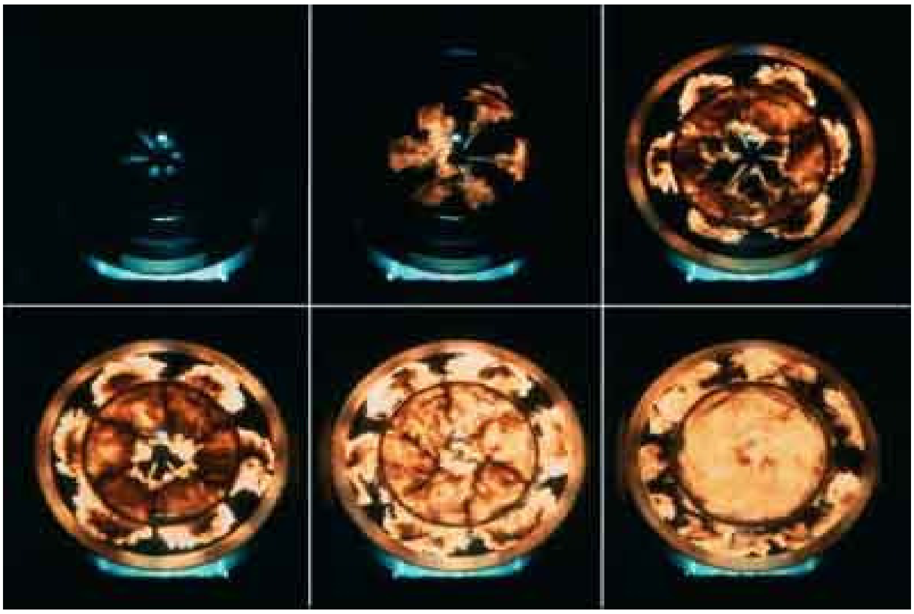

Figure 1.14: Dynamics of a conventional Diesel combustion [100].

On the other hand, in HCCI combustion, the mixture inside the cylinder is homogeneous. Hence, chemical kinetics play the most important role in the combustion process. The dynamics of a Diesel HCCI combustion are shown in figure 1.15.

As shown in this figure, because of the homogeneity of the mixture, all the gas auto-ignites simultaneously. As a consequence, HCCI combustion is characterized by a high Heat Release Rate (HRR).

1.2 The global engine system study

An ICE is a complex system to study for the following reasons :

- many different branches of physics are involved in the study of its fundamental principles of functioning,

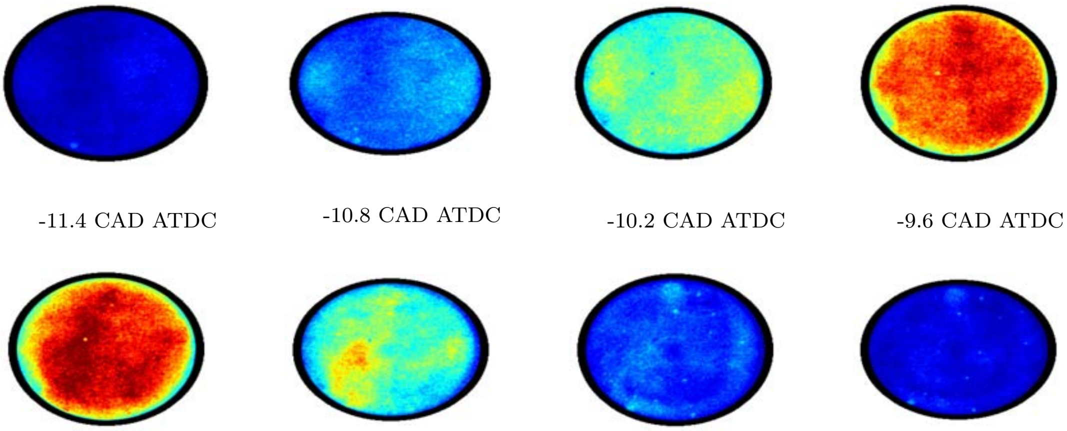

-11.4 CAD ATDC -10.8 CAD ATDC -10.2 CAD ATDC -9.6 CAD ATDC

-9.0 CAD ATDC -8.4 CAD ATDC -7.8 CAD ATDC -7.2 CAD ATDC

Figure 1.15: Dynamics of a Diesel HCCI combustion [98].

- complex interactions between physical phenomena occur,
- the large number of devices integrated in the engine architecture, which are necessary in order to guarantee the required flexibility to the system, constitute a complex system to optimize,
- prototypes are expensive to manufacture and need time to be tested.

For these reasons, the optimisation of the entire engine system is a hard task, expensive and time consuming. In the following, two devices for optimizing the performance of global engine systems are presented :

- experimental global engine test bench,
- global engine simulation numerical models.

1.2.1 The global engine system test bench

In the past, the global engine test-bench was widely used for engine-control calibration, figure 1.16. This methodology of calibration was possible essentially because :

- only a reduced number of devices were integrated in the engine architecture,
- the engine systems were less flexible,
- there were less constraints in terms of pollutant emissions,
- it was the only solution available then.

The major inconvenients associated to this methodology are :

- the cost in terms of facilities and human resources,

- the length of time needed for the experiments.

Today, the role of the engine test-bench in the engine development process has changed. In fact, it is essentially used for :

- testing very particular engine operating points,
- testing new engine control strategies,
- validating the ICE numerical simulations,

and no longer used for optimizing engine control strategies.

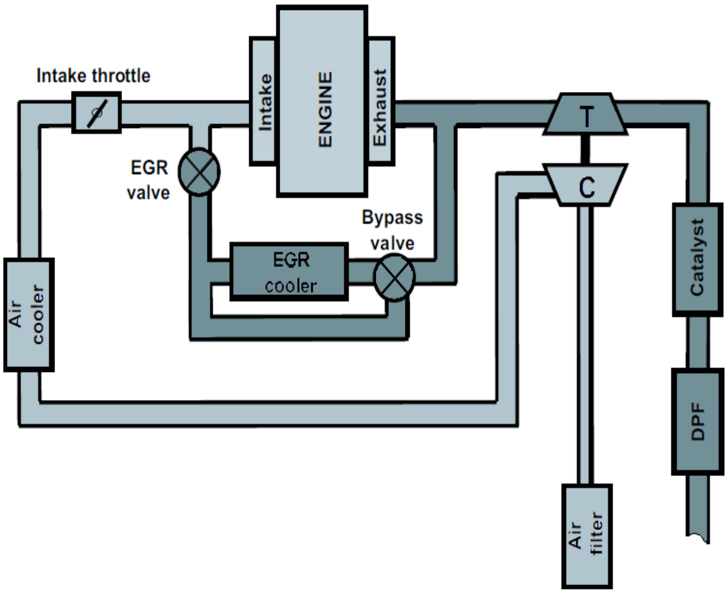

Figure 1.16: Schematic of a global-engine test-bench.

1.2.2 The global engine system simulation

In recent years, consequently to the rapid progress in CPU performance and the large increase in data storage capabilities, numerous softwares for global engine system numerical simulation have been developed (e.g. GT-power, AMESim, GASDYN, etc...). As mainframe for the development of dual-CM, the environment of simulation AMESim has been choosen, appendix A. Compared to global engine test bench approach, the global engine system simulation presents the following advantages, figure 1.17 :

- the cost in term of facilities and human resources is relatively low,
- computations are performed in a short interval of time,
- the models can be easily transported from one place to another.

On the other hand, global engine system simulation is not a stand alone device : it needs experimental data from laboratory facilities in order to validate the engine model. In industry, global engine system simulation is mainly used in the following domains :

- engine architecture conception phase,
- engine-control strategies definition,
- engine performance investigation, (e.g. engine tests on standard vehicle homologation driving cycles).

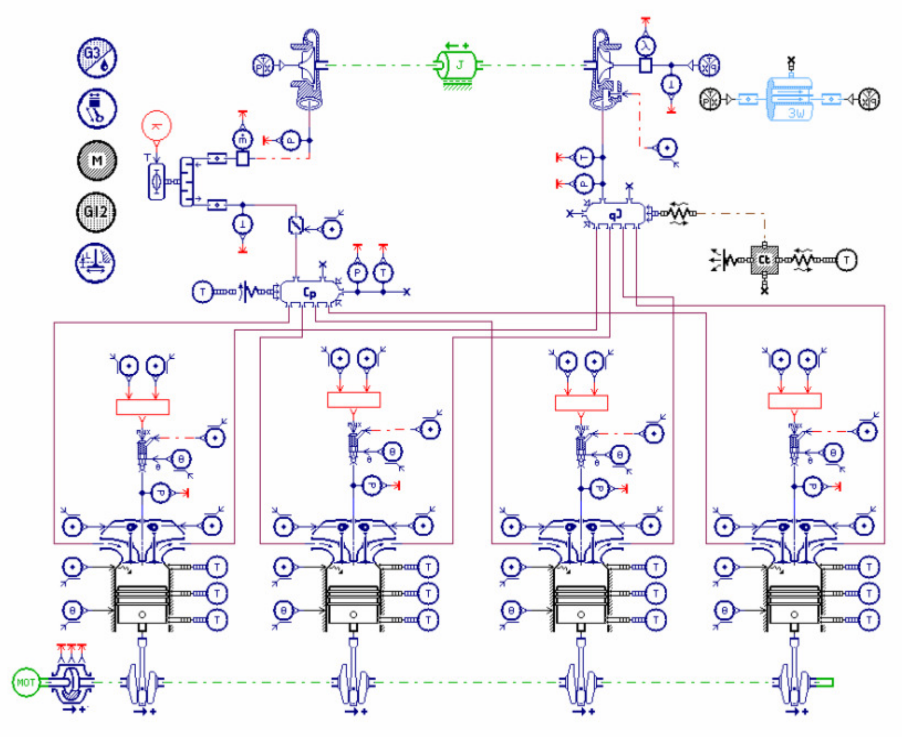

Figure 1.17: Schematic of a global-engine system simulator.

1.3 Objective and methodology

The aim of this work is to develop a numerical model able to simulate the ICE combustion process in both conventional Diesel and Diesel HCCI regimes. The model has been conceived for global system simulation applications. In this context, the model must be able to respond properly to turbocharger pressure variations, which modify the thermodynamic conditions of the inlet gases in the cylinder in term of pressure and temperature, fuel injection pattern variations, Exhaust Gas Recirlculation (EGR) mass flow rate variations, etc...

The development of such models is a challenge especially because :

- the large number of physical fields that occur in ICEs (multidisciplinary competences),
- the complex interaction between the different physical phenomena during the combustion process,
- the large magnitude ranges on spatial and temporal scales associated to the phenomena that must be modeled and taken into account,
- the wide range of engine conditions constituting the engine operating domain,
- the fact that global system simulation tools are limited to 0D approaches requires more modeling and parametrization than classical 3D CFD.

In the following, the dissertation focuses on the study and comprehension of the combustion process in Diesel HCCI engines, that is engines that are able to run using conventional Diesel and Diesel HCCI combustion regimes. In chapter 2, the developed model, dual Combustion Model (*dual-CM*), is introduced and detailed. The different submodels constituting dual-CM have been developed and validated on the base of the observations made by using experimental facilities : both published in literature or coming from the IFP laboratories. When experiments were not available, submodel validations were done on the basis of computed results obtained by using numerical solvers considered to provide reliable physical results. In chapter 3, the engine validation results of the dual-CM are presented. The model has been validated using engine test bench experimental results when available and 3D CFD simulation results when experimental data were not available. In chapter 4, the limits of the model are investigated and precision analysis are carried out.

Chapter 2

The dual Combustion Model (*dual-CM*)

In this chapter the dual Combustion Model (*dual-CM*) is presented. Dual-CM has been conceived following the outline of the promising approach developed by Mauviot [13] at IFP.

During this Ph.D, the original model of Mauviot [13] was improved following three major axis of development :

- introducing new features in order to extend the application domain of the combustion model. This aspect essentially concerns the introduction of a new formalism able to take into account multiple injection strategies : from the description of the evolutions and interactions of the different sprays within the cylinder, up to the description of the complex chemical kinetics,

- introducing more physics in the different submodels, in order to make the combustion model more predictive. In particular :

  - a description of the liquid-gas interface during the evaporation process was introduced. This aspect is very important in the determination of the local thermochemical properties of the gaseous mixture and, consequently, on the determination of the mixture auto-ignition delay,
  - a new equation for the fuel mixture fraction variance was developed. The new formula takes into account the fact that liquid fuel evaporates in ambient-air at saturated conditions and not as a pure fuel. Moreover, the new equation is adapted to be used in a multiple-injection context, in which the spray associated with the different fuel injections can interact with one another,
  - a new formulation of the chemical kinetic model, permitting us to have a better description of the species evolutions during the combustion process and a better estimation of the final composition of the exhaust gases was adopted. In particular, the new chemical kinetic model is based on a *species mass fraction* complex chemistry tabulation method instead of a *species reaction rate* complex chemistry tabulation method,
  - the chemical kinetics mechanism used for generating the table is the one proposed by Anderlohr [86] for n-heptane. This mechanism, compared to the

one used in the original version of the model [64], permits to have a better estimate of the mixture auto-ignition delays,

- optimizing the source code in order to reduce to the bare minimum the computational time, compatibly with the modeling solutions that were retained.

All these aspects will be discussed in detail in the following of this chapter.

First of all the context and the specifications of dual-CM are introduced, section 2.1. After that, starting from the state of the art in combustion science applied to modern Diesel HCCI ICE, section 1.1, several physical topics are retained and considered as fundamental for the description of the in-cylinder combustion process and consequently studied, interpreted, modeled and integrated in dual-CM. Essentially, the physical topics retained and presented in section 2.3 to 2.6 are the following :

- liquid fuel injection,
- composition evolution,
- turbulence,
- chemical reactions,
- thermal exchange losses,
- combustion chamber geometry variations,
- fluid thermodynamics.

A parametric study of dual-CM, section 2.7, shows the sensitivity of the model to the different modeling parameters. Finally, the dual-CM computational time is discussed, section 2.8.

2.1 Context and model specifications

The dual-CM is a 0D phenomenological combustion model formulated for global engine system simulation, subsection 1.1, and especially for Diesel HCCI engines, section 1.2.2. In this sense, the model must be able to provide reliable results in short computational time. The model has been conceived by reducing physical 3D CFD models to a 0D formalism. The different submodels constituting dual-CM have been developed by using as much as possible physical information and reducing to the bare minimum the use of abstract empirical/mathematical laws. This choice is a scientific challenge because reducing the number of pure modeling adjustment coefficients, reduces the possibility to tune computed results in order to fit experimental data. On the other hand, it brings the following advantages :

- using the model is intuitive because adjustment parameters are associated with physical phenomena,
- computed variables can be interpreted as representative of the real physical process and, consequently, used to study trends and limiting factors of the real system,
- once the model is tuned to a given set of engine operating points, it is expected to be able to predict the behavior of the system for different operating conditions, too,
- the model can be used in the engine architecture design process,
- the model can be used in engine-control strategy definition in which predictivity is a fundamental need.

The aim of the model is to be able to predict the in-cylinder combustion process once :

- devices such as turbochargers, EGR system, intercoolers, wastegate valve, Variable Valve Actuators (VVA) have imposed in the cylinder a mixture of air and eventually EGR at given thermodynamic conditions,
- a fuel injection strategy pattern has been defined.

Essentially, during the Ph.D, modeling efforts have focused on :

- liquid fuel evaporation,
- reactive gaseous mixture zones (spray regions),
- Auto-Ignition (AI) delays of reactive mixtures,
- Heat Release (HR),
- major pollutant species chemical-kinetics,
- Indicated Mean Effective Pressure ($IMEP$).

A model being able to satisfy all these requirements is suitable for the integration in a global engine system simulator. In fact, such a model is able to fully interact with the other devices integrated in the engine architecture : responding to the different system inputs and providing the necessary outputs to the system. In the following, the presentation will focus on the modeling of compression and expansion strokes of the Diesel thermodynamic cycle, which are the only phases of the engine cycle concerned with the combustion model.

2.2 Synoptical diagram of the model

In dual-CM the different physical phenomena, taking place in the cylinder of a Diesel HCCI engine, are taken into account and described by proper submodels, figure 2.1. In the following, the investigation will focus on the interval of the engine thermodynamic cycle going from Inlet Valve Closure (IVC) crank angle, during the compression stroke, to Exhaust Valve Opening (EVO) crank angle, during the expansion stroke, considered as being the only crank angle interval in which combustion conditions occur in the cylinder. At IVC crank angle, an ambient gaseous mixture, consisting of pure air and eventually EGR, is compressed by the piston. This ambient mixture is here supposed to be a perfectly stirred mixture. As shown in figure 2.1, the event triggering the combustion computation is the injection of liquid fuel in the combustion chamber (Injection rate model, section 2.3). At that point liquid fuel and ambient air coexist within the cylinder. The region where both fuel and ambient-air are simultaneously observed is called spray region (Spray model, section 2.4), figure 2.2. Two main phenomena occur in the spray region :

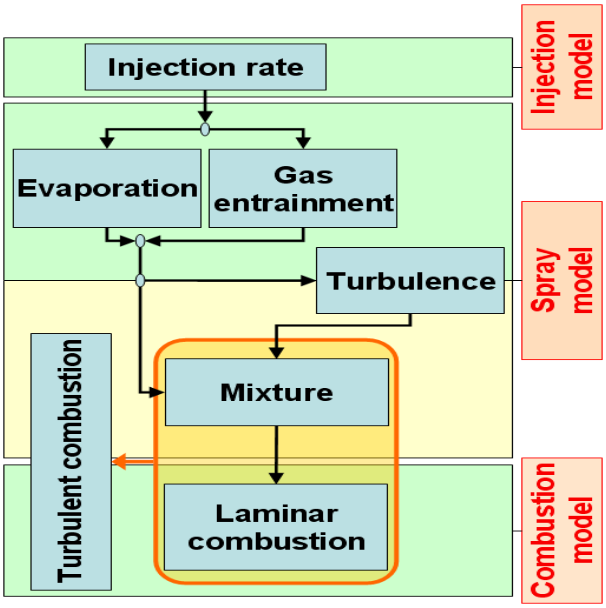

Figure 2.1: Synoptical diagram of the model dual-CM in a case of single injection strategy.

- the liquid fuel evaporation (Evaporation submodel, section 2.4.1),
- the entrainment of ambient air in the spray (Gas entrainment submodel, section 2.4.2).

As liquid fuel evaporation and ambient air entrainment go along, the spray region grows. The injection of liquid fuel at high speed in the cylinder introduces a large quantity of

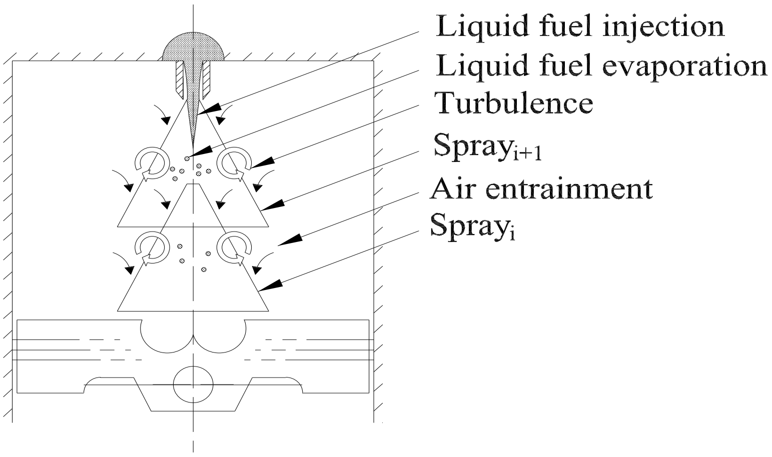

Figure 2.2: Schematic of the liquid-fuel injection phisics within the cylinder of a Direct Injection Diesel engine.

kinetic energy which is finally transformed in a strong turbulent motion (Turbulence submodel, section 2.4.3). The presence of turbulence in the combustion chamber favors the mixing between gaseous fuel and ambient gas. Consequently, a continuous distribution of mixture compositions varying from a maximum fuel mixture fraction (corresponding to ambient-air saturated with fuel, $Z = Z_s$[1]) to pure ambient-air (corresponding to $Z = 0$) is present in the cylinder, section 2.4.4. Because of the turbulent mixing process, the mixture inside the cylinder tends to become progressively more homogeneous. Among the wide spectrum of mixture compositions within the cylinder, the compositions contained between the fuel inflammability limits are named reactive mixtures. Once favorable thermodynamic conditions are reached, the combustion process takes place (Combustion model, section 2.5). Focusing on a given composition belonging to the reactive mixtures, the oxidation process takes place once the auto-ignition delay is reached. At that instant, combustion begins. During the combustion process, thousands of intermediate chemical species appear and interact with one another eventually forming products of combustion and pollutant species (Laminar combustion submodel, section 2.5.1). In a Diesel HCCI combustion chamber, mixture is not homogeneous and local composition varies in time because of the turbulence action (turbulent mixing). Those are very important aspects to be accounted for in Diesel HCCI combustion and they influence the whole combustion process from the auto-ignition delay to final mixture composition (Turbulent combustion submodel, section 2.5.3). Until now, the discussion has been limited to single injection strategy configurations. Things change slightly for multiple injection strategy configurations. A diagram representing a multiple injection strategy configuration is shown in figure 2.3 for double injection strategies. Obviously, before the start of the second injection, the diagram of the model is identical to that

---

[1] Definition and modeling of Z_s are discussed in detail in section 2.4.1.1.

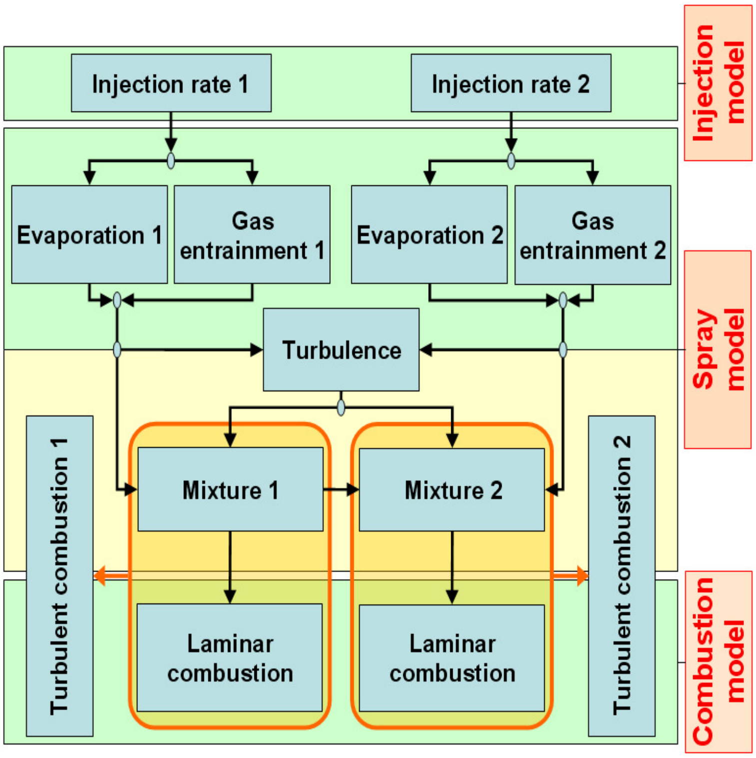

Figure 2.3: Synoptical diagram of the model dual-CM in a case of multiple injection strategy.

of the single injection case. When the second injection starts, the diagram is modified because the two injections interact : the impact of the second injection on the first one can be summarized as an enhancement of its kinetic energy. On the other hand, the impact of the first injection on the second one is much more important :

- the velocity field within the cylinder has been modified by the first injection,
- the thermodynamic conditions within the cylinder have been modified by the combustion of the fuel of the first injection,
- the entrained air in the spray region of the second injection has a chemical composition that is different from that of the ambient air, as it has been modified by the combustion of the fuel of the first injection,
- the chemical kinetics of the mixture formed by the second injection is influenced by both the different chemical composition and the different thermodynamic conditions of the entrained ambient-air.

Certainly, other effects associated to the interaction of different sprays exist. In a first approximation, all these are neglected.

2.3 Injection rate model

The fuel injection rate model is fundamental in order to perform an engine cycle computation. It simulates the response of the high pressure injection system to the inputs received from the Engine Control Unit (ECU). In particular, it computes the liquid-fuel mass introduction rate, $\dot{m}_{F_l}$, in the cylinder. As can be seen in figures 2.1 and 2.3, it is the main input of the dual-CM spray model, section 2.4, and in particular it directly communicates with the evaporation submodel, section 2.4.1, and the gas entrainment submodel, section 2.4. In order to correctly characterize an injection rate profile (fuel flow rate versus time), the aspects that must be accounted for are, figure 2.4 :

- the initial slope, describing the opening transitory of the injector needle (the needle opening transitory is mainly due to the unbalanced fluid pressures acting on the needle and the needle inertia),
- the maximum value of the injection rate, corresponding to a steady opening state,
- the final slope, describing the closing transitory of the injector needle (the needle closing transitory is mainly due to a mechanical force acting on the needle),
- the integration of the fuel injection rate curve must be equal to the injected fuel mass.

All these aspects vary with the technological parameters of the injection system :

- the injection pressure, p_{inj},
- the energizing time, ET,
- the nozzle permeability,
- the injector geometry,
- the type of fuel.

In order to account for all these aspects, an injector model has been developed at IFP. For a given fuel, injector and nozzle, the model is able to describe the fuel injection rate as function of the time. Moreover, the model is sensitive to injection pressure and energizing time variations. In this approach, an injection rate profile relative to high injection pressure (here $p_{inj}^{ref} = 1600$ bar) and sufficiently long energizing time[2] (here $ET^{ref} = 2.25$ ms) is chosen as reference injection profile, figure 2.4. Figure 2.4 shows the main features of a reference fuel introduction rate profile. In particular, the three different regions characterizing the injection profile can be clearly distinguished :

---

[2] A correct energizing time value must guarantee the complete lifting of the injector needle.

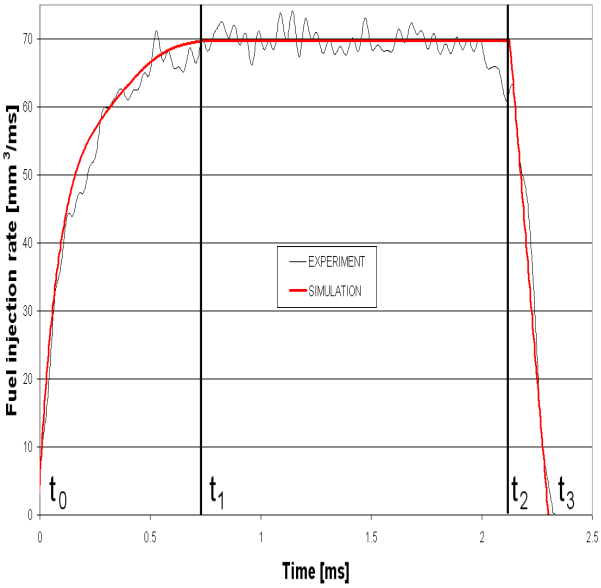

Figure 2.4: Description of the main features of a reference fuel introduction rate profile.

the initial transitory (left), the steady condition (middle) and the final transitory (right). The first step, in order to have an analitical expression of the reference liquid fuel injection rate, $\dot{m}_{F_l}^{ref}$, consists in fitting the experimental reference injection rate with appropriate equations, in each region :

- the opening period (from t_0^{ref} to t_1^{ref}) is modeled by using a sixth order polynomial :

$$\dot{m}_{F_l}^{ref} = a_0 + a_1 \cdot t + a_2 \cdot t^2 + a_3 \cdot t^3 + a_4 \cdot t^4 + a_5 \cdot t^5 + a_6 \cdot t^6 \tag{2.1}$$

- the steady injection rate time (from t_1^{ref} to t_2^{ref}) is modeled by using a zeroth order polynomial (constant value) :

$$\dot{m}_{F_l}^{ref} = \dot{m}_{F_l}^{st} \tag{2.2}$$

- the closing period (from t_2^{ref} to t_3^{ref}) is modeled by using a first order polynomial :

$$\dot{m}_{F_l}^{ref} = \dot{m}_{F_l}^{st} - b_0 \cdot (t - t_2^{ref}) \tag{2.3}$$

  experiments showed that the closing transitory slope is independent of the injection pressure,

where a_0, a_1, a_2, a_3, a_4, a_5, a_6 and b_0 are adjustment coefficients depending on the injection system, $\dot{m}_{F_l}^{st}$ represents the mean experimental injection rate on the time interval $t_1^{ref} \leq t < t_2^{ref}$, and t_2^{ref} corresponds to the beginning of the closing transitory.

These polynomial expressions are then parametrized with the injection pressure, in order to obtain injection rate profiles for different injection conditions :

- the opening transitory end-time value, t_1, depends on the injection pressure as :

$$t_1 = t_1^{ref} \cdot \sqrt{\frac{\Delta p}{\Delta p^{ref}}} \tag{2.4}$$

  where Δp and Δp^{ref} are the pressure drops through the injector nozzle for the present and reference injection pressure conditions,

- the injection rate for the time period from t_0 to t_1 is computed as :

$$\begin{aligned} \dot{m}_{F_l} &= \dot{m}_{F_l}^{ref} \cdot \left(\sqrt{\frac{\Delta p}{\Delta p^{ref}}} \cdot \left(\frac{p_{inj}}{p_{inj}^{ref}} - 1 \right) \cdot \left(\frac{t}{t_1} \right)^2 + \right. \\ & \left. -2 \cdot \left(\sqrt{\frac{\Delta p}{\Delta p^{ref}}} \cdot \left(\frac{p_{inj}}{p_{inj}^{ref}} - 1 \right) \cdot \frac{t}{t_1} \right) + \sqrt{\frac{\Delta p}{\Delta p^{ref}}} \cdot \frac{p_{inj}}{p_{inj}^{ref}} \right) \end{aligned} \tag{2.5}$$

- the injection rate for the time period from t_1 to t_2 is computed as :

$$\dot{m}_{F_l} = \dot{m}_{F_l}^{ref} \cdot \sqrt{\frac{\Delta p}{\Delta p^{ref}}} \tag{2.6}$$

- the injection rate for the time period from t_2 to t_3 is computed as :

$$\dot{m}_{F_l} = \dot{m}_{F_l}^{ref} \cdot \sqrt{\frac{\Delta p}{\Delta p^{ref}}} - b_0 \cdot (t - t_2) \tag{2.7}$$

The profile given by using equations 2.4 to 2.7 defines the overall shape on the fuel injection rate for a given injection pressure, p_{inj}, with time. By using the additional information of the global fuel injected mass, m_{F_l}, (obtained experimentally), the time t_2 is then chosen in such a way that the integral of the computed fuel injection rate equals the measured fuel injected mass. Figure 2.5 shows different profiles of the fuel introduction rate as a function of the time and of the injection pressure. Computed injection rates are compared with experiments. As shown, a good agreement is found between the curves. To resume, the above detailed injection rate model returns, for a given fuel and injection system, the fuel introduction rates as a function of two variables measured experimentally at the engine test-bench : the injection pressure, p_{inj}, and the injected liquid fuel mass, m_{F_l}.

2.4 Spray model

The spray model describes the formation of the regions containing both fuel and ambient air, defined previously as *spray regions*. Combustion takes place in these regions and a detailed description of the sprays is of capital importance for Diesel HCCI combustion modeling as local thermochemical conditions of the mixture determine the kinetics of combustion. As can be seen in figures 2.1 and 2.3, in the global context of dual-CM, the

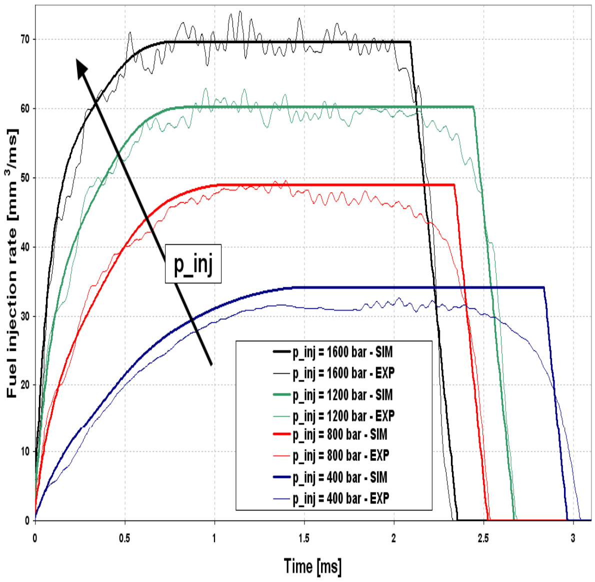

Figure 2.5: Fuel introduction rate profiles as function of the time and of the injection pressure, p_{inj} (legend). Computed introduction rates (thin solid lines) are compared with experiments (thick solid lines).

spray model is positioned between the injection rate model and the combustion model. Starting from the liquid fuel injection rate events, section 2.3, the physical phenomena occurring in the cylinder such as fuel evaporation, ambient-air entrainment and turbulent mixing have been identified, investigated and modeled. The fuel is heptane ($n - C_7H_{16}$). This choice has been done mainly for the following reasons :

- thermochemical properties of n-heptane are well-known in literature,
- complex chemistry kinetic mechanisms exist and have been validated on a wide range of thermodynamic conditions,
- auto-ignition delays are comparable to those of commercial hydrocarbon Diesel blends.

The main aim of the spray model is to give a description of the spray region in order to transfer this information to the combustion model, section 2.5.

2.4.1 Evaporation submodel

The evaporation of liquid fuel in the combustion chamber is the first and one of the most important aspects that must be handled in combustion modeling. Intuitively[3], the major factors that influence the rate of evaporation of a given mass of fuel are :

- injected fuel temperature,

---

[3] Experimental evidences of these phenomena confirm the above statements [52, 49].

- interface surface extent,
- ambient-air temperature, pressure and composition,
- slip velocity between liquid fuel and surrounding gas.

The complex scenario representing the dynamics associated with the physics of a spray observed when liquid fuel injection is performed in a gaseous environment is presented schematically in figure 2.6. Three different regions can be distinguished in a typical spray, figure 2.6 :

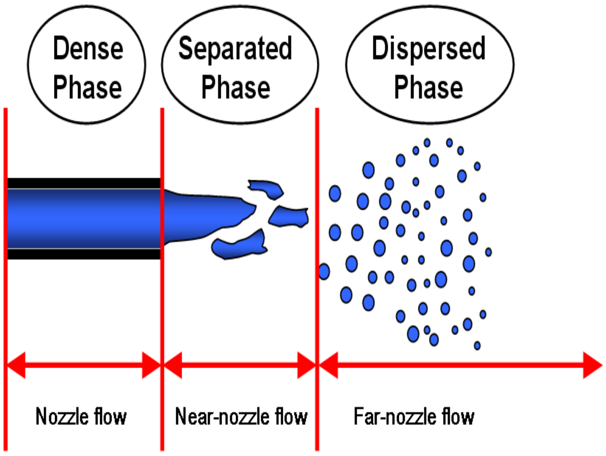

Figure 2.6: Scenario associated to the physics of a spray [92].

- the dense phase region,
- the separated phase region,
- the dispersed phase region.

Within the injector nozzle, the fluid flow is dense, and can be considered as a continuum. Once outside the injector nozzle, the near-nozzle flow is subject to the primary atomization process, which allows the continuous liquid-phase to be fragmented in ligaments and droplets with relatively large diameters (separated phase). Further downstream, the liquid fuel is subject to the secondary atomization process, which breaks ligaments and droplets of fluid in a large number of droplets with very small mean diameter. The fluid is said to be in a dispersed phase. In the dispersed phase region, as droplets have different velocities and diameters, they form a sort of cloud in the spatial domain of the spray. Experimental studies on spray clouds show that the overall statistical behaviors of droplets can be put in evidence. In fact, droplets can be classified according to different criteria (e.g. diameter size, volume and velocity) constituting distributions evolving in time due to the spray dynamics. Several numerical models exist for representing such kind of distributions (e.g. Nukiyama and Tanasawa, Rosin-Rammler for droplet sizes).

Of course, the shapes of these distributions must account for primary and secondary atomization process variables, as well as evaporation process. It is important now to make a distinction between two different evaporation regimes : mixing controlled evaporation and local interphase transport controlled evaporation. The major implications of being in one regime rather than in the other are :

- if mixing controlled, the local interphase transport rates of mass, momentum, and energy that control liquid breakup and droplet evaporation must be fast relative to turbulent mixing rates. In this limit, no local velocity or temperature differences exist between the phases in the spray, and the phases are in equilibrium locally [74]. Turbulent mixing controls vaporization by determining the rate at which energy is entrained into the spray for heating and vaporizing the fuel. In turbulent mixing controlled regime, the influence of diameter and velocity droplet distributions on the evaporation process can be neglected.

- if local interphase controlled, transport rates of mass, momentum and energy limit the overall vaporization rate, and the turbulent mixing must be fast relative to those processes. In other words, sufficient energy is entrained into the spray, but the transfer to the liquid phase is limited, and local velocity and temperature differences exist between the phases in the spray. In local interface controlled regimes, diameter and velocity droplet distributions must be taken into account.

According to [52], vaporization in a Diesel spray is controlled by air entrainment into the spray (i.e., by turbulent mixing). The local interphase transport rates of mass, momentum, and energy that control liquid breakup and droplet evaporation do not limit the overall rate of vaporization, section 2.4.1.2. The outline of the approach was developed in [13]. The model :

- computes an evaporation rate,
- is developed considering a mixing controlled vaporization approach,
- is sensitive to thermochemical properties of fluids.

At this point, it is important to determine the requirements that the evaporation submodel must have. In particular, it must be able to compute :

- the thermochemical properties of the gaseous mixture at the droplet interface. This information is important for the description of the mixture within the cylinder, section 2.4.4, as well as for evaluating the mixture auto-ignition delay, section 2.5,

- the value of the liquid fuel penetration length. Overpredicted penetrations of the fuel liquid-phase can lead to greater emissions if liquid fuel impinges and collects on the piston bowl wall,

- the overall fuel mass evaporation rate, which controls the rate of kinetic energy production associated with fuel injection, section 2.4.3, and mixing, section 2.4.4.

Moreover, the model must have a high accuracy/computational time ratio. Figure 2.7 shows how the evaporation model is structured in dual-CM. The white arrow in figure 2.7 indicates the order used to present the parts of the evaporation model, in the following presentation. As shown in figure 2.7, three stages can be distinguished in the model :

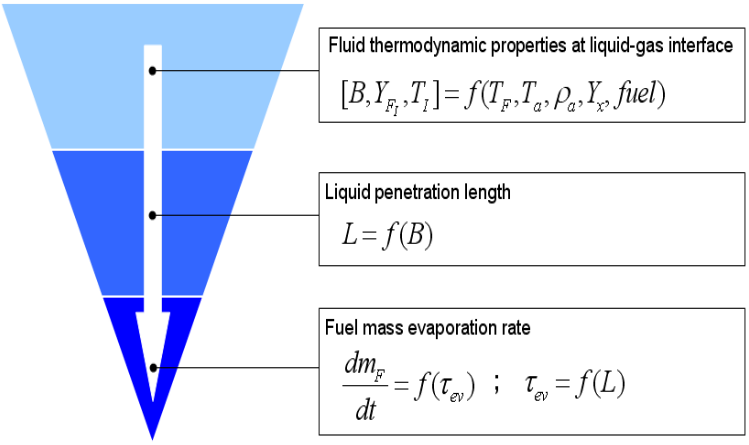

Figure 2.7: Schematic representation of the evaporation submodel structure.

- *Fluid thermodynamic properties at liquid gas interface*, section 2.4.1.1 : this model provides an evaluation of the transfer number, B, and of the mixture thermodynamic properties at the liquid-gas interface expressed in terms of temperature, T_I, and fuel mixture fraction, Y_{F_I}, at saturated conditions, associated to steady-state evaporation process for given boundary conditions in terms of fuel and ambient-gas thermochemical properties. The model is inspired by the theory on evaporation proposed in [49],

- *Liquid penetration length*, section 2.4.1.2 : this model permits us to compute the liquid-phase penetration length (L) in the cylinder. It is based on the theory proposed in [53] and uses a scaling law relating the liquid-fuel penetration length to the transfer number, B[4], commonly used in liquid vaporization studies,

- *Fuel mass evaporation rate*, section 2.4.1.3 : this model permits us to compute the overall evaporation rate in the dual-CM of the total fuel liquid mass present in the cylinder, $\dot{m}_F$. The fuel evaporation rate value depends on the value of a characteristic time of evaporation, τ_{ev}, which is computed by using an approach first proposed in [13] : this approach relates the evaporation characteristic time to the fuel liquid-phase penetration length, L.

---

[4] The considered transfer number refers to steady-state evaporation processes, that is, heating of liquid fuel an convective influence on evaporation are void.

2.4.1.1 Fluid thermodynamic properties at liquid-gas interface

This section deals with the computation of the steady-state transfer number, B, and of the fluid thermodynamic properties at liquid-gas interface, such as the the gaseous mixture temperature, T_I, and fuel mixture fraction, Y_{F_I}. It represents the first step of the set up evaporation-model and it gives information needed for computing the fuel liquid-phase penetration length, L, figure 2.7. The droplet evaporation in a spray involves simultaneous heat and mass transfer processes in which heat is transferred to droplets by the gas stream. The overall rate of evaporation depends on pressure, temperature and transport properties of the ambient-gas, and temperature, volatility and diameter of the droplets in the spray. Many fundamental studies were carried out to understand evaporation of a single droplet at rest in a quiescent ambient gas [49, 58, 61]. In particular, the academic configuration concerning the evaporation process of single droplet at rest surrounded by a given gaseous mixture in quiescent conditions has been widely studied from both experimental and theoretical points of view. Experiments show that once a droplet immersed in a given ambient-gas mixture attains steady-state evaporation conditions[5], its squared diameter diminishes linearly with time [49, 58, 51, 80]. From the theoretical point of view, a physical evaporation-model, better known as $D^2 law$ approach, was developed [49, 58]. This model correctly describes the above-mentioned configuration and well represents experimental observations showing that once established the evaporation steady state conditions, the drop diameter diminishes with time according to the following relation :

$$D_{d_0}^2 - D_d^2 = \lambda \cdot t \tag{2.8}$$

where D_{d_0} is the reference initial drop diameter, D_d is the drop diameter, λ is the evaporation constant and t is the time. Concerning the present context, even if a Diesel engine spray configuration differs from the academic one, the D^2 law approach is useful to :

- give an insight about the thermochemical properties of the mixture at liquid-gas interface in terms of saturated fuel mixture fraction, Y_{F_I}, and temperature, T_I. This data is needed to :
  - estimate the value of the transfer number, B, necessary for computing the fuel liquid penetration length, figure 2.7. In fact the penetration model, that is based on the hypothesis of turbulent mixing limited evaporation process[6], assumes the thermodynamic equilibrium at liquid-gas interface and no slip velocity between gaseous and liquid phases, as supposed in the present model,

---

[5] Steady-state assumption implies thermodynamic equilibrium of the mixture at liquid-gas interface.

[6] Justifications of this hypothesis are given in section 2.4.1.2.

  - estimate the local thermodynamic conditions of the mixture within the spray region, section 2.4.4,

- validate the computed physical interface properties. The evaporation constant, λ[7], which is directly dependent to T_I and Y_{F_I}, is measurable experimentally. Consequently, the validation of the computed λ with experiments allows the validation of the computed interface properties,

- dispose of a model that can be applied to particular Diesel engine operating conditions (i.e. cold start transient regimes).

In what follows, the major equations of the theoretical approach are introduced, and computed results are compared to experiments in order to validate the model. According to [49], the approach generally used is to assume a spherically symmetric model of a vaporizing drop in which the rate-controlling process is that of molecular diffusion, figure 2.8.

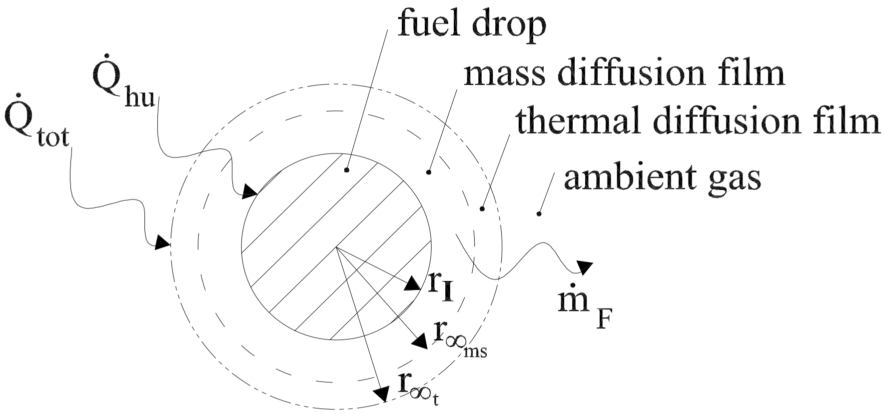

Figure 2.8: Evaporation model of a liquid fuel drop. In figure, $\dot{Q}_{tot}$ and $\dot{Q}_{hu}$ represent respectively the total and the heat-up heat flows absorbed by the drop, r_I, $r_{\infty_{ms}}$ and r_{∞_t} represent respectively the drop, and the mass and thermal boundary layer radius, and $\dot{m}_F$ is the fuel evaporation mass flow-rate.

In this theory, the following assumptions are usually made :

- the droplet is considered to be spherical,

- the fuel is a pure liquid with a well-defined boiling point,

- radiation heat transfer is neglected,

- evaporation is assumed to be a quasi-steady process, in order to avoid consideration of time variations associated with the droplet regression process,

---

[7] A good estimate of λ implies a good estimate of B, see below in this section.

- ambient gas flux through the liquid surface is neglected (insolubility hypothesis); this means that below the droplet surface only pure fuel exists.

Except at very extreme pressures, these assumptions are generally considered valid.

The details of the D^2 *law* derivation are given in appendix C. The main results for steady-state evaporating conditions are summarized below. According to the theory developed in [58], an evaporation process can be characterized by two parameters :

$$B_M = \frac{Y_{F_I}}{1 - Y_{F_I}} \tag{2.9}$$

$$B_T = \frac{c_{p_g} \cdot (T_\infty - T_I)}{l_I} \tag{2.10}$$

where B_M and B_T are the mass transfer number and the thermal transfer number, respectively. The other terms represent :

- Y_{F_I}, the saturated fuel mixture fraction at liquid/gas interface,
- c_{p_g}, the specific constant-pressure heat-capacity of the gaseous mixture,
- T_∞, the temperature of the ambient gas,
- T_I, the temperature of the gaseous mixture at liquid/gas interface,
- l_I, the latent heat of vaporization at the temperature T_I.

The relation between Y_{F_I} and T_I is given by the following equations :

$$\ln\left(\frac{p_{vp_I}}{p_{cr}}\right) = \frac{T_{bn}}{T_{cr}} \cdot \frac{\ln\left(\frac{p_{cr}}{101325}\right)}{1 - \frac{T_{bn}}{T_{cr}}} \cdot \left(1 - \frac{1}{\frac{T_I}{T_{cr}}}\right) \tag{2.11}$$

$$Y_{F_I} = \left[1 + \left(\frac{p}{p_{vp_I}} - 1\right) \cdot \frac{\mathcal{M}_a}{\mathcal{M}_F}\right]^{-1} \tag{2.12}$$

in which :

- p, the ambient-gas pressure,
- p_{vp_I}, the liquid saturation pressure at the temperature T_I,
- p_{cr}, the critical pressure of the liquid,
- T_{bn}, the normal boiling temperature of the liquid,
- T_{cr}, the critical temperature of the liquid,
- $\mathcal{M}_a$, the molar mass of the ambient-gas,
- $\mathcal{M}_F$, the molar mass of the fuel.

Under steady conditions, the following identity is verified :

$$B_M = B_T = B \tag{2.13}$$

The values of T_I, Y_{F_I} and B are obtained from equations 2.9 to 2.13 by using an iterative method[8].

The constant of evaporation for steady-state conditions, λ_{st}, is then computed as :

$$\lambda_{st} = \frac{8 \cdot k_g \cdot \ln(1+B)}{Le \cdot c_{p_g} \cdot \rho_{F_l}} \tag{2.14}$$

where k_g, Le and ρ_{F_l} are respectively the thermal conductivity of the gasous mixture, the Lewis' number, here supposed to be equal to unity, and the density of the liquid fuel at the temperature T_I.

The developed model has then been validated with experiments : the steady-state regime has been compared to experimental data relative to n-heptane (C_7H_{16}) drop evaporation [49] in well-known test conditions, table 2.1.

Limit condition	Unit	Value
T_∞	[K]	773
p	[Pa]	101330
D_{d_0}	[μm]	200

Table 2.1: Limit conditions of the steady-state evaporation process.

In table 2.2 the comparison between the known values of the test from literature [49, 72][9] and the relative model output values are shown.

Table 2.2 shows that the steady-state evaporation model gives output values that are very close to those found in literature. Further validations of the model have been performed by comparing computed results with experimental results obtained by [51], figures 2.9 and 2.10. Figures 2.9 and 2.10 show the dependence of the evaporation constant on the ambient pressure and temperature conditions for n-heptane.

As shown, there is a good agreement between the model and the experimental data [51].

Figure 2.11 shows the influence of ambient thermodynamic conditions on the mixture temperature at the liquid-gas interface.

To summarize, the thermochemical properties of the mixture at liquid-gas interface, characterized by Y_{F_I} and T_I, are key parameters of dual-CM. These parameters will be used in the mixture and combustion models, which will be presented in section 2.4.4 and 2.5, respectively. As shown, the evaporation model proposed in [49] allows to determine the thermochemical conditions of the fluid at the droplet surface in steady-state

---

[8] At each iteration all the properties of the fluids are reevaluated.

[9] In the case both values from Lefebvre [49] and from FLUIDAT [72] are available, the last one is considered to be more reliable : more accurate formulas are used to determine the value.

Physical property	Unit	Simulated Value	Values from Lefebvre [49]	Values from FLUIDAT [72]
Y_{F_I}	[-]	0.675	0.679	–
T_I	[K]	340.0	341.8	–
B	[-]	2.08	2.12	–
p_{vp} at T_I	[Pa]	37931	38420	36260
l_{bn}	[J/kg]	313630	371800	310900
l_I	[J/kg]	334372	339000	331100
ρ_{F_l} at T_I	[kg/m^3]	640.8	638.0	641.8
c_{p_a}	[J/kg/K]	1028	1026	–
c_{p_F}	[J/kg/K]	2309	2450	–
c_{p_g}	[J/kg/K]	1604	1671	–
μ_{O_2}	[kg/m/s]	226840	–	227800
μ_{N_2}	[kg/m/s]	194960	–	196200
$\mu_{C_7H_{16}}$	[kg/m/s]	66144	–	–
μ_g	[kg/m/s	107000	–	–
k_a	[J/m/s/K]	0.03925	0.0384	–
k_F	[J/m/s/K]	0.03069	0.0307	–
k_g	[J/m/s/K]	0.0354	0.0349	–
λ_{st}	[m^2/s]	$3.09e-7$	$3.00e-7$	–

Table 2.2: Physical properties during the steady-state evaporation process.

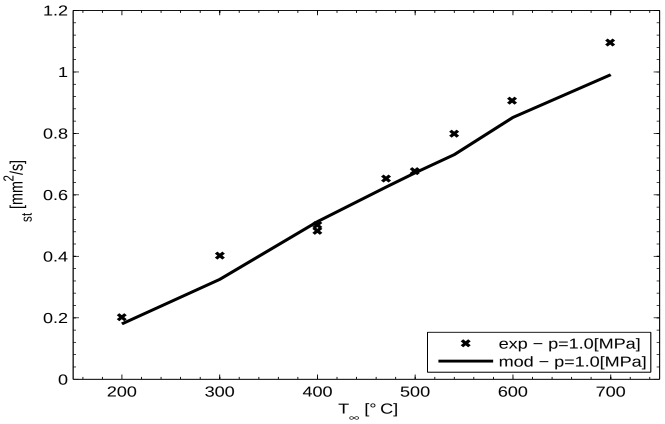

Figure 2.9: Dependence of the evaporation constant on the ambient conditions (Fuel : n-heptane).

evaporation conditions. This model has been validated with experimental data and has shown to be able to predict the evaporation constant λ_{st}. As λ_{st} is strongly dependent on the transfer number value B through equations 2.9, 2.10 and 2.13, which in turn depends on the thermodynamic interface conditions, it is possible to affirm that the computed values of temperature and fuel mixture fraction at the interface are reliable.

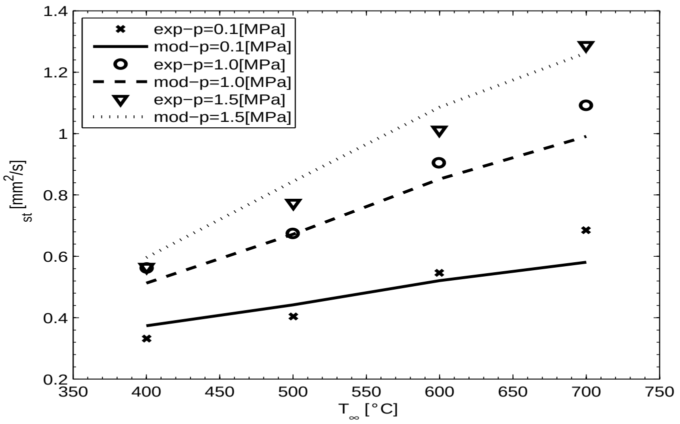

Figure 2.10: Dependence of the evaporation constant on the ambient conditions (Fuel : n-heptane).

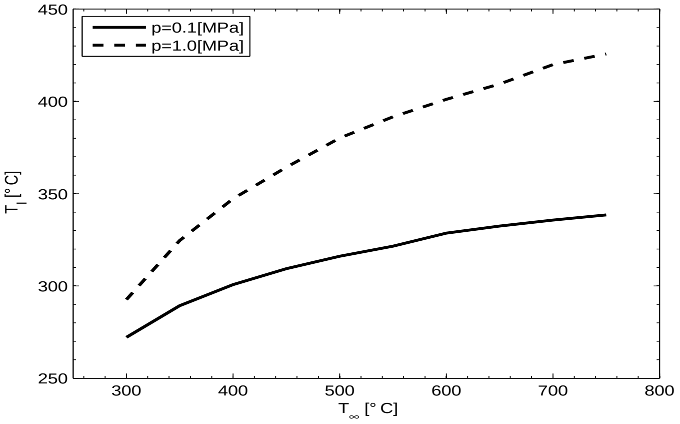

Figure 2.11: Dependence of the temperature at the liquid-gas interface on the ambient conditions (Fuel : n-heptane).

2.4.1.2 Liquid penetration length

This section deals with the computation of the fuel liquid-phase penetration length, L. It represents the second step of the set up evaporation-model and it allows us to have access to information needed for computing the overall fuel evaporation rate, $\dot{m}_F$, figure 2.7. Liquid fuel penetration is one of the important issues with respect to optimizing in-cylinder processes in Diesel engines, especially for the small-bore Direct Injection (DI) Diesels being developed for automotive applications. Overpredicted penetrations of the fuel liquid-phase can lead to higher emissions if liquid fuel impinges and collects on the piston bowl wall. As a result, developing a better understanding of the parameters that control the extent of the liquid-phase fuel in a Diesel spray is important.

Figure 2.12 is a plot of the liquid lengths expected in a standard commercial light-duty Diesel engine as a function of realistic Top Dead Center (TDC) temperature. This analysis immediately shows which constraints must be taken into account during engine-control calibration. The upper gray region represents the range of liquid lengths expected for cold start engine conditions. The gray horizontal band running through the center of the figure between 22 and 28 mm represents typical distances between the injector and the far wall of the piston bowl in light-duty Diesel engines. The upper and lower edges of the region for warm running conditions represent operation at boost pressures of 0.7 and 3 atm, respectively. The left and right sides of this region correspond to operation at the lowest and the highest intake temperatures, respectively. For reference, the typical liquid lengths predicted with the scaling law (detailed in the following) for lines of constant density (the light-gray solid curves) are included. The scaling law gives the average liquid length, but turbulence in classical engine conditions causes approximately ±10% fluctuations in the instantaneous liquid length [52]. The dashed lines above and below the upper border of the warm running conditions region in figure 2.12 represent the effect of turbulent fluctuations in the liquid length on the upper border. Experimental results in an engine indicate that combustion thermal radiation potentially shorten the liquid length slightly, but that vaporization is almost complete before the combustion zone is reached [77, 78]. According to figure 2.12, sensitive regions in which liquid is likely to impinge on the piston bowl are those associated to cold start conditions and lightest load warm running operating conditions which correspond to the upper left corner of the lower gray region.

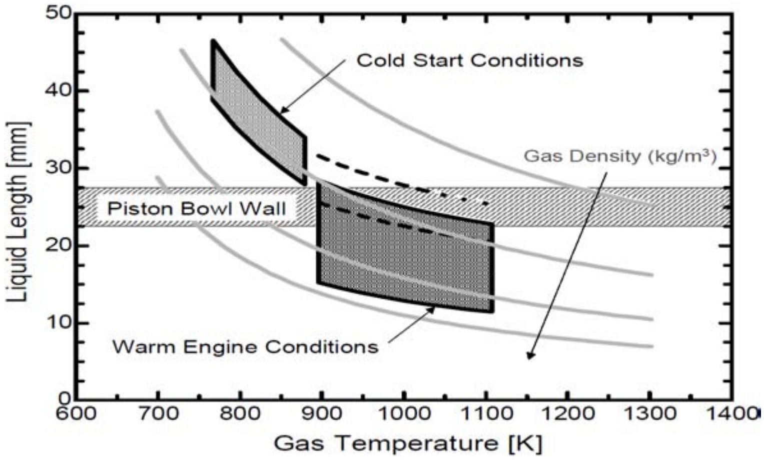

Figure 2.12: Liquid lengths expected in light-duty Diesel engine. The lower gray region represents the range of liquid lengths expected for warm running engine conditions. The upper gray region represents the range of liquid lengths expected for cold start engine conditions. The gray horizontal band across the middle of the figure represents typical maximum distances from the injector to the piston bowl wall. The light-gray solid curves are liquid lengths for lines of constant density [52].

Investigations on the liquid fuel penetration [75, 76, 77, 52] show that liquid fuel initially defines the penetrating tip of a Diesel spray. This continues until the liquid phase region penetrates to a point where the total fuel evaporation rate in the spray equals the fuel injection rate. When this condition occurs, the tip of the liquid region stops penetrating and, because of the interactions between the liquid with turbulent structures having an aleatory motion, it begins fluctuating about a mean axial location. The primary source of energy for fuel vaporization is the hot air entrained into the spray and not the energy from combustion, since the liquid lengths were established before ignition occurred. Liquid lengths were obtained from time averaged images, such as those shown in figure 2.13, by selecting an intensity threshold and determining the maximum spray axial distance with a light intensity above the threshold [52]. Figure 2.13 shows three time-averaged images of the Mie-scattered light from an evaporating Diesel spray : the liquid-phase penetration length diminishes with increasing ambient air density. Results from an experimental investigation of the effects of several key parameters on the liquid length in Diesel sprays over extremely wide ranges of conditions obtained by [52, 54] are reported in figures 2.14 to 2.18. The investigation of liquid phase fuel penetration was conducted in inert, high-temperature, high-density conditions generated in a constant-volume combustion vessel. Inert conditions allowed the penetration and vaporization of the liquid phase to be examined optically without interference from ignition and combustion processes. The parameters considered were injector orifice diameter, injection pressure, ambient gas density and temperature, and fuel temperature and volatility. Three different fuels were tested : a Phillips research grade Diesel fuel ($DF2$), heptamethylnonane (HMN) and n-hexadecane ($Cetane$). Figure 2.14 shows one dominant trend : namely, the liquid length in a Diesel spray is linearly dependent on orifice diameter and approaches a value of zero as the orifice diameter decreases toward

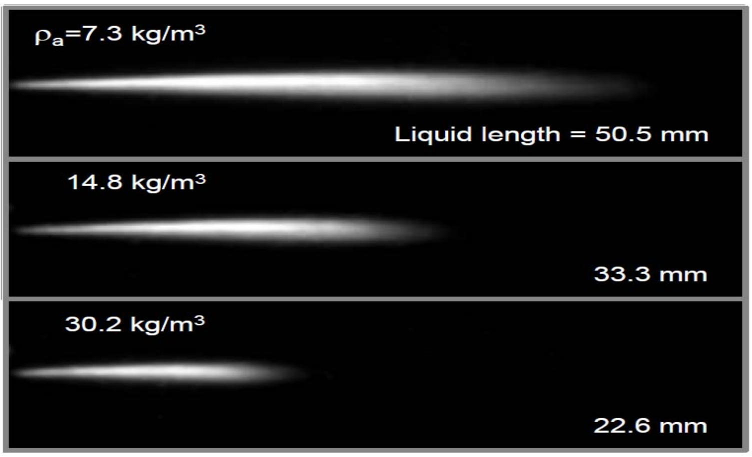

Figure 2.13: Time-averaged Mie-scattered light images showing the liquid-phase penetrations for three sprays injected from left to right into the ambient-gas density (ρ_a). Liquid penetration and gas density values are given in each image. The orifice pressure drop and diameter, the ambient gas temperature, the fuel temperature, and the fuel were 1350 bar, 246 μm, 1000 K, 438 K and DF2, respectively [52].

zero. The linear dependence on orifice diameter is an important result for the small-bore ($\sim$ 80 mm) DI Diesel engines currently being developed, since liquid impingement on piston bowl walls is a concern in these engines. Figure 2.15 shows that the orifice pressure drop[10] has a negligible effect on the liquid length over a very large pressure range. The lack of injection pressure effect on liquid length indicates that the change in the fuel flow rate that occurs with a change in injection pressure must cause exactly the same change in the overall fuel evaporation rate. This result shows that use of higher injection pressures does not lead to enhanced problems with liquid impingement on piston bowl walls in engines.

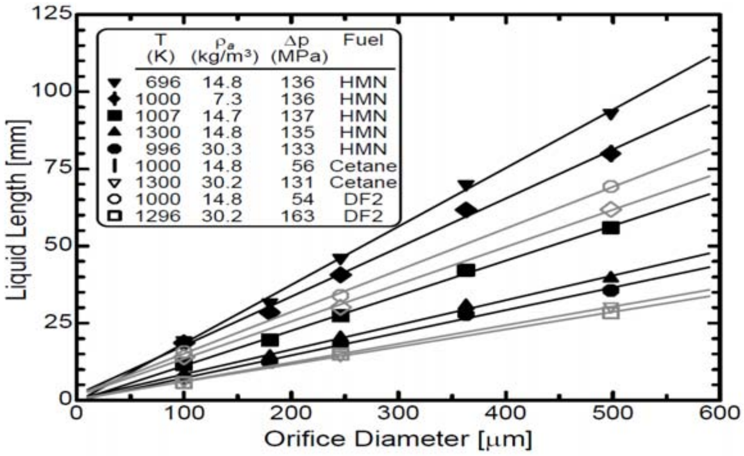

Figure 2.14: Liquid length versus orifice diameter for a wide range of conditions. The terms in the legend are the ambient gas temperature (T) and density (ρ_a), the orifice pressure drop (Δp), and the fuel. The aspect ratio of the orifices and the fuel temperature were nominally 4.2 and 438 K, respectively [52].

The liquid length dependence on orifice diameter and injection pressure shown in figures 2.14 and 2.15, respectively, strongly suggest that fuel vaporization in a Diesel spray is controlled by air entrainment (i.e., turbulent mixing processes) [52]. Control by mixing in turn implies that the local interphase transport rates of mass, momentum, and energy controlling liquid breakup and droplet evaporation are not the processes limiting fuel evaporation in a Diesel spray. In the following, in order to justify the statement above, the exhaustive analysis comparing turbulent mixing control and local interphase transport control implications made in [52] is presented.

If turbulent mixing controls vaporization, the local interphase transport rates of mass, momentum, and energy that control liquid breakup and droplet evaporation must be fast relative to turbulent mixing rates. In this limit, no local velocity or temperature differences exist between the phases in the spray and the phases are in equilibrium

---

[10] Pressure drop through the nozzle orifice is defined as the difference between liquid-fuel pressure inside the nozzle and ambient-air pressure within the cylinder.

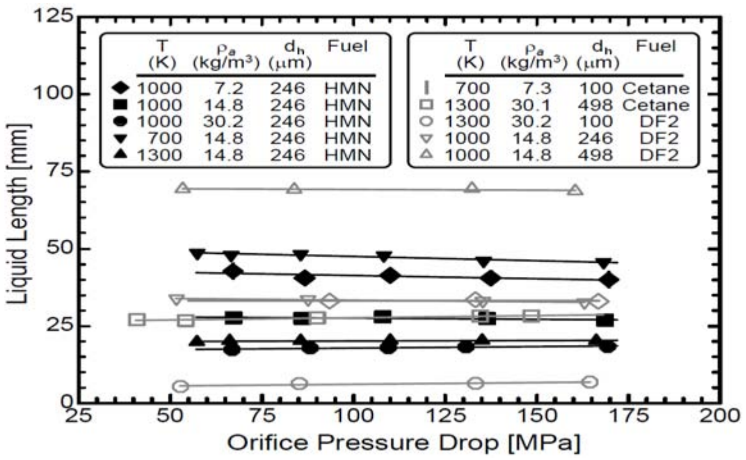

Figure 2.15: Liquid length versus the pressure drop across the injector orifice for a wide range of conditions. The terms in the legend are the orifice diameter (d_h), the ambient gas temperature (T) and density (ρ_a) and the fuel. The aspect ratio of the orifices and the fuel temperature were nominally 4.2 and 438 K, respectively [52].

locally [74]. Consequently, in this context, the model developed in section 2.4.1.1 gives an insight on the thermochemical properties of the gaseous fuel at liquid-gas interface. Turbulent mixing controls vaporization in this limit by determining the rate at which energy is entrained into the spray for heating and vaporizing the fuel. By conservation of energy, the energy entrainment rate is directly proportional to the ambient gas mass entrainment rate. The net result is that a change in the injected fuel mass flow rate will have to be matched by a change in the entrained air mass flow rate to supply the energy needed to vaporize the new quantity of fuel injected. In this situation, the expressions for the fuel injection rate and the entrained gas flow rate, can be derived to show the dependence of liquid length on orifice diameter and injection pressure. These relationships can be derived by applying conservation of mass and momentum principles to a simple conceptual model for a spray [53]. The schematic of the model is presented in figure 2.19. It is the basis of the development of the liquid-phase penetration scaling law presented below. At this point, in order to have a complete understanding of the implications of the results shown in figures 2.14 and 2.15, two relationships giving the mass flow rates of injected fuel, $\dot{\mathbf{m}}_F$[11], and of total entrained ambient gas mass, $\dot{\mathbf{m}}_a$, through a cross-section at any axial location in a spray are introduced :

$$\dot{\mathbf{m}}_F \propto \rho_{F_l} \cdot d_h^2 \cdot u_F \tag{2.15}$$

$$\dot{\mathbf{m}}_a \propto \sqrt{\rho_a \cdot \rho_{F_l}} \cdot d_h \cdot x \cdot u_F \cdot \tan\left(\frac{\theta}{2}\right) \tag{2.16}$$

The terms in the equations are the ambient gas density, ρ_a, the liquid fuel density, ρ_{F_l}, the orifice diameter, d_h, the injected fuel velocity, u_F[12], the axial distance from the

---

[11] The notation $\dot{\mathbf{m}}_F$ refers to both liquid and gaseous fuel.

[12] For more information concerning the procedure to compute u_F, refer to section 2.4.2.

orifice, x, and the spreading angle of the spray, θ.

The first relationship states that the mass flow rate of fuel at any axial location in a spray is the injected fuel mass flow rate. The second relationship applies after a distance of several orifice diameters from the injector tip. It shows that the total entrained gas flow rate depends linearly on the orifice diameter, the axial location in the spray, and the injected fuel velocity (where injected fuel velocity is proportional to the square-root of the pressure drop across the orifice). Assuming all other parameters are fixed, equations 2.15 and 2.16 show a linear dependence results between the orifice diameter and the length of the spray needed to entrain the appropriate air (i.e., energy) to vaporize the fuel, as observed in figure 2.14. Concerning the injection pressure, equations 2.15 and 2.16 show that the entrained gas (i.e., energy) and the quantity of fuel injected have the same dependence on injection pressure, since the injection velocity is proportional to the square-root of the pressure drop across the injector orifice. As a consequence, no change in the spray entrainment length is required when the injection pressure changes, resulting in no change in the liquid length as observed in figure 2.15. This observation with respect to injection pressure does not mean that the rate of vaporization is unchanged with an increase in injection pressure. As discussed previously, the vaporization rate must be increasing with increasing injection pressure. The existence of a well defined liquid length means that the total rate of vaporization in the spray upstream of the liquid length location is equal to the fuel injection rate. Therefore, the total spray evaporation rate increases in proportion to the fuel injection rate.

If local interphase transport rates of mass, momentum, and energy that control the liquid breakup and droplet evaporation would limit the overall vaporization rate, the turbulent mixing rate should be fast relative to those processes. In other words, sufficient energy is entrained into the spray, but transfer to the liquid phase is limited and local velocity and temperature differences exist between the phases in the spray. In this limit a different dependence of liquid length on orifice diameter and injection pressure would be expected. Concerning the influence of the orifice diameter, experimental results have shown that the orifice diameter does not have a strong effect on the mean droplet size in a Diesel spray in the injection pressure range considered in figure 2.14 [79]. This implies that if atomization processes and the ensuing individual droplet evaporation rates limit the overall rate of vaporization, the orifice diameter should have very little effect on the liquid length, which contrasts with experimental evidence. Concerning the injection pressure, research has shown that there is virtually no change in mean droplet size with a change in injection pressure for the range of injection pressures covered in figure 2.15 [79]. The primary effect of injection pressure is on the heat and mass transfer rates at the droplet surface and the penetration rate of the droplets in a spray. The net effect of an increase in injection pressure is a longer droplet penetration distance before evaporation, even though the droplet lifetime is shorter than before. No such changes in liquid length were observed in figure 2.15.

Consequently, the trends in figures 2.14 and 2.15 can only be explained by a mixing-controlled vaporization process in the spray. The effects of ambient gas density and temperature on liquid length are shown in figures 2.16 and 2.17. The orifice diameter, the injection pressure drop across the orifice, the fuel, and the fuel temperature for the data were 246 μm, 1360 bar, HMN and 438 K, respectively. Figure 2.16 shows that the ambient gas density has a non-linear effect on liquid length. As the gas density increases, the liquid length decreases. At the highest densities, the effect of density becomes smaller. The trend with respect to density is similar at all gas temperatures. Figure 2.17 shows that the gas temperature has also a strong effect on liquid length. As the gas temperature is increased, the liquid length decreases. The reason for the decrease in liquid length with increasing temperature is obvious and expected. The entrained higher temperature ambient gas contains more energy and will heat the liquid fuel to a higher temperature. The result is an overall increase in the vaporization rate and a shortening of the length of spray required to entrain enough hot gas to vaporize the fuel. Some of the reasons for the ambient gas density effect are contained in equation 2.16. This equation indicates that the entrained gas increases in proportion to the square-root of the gas density, providing more energy for vaporization. Also, since the spreading angle (θ) of a spray increases with increasing gas density [55], equation 2.16 indicates that additional energy will be available for fuel vaporization indirectly as a result of an increase in the gas density.

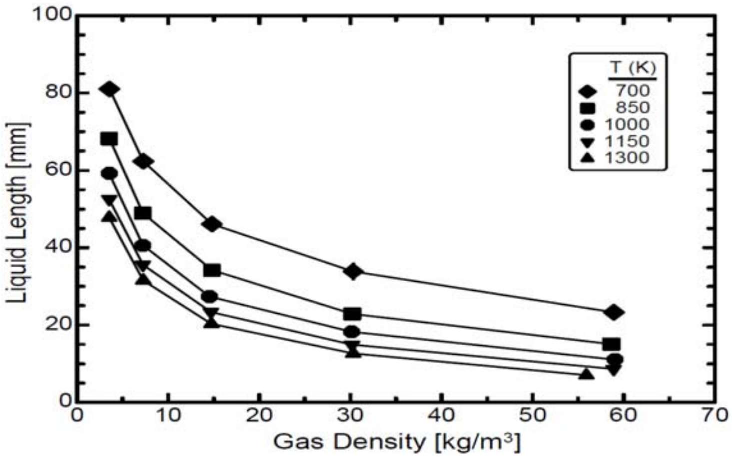

Figure 2.16: Liquid length as a function of gas density for five gas temperatures. The orifice diameter, the injection pressure drop across the orifice, the fuel temperature, and the fuel were 246 μm, 1360 bar, 438 K, and HMN, respectively [52].

Figure 2.18 shows that as fuel temperature increases the liquid length decreases linearly with fuel temperature. The effect of fuel temperature is most significant at low gas

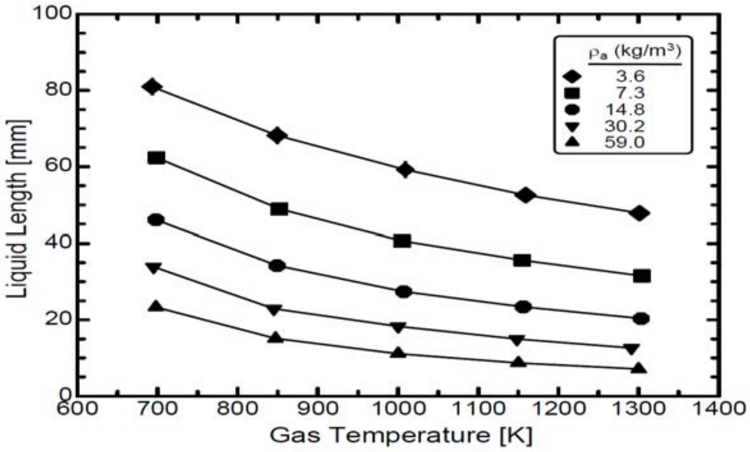

Figure 2.17: Liquid length as a function of gas temperature for five gas densities. The orifice diameter, the injection pressure drop across the orifice, the fuel temperature, and the fuel were 246 μm, 1360 bar, 438 K, and HMN, respectively [52].

temperature/density conditions. At the highest gas temperature/density conditions, the effect appears smaller. Based on a mixing control of vaporization, the cause of the fuel temperature effect is straightforward. As fuel temperature increases, less energy is required to heat and vaporize the liquid fuel. This shortens the spray length required to entrain the energy needed to vaporize the fuel, resulting in a shorter liquid length.

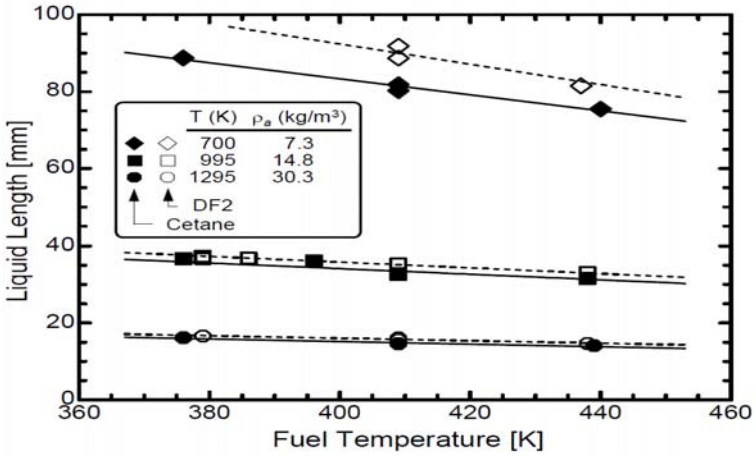

Figure 2.18: Liquid length versus the injected fuel temperature for three different ambient gas conditions and two different fuels as given in the legend. The orifice diameter and injection pressure drop across the orifice were 246 μm and 1350 bar, respectively [52].

According to the experimental data of figures 2.14 to 2.18, a scaling law for the maximum penetration distance of liquid-phase fuel in a Diesel spray was developed in [53] by applying jet theory to a simplified spray model, figure 2.19. The scaling law, developed by using principles of conservation of mass, momentum and energy, accounts for injector specifications, fuel and in-cylinder thermodynamic conditions on liquid length. The idealized spray is assumed to have the following physical characteristics :

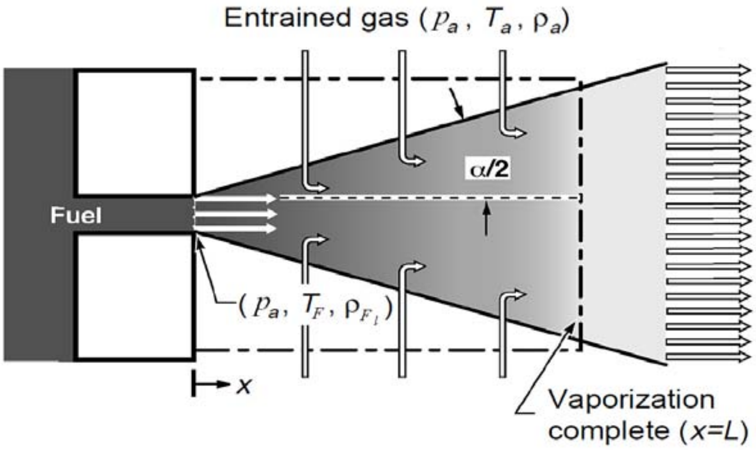

Figure 2.19: Schematic of the idealized spray model used to develop the liquid length scaling law [53].

- quasi-steady flow with a uniform growth rate (i.e. a constant spreading angle α),
- uniform velocity, fuel concentration, and temperature profiles,
- in a spray cross section, the area associated to the liquid fuel is negligible,
- no velocity slip between the injected fuel and the entrained ambient gas.

The last assumption is doubtful close to the injector orifice exit, but it has been shown to apply very well before the complete vaporization axial distance from the injector nozzle outlet section. In figure 2.19, the downstream side of the control surface ($x = L$) is defined as being at the axial location in the spray where the fuel has just completely vaporized. The thermodynamic assumption up to this location in the spray are :

- the vapor phase fuel is at saturated condition,
- the vapor phase fuel is in thermodynamic equilibrium with the entrained ambient gas and the liquid phase fuel (i.e. they are at the same temperature),
- idealized phase equilibrium assumption (i.e. Raoult's and Dalton's rules) apply,
- gas absorption in the liquid phase is neglected,
- the recovery of kinetic energy in the fuel vaporization region of the spray is neglected.

The spray spreading angle is due to the turbulent entrainment of air into the spray region. It depends on injector nozzle geometry (i.e. hole diameter and orifice aspect ratio), and fuel and ambient air density. The fuel fluid dynamics through the injector orifice is not completely understood today, and the given analytical expression of the spreading angle, equation 2.17, is a correlation, function of the influencing parameters, that permits us to have an estimate of the experimental spreading angle values, θ :

$$\tan\left(\frac{\theta}{2}\right) = c \cdot \left[\left(\frac{\rho_a}{\rho_{F_l}}\right)^{0.19} - 0.0043 \cdot \left(\frac{\rho_{F_l}}{\rho_a}\right)^{0.5}\right] \tag{2.17}$$

where c is a constant taking into account the effect of injector orifice geometry on spreading angle. Authors recommend $c = 0.260$. The first term of equation 2.17 takes into account the spreading-angle density-dependence, while the second term takes into account the fact that the cooling of the entrained hot ambient air causes a contraction of the spray [55]. The angle α in the model, figure 2.19, must be related to the measured angle, θ, in order to use in the model the correlation expressed in equation 2.17. By making the assumption of self-preserved flow in the spray, the tangents of these two angles are related by a constant :

$$\tan\left(\frac{\alpha}{2}\right) = a \cdot \tan\left(\frac{\theta}{2}\right) \tag{2.18}$$

where a is the constant. Authors recommend $a = 0.66$. This value of a was obtained by assuming self preserving flow and equivalence between the mass and the momentum flow rates of real spray and idealized spray [55]. Moreover, experiments on the evaluation of spreading angle have shown that there is no dependence between spreading angle and type of fuel, ambient air temperature and injection pressure. The determination of a mathematical relation giving the liquid-phase penetration length has been obtained by using mass, momentum and energy balances. In that way, it has been possible to identify the spray axial coordinate at which liquid has completely vaporized, figure 2.19. For fuel and ambient air, the mass balance equations are :

$$\dot{\mathbf{m}}_F(0) = \rho_{F_l}(0) \cdot A(0) \cdot u(0) = \dot{\mathbf{m}}_F(L) = \rho_F(L) \cdot A(L) \cdot u(L) \tag{2.19}$$

$$\dot{\mathbf{m}}_a(L) = \rho_a(L) \cdot A(L) \cdot u(L) \tag{2.20}$$

where 0 and L represents respectively the values of the axial coordinate, x, at the exit of the injector and at which liquid fuel is completely vaporized, $\dot{\mathbf{m}}_F(x)$ and $\dot{\mathbf{m}}_a(x)$ are respectively the fuel and ambient air mass flow rates[13], $\rho_F(x)$ and $\rho_a(x)$ are respectively the fuel and air partial density, and $A(x)$ and $u(x)$ represent respectively the spray cross section and fluid velocity, respectively. The cross sections being computed as :

$$A(x) = \pi \cdot \left[x \cdot \tan\left(\frac{\alpha}{2}\right)\right]^2 \tag{2.21}$$

$$A(0) = \frac{\pi}{4} \cdot d_{vc}^2 \tag{2.22}$$

---

[13] $\dot{\mathbf{m}}_a(x)$ corresponds to the total entrained mass ambient air flow rate up to the coordinate x.

where the diameter of the vena contracta, d_{vc}, is defined as :

$$d_{vc} = \sqrt{C_a} \cdot d_h \tag{2.23}$$

where C_a and d_h are the area-contraction coefficient [14] and the injector orifice hole diameter. By definition at $x = L$, the fuel is completely vaporized and in thermodynamic equilibrium with the ambient air (fuel saturation condition). Consequently, both fuel and ambient-air are at the same temperature and the partial densities of the fuel and the ambient gas are dependent on their respective partial pressures. Consequently, the energy balance equation at $x = L$ holds :

$$\dot{\mathbf{m}}_F(L) \cdot h_F(T_F, p_a) + \dot{\mathbf{m}}_a(L) \cdot h_a(T_a, p_a) = \dot{\mathbf{m}}_F(L) \cdot h_F(T_s, p_s) + \dot{\mathbf{m}}_a(L) \cdot h_a(T_s, p_a - p_s) \tag{2.24}$$

where $h_F(T, p)$ and $h_a(T, p)$ are respectively the fuel and air specific enthalpies at given thermodynamic conditions (expressed in terms of temperature, T, and partial pressure, p), T_F, T_a and T_s are respectively the fuel, ambient air and fuel saturation temperatures, and p_a and p_s are respectively the ambient air and fuel-saturation pressures. Rearranging equations 2.19 to 2.24, it is possible to explicit the ratio of fuel and ambient air mass flow rates required for completely vaporizing the fuel at $x = L$:

$$\frac{\dot{\mathbf{m}}_F(L)}{\dot{\mathbf{m}}_a(L)} = \frac{h_a(T_a, p_a) - h_a(T_s, p_a - p_s)}{h_F(T_s, p_s) - h_F(T_F, p_a)} \tag{2.25}$$

where the enthalpy difference in the numerator is the specific enthalpy transferred from the entrained ambient gas to heat and vaporize the fuel, and the enthalpy difference in the denominator is the specific enthalpy required to heat and vaporize the liquid fuel[15]. In equation 2.25, the saturation temperature and pressure are dependent through the saturation temperature-pressure relationship. Consequently, the only unknown is T_s in order to determine the thermodynamic condition of the gas at the coordinate corresponding to the liquid-phase penetration length. Note that the ratio of fuel and ambient air mass flow rates defined in equation 2.25 corresponds to the thermal transfer number, B_T, used in droplet vaporization studies [53]. Moreover, according to the hypotheses used in developing the liquid penetration length model, it is possible to affirm that at the maximum penetration length section the thermal transfer number is equal to the mass transfer number, B_M and that the gaseous mixture thermodynamic state of the fluid corresponds to the fuel saturated condition at the liquid-gas interface of an evaporating droplet at rest in a quiescent gaseous mixture, section 2.4.1.1.

Equation 2.25 can be rewritten as :

$$\frac{\dot{\mathbf{m}}_F(L)}{\dot{\mathbf{m}}_a(L)} = B_T = B_M = B \tag{2.26}$$

---

[14] For more information about the implications and the determination of this coefficient, refer to section 2.4.2.

[15] It is comprehensive of the latent enthalpy of vaporization and sensible enthalpy of heating.

In order to derive an equation describing the axial variation of the fuel/ambient gas ratio with the axial coordinate, an additional assumption is made. The assumption is that axial variation of this ratio in the vaporizing spray is similar to that in a non-vaporizing, isothermal spray[16]. It is now possible to rewrite mass and momentum balance equations for the generic abscissa x as :

$$\dot{\mathbf{m}}_F\left(x\right) = \dot{\mathbf{m}}_F\left(0\right) \tag{2.27}$$

$$\dot{\mathbf{m}}_a\left(x\right) = \rho_a\left(x\right) \cdot A\left(x\right) \cdot u\left(x\right) \tag{2.28}$$

$$\dot{\mathbf{m}}_F\left(x\right) \cdot u\left(x\right) + \dot{\mathbf{m}}_a\left(x\right) \cdot u\left(x\right) = \dot{\mathbf{m}}_F\left(0\right) \cdot u\left(0\right) \tag{2.29}$$

Defining a non-dimensional penetration coordinate defined as :

$$\widetilde{x} = \frac{x}{x^+} \tag{2.30}$$

where the penetration length scale x^+ is defined as :

$$x^+ = \sqrt{\frac{\rho_{F_l}}{\rho_a}} \cdot \frac{d_{vc}}{\tan\frac{\alpha}{2}} \tag{2.31}$$

and rearranging equations 2.27 to 2.29 and using the definition given in equation 2.18 and in equations 2.21 to 2.23, the dimensionless form of the axial variation of the ratio of the fuel/ambient gas mass flow rates is :

$$\frac{\dot{\mathbf{m}}_F\left(x\right)}{\dot{\mathbf{m}}_a\left(x\right)} = \frac{2}{\sqrt{1 + 16 \cdot \widetilde{x}^2} - 1} \tag{2.32}$$

The non-dimensional liquid-phase penetration-length, $\widetilde{L}$, is obtained from equation 2.32 for the coordinate $x = L$ (according to equation 2.26, in that case, the left-hand side of the equation is equal to the transfer number, B) and solving for the value of $\widetilde{L}$:

$$\widetilde{L} = b \cdot \sqrt{\left(\frac{2}{B} + 1\right)^2 - 1} \tag{2.33}$$

where b is a constant coefficient. Authors recommend $b = 0.41$. The dimensional expression of the liquid-phase penetration is simply obtained as :

$$L = \widetilde{L} \cdot x^+ \tag{2.34}$$

or, introducing the definitions given in equation 2.18, equations 2.21 to 2.23, and equations 2.30 and 2.31 into equations 2.34 :

$$L = \frac{b}{a} \cdot \sqrt{\frac{\rho_{F_l}}{\rho_a}} \cdot \frac{\sqrt{C_a} \cdot d_h}{\tan\frac{\theta}{2}} \cdot \sqrt{\left(\frac{2}{B} + 1\right)^2 - 1} \tag{2.35}$$

The penetration law for n-heptane has been tested on a wide range of configurations typical of commercial Diesel engines including injector orifice diameter, injection pressure, ambient air thermodynamic state and injected fuel temperature variations.

---

[16] It means that droplets are small enough to follow the gas flow.

Figures 2.20 to 2.24 show the obtained trends. The aim of this qualitative validation is to show the model sensitivity to the considered parameters as well as to confirm the trends found in [52]. Figure 2.20 shows the variation of the computed liquid-phase penetration length with the injector orifice diameter and ambient air density. According to experimental data, figure 2.14, the trends show that liquid-phase penetration varies linearly with injector orifice diameter. Further, it decreases with an increase in the ambient air density. Figure 2.21 shows the variation of the computed liquid-phase penetration length with the pressure drop through the injector nozzle and ambient air temperature. According to experimental data, figure 2.15, the trends show that liquid-phase penetration is independent of pressure drop variations. Further, it decreases with an increase in the ambient air temperature. Figure 2.22 shows the variation of the computed

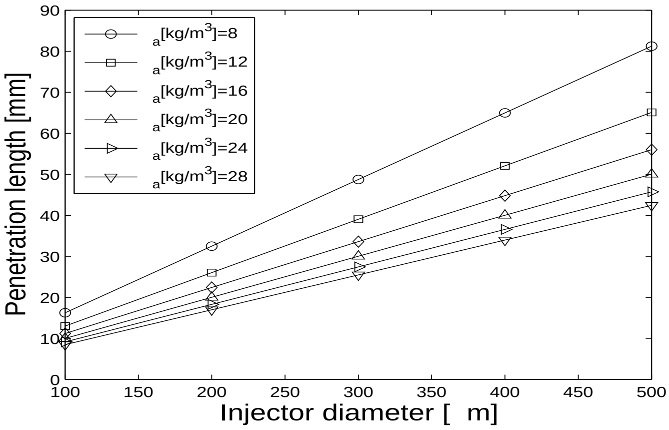

Figure 2.20: Computed liquid-phase penetration length variations as function of injector orifice diameter and ambient air density (legend). Other parameters were kept constant. In particular, ambient air temperature, pressure drop through the orifice and injected fuel temperature were 800 K, 1000 bar and 350 K, respectively.

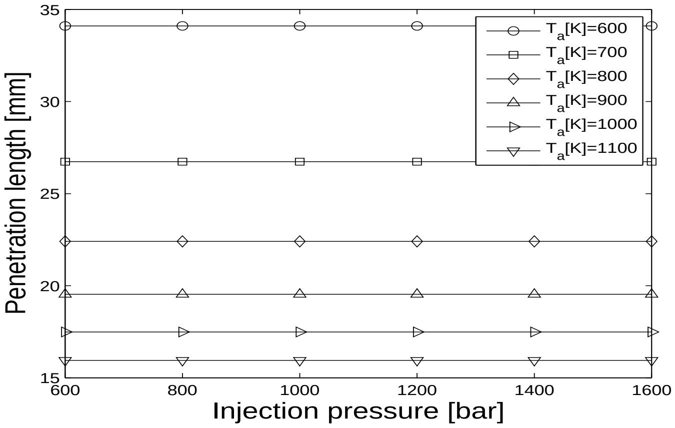

Figure 2.21: Computed liquid-phase penetration length variations as function of pressure drop across the injector orifice and ambient air temperature (legend). Other parameters were kept constant. In particular, the orifice diameter, ambient air density and injected fuel temperature were 200 μm, 16 kg/m^3 and 350 K, respectively.

liquid-phase penetration length with the ambient air density and ambient air temperature. According to experimental data, figure 2.16, the trends show that liquid-phase penetration decreases with an increase in the ambient air density. Further, it decreases with an increase in the ambient air temperature. Figure 2.23 shows the variation of

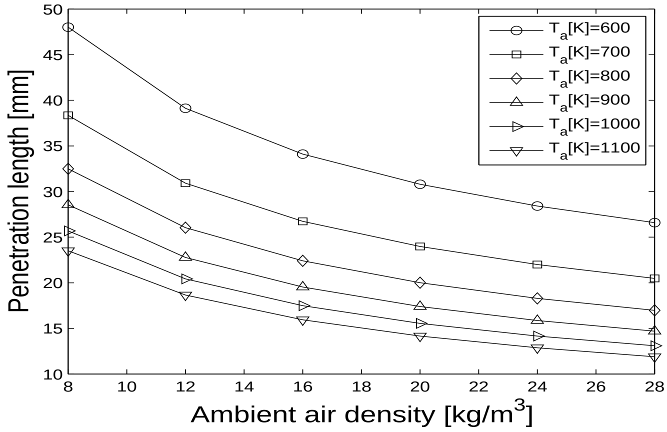

Figure 2.22: Computed liquid-phase penetration length variations as function of ambient air density and temperature (legend). Other parameters were kept constant. In particular, the orifice diameter, pressure drop through the orifice and injected fuel temperature were 200 μm, 1000 bar and 350 K, respectively.

the computed liquid-phase penetration length with the ambient air temperature and ambient air density. According to experimental data, figure 2.17, the trends show that the liquid-phase penetration decreases with an increase in the ambient air temperature. Further, it decreases with an increase in the ambient air density. Figure 2.24 shows the

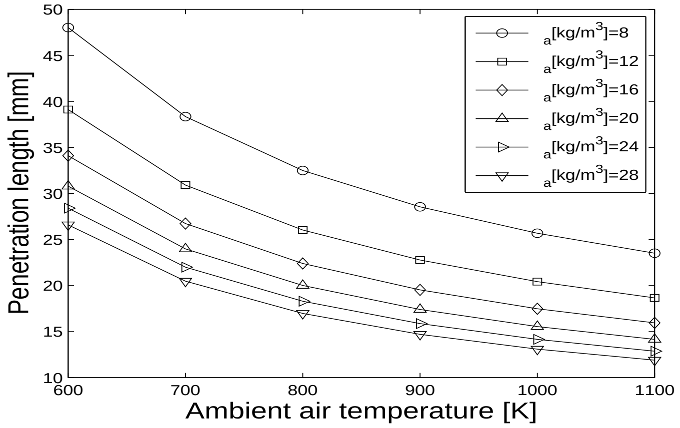

Figure 2.23: Computed liquid-phase penetration length variations as function of ambient air temperature and density (legend). Other parameters were kept constant. In particular, the orifice diameter, pressure drop through the orifice and injected fuel temperature were 200 μm, 1000 bar and 350 K, respectively.

variation of the computed liquid-phase penetration length with the injected fuel temperature and ambient air density. According to experimental data, figure 2.18, the trends show that liquid-phase penetration decreases linearly with a decrease in the injected fuel temperature. Further, it decreases with an increase in the ambient air density.

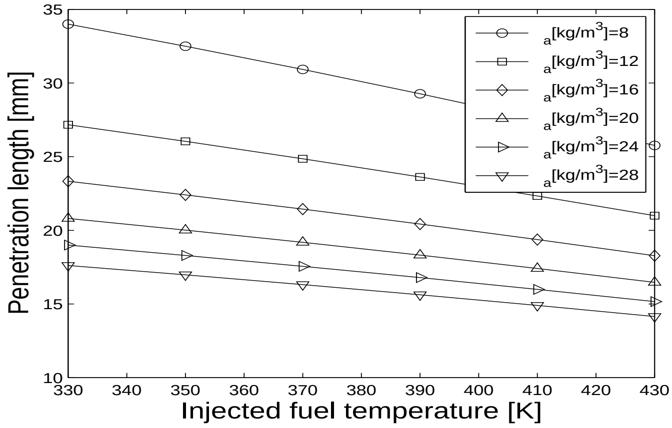

Figure 2.24: Computed liquid-phase penetration length variations as function of fuel temperature and ambient air density (legend). Other influent parameters were kept constant. In particular, the orifice diameter, pressure drop through the orifice and injected fuel temperature were 200 μm, 1000 bar and 350 K, respectively.

Other interesting results can be obtained by using the implemented liquid-phase penetration-length scaling law, figures 2.25 to 2.29. Figure 2.25 shows the variation of the computed spray spreading angle with the ambient air temperature and ambient air density. According to experimental data obtained in [53], the trends show that the spreading angle is independent of ambient air temperature variations. Further, it increases with an increase in the ambient air density. Figure 2.26 shows the variation of the computed fuel mixture fraction at the liquid-gas interface with the ambient air temperature and ambient air density. According to experimental data [80], fuel mixture

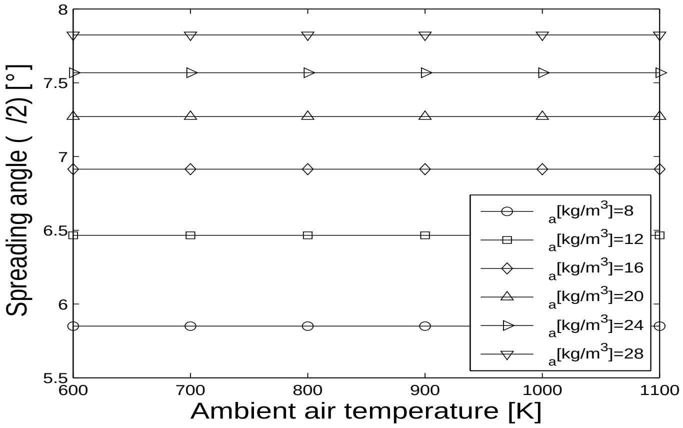

Figure 2.25: Computed spreading angle variations as function of ambient air temperature and density (legend). Other influent parameters were kept constant. In particular, the orifice diameter, pressure drop through the orifice and injected fuel temperature were 200 μm, 1000 bar and 350 K, respectively.

fraction increases with ambient air temperature and decreases with an increase in the ambient air density. Figure 2.27 shows the variation of the computed equivalence ratio

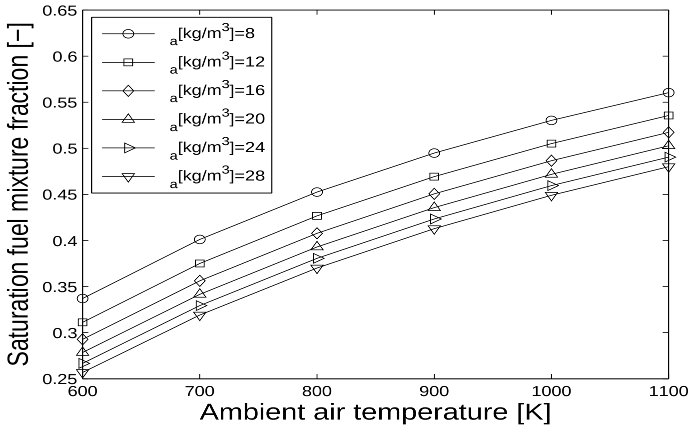

Figure 2.26: Computed fuel mixture fraction variations at liquid-gaseous interface as function of ambient air temperature and density (legend). Other influent parameters were kept constant. In particular, the orifice diameter, pressure drop through the orifice and injected fuel temperature were 200 μm, 1000 bar and 350 K, respectively.

at the liquid-gas interface with the ambient air temperature and ambient air density. In a similar fashion as in figure 2.26, the trends show that equivalence ratio increases with an increase in ambient air temperature. Further, it decreases with an increase in the ambient air density. Figure 2.28 shows the variation of the computed transfer

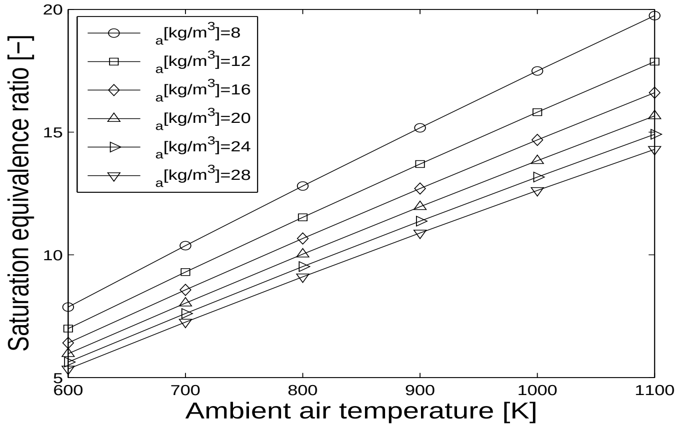

Figure 2.27: Computed equivalence ratio variations at liquid-gaseous interface as function of ambient air temperature and density (legend). Other influent parameters were kept constant. In particular, the orifice diameter, pressure drop through the orifice and injected fuel temperature were 200 μm, 1000 bar and 350 K, respectively.

number at the liquid-gas interface with the ambient air temperature and ambient air density. The trends show that transfer number increases with ambient air temperature. Further, it decreases with an increase in the ambient air density. Finally, figure 2.29 shows the variation of the computed saturation temperature at the liquid-gas interface

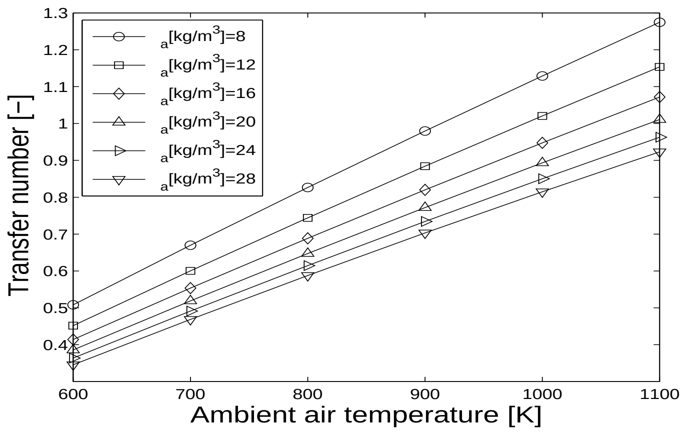

Figure 2.28: Computed transfer number variations as function of ambient air temperature and density (legend). Other influent parameters were kept constant. In particular, the orifice diameter, pressure drop through the orifice and injected fuel temperature were 200 μm, 1000 bar and 350 K, respectively.

with the ambient air temperature and ambient air density. According to experimental data obtained in [53, 80], the trends show that saturation temperature increases with an increase in the ambient air temperature. Further, it increases with an increase in the ambient air density. An important observation regarding figure 2.29 is that for common Diesel engine operating conditions, the saturation temperature never attains the value of 540.2 K corresponding to the critical temperature[17] of normal heptane (dashed line in figure 2.29).

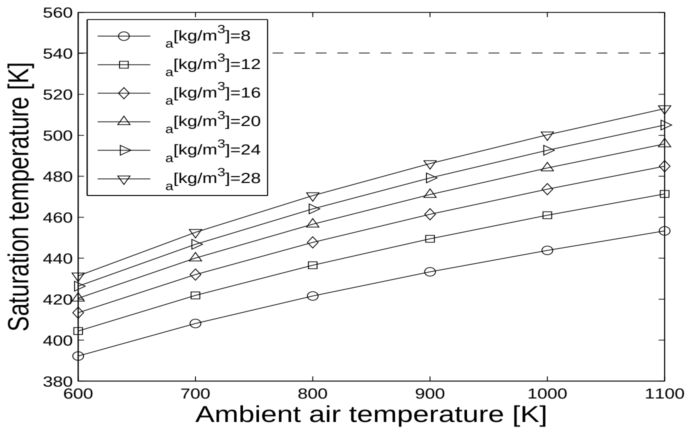

Figure 2.29: Computed saturation temperature variations at liquid-gas interface as function of ambient air temperature and density (legend). Other influent parameters were kept constant. In particular, the orifice diameter, pressure drop through the orifice and injected fuel temperature were 200 μm, 1000 bar and 350 K, respectively. The dashed line represents the critical temperature of n-C_7H_{16}.

By comparing figures 2.14 to 2.18 to figures 2.20 to 2.24, it is possible to note that

---

[17] The critical temperature of a liquid fluid is the maximum temperature that fluid can reach.

the computed penetration lengths are shorter than the experimental ones. This is essentially due to the different thermodynamic properties of the two fuels : Phillips research grade Diesel fuel ($DF2$) for experimental data, and normal heptane for computed results. In fact the volatility of normal heptane is higher than that of DF2. Consequently, it evaporates in a shorter time interval. Experimental studies show that for given ambient gas conditions in terms of temperature and density, fuel temperature and orifice diameter, penetration lengths change with the type of fuel, figure 2.30 [54]. As shown in figure 2.30, a simple linear correlation between liquid-phase penetration length and fuel volatility[18], as was supposed in [78, 52], is not sufficient to accurately predict the measured liquid lengths. For this reason, the dependence of liquid penetration length on

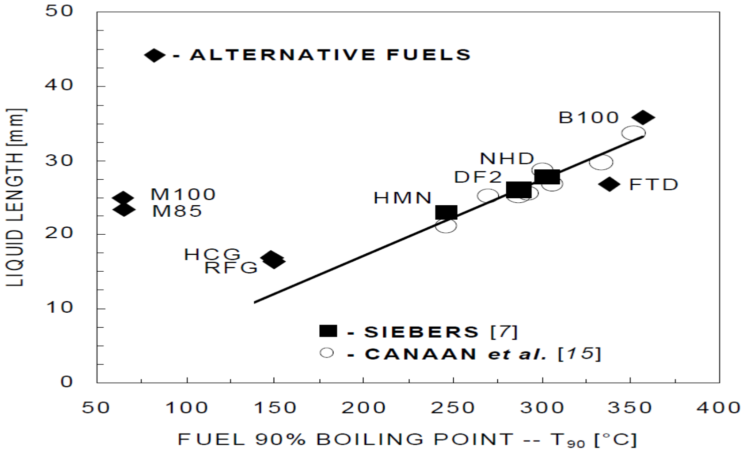

Figure 2.30: A linear scaling of liquid length with fuel volatility (i.e., boiling point) is not accurate for some fuels, especially those containing methanol [54]. All results have been scaled to ambient air density and temperature of 16.6 kg/m^3 and 992 K respectively, and an orifice diameter of 194 μm. Open circles represent various Diesel-like fuels examined by [78].

physical properties of the fuels was investigated in [54], and an engineering correlation was developed to explicit the dependence of liquid-phase penetration length on the type of fuel. The factors considered as to be influent in this analysis were :

- the ratio of fluid densities :

$$\widehat{\rho} = \frac{\rho_{F_l}}{\rho_a} \tag{2.36}$$

- the ratio of the heat available from the gases entrained in the spray and the heat necessary to heat the fuel (latent plus sensible) up to the boiling temperature; this term is nothing other than the thermal transfer number at boiling temperature :

$$B = \frac{c_{p_a} \cdot (T_a - T_{bn})}{c_{p_F} \cdot (T_{bn} - T_F) + l} \tag{2.37}$$

  where c_{p_a} and c_{p_F} are respectively the specific heat capacity at constant pressure for the ambient-air and the gaseous fuel, l is the fuel latent heat of evaporation,

---

[18] As characterized by the fuel distillation curve. Consequently fuel volatility is correlated to boiling point.

and T_a, T_F and T_{bn} are the ambient air temperature, the injected fuel temperature and the boiling temperature of the fuel,

- the injector orifice diameter, d_h,
- the injector orifice aspect ratio.

The engineering correlation giving the liquid-phase penetration length, L_{ec}, takes the form :

$$\frac{L_{ec}}{d_h} = k \cdot \widehat{\rho}^{\alpha} \cdot B^{-\beta} \tag{2.38}$$

where k, α and β are constant coefficients determined in order to have the best fit of the experimental data[19] and their values are 10.5 ,0.58 and 0.59, respectively. The correlation is able to give reliable results with a standard deviation of 12%. In order to show that the computed penetration lengths computed with the liquid-phase penetration model are quantitatively correct, equation 2.38 is now used with the aim of having an estimate of the order of magnitude of those penetrations for normal heptane. Physical data [72] and geometrical specifications of the computation are reported in table 2.3. The result obtained using the engineering correlation, equation 2.38, is $L_{ec} = 15.1 \pm 1.8$ mm while the result given by the liquid-phase penetration model, equation 2.35, is $L = 17.4$ mm. The slight difference between the two values can be attributed to a different estimation of the orifice aspect ratio influence that impacts the flow coefficients describing the flow through the injector, section 2.4.2. Nevertheless, the two values show that the model is able to correctly predict the liquid penetration length. To conclude this section concerning the liquid-phase penetration length, it is worth mentioning two second order trends concerning the penetration scaling law that have been highlighted in [53]. In particular, the scaling law slightly overestimates liquid lengths at very high and very low

Variable	Unit	Value
d_h	[μm]	200
T_a	[K]	1000
T_F	[K]	330
T_{bn}	[K]	371.6
ρ_a	[kg/m^3]	16
ρ_{F_l}	[kg/m^3]	684
c_{p_a}	[J/kg/K]	1011
c_{p_F}	[J/kg/K]	2576
l	[kJ/kg]	338.6

Table 2.3: Physical data [72] and geometrical specifications used in the liquid-phase penetration length computation for normal heptane.

---

[19] Best values of the constant coefficients k, α and β can slightly vary as function of the injector aspect-ratio value.

ambient-air temperature, T_a, and density, ρ_a. The reasons of those deviations have been found to be related to :

- for high T_a and ρ_a conditions : the hypotheses of perfect gas and neglecting the gas dissolution in liquid do not completely apply. Those kind of conditions are typical of high load engine operating points,
- for low T_a and ρ_a conditions : the hypothesis of considering the turbulent mixing the only limiting factor to vaporization is not completely justified : other phenomena related to local transport processes at droplet surface ultimately begin controlling fuel vaporization. Those kind of conditions are typical of cold start engine operating points.

Cold engine operating points present some peculiarities when compared to hot engine operating points such as :

- liquid jet/combustion chamber wall impingement, and formation of a fuel liquid film,
- irregular crankshaft speed,
- very low ambient gas temperature and consequent slowdown of chemical kinetics,
- high equivalence ratios,
- heating plug influence on ignition,

that represent new challenges for numerical modeling and are beyond the purposes of dual-CM.

2.4.1.3 Fuel mass evaporation rate

This section deals with the computation of the overall evaporation rate within the spray region, $\dot{m}_F$. It represents the last modeling step for completely fulfilling the set up evaporation-model requirements, figure 2.7. In order to do that, the approach developed in [12] has been retained. This approach is based on the theory developed in [55] (presented in section 2.4.2) which provides a non-dimensional scaling law, relating the gaseous-phase tip penetration of a Diesel spray with time. According to experiments [55, 52], the gaseous-phase tip penetration is initially coincident with the liquid-phase tip penetration. Once the liquid-phase tip penetration reaches its maximum extent, it stabilizes about this value, while the gaseous-phase tip penetration continues to grow according to the scaling law. The original approach proposed in [12] consists in obtaining an estimate of the evaporation characteristic-time, τ_{ev}, by inverting the gaseous-phase tip penetration scaling law, once the penetration length is coincident with the steady liquid penetration length, L. This time is representative of the interval necessary for the injected mass to completely evaporate. The relation between the reduced time, $\widetilde{t}$, and the reduced penetration length, $\widetilde{x}$, is :

$$\widetilde{t} = \frac{\widetilde{x}}{2} + \frac{\widetilde{x}}{4} \cdot \sqrt{1 + 16 \cdot \widetilde{x}^2} + \frac{1}{16} \cdot \ln\left(4 \cdot \widetilde{x} + \sqrt{1 + 16 \cdot \widetilde{x}^2}\right) \tag{2.39}$$

where $\widetilde{x}$ is defined in equation 2.30, $\widetilde{t}$ is defined as :

$$\widetilde{t} = \frac{t}{t^+} \tag{2.40}$$

in which :

$$t^+ = \frac{x^+}{u_F} \tag{2.41}$$

where x^+ is defined by equation 2.31 and u_F is the fuel velocity at the orifice exit[20] $(u_F = u\,(0))$. Consequently, for a penetration length $\widetilde{x} = \widetilde{L}$ equation 2.39 gives a reduced evaporation characteristic time, $\widetilde{\tau}_{ev}$, equal to :

$$\widetilde{\tau}_{ev} = \frac{\widetilde{L}}{2} + \frac{\widetilde{L}}{4} \cdot \sqrt{1 + 16 \cdot \widetilde{L}^2} + \frac{1}{16} \cdot \ln\left(4 \cdot \widetilde{L} + \sqrt{1 + 16 \cdot \widetilde{L}^2}\right) \tag{2.42}$$

that corresponds to a physical evaporation characteristic time, τ_{ev} :

$$\tau_{ev} = \widetilde{\tau}_{ev} \cdot t^+ \tag{2.43}$$

Figure 2.31 shows the variation of the computed physical evaporation characteristic time with the ambient air temperature and density. The boundary conditions are those used in figure 2.23. The trends show that physical evaporation characteristic time decreases with an increase in the ambient air temperature. It also decreases with an increase in the ambient air density. These results are coherent with those shown in figure 2.23. As seen in figure 2.31, the variations of τ_{ev} are relatively small on the investigated domain. The overall liquid-mass evaporation-rate has then been estimated by using the following first order model expression :

$$\dot{m}_F = C_{ev} \cdot \frac{m_{F_l}}{\tau_{ev}} \tag{2.44}$$

where C_{ev} is a dimensionless adjustment coefficient, here set to unity, and m_{F_l} is the total liquid mass of fuel present in the spray. This model requires a very reduced CPU time. It is validated in chapters 3 and 4 by comparing its outputs to a 3D CFD code IFP-C3D [73].

---

[20] For more information concerning the procedure to compute u_F, refer to section 2.4.2.1.

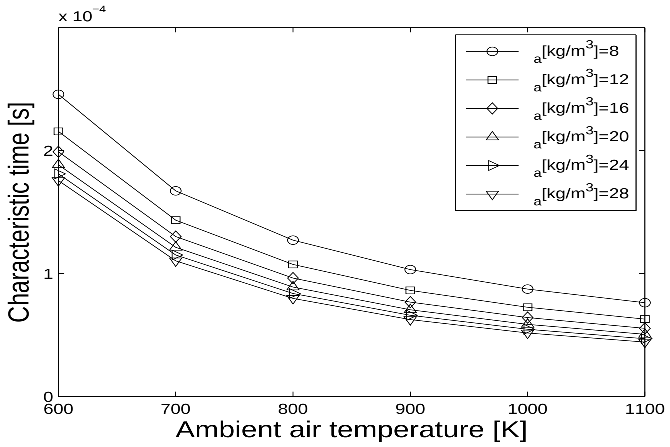

Figure 2.31: Computed evaporation characteristic-time variations as function of ambient air temperature and density (legend).

2.4.2 Gas entrainment submodel

In this section, modeling of the gas entrainment phenomenon in a spray is discussed. Section 2.4.2.1 discusses the impact of the pressure drop through the injector orifice on the gas entrainment process. Section 2.4.2.2 describes a formalism able to take into account the entrainment of ambient air in a Diesel engine spray. Finally in section 2.4.2.3, the extension of the model to multiple injection strategies is detailed.

2.4.2.1 Injector orifice performance

In order to describe the air entrainment, it is important to estimate both the mass and momentum flow rates from an orifice. This implies characterizing the injector orifice performance [53]. The three coefficients that permit to describe the flow through the injector orifice are :

C_d the discharge coefficient[21], it accounts for global charge-loss through an injector orifice,

C_a the area contraction coefficient[22], it accounts for loss of flow area in an orifice due

---

[21] In [53] the discharge coefficient was measured by the standard method of collecting and weighing fuel, Δm_{F_l}, injected over a period of time, Δt :

$$C_d = \frac{\Delta m_{F_l}}{\Delta t \cdot \left(\frac{d_h^2}{4}\right) \cdot \rho_{F_l} \cdot \sqrt{2 \cdot \frac{\Delta p}{\rho_{F_l}}}}$$

This was done both at low pressure and typical Diesel engine injection pressure. The measurements at the two pressures agreed within 2%.

[22] In [53] the area contraction coefficient was determined from spray momentum, $\dot{M}_{F_l}$, measured with a force transducer by using the following equation :

$$C_a = 2 \cdot \left(\frac{d_h^2}{4}\right) \cdot C_d^2 \cdot \frac{\Delta p}{\dot{M}_{F_l}}$$

to the presence of bubbles of cavitation at the orifice exit,

C_v the velocity coefficient[23], it accounts for the non-uniform velocity profile.

They are not independent and are related by the following equation :

$$C_d = C_a \cdot C_v \tag{2.45}$$

Any two of the three coefficients can be used to characterize the mass and momentum flows through an orifice. For instance, using C_a and C_v, the mass flow rate, $\dot{m}_{F_l}$, and momentum flow rate, $\dot{M}_{F_l}$, through an orifice of diameter d_h are computed respectively as :

$$\dot{m}_{F_l} = C_a \cdot \left(\frac{\pi \cdot d_h^2}{4} \right) \cdot \rho_{F_l} \cdot C_v \cdot u_B \tag{2.46}$$

$$\dot{M}_{F_l} = \dot{m}_{F_l} \cdot C_v \cdot u_B \tag{2.47}$$

where u_B is the velocity computed using Bernoulli's equation.

u_B represents the maximum potential velocity at the exit of an orifice and is computed as :

$$u_B = \sqrt{\frac{2 \cdot (\Delta p)}{\rho_{F_l}}} \tag{2.48}$$

where Δp is the fluid pressure drop through the orifice. The real mean fluid velocity at the injector exit is :

$$u_F = C_v \cdot u_B \tag{2.49}$$

Figure 2.32 shows C_d, C_a and C_v as function of the pressure drop through an injector orifice having a diameter of 267 μm and an aspect ratio of 8 : C_a decreases with increasing injection pressure, while C_d remains nearly constant. This means the flow area decreases as injection pressure increases, most likely as a result of increasing cavitation. Moreover, the corresponding increase in C_v indicates that fluid velocity at the orifice exit approaches the Bernoulli's velocity, equation 2.48. In all computations performed in this document, values of C_a and C_v were chosen to be 0.82 and 0.93, respectively, and kept constant. As shown in figure 2.32, those values well characterize the injector orifice in a range of pressure drops through the nozzle orifice from 1000 to 1600 bar.

2.4.2.2 Gas entrainment modeling

The aim of the gas entrainment submodel is to quantify, relatively to the spray region volume, the incoming ambient air[24] mass flow rate. The spray region is defined as the volume where, locally, ambient air and fuel coexist. It is important to describe the characteristics of the spray region because it is in this volume where reactive mixture

---

[23] In [53] the velocity coefficient was obtained by using equation 2.45.

[24] Ambient air in the most general case is a perfectly stirred mixture of pure air and EGR.

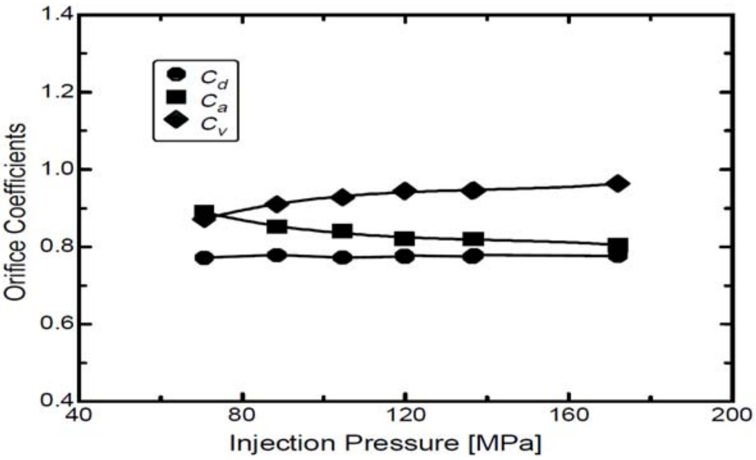

Figure 2.32: Experimental data for orifice discharge coefficient (C_d), area-contraction coefficient (C_a) and velocity coefficient (C_v) versus pressure drop through the injector orifice. Orifice diameter and aspect-ratio values are 267 μm and 8 respectively [53].

forms. As shown in section 2.4.1.2, knowing the entrained ambient air flow rate is important because the dynamics of the evaporation process depend on it. Moreover, it is important to know the total entrained ambient air mass because it is an essential information for computing the mean composition of the spray mixture. In fact, in terms of equivalence ratio, the mean composition within the spray can be expressed as[25] :

$$\widetilde{\Phi} = \frac{\frac{m_{F_\tau}}{m_S}}{\left(1 - \frac{m_{F_\tau}}{m_S}\right) \cdot (1 - Y_D|_a)} \cdot \left(\frac{A}{F}\right)_{st} \tag{2.50}$$

where $\widetilde{\Phi}$ is the mean equivalence ratio, m_{F_τ} is the tracer mass of fuel within the spray[26], the term $(A/F)_{st}$ represents the mass Air/Fuel ratio at stoichiometric conditions [6], and $Y_D|_a$ represents the mass fraction of Burned Gases (BG) conditioned to ambient gas, defined as :

$$Y_D|_a = \frac{m_D}{m_D + m_{pa}} \tag{2.51}$$

in which m_D is the mass of BG and m_{pa} is the mass of pure air. Here, the BG are supposed to be at stoichiometric composition, and neutral with respect to combustion. Experimental investigations [55] for a wide range of operating conditions describe the effect of ambient gas and fuel vaporization on the gaseous penetration and dispersion of Diesel sprays. Injections were performed in a constant-volume combustion vessel using a high pressure injection system for non-vaporizing and vaporizing ambient gas conditions[27]. For instance, figure 2.33 shows three different sprays relative to three different ambient air density values. The outer boundaries and the cone angle of the

---

[25] This formula adapts well to the most general situation in which ambient air is a perfectly stirred mixture of pure air and EGR.

[26] The adjective *tracer* in this dissertation is used as a synonymous of *combustion independent*. In the specific, it represents the total mass of vaporized fuel in the spray.

[27] Non-vaporizing conditions refer to ambient air temperature lower than 450 K, while vaporizing conditions refer to ambient gas temperature higher than 600 K.

dark region are the time averaged outer boundaries and spreading angle of the gaseous phase of the spray, respectively, while the bright region within the dark region is the time averaged liquid phase of the spray. The three images in figure 2.33 demonstrate that the liquid region in a vaporizing spray occupies a decreasing fraction of the spray cross-sectional area with increasing axial distance and that it has a limited axial extent. The experimental opening angle, θ, is independent of axial location and time [55]. Moreover, the spreading angle has been found to be mostly dependent on :

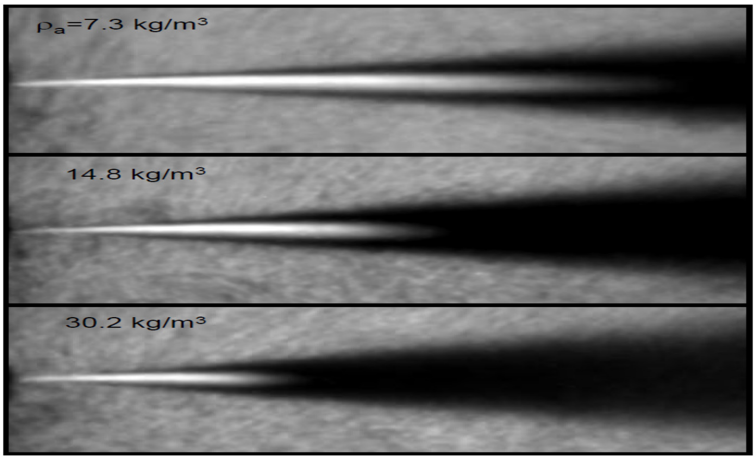

Figure 2.33: Experimental time-averaged Mie-scattered light images of gaseous-phase and liquid-phase penetrations for three sprays injected from left to right into the ambient gas density (ρ_a), given in each image. Test conditions are those used in figure 2.13. The orifice pressure drop and diameter, the ambient gas temperature, the fuel temperature, and the fuel were 1350 bar, 246 μm, 1000 K, 438 K and DF2, respectively [52].

- the ambient air/fuel density ratio,
- the orifice geometrical parameters.

It is independent of the fuel type, injection pressure and ambient air temperature. More details concerning the mathematical correlation relating the measured opening angle to influent factors can be found in section 2.4.1.2, equation 2.17. Figure 2.34 is a schematic of a simplified gaseous spray. As can be seen, the gaseous spray is considered to be a perfect truncated cone whose height, S, and opening angle, α represent the gaseous-phase tip penetration and spreading angle of the spray. The relation between the measured and the idealized spreading angle is explicit in equation 2.18 : the spray volume is completely defined once S and α are fixed. As the flow is supposed to be self-preserving, a constant spreading angle value implies that the rate of entrained air along the spray is constant; that is, the mass in the spray grows linearly with axial distance. With reference to figure 2.34, at a given x of the axial spray coordinate, the ambient air mass flow rate through the corresponding spray cross section, $\dot{\mathbf{m}}_a\left(x\right)$, is found to be directly

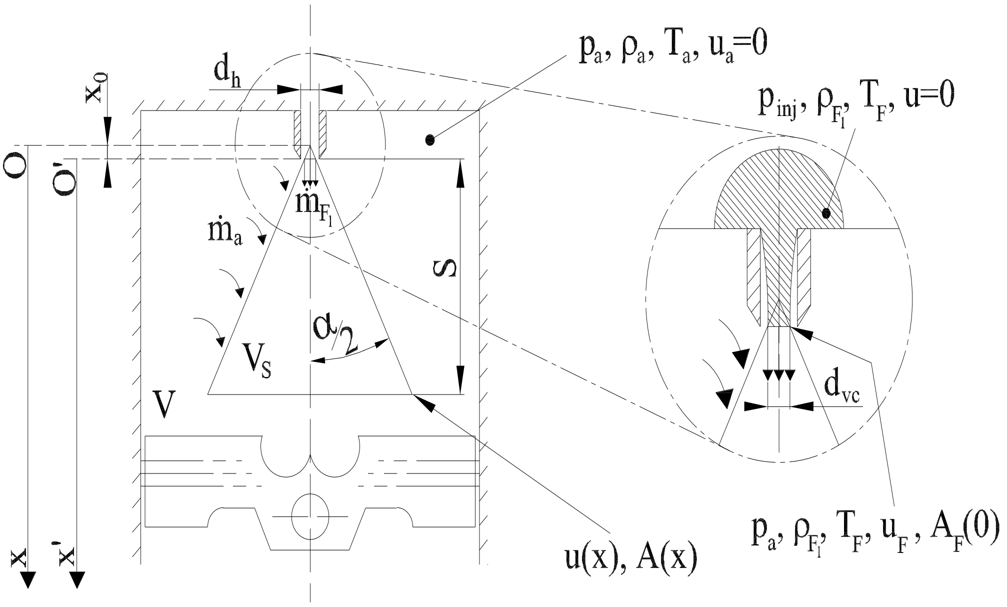

Figure 2.34: Gaseous spray model scheme [55].

proportional to the following variables :

$$\dot{\mathbf{m}}_a\left(x\right) \propto \sqrt{\rho_a \cdot \rho_{F_l}} \cdot d_h \cdot x \cdot u_F \cdot \tan\left(\frac{\theta}{2}\right) \tag{2.52}$$

Equation 2.52 and 2.17 reveal that consequently to an increase of ambient-air density, the entrained ambient-air mass flow rate grows for two reasons :

- the ambient-air density increase,
- the spreading angle increase.

On the schematic representation of a spray shown in figure 2.34, a model for the description of the gaseous-phase penetration length was derived by using an integral control surface technique applicable to isothermal-incompressible jets and sprays, in which injected and ambient fluids can be any combination of high and low density fluids [55]. The following assumptions were used :

- a uniform velocity profile at a given cross-section,
- constant injection velocity with an instantaneous start,
- no velocity slip between fuel and entrained air,
- quasi steady flow with constant growth rate (constant spreading angle).

The fuel-mass and overall momentum balance-equations are, respectively :

$$\rho_{F_l} \cdot A_F\left(0\right) \cdot u_F = \rho_F \cdot A_F\left(x\right) \cdot u\left(x\right) \tag{2.53}$$

and :

$$\rho_{F_l} \cdot A_F(0) \cdot u_F^2 = \rho_F \cdot A_F(x) \cdot u(x)^2 + \rho_a \cdot A_a(x) \cdot u(x)^2 \tag{2.54}$$

where $A_F(x)$ and $A_a(x)$ are the cross-sectional areas occupied by the fuel and ambient air at a given value of penetration, x. $A_F(x)$ and $A_a(x)$ are related to the total cross-sectional area $A(x)$ at the location x in the spray by the following equation :

$$A(x) = A_a(x) + m \cdot A_F(x) \tag{2.55}$$

where m is 0 or 1 depending on whether the fuel cross-sectional area is neglected or accounted for, respectively. Combining equations 2.53 to 2.55 and solving for the fluid velocity, $u(x)$, at a given spray location, x :

$$u(x) = \frac{dx}{dt} = \frac{u_F}{2} \cdot \frac{A_F(0)}{A(x)} \cdot \left(\frac{\rho_{F_l}}{\rho_a} - m\right) \cdot \left(\sqrt{1 + 4 \cdot \frac{\frac{A(x)}{A_F(0)} \cdot \frac{\rho_{F_l}}{\rho_a}}{\left(\frac{\rho_{F_l}}{\rho_a} - m\right)^2}} - 1\right) \tag{2.56}$$

By using the definitions given in equations 2.17, 2.18, 2.23, 2.48 and 2.49, introducing the following definitions :

$$x_0 = \frac{m}{2} \cdot \frac{d_{vc}}{\tan\left(\frac{\alpha}{2}\right)} \tag{2.57}$$

$$x' = x + x_0 \tag{2.58}$$

$$\frac{dx'}{dt'} = \frac{dx}{dt} = u(x) \tag{2.59}$$

$$A(x) = \pi \cdot \left(x' \cdot \tan\left(\frac{\alpha}{2}\right)\right)^2 \tag{2.60}$$

$$A_F(0) = \frac{\pi}{4} \cdot d_{vc}^2 \tag{2.61}$$

and defining the spatial and temporal characteristic dimensionless variables as :

$$\widehat{\rho} = \frac{\rho_{F_l}}{\rho_a} \tag{2.62}$$

$$\widetilde{x} = \frac{x'}{x^+} \tag{2.63}$$

$$\widetilde{t} = \frac{t'}{t^+} \tag{2.64}$$

where x^+ and t^+ are the spatial and temporal scaling parameters defined, respectively, as :

$$x^+ = d_{vc} \cdot \sqrt{\widehat{\rho}} \cdot \left(\frac{\widehat{\rho} - m}{\widehat{\rho}}\right) \cdot \frac{1}{\tan\left(\frac{\alpha}{2}\right)} \tag{2.65}$$

$$t^+ = d_{vc} \cdot \sqrt{\widehat{\rho}} \cdot \left(\frac{\widehat{\rho} - m}{\widehat{\rho}}\right)^2 \cdot \frac{1}{u_F \cdot \tan\left(\frac{\alpha}{2}\right)} \tag{2.66}$$

then equation 2.56 simplifies to :

$$\widetilde{u}(\widetilde{x}) = \frac{d\widetilde{x}}{d\widetilde{t}} = \frac{2}{\sqrt{1 + 16 \cdot \widetilde{x}^2} + 1} \tag{2.67}$$

Finally, integrating equation 2.56 between $\widetilde{x}=0$ and $\widetilde{x}=\widetilde{S}$, where :

$$\widetilde{S}=\frac{S'}{x^{+}} \tag{2.68}$$

with S' the spray tip location relative to the projected origin, figure 2.34, yields the dimensionless penetration time, $\widetilde{t}$, as a function of the dimensionless penetration distance, $\widetilde{S}$, both referenced to the projected spray origin :

$$\begin{aligned}\widetilde{t} \;&=\; \frac{\widetilde{S}}{2}+\frac{\widetilde{S}}{4}\cdot\sqrt{1+16\cdot\widetilde{S}^{2}}\;+\\ &\;+\frac{1}{16}\cdot\ln\left(4\cdot\widetilde{S}+\sqrt{1+16\cdot\widetilde{S}^{2}}\right)\end{aligned} \tag{2.69}$$

In the above equations, x' and t' are the spatial and temporal physical coordinates referred to the projected origin of the spray, and $\widetilde{x}$ and $\widetilde{t}$ are the spatial and temporal non-dimensional coordinates. An accurate inverse correlation, allowing us to compute the value of $\widetilde{S}$ as function of $\widetilde{t}$, is obtained by combining the equations of the two asymptotical limits of equation 2.69, equations 2.4.2.2 and 2.4.2.2 :

$$\widetilde{S}=\left(\left(\frac{1}{\widetilde{t}}\right)^{n}+\left(\frac{1}{\sqrt{\widetilde{t}}}\right)^{n}\right)^{-\frac{1}{n}}=\frac{\widetilde{t}}{\left(1+\widetilde{t}^{\frac{n}{2}}\right)^{\frac{1}{n}}} \tag{2.70}$$

where n is a constant coefficient. Authors recommend $n=2.2$. It is worth a comment on the coefficient m introduced in equation 2.55. If its value is set equal to unity the cross-sectional area occupied by the fuel is not neglected. Consequently :

- as the projected origin is positioned inside the nozzle orifice, $x'=0$, in order to obtain the right values of spatial and temporal evolution of the spray penetration within the combustion chamber, the computed values of penetration and associated time interval, must be reduced of the values x_0 and t_0, respectively, where x_0 is defined in equation 2.57 and t_0 is the time that the fluid needs to cover the distance x_0,

- because of the model simplifications, if the spray origin is positioned at $x'=0$, the liquid fuel, passing through the length interval x_0, entrains ambient air and this is not physical. Moreover, as a direct consequence, the gaseous mixture crosses the orifice exit with a velocity lower than the original injection velocity (momentum balance).

As a consequence, another assumption was introduced [55] : the cross-sectional area occupied by the fuel is neglected. This assumption implies that in the above equations, the value of the coefficient m is set equal to zero. The repercussions of this assumption on the model results are that :

- the computed gaseous spray tip penetration has its origin at $x = 0$, that is at the very exit of the nozzle orifice, figure 2.34,
- the injected fuel is treated as a point source of momentum.

Figure 2.35 shows the logarithmic plot of the correlation in equation 2.69. The solid line represents the correlation law, the dash-dotted lines represent asymptotic limits and dashed lines represent the ±10% of deviation from the correlation, representing the uncertainty due to turbulent aleatory effects. An asymptotical investigation of equation 2.69 shows that the trends which were observed experimentally in [43] are correctly taken into account :

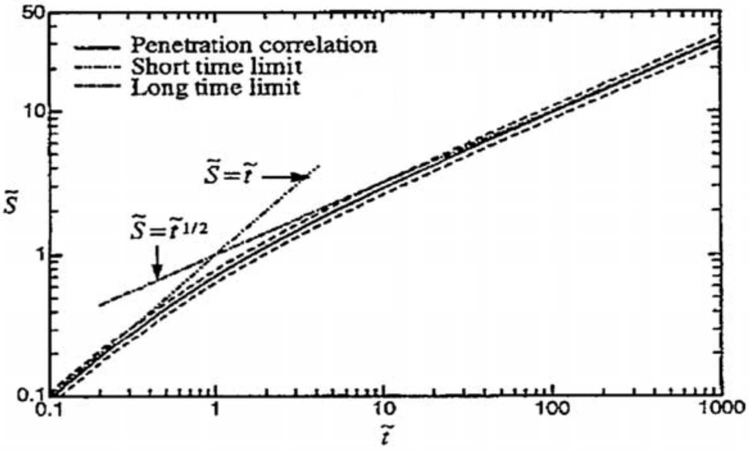

Figure 2.35: The dimensionless penetration correlation given in equation 2.69 (solid line), deviations of ±10% (dashed lines) and asymptotic limits (dash-dotted lines) [55].

- short time limit :

  $$\text{Limit } \widetilde{t} \to 0 \Longrightarrow \widetilde{S} = \widetilde{t}$$

  this shows a linear dependence on time of the spray penetration during the first instants of the injection,

- long time limit :

  $$\text{Limit } \widetilde{t} \to +\infty \Longrightarrow \widetilde{S} = \sqrt{\widetilde{t}}$$

  this shows a square root dependence on time of the spray penetration as in gaseous-jets, after a sufficiently long period of time.

Figure 2.36 shows experimental-data compared to the scaling law given in equation 2.69 : the penetration correlation fits the experimental points. The value of the physical gaseous spray tip penetration can finally be computed using equation 2.68 as :

$$S \equiv S' = \widetilde{S} \cdot x^{+} \tag{2.71}$$

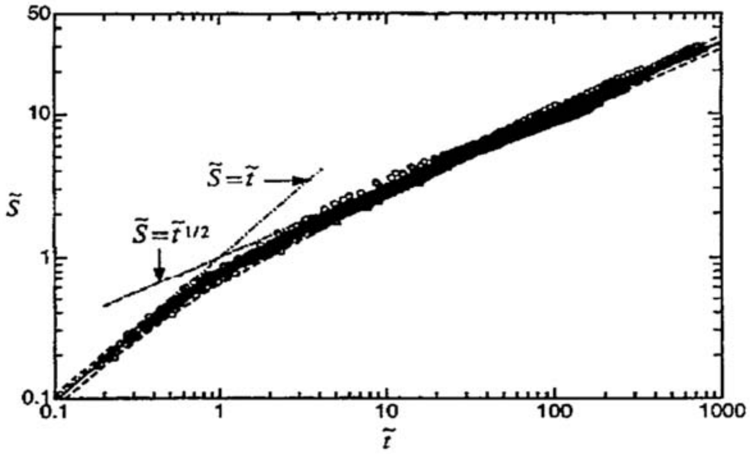

Figure 2.36: Scattered plot of a large amount of gaseous penetration experimental data versus time in non-dimensional logarithmic coordinates (circles) compared to dimensionless penetration correlation given in equation 2.69 (solid line). Deviations of ±10% from correlation (dashed lines) and asymptotic limits (dash-dotted lines) are plotted, too [55].

Through experimentation of injection in a constant volume vessel containing a gas at a given pressure and temperature, equations 2.17 and 2.71 correlations have been widely validated [20, 42, 55, 56]. In order to validate the model of gaseous spray tip penetration, Diesel-like injections of normal heptane in a closed pressurized constant-volume vessel were simulated. Computed results were then compared to experiments [42]. Figures 2.37 and 2.38 compare the computed spray penetrations with experimental data obtained in a high pressure vessel [42] for low and high ambient-air temperature conditions, respectively.

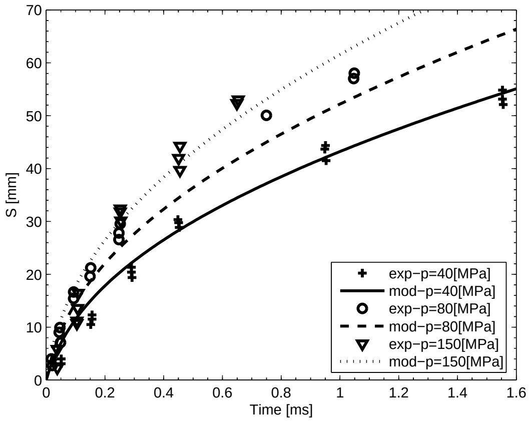

Figure 2.37: Gaseous-phase spray tip penetration. Experimental conditions : fuel = n-heptane, $T_a = 387$ K, $\rho_a = 25$ kg/m^3 and $d_h = 200$ μm.

The results are in good agreement with experiments : the model is sensitive to parameters such as injection pressure and the thermodynamic state of the ambient gas. According to the simplified spray model, figure 2.34, the spray region is represented by a truncated cone characterized by its height, S, and opening angle, α. From geometrical

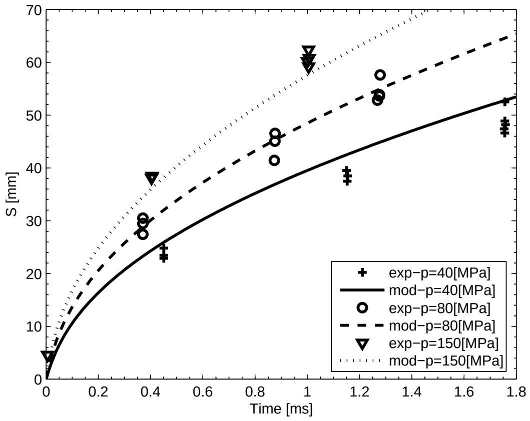

Figure 2.38: Gaseous-phase spray tip penetration. Experimental conditions : fuel = n-heptane, $T_a = 800$ K, $\rho_a = 30$ kg/m^3 and $d_h = 200$ μm.

considerations, the volume of the spray, V_{S_h}, is computed as :

$$V_{S_h} = \frac{\pi}{3} \cdot \tan^2\left(\frac{\alpha}{2}\right) \cdot \left[(S + x_0)^3 - x_0^3\right] \tag{2.72}$$

In ICEs every single injector can have several orifices (up to twelve) disposed on a circumference coaxial with the nozzle axis, section 1.1.2. The number of orifices will be indicated in the following with the notation n_h. With the assumption that all the injection cones of the different orifices have the same identical behaviour[28], the overall spray volume, V_S, is computed as :

$$V_S = n_h \cdot V_{S_h} = n_h \cdot \frac{\pi}{3} \cdot \tan^2\left(\frac{\alpha}{2}\right) \cdot \left[(S + x_0)^3 - x_0^3\right] \tag{2.73}$$

The ambient air mass within the spray volume, m_a, is considered to be, in the most general situation, a perfectly stirred mixture of pure air mass, m_{pa}, and BG, m_D. On the basis of geometrical considerations regarding the spray volume evolution, equation 2.73, it is possible to quantify the ambient-gas mass flow rate into the spray region due to entrainment :

$$\frac{dm_a}{dt} = \sum_x \left.\frac{dm_x}{dt}\right|_{entr} \tag{2.74}$$

where :

$$\left.\frac{dm_x}{dt}\right|_{entr} = \rho_{x0} \cdot \frac{dV_S}{dt} = \rho_{x0} \cdot \dot{V}_S \tag{2.75}$$

in which $\dot{V}_S$ is the time derivative of the spray volume, V_S, and ρ_{x0} is the partial density of the species x outside the spray region computed as :

$$\rho_{x0} = \frac{m_{x0}}{V - V_S} \tag{2.76}$$

---

[28] The interactions between the injection cones of the different orifices are not taken into account.

where m_{x_0} is the mass of the species x outside the spray regions and V is the cylinder volume. $\dot{V}_S$, obtained by deriving equation 2.73, is computed as :

$$\begin{aligned}\frac{dV_S}{dt} &= \frac{a^2 \cdot \pi \cdot n_h}{3} \cdot \Bigg[\left(3 + (S+x_0)^2 \cdot \left(\frac{dS}{dt} + \frac{dx_0}{dt}\right) - 3 \cdot x_0^2 \cdot \frac{dx_0}{dt}\right) \cdot \tan^2\left(\frac{\theta}{2}\right) + \\ &\quad + \left((S+x_0)^3 - x_0^3\right) \cdot 2 \cdot \tan\left(\frac{\theta}{2}\right) \cdot \frac{d}{dt}\left(\tan\left(\frac{\theta}{2}\right)\right)\Bigg] \qquad (2.77)\end{aligned}$$

where :

$$\begin{aligned}\frac{dS}{dt} = \frac{d(\tilde{S} \cdot x^+)}{dt} &= C_s \cdot \left[\frac{d}{dt}\left((t-t_0) \cdot u_F\right) \cdot \left(1 + \left(\frac{t-t_0}{x^+} \cdot u_F\right)^{\frac{n}{2}}\right)^{-\frac{1}{n}} + \right. \\ &\quad \left. + (t-t_0) \cdot u_F \cdot \frac{d}{dt}\left(\left(1 + \left(\frac{t-t_0}{x^+} \cdot u_F\right)^{\frac{n}{2}}\right)^{-\frac{1}{n}}\right)\right] \qquad (2.78)\end{aligned}$$

$$\frac{dx_0}{dt} = \frac{d}{dt}\left(\frac{d_{vc}}{2 \cdot a \cdot \tan\left(\frac{\theta}{2}\right)}\right) = -\frac{d_{vc}}{2 \cdot a \cdot \tan^2\left(\frac{\theta}{2}\right)} \cdot \frac{d}{dt}\left(\tan\left(\frac{\theta}{2}\right)\right) \qquad (2.79)$$

$$\begin{aligned}\frac{d}{dt}\left(\tan\left(\frac{\theta}{2}\right)\right) &= \frac{d}{dt}\left(c \cdot \left(\left(\frac{\rho_a}{\rho_{F_l}}\right)^{0.19} - 0.0043 \cdot \sqrt{\frac{\rho_a}{\rho_{F_l}}}\right)\right) \\ &= c \cdot \left(0.19 \cdot \rho_{F_l}^{-0.19} \cdot \rho_a^{-0.81} \cdot \frac{d\rho_a}{dt} + \frac{0.0043}{2} \cdot \rho_{F_l}^{0.5} \cdot \rho_a^{-1.5} \cdot \frac{\rho_a}{dt}\right) \qquad (2.80)\end{aligned}$$

in which :

$$\begin{aligned}\frac{d}{dt}\left((t-t_0) \cdot u_F\right) &= u_F + (t-t_0) \cdot \frac{d}{dt}\left(C_v \cdot \left(2 \cdot \frac{p_{inj} - p}{\rho_{F_l}}\right)^{\frac{1}{2}}\right) \\ &= u_F - \frac{C_v \cdot (t-t_0)}{\left(2 \cdot (p_{inj} - p) \cdot \rho_{F_l}\right)^{\frac{1}{2}}} \cdot \frac{dp}{dt} \qquad (2.81)\end{aligned}$$

$$\begin{aligned}\frac{d}{dt}\left(\left[1 + \left(\tfrac{(t-t_0) \cdot u_F}{x^+}\right)^{\frac{n}{2}}\right]^{-\frac{1}{n}}\right) &= -\tfrac{1}{2} \cdot \left[1 + \left(\tfrac{(t-t_0) \cdot u_F}{x^+}\right)^{\frac{n}{2}}\right]^{-\frac{1}{n}-1} \cdot \\ &\quad \cdot \left(\tfrac{(t-t_0) \cdot u_F}{x^+}\right)^{\frac{n}{2}-1} \cdot \left(\tfrac{1}{x^+} \cdot \tfrac{d}{dt}\left((t-t_0) \cdot u_F\right) - \tfrac{(t-t_0) \cdot u_F}{x^+}^2 \cdot \tfrac{dx^+}{dt}\right) \\ &= -\tfrac{1}{2} \cdot \left[1 + \tilde{t}^{\frac{n}{2}}\right]^{-\frac{1}{n}-1} \cdot \tilde{t}^{\frac{n}{2}-1} \cdot \left(\tfrac{1}{x^+} \cdot \tfrac{d}{dt}\left((t-t_0) \cdot u_F\right) + \right. \\ &\quad \left. - \tfrac{1}{{x^+}^2} \cdot (t-t_0) \cdot u_F \cdot \tfrac{dx^+}{dt}\right) \qquad (2.82)\end{aligned}$$

$$\begin{aligned}\frac{dx^+}{dt} &= \frac{d}{dt}\left(\frac{d_{vc} \cdot \sqrt{\frac{\rho_{F_l}}{\rho_a}}}{a \cdot \tan\left(\frac{\theta}{2}\right)}\right) = \frac{\sqrt{\rho_{F_l}} \cdot d_{vc}}{a} \cdot \frac{d}{dt}\left(\frac{1}{\sqrt{\rho_a} \cdot \tan\left(\frac{\theta}{2}\right)}\right) \\ &= -\frac{\sqrt{\rho_{F_l}} \cdot d_{vc}}{a} \cdot \frac{\frac{\tan\left(\frac{\theta}{2}\right)}{2 \cdot \sqrt{\rho_a}} \cdot \frac{d\rho_a}{dt} + \sqrt{\rho_a} \cdot \frac{d}{dt}\left(\tan\left(\frac{\theta}{2}\right)\right)}{\left(\sqrt{\rho_a} \cdot \tan\left(\frac{\theta}{2}\right)\right)^2} \qquad (2.83)\end{aligned}$$

and :

$$\begin{aligned}\frac{d\rho_a}{dt} &= \frac{d}{dt}\left(\frac{m_{tot}}{V}\right) = \frac{dm_{tot}}{dt}\cdot\frac{1}{V} - \frac{m_{tot}}{V^2}\cdot\frac{dV}{dt}\\ &= \left(\frac{dm^{i/o}}{dt} + \frac{dm_{F_\tau}}{dt}\right)\cdot\frac{1}{V} - \frac{m_{tot}}{V^2}\cdot\frac{dV}{dt}\\ &= \left(\frac{dm^{i/o}}{dt} + \frac{dm_{F_\tau}}{dt}\right)\cdot\frac{1}{V} - \rho_a\cdot\frac{1}{V}\cdot\frac{dV}{dt} \qquad (2.84)\end{aligned}$$

where t_0 is the origin of the relative time coordinate representing the start of the spray penetration, m_{tot} is the total gaseous mass in the cylinder, and $\frac{dm^{i/o}}{dt}$ represents the fluxes of mass through the inlet and outlet valves, respectively.

Further validations of the developed ambient-gas entrainment submodel in ICE configurations are provided by direct comparison of $3D$ and $0D$ computations, sections 3.4 and 4.

2.4.2.3 Extension of the model to multiple injection strategies

The model of ambient air entrainment into the spray region developed in section 2.4.2.2 applies well to single injection configurations. An extension of the model to multiple injection configurations is proposed here. In ICE simulations, different additional challenges appear when dealing with multiple injection spray dynamics, section 2.2. For instance, when dealing with double injections :

- the former fuel injection modifies the velocity field within the cylinder, consequently the second injection penetration and spreading angle are potentially influenced by this different environment,

- the fuel of the first injection begins to burn in the cylinder before the injection of the second one, and, in general, its combustion process is still in progress when the second injection is performed. This is a complex aspect to manage, especially because :

  - the heat release associated to the first injection fuel combustion modifies the thermodynamic properties of the gas entrained into the second spray zone and, consequently, has an influence on the penetration and on the spreading angle of the second spray,
  - the chemical kinetics associated to the first injection fuel combustion modifies the chemical properties of the ambient-gas entrained into the second spray zone and, consequently, has an impact on the chemical kinetics associated to the second injection event,

- the spray volumes of the two injections sooner or later interact. This interaction must be taken into account as it influences many important aspects relative to combustion. For instance, local fuel concentration and chemical composition of the mixture are fundamental aspects in this sense.

Figure 2.39 shows two opposite ideal spray dynamics for a short dwell-time double-injection strategy : configurations (a) and (b). In configuration (a), after the end of the first injection event, the spray region moves away from the injector tip. Consequently, when the second injection starts, the ambient gases entrained into the second spray-volume do not contain fuel injected during the first injection event. The opposite situation is shown in configuration (b). After the end of the first injection event, the spray region stays close to the injector tip. Therefore, when the second injection starts, the fuel of this is injected into the first spray volume. Thereby, the ambient gases entrained into the second spray volume contain fuel injected during the first injection event, too. Evidently, the presented configurations are simplified to give an idea of the different dynamics that can be expected. Several investigations concerning spray interactions in the case of Diesel-like multiple injection strategies have been published [81, 82, 83]. In order to develop a phenomenological model representative of the physics phenomena that occur when multiple injections are performed, it is important to have a view of the possible scenarios encountered. To do that, in the first instance, a brief description of the differences between single injection and multiple injections in terms of engendered equivalence ratio distributions and velocity fields is presented. Then, the differences between the overall behavior of the first and the second injection sprays for a case of

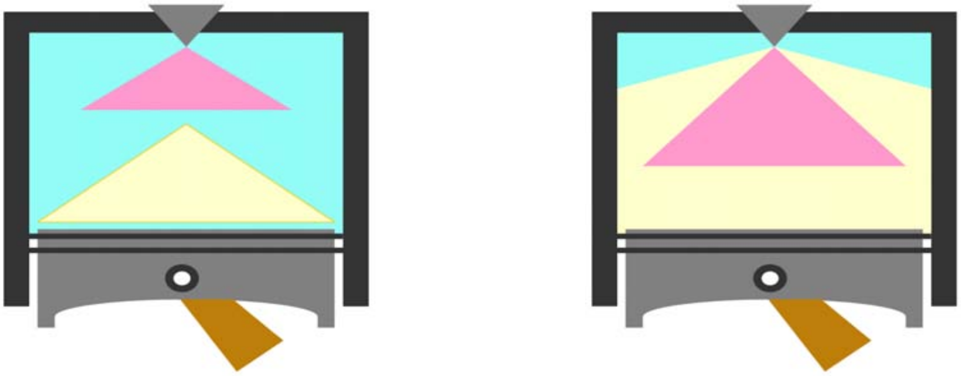

(a) (b)

Figure 2.39: Representation of two opposite spray dynamics for a short dwell-time double-injection strategy. Case (a) : when second injection is performed, first injection spray volume is parted from the injector tip; entrained ambient-air in the second spray does not contain fuel belonging to the first injection. Case (b) : when second injection is performed, first injection spray volume is close to the injector tip; entrained ambient-air in the second spray contains fuel belonging to the first injection.

double injection are given. Figure 2.40 shows three spray images obtained by using a Laser Absorption Spectrometry technique (LAS) [83]. Figure 2.40 (a) defines the tail and the tip of a spray, while figure 2.40 (b) and (c) represent the fuel distribution within the spray region for a single injection and double injection strategies, respectively. In both configurations, the same fuel mass is injected : all together for the single injection, figure 2.40 (b), split into two equal parts for the double injection strategy, figure 2.40 (c). Pictures are taken after the same interval of time, computed starting from the first SOI. Details are given in figure 2.40. As shown in figure 2.40 (b) concerning the spatial fuel distribution, the spray essentially develops by extending its length : fuel accumulates at the leading edge of the spray, due to the air resistance to penetration, while extended lean region of mixture is observed in the spray tail. Moreover, concerning the velocity field generated by the injection, two counter rotating vortices can be distinguished on the left and right of the spray region. Differently in figure 2.40 (c), concerning the spatial fuel distribution, two zones with higher fuel concentration can be distinguished : one relative to the first injection (bottom), and one relative to the second injection (top). Because of the smaller quantity of fuel injected during the first injection, the accumulation of fuel in the tip of the injection is reduced. Furthermore, the lean mixture region in the spray tail disappears because of the second-injection fuel. Finally, when the second injection is performed, the two counter-rotating vorteces generated by the first one still exist and interact with the vorteces generated by the second injection. The global action of turbulence on the second spray contributes to accelerate the evaporation of the

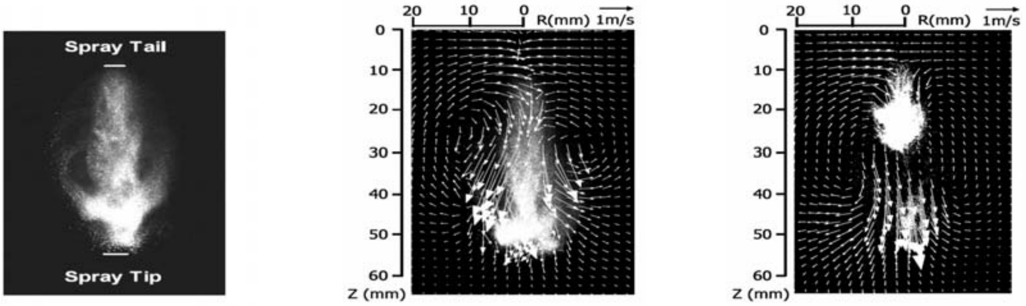

(a) (b) (c)

Figure 2.40: Three spray images obtained by using a Laser Absorption Spectrometry technique (LAS), for fuel distribution visualization, coupled with Laser Induced Fluorescence - Particle Image Velocimetry ($LIF-PIV$), for spray-induced air motion investigation. Injection from the top [83]. In (a), the definitions of tail and tip of the spray are given, while (b) and (c) represent the fuel distribution within the spray region for a single injection and double injection strategies, respectively. For both cases, the total injected fuel ($p-xilene$) mass is 9.4 mg, injection pressure is 4.6 MPa, ambient gas temperature is 300 K, ambient gas pressure is 0.6 MPa. For the single injection, (b), the ET is 1.62 ms, while the two injections of the split strategy, (c), have an energizing time of 0.8 ms and are separated by a DT of 0.7 ms. Pictures are taken 2.5 ms after the first SOI.

second-injection fuel. Due to the positive effect of the ambient air motion, the vapor of the second spray combined with the vapor of the first spray results in a higher and more homogeneous fuel concentration. The same conclusions were drawn up in [82] for split injection Diesel sprays impinging on a flat wall. Figure 2.41 permits us to have a deeper understanding of the spray interaction dynamics.

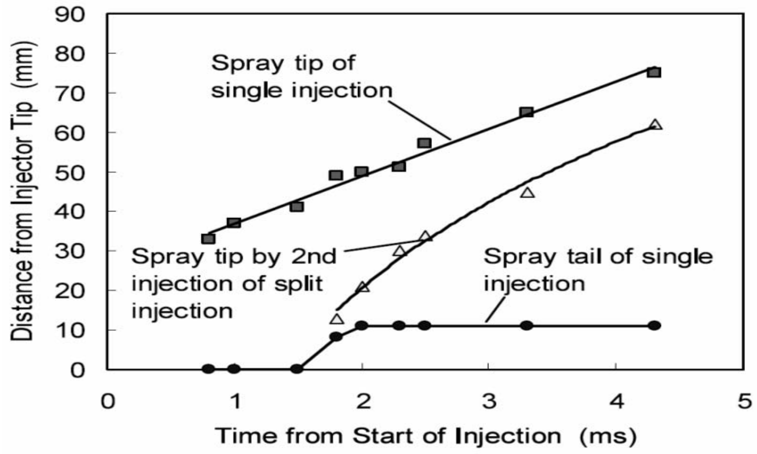

Figure 2.41: Variation of the positions of spray tail and tip of the single injection, and penetration of the tip of the second injection of the split injection [83]. Experimental conditions are given in figure 2.40.

As shown in figure 2.41, the tip penetration of the single injection increases with time, while its tail remains at a constant distance from the injector nozzle, after 1.8 ms. The penetration of the single injection, in a first approximation, is almost the same as that of the first spray of the split injection, figures 2.40 (b) and (c). According to figure 2.41, the tip penetration of the second injection crosses the tail position of the single injection. In other words, the second-injection fuel mass of the split injection is injected into the tail region of the spray of the first injection. For instance, as seen by comparing figures 2.40 (b) and (c) and figure 2.41, after 2.5 ms from the beginning of the first injection, the first injection tip penetration is about 60 mm, while the second-injection tip penetration is about 30 mm. For a case of double injection, the overall differences between the first and the second injection sprays can be expressed in terms of tip penetrations, mean velocities and representative droplet mean-diameters. This last part concerning the investigation of the dynamics of sprays in multiple injection strategies, is focused on capturing the differences between the overall behaviors of the sprays. Figure 2.42 shows how the pilot injection influences the penetration length of the main-injection spray. In figure 2.42, the main-injection tip penetrates faster than the pilot-injection tip. According to [81], this is essentially due to the in-cylinder velocity field generated by the pilot injection, that reduces the resistance to the penetration of the main-injection fuel. Moreover, by using a phase Doppler particle analyzer system,

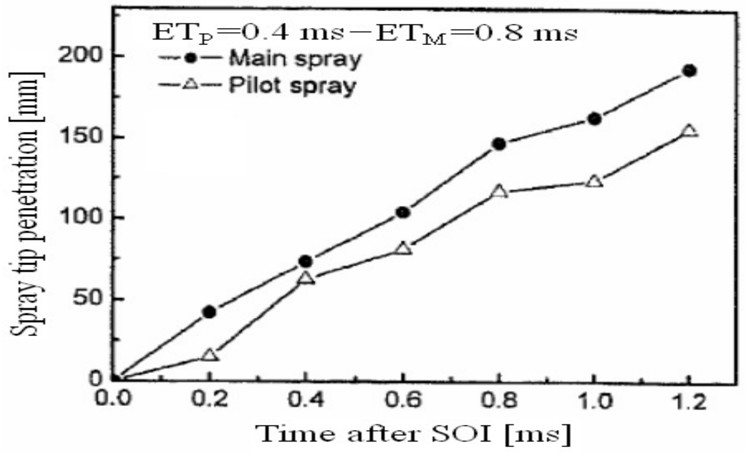

Figure 2.42: Effect of pilot injection on spray tip penetration [81]. The mean velocities of spray tips are 130 m/s and 162 m/s for pilot and main injections, respectively, for an injection pressure of 60 MPa. The pilot injection energizing time, ET_P, and the main injection energizing time, ET_M, are given in the figure.

the evolutions of microscopic characteristics of the spray such as Sauter Mean Diameter (SMD)[29] and mean velocity of droplets where investigated, figure 2.43 [81]. Figure 2.43

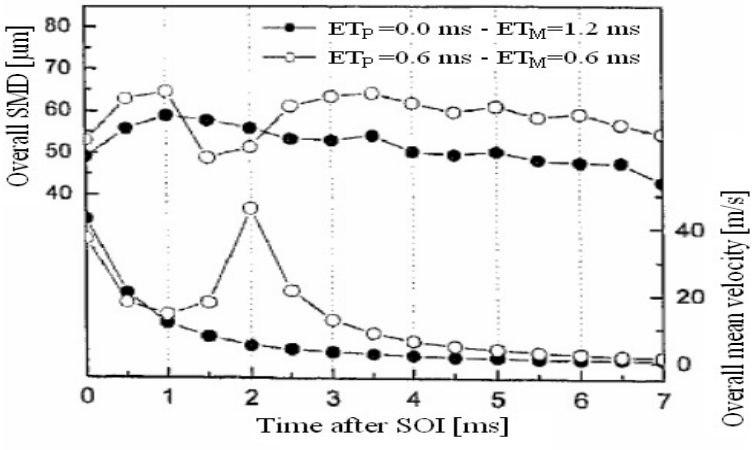

Figure 2.43: Effect of pilot injection on overall SMD and mean velocity [81]. The injection pressure is 60 MPa. Two configurations, relative to a single and a multiple injection strategies, were tested. The pilot injection energizing time, ET_P, and the main injection energizing time, ET_M, are given in the figure.

shows that for the multiple injection strategy, the mean velocity associated to the second injection event is higher than that associated to the first injection : in multiple injection configurations, the first injection generates a velocity field in the chamber that favors the penetration of the following injection. A further confirmation of this phenomenon comes from the information relative to the SMD : $SMDs$ for the multiple injection strategy are larger than for the single injection strategy, because of the smaller relative velocity

---

[29] According to the analysis done in section 2.4.1.2, that is turbulent mixing is the limiting factor for liquid fuel evaporation, information given by SMD measurements in this presentation is not used as an absolute indicator of fuel mass evaporation rate, but instead as a relative indicator used for extrapolating useful information on the spray dynamics.

between injected fuel and ambient gas.

On the basis of the above-mentioned observations, a methodology has been developed in dual-CM to account for spray interaction dynamics. Figure 2.44 shows a schematic of the multiple injection modeling approach. Using the subscripts i for referring to the i^{th} injection, the following assumptions are used :

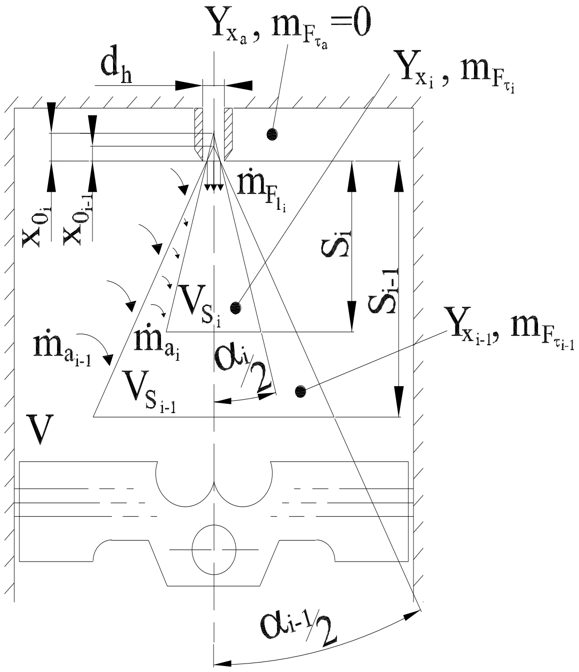

Figure 2.44: Scheme of the multiple injection modeling approach. Subscripts i refers to the i^{th} injection.

- to each injection of liquid fuel mass, $m_{F_{l_i}}$, is associated a spray volume, V_{S_i}, defining the control volume in which injected fuel and ambient air coexist,
- $m_{F_{l_i}}$ vaporizes and increases the fuel tracer variable, $m_{F_{\tau_i}}$, which is a dummy species representing the total vaporized mass of fuel in the spray, supposed to be independent of the combustion process[30],
- each spray volume grows according to the theory developed in section 2.4.2.2. Consequently each cone is characterized by its own penetration and opening angle,
- each spray has its own composition expressed in terms of chemical species masses, m_{x_i}[31], where x indicates the generic chemical species x. Chemical species in each spray evolve in time because of liquid fuel evaporation, entrained gases and chemical kinetics,

---

[30] For more information about the definition and computation of fuel tracer variables refer to section 2.5.

[31] For more information about the definition and computation of chemical species masses refer to section 2.5.

- mixture flow rates between spray volumes occur :
  - the flow rates are computed on the basis of geometrical considerations regarding the spray volume evolutions,
  - the liquid fuel mass relative to the i^{th} injection (here $i \geq 2$) is injected in the spray region associated to the $(i-1)^{th}$ injection. Therefore, the i^{th} spray volume grows in the $(i-1)^{th}$ spray region, figure 2.44,
  - when the gaseous mixture flows from $(i-1)^{th}$ to i^{th} spray (here $i \geq 2$), the transferred mass composition is supposed to be equal to the mean composition of the $(i-1)^{th}$ spray.

The last hypothesis that a given spray entrains gases strictly from the previous spray could appear at first sight quite strong. Figure 2.45 presents two configurations where this hypothesis applies. For high dwell-time values (top of figure 2.45) the hypothesis is exact : as the first spray occupies the whole cylinder volume, the second spray volume can only grow within the first one. This configuration occurs for the majority of the tested engine operating points. For low dwell-time values (bottom of figure 2.45), as

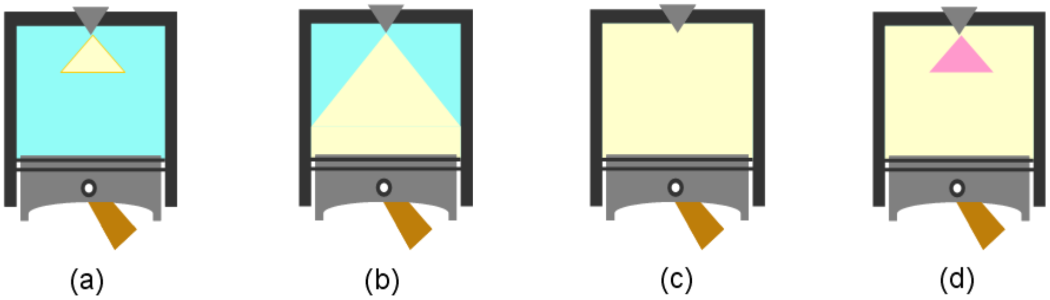

High dwell-time value between injections. After the first injection event, (a), the first spray grows, (b), until occupying the whole cylinder volume, (c). Then, the second injection is performed, (d).

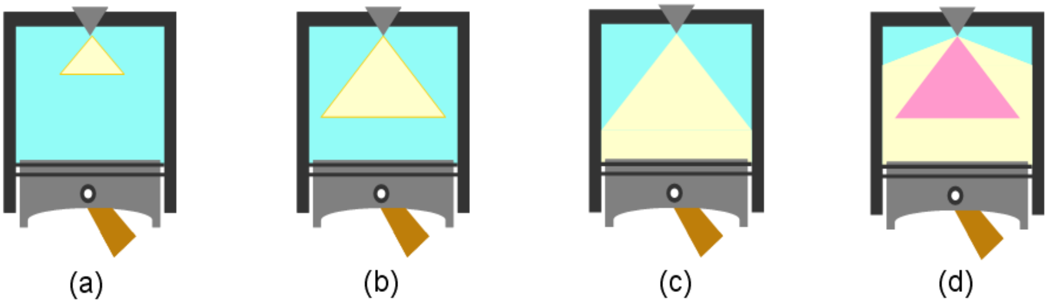

Low dwell-time value between injections. After the first injection event, (a), the first spray grows, (b) and (c). Then, the second injection is performed, before the first injection volume had the time to completely fill the cylinder volume, (d).

Figure 2.45: Representation of two different spray dynamics occurring in multiple injection strategies.

the first volume has not completely filled the cylinder volume, the second spray could entrain both first spray gases and ambient air gases (the last not being accounted for in the present hypothesis). The validity of the hypothesis for low dwell-time values proved by experimental results, in figure 2.42, and by CFD computations, section 4. According to the proposed multiple-injection spray-dynamics modeling, the volumes of the sprays are computed as :

$$V_{S_i} = \int \underline{\dot{V}}_{S_i} \cdot dt \tag{2.85}$$

where $\underline{\dot{V}}_{S_i}$ is the net variation of the i^{th} spray volume, defined as :

$$\underline{\dot{V}}_{S_i} = \dot{V}^{+}_{S_i} - \dot{V}^{-}_{S_i} \tag{2.86}$$

In equation 2.86, $\dot{V}^{+}_{S_i}$ is the positive contribution to the i^{th} spray growth associated to the i^{th} spray penetration, computed according to equation 2.77 and rewritten here in equation 2.87 for the i^{th} spray; $\dot{V}^{-}_{S_i}$ is the negative contribution to the i^{th} spray growth associated to the growth of the $(i+1)^{th}$ spray, if existing, computed according to equation 2.77 for the $(i+1)^{th}$ spray, equation 2.88 :

$$\begin{aligned}\left(\frac{dV_{S_i}}{dt}\right)^{+} &= \frac{a^2 \cdot \pi \cdot n_h}{3} \cdot \left[\left(3 + (S_i + x_{0_i})^2 \cdot \left(\frac{dS_i}{dt} + \frac{dx_{0_i}}{dt}\right) - 3 \cdot x_{0_i}^2 \cdot \frac{dx_{0_i}}{dt}\right) \cdot \right.\\ &\left. \cdot \tan^2\left(\frac{\theta_i}{2}\right) + \left((S_i + x_{0_i})^3 - x_{0_i}^3\right) \cdot 2 \cdot \tan\left(\frac{\theta_i}{2}\right) \cdot \frac{d}{dt}\left(\tan\left(\frac{\theta_i}{2}\right)\right)\right]\end{aligned} \tag{2.87}$$

and :

$$\left(\frac{dV_{S_i}}{dt}\right)^{-} = \left(\frac{dV_{S_{i+1}}}{dt}\right)^{+} \tag{2.88}$$

Then, the global mass flow rate for a given species x associated to the i^{th} spray is computed as :

$$\underline{\dot{m}}_{x_i} = \dot{m}^{+}_{x_i} - \dot{m}^{-}_{x_i} \tag{2.89}$$

in which $\dot{m}^{+}_{x_i}$ is the positive contribution to the species mass of the i^{th} spray coming from the $(i-1)^{th}$ spray [32], computed according to equation 2.90, and $\dot{m}^{-}_{x_i}$ is the negative contribution to the species mass of the i^{th} spray associated to the mass transfer from the i^{th} spray to the $(i+1)^{th}$ spray, if existing, computed according to equation 2.92 :

$$\left(\frac{dm_{x_i}}{dt}\right)^{+} = \rho_{x_{i-1}} \cdot \left(\frac{dV_{S_i}}{dt}\right)^{+} \tag{2.90}$$

where $\rho_{x_{i-1}}$ is the partial density of the species x in the $(i-1)^{th}$ spray defined as :

$$\rho_{x_{i-1}} = \frac{m_{x_{i-1}}}{V_{S_{i-1}}} \tag{2.91}$$

---

[32] When $i = 1$, the subscript $(i-1) = 0$ refers to ambient-gas in the cylinder, but outside the spray regions.

where $m_{x_{i-1}}$ is the the mass of the species x in the $(i-1)^{th}$ spray, and :

$$\left(\frac{dm_{x_i}}{dt}\right)^{-} = \rho_{x_i} \cdot \left(\frac{dV_{S_i}}{dt}\right)^{-} \tag{2.92}$$

where ρ_{x_i} is the partial density of the species x in the i^{th} spray defined as :

$$\rho_{x_i} = \frac{m_{x_i}}{V_{S_i}} \tag{2.93}$$

where m_{x_i} is the the mass of the species x in the i^{th} spray.

In equations 2.89 to 2.93, the subscript x refers to the considered chemical species (i.e. C_7H_{16}, C_7H_{14}, H_2O, CO_2, CO, O_2, H_2, H and N_2), as well as to the fuel tracer masses ($m_{F_{\tau_i}}$).

Figure 2.46 represents a particular case of triple-spray injection in non-reactive conditions. As shown, although the liquid-fuel injection-rates are all the same for the three injections, figure 2.46 (a), the evolutions of the spray volumes are very different from each other because of thermodynamic conditions of the ambient gas and the piston movement, figure 2.46 (b). Figure 2.46 (c) shows the oxygen mass-transfers from one spray to another. As shown, because of the non-reactive conditions, the total initial mass of oxygen is conserved. Finally, the gaseous-fuel mass in the different sprays as well as its global value, are plotted and compared to the total liquid-fuel injected mass, figure 2.46 (d).

2.4.3 Turbulence submodel

In ICE, turbulence plays a very important role, increasing mass, momentum and energy transfer rates. The dynamics of turbulent motion can be described as follows. At first, kinetic energy associated with the mean flow is transferred to the large scales of the fluctuating motion (integral scale). After that, kinetic energy is transferred isentropically from large to small scales of turbulence (Kolmogorov scale). Finally, the kinetic energy is dissipated by viscous forces and is transformed into thermal energy. Here, the aim of the turbulence submodel is to obtain an estimate of the turbulence characteristic time, τ_t, which controls the mixing process modelling.

The approach used in the dual-CM is the one developed in [13], here adopted in its original formulation. This approach is based on the well-known $\kappa - \epsilon$ turbulence-model theory. According to this theory, the global kinetic energy, E_c, is decomposed into two contributions :

$$E_c = m_S \cdot \widetilde{K} + m_S \cdot \widetilde{\kappa} \tag{2.94}$$

where $\widetilde{K}$ is the mean specific kinetic energy associated to the big structures of the mixture flow, $\widetilde{\kappa}$ is the turbulent specific kinetic energy associated to the local mixture velocity-fluctuations and m_S is the total mass of the spray.

The procedure to estimate τ_t is detailed in the following.

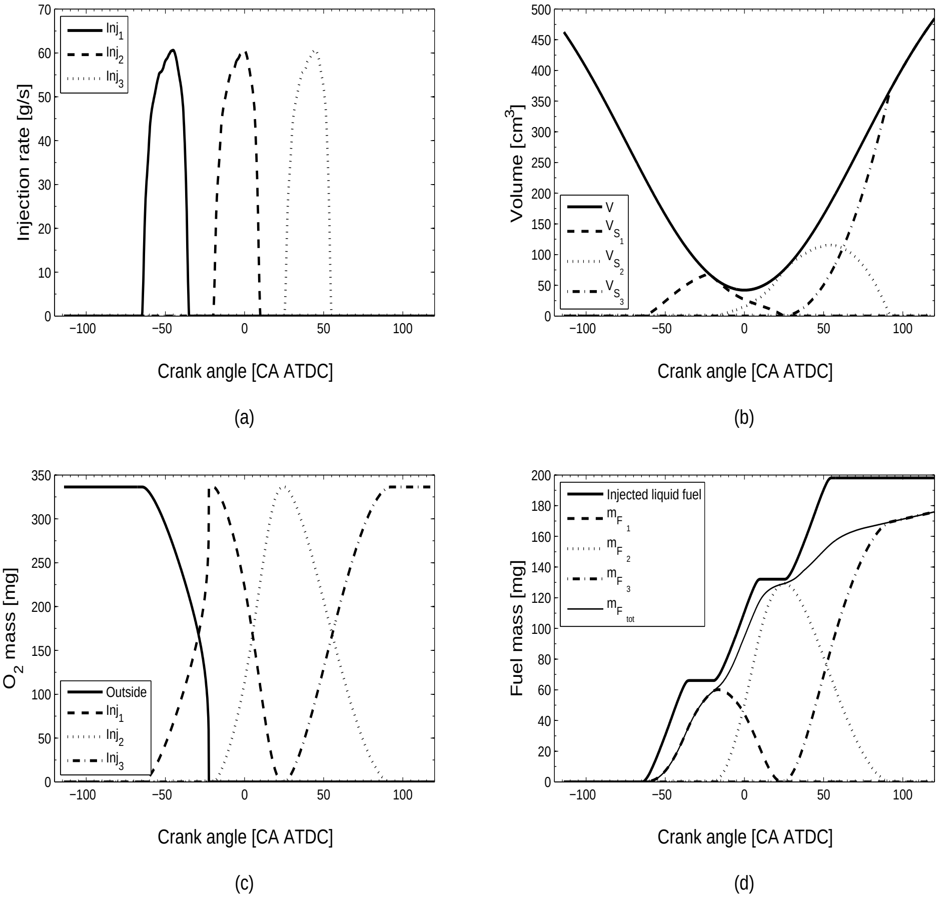

Figure 2.46: Triple-injection spray evolutions in non-reactive conditions. Injection rates, (a), spray volume evolutions, (b), oxygen mass-transfer between sprays, (c) and fuel-tracer mass transfer between sprays, (d). Global liquid-fuel injected-mass is compared to the total fuel-tracer mass (d).

Spray global kinetic-energy

The spray global kinetic-energy rate, $\dot{E}_c$, can be expressed as the sum of a production term, $\left.\frac{dE_c}{dt}\right|_{pr}$, and a dissipation term, $\left.\frac{dE_c}{dt}\right|_{ds}$:

$$\dot{E}_c = \frac{dE_c}{dt} = \left.\frac{dE_c}{dt}\right|_{pr} + \left.\frac{dE_c}{dt}\right|_{ds} \tag{2.95}$$

The production term in a Diesel ICE application can be detailed as follows :

$$\left.\frac{dE_c}{dt}\right|_{pr} = \frac{dE_{c_{swirl}}}{dt} + \frac{dE_{c_{squish}}}{dt} + \frac{dE_{c_S}}{dt} \tag{2.96}$$

in which $E_{c_{swirl}}$, $E_{c_{squish}}$ and E_{c_S} represent the production terms associated with the swirl, the squish and the spray, respectively.

E_{c_S} represents about 98% of the total kinetic energy, according to [20]. For that reason, with good approximation, it is possible to affirm that :

$$\left.\frac{dE_c}{dt}\right|_{pr} \approx \frac{dE_{c_S}}{dt} = \frac{u_F^2}{2} \cdot \left.\frac{dm_{F_l}}{dt}\right|_{inj} \tag{2.97}$$

in which :

$$u_F = \frac{1}{C_d \cdot n_h \cdot \rho_{F_l} \cdot \left(\frac{\pi}{4} \cdot d_h^2\right)} \cdot \left.\frac{dm_{F_l}}{dt}\right|_{inj} \tag{2.98}$$

where m_{F_l} is the mass of injected fuel, C_d is the discharge coefficient of the orifice and n_h is the number of holes of the nozzle.

The spray global kinetic-energy dissipation-term, mainly due to flow viscous forces, has been modeled by using empirical closure terms [13] :

$$\left.\frac{dE_c}{dt}\right|_{ds} = -m_S \cdot \left(C_K \cdot \widetilde{K}^{N_K} + C_\kappa \cdot \widetilde{\kappa}^{N_\kappa}\right) \tag{2.99}$$

where C_K and N_K are empirical dissipation-term constant-coefficients associated to the mean specific kinetic-energy, $\widetilde{K}$, and C_κ and N_κ are empirical dissipation-term constant-coefficients associated to the mean specific turbulent kinetic-energy, $\widetilde{\kappa}$.

Equation 2.95 can now be rewritten as :

$$\frac{dE_c}{dt} = \frac{u_F^2}{2} \cdot \left.\frac{dm_{F_l}}{dt}\right|_{inj} - m_S \cdot \left(C_K \cdot \widetilde{K}^{N_K} + C_\kappa \cdot \widetilde{\kappa}^{N_\kappa}\right) \tag{2.100}$$

Mean specific kinetic-energy

Similarly to $\kappa - \epsilon$ theory, by spatially averaging the 3D momentum balance-equation, it is possible to obtain an expression for the temporal evolution of the mean specific kinetic-energy[33] [13] :

$$\frac{d\widetilde{K}}{dt} = \frac{\sqrt{2 \cdot \widetilde{K}}}{m_S} \cdot \left[u_F \cdot \left.\frac{dm_{F_l}}{dt}\right|_{inj} - \sqrt{2 \cdot \widetilde{K}} \cdot \left(\frac{dm_a}{dt} + \left.\frac{dm_{F_l}}{dt}\right|_{inj}\right)\right] - C_K \cdot \widetilde{K}^{N_K} \tag{2.101}$$

where the last right-hand-side term represents the mean specific kinetic-energy dissipation-term, already present in equation 2.100. The control volume used to obtain equation 2.101 is the spray volume, V_S.

Characteristic time of turbulence

By using equation 2.94, it is now possible to compute the mean specific turbulent kinetic-energy value as :

$$\widetilde{\kappa} = \frac{E_c}{m_S} - \widetilde{K} \tag{2.102}$$

The term indicating the mean specific turbulent-kinetic-energy dissipation-rate, $\widetilde{\epsilon}$, is supposed to have an expression similar to the one used to represent the dissipation rate of the mean specific kinetic-energy :

$$\widetilde{\epsilon} = C_\kappa \cdot \widetilde{\kappa}^{N_\kappa} \tag{2.103}$$

as shown in equation 2.100.

---

[33] The proof of equation 2.101 is detailed in [13].

According to the $\kappa - \epsilon$ turbulent model theory, the characteristic time associated to turbulence is defined as :

$$\tau_t = \frac{\widetilde{\kappa}}{\widetilde{\epsilon}} \tag{2.104}$$

The presented 0D turbulence model, derived from the 3D approach, has the advantage of describing well the mechanism involving the transfer of kinetic energy in the frequency domain from large to small scales of turbulence due to the shear forces. Results concerning the turbulence submodel will be discussed in chapter 3.

2.4.4 Mixture submodel

One of the main issues in Diesel HCCI combustion modelling is that the auto-ignition and the combustion process take place in stratified-mixture conditions, section 1.1.3. In order to define a model able to predict both these phenomena, the modelling of the mixture stratification is of primary importance. Using a 0D formalism, to account for this aspect, which is essentially related to fuel spatial distributions, is not straightforward. To improve this aspect in the model, one solution is to use presumed PDFs, commonly used in 3D codes, for describing the mixture stratification using a statistical approach. The PDF is then used to estimate several local variables, such as mixture composition, temperature and reaction rates. Moreover, using a PDF approach implies the addition of only one more state variable per spray and a minimum impact on the CPU time cost. The mixture stratification model used in dual-CM, is based on the approach proposed in [13]. During this Ph.D the original approach has been extended in order to take into account phenomena such as fuel evaporation at saturated conditions and the spray interactions in configurations adopting multiple injection strategies.

Mixture fraction variable

According to the theory developed to study laminar diffusion flames [48], combining the transport equations of fuel mass fraction, Y_F, and oxidizer mass fraction, Y_O, it is possible to define a combustion-independent scalar (Schwab-Zeldovitch variable), φ, as :

$$\varphi = Y_F - \frac{Y_O}{s} \tag{2.105}$$

where s, the mass stoichiometric coefficient, is defined as :

$$s = \frac{\nu_O}{\nu_F} \cdot \frac{\mathcal{M}_O}{\mathcal{M}_F} \tag{2.106}$$

Here, ν_x represents the molar coefficient of the global combustion reaction and $\mathcal{M}_x$ is the species molar weight.

The normalization of the variable φ with the mass fractions relative to the fuel and oxidizer streams gives the mixture fraction variable, Z, whose values through the diffusive layer vary between 0, in pure oxidizer, and 1, in pure fuel. Z can be expressed as :

$$Z = \frac{\Phi \cdot \frac{Y_F}{Y_{F_0}} - \frac{Y_O}{Y_{O_0}} + 1}{\Phi + 1} \tag{2.107}$$

where Y_{F_0} is the fuel mass fraction in the fuel feeding stream and Y_{O_0} is the oxidizer mass fraction in the oxidizer stream. Φ is the equivalence ratio of the non-premixed flame defined as :

$$\Phi = \frac{Y_{F_0}}{Y_{O_0}} \cdot s \tag{2.108}$$

It is possible to demonstrate that :

$$Z = Y_{F_\tau} \tag{2.109}$$

where Y_{F_τ} is the fuel-tracer mass-fraction, that is the local fuel mass-fraction in the case of a non-reactive mixture (pure mixing line).

Presumed PDF

Different kinds of PDF are available in the literature. In order to simulate the mixing process taking place in diffusion flames, the PDF described by a β-function is usually the best choice [57]. A β-PDF function is a normalized statistical tool representing the probability, $\mathcal{P}(X^*)$, of a generic variable X, defined in its own domain of existence $(0 \leq X \leq 1)$.

A β-PDF is completely described by two parameters. The first one is the mean value of the distribution, $\bar{X}$, defined as :

$$\bar{X} = \int_0^1 X^* \cdot \mathcal{P}(X^*) \cdot dX^* \tag{2.110}$$

and the second is the segregation factor of the distribution, δ, defined as :

$$\delta = \frac{\overline{X'^2}}{\overline{X'^2}_{max}} \tag{2.111}$$

where $\overline{X'^2}$ is the value of the variance of the distribution computed as :

$$\overline{X'^2} = \int_0^1 (X^* - \bar{X})^2 \cdot \mathcal{P}(X^*) \cdot dX^* \tag{2.112}$$

and $\overline{X'^2}_{max}$ is the maximum value of the variance defined as :

$$\overline{X'^2}_{max} = \bar{X} \cdot (1 - \bar{X}) \tag{2.113}$$

The mathematical expression of $\mathcal{P}(X)$ is :

$$\mathcal{P}(X) = \frac{\Gamma(\alpha + \beta)}{\Gamma(\alpha) \cdot \Gamma(\beta)} \cdot X^{\alpha-1} \cdot (1 - X)^{\beta-1} \tag{2.114}$$

with :

$$\Gamma(a) = \int_0^{+\infty} e^{-t} \cdot t^{a-1} \cdot dt \tag{2.115}$$

and the coefficients α and β are defined as :

$$\alpha = \bar{X} \cdot \left[\frac{1}{\delta} - 1\right] \quad \text{and} \quad \beta = \frac{\alpha}{\bar{X}} - \alpha \tag{2.116}$$

Figure 2.47 shows the typical evolution of the β-PDF.

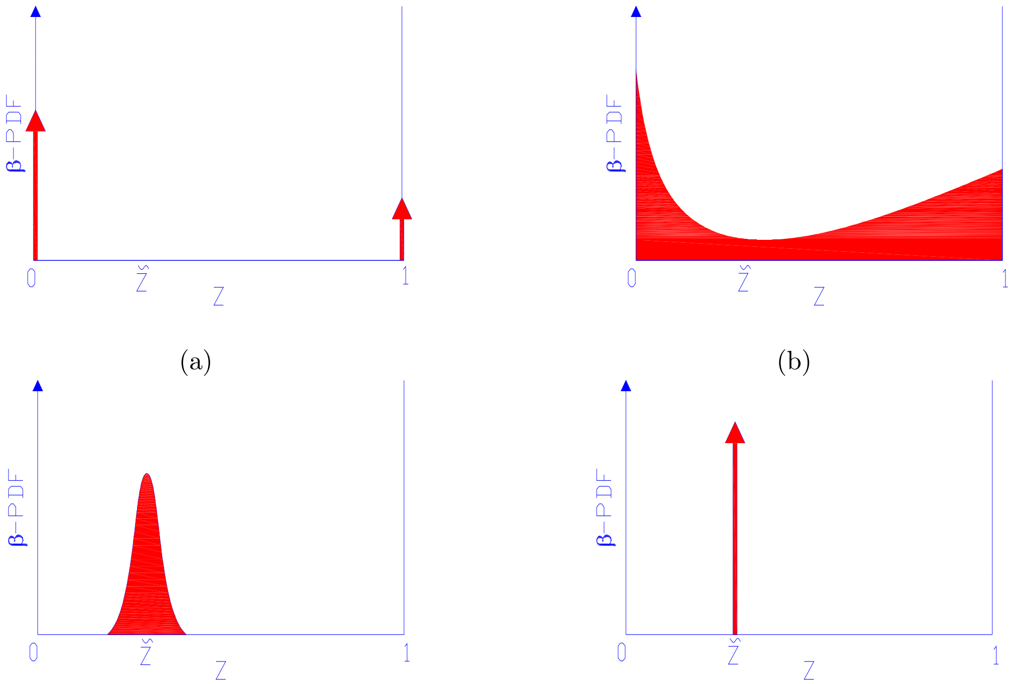

(a) (b)

(c) (d)

Figure 2.47: Representation of β-PDF evolution. At the beginning representing a perfectly unmixed mixture (a); at an intermediary stage still presenting a bimodal mixture fraction (b); at a later stage presenting a monomodal mixture fraction (c); and at the end of the mixing process a perfectly stirred mixture (d).

The configuration shown in figure 2.47 represents the mixing process taking place in a closed constant volume initially containing pure fuel and oxidizer. The value of $\widetilde{Z}$ is constant in time once the mass proportion of the two gases is fixed. $\widetilde{Z}$ can be computed as :

$$\widetilde{Z} = \frac{m_F}{m_F + m_O} \tag{2.117}$$

At $t = 0$, the oxidizer and fuel are perfectly unmixed ($\delta = 1$). In this case, the β-PDF presents two peaks : one representing the pure oxidizer (at $Z = 0$), and the other representing the pure fuel (at $Z = 1$). At times t_1 and t_2, two intermediary configurations are presented. The mixing process is going as δ decreases. At $t = t_{end}$, the mixture is perfectly stirred, and in this case, the β-PDF presents one peak centered at $\widetilde{Z}$.

Application of the submodel to ICE

As shown above, the β-PDF is a tool potentially adapted to reproduce the mixture stratification evolution during a mixing process [57]. The last step in completing the mixture model is to determine the equations giving the temporal evolution of the two parameters, the mean value, $\widetilde{Z}$, and the variance, $\widetilde{Z"^2}$, of the distribution, defining the PDF (and the mixture stratification). Remember that the mixture submodel addresses the gas mixture composition inside the spray volume.

Compared with the previous example, which refers to two perfectly-unmixed gases in a closed constant-volume, the ICE application is much more complicated :

- both volume and total mass grow in time,
- the upper limit of the mixture-fraction, Z_s, that corresponds to the fuel mass fraction at saturated conditions Y_{F_s} computed by the evaporation submodel, evolves in time as a function of the in-cylinder thermodynamic conditions,
- the fuel/ambient-gas ratio and the mean value of the mixture fraction vary in time,
- in a case of multiple injection strategy, several sprays coexist and interact with each other. Figure 2.48 represents a multiple injection configuration. In particular, a triple injection case is illustrated. As seen, at the shown instant of time, the first spray has completely filled the cylinder, while the second and the third spray volumes are growing in time. In the following, using the indice i for refering to the i^{th} injection, the mean value and the variance equations are given.

Distribution mean value equation

For the injection i, the mean value is computed as the ratio of the total fuel-evaporated mass, $m_{F_{\tau_i}}$, and the total mass of gas in the spray volume, m_{S_i} :

$$\widetilde{Z}_i = \frac{m_{F_{\tau_i}}}{m_{S_i}} = \frac{m_{F_{\tau_i}}}{m_{F_{\tau_i}} + m_{a_i}} \tag{2.118}$$

$m_{F_{\tau_i}}$ and m_{a_i} are easily obtained by integration of the evaporation and entrainment gas submodel-outputs, figure 2.3.

Distribution variance equation

By definition, the variance of the distribution of Z in the i^{th} spray is :

$$\widetilde{Z"^2}_i = \frac{1}{m_{S_i}} \cdot \int_{m_{S_i}} \left(Z - \widetilde{Z}_i\right)^2 \cdot dm \tag{2.119}$$

Differentiating equation 2.119 and making the following hypotheses (referred to the i^{th} injection spray) :

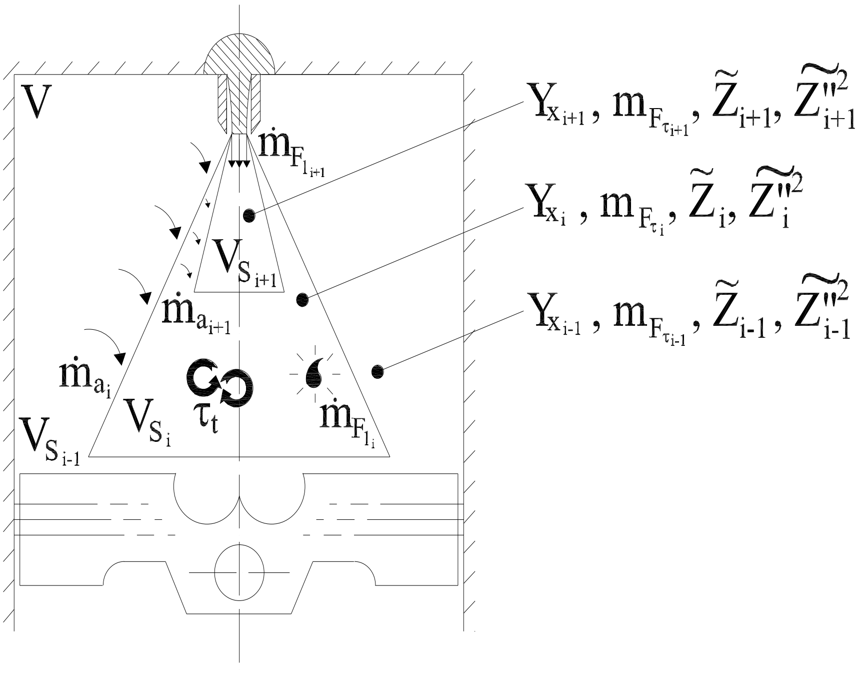

Figure 2.48: Representation of a multiple injection spray dynamics. In the figure, the indice i refers to the second injection event.

- the incoming mass in the spray has a composition equal to the mean composition of the $(i-1)^{th}$ injection spray,
- the outgoing mass of the spray has a composition equal to the mean composition of the spray,
- the liquid fuel evaporates at saturated conditions in pure ambient air $(Z = 0)$,
- the variance dissipation is proportional to the turbulent mixing frequency and to the variance value,

the variance rate is written as[34] :

$$\frac{d\widetilde{Z''^2}_i}{dt} = -\underbrace{2 \cdot C_{ds_i} \cdot \frac{\widetilde{\epsilon}}{\widetilde{\kappa}} \cdot \widetilde{Z''^2}_i}_{I} + \underbrace{\frac{1}{m_{S_i}} \cdot \left(\left(\widetilde{Z}_{i-1} - \widetilde{Z}_i\right)^2 - \widetilde{Z''^2}_i\right) \cdot \frac{dm_{in_i}}{dt}}_{II} +$$
$$+ \underbrace{\frac{1}{m_{S_i}} \cdot \left(\widetilde{Z}_i^2 \cdot \left(1 - \frac{1}{Z_{s_i}}\right) + \left(Z_{s_i} - \widetilde{Z}_i\right)^2 \cdot \frac{1}{Z_{s_i}} - \widetilde{Z''^2}_i\right) \cdot \frac{dm_{F_i}}{dt}}_{III} +$$
$$+ \underbrace{\frac{1}{m_{S_i}} \cdot \widetilde{Z''^2}_i \cdot \frac{|dm_{out_i}|}{dt}}_{IV} \tag{2.120}$$

The use of the β-function to represent the PDF, as already seen, brings several positive aspects, but also imposes some limitations on the mixture-distribution description.

---

[34] Complete proof of the equation 2.120 is given in appendix D.

For instance, figure 2.49 shows a situation that cannot be represented by a β-function. More generally, the β-function can not represent mixture fraction variable distributions having more than two peaks. To reduce the impact of these limitations on modeling, in the following the upper limit of the distribution domain will be considered as constant and equal to the maximum value reached during the evaporation process, $Z_{s_{max}}$. In section 3, 3D computations have been performed to have an estimate of this variable.

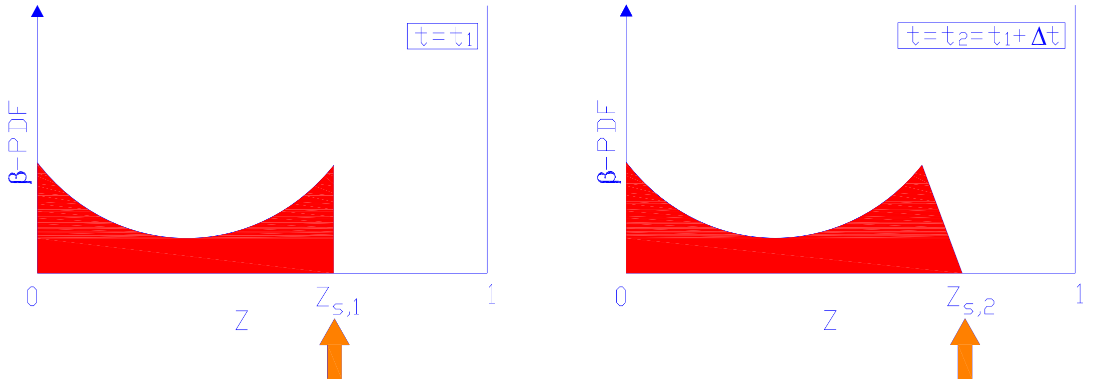

(a) (b)

Figure 2.49: Representation of β-PDF limitation : mixture fraction distribution at the instant $t = t_1$ (a), mixture fraction distribution at the instant $t = t_2 = t_1 + \Delta t$ (b). During Δt temperature increases and liquid fuel evaporates at $Z = Z_{s,2}$.

In equation 2.120, it is possible to distinguish four contributions. The first term, I, corresponds to the mixing-process contribution (term of dissipation of the variance). It depends on turbulence[35] and is proportional to the turbulence characteristic-frequency via the adjustment coefficient C_{ds}. The composition of the entrained mass is equal to the mean composition of the region $(i-1)$. The second term, II, corresponds to the entrained gaseous mixture contribution. The third term, III, corresponds to the fuel-evaporation contribution and is obtained by assuming that liquid fuel evaporates at the saturated thermodynamic conditions in pure ambient gas ($Z = 0$). The last term, IV, corresponds to the outgoing mass contribution assuming that the outgoing mass has the mean spray composition.

β-PDF parameters

Once the mean value and the variance of the mass fraction distribution have been computed for the spray, they have to be normalized for use with a presumed PDF.

The proposed normalization takes into account the fact that $Z_{s_{max_i}}$ can be smaller

---

[35] The laminar species diffusion is neglected.

than unity [87]. Mean value and variance are respectively normalized as follows :

$$\widetilde{Z}_{\beta-PDF_i} = \frac{\widetilde{Z}_i}{Z_{s_{max_i}}} \tag{2.121}$$

and :

$$\delta_{\beta-PDF_i} = \frac{\widetilde{Z"^2}_i}{\widetilde{Z"^2}_{max_i}} = \frac{\widetilde{Z"^2}_i}{\widetilde{Z}_i \cdot \left(Z_{s_{max_i}} - \widetilde{Z}_i\right)} \tag{2.122}$$

For the sake of completeness, it is worthwhile to point out that, when dealing with Diesel ICEs, trans/super-critical evaporation phenomena can take place at particular engine operating conditions [58, 59]. Under trans/super-critical evaporation regimes :

- the perfect gas hypothesis is no longer valid,
- Clapeyron's law is not valid,
- the ambient-gas dissolution in liquid fuel is no longer negligible,
- the concept of a liquid-gas interface vanishes.

According to [58, 61], when trans/super-critical evaporation phenomena occur, using a subcritical evaporation model, as the one adopted in dual-CM, instead of a tran/super-critical one, leads to an under-estimation of the value of the maximum fuel mass-fraction. At present time in the literature, trans/super-critical evaporation models are adopted only for very particular applications.

These particular evaporation regimes are not accounted for in dual-CM.

In the following, the value of the maximum mixture fraction has been arbitrarely fixed at $Z_{s_{max_i}} = 0.8$. The choice of this particular value will be discussed more in detail in chapter 3.

2.5 Combustion model

The combustion model computes the chemical kinetics that take place within the reactive mixture in the engine combustion chamber. As seen in figures 2.1 and 2.3, it represents the last brick of dual-CM. Its role is to compute, according with the thermochemical composition of the in-cylinder gaseous mixture, given by the spray model (section 2.4), the heat release and the pollutant species emissions relative to the considered engine cycle. Several approaches to chemical kinetics computation exist : one-step reaction, reduced kinetics and detailed kinetics approaches. As shown in figure 1.13, a solution for getting off the region relative to NO_x and soot emissions is to obtain a combustion process characterized by lower temperatures and a higher level of local air-excess ratio. Nowadays, to reduce the combustion temperatures, it is usual to dilute the fuel-air mixture with EGR because of its high specific heat-capacity and immediate availability. The

EGR dilution has a direct impact on the chemical kinetics of combustion. In particular, it slows down the formation process of active radicals of combustion and reduces their local concentration. It is common, by using high EGR rates, to increase the auto-ignition delay of the reactive mixture, and split the heat release process into two stages : the first, called cold flame, associated to the fuel decomposition in intermediary species; and the second, called main flame, associated to the oxidation process. To predict all these scenarios is a real challenge in computational combustion science :

- in order to account for all the concerned combustion regimes and in order to have a good estimate of the pollutant-species emissions, a detailed chemical kinetics approach is required,

- the computational time[36] should remain compatible with practical requirements.

In the last decade, a technique based on the analysis of chemical characteristic times in the phase space, Intrinsic Low-Dimensional Manifolds ($ILDM$), was developed in [65]. The main idea is to compute a low-dimensional surface as a function of physical parameters describing the thermochemical state of the chemical system, by solving for the system eigenvalues and eigenvectors. The composition of the whole chemical system can then be parameterized as a function of a small number of coordinates. These values are stored in a look-up table, which is finally used in computational solvers. The computational time associated to this kind of approach is enormously reduced if compared to detailed chemical kinetics computations. More recently, an extension of the ILDM approach to premixed flame computations, the Flame Prolongation of ILDM (FPI) approach, was proposed in [47]. In particular, the FPI approach permits the prolongation of the ILDM manifolds in the low-temperature domain. In fact in the original approach, because of the fast reaction characteristic times, the chemical kinetics at low temperature were not taken into account. In a similar fashion, the FPI method was then extended to computations of non-premixed flames [87] and auto-ignition of homogeneous reactors [67]. The tabulated chemistry approach was then successfully applied to ICE computations [85].

Concerning the 0D model dual-CM, as it is dedicated to a global-system simulation context in which the CPU computation-cost is a first order evaluation parameter, it is an unreasonable choice to solve for the complete chemical scheme. Nevertheless, the complex-chemistry species interactions must be taken into account, as one of the main issues of the dual-CM is to be able to correctly compute the auto-ignition delay of the

---

[36] The use of a detailed chemical kinetics approach implies very high computational times mainly for two reasons. The former is that detailed chemical schemes involve hundreds of species and hundreds of chemical reactions, consequently, the size of the system to solve is very large. The second is that many of the considered reactions are stiff, consequently, for correctly solving the chemical system, short time steps are required.

reactive mixture. In fact, a good estimate of this variable allows us to define and optimize the engine-control strategies in conventional Diesel and Diesel HCCI engines.

For that reason, a tabulated complex chemistry method (FPI-like approach) adapted to the computation of auto-ignition reactions, inspired by the 3D approach [85], was retained.

The choice of using a detailed chemistry approach for the oxidation process modeling permits of capturing highly non-linear phenomena related to the combustion process, otherwise not captured by reduced chemistry. In particular, for a correct modeling of the new combustion regimes such as PCCI, LTC and HCCI, it is important to capture the influence on the combustion process of variables such as the thermochemical conditions of the reactive mixture. Figures 2.50 and 2.51 show two non-linear phenomena that imperatively must be taken into account for a correct description of the combustion process in ICEs. Figure 2.50 shows the temperature evolutions taking place during the combustion processes of two gaseous mixtures with different compositions. Both configurations are relative to the combustion of a homogeneous fuel/air mixture in an adiabatic constant-volume reactor. Initial conditions do not change between the two configurations, except for the EGR dilution rate. Nevertheless, in the configuration with a higher EGR rate, it is possible to clearly distinguish a two-step auto-ignition process and a reduction of the final combustion temperature. Figure 2.51 shows the evolution of the main combustion ignition-delay for a given mixture at a given initial pressure as a function of initial temperature. Values computed using the solver SENKIN, from the CHEMKIN package [63], are plotted against experimental data [68]. The ignition delays are determined from the maximum temperature gradients. It is interesting to note the Negative Temperature Coefficient (NTC) zone in the interval of temperature from

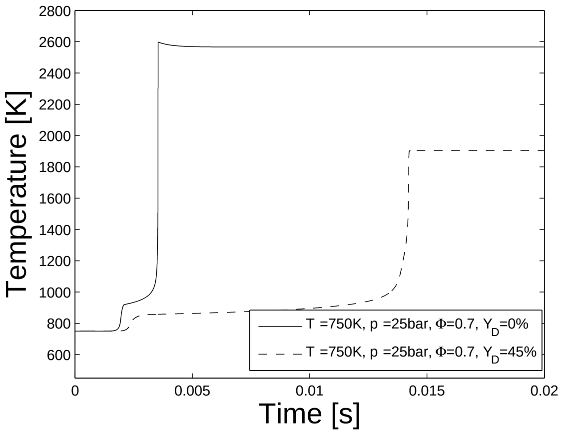

Figure 2.50: Results from SENKIN for EGR rate influence on auto-ignition of a perfectly stirred mixture of n-heptane/air/EGR in a constant volume reactor. Initial states : $T_\tau = 750$ K, $p_\tau = 25$ bar, $\Phi = 0.7$, and $Y_D = 0\%$ and 45% for solid and dashed lines, respectively.

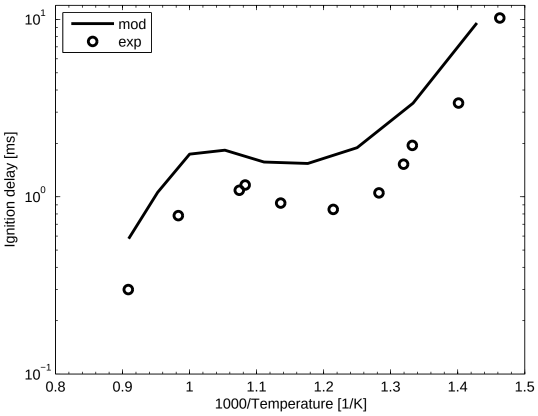

Figure 2.51: Dependence of the main ignition-delay on the temperature for a perfectly stirred mixture of n-heptane/air in a constant pressure reactor. SENKIN results are compared with experimental data. Initial state : $p_\tau = 42$ bar, $\Phi = 0.5$.

850 K to 950 K. In that interval, an increase of the initial temperature corresponds to an increase of the ignition delay due to endothermic radical reactions appearing before the main combustion process.

The dual-CM combustion model is based on the first order Presumed Conditional Moment (PCM) approach as it was proposed in [87].

The PCM approach supposes that the local combustion process progress can univocally be described by a progress variable, Y_c, defined as a linear combination of the local species mass fractions, Y_x. In the PCM original formulation :

$$Y_c = Y_{CO} + Y_{CO_2} \tag{2.123}$$

When dealing with diffusion flames, the local fuel mixture fraction value, Z, can strongly vary between two different points of the flow. As a consequence, the final value (at chemical equilibrium) of the progress variable changes. Accordingly, it is convenient to normalize the progress variable by its equilibrium value, $Y_{c_{eq}}(Z)$, as :

$$c = \frac{Y_c}{Y_{c_{eq}}(Z)} \tag{2.124}$$

The Y_c reaction rate, $\dot{\omega}_{Y_c}$, and the species concentrations, Y_x, evolutions are then stored in look-up tables (FPI tables) as a function of the fuel mixture fraction and the progress variable :

$$\dot{\omega}_{Y_c} = \dot{\omega}_{Y_c}^{TAB}(Z, c) \tag{2.125}$$

$$Y_i = Y_i^{TAB}(Z, c) \tag{2.126}$$

The mean value on the domain of a generic variable, $\widetilde{\phi}$, is then computed as :

$$\widetilde{\phi} = \int_0^1 \int_0^1 \phi^{TAB}(Z^*, c^*) \cdot \mathcal{P}(c^* | Z^*) \cdot \mathcal{P}(Z^*) \cdot dc^* \cdot dZ^* \tag{2.127}$$

where $\mathcal{P}\left(c^*|\,Z^*\right)$ and $\mathcal{P}\left(Z^*\right)$ are the probability density function of c conditioned to Z and the probability density function of Z, respectively. In the first order PCM approach, the progress variable is considered to be homogeneous on the fuel mixture fraction domain, and equal to the mean progress variable value :

$$\mathcal{P}\left(c^*|\,Z^*\right) = \delta\left(c^* - \widetilde{c}\right) \tag{2.128}$$

where $\widetilde{c}$ is computed as :

$$\widetilde{c} = \frac{\widetilde{Y_c}}{\widetilde{Y_{c_{eq}}}} \tag{2.129}$$

in which $\widetilde{Y_c}$ and $\widetilde{Y_{c_{eq}}}$ are computed according with equation 2.127.

In the following the dual-CM combustion model is presented more in detail. The description of the model is organized in three sections :

- the first concerning the creation of the FPI look-up table, section 2.5.1,
- the second dealing with the modeling of laminar combustion processes, section 2.5.2
- the last concerning the extension of the laminar combustion submodel to turbulent combustion in ICEs, section 2.5.3.

2.5.1 Tabulation of laminar combustion processes

In this section, the methodology that has been used in order to create and set up the database of detailed chemistry computations is detailed.

Complex chemistry solver

The detailed chemistry solver used for computing the kinetics of the chemical reactions is the CHEMKIN package [63]. Two tools of the CHEMKIN package were used :

- SENKIN, a solver for chemical kinetics computations of perfectly stirred gaseous mixtures reacting in a closed-volume reactor,
- EQUIL, a solver able to compute the thermochemical equilibrium composition of a given initial reactive mixture.

Diesel fuel surrogate and chemical mechanism

It is important to note that commercial Diesel fuel is not a pure hydrocarbon but a mixture of many different ones and a unique formulation of the Diesel fuel does not exist. Nevertheless the mixture, in order to be commercialized as Diesel fuel, must respect rigorous specifications.

For that reason in combustion modeling, a Diesel fuel-surrogate is often adopted : it is usually a pure fuel that has the same auto-ignition properties as the real fuel. Normal heptane has been chosen as the Diesel fuel substitute, in this work. According to section 2.4, this choice has been done mainly for the following reasons :

- thermochemical properties of n-heptane are well-known in the literature,
- complex chemistry kinetic mechanisms exist and have been validated on a wide range of thermodynamic conditions,
- auto-ignition delays are comparable to that of commercial hydrocarbon Diesel blends : n-heptane like real Diesel fuel blends has a NTC zone, figure 2.51.

In order to be consistent with Diesel-like fuels in terms of energy balance, for combustion heat release computations, the mass enthalpy of normal heptane was replaced with that of DFL1 (reference Diesel fuel used at IFP).

Several complex chemical kinetics schemes exist for n-heptane : here, the complete scheme proposed in [86] was used. It involves 536 species and 3000 reactions.

FPI table inputs

A first challenge is to define a reduced set of variables to describe a homogeneous mixture of unburned gases. In fact, when dealing with ICEs, a wide range of thermochemical conditions can be encountered in terms of pressure, temperature, species concentration, EGR rate, equivalence ratio, etc.

The thermochemical state of the gaseous mixture of fuel, air and EGR can be completely described with the following four variables :

- T_τ : temperature,
- p_τ : pressure,
- Φ : equivalence ratio,
- Y_D : Burned Gas mass fraction in ambient-gas[37]. It is defined as :

  $$Y_D = \frac{m_D}{m_{pa} + m_D} \tag{2.130}$$

  where m_D and m_{pa} are the BG and pure air masses in the in-cylinder ambient-air, respectively. Here, BG are supposed to be at stoichiometric composition and neutral with respect to combustion.

---

[37] Here the ambient-gas is a perfectly stirred mixture of pure air and EGR. Pure air is supposed to be a mixture of oxygen and nitrogen in the molar proportion of 1 : 3.76.

.

They constitute an orthogonal base in the phase space, and they have been chosen as inputs of the table. In order to describe the progress of the combustion process additional parameters are required.

The strategy is to represent the chemical path of the reaction through a unique parameter, here called the *progress variable* of the combustion, c. The progress variable describes the mixture composition variation from unburned gases up to burned gases, its value varying from 0 up to 1, respectively. The progress variable must satisfy the following properties :

- c varies with the mixture composition variation during the combustion process in a closed interval between 0 and 1 : 0 in the fresh gases and 1 in the burnt gases,
- c must be monotonic with the progress of combustion,
- c must be representative of all main reactions.

Accordingly, a generic variable ϕ is stored in the table as a function of the five table inputs :

$$\phi = \phi \left(T_\tau, p_\tau, \Phi, Y_D, c \right) \tag{2.131}$$

Figure 2.52 shows the computed progress variable associated with the combustion processes presented in figure 2.50. In figure 2.52, note that even if in figure 2.50, at the end of combustion the temperature relative to the combustion process without EGR diminishes (because of endothermic chemical reactions), the relative progress variable continues to be monotonic.

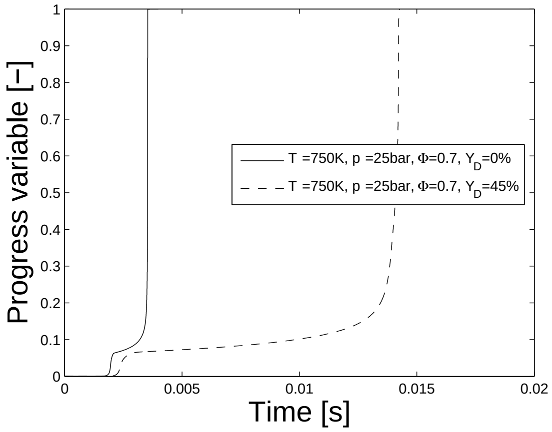

Figure 2.52: Computed progress variables evolutions for the two combustion processes presented in figure 2.50. Initial states : $T_\tau = 750$ K, $p_\tau = 25$ bar, $\Phi = 0.7$, and $Y_D = 0\%$ and 45% for solid and dashed lines, respectively.

The species mass fraction tabulation method

With the five parameters defined above, the combustion is completely parametrized. For each set of initial conditions, it is now possible to store the information related to the combustion process, permitting us to reconstruct at each instant the species reaction rates in the burning mixture. Two approaches are possible :

- species reaction rates, $\dot{\omega}_x^{cb}$, are extracted from the detailed chemistry computations and stored in the table,
- species mass/molar concentrations, Y_x, are extracted from the detailed chemistry computations and stored in the table. The species reaction rates, $\dot{\omega}_x^{cb}$, are then reconstructed by the computational solver.

In order to have reliable computed results by using the species reaction rate approach, a dense discretization of the axes of the input variables of the table is required. If not, at each computational step, an error in the determination of the species reaction rates could appear, and its accumulation could induce trajectory inconsistencies in the phase space [88], appendix E.

On the other hand, the species mass/molar concentration tabulation approach permits us to have reliable results even if a rather coarse discretization of the table axes is adopted.

In ICE applications, because of the hardware memory limitations and the wide domain of thermochemical conditions occurring in computations, only a relatively coarse discretization can be envisaged. For this reason, the species mass/molar concentration approach has been retained. In particular, as dual-CM deals with species masses, a species mass fraction approach was preferred.

Definition of the major species

Complex chemistry for hydrocarbons involves hundreds of species, N. One of the advantages of the tabulation methods is to be able to reconstruct the mixture thermochemical properties of interest with a limited number of species, M. Evidently, in order to limit the table dimensions and take as much advantage as possible of the tabulation method, the number of retained species must be reduced to the bare minimum. The choice of these species is crucial, because their evolutions have to be sufficient to represent the combustion process on the whole chemical scheme domain. Here, nine major species have been retained according to the following considerations :

- *species interest considerations* dealing with the needs to have a good knowledge of given species concentrations. For instance, in order to have an estimate of the pollutant emissions at the end of the engine cycle, the considered pollutant species must be computed,

- *mass considerations* require to retain species whose mass fractions in the mixture are not negligible,

- *energy considerations* require to retain species whose energetic contribution to the mixture energy is not negligible. This aspect is important as in dual-CM the heat-release associated with the combustion process, $\dot{Q}^{cb}$, is associated to the species concentration variations :
$$\dot{Q}^{cb} = \sum_{x=1}^{M<N} h_x \cdot \dot{\omega}_x^{cb} \tag{2.132}$$
where h_x is the total enthalpy of the species x.

The retained species are : C_7H_{16}, C_7H_{14}, N_2, O_2, H_2O, CO_2, CO, H_2 and H [85]. Amongst them, only five species are tabulated (C_7H_{16}, H_2O, CO_2, CO and H), three are reconstructed by using atomic balance equations for C, O and H atoms (C_7H_{14}, O_2 and H_2), and one is considered as a combustion independent and its mass does not vary in time (N_2). This method permits us to conserve the total mass of the system. The selection of the reconstructed species is rather tricky. In fact, as they are reconstructed, the evolution of a reconstructed species x differs from the evolution of the species x computed using the detailed chemistry. Moreover, the energetic contribution of a reconstructed species x must be representative of the energetic contribution of all the neglected species of the complex mechanism that the species x represents.

Definition of the progress variable

As said above, the FPI approach assumes that, for a given set of initial conditions, the combustion state is uniquely defined by a unique progress variable c. The progress variable is commonly defined as a linear combination of the computed tabulated-species concentrations. The generic definition of c used in a FPI approach is :

$$c = \frac{Y_c(t) - Y_c(t=0)}{Y_c(t=t_{eq}) - Y_c(t=0)} \tag{2.133}$$

where Y_c represents the species mass fraction linear combination, and it is defined as :

$$Y_c = \sum_{x=1}^{M} \sigma_x \cdot Y_x \tag{2.134}$$

where t_{eq} stands for the time necessary to reach chemical equilibrium, σ_x is a coefficient depending on the species and M is the number of species.

Hence :

- $c = 0$ corresponds to the fresh gaseous mixture at the time $t = 0$,
- $c = 1$ corresponds to the burnt gaseous mixture at the time $t = t_{eq}$.

In the literature different definitions of Y_c can be found. In particular :

- $Y_c = Y_{CO} + Y_{CO_2}$ was used in [87] and [85] for the description of the combustion process of light and heavy hydrocarbons, respectively,
- $Y_c = -Y_{O_2} + Y_{CO} + Y_{CO_2}$ was used in [13] because of the relatively regular consumption of oxygen during the combustion process,
- $Y_c = -Y_F + Y_{CO} + Y_{CO_2}$ was used in [67] for the description of the combustion process of heavy hydrocarbons, in order to better visualize the auto ignition and cold flame phenomena on the progress variable curve.

In dual-CM, the retained choice is the one proposed in [85].

As said above in this section, in ICE applications EGR can be present in ambient air. In the following, the hypothesis will be that the composition of BG contained in EGR does not influence the combustion process. According to this hypothesis, the table generation was done considering the BG as pure nitrogen. At first sight this could seem a strong hypotheses. For that reason, it is worthwhile to use more words in order to justify it :

- the fact of considering a mixture of pure nitrogen instead of the real BG mixture composition, does not modify significantly the molar mass of the EGR and its heat capacity. In fact, being lean the global equivalence ratios of Diesel engine operating points, the mixture fraction of nitrogen is much higher than the others. Consequently, the mixture thermodynamic properties are similar to those of nitrogen,
- the combustion products other than N_2 such as H_2O, CO_2 are relatively stable if compared to the fresh mixture species. Hence, when replaced with nitrogen, a minor impact on the combustion kinetics can be supposed. This is especially true for auto-ignition delays computations as shown in [85],
- taking into account the EGR real composition for an exact description of the thermochemical properties of the initial mixture would bring additional table coordinates and, consequently to a non-manageable table size.

.

According to the hypothesis done, if CO or CO_2 mass fractions exist in the ambient gases, their contribution to the progress variable computation must be null.

Hence, in order to correctly compute the combustion dynamics, it is important to split the in-cylinder species mass fractions, Y_x, into two contributions :

- the first referred to the species mass introduced in the cylinder with EGR, which does not play any role on the combustions process, Y_x^D,
- the second referred to the species mass involved in the combustion process, Y_x^{cb}.

As an example, when EGR is used, the CO$_2$ mass fraction in unburned ambient-gas is not null. As the CO$_2$ belonging to EGR does not participate to combustion, it must be differentiated from that generated during combustion. Accordingly, the in-cylinder mass fraction of a generic species x, Y_x, can be written as :

$$Y_x = Y_x^{cb} + Y_x^D \tag{2.135}$$

According to this hypothesis, using equation 2.135, Y_c is defined as :

$$Y_c = Y_{CO}^{cb} + Y_{CO_2}^{cb} = Y_{CO} - Y_{CO}^D + Y_{CO_2} - Y_{CO_2}^D \tag{2.136}$$

Hence, according to equation 2.133, the progress variable is computed as :

$$\begin{aligned} c &= \frac{\left(Y_{CO}^{cb}(t) + Y_{CO_2}^{cb}(t)\right) - \left(Y_{CO}^{cb}(0) + Y_{CO_2}^{cb}(0)\right)}{\left(Y_{CO}^{cb}(t_{eq}) + Y_{CO_2}^{cb}(t_{eq})\right) - \left(Y_{CO}^{cb}(0) + Y_{CO_2}^{cb}(0)\right)} \\ &= \frac{\left(Y_{CO}(t) - Y_{CO}^D(t)\right) + \left(Y_{CO_2}(t) - Y_{CO_2}^D(t)\right)}{\left(Y_{CO}(t_{eq}) - Y_{CO}^D(t_{eq})\right) + \left(Y_{CO_2}(t_{eq}) - Y_{CO_2}^D(t_{eq})\right)} \end{aligned} \tag{2.137}$$

An advantage of using the definition given in [85] for the progress variable is that all species appearing in the Y_c, namely CO and CO$_2$, have null initial values. This avoids the propagation of numerical errors due to an erroneous computation of the progress variable. For instance, using a definition as the one given in [13], the oxygen appears in the definition of Y_c. When the table is generated, for a given set of initial conditions $(T_\tau, p_\tau, \Phi, Y_D)$, a certain value of $Y_{O_2}^{TAB}(0) = Y_{O_2}\left(T_\tau, p_\tau, \Phi, Y_D, c = 0\right)$, representing the oxygen mass fraction in the fresh gases, is stored in the table with a certain numerical precision. For the sake of clarity, suppose here $Y_D = 0$. Once the table is integrated in a computational solver and a computation is performed by setting the above mentioned initial conditions in the code, T_τ, p_τ, Φ and Y_D, the mass fractions of the fresh gases can be recovered. In particular, a value for the computation initial oxygen mass fraction, $Y_{O_2}^{COMP}(0)$, is obtained with a certain numerical precision, potentially different from the one used for storing the data in the table. If this is the case, at the time $t = 0$, the computation of the progress variable in fresh gases is (equation 2.133) :

$$\begin{aligned} c &= \frac{\left(-Y_{O_2}^{COMP}(0) + Y_{CO}^{COMP}(0) + Y_{CO_2}^{COMP}(0)\right) - \left(-Y_{O_2}^{TAB}(0) + Y_{CO}^{TAB}(0) + Y_{CO_2}^{TAB}(0)\right)}{\left(-Y_{O_2}^{TAB}(t_{eq}) + Y_{CO}^{TAB}(t_{eq}) + Y_{CO_2}^{TAB}(t_{eq})\right) - \left(-Y_{O_2}^{TAB}(0) + Y_{CO}^{TAB}(0) + Y_{CO_2}^{TAB}(0)\right)} \\ &= \frac{-Y_{O_2}^{COMP}(0) + Y_{O_2}^{TAB}(0)}{\left(-Y_{O_2}^{TAB}(t_{eq}) + Y_{CO}^{TAB}(t_{eq}) + Y_{CO_2}^{TAB}(t_{eq})\right) + Y_{O_2}^{TAB}(0)} \neq 0 \end{aligned} \tag{2.138}$$

As shown in equation 2.138, even if the combustion process has not begun, the progress variable is different from zero. This error, associated to numerical precision, occurs at every single computational step when computing c. Its integration in time leads to a modification of the combustion process chemical kinetics.

Discretization of the table definition domain and filling of the table

As mentioned above in this section, the independent physical variables used for describing the initial thermochemical domain of existence of the combustion process are the initial temperature, T_τ, the initial pressure, p_τ, the equivalence ratio, Φ, and the mass fraction of BG in the ambient-air, Y_D; the progress variable is an additional variable used for describing the state of the combustion. In dual-CM the following ranges and discretizations have been retained for the table input variables :

- 19 initial temperatures varying between 590 K and 1300 K. More refined discretization was done for the lower temperatures domain, in order to well describe the NTC region,
- 13 initial pressures varying between 1 bar and 150 bar,
- 9 initial equivalence ratios varying between 0.1 and 4,
- 6 initial BG rates varying between 0% and 75%,
- 31 values of progress variable varying between 0 and 1. More refined discretization was done for very low and very high progress variable values, in order to better describe the beginning and the end of combustion, respectively.

Figure 2.53 shows an example of progress variable discretization. The discretization of the table definition domain leads to an initial condition map of 13338 operating points.

The combustion process computation using SENKIN [63] is then performed at each operating point, considering a perfectly stirred adiabatic constant-volume reactor and adopting the complete chemical kinetics scheme [86]. Homogeneous reactors were chosen as the main interest here is to capture the auto-ignition delay of the mixture. The constant-volume reactor choice was preferred to the constant-pressure reactor essentially for the following reasons :

- auto-ignition in Diesel ICEs most of the time takes place in the proximity of TDC where volume variations are small,
- once reactive mixture auto-ignites, strong pressure gradients are observed.

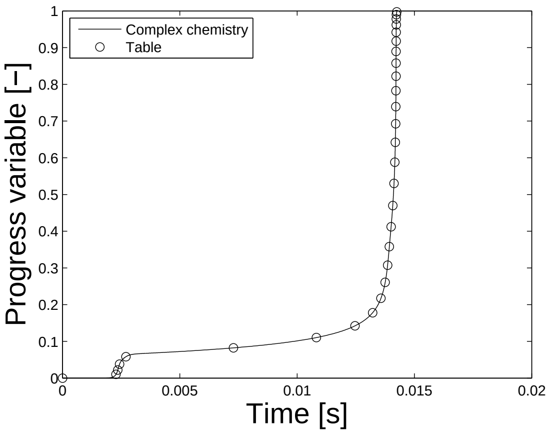

Figure 2.53: Progress variable discretization. Combustion refers to a homogeneous mixture of n-heptane/air/EGR in a constant volume reactor. The initial state : $T_\tau = 750$ K, $p_\tau = 25$ bar, $\Phi = 0.7$ and $Y_D = 45\%$, figure 2.50. The solid line represents the SENKIN computation, while the circles are the value of c stored in the table.

The fact of generating the table by using constant-volume reactor results is a constraining hypothesis when computing the species evolutions during an engine cycle expansion stroke. In fact, in this case, the volume variation is no more negligible. As a consequence, the final composition of the gases within the cylinder can be slightly different from experimental measurements. Nevertheless, the error remains acceptable.

At present, IFP is working on this aspect, and encouraging results were obtained. The formalism used in developing the new approach is the same as the one used in the dual-CM. Consequently, once the new approach is validated, the update of the dual-CM combustion model will be straightforward.

Finally, the table is filled in with the mass fractions of each tabulated species. Regarding the table outputs, tabulated species mixture fractions are obtained as function of the table inputs; that is, for the species x, $Y_x^{TAB} = Y_x^{TAB}\left(T_\tau, p_\tau, \Phi, Y_D, c\right)$.

Figure 2.54 shows the evolutions of CO and CO_2 mass fractions as a function of the progress variable, for a lean mixture with high EGR rate.

An additional information concerning the combustion process progress is stored in the table : the Y_c reaction rate, $\dot{\omega}_{Y_c} = \dot{\omega}_{Y_c}\left(T_\tau, p_\tau, \Phi, Y_D, c\right)$. This variable, containing the temporal information of the combustion kinetics, is in fact necessary for computing the progress variable reaction rate, $\dot{\omega}_c$, through the relation :

$$\begin{aligned}
\dot{\omega}_c &= \frac{d}{dt}\left(\frac{Y_c(c) - Y_c(c=0)}{Y_c(c=1) - Y_c(c=0)}\right) = \frac{1}{Y_c(c=1) - Y_c(c=0)} \cdot \frac{d}{dt}\left(Y_c(c)\right) \\
&= \frac{\dot{\omega}_{Y_c}(c)}{Y_c(c=1) - Y_c(c=0)} \qquad (2.139)
\end{aligned}$$

It has to be noticed, that $\dot{\omega}_{Y_c}$ is not directly retrieved by complex chemistry computations, but it is reconstructed from progress variable evolution assuming a constant

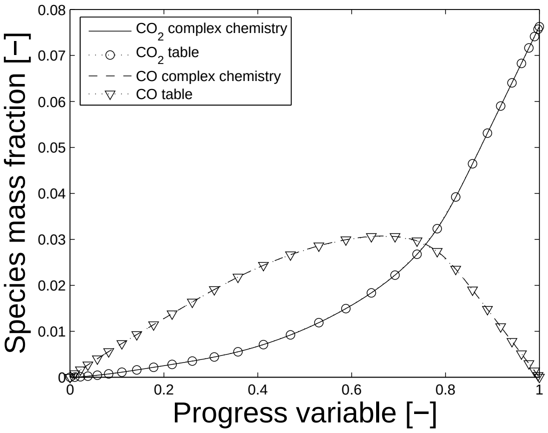

Figure 2.54: Discretization of species evolution curves. In this figure, are presented the evolutions of CO and CO$_2$. The combustion process refers to a homogeneous mixture of n-heptane/air/EGR in a constant volume reactor. The initial state : $T_\tau = 750$ K, $p_\tau = 25$ bar, $\Phi = 0.7$ and $Y_D = 45\%$, figure 2.50. The solid lines represent the SENKIN computations, while the markers indicate the values of CO and CO_2 stored in the table.

reaction rate in each interval $[c_j,\ c_{j+1})$:

$$\dot{\omega}_{Y_c}(c) = \dot{\omega}_{Y_c}(c_j) = \frac{Y_{c_{j+1}} - Y_{c_j}}{t_{j+1} - t_j} \quad \text{for } c \in [c_j,\ c_{j+1}) \tag{2.140}$$

where t_j is the time defined as $c(t_j) = c_j$, and j is a pointer mapping the table progress variable axis. The linear increase of Y_c ensures that the manifold trajectory can be followed with a reduced number of progress variable points.

Figure 2.55 shows the discretization of the temporal progress variable evolution and the corresponding Y_c reaction rate, $\dot{\omega}_{Y_c}$. As shown in figure 2.55, the evolution of c is piecewise linear with time (top), which implies a constant reaction rate on each interval (bottom).

Computation of the species reaction rates

As the choice was done to use a species mass fraction tabulation approach, the species reaction rates must be reconstructed [85]. The methodology is detailed below.

The reaction rate of the species x is obtained from species tabulation by introducing a relaxation time, τ, as :

$$\dot{\omega}_x^{cb} = \frac{\partial Y_x^{cb}}{\partial t} = \frac{Y_x^{TAB}(c(t+\tau)) - Y_x^{cb}(t)}{\tau} \tag{2.141}$$

where t is the current time, τ is the characteristic time-scale permitting us to relax towards the tabulated chemistry, $c(t+\tau)$ is the progress variable value at the time $t+\tau$ and $Y_x^{TAB}(c(t+\tau))$ is the tabulated species mass fraction value at $c = c(t+\tau)$.

More details concerning the physical meaning of the relaxation time are given in appendix E.

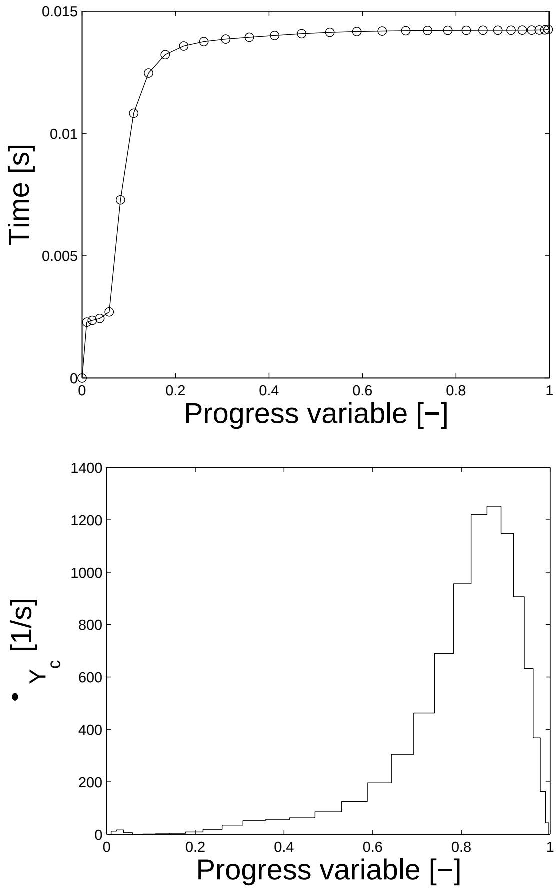

Figure 2.55: Evolution of the progress variable with time (top), and the corresponding Y_c reaction rate, ω_{Y_c} (bottom). The curve refers to the combustion process of a perfectly stirred mixture of n-heptane/air/EGR in a constant volume reactor. Initial state : $T_\tau = 750$ K, $p_\tau = 25$ bar, $\Phi = 0.7$, and $Y_D = 45\%$.

Supposing τ small compared to the chemical time, $c\,(t+\tau)$ is approximated as :

$$c\,(t+\tau) = c\,(t) + \tau \cdot \dot{\omega}_c\,(c(t)) \tag{2.142}$$

where $\dot{\omega}_c$ represents the progress variable reaction rate, equation 2.139.

The value of τ is determined according to the following considerations :

- τ must be smaller than the chemical characteristic time, τ_{chem}, in order to capture the combustion kinetics,
- τ must be strictly greater than the computational time step, dt, in order to guarantee the stability of the numerical scheme. In practice, $\tau = dt$ is often chosen.

The dual-CM was developed in the environment AMESim, appendix A. AMESim permits us to use a fixed or variable time step (dt) in computations. If fixed time step is adopted, the constraints to respect on the choice of τ are $dt \leq \tau < \tau_{chem}$, where τ_{chem} is the chemical time scale. Values for τ of the order of $10^{-6} \div 10^{-5}$ s were found to be sufficient for obtaining accurate results. If variable time step is adopted, as in AMESim dt can vary over several orders of magnitude, for instance $dt = 10^{-30} \div 10^{30}$ s, it is capital to limit the maximum value of dt to $10^{-6} \div 10^{-5}$ s, and fix the value of τ according to the relation $dt \leq \tau < \tau_{chem}$.

The atomic balance equations for C_7H_{14}, O_2 and H_2 are, respectively :

$$\dot{\omega}^{cb}_{C_7H_{14}} = \left(\frac{dm_{C_7H_{14}}}{dt}\right)^{cb} = -\left(7 \cdot \left(\dot{\omega}^{cb}_{C_7H_{16}} \cdot \frac{1}{\mathcal{M}_{C_7H_{16}}}\right) + \left(\dot{\omega}^{cb}_{CO_2} \cdot \frac{1}{\mathcal{M}_{CO_2}}\right) + \right.$$
$$\left. + \left(\dot{\omega}^{cb}_{CO} \cdot \frac{1}{\mathcal{M}_{CO}}\right)\right) \cdot \frac{\mathcal{M}_{C_7H_{14}}}{7} \tag{2.143}$$

$$\dot{\omega}^{cb}_{O_2} = \left(\frac{dm_{O_2}}{dt}\right)^{cb} = -\left(\left(\dot{\omega}^{cb}_{CO} \cdot \frac{1}{\mathcal{M}_{CO}}\right) + 2 \cdot \left(\dot{\omega}^{cb}_{CO_2} \cdot \frac{1}{\mathcal{M}_{CO_2}}\right) + \right.$$
$$\left. \left(\dot{\omega}^{cb}_{H_2O} \cdot \frac{1}{\mathcal{M}_{H_2O}}\right)\right) \cdot \frac{\mathcal{M}_{O_2}}{2} \tag{2.144}$$

$$\dot{\omega}^{cb}_{H_2} = \left(\frac{dm_{H_2}}{dt}\right)^{cb} = -\left(16 \cdot \left(\dot{\omega}^{cb}_{C_7H_{16}} \cdot \frac{1}{\mathcal{M}_{C_7H_{16}}}\right) + 14 \cdot \left(\dot{\omega}^{cb}_{C_7H_{14}} \cdot \frac{1}{\mathcal{M}_{C_7H_{14}}}\right) + \right.$$
$$\left. 2 \cdot \left(\dot{\omega}^{cb}_{H_2O} \cdot \frac{1}{\mathcal{M}_{H_2O}}\right) + \left(\dot{\omega}^{cb}_{H} \cdot \frac{1}{\mathcal{M}_{H}}\right)\right) \cdot \frac{\mathcal{M}_{H_2}}{2} \tag{2.145}$$

where $\dot{\omega}^{cb}_x$, m_x and $\mathcal{M}_x$ are the combustion mass reaction rate, the mass and the molar mass of the species x, respectively. As the NO_x chemistry, at this stage of development of the model, is not taken into account, the combustion reaction rate associated to the nitrogen is null ($\dot{\omega}^{cb}_{N_2} = 0$).

Computation of tabulated combustion processes

For a given set of initial conditions expressed in terms T_τ, p_τ, Φ and Y_D corresponding to the initial conditions of a tabulated combustion process, by using equations 2.133, 2.136, 2.139, and 2.141 to 2.145, it is now possible to compute the combustion process of the gaseous mixture.

For instance, figure 2.56 shows the evolutions of two major species (O_2 and CO) during the combustion process. Results computed using the tabulated chemistry and the complete chemical scheme (SENKIN) are compared.

Both figures 2.55 and 2.56 concern an homogeneous lean-mixture with 45% of BG :

- the species evolution is well predicted if the species is a tabulated one (e.g. CO). This is less the case for oxygen, as it is a reconstructed species that accounts for all oxygenated species other than H_2O, CO and CO_2,
- potentially, the tabulated-chemistry method allows for the description of any species evolution during combustion. Concerning the study of pollutant emissions, this aspect makes the approach a promising one.

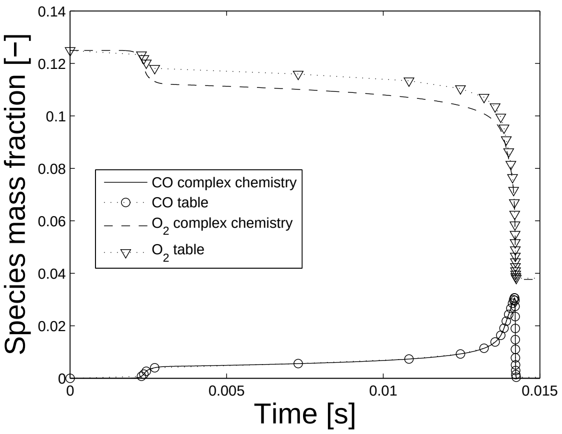

Figure 2.56: Evolutions of O_2 and CO during combustion. Comparison between complete chemical scheme and tabulated chemical scheme. The difference between reconstructed (tabulation method) and computed (complex chemistry method) evolutions concerning the oxygen is put in evidence. Curves refer to the combustion process of a perfectly stirred mixture of n-heptane/air/EGR in a constant volume reactor. Initial state : $T_\tau = 750$ K, $p_\tau = 25$ bar, $\Phi = 0.7$, and $Y_D = 45\%$.

Influence of the relaxation time on combustion

Figure 2.57 shows the influence of the value of the parameter τ on the computed combustion process, equation 2.141. As can be seen in figure 2.57, for values of τ up to $\tau = 100 \cdot dt$ the results are almost superimposed. Further increasing τ leads to differences on the combustion dynamic. Nevertheless, it is worth noting that the right final composition is always obtained.

2.5.2 Laminar combustion submodel

The FPI table contains information which concern a limited number of combustion processes relative to perfectly-stirred adiabatic constant-volume reactors. In order to extend the table application domain to the combustion computation of different system configurations (systems having initial conditions other than the tabulated ones, or variable volume systems), methodologies must be developed and validated.

In the following of this section, two aspects concerning the use of the FPI table for laminar chemistry (perfectly stirred reactors) computations are investigated :

- the determination of the table outputs when the table inputs do not exactly correspond to the coordinates of a tabulated point : the interpolation method,
- the determination of the table inputs when the system control-volume varies; that is, it does/receives work which causes a modification of the combustion process.

Then, in order to validate the combustion model, the dual-CM results are compared with the combustion processes computed by using the complex chemistry solver

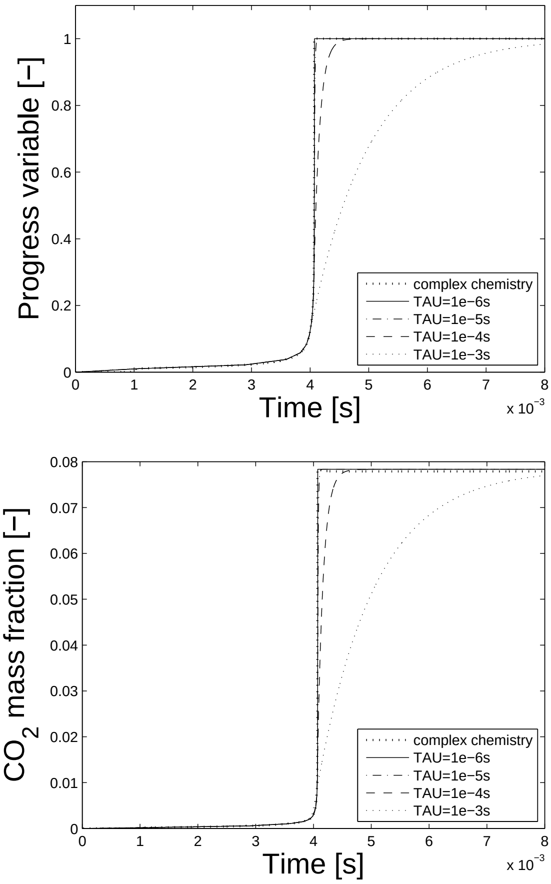

Figure 2.57: Influence of the parameter τ on the progress variable (top) and on the CO_2 evolutions. The complex chemistry result is compared to dual-CM results obtained for different values of τ, ranging from 10^{-6} to 10^{-3} s. The time step for all the computations is $dt = 10^{-6}$ s.

CHEMKIN. The interpolation method is validated by computing the combustion processes in constant volume homogeneous reactor configurations, for different thermochemical initial conditions of the gaseous mixture. Then, the validation is extended to the computation of combustion processes taking place in variable volume[38] homogeneous reactor configurations, for different thermochemical initial conditions of the gaseous mixture.

Interpolation method

The species mass fractions stored in the look-up table are exact only if the set of inputs refers to a table definition node. For all the other conditions, that is in the cases in which table inputs do not exactly correspond to the coordinates of a tabulated point, the species mass fractions are computed using extrapolation and linear interpolation techniques. It is worth investigating both these aspects.

With regard to extrapolation, different choices were done for the different variables

---

[38] The used volume variation law is representative of a classical kinematic law adopted in ICEs.

of the table definition domain. In particular, because of the highly non-linear behavior of the chemical kinetics with equivalence ratio, all kinds of extrapolation along the Φ dimension have been avoided. That is, in reading the look-up table, a mixture composition which does not belong to the table definition domain is considered as being not reactive. Concerning the EGR rate dimension, Y_D, the table definition domain is wide enough to contain all the tested operating conditions; consequently, this dimension does not need any kind of extrapolation. Finally, when dealing with table inputs such as pressure, p_τ, or temperature, T_τ, which are outside the table definition domain, they are considered as being equal to the nearest tabulated value.

On the other hand, with regard to the determination of the table outputs when the table inputs do not exactly correspond to the coordinates of a tabulated point, a linear interpolation method in the composition space of the table values has been set up. Once again, attention must be paid relatively to the Φ coordinate. In fact, as already said, the equivalence ratio is a variable highly non-linear with species mass fraction. In particular, the equivalence ratio, Φ, is related to fuel mixture-fraction, Z, through the relation :

$$\Phi = \frac{Z}{(1-Z)\cdot(1-Y_D)} \cdot \left(\frac{A}{F}\right)_{st} \tag{2.146}$$

where $(A/F)_{st}$ represents the mass Air/Fuel ratio at stoichiometric conditions [6]. Consequently, from equation 2.146, $Y_F = 0 \rightarrow \Phi = 0$ and $Y_F = 1 \rightarrow \Phi = \infty$. For that reason, linear interpolations will not be done in the phase space $(T_\tau, p_\tau, \Phi, Y_D)$ but in the transformed phase space (T_τ, p_τ, Z, Y_D). In the new system of coordinates for the phase space, the variables are not independent from each other; equation 2.146 explicit the relation between Φ, Y_D and Z. For that reason, particular attention must be paid in the interpolation method. Concerning the interpolation done along the dimensions T_τ and p_τ, a simple multi-linear interpolation is done. Figure 2.58 illustrates the schematic of the interpolation method relative to the coordinates Φ and Y_D. In figure 2.58, the subscripts/superscripts S and I are relative to the higher and lower tabulated values (with respect to the reference input value), respectively. If subscripts, they are associated to the EGR rate, otherwise, if superscripts, they are associated to the equivalence ratio. The interpolation method used to find the reaction rate associated to generic Φ and Y_D is resumed in the following steps :

- determining of the upper and lower tabulated values of Y_D in the table,
- once the value of the variable Y_D is fixed as $Y_{D-S/I}$, respectively, using equation 2.146, species mass fractions $Y\left(\Phi, Y_{D-S/I}\right)$ can be expressed as $Y\left(Z_{S/I}, Y_{D-S/I}\right)$,
- determining the upper and lower values of $Z_{S/I}$ with respect to the Φ coordinate : $Z^S_{S/I}$ and $Z^I_{S/I}$, respectively,

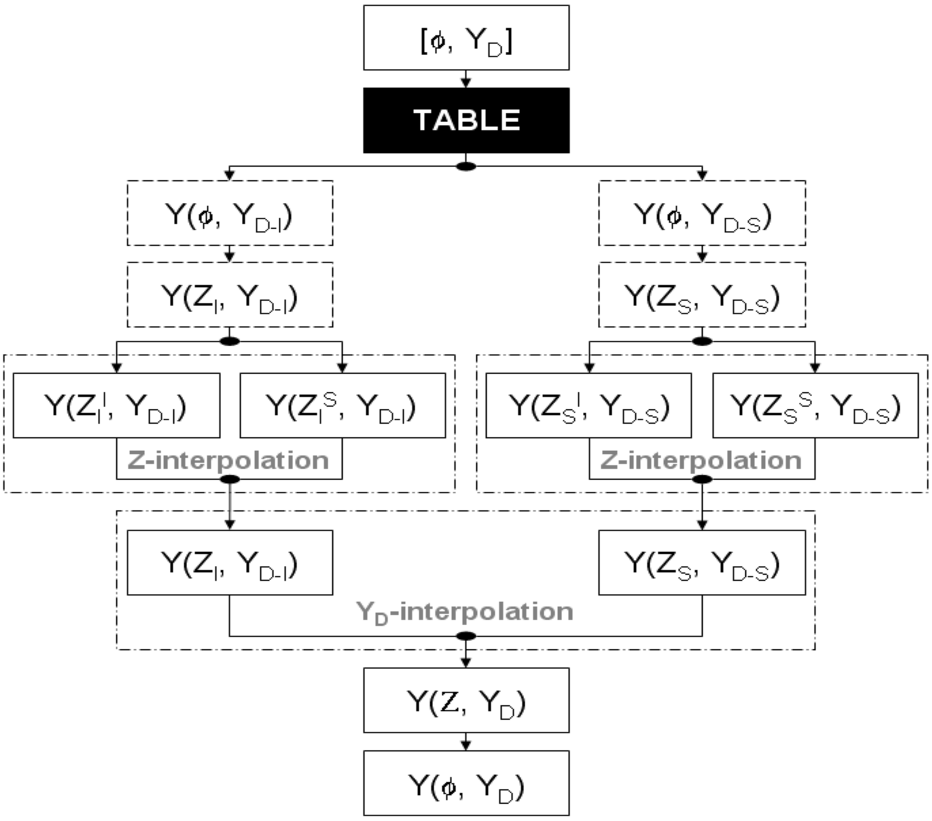

Figure 2.58: Interpolation method in the phase space (T_τ, p_τ, Z, Y_D).

- linear interpolation in $Z_{S/I}$,
- linear interpolation in Y_D,
- the obtained species mass fraction corresponds to the value relative to table input conditions Φ and Y_D.

Figure 2.59 refers to an interpolation along the BG mass fraction dimension of the table.

Figure 2.60 refers to an interpolation along the equivalence ratio dimension of the table.

As shown in figures 2.59 and 2.60, the set up interpolation method permits us to obtain reliable results although the computed combustion process has initial conditions that do not correspond to a tabulated point of the table. In particular, the right kinetics and final compositions are reproduced. Figure 2.59 shows that a slight error appears relatively to the chemical kinetics. This could suggest that, because of the highly non linear impact of the EGR on combustion, a more accurate discretization would be necessary along the BG mass fraction axis. Nevertheless, the error is small and it was judged as acceptable.

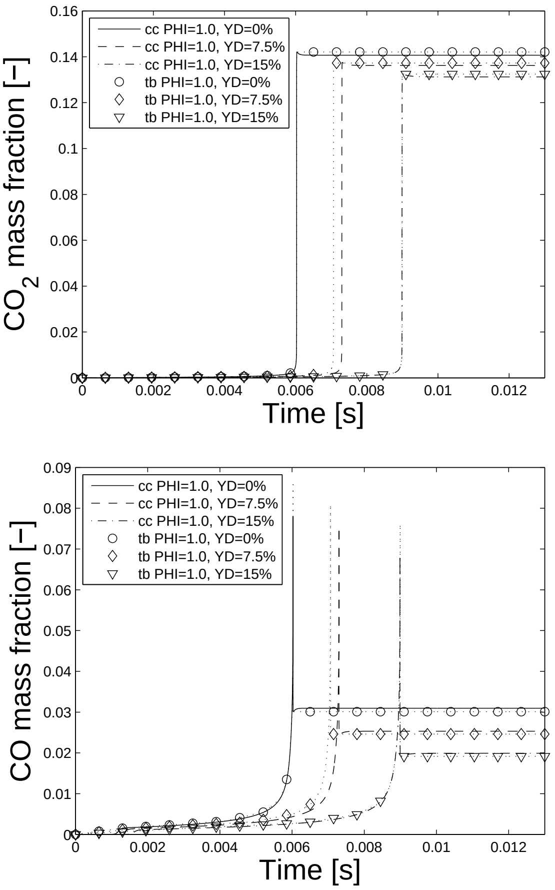

Figure 2.59: Interpolation along the BG mass fraction dimension of the table. Three combustion processes are computed. The initial conditions of the mixture are : $T_\tau = 850$ K, $p_\tau = 10$ bar and $\Phi = 1$. The BG mass fraction value varies from 0% to 15%. The mass fractions of CO_2 (top) and CO (bottom) computed using complex chemistry (*cc*) are compared to those computed using the look-up table (*tb*).

Control volume variation

As the FPI table was generated by using homogeneous adiabatic constant-volume reactors, the use of the FPI table for computing combustion processes taking place in homogeneous adiabatic variable-volume reactors requires the development of a methodology permitting us to take into account the impact of the system volume variations on the combustion process and, consequently, on the table inputs, T_τ and p_τ, used for reading the FPI table.

The methodology used in the dual-CM is based on the following observations :

- the combustion process does not have any impact on the values of the table inputs T_τ and p_τ, as their values are referred to the corresponding fresh gaseous mixture thermodynamic state,
- when a work is done on the system, the thermodynamic state defined by T_τ and p_τ of the fresh gaseous mixture varies.

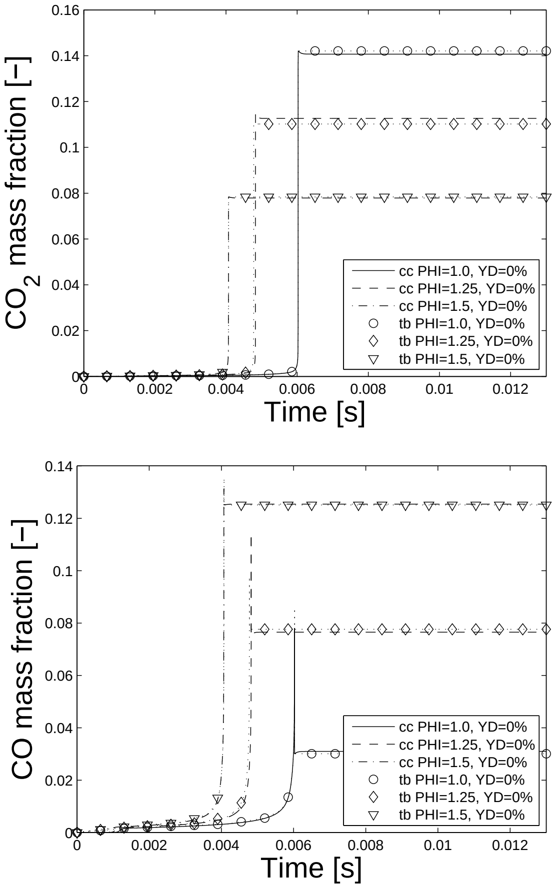

Figure 2.60: Interpolation along the equivalence ratio dimension of the table. Three combustion processes are computed. The initial conditions of the mixture are : $T_\tau = 850$ K, $p_\tau = 10$ bar and $Y_D = 0\%$. The equivalence ratio value varies from 1 to 1.5. The mass fractions of CO_2 (top) and CO (bottom) computed using complex chemistry (*cc*) are compared to those computed using the look-up table (*tb*).

According with the above-mentioned statements, in a case of variable control-volume, the table input variables T_τ and p_τ vary in time. In the particular case of a closed gaseous homogeneous adiabatic system, the table input variables are computed using an isentropic evolution of the fresh gases. As a consequence, the relation between the system volume and the pressure, p_τ, is given by the relation :

$$p_{\tau 0} \cdot V_0^\gamma = p_\tau \cdot V^\gamma = constant \tag{2.147}$$

where $p_{\tau 0}$ and V_0 are the pressure and the volume of the system at the instant $t = t_0$ representing the initial conditions of the computation, V is the volume of the system at a given instant of time, and γ is the isentropic coefficient depending on the mixture molecular properties. As the volume variation law is known, at each instant of time through equation 2.147 it is possible to know the value of p_τ. It is important to note that equation 2.147 is obtained by integrating the most general tracer pressure equation, equation 2.165, applied to the particular case of a closed gaseous homogeneous adiabatic system. Then, the temperature value, T_τ, can be obtained by using the perfect gas state equation as :

$$T_\tau = \frac{p_\tau \cdot V}{n \cdot \mathcal{R}} \tag{2.148}$$

where $\mathcal{R}$ is the universal constant of gases and n is the total number of moles in the fresh gaseous mixture. As combustion is not accounted for, n does not change.

Figure 2.61 and 2.62 refer to the results of two simulations of homogeneous adiabatic variable-volume reactors. In particular, figure 2.61 refers to a configuration having a short auto-ignition delay, while figure 2.62 refers to a configuration having a long auto-ignition delay. The results obtained using the complex chemistry solver SENKIN are compared with the results obtained by using dual-CM. The initial and boundary conditions of the tested cases are given in table 2.4.

	Late injection case	Early injection case
Bore [mm]	86.0	85.0
Stroke [mm]	73.4	88.0
Connecting rod [mm]	149.9	145.0
Compression ratio [-]	8.55	17.8
Engine speed [rpm]	2000	1640
Initial temperature [K]	710	300
Initial pressure [bar]	20.0	1.358
EGR rate [%]	0	0
Equivalence ratio [-]	0.7	0.7
Initial crank angle [CAD ATDC]	-30	-146

Table 2.4: Initial and boundary conditions of the two variable-volume combustion reactor test cases.

As shown, the set up methodology, used for reading the table when the control volume varies in time, permits to correctly estimate the auto-ignition delay of the mixture. In both cases, the method has been shown to correctly predict the auto ignition-delays and the in-cylinder thermodynamic conditions. Furthermore, the good agreement of the curves concerning the evolution of the species CO reveals that the model can predict the species evolutions. Nevertheless, some discrepancies appear about the end of the combustion. This differences can be seen on the CO mass fraction evolutions. They are essentially due to the fact that the table has been generated by using a constant volume hypothesis : this hypothesis, reasonable around TDC, defeats during the expansion stroke. Recently, a solution in order to accounting for the effects of expansion on the chemical kinetics has been developed at IFP, but at the present time it has not been integrated in the dual-CM.

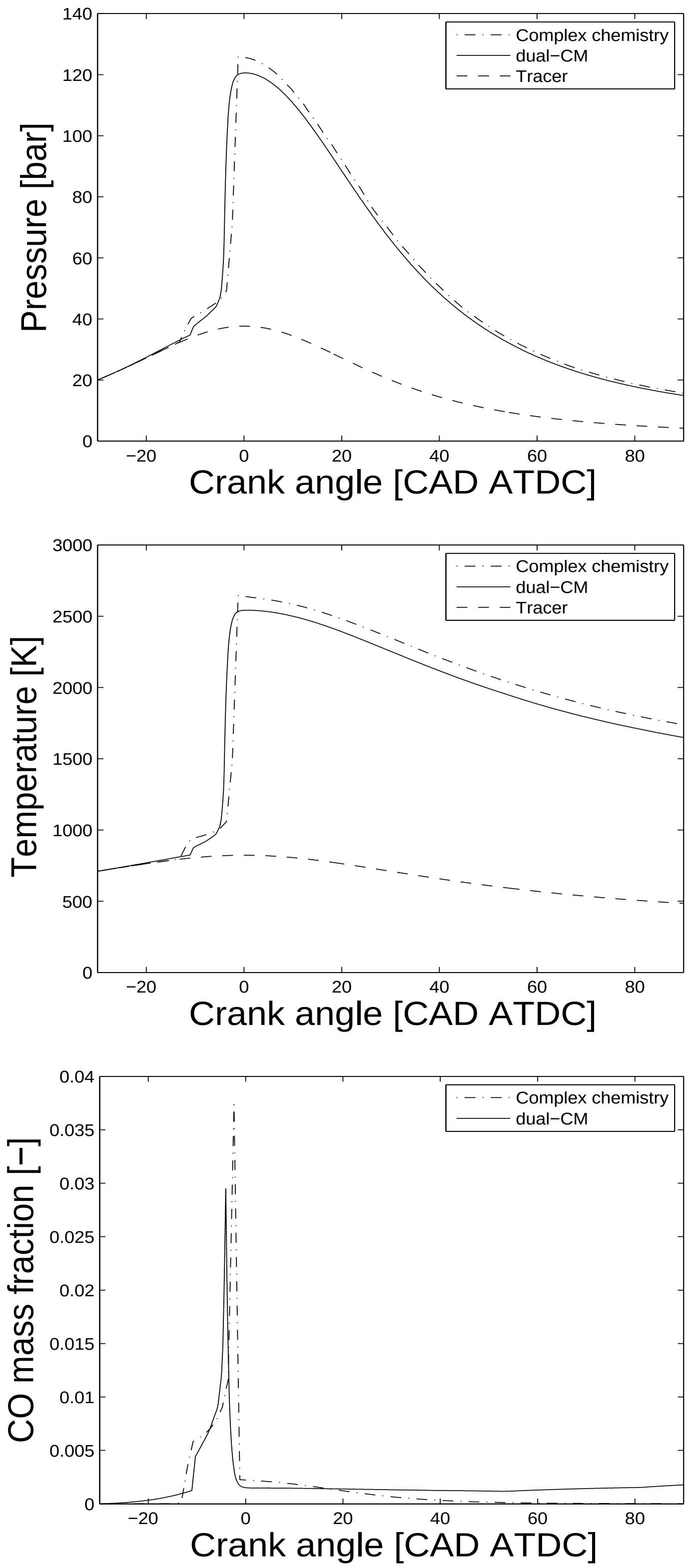

Figure 2.61: A variable volume combustion process is presented. The tested case is representative of a late injection strategy. The initial and boundary conditions of the computation are given in table 2.4. The pressures (top), temperatures (middle) and the CO mass fractions (bottom) are compared. The tracer contitions, expressed in terms of temperature and pressure, used for the lecture of the table are reported, too.

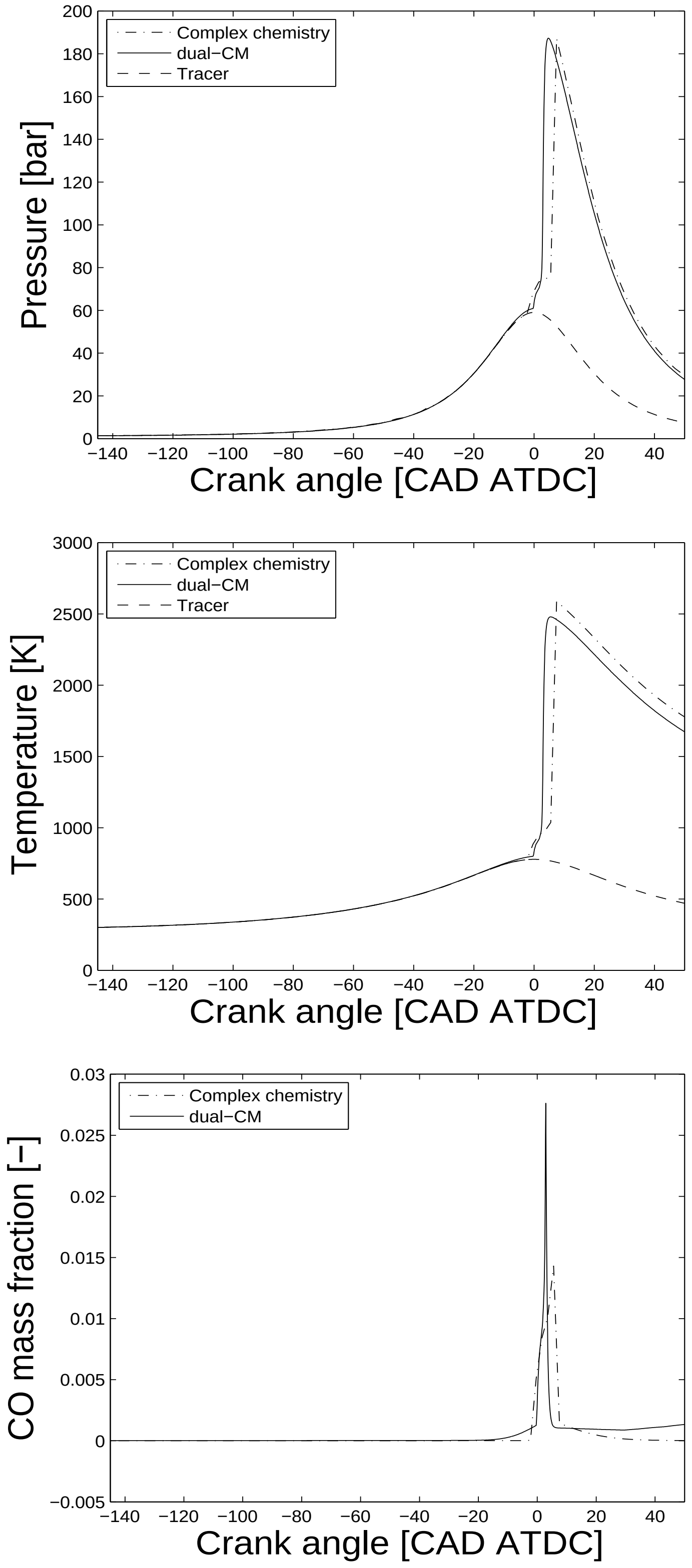

Figure 2.62: A variable volume combustion process is presented. The tested case is representative of an early injection strategy. The initial and boundary conditions of the computation are given in table 2.4. The pressures (top), temperatures (middle) and the CO mass fractions (bottom) are compared. The tracer contitions, expressed in terms of temperature and pressure, used for the lecture of the table are reported, too.

2.5.3 Turbulent combustion submodel

In this section the turbulent combustion modeling is detailed. If compared to the simpler configurations presented in section 2.5.2 (homogeneous adiabatic constant/variable volume reactors), the additional challenges for ICE combustion modeling are :

- the system is not adiabatic because of heat losses through the walls,
- the injected liquid fuel evaporates within the cylinder subtracting energy to the gaseous mixture,
- the burning gaseous mixture within the cylinder is not homogeneous. From the thermochemical point of view, this spatial non-homogeneity appears as differences between local temperatures and equivalence ratios.

In what follows, the methodology developed and adopted in the dual-CM for computing turbulent combustions in ICEs by using the FPI table (section 2.5.1) is detailed. In particular, attention will be paid on the determination of the table input variable values : $T_{\mathcal{T}}$, $p_{\mathcal{T}}$, Φ, Y_D and c.

First of all, it is worthwhile to recall the relation between the fuel mass-fraction, Z, used to characterize the mixture stratification (β-PDF) and the equivalence ratio, Φ, representing an input variable of the look-up table, equation 2.146. In order to facilitate the reading of the manuscript, this equation is repeated below :

$$\Phi = \frac{Z}{(1-Z)\cdot(1-Y_D)} \cdot \left(\frac{A}{F}\right)_{st}$$

As seen in section 2.5.2, the table input variables $T_{\mathcal{T}}$ and $p_{\mathcal{T}}$ refer respectively to the temperature and pressure that would characterize the thermodynamic state of the gaseous mixture, if it was not influenced by combustion. For that reason, in order to be consistent with the nomenclature commonly used in literature, in the following $T_{\mathcal{T}}$ and $p_{\mathcal{T}}$ will be indicated with the names of tracer temperature and tracer pressure respectively[39].

Accordingly, when dealing with engine operating points adopting single injection strategies, $T_{\mathcal{T}}$ and $p_{\mathcal{T}}$ are referred to the in-cylinder temperature and pressure conditions corresponding to the motored engine cycle.

The concept of tracer variables is extended here to the multiple injection context : in the following, the notations $p_{\mathcal{T}_i}$ and $T_{\mathcal{T}_i}$ refer to the pressure and temperature tracer conditions associated with the i^{th} injection, respectively.

Hence, they represent the gaseous mixture thermodynamic conditions computed by neglecting the energy released by the combustion of the fuel of the i^{th} injection, but sensitive to the fuel combustion of the j^{th} injection (with $j \neq i$).

---

[39] For more information concerning the definition of tracer conditions refer to [34].

As seen, $p_{\mathcal{T}_i}$ and $T_{\mathcal{T}_i}$ evolve in time, because of the thermal losses, the liquid fuel evaporation, the fuel combustion of the j^{th} injection and the cylinder volume variation.

In dual-CM, in order to compute $p_{\mathcal{T}_i}$, a dedicated energy balance-equation, independent of the fuel combustion of the i^{th} injection, but taking into account the thermal losses, the liquid fuel evaporation, the energy released by the combustion of the fuel of the j^{th} injection (with $j \neq i$) and the cylinder volume variation, has been set up.

The combustion chamber, representing the studied system, is an open system in which liquid and gaseous phases coexist. In order to set up the energy equation for the i^{th} tracer pressure, only the gaseous phase will be accounted for. Accordingly, the following hypotheses have been made :

- the perfect-gas state equation applies to the gaseous mixture,
- the liquid fuel is injected at temperture T_F, the temperature of the fuel within the injector, and, once in the combustion chamber, it heats up to the liquid-gas saturation temperature before vaporizing,
- the volume occupied by the liquid is negligible.

As seen in section 2.5.1, in the present combustion model approach M major species are retained : C_7H_{16}, C_7H_{14}, N_2, O_2, H_2O, CO_2, CO, H_2 and H.

Consequently for a given spray i, in order to be able to compute the corresponding in-cylinder tracer pressure, $p_{\mathcal{T}_i}$, and mean tracer temperature, $\widetilde{T}_{\mathcal{T}_i}$, an entire set of M species, which evolve during the engine cycle independently from the i^{th} combustion process, must be computed. In the following, the generic mass of the species x, associated with the computation of the tracer conditions relative to the i^{th} spray, and belonging to the j^{th} spray region is noted as ${}^{i}m_{x_j}$, figure 2.63. Hence in the cylinder, the total mass of the species x associated with the computation of the tracer conditions relative to the i^{th} spray, ${}^{i}m_x$, and its mass fraction, ${}^{i}Y_x$, are computed respectively as :

$${}^{i}m_x = \sum_{j=0}^{NI} {}^{i}m_{x_j} \tag{2.149}$$

and :

$${}^{i}Y_x = \frac{{}^{i}m_x}{m_{tot}} \tag{2.150}$$

where NI is the number of injections and m_{tot} is the total gaseous mass within the cylinder[40].

For a given species x associated with the i^{th} spray tracer condition computation, the mass balance equation is :

$${}^{i}\dot{m}_x = {}^{i}\dot{m}_x^{cb} + {}^{i}\dot{m}_x^{i/o} \tag{2.151}$$

---

[40] In equation 2.149, the subscript $j = 0$ indicates the in-cylinder gaseous mass of the species x which does not belong to any spray.

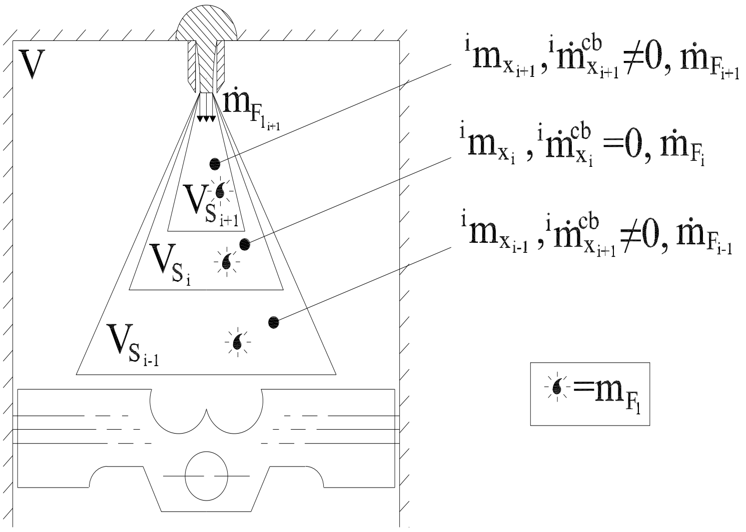

Figure 2.63: Schematic of the system showing the variables used for the computation of the in-cylinder tracer conditions associated with the i^{th} spray combustion process.

where superscripts cb and i/o refer respectively to species mass variations due to the combustion process and to input/output mass flow rates relatively to the system control volume. As the i^{th} spray tracer conditions are independent of the combustion process associated with the i^{th} spray, the term ${}^{i}\dot{m}_x^{cb}$ in equation 2.151, associated with species mass variations due to combustion, is computed as :

$$ {}^{i}\dot{m}_x^{cb} = \sum_{\substack{j=1,NI \\ j\neq i}} \widetilde{\dot{\omega}}_{x_j} \tag{2.152}$$

where $\widetilde{\dot{\omega}}_{x_j}$ represents the mean mass reaction rate of the species x computed for the j^{th} spray, equation 2.178. Then, with the assumption that when combustion occurs the engine inlet/outlet valves are closed (no mass flow rates through the system control volume), the only gaseous mass source term is associated with liquid fuel evaporation, $\dot{m}_F$. Hence, the term ${}^{i}\dot{m}_x^{i/o}$ in equation 2.151 simplifies to :

$$ {}^{i}\dot{m}_x^{i/o} = \dot{m}_F \tag{2.153}$$

where $\dot{m}_F$ is computed as :

$$ \dot{m}_F = \sum_{j=1}^{NI} \dot{m}_{F_j} \tag{2.154}$$

in which $\dot{m}_{F_j}$ is the liquid fuel evaporation rate associated with the j^{th} injection.

The global enthalpy variation, ${}^{i}dH$, is computed applying the first principle of thermodynamics to the system :

$$ {}^{i}dH = d\left(\sum_{x=1}^{M} h_x \cdot {}^{i}m_x\right) = \delta Q_{th} + \delta Q_{ev} + V \cdot dp_{\tau_i} + h_F \cdot dm_F \tag{2.155}$$

with h_x the specific enthalpy of the species x, Q_{th} the term representing the heat losses, section 2.6.3, and Q_{ev} the source term relative to the liquid fuel evaporation. The term Q_{ev} is computed as :

$$\delta Q_{ev} = -\left(l\left(T_F\right) + \left(h_F\left(\widetilde{T}_{\tau_i}\right) - h_F\left(T_F\right)\right)\right) \cdot \dot{m}_F \tag{2.156}$$

where l is the latent heat of evaporation of n-heptane at the fuel injection temperature T_F, computed according to equation C.41. For perfect gases :

$$dh_x = \left.\frac{\partial h_x\left(\widetilde{T}_{\tau_i}\right)}{\partial \widetilde{T}_{\tau_i}}\right|_p \cdot d\widetilde{T}_{\tau_i} = c_{p_x}\left(\widetilde{T}_{\tau_i}\right) \cdot d\widetilde{T}_{\tau_i} \tag{2.157}$$

and by definition :

$$^{i}c_p\left(\widetilde{T}_{\tau_i}\right) = \sum_{x=1}^{M} c_{p_x}\left(\widetilde{T}_{\tau_i}\right) \cdot^{i} Y_x \tag{2.158}$$

where $^{i}c_p$ is the specific constant-pressure heat capacity of the tracer gaseous mixture associated with the i^{th} spray. The specific constant-pressure heat capacities, $c_{p_x}\left(\widetilde{T}_{\tau_i}\right)$, are computed by using the Janaf's polynomials.

Consequently, the left-hand side term of equation 2.155 can be written as :

$$d\left(\sum_{x=1}^{M} h_x \cdot^{i} m_x\right) = \sum_{x=1}^{M} h_x \cdot d\,^{i}m_x^{cb} + m_{tot} \cdot^{i} c_p \cdot d\widetilde{T}_{\tau_i} \tag{2.159}$$

The expression giving the variation of the temperature, $d\widetilde{T}_{\tau_i}$, is obtained by differentiating the perfect gas equation, equation 2.148 :

$$\frac{d\widetilde{T}_{\tau_i}}{\widetilde{T}_{\tau_i}} = \frac{dp_{\tau_i}}{p_{\tau_i}} + \frac{dV}{V} - \frac{d\,^{i}n}{^{i}n} \tag{2.160}$$

where the terms dV and V are given by the kinematic piston law, section 2.6.2, and the terms $d\,^{i}n$ and ^{i}n, where ^{i}n represents the number of moles associated with the i^{th} spray trace conditions, are given by the relations :

$$d\,^{i}n = \sum_{x=1}^{M} \frac{d\,^{i}m_x}{\mathcal{M}_x} \quad \text{and} \quad ^{i}n = \sum_{x=1}^{M} \frac{^{i}m_x}{\mathcal{M}_x} \tag{2.161}$$

in which $\mathcal{M}_x$ is the molar mass of the species x. Combining equations 2.155, 2.159 and 2.160 gives :

$$\begin{aligned} dp_{\tau_i} = \; & \tfrac{^{i}c_p}{^{i}c_p - ^{i}R} \cdot p_{\tau_i} \cdot \left(\tfrac{d\,^{i}n}{^{i}n} - \tfrac{dV}{V}\right) + \tfrac{^{i}R}{^{i}c_p - ^{i}R} \cdot \tfrac{1}{V} \cdot \left(\delta Q_{th} + \delta Q_{ev}\right) + \\ & + \tfrac{^{i}R}{^{i}c_p - ^{i}R} \cdot \tfrac{1}{V} \cdot \left(h_F \cdot dm_F - \textstyle\sum_{x=1}^{M} h_x \cdot d\,^{i}m_x^{cb}\right) \end{aligned} \tag{2.162}$$

where ^{i}R is the gas constant of the mixture, associated with the i^{th} spray tracer conditions, computed as :

$$^{i}R = \mathcal{R} \cdot \sum_{x=1}^{M} \frac{^{i}Y_x}{\mathcal{M}_x} \tag{2.163}$$

The total enthalpy term of the species x, h_x, can be decomposed in a term of formation enthalpy, h_x^0, and a term of sensible enthalpy, h_{s_x}, as :

$$h_x\left(\widetilde{T}_{\tau_i}\right) = h_x^0 + h_{s_x}\left(\widetilde{T}_{\tau_i}\right) \tag{2.164}$$

where the formation enthalpy is computed at a given reference temperature, T_0.

Introducing the definitions given in equations 2.161, the final expression for the tracer pressure derivative is :

$$\begin{aligned} \frac{dp_{\tau_i}}{dt} = \quad & \frac{{}^i c_p}{{}^i c_v} \cdot p_{\tau_i} \cdot \left(\frac{1}{\sum_{x=1}^{M} \frac{{}^i m_x}{\mathcal{M}_x}} \cdot \sum_{x=1}^{M} \frac{1}{\mathcal{M}_x} \cdot^i \dot{m}_x - \frac{1}{V} \cdot \frac{dV}{dt} \right) + \\ & + \frac{{}^i R}{{}^i c_v} \cdot \frac{1}{V} \cdot \left(\dot{Q}_{th} + \dot{Q}_{ev} +^i \dot{Q}_{cb} + h_F \cdot \dot{m}_F \right) \end{aligned} \tag{2.165}$$

where the specific constant-volume heat capacity of the mixture, ${}^i c_v$, is computed as :

$${}^i c_v =^i c_p -^i R \tag{2.166}$$

and the term ${}^i\dot{Q}_{cb}$, representing the heat release due to combustion processes associated to spray other than the i^{th}, is computed as :

$${}^i\dot{Q}_{cb} = -\sum_{x=1}^{M} h_x \cdot^i \dot{m}_x^{cb} \tag{2.167}$$

in which ${}^i\dot{m}_x^{cb}$ is given by equation 2.152.

Equation 2.165 is integrated by the solver to compute the i^{th} spray tracer-pressure evolution[41]. Finally, the i^{th} spray mean tracer-temperature, $\widetilde{T}_{\tau_i}$, is computed using the perfect gas equation as :

$$\widetilde{T}_{\tau_i} = \frac{p_{\tau_i} \cdot V}{m_{tot} \cdot^i R} \tag{2.168}$$

Using the PCM approach, the general equation used to compute the mean value of a generic tabulated variable ϕ in the i^{th} spray is :

$$\widetilde{\phi}_i^{PCM} = \int \phi\left(T_{\tau_i}^*, p_{\tau_i}^*, Z^*, Y_D^*, c_i^*\right) \cdot \mathcal{P}_{co_i}\left(T_{\tau_i}^*, p_{\tau_i}^*, Z^*, Y_D^*, c_i^*\right) \cdot dT_{\tau_i}^* \cdot dp_{\tau_i}^* \cdot dZ^* \cdot dY_D^* \cdot dc_i^* \tag{2.169}$$

where $\mathcal{P}_{co_i}$ is the coupled PDF giving the probability of having in the i^{th} spray a local mixture characterized by a temperature, $T_{\tau_i}^*$, a pressure, $p_{\tau_i}^*$, a fuel mixture fraction, Z^*, an BG mass fraction, Y_D^* and a combustion process progress, c_i^*. Equation (2.169) is very difficult to solve because of the complex interactions between the different variables.

For that reason, in order to compute the mean value of the generic tabulated variable ϕ, several assumptions have to be made :

- p_{τ_i} and Y_D are uniform in the domain,

---

[41] Note that equation 2.165 when used for computing the tracer pressure evolution of homogeneous adiabatic gaseous reactors reduces to equation 2.147.

- T_{τ_i} depends only on the fuel mixture fraction, Z,
- c_i is considered to be homogeneous in the spray region and equal to the spray mean progress variable value, $\widetilde{c}_i$, (first order PCM approach). In particular the PDF of c_i conditioned to Z, $\mathcal{P}_i\left(c_i \middle| Z\right)$, is :

$$\mathcal{P}_i\left(c_i \middle| Z\right) = \delta\left(c_i - \widetilde{c}_i\right) \quad \text{valid} \quad \forall Z \tag{2.170}$$

  This assumption, certainly the strongest one, has probably an impact on the combustion process. The validity of this assumption will be investigated in section 4.2. However, it is worth noting that it does not impact the computation of the start of combustion [13].

According to the aforementioned assumptions, for the i^{th} spray, the coupled PDF, $\mathcal{P}_{co_i}$, reduces to a simpler PDF, $\mathcal{P}_i$, giving the probability of having within the spray a local fuel mixture fraction, Z, at a given tracer temperature, T_{τ_i}. Moreover, as the local tracer temperature is supposed to depend only by the local fuel mixture fraction value, the $\mathcal{P}_i$ is written as a single-variable PDF, only depending by the fuel mixture fraction variable Z :

$$\mathcal{P}_{co_i}\left(T^*_{\tau_i}, p^*_{\tau_i}, Z^*, Y^*_D, c^*_i\right) = \mathcal{P}_i\left(Z^*\right)\cdot\delta\left(T^*_{\tau_i} - T_{\tau_i}\left(Z^*\right)\right)\cdot\delta\left(p^*_{\tau_i} - p_{\tau_i}\right)\cdot\delta\left(Y^*_D - Y_D\right)\cdot\delta\left(c^*_i - \widetilde{c}_i\right) \tag{2.171}$$

Now, the mean value of the generic variable ϕ_i in the i^{th} spray is computed as :

$$\widetilde{\phi}_i^{PCM} = \int \phi_i\left(T_{\tau_i}\left(Z^*\right), p_{\tau_i}, Z^*, Y_D, \widetilde{c}_i\right) \cdot \mathcal{P}_i(Z^*) \cdot dZ^* \tag{2.172}$$

The equation defining the local tracer temperature of the mixture in the i^{th} spray, T_{τ_i}, as a function of the fuel mixture fraction, Z, is :

$$T_{\tau_i} = T_{\tau_i}\left(Z\right) = \widetilde{T}_{\tau_i} + \left(\frac{T_{s_i} - \widetilde{T}_{\tau_i}}{Z_{s_i} - \widetilde{Z}_i}\right) \cdot \left(Z - \widetilde{Z}_i\right) \tag{2.173}$$

where Z_{s_i} and T_{s_i} are the values of the mixture fraction and the temperature at the liquid-gas interface under evaporating conditions respectively as computed in section 2.4.1.1, and $\widetilde{T}_{\tau_i}$ is the value of the mean tracer temperature of the domain, equation 2.168.

In what follows, the methodology used for reconstructing the mean reaction rate of the species x in the i^{th} spray region at a given time t, $\widetilde{\dot{\omega}}_{x_i}$, is detailed.

The mean progress variable is computed as :

$$\widetilde{c}_i = \frac{\widetilde{Y}_{c_i}}{\widetilde{Y}^{PCM}_{c_{eq_i}}} \tag{2.174}$$

in which $\widetilde{Y}_{c_i}$ and $\widetilde{Y}^{PCM}_{c_{eq_i}}$ are computed respectively as :

$$\widetilde{Y}_{c_i} = Y_{CO_i} + Y_{CO_{2_i}} \tag{2.175}$$

and :

$$\widetilde{Y}_{c_{eq_i}}^{PCM} = \int Y_{c_i}\left(T_{\tau_i}\left(Z^*\right), p_{\tau_i}, Z^*, Y_D, c_i = 1\right) \cdot \mathcal{P}_i(Z^*) \cdot dZ^* \tag{2.176}$$

where Y_{CO_i} and $Y_{CO_{2_i}}$ are the CO and CO_2 mass fractions within the i^{th} spray, and the fuel mixture fraction PDF associate with the i^{th} spray, $\mathcal{P}_i\left(Z^*\right)$, is computed as shown in section 2.4.2.3.

Then, the mean progress variable reaction rate is computed as :

$$\widetilde{\dot{\omega}}_{c_i} = \frac{\widetilde{\dot{\omega}}_{Y_{c_i}}^{PCM}}{\widetilde{Y}_{c_{eq_i}}^{PCM}} \tag{2.177}$$

where $\widetilde{\dot{\omega}}_{Y_{c_i}}^{PCM}$ is obtained from the FPI table through equation 2.172.

Finally, the reaction rate of the species x is computed as :

$$\widetilde{\dot{\omega}}_{x_i} = \frac{\widetilde{Y}_{x_i}^{PCM}\left(\widetilde{c}_i + d\widetilde{c}_i\right) - Y_{x_i}}{\tau} \tag{2.178}$$

where $\widetilde{Y}_{x_i}^{PCM}\left(\widetilde{c}_i + d\widetilde{c}_i\right)$ is computed through equation 2.172 using a progress variable value equal to $\widetilde{c}_i + d\widetilde{c}_i$, and Y_{x_i} is the mass fraction of the species x in the i^{th} spray. The value of $d\widetilde{c}_i$ is computed as :

$$d\widetilde{c}_i = \widetilde{\dot{\omega}}_{c_i} \cdot \tau \tag{2.179}$$

The behavior of the turbulent combustion submodel will be further investigated in sections 3 and 4.

2.6 Auxiliary models

In order to perform engine cycle computations, the model of combustion, dual-CM, is coupled with other models commonly used in ICE simulations. In particular, three models will be detailed here :

- a thermodynamic model describing the gaseous mixture evolution within the cylinder, section 2.6.1,
- a kinematic model for the piston motion, section 2.6.2,
- a thermal loss model describing the heat losses through the walls, section 2.6.3.

2.6.1 In cylinder gas mixture thermodynamic model

The dual-CM approach set up in this chapter is a multi-zone model : a zone for each spray plus an additional zone corresponding to the gases outside the spray regions. The pressure is supposed to be homogeneous in the cylinder, but the mean temperatures vary from one zone to another. The combustion chamber, representing the studied system, is an open system in which liquid and gaseous phases coexist. In order to set up the energy equation for the pressure, only the gaseous phase will be accounted for. Accordingly, the following hypotheses have been made :

- the perfect-gas state equation is applied to the gaseous mixture,
- the liquid fuel is injected at temperature T_F, the temperature of the fuel within the injector, and, once in the combustion chamber, it heats up to the liquid-gas saturation temperature before vaporizing,
- the volume occupied by the liquid is negligible.

For a given species x, the mass balance equation is :

$$\dot{m}_x = \dot{m}_x^{cb} + \dot{m}_x^{i/o} \tag{2.180}$$

where superscripts cb and i/o refer to mass species variations due to the combustion process and to input/output mass flow rates relatively to the control volume of the system (that is the mass flow rates through the inlet/outlet valves and the fuel evaporation rate), respectively. The term $\dot{m}_x^{i/o}$ is defined as :

$$\dot{m}_x^{i/o} = \dot{m}_x^{i} - \dot{m}_x^{o} \tag{2.181}$$

The global enthalpy variation, dH, is computed applying the first principle of thermodynamics to the system :

$$dH = d\left(\sum_{x=1}^{M} h_x \cdot m_x\right) = \delta Q_{th} + \delta Q_{ev} + V \cdot dp + \sum_{i/o}\sum_{x=1}^{M} h_x^{i/o} \cdot dm_x^{i/o} \tag{2.182}$$

with h_x the specific enthalpy of the species x, Q_{th} the term representing the heat losses, section 2.6.3, and Q_{ev} the source term relative to the liquid fuel evaporation. The term Q_{ev} is computed as :

$$\delta Q_{ev} = -\left(l\left(T_F\right) + \left(h_F\left(T\right) - h_F\left(T_F\right)\right)\right) \cdot \dot{m}_F \tag{2.183}$$

where l is the latent heat of evaporation of n-heptane at the temperature T_F, computed according to equation C.41. Knowing that for perfect gases :

$$dh_x = \left.\frac{\partial h_x\left(T\right)}{\partial T}\right|_p \cdot dT = c_{p_x}\left(T\right) \cdot dT \tag{2.184}$$

and by definition :

$$c_p\left(T\right) = \sum_{x=1}^{M} c_{p_x}\left(T\right) \cdot Y_x \tag{2.185}$$

where c_p is the specific constant-pressure heat capacity of the gaseous mixture, the left-hand side term of equation 2.182 can be written :

$$d\left(\sum_{x=1}^{M} h_x \cdot m_x\right) = \sum_{x=1}^{M} h_x \cdot dm_x^{cb} + m_{tot} \cdot c_p \cdot dT \tag{2.186}$$

where m_{tot} is the total mass within the cylinder. The specific constant-pressure heat capacities, $c_{p_x}(T)$, are computed by using the Janaf's polynomials. The expression giving the variation of the temperature, dT, is computed by differentiating the perfect gas equation, equation 2.148 :

$$\frac{dT}{T} = \frac{dp}{p} + \frac{dV}{V} - \frac{dn}{n} \tag{2.187}$$

where the terms dV and V are given by the kinematic piston law, section 2.6.2, and the terms dn and n are given by the relations :

$$dn = \sum_{x=1}^{M} \frac{dm_x}{\mathcal{M}_x} \quad \text{and} \quad n = \sum_{x=1}^{M} \frac{m_x}{\mathcal{M}_x} \tag{2.188}$$

Combining equations 2.182, 2.186 and 2.187 gives :

$$\begin{aligned} dp = & \quad \tfrac{c_p}{c_p - R} \cdot p \cdot \left(\tfrac{dn}{n} - \tfrac{dV}{V}\right) + \tfrac{R}{c_p - R} \cdot \tfrac{1}{V} \cdot \left(\delta Q_{th} + \delta Q_{ev}\right) + \\ & + \tfrac{R}{c_p - R} \cdot \tfrac{1}{V} \cdot \left(\textstyle\sum_{i/o} \sum_{x=1}^{M} h_x^{i/o} \cdot dm_x^{i/o} - \sum_{x=1}^{M} h_x \cdot dm_x^{cb}\right) \end{aligned} \tag{2.189}$$

The total enthalpy term of the species x, h_x, can be decomposed in a term of formation enthalpy, h_x^0, and a term of sensible enthalpy, h_{s_x} :

$$h_x(T) = h_x^0 + h_{s_x}(T) \tag{2.190}$$

where the formation enthalpy is computed at a given reference temperature, T_0. Introducing the definition given in equation 2.188, the final expression for the temporal pressure rate is :

$$\begin{aligned} \frac{dp}{dt} = & \quad \tfrac{c_p}{c_v} \cdot p \cdot \left(\frac{1}{\sum_{x=1}^{M} \frac{m_x}{\mathcal{M}_x}} \cdot \textstyle\sum_{x=1}^{M} \frac{1}{\mathcal{M}_x} \cdot \dot{m}_x - \frac{1}{V} \cdot \frac{dV}{dt}\right) + \\ & + \tfrac{R}{c_v} \cdot \tfrac{1}{V} \cdot \left(\dot{Q}_{th} + \dot{Q}_{ev} + \dot{Q}_{cb} + \textstyle\sum_{i/o} \sum_{x=1}^{M} h_x^{i/o} \cdot \dot{m}_x^{i/o}\right) \end{aligned} \tag{2.191}$$

where the term $\dot{Q}_{cb}$, representing the heat release due to the combustion process, is defined as :

$$\dot{Q}_{cb} = -\sum_{x=1}^{M} h_x \cdot \dot{m}_x^{cb} \tag{2.192}$$

and the specific constant-volume heat capacity, c_v, is computed as :

$$c_v = c_p - R \tag{2.193}$$

Equation 2.191 is integrated by the solver to compute the pressure evolution within the cylinder. Finally, the temperature of the gaseous mixture is computed using the perfect gas equation :

$$T = \frac{p \cdot V}{m_{tot} \cdot R} \tag{2.194}$$

2.6.2 Kinematic model of the piston motion

In this section the kinematic model of the piston motion is detailed. It permits us to obtain at each instant the combustion chamber volume, V, and its temporal derivative, dV/dt, as function of the engine geometrical specifications and operating conditions. These two variables are fundamental for computing the energy equations as detailed in sections 2.5.3 and 2.6.1. Figure 2.64 represents a schematic of a mono-cylinder. In particular in the figure the following entities can be distinguished :

- $\boldsymbol{B}$, the bore,
- $\boldsymbol{s}$, the stroke,
- $\boldsymbol{b}$, the connecting rod length,
- $\boldsymbol{a}$, the crank radius,
- $\boldsymbol{e}$, represents the squish height,
- $\boldsymbol{x}$, is a coordinate defining the distance between the top of the piston and the engine head,
- $\boldsymbol{g}$, is the projection of the connection rod and crank radius on the cylinder axis,
- V_b, is the volume of the bowl,
- $\boldsymbol{\theta}$, is the crank angle,
- $\dot{\boldsymbol{\theta}}$, is the crank speed,
- $\ddot{\boldsymbol{\theta}}$, is the crank acceleration,
- TDC, indicates the Top Dead Center piston position,
- BDC, indicates the Bottom Dead Center piston position.

According to the used notations, the dead volume, V_d, defined as the volume when piston is at TDC, is computed as :

$$V_d = V_b + \left(\frac{\pi \cdot \boldsymbol{B}^2}{4}\right) \cdot \boldsymbol{e} \tag{2.195}$$

then the instantaneous cylinder volume is computed as :

$$V = V_d + \left(\frac{\pi \cdot \boldsymbol{B}^2}{4}\right) \cdot (\boldsymbol{b} + \boldsymbol{a} - \boldsymbol{g}) \tag{2.196}$$

in which $\boldsymbol{g}$ is computed as :

$$\boldsymbol{g} = \boldsymbol{a} \cdot \cos \boldsymbol{\theta} + \sqrt{\boldsymbol{b}^2 - \boldsymbol{a}^2 \cdot \sin^2 \boldsymbol{\theta}} \tag{2.197}$$

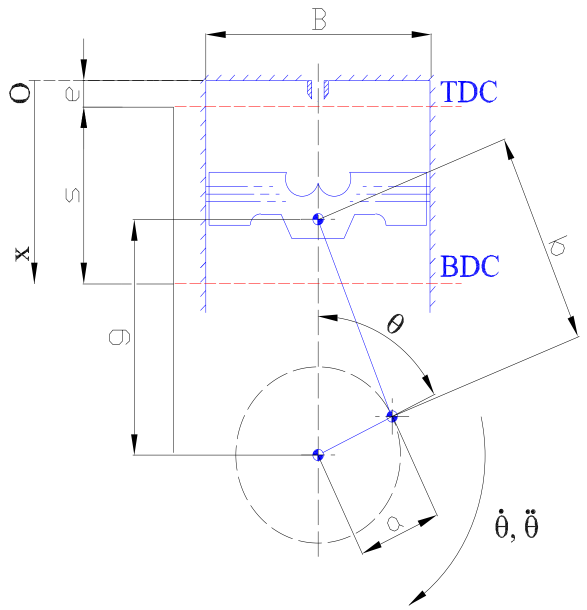

Figure 2.64: Kinematic model of the piston motion.

Concerning the computation of the temporal volume derivative :

$$\frac{dV}{dt} = \frac{dV}{d\boldsymbol{\theta}} \cdot \frac{d\boldsymbol{\theta}}{dt} = \frac{dV}{d\boldsymbol{\theta}} \cdot \dot{\boldsymbol{\theta}} \tag{2.198}$$

the term $dV/d\boldsymbol{\theta}$ is then computed deriving the equation 2.196 :

$$\frac{dV}{d\boldsymbol{\theta}} = \left(\frac{\pi \cdot \boldsymbol{B}^2}{4}\right) \cdot \boldsymbol{a} \cdot \sin\boldsymbol{\theta} \cdot \left(1 + \frac{\cos\boldsymbol{\theta}}{\sqrt{\frac{\boldsymbol{b}^2}{\boldsymbol{a}^2} - \sin^2\boldsymbol{\theta}}}\right) \tag{2.199}$$

2.6.3 Thermal loss model

The purpose of this model is to quantify the energy losses due to the thermal transfers through the walls during the engine-cycle phases. The retained model is the one proposed in [69]. Here in the following the most important results will be presented. In the model, the heat transfer by radiation is neglected. Consequently, only the convection mechanism is taken into account. The heat loss flow rate is modeled as :

$$\dot{Q}_{th} = h_c \cdot (T - T_w) \cdot S_w \tag{2.200}$$

where T_w is the wall temperature, S_w is the heat exchange surface and h_c is the convection coefficient computed as :

$$h_c = 3.26 \cdot \boldsymbol{B}^{-0.2} \cdot \left(\frac{p}{1000}\right)^{0.8} \cdot T^{-0.55} \cdot u_g^{0.8} \tag{2.201}$$

where $\boldsymbol{B}$ is the cylinder bore, p is the in-cylinder pressure and u_g is the local velocity of the gas computed by using the following empirical correlation :

$$u_g = \left[C_1 \cdot \bar{S}_P + C_2 \cdot \frac{V_{displ} \cdot T_0}{p_0 \cdot V_0} \cdot (p - p_T)\right] \tag{2.202}$$

with $\bar{S}_P$ the mean piston velocity as defined in [6], V_{displ} the single cylinder displacement, p_τ the in-cylinder pressure when no combustion occurs, and T_0, p_0 and V_0 are the temperature, pressure and volume at the beginning of combustion[42]. The two coefficients, C_1 and C_2, change during the engine-cycle according to the engine-cycle phase :

- $C_1 = 6.18$ and $C_2 = 0$ during the intake and exhaust strokes,
- $C_1 = 2.28$ and $C_2 = 0$ during the compression stroke,
- $C_1 = 2.28$ and $C_2 = 3.24 \cdot 10^{-3}$ during the expansion stroke.

2.7 Parametric study of the model

In this section a parametric study of the dual-CM is presented : the aim here is to show how the different adjustment parameters influence the combustion process, and the sensitivity of the dual-CM to variations of those parameters.

The dual-CM adjustment parameters are :

- b, which has an influence on the liquid fuel penetration and, consequently, on the liquid fuel evaporation rate[43] (section 2.4.1.2, equation 2.35),
- C_S, which has an influence on the gaseous spray penetration and, consequently, on the spray volume growth and the ambient-gas entrainment within the spray region (section 2.4.2.2, equation 2.78),
- C_K and C_κ, which are pre-exponential coefficients of the dissipation terms associated with the mean specific kinetic energy, K, and the turbulent specific kinetic energy, κ, respectively and, consequently, they have an influence on the in-cylinder gaseous-mixture kinetic energy, E_c, dissipation (section 2.4.3, equation 2.100),
- N_K and N_κ, which are exponential coefficients of the dissipation terms associated with the mean specific kinetic energy, K, and the turbulent specific kinetic energy, κ, respectively and, consequently, they have an influence on the in-cylinder gaseous-mixture kinetic energy, E_c, dissipation (section 2.4.3, equation 2.100),
- C_{ds}, which has an influence on the fuel-mixture-fraction distribution variance and, consequently, on the in-cylinder gaseous mixture mixing process (section 2.4.4, equation 2.120),
- $Z_{s_{max}}$, which has an influence on the fuel-mixture-fraction distribution variance (section 2.4.4, equation 2.120),

---

[42] The beginning of combustion is the instant at which Heat Release, associated with chemical reactions, begins.

[43] In [53], the author recommends $b = 0.41$.

The above mentionned adjustment parameters once fixed were maintained constant for all the computations presented in chapter 3 : their values are given in table 2.5.

Parameter	Value
b	0.41
C_S	1.3
C_K,C_κ	15
N_K,N_κ	1.9
C_{ds}	0.67
$Z_{s_{max}}$	0.8

Table 2.5: Set of adjustment parameters used in dual-CM. The parameters once fixed were maintained constant for all the computations presented in chapter 3.

Figure 2.65 shows the comparison of the dual-CM in-cylinder pressure curve, computed by using the adjustment parameter values given in table 2.5, with experiments[44]; the engine operating point specifications are given in table 2.6.

Variable	Unit	Value
Engine speed	[rpm]	1497
$IMEP$	[bar]	6.1
Y_D	[%]	36.3
AVI	[CAD BTDC]	6
Φ	[-]	0.89
p_{inj}	[bar]	1600

Table 2.6: Engine operating point specifications.

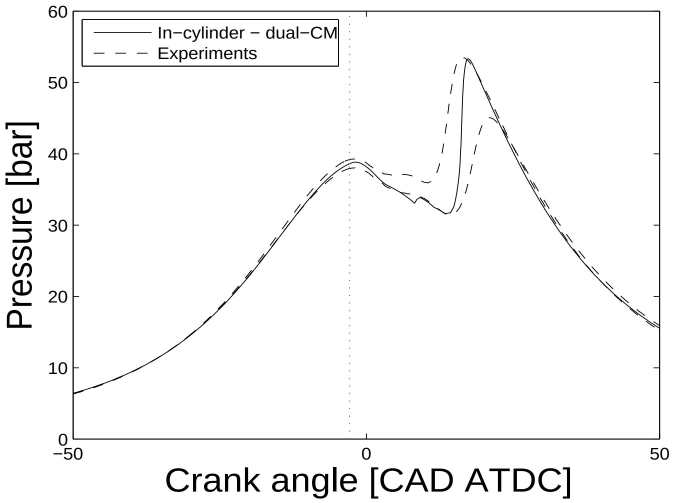

Figure 2.65: Comparison of the dual-CM in-cylinder pressure curve with experiments : the engine operating point specifications are given in table 2.6. The red dotted vertical line represents the SOI.

---

[44] The two experimental curves represent the limits of the measured in-cylinder pressure variation domain.

Figures 2.66 to 2.71 show the results of the dual-CM parametric study : the adjustment parameter values were varied around their reference values, as specified in table 2.7.

Parameter	Values		
b	0.16	**0.41**	0.66
C_S	0.9	**1.3**	1.7
C_K,C_κ	5	**15**	25
N_K,N_κ	1.7	**1.9**	2.1
C_{ds}	0.52	**0.67**	0.82
$Z_{s_{max}}$	0.6	**0.8**	1.0

Table 2.7: Variation limits of the adjustment parameters used in the dual-CM parametric study. The bold numbers in the table represent the parameter reference values.

Figure 2.66 shows the influence of the adjustment parameter b, associated with the evaporation rate, on the in-cylinder pressure curve and on the liquid fuel mass within the spray. As seen, an increase of this parameter (corresponding to an increase of the liquid penetration length and, consequently, to a decrease of the fuel evaporation rate) corresponds to a decrease of the reactivity of the in-cylinder gaseous mixture (top) and an increase of the liquid fuel mass within the spray (bottom), and vice versa.

Figure 2.67 shows the influence of the adjustment parameter C_S, associated with the gaseous spray penetration, on the in-cylinder pressure curve and on the spray volume. As seen, an increase of this parameter (corresponding to an increase of the gaseous spray penetration) corresponds to a decrease of the reactivity of the in-cylinder gaseous mixture (top) and an increase of the spray volume growth rate (bottom), and vice versa. This agrees with the results shown in figure 2.66 : in fact, an increase of the gaseous spray penetration corresponds to an increase of the ambient-air entrainment in the spray region and, as a consequence, a poorer mixture within the spray; the same result can be obtained by reducing the fuel evaporation rate.

Figure 2.68 shows the influence of the adjustment parameters C_K and C_κ, associated with the mean and turbulent specific kinetic energies dissipation, on the in-cylinder pressure curve and on the spray kinetic energy. The two parameters playing the same role in the dissipation of the spray kinetic energy were fixed at the same values. As seen, an increase of those parameters (corresponding to an increase of the kinetic energy dissipation rate) corresponds to an increase of the reactivity of the in-cylinder gaseous mixture (top) and a decrease of the spray kinetic energy (bottom), and vice versa. This is due to the fact that the dissipation of the kinetic energy is associated with mixing : the higher the kinetic energy dissipation, the higher the mixing frequency is and, consequently, the faster the creation of a more reactive gaseous mixture within the cylinder.

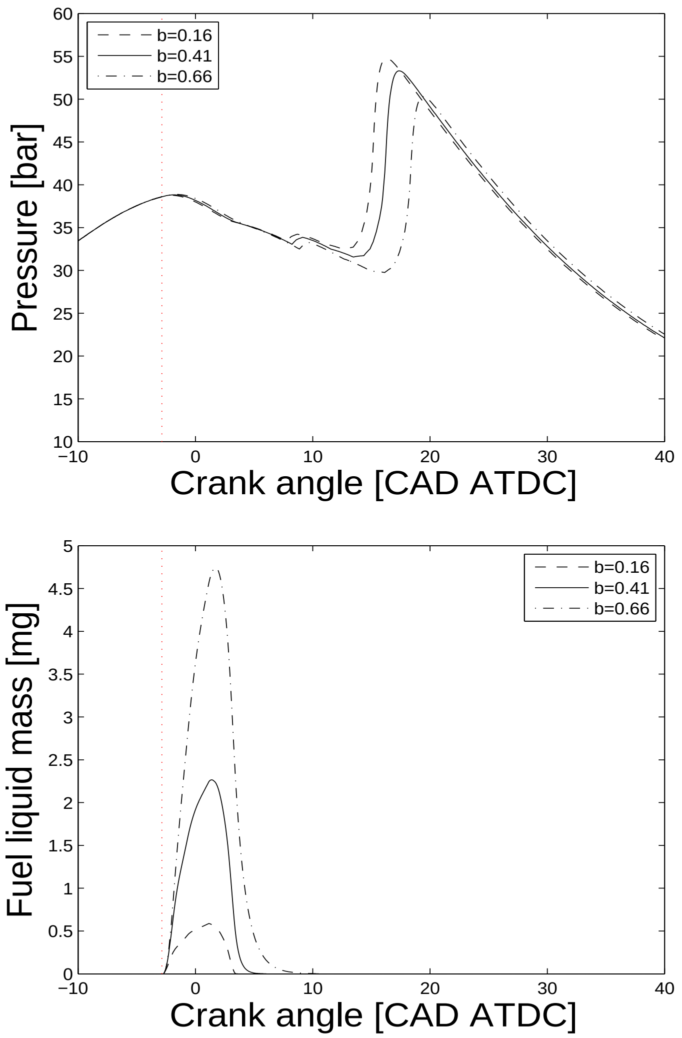

Figure 2.66: Influence of the adjustment parameter b associated with the fuel evaporation rate : on the in-cylinder pressure curve (top) and on the liquid fuel mass (bottom). The red dotted vertical line represents the SOI.

Figure 2.69 shows the influence of the adjustment parameters N_K and N_κ, associated with the mean and turbulent specific kinetic energies dissipation, on the in-cylinder pressure curve and on the spray kinetic energy. The two parameters playing the same role in the dissipation of the spray kinetic energy were fixed at the same values. As seen, an increase of those parameters (corresponding to an increase of the kinetic energy dissipation rate) corresponds to an increase of the reactivity of the in-cylinder gaseous mixture (top) and a decrease of the spray kinetic energy (bottom), and vice versa. This is due to the fact that the dissipation of the kinetic energy is associated with mixing : the higher the kinetic energy dissipation, the higher the mixing frequency is and, consequently, the faster the creation of a more reactive gaseous mixture within the cylinder. These results agree with the ones shown in figure 2.68.

Figure 2.70 shows the influence of the adjustment parameter C_{ds}, associated with the

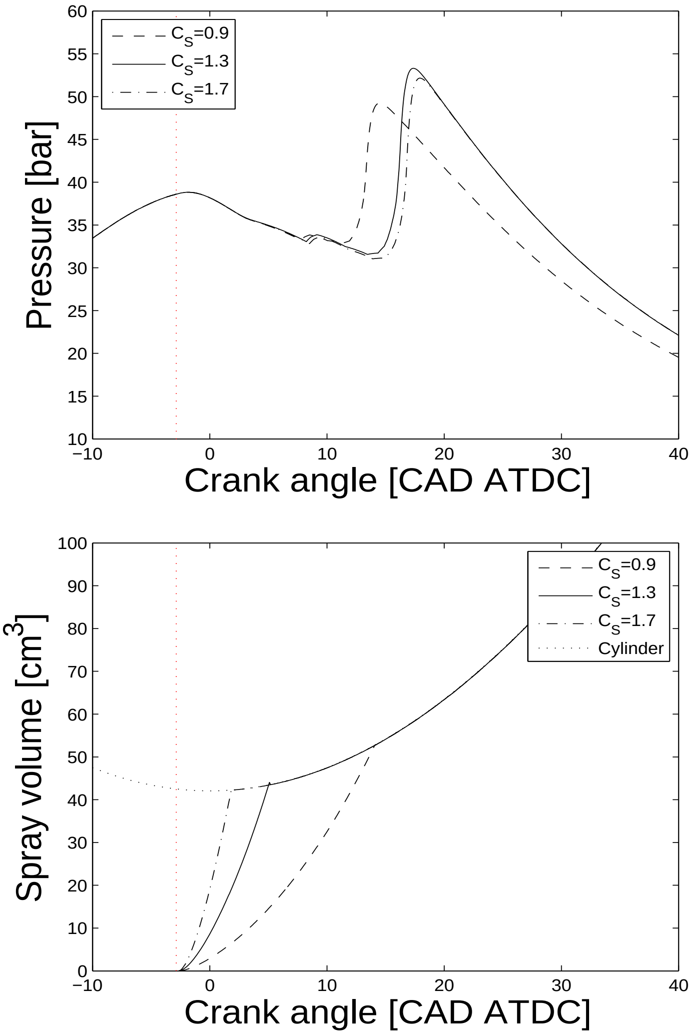

Figure 2.67: Influences of the adjustment parameter C_S associated with the gaseous spray penetration : on the in-cylinder pressure curve (top) and on the spray volume (bottom). The red dotted vertical line represents the SOI.

fuel mixture-fraction distribution variance dissipation, on the in-cylinder pressure curve and on the variance. As seen, an increase of this parameter (corresponding to an increase of the variance dissipation) corresponds to an increase of the reactivity of the in-cylinder gaseous mixture (top) and a decrease of the variance (bottom), corresponding to a more homogeneous gaseous mixture within the spray, and vice versa.

To conclude this parametric study, figure 2.71 shows the influence of the adjustment parameter $Z_{s_{max}}$, associated with the fuel mixture-fraction distribution variance creation, on the in-cylinder pressure curve and on the variance. As seen, a decrease of this parameter corresponds to an increase of the reactivity of the in-cylinder gaseous mixture (top) and a decrease of the variance (bottom), corresponding to a more homogeneous gaseous mixture within the spray, and vice versa.

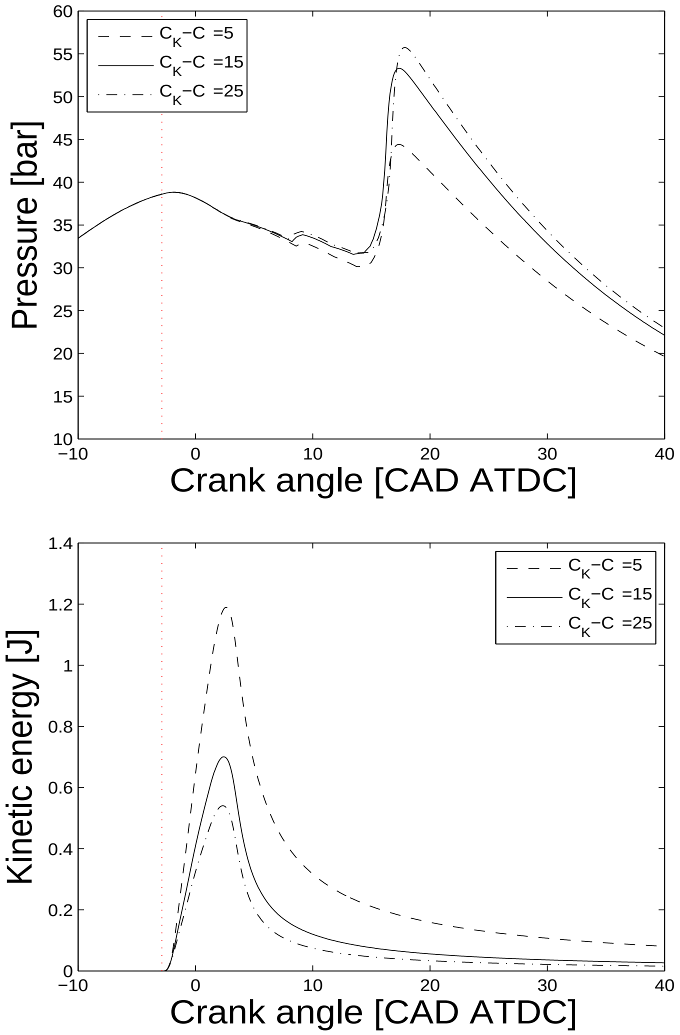

Figure 2.68: Influences of the adjustment parameters C_K and C_κ associated with the dissipation of the mean and turbulent specific kinetic energies : on the in-cylinder pressure curve (top) and on the kinetic energy (bottom). The red dotted vertical line represents the SOI.

2.8 Computational time

This section investigates the impact of the numerical approach used to solve the system and of the time-step value used in the computation, on the computational time.

The dual-CM is developed in the AMESim environment, appendix A. AMESim allows us to use two approaches for solving the numerical system : the first adopting a fixed time-step and the second adopting a variable time-step able to adapt the time-step value to the dynamic of the system.

Because of the specific way of computing the species reaction rates used in dual-CM, equation 2.141, in order to compute reliable species reaction rates, the maximum time-step value must be strictly lower than the value of the relaxation characteristic time, τ[45].

---

[45] As a consequence, a constraint on the maximum value of the relaxation characteristic time has an

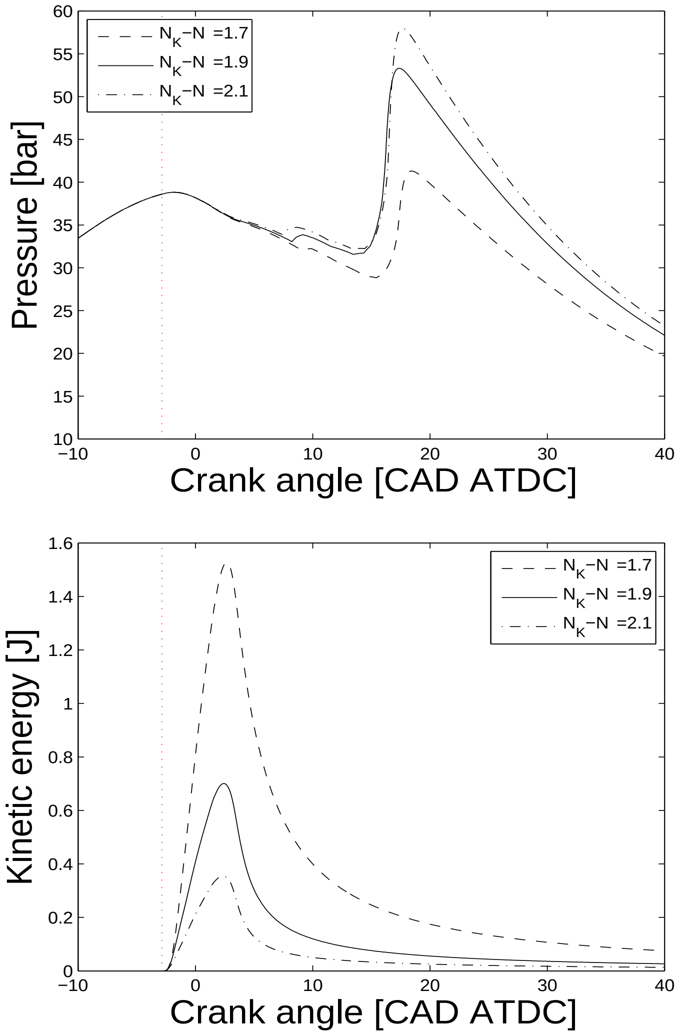

Figure 2.69: Influences of the adjustment parameters N_K and N_κ associated with the dissipation of the mean and turbulent specific kinetic energies : on the in-cylinder pressure curve (top) and on the kinetic energy (bottom). The red dotted vertical line represents the *SOI*.

Values for the maximum time-step, *dt*, of the order of 10^{-6} up to 10^{-5} s were found to be sufficient for obtaining accurate results.

Table 2.8 shows the influence of the numerical approach (fixed/variable time-step) and of the maximum time-step value, *dt*, on the computational time. In all the computations, a value of $\tau = 5\ dt$ was used. Results refer to the engine operating point described in table 2.6.

	$dt = 10^{-6}$ s	$dt = 10^{-5}$ s
Variable time-step	$8.2 \cdot 10^3$ RT (220 s)	$2.6 \cdot 10^3$ RT (69 s)
Fixed time-step	$2.7 \cdot 10^3$ RT (71 s)	$3.7 \cdot 10^2$ RT (10 s)

Table 2.8: Influence of the numerical approach and of the maximum time-step value on the computational time. In the table, the computational times are expressed in terms of *times the Real Time*, (*RT*), and physical time, s.

---

impact on the constraints associated with the value of the maximum time-step value.

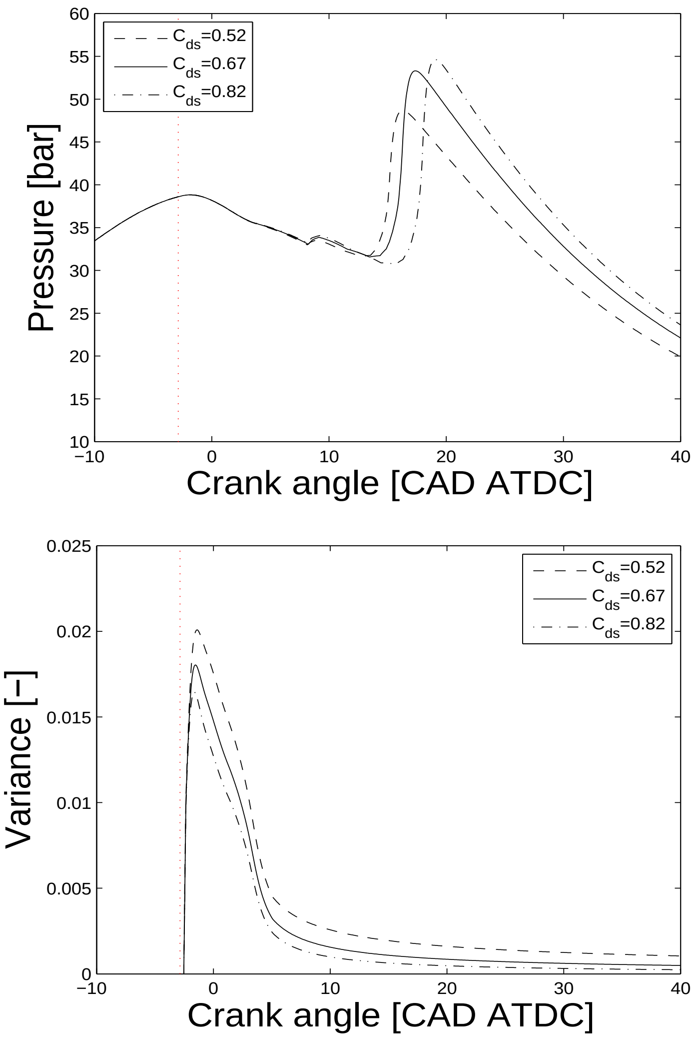

Figure 2.70: Influences of the adjustment parameter C_{ds} associated with the fuel mixture-fraction distribution variance : on the in-cylinder pressure curve (top) and on the variance (bottom). The red dotted vertical line represents the SOI.

Figure 2.72 shows the computed in-cylinder pressure curves obtained for the different configurations presented in table 2.8.

Looking at the data of table 2.8 and the curves shown in figure 2.72, it is clear that the fact of using a fixed or variable time-step approach has a strong influence on the CPU time of the computation, the fixed time-step approach being much faster. Nevertheless, the fact of using a variable time-step, has the advantage to better capture the dynamics of the system. In fact, even in the case of a greater maximum time-step, the beginning of the rise of the in-cylinder pressure curve due to combustion is always well captured when using the variable time-step approach, figure 2.72. On the other hand, when using the fixed time-step approach, this lack can be easily eliminated by reducing the maximum time-step value. Finally in figure 2.72, it is shown that when a maximum time-step $dt = 10^{-5}$ s is used, the stiff dynamics of the combustion is less correctly

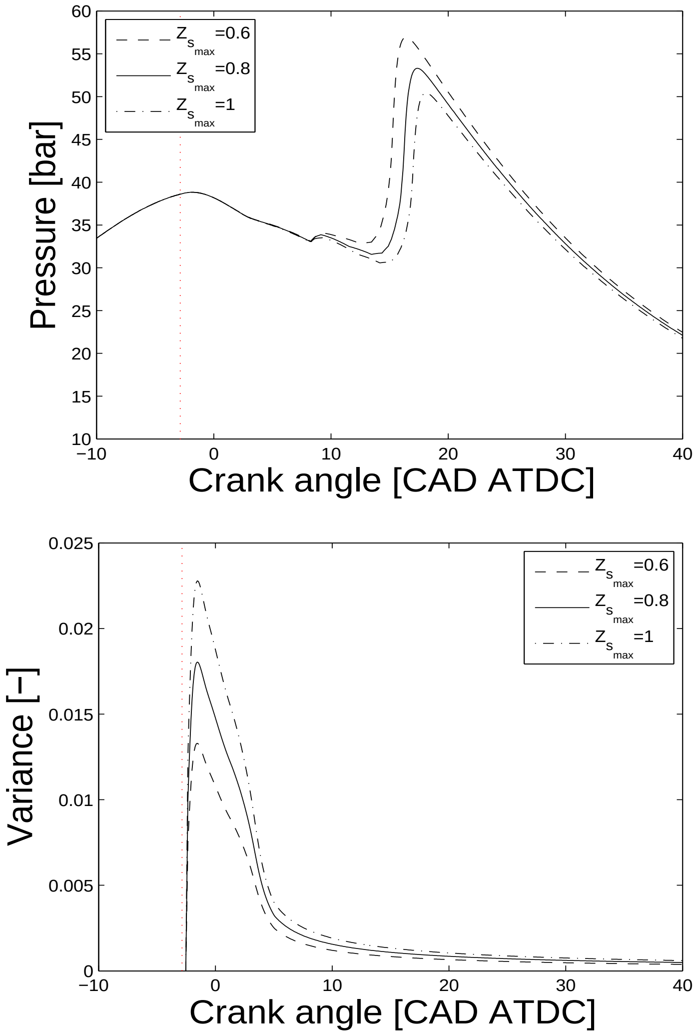

Figure 2.71: Influences of the adjustment parameter $Z_{s_{max}}$ associated with the fuel mixture-fraction distribution variance : on the in-cylinder pressure curve (top) and on the variance (bottom). The red dotted vertical line represents the SOI.

represented. This is due to the fact that for all the curves presented in figure 2.72, the ratio between the characteristic relaxation time and the time-step is kept constant ($\tau/dt = 5$). Accordingly, an increase of the time-step, dt, corresponds to an increase of the characteristic relaxation time, τ, and, consequently, the species evolutions within the cylinder are smoothed, section 2.5.1.

To summarize, both the choices concerning the numerical approach used to solve the system and the computation time-step have an impact on the computational time and on the results of the computation. However, the impact is much more important on the computational time rather than on the results of the computation.

All the results presented in this document were obtained using the variable time-step solver and limiting the maximum time-step to 10^{-6} s.

To conclude, it is worthwhile to spend more words on the perspective of having in a

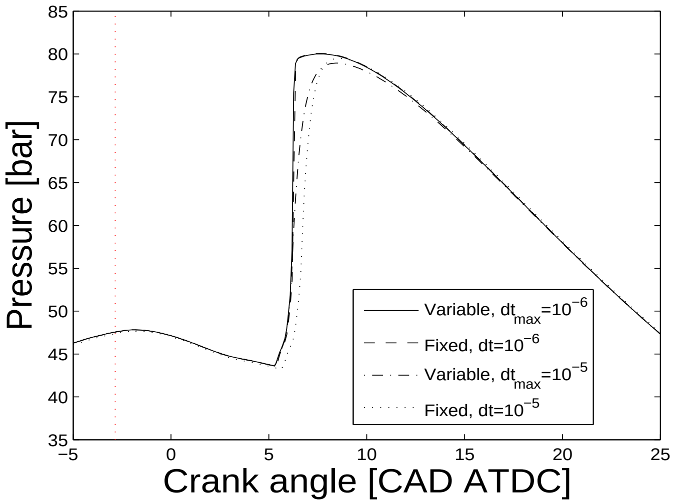

Figure 2.72: Influence of the numerical approach and of the maximum time-step value on the computed in-cylinder pressure. The engine operating point specifications are given in table 2.6. The red dotted vertical line represents the SOI.

near future a version of the dual-CM able to compute engine operating points in Real Time. As shown in table 2.8, the present dual-CM computational time is far from the target of the Real Time. The major limiting factor it was found to be associated with the use of the FPI table :

- the size of the table can strongly grows if more refined discretizations of the table axes are done, or if additional table inputs are necessary (as it is the case for the new tabulation method accounting for the combustion chamber expansion effects on chemical kinetics),
- the AMESim numerical scheme adopting a variable time step, is not optimized to manage FPI tables storing species mass fractions. In fact, as the FPI trajectories are supposed to be piecewise linear, their first derivatives are discontinuous. These discontinuities strongly slow down the solver computational speed.

Accordingly, in order to overcome these limitations, a possible solution consists in generating the FPI table, as usual, and then learning it by using an adapted neural network. In such a way, a multi-dimensional polynomial surface containing all the information stored in table is generated, and it can be used in the dual-CM. The polynomial surface, compared to the FPI table, has the advantages of having a very small size and continuous derivatives.

Chapter 3

Dual-CM engine validation

In this chapter, the dual-CM, developed in chapter 2, is validated against two types of results :

- experimental data from engine test-bench are used to validate the overall behavior of dual-CM,
- 3D CFD simulation results obtained with the IFP-C3D solver, section 3.2, are used to validate more specific aspects of the dual-CM, and in particular aspects associated to fuel evaporation and mixing. Although IFP-C3D calculations are not exact, they give results close to experiments and above all they allow, thanks to the Diesel combustion model ECFM3Z developed by Colin et al. [34], to give access to the basic physics of combustion in Diesel engines, which is unfeasible with experimental measurements.

Concerning this chapter, after a brief description of the tested engine, section 3.1, and of the IFP-C3D solver, section 3.2, the methodology used for determining the simulation initial conditions starting from the experimental data is detailed, section 3.3. Then, the dual-CM results are investigated and compared with the IFP-C3D results, section 3.4. Furthermore, the sensitivity of the dual-CM to isoparametric variations and its adaptation capability to a wide range of engine operating conditions are presented in section 3.5 and section 3.6, respectively. To conclude, statistics relative to the dual-CM behavior on the entire engine operating domain are presented, section 3.7.

3.1 Tested engine : Renault G9T NADI™ concept engine

The tested engine is a turbo-charged Renault G9T NADI™ concept engine [93]. The specifications of the engine are given in table 3.1. This engine has the particularity

Engine type	in-line 4 cylinder
Bore [mm]	87.0
Stroke [mm]	92.0
Connecting rod [mm]	149.9
Compression ratio [-]	14.0
Unitary piston displacement [cm^3]	546.91
Injection system	Bosch GmbH CRI 2.2

Table 3.1: Renault G9T NADI™ concept engine specifications.

of being able to operate in both conventional Diesel and HCCI combustion regimes. Figure 3.1 shows the original scheme published in the Narrow Angle Direct Injection ($NADI^{TM}$) concept patent. A better illustration of the NADI™ concept principle is given in figure 3.2. Figure 3.2 shows the difference between the conventional Diesel bowl and the NADI™ concept bowl. In particular, in a conventional Diesel configuration the injection sprays impact the outer part of the bowl and are then wall-guided towards the inner part of the combustion chamber. Differently, in the NADI™ concept, because of the narrow angle β between the sprays ($\beta < 100°$), the injections directly impact the inner part of the bowl and are then wall-guided towards the outer part of the combustion chamber. When compared to conventional Diesel engines, the NADI™ concept geometry has shown to have two main advantages [93] :

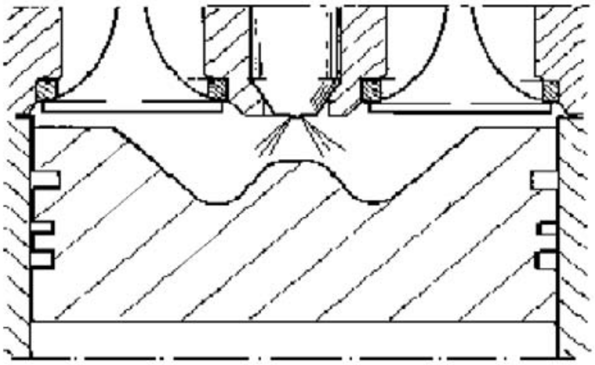

Figure 3.1: Scheme of the NADI™ concept.

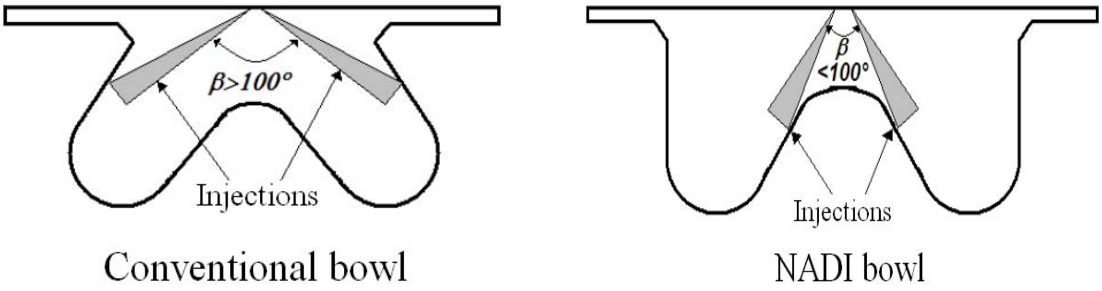

Figure 3.2: Difference between the conventional Diesel bowl and the Narrow Angle Direct Injection ($NADI^{TM}$) bowl. The angle β indicates the opening of the solid angle containing the axes of the fuel injection sprays.

- reducing the liquid fuel cylinder wall impingement, which is the cause of unburned hydrocarbon emissions,
- improving the mixing of fuel and ambient gases in the combustion chamber, especially for engine operating points having high EGR rates, as common for HCCI

engine operating points. As a consequence, the emissions of NO_x and soot are reduced.

In order to put in evidence the impact of the piston shape on the spray dynamics, two different bowls were used, figure 3.3. As will be shown in sections 3.4 and 4, the geometry

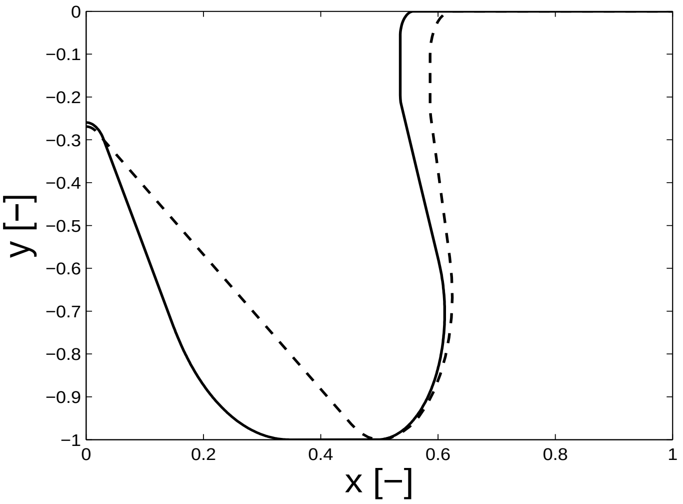

Figure 3.3: Two different profiles of NADI™ concept piston bowls (out of scale).

of the piston bowl can have a strong influence on the mixing process of injected fuel with the in-cylinder ambient air.

3.1.1 The engine operating domain

The Renault G9T NADI™ engine was installed on an engine test-bench and tested on the entire engine operating domain [95]. Figure 3.4 represents the engine operating domain expressed in terms of Indicated Mean Effective Pressure ($IMEP$) and engine speed.

The region of the engine operating domain associated to HCCI operating conditions, that is the low load and low engine speed region, is rather unstable and difficult to control. For this reason a thorough investigation of this region was performed, figure 3.4. This experimental database represents the basis on which the overall behavior of the dual-CM has been validated. In section 3.7, the statistics of the results of the dual-CM on the entire engine operating domain are presented.

3.2 The 3D Computational Fluid Dynamics Code IFP-C3D

IFP-C3D is a 3D Computational Fluid Dynamics (CFD) code using unstructured meshes and Arbitrary Lagrangian Eulerian (ALE) finite volume method dedicated to ICE simulations. IFP-C3D integrates a combustion model entirely developed at IFP : ECFM3Z [34][1].

---

[1] The ECFM3Z equations are reported in appendix B.

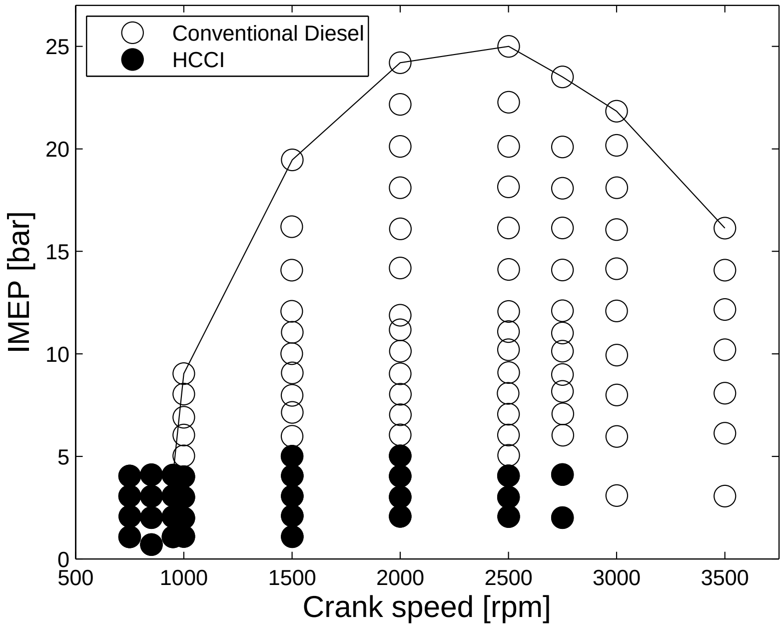

Figure 3.4: Renault G9T NADI™ concept engine operating domain. Each circle corresponds to a different engine operating point : empty and filled circles correspond to conventional Diesel and Diesel HCCI conditions, respectively. The solid line represents the upper load limit as function of the engine speed.

Nowadays, this model is widely used by car manufacturers for several and diversified applications. In particular, ECFM3Z is able to compute conventional Diesel and Diesel HCCI combustion regimes. This model has been retained as a reference model especially for two reasons :

- it is able to compute all the combustion regimes : auto-ignition, premixed flames and diffusion flames,
- the details given by a 3D calculation permit us to have a deep understanding of the flow in terms of turbulence, fuel mixture fraction distribution and fuel evaporation rate otherwise inaccessible with experimental devices.

Principle of ECFM3Z

Figure 3.5 shows the different zones computed by the model :

- a pure ambient air zone, which in the most general case contains a perfectly stirred mixture of pure air and EGR $\left(A = A^u + A^b\right)$,
- a pure gaseous fuel zone $\left(F = F^u + F^b\right)$,
- a zone in which ambient air and fuel are mixed with each other $\left(M = M^u + M^b\right)$.

As seen, each of these zones is further subdivided into two parts representing the unburned and burned gases. On the left of figure 3.5 is represented the unburned gas region ($A^u + M^u + F^u$), while on the right the burned gas region ($A^b + M^b + F^b$).

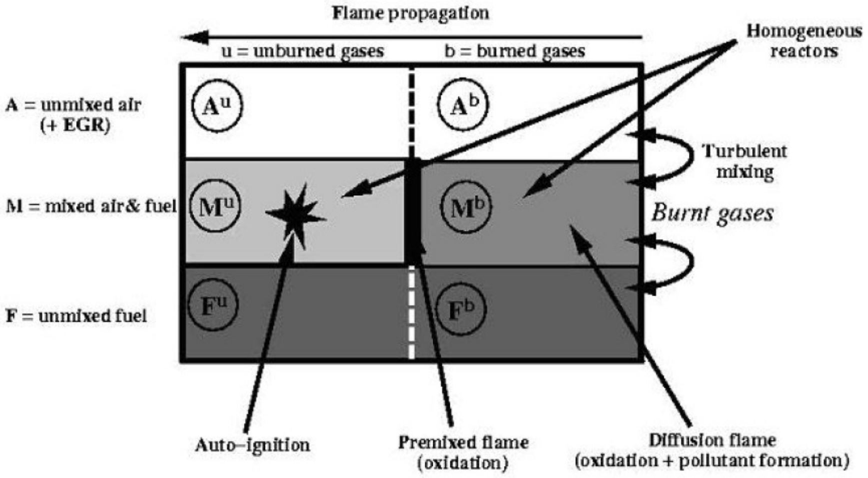

Figure 3.5: Schematic representation of the ECFM3Z combustion model.

Diesel combustion process dynamics in ECFM3Z

Figure 3.6 shows the initial state of the combustion chamber : the gaseous mixture inside the reactor is a perfectly stirred mixture of pure air and eventually EGR at a given thermodynamical state. At this stage, all the gases belong to the pure ambient air zone of the unburned gases (A^u), figure 3.5. When the liquid fuel is injected in the cylinder, a second zone containing pure gaseous fuel appears in the cylinder (F^u). Once the pure ambient air and pure fuel zones coexist, they exchange mass with each other. Consequently, a third zone, containing pure air, EGR and gaseous fuel, is formed (M^u), figure 3.7. At this stage, the whole gaseous mixture belongs to the unburned gas region, figure 3.5. Once the mixing region is created, the computation of the auto-ignition delay

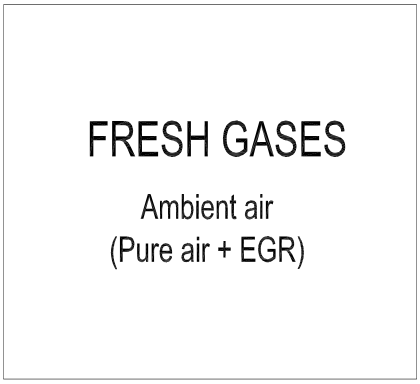

Figure 3.6: Diesel combustion process dynamics in ECFM3Z : initial state.

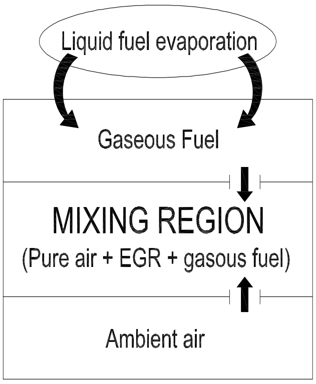

Figure 3.7: Diesel combustion process dynamics in ECFM3Z : mixing phase.

of the gaseous mixture starts. When the auto-ignition delay is attained, the combustion process begins. At this point, three other zones relative to the burned gas region appear figure 3.8 :

- a zone containing pure ambient air, A^b, identical to A^u,
- a zone containing pure fuel, F^b, identical to F^u; this zone is fed by the liquid fuel mass evaporation rate, which is partitioned between the burned and burned pure fuel zones,
- a zone containing a gaseous mixture of fuel, air and products of combustion, M^b.

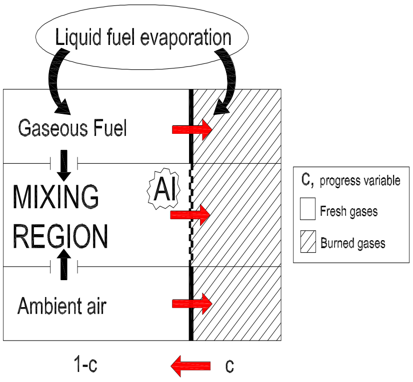

Figure 3.8: Diesel combustion process dynamics in ECFM3Z : auto-ignition of the gaseous mixture.

The mixing process between pure ambient air and pure fuel takes place in the burned gas region, too, figure 3.9. Thus, the mass fluxes from pure ambient air and pure fuel feed the mixing zone and burn in diffusion combustion. This kind of modeling is integrated in each computational cell used for representing the physical volume of the combustion chamber. One of the main contributions of the ECFM3Z approach is the representation of the mixing dynamics, which is capital for a correct computation of the combustion process. A fundamental variable of the ECFM3Z approach is the progress variable, c.

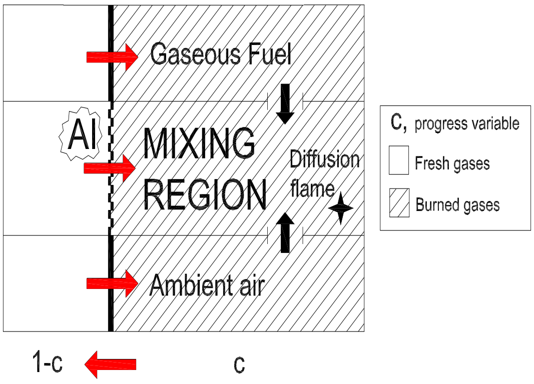

Figure 3.9: Diesel combustion process dynamics in ECFM3Z : diffusion flame.

In fact, the gaseous mixture repartition between unburned and burned gases depends on its value. For this reason, it is a very important variable for the combustion description.

3.3 Methodology for determining initial and boundary conditions

The dual-CM is a model that has been created for global engine system simulations, section 1.2.2.

Accordingly, one of the major purposes of the combustion model is to reproduce the behavior of a real engine, as observed at the engine test-bench, on the whole engine operating domain. When dealing with a real engine, the combustion process is controlled by varying the in-cylinder thermochemical conditions and the injection strategy, both of them imposed by the simultaneous action of the devices integrated in the engine architecture (turbo-charger, injection system, EGR loop, etc.). In a similar fashion, when dealing with a virtual engine, the combustion model must be sensitive to variations of the in-cylinder thermochemical conditions and of the injection strategy; that is, from a numerical point of view, the combustion model must be sensitive to initial and boundary conditions, respectively. In order to validate this aspect, the dual-CM combustion model has been tested on the whole engine operating domain and the results compared to experiments. Due to the large number of engine operating points to simulate in such a kind of application, an automatic data processing methodology for determining the computation initial and boundary conditions, expressed in terms of initial pressure, p_{ini}, initial temperature, T_{ini} and initial gaseous mixture composition, $Y_{x_{ini}}$, and engine speed, Ω_{eng}, injection pressure, p_{inj}, Start Of Injection for the i^{th} injection, SOI_i, and injected liquid fuel mass for the i^{th} injection, $m_{F_{inj_i}}$, respectively, must be set-up. For this purpose, the engine test-bench experimental database contains fundamental information. Once the methodology is defined, it will be used for computing the initial conditions of all the engine operating points of the engine operating domain. It must be pointed out that this is a hard constraint for the model. In fact,

- the adjustment parameters of the model were fixed once, and kept constant for all the computations,
- the initial and boundary conditions are determined by using the set up methodology and they do not constitute adjustment parameters of the computation.

Table 3.2 lists the data stored in the experimental database used for the determination of the computation initial and boundary conditions.

Data refer to the four cylinder turbo-charged Renault G9T NADI™ concept engine, section 3.1.

In-cylinder pressure curves	p_{exp_k}	[bar]
Engine speed	Ω_{eng}	[CAD/s]
Injection pressure	p_{inj}	[Pa]
Injection timing for the i^{th} injection	AVI_i	[CAD ATDC]
Energizing Time for the i^{th} injection	ET_i	[s]
Injected liquid fuel mass flow rate	$\dot{m}_{F_{inj}}$	[kg/h]
Pure air mass flow rate in the upstream intake manifold	$\dot{m}_{pa}$	[kg/h]
EGR mass flow rate in the EGR loop manifold	$\dot{m}_{EGR}$	[kg/h]

Table 3.2: Data stored in the experimental database used for the determination of the computation initial and boundary conditions.

Initial conditions

In order to determine the initial composition of the ambient air within the cylinder, the mass flow rates $\dot{m}_{F_{inj}}$, $\dot{m}_{pa}$ and $\dot{m}_{EGR}$ are expressed in terms of mass per cylinder per cycle (kg/cyl/cyc) :

$$m_{F_{inj}}\Big|_{cc} = \frac{2}{3600 \cdot n_{cyl} \cdot \Omega_{eng}} \cdot \dot{m}_{F_{inj}} \tag{3.1}$$

$$m_{pa}\big|_{cc} = \frac{2}{3600 \cdot n_{cyl} \cdot \Omega_{eng}} \cdot \dot{m}_{pa} \tag{3.2}$$

$$m_{EGR}\big|_{cc} = \frac{2}{3600 \cdot n_{cyl} \cdot \Omega_{eng}} \cdot \dot{m}_{EGR} \tag{3.3}$$

where n_{cyl} is the number of cylinders. Then, an apparent equivalence ratio[2], $\widehat{\Phi}$ is computed as :

$$\widehat{\Phi} = \frac{m_{F_{inj}}\Big|_{cc}}{m_{pa}\big|_{cc}} \cdot \left(\frac{A}{F}\right)_{st} \tag{3.4}$$

By doing the assumption that all the fuel burns at stoichiometric conditions according to the equation below :

$$C_7H_{16} + 11 \cdot (O_2 + 3.76 \cdot N_2) \rightarrow 7 \cdot CO_2 + 8 \cdot H_2O + 11 \cdot 3.76 \cdot N_2 \tag{3.5}$$

---

[2] $\widehat{\Phi}$ is called apparent equivalence ratio because it does not take into account the air contained in the EGR.

it is possible to compute the pure air mass fraction, $Y_{pa}|_{EGR}$, and Burned Gas (BG) mass fraction[3], $Y_D|_{EGR}$, relatively to the EGR mixture[4] :

$$Y_{pa}|_{EGR} = \left(1 - \widehat{\Phi}\right) \cdot \frac{m_{pa}|_{cc}}{m_{F_{inj}}\Big|_{cc} + m_{pa}|_{cc}} \tag{3.6}$$

$$Y_D|_{EGR} = \frac{\widehat{\Phi} \cdot m_{pa}|_{cc} + m_{F_{inj}}\Big|_{cc}}{m_{F_{inj}}\Big|_{cc} + m_{pa}|_{cc}} \tag{3.7}$$

With the assumption that at each engine cycle the mass of internal EGR[5], $m_{IEGR}|_{cc}$ corresponds to a given percentage $Tx_{IEGR} = 4\%$ of the total mass of air and EGR passing through the intake valve[6], the total mass of pure air trapped in the cylinder after the intake valve closure, m_{pa}, is :

$$m_{pa} = m_{pa}|_{cc} + \left(m_{EGR}|_{cc} + \left(m_{pa}|_{cc} + m_{EGR}|_{cc}\right) \cdot Tx_{IEGR}\right) \cdot Y_{pa}|_{EGR} \tag{3.8}$$

in the same way, the total mass of BG trapped in the cylinder after the intake valve closure, m_D, is :

$$m_D = \left(m_{EGR}|_{cc} + \left(m_{pa}|_{cc} + m_{EGR}|_{cc}\right) \cdot Tx_{IEGR}\right) \cdot Y_D|_{EGR} \tag{3.9}$$

Accordingly, the initial mass fractions of pure air Y_{pa}, burned gases Y_D and fuel Y_F are :

$$Y_{pa} = \frac{m_{pa}}{m_D + m_{pa}} \tag{3.10}$$

$$Y_D = \frac{m_D}{m_D + m_{pa}} \tag{3.11}$$

$$Y_F = 0 \tag{3.12}$$

Y_F has been set to zero as in a Diesel engine the fuel is injected after the inlet valve closure.

To conclude the determination of the initial conditions, the initial pressure and temperature must be fixed.

Once computed the mean in-cylinder experimental pressure curve, $p_{exp_{mean}}$, as[7] :

$$p_{exp_{mean}} = \frac{1}{n_{cyl}} \cdot \sum_{k=1}^{n_{cyl}} p_{exp_k} \tag{3.13}$$

---

[3] As in Diesel engine the gaseous mixture has a poor overall equivalence ratio, the burned gases are here considered as having a stoichiometric composition.

[4] Usually in Diesel engines, the overall equivalence ratio of the mixture within the cylinder is poor ($\Phi < 1$). Consequently, in the EGR gases the oxygen concentration is not null. Accordingly, doing the hypothesis of a stoichiometric combustion, an amount of pure air in the EGR mixture can be quantified.

[5] The internal EGR is the gaseous mass, having a composition identical to that of EGR, that rests trapped in the cylinder when the exhaust valves close.

[6] Studies carried out at IFP have validated this hypothesis.

[7] The subscript k in p_{exp_k}, varying from 1 to 4, refers to the cylinder number. For each cylinder the pressure curve represents the mean curve of hundreds of engine cycles.

the initial pressure, p_{ini}, is read directly on the experimental curve for the desired initial crank angle, $\boldsymbol{\theta}_{ini}$:

$$p_{ini} = p_{exp_{mean}} \left(\boldsymbol{\theta}_{ini}\right) \tag{3.14}$$

Then, by using the perfect gas equation, the mixture initial temperature, T_{ini}, is :

$$T_{ini} = \frac{p_{ini} \cdot V_{ini}}{\mathcal{R} \cdot m_{tot} \cdot \left(\frac{Y_{pa}}{\mathcal{M}_{pa}} + \frac{Y_D}{\mathcal{M}_D}\right)} \tag{3.15}$$

where $\mathcal{M}_{pa}$ and $\mathcal{M}_D$, are the molar masses of the pure air and of the stoichiometric burned gases, respectively, and V_{ini} is the cylinder volume at $\boldsymbol{\theta}_{ini}$, section 2.6.2.

Boundary conditions

The boundary conditions of interest for the computation are :

- the engine speed, Ω_{eng},
- the injection pressure, p_{inj},
- the Start Of Injection for the i^{th} injection, SOI_i,
- the injected liquid fuel mass for the i^{th} injection, $m_{F_{inj_i}}$.

Ω_{eng} and p_{inj} are directly read in the experimental database. The SOI_i is computed as :

$$SOI_i = AVI_i + \Omega_{eng} \cdot t_{nod} \tag{3.16}$$

where $AVIi$ and t_{nod} are the ECU injection timing and the needle opening delay. In fact, because of mechanical and hydraulic inertia, an interval of time equal to $t_{nod} = 350\ \mu$s[8] elapses between the start of the electrical signal given to the injector solenoid and the beginning of the liquid fuel injection.

The total fuel mass injected per cycle, $m_{F_{inj}}\Big|_{cc}$, is known, equation 3.1.

In the case of a single injection strategy, the liquid fuel mass is injected at once. Hence, the values of the injection pressure, p_{inj}, and of the injected fuel mass, m_{F_l}, being known, the injection rate model is used to compute the fuel injection rate, section 2.3.

In the case of multiple injections, the measured injected fuel mass, $m_{F_{inj}}\Big|_{cc}$, corresponds to the total injected mass per cycle, that is the sum of the fuel masses of the injections. Consequently, in order to compute the liquid fuel injection rates for the different injections by using the injection rate model (section 2.3), the total injected fuel mass must be apportioned between the different injections. For doing that, a look-up table was generated at IFP, containing the characteristic curves of the injector[9], figure 3.10.

---

[8] The value of t_{nod} depends of the injection system.

[9] A characteristic curve of the injector represents the injected fuel mass as a function of the energizing time, for a given injection pressure.

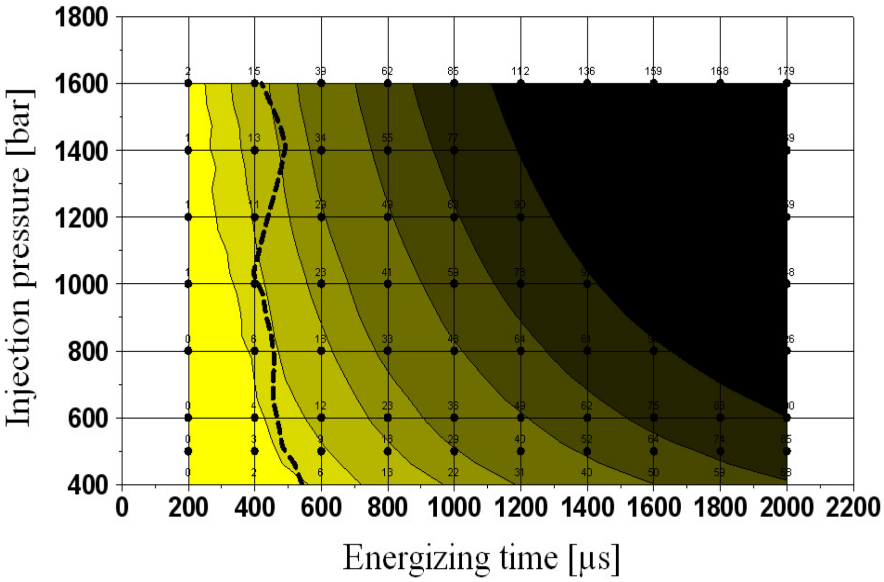

Figure 3.10: Bosch GmbH CRI 2.2 injector characteristic map.

Thus, from this table it is possible to have an estimate of the value of the injected fuel mass, $\widehat{m}_{F_{l_i}}$, as a function of the injection pressure and of the Energizing Time :

$$\widehat{m}_{F_{l_i}} = f\left(p_{inj}, ET_i\right) \tag{3.17}$$

Once the $\widehat{m}_{F_{l_i}}$ have been computed for each injection, in order to be sure of injecting the right total mass of fuel, the $\widehat{m}_{F_{l_i}}$ values are normalized by using the following relation :

$$m_{F_{l_i}} = \frac{\widehat{m}_{F_{l_i}}}{\sum_i \widehat{m}_{F_{l_i}}} \cdot m_{F_{inj}}\Big|_{cc} \tag{3.18}$$

The normalized injected fuel masses, $m_{F_{l_i}}$, together with the injection pressure, p_{inj}, are the inputs of the injection rate model.

3.4 Investigation of physical models using a comparison with a 3D code

Experimental data obtained by using engine test benches only give information about the over-all combustion process, such as the in-cylinder pressure curve, the fuel consumption, pollutant emissions, etc. In order to validate the different submodels of dual-CM in a global ICE context, a solution is to use results obtained by using CFD solvers (here IFP-C3D). Accordingly, the combustion process of a given engine operating point, whose specification are given in table 3.3, was computed by using both the dual-CM and ECFM3Z. The results are compared in figures 3.11 to 3.25. Initial and boundary conditions of the computations were computed by using the method presented in section 3.3, and they were used for both models.

Variable	Unit	Value
Ω_{eng}	[rpm]	1497
$IMEP$	[bar]	6
Y_D	[%]	9.3
AVI	[CAD BTDC]	6
Φ	[-]	0.489
p_{inj}	[bar]	1600

Table 3.3: Engine operating point specifications.

Figure 3.11 shows a comparison of the computed in-cylinder pressure curves with experiments[10]. Both simulations are in good agreement with the experimental pressure curves. Consequently, a comparison between the spray dynamics of the two models is possible.

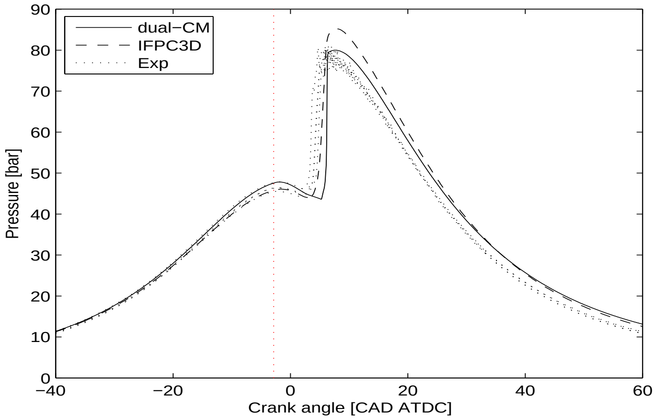

Figure 3.11: Comparison of the dual-CM, IFP-C3D and experimental in-cylinder pressure curves. The engine operating conditions are given in table 3.3. The red dotted vertical line represents the SOI.

Figures 3.12 to 3.15 are relative to the liquid and gaseous masses within the spray. In figures 3.12 the fuel liquid masses within the sprays are compared[11] : good agreement between the two models is found. In particular, the dual-CM correctly predicts the magnitude of the liquid mass and the crank angle interval on which liquid fuel exists. Figures 3.13 compares the spray volumes. The spray volume in IFP-C3D was computed as the sum of the volumes of the cells containing a tracer fuel mass fraction $Y_{F_{\tau}} \geq 10^{-5}$. Also in this case, good agreement between the curves is found in terms of growth rates. Figures 3.14 shows the total quantity of evaporated fuel in the sprays : the two models give similar results. In IFP-C3D, the total gaseous fuel mass within the spray,

---

[10] As shown in figure 3.11, the pressure curve computed by using IFP-C3D presents a slightly higher peak. This difference can be easily reduced by varying the initial conditions of the computation (in the limit of experimental uncertainty). As the main purpose here is to investigate the spray dynamics and mixture formation, the most important thing for having a reliable comparison of the variables computed by the two models is to use the same initial conditions.

[11] In IFP-C3D, the liquid fuel represents the total mass of liquid fuel within the cylinder.

corresponding to the total tracer fuel mass, was computed as :

$$m_{F_\tau}^{IFP-C3D} = \sum_{k=1}^{NSC} Y_{F_{\tau_k}} \cdot \rho_k \cdot V_k \tag{3.19}$$

where NSC is the number of cells belonging to the spray region.

Finally, figure 3.15 compares the total gaseous masses within the sprays computed in IFP-C3D as :

$$m_S^{IFP-C3D} = \sum_{k=1}^{NSC} \rho_k \cdot V_k \tag{3.20}$$

Looking at these curves, a slight difference at around 5 CAD ATDC is noticed : it is due to a difference in the spray growth evolution associated to the combustion chamber geometry. This aspect is represented in figure 3.16 showing the spray dynamics computed by IFP-C3D. Figure 3.16 represents the equivalence ratio distribution within the cylinder at four crank angle values. As shown, according to the NADI™ concept, the spray impacts the bowl on its inner part, figure 3.16 (a), it is then wall guided towards the outer part of the bowl, figure 3.16 (b), and finally curved on it self, figures 3.16 (c) and (d). In particular, figure 3.16 (c) shows the equivalence ratio distribution at 5 CAD ATDC. As seen, at that time, there are two regions that do not belong to the spray, because of bowl geometry :

- the core of the macroscopic vortex (represented by an arrow in figure 3.16 (d)),
- the ambient air situated in the squish volume (represented by an oval in figure 3.16 (d)).

These two aspects due to the combustion chamber geometry are not accounted for in dual-CM. Nevertheless, the behavior of the spray is predicted with sufficiently accuracy.

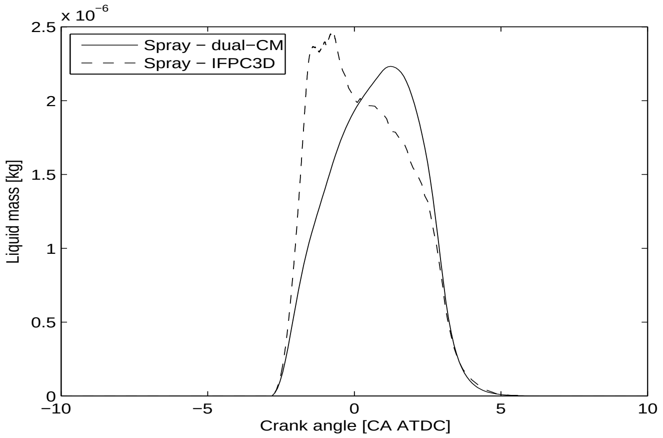

Figure 3.12: Comparison of the dual-CM and IFP-C3D liquid fuel masses. The engine operating conditions are given in table 3.3.

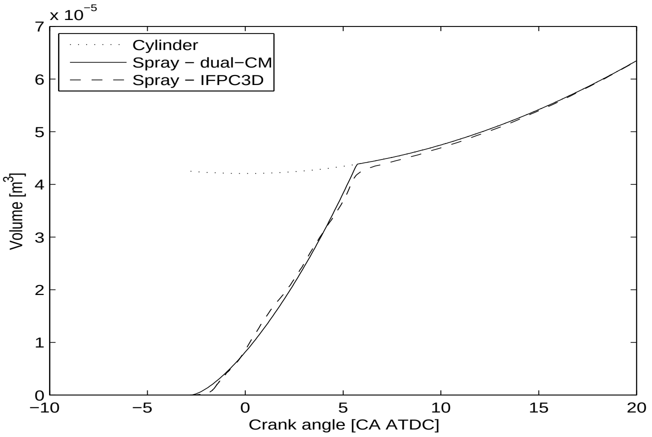

Figure 3.13: Comparison of the dual-CM and IFP-C3D spray volumes. The engine operating conditions are given in table 3.3.

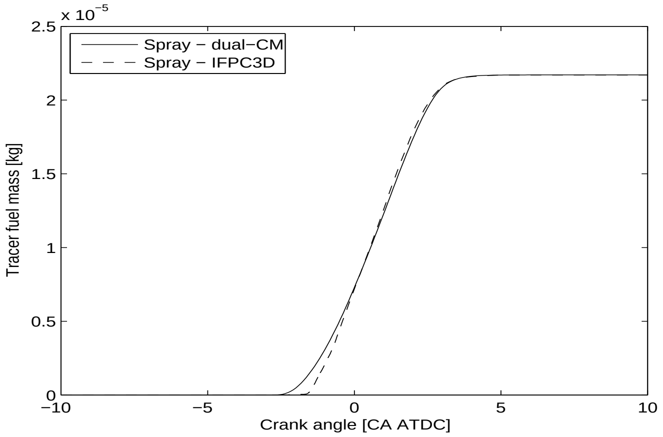

Figure 3.14: Comparison of the dual-CM and IFP-C3D tracer fuel mass. The engine operating conditions are given in table 3.3.

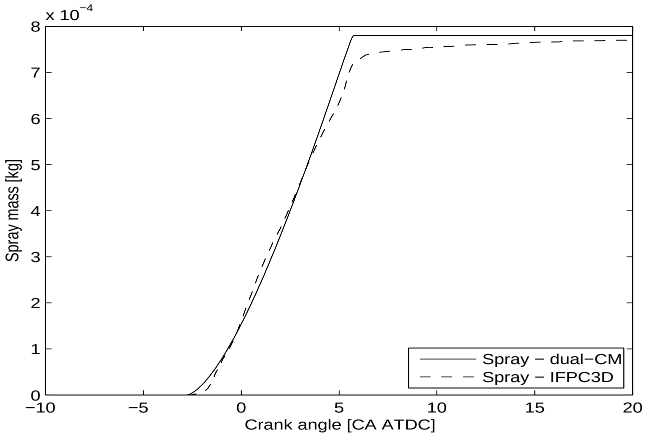

Figure 3.15: Comparison of the dual-CM and IFP-C3D total spray masses. The engine operating conditions are given in table 3.3.

Figures 3.17 and 3.18 show the global kinetic energy, equation 2.100, and the mean specific kinetic energy, equation 2.101, of the spray, respectively.

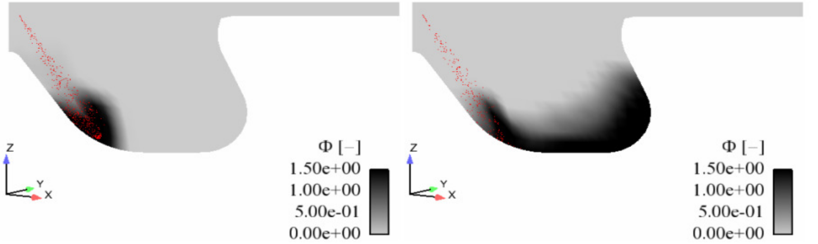

(a) -1 [CA ATDC] (b) 2 [CA ATDC]

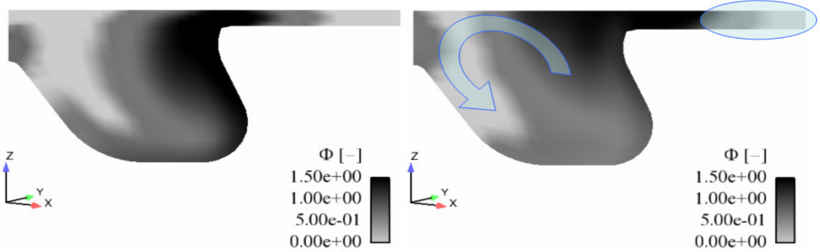

(c) 5 [CA ATDC] (d) 8 [CA ATDC]

Figure 3.16: Equivalence ratio distribution within the cylinder for different crank angle values (shown in the figure). The engine operating conditions are given in table 3.3. Droplets of liquid fuel injection can be observed in the figures (a) and (b), colored in red. In the figure (d) : the oval indicates a region hardly accessible to fuel, the arrow indicates a macroscopic vortex generated by the bowl geometry.

In IFP-C3D the spray global kinetic energy, $E_c^{IFP-C3D}$, and mean specific kinetic energy, $\widetilde{K}^{IFP-C3D}$, were respectively computed as :

$$E_c^{IFP-C3D} = \frac{1}{2} \cdot \sum_{k=1}^{NSC} \left[\frac{1}{NV} \cdot \rho_k \cdot V_k \cdot \sum_{l=1}^{NV} |u_{k_l}|^2 + \rho_k \cdot V_k \cdot \kappa_k \right] \tag{3.21}$$

and :

$$\widetilde{K}^{IFP-C3D} = \frac{\frac{1}{2} \cdot \sum_{k=1}^{NSC} \left[\frac{1}{NV} \cdot \rho_k \cdot V_k \cdot \sum_{l=1}^{NV} |u_{k_l}|^2 \right]}{\sum_{k=1}^{NSC} \rho_k \cdot V_k} \tag{3.22}$$

where NV is the vertex number of the cell.

Regarding the global kinetic energy, the dual-CM and IFP-C3D results are very similar in terms of magnitude and dissipation characteristic time, figures 3.17. Differences can be noticed in the estimation of the specific kinetic energy of the spray, figures 3.18 : the dual-CM underestimates this variable by a factor five, approximatively. Nevertheless, it can be noticed that the dissipation characteristic time is correctly reproduced.

To conclude, the fuel mixture fraction distributions within the spray are compared, figures 3.19 to 3.21. Figure 3.19 and figure 3.20 show the mean value and the variance of the fuel mixture fraction distribution, respectively. In IFP-C3D, the mean fuel mixture fraction and its variance are computed respectively as :

$$\widetilde{Z}^{IFP-C3D} = \frac{\sum_{k=1}^{NSC} Y_{F_{\tau_k}} \cdot \rho_k \cdot V_k}{\sum_{k=1}^{NSC} \rho_k \cdot V_k} \tag{3.23}$$

and :

$$\widetilde{Z"^2}^{IFP-C3D} = \frac{\sum_{k=1}^{NSC} \left(Z_k - \widetilde{Z}^{IFP-C3D} \right)^2 \cdot \rho_k \cdot V_k}{\sum_{k=1}^{NSC} \rho_k \cdot V_k} \tag{3.24}$$

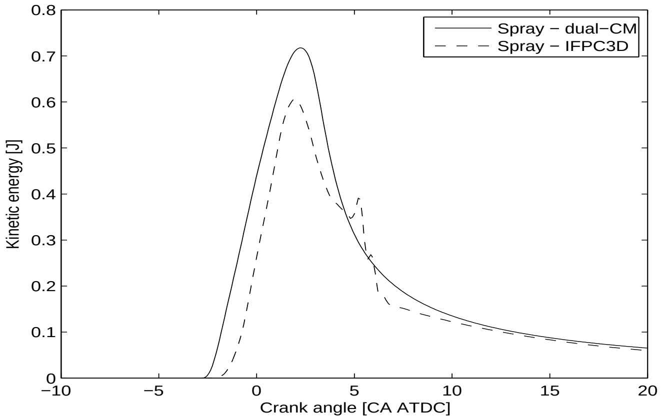

Figure 3.17: Comparison of the dual-CM and IFP-C3D kinetic energies. The engine operating conditions are given in table 3.3.

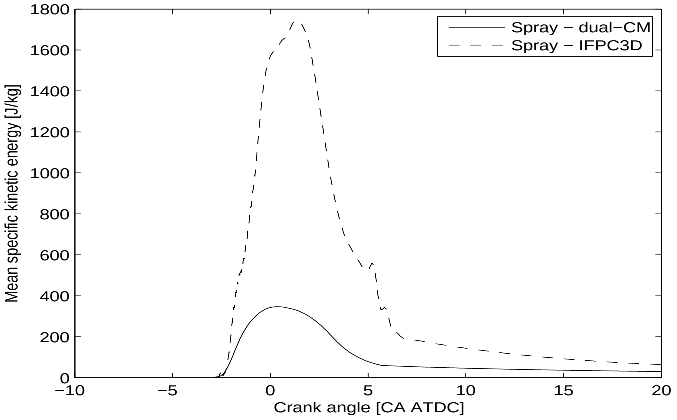

Figure 3.18: Comparison of the dual-CM and IFP-C3D mean specific kinetic energies. The engine operating conditions are given in table 3.3.

where the fuel mixture fraction of the cell, Z_k, corresponds to the cell tracer fuel mass fraction, $Y_{F_{\tau_k}}$.

Note that equation 3.24 does not represent the total fuel mixture fraction distribution variance associated with the spray. In fact for each cell, there is a further contribution to the spray mixture fraction variance associated with subgrid-scale mixture-fraction fluctuations. In fact, as shown in section 3.2, the ECFM3Z fuel mixture fraction PDF is represented by three Dirac functions : one corresponding to the pure air region, $Z = 0$, one corresponding to the mean fuel mixture fraction value of the mixing region, figure 3.5, and the last corresponding to the pure fuel region, $Z = 1$. Here, as a first approximation, the subgrid scale variance contributions were neglected.

As seen, the mean fuel mixture fraction is in good agreement between dual-CM and ECFM3Z. Concerning the variance, the overall behavior of the two curves is very similar, but their magnitudes differ by a factor 2.5, approximatively.

It is not surprising that the fuel mixture fraction distribution variance computed by IFP-C3D is lower than the one computed by the dual-CM, as in computing the IFP-C3D mixture fraction variance, the subgrid scale variance contributions were neglected. However, at this stage, it is not possible to quantify the global contribution to the spray mixture fraction variance associated with the subgrid scale mixture fraction fluctuations.

This aspect will be discussed more in detail in chapter 4. Finally, the comparison of the mixture fraction PDF of the two sprays for different crank angle values is shown in figure 3.21 : the overall evolution of the spray mixture is captured by dual-CM, as well as the magnitude for the different fuel mixture fractions.

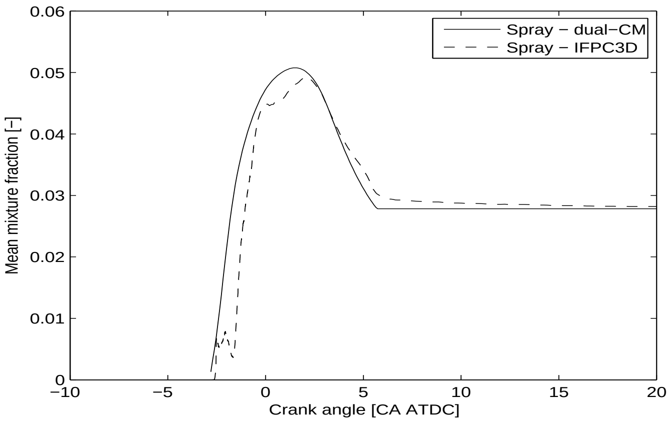

Figure 3.19: Comparison of the dual-CM and IFP-C3D mixture fractions. The engine operating conditions are given in table 3.3.

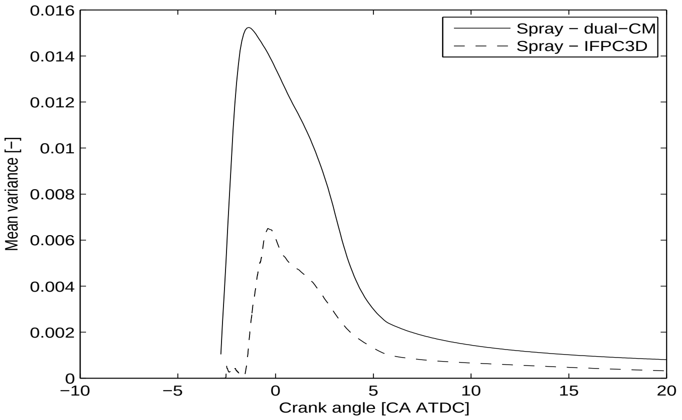

Figure 3.20: Comparison of the dual-CM and IFP-C3D spray variances. The engine operating conditions are given in table 3.3.

Figure 3.22 represents the turbulent mixing frequency computed in dual-CM as $1/\tau_t$, equation 2.104, by which depends the variance dissipation of the mixture fraction distribution, equation 2.120.

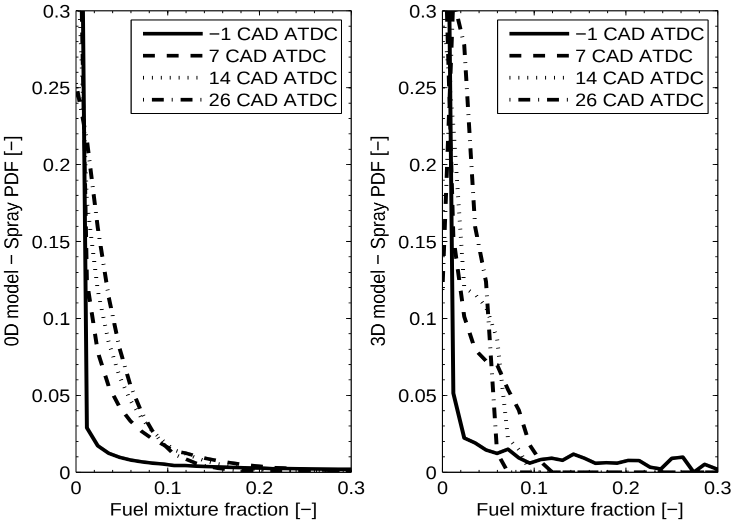

Figure 3.21: Comparison of the dual-CM and IFP-C3D PDFs. The engine operating conditions are given in table 3.3.

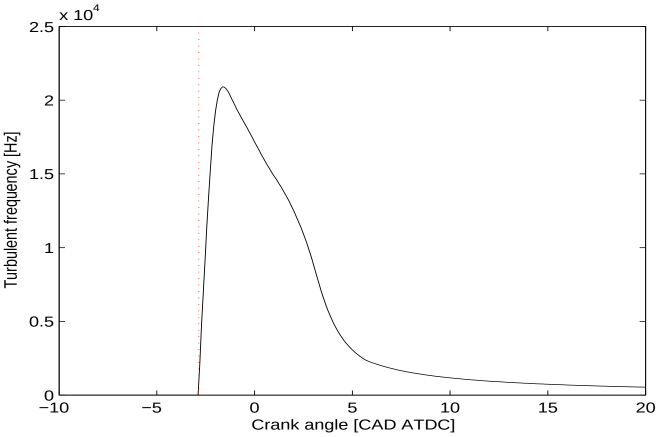

Figure 3.22: Turbulent mixing frequency computed by dual-CM. The engine operating conditions are given in table 3.3. The red dotted vertical line represents the *SOI*.

Figure 3.23 compares the dual-CM (top) and IFP-C3D (bottom) results concerning the evolutions of some between the major species (O_2, CO_2 and H_2O), during the combustion. As can be seen in figure 3.23, the overall behaviors of the main species is captured. It is worthwhile to point out that the chemistry computational approaches used in the dual-CM, section 2.5, and ECFM3Z, section 3.2, are different. Consequently, at this stage of the comparison between the two models, it would not be expected to obtain results close to each other.

Figure 3.24 shows a comparison of the dual-CM and IFP-C3D Heat Releases. As seen by comparing the figures 3.11 and 3.24, the IFP-C3D model overestimates the mass of the reactive mixture burning in a premixed-combustion regime. On the other hand, once the premixed combustion is finished, both models predict the same diffusion combustion dynamics.

Finally, figure 3.25 shows the Heat Release Rate curve computed by dual-CM. The high peak at about 5 CAD ATDC seen in the HRR curve is related to the combustion model : hypothesis of considering a unique progress variable for the description of the combustion process, computed using the mean species concentrations within the spray region. Accordingly, once attained the auto-ignition delay, the gaseous reactive mixture within the cylinder burns *at the same time* regardless of the local mixture composition. This aspect will be detailed more in chapter 4.

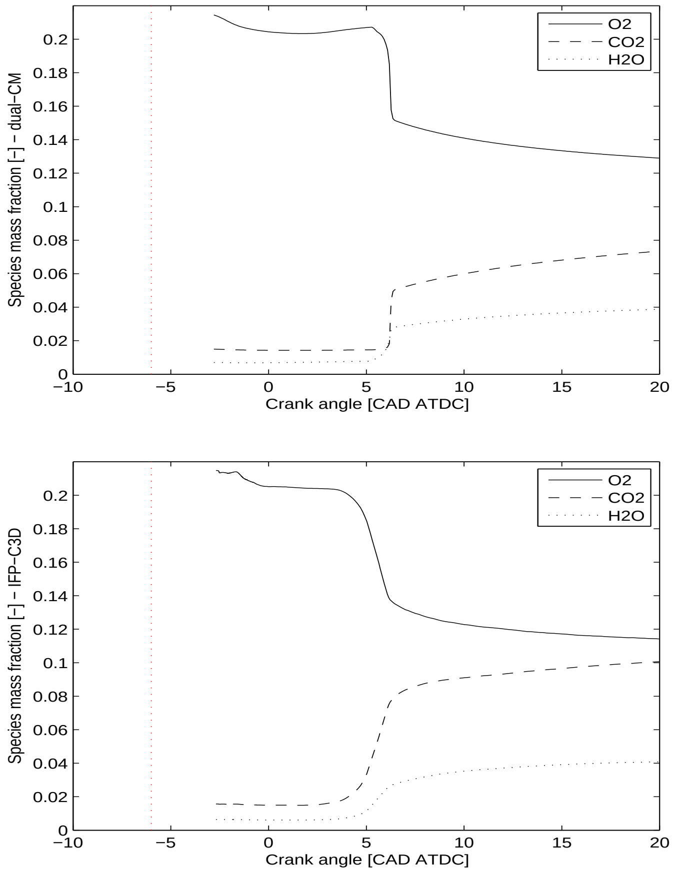

Figure 3.23: Comparison of the dual-CM (top) and IFP-C3D (bottom) O_2, CO_2 and H_2O mass fraction evolutions within the spray region. The engine operating conditions are given in table 3.3. In each figure, the red dotted vertical line represents the SOI.

3.5 Sensitivity of dual-CM to isoparametric variations

One of the major challenges for the dual-CM is to be predictive on the entire engine map. An engine operating point is completely defined once initial and boundary conditions are fixed, section 3.3. In this section, a set of engine operating points, table 3.4, representative of the entire engine operating domain, was extracted from the experimental database, section 3.1.1. The engine operating point n° 1, written using a bold font in

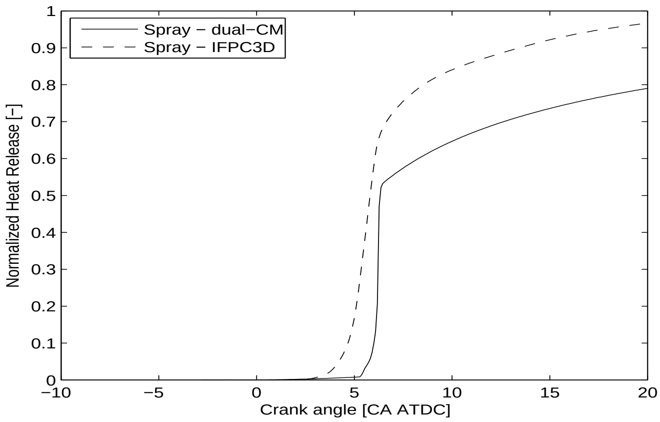

Figure 3.24: Comparison of the dual-CM and IFP-C3D Heat Releases. The engine operating conditions are given in table 3.3. The red dotted vertical line represents the *SOI*.

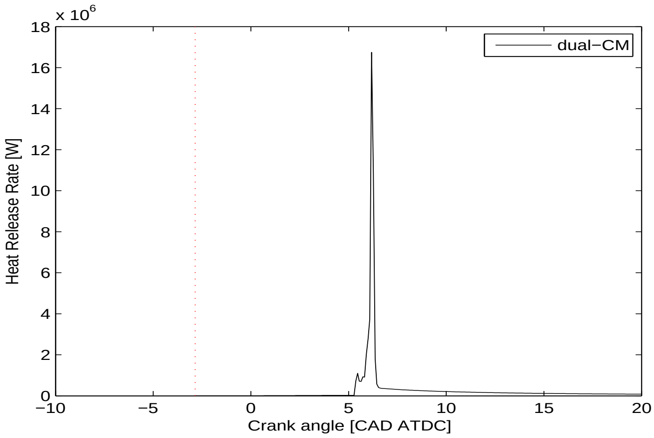

Figure 3.25: Heat Release Rate computed by dual-CM. The engine operating conditions are given in table 3.3. The red dotted vertical line represents the *SOI*.

table 3.4, is the one already investigated in section 3.4.

Point [-]	Ω_{eng} [rpm]	$IMEP$ [bar]	$EGR\ rate$ [%]	AVI [CAD BTDC]	Φ [-]	p_{inj} [bar]
1	**1497**	**6.0**	**9.3**	**6**	**0.489**	**1600**
2	1497	6.1	19.8	6	0.613	1600
3	1497	6.1	36.3	6	0.885	1600
4	3491	6.1	0.2	15	0.356	1600
5	3494	10.1	0.3	18	0.465	1600
6	3491	20.2	0.3	27	0.674	1600
7	1497	6.3	36.8	10	0.888	1600
8	1497	6.2	36.7	8	0.886	1600

Table 3.4: Set of experimental engine operating points used to investigate the sensitivity of the dual-CM to isoparametric variations.

Figures 3.26 to 3.28 show the in-cylinder pressures relative to eight different engine operating points. Computed results are plotted against experimental data.

Figure 3.26 shows the model sensitivity to a variation of $IMEP$ (points n° 4, 5 and 6). Computed pressure evolutions agree well with the experimental curves. The most important aspects in combustion prediction, such as Start Of Combustion (SOC), pressure peak value, and pressure peak position, are well reproduced. All three combustion processes are representative of conventional Diesel combustion.

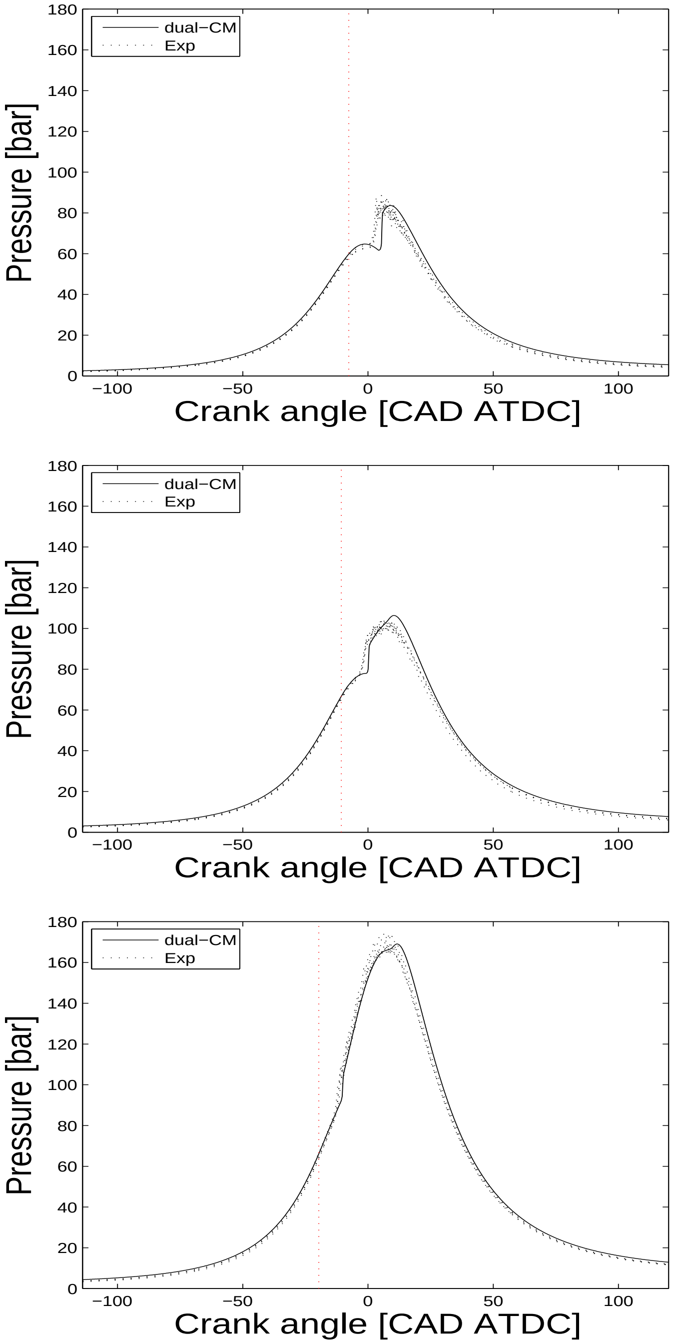

Figure 3.26: Sensitivity of the 0D model to $IMEP$ variations. Comparison of 0D modelling with experimental data. Curves of pressure refer to the operating points n° 4 (top), 5 (middle), 6 (bottom). The red dotted vertical line represents the SOI.

Figure 3.27 shows the model sensitivity to a variation of the SOI value while the other parameters remain constant (points n° 7, 8 and 3). The computed pressures follow the experimental results well. In particular, the main ignition-delay growth and the reduction of the pressure peaks, with a reduction in the SOI, are well reproduced. All three operating points concern high $EGR\ rates$ that, as already seen, favor cold-flame phenomena. Thus, the combustion processes are representative of HCCI combustion. This aspect is clearly put in evidence by the presence of two peaks in the pressure curves : the first associated with the cold-flame heat-release, and the second associated with the main heat-release.

Finally, Figure 3.28 shows the model sensitivity to a variation of the $EGR\ rate$ value (points n° 1, 2 and 3). This series of operating points considered highlights the potential of the model to predict the combustion process. In fact, with the growth of the $EGR\ rate$, the combustion process changes from conventional Diesel to HCCI.

3.6 Representative engine operating points of the experimental database

In this section, the dual-CM results relative to a set of engine operating points, figure 3.29, representative of the entire engine operating domain are shown, figures 3.30 to 3.34. In particular, as shown in figure 3.29, in the following are shown three $IMEP$ variations relative to low (750 rpm), moderate (1500 rpm) and high (2500 rpm) engine speeds, and two engine speed variations relative to low (3 bar) and middle (7 bar) loads.

The specifications of the engine operating points are given in table 3.5.

Point [-]	Ω_{eng} [rpm]	$IMEP$ [bar]	$EGR\ rate$ [%]	AVI_1 [CAD BTDC]	AVI_2 [CAD BTDC]	Φ [-]	p_{inj} [bar]
1	750	1	4	10	2	0.18	300
2	750	2	4	10	-3	0.26	400
3	750	3	21	5	-2	0.43	500
4	750	4	21	11	3	0.56	600
5	850	3	23	7	0	0.44	600
6	950	3	45	24	9	0.57	700
7	1500	3	52	-	18	0.65	800
8	1500	12	0	28	3	0.68	1400
9	1500	16	0	20	9	0.80	1560
10	1500	19	0	-	10	0.92	1460
11	2000	7	24	21	1	0.62	1050
12	2500	2	46	-	20	0.41	800
13	2500	7	25	21	0	0.54	1250
14	2500	9	21	24	2	0.54	1350
15	2500	12	0	35.5	7.5	0.44	1500
16	3000	8	0	30.5	8	0.34	1400
17	3500	8	0	30.5	9	0.36	1600

Table 3.5: Set of experimental engine operating points used to investigate the behavior of the dual-CM on the entire engine operating domain.

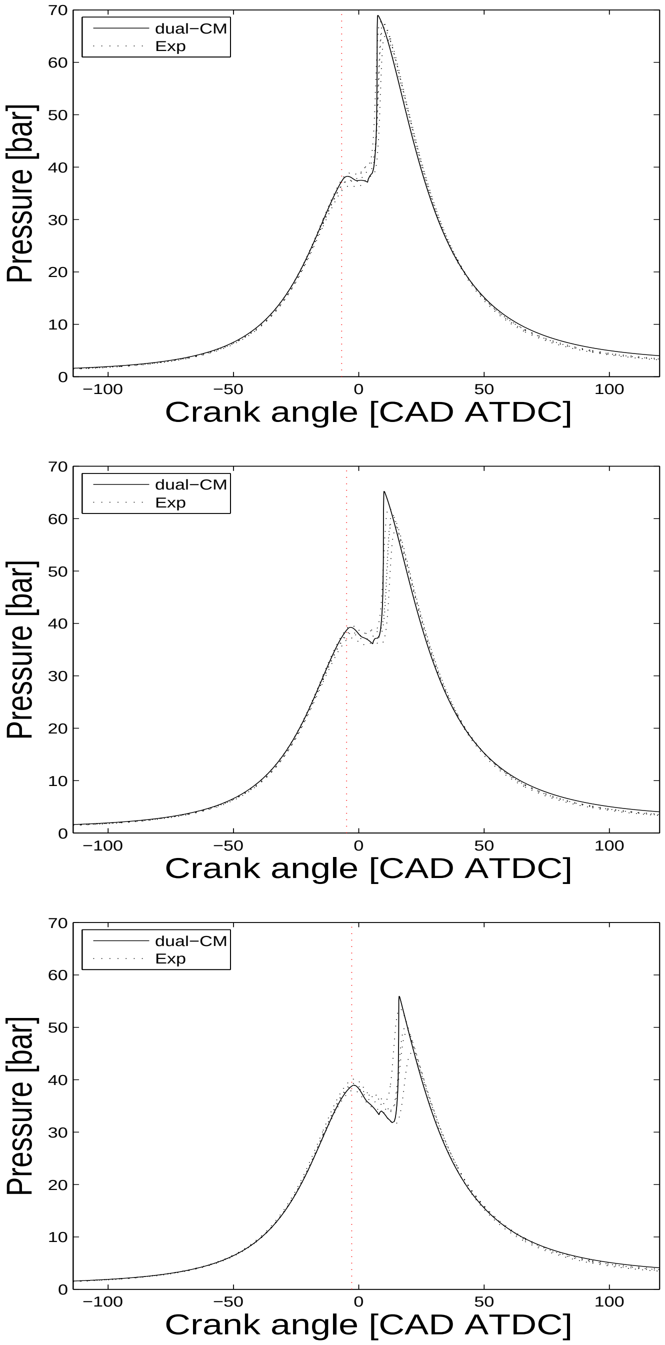

Figure 3.27: Sensitivity of the 0D model to *SOI* variations. Comparison of 0D modelling with experimental data. Curves of pressure refer to the operating points n° 7 (top), 8 (middle), 3 (bottom). The red dotted vertical line represents the *SOI*.

As shown in table 3.5, the tested engine operating points strongly differ from each other in terms of engine speeds, $IMEPs$, $EGR\ rates$, $AVIs$, engine loads and injection pressures.

Figures 3.30 to 3.34 show on the left hand sides the comparison of the dual-CM in-cylinder pressure curves with experiments. In each of these pictures, the tracer pressure curves giving the pressure values for reading the complex chemistry look-up tables are

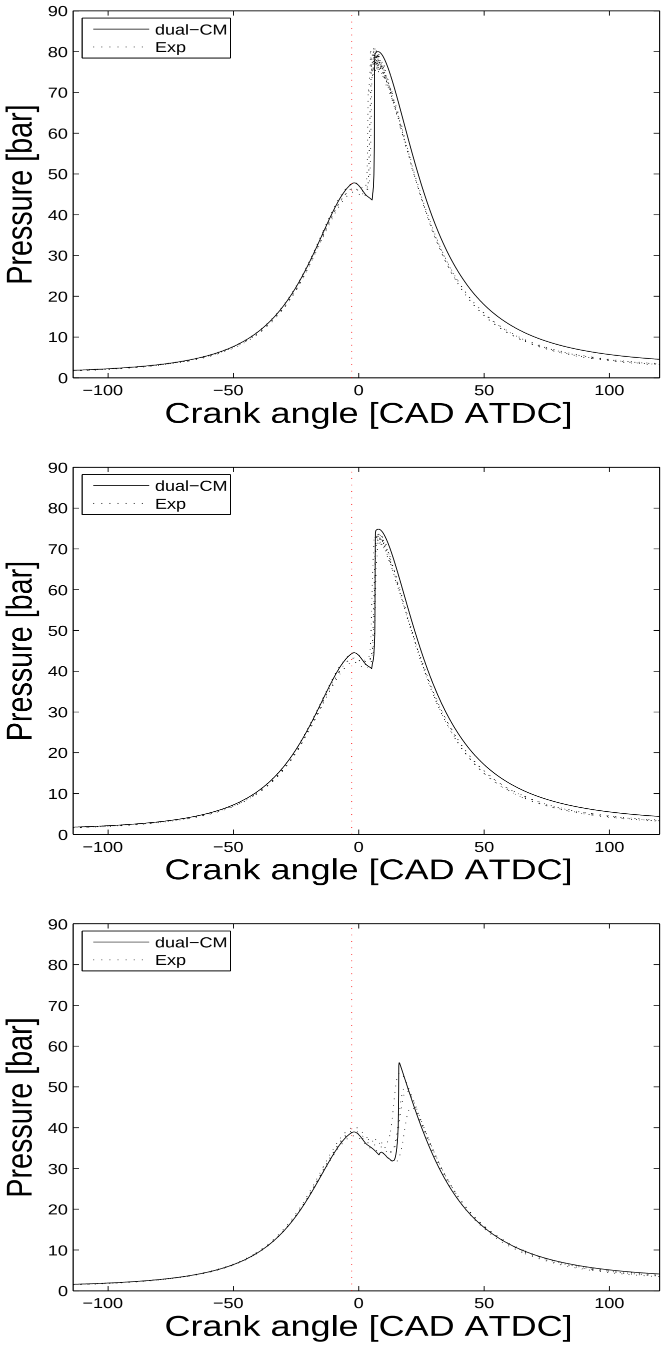

Figure 3.28: Sensitivity of the 0D model to *EGR rate* variations. Comparison of 0D modelling with experimental data. Curves of pressure refer to the operating points n° 1 (top), 2 (middle), 3 (bottom). The red dotted vertical line represents the *SOI*.

shown, as well. On the right hand sides, the cylinder volumes, and spray volumes and liquid masses evolutions are presented. As seen, the dual-CM pressure curves are in good agreement with experiments : the overall shape of the pressure curves and the auto-ignition delays, as well as the maximum pressure values and their locations are well predicted. Concerning the spray evolutions, it is noticed that in the most general case, when the second injection event takes place, the liquid fuel mass belonging to the

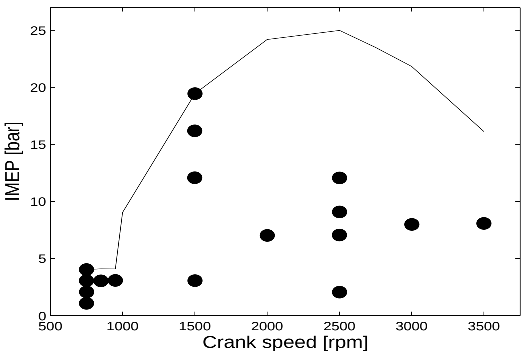

Figure 3.29: Location of the retained engine operating points on the whole engine operating domain.

first spray is completely vaporized and this latter has completely fulfilled the cylinder volume : in those conditions the hypothesis done on the spray interaction, section 2.4.2.3, is exact.

Regarding the pressure curves shown in figure 3.30, it is seen (especially on the third row from the top) that experiments have at Top Dead Center (TDC) a lower value of pressure than computations. This difference is probably due to blow-by phenomena existing in the real system, but not taken into account by the dual-CM. In fact in a real engine running at low engine speed, part of the gases in the combustion chamber have the time to flow away passing through the clearance between the cylinder-liner and the piston wall.

To conclude, differences between computed and experimental pressure curves are noticed looking at the last two rows of figure 3.34, regarding the maximum pressure values. This is essentially due to an underestimation of the reactivity of the second injection mixture. This aspect will be detailed more in chapter 4.

3.7 Statistics on the entire engine operating domain

In this section, the statistics relative to the dual-CM behavior on the entire engine operating domain are presented. Figures 3.36 to 3.38 refer to the three criteria that are commonly adopted for estimating the quality of an engine operating point computation for global engine system simulation :

- the $IMEP$ value,
- the maximum in-cylinder pressure value (due to combustion[12]) of the engine cycle,
- the angle at which the maximum in-cylinder pressure value is obtained.

---

[12] It could happen for given late injection strategies, that the maximum in-cylinder pressure values correspond to the pressure values associated to the motored engine cycles : for those conditions there is no interest of determining their values and locations.

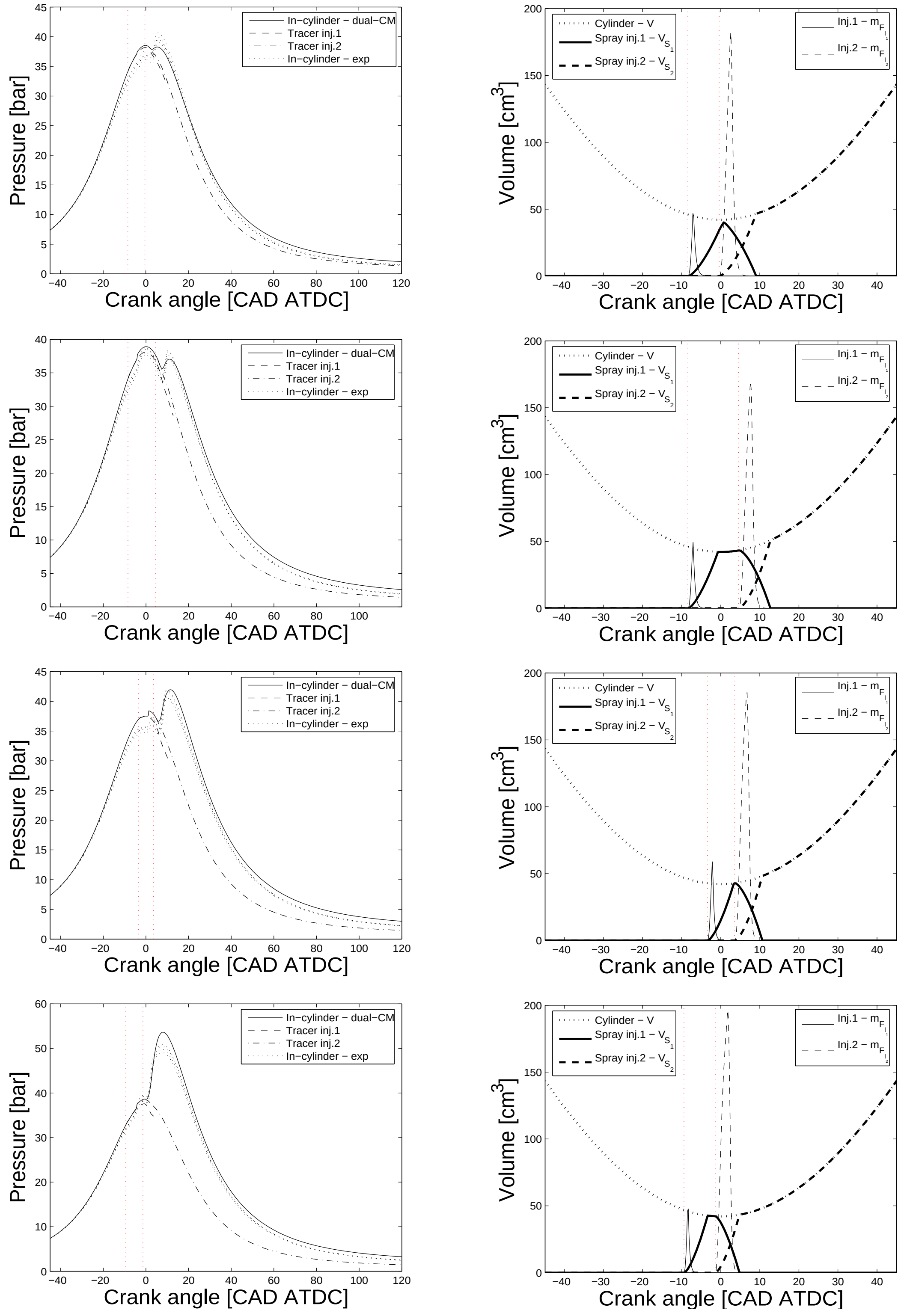

Figure 3.30: Set of engine operating points representing a load variation from 1 up to 4 bar; the engine speed is kept constant to 750 rpm. From the top, curves correspond to the engine operating points n° 1, 2, 3 and 4 detailed in table 3.5. The figure shows the comparison of the computed pressure curves with experiments (left), and the computed volumes and fuel liquid masses relative to the two sprays (right). The red dotted vertical lines represent the *SOIs*.

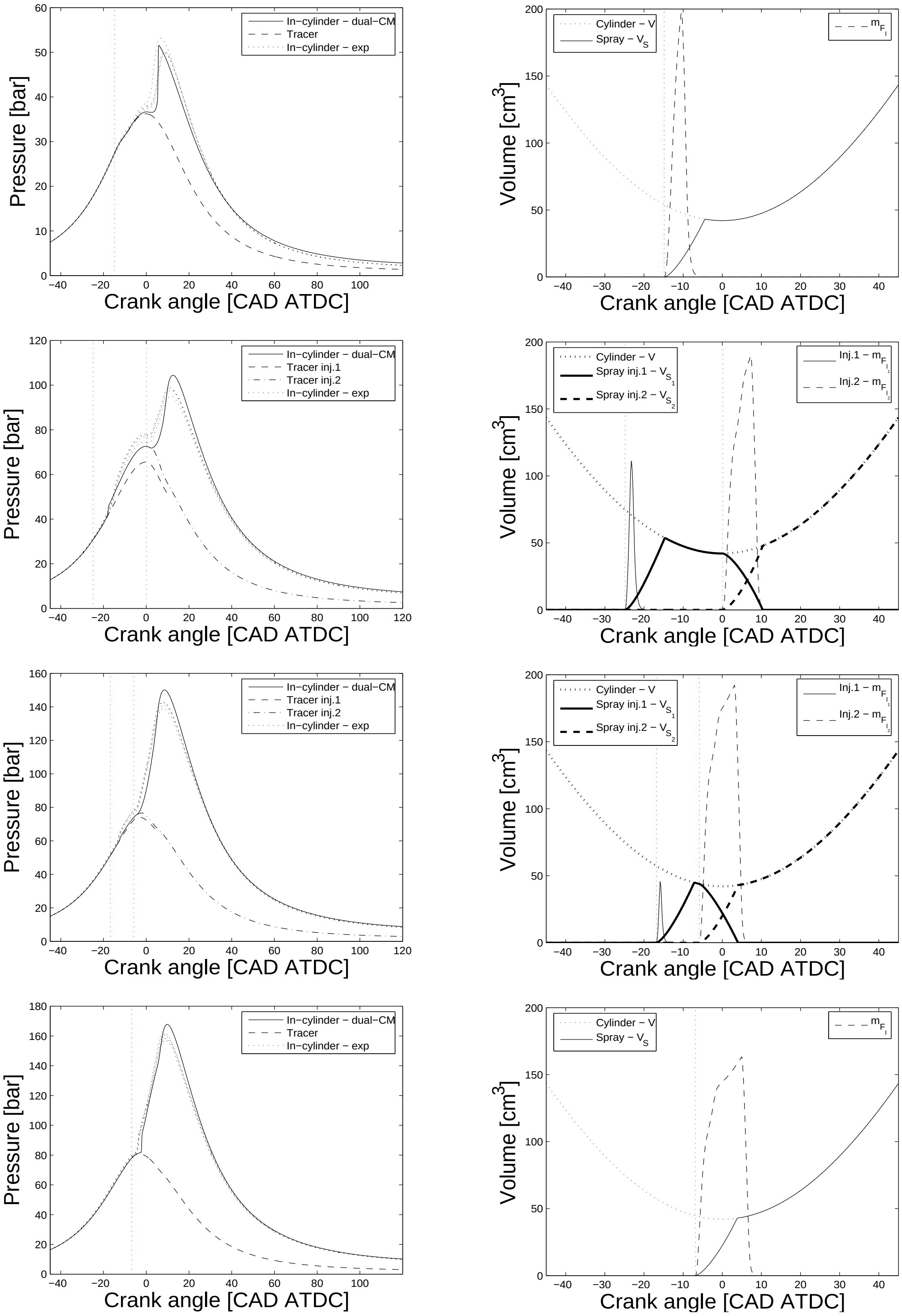

Figure 3.31: Set of engine operating points representing a load variation from 3 up to 19 bar; the engine speed is kept constant to 1500 rpm. From the top, curves correspond to the engine operating points n° 7, 8, 9 and 10 detailed in table 3.5. The figure shows the comparison of the computed pressure curves with experiments (left), and the computed volumes and fuel liquid masses relative to the two sprays (right). The red dotted vertical lines represent the *SOIs*.

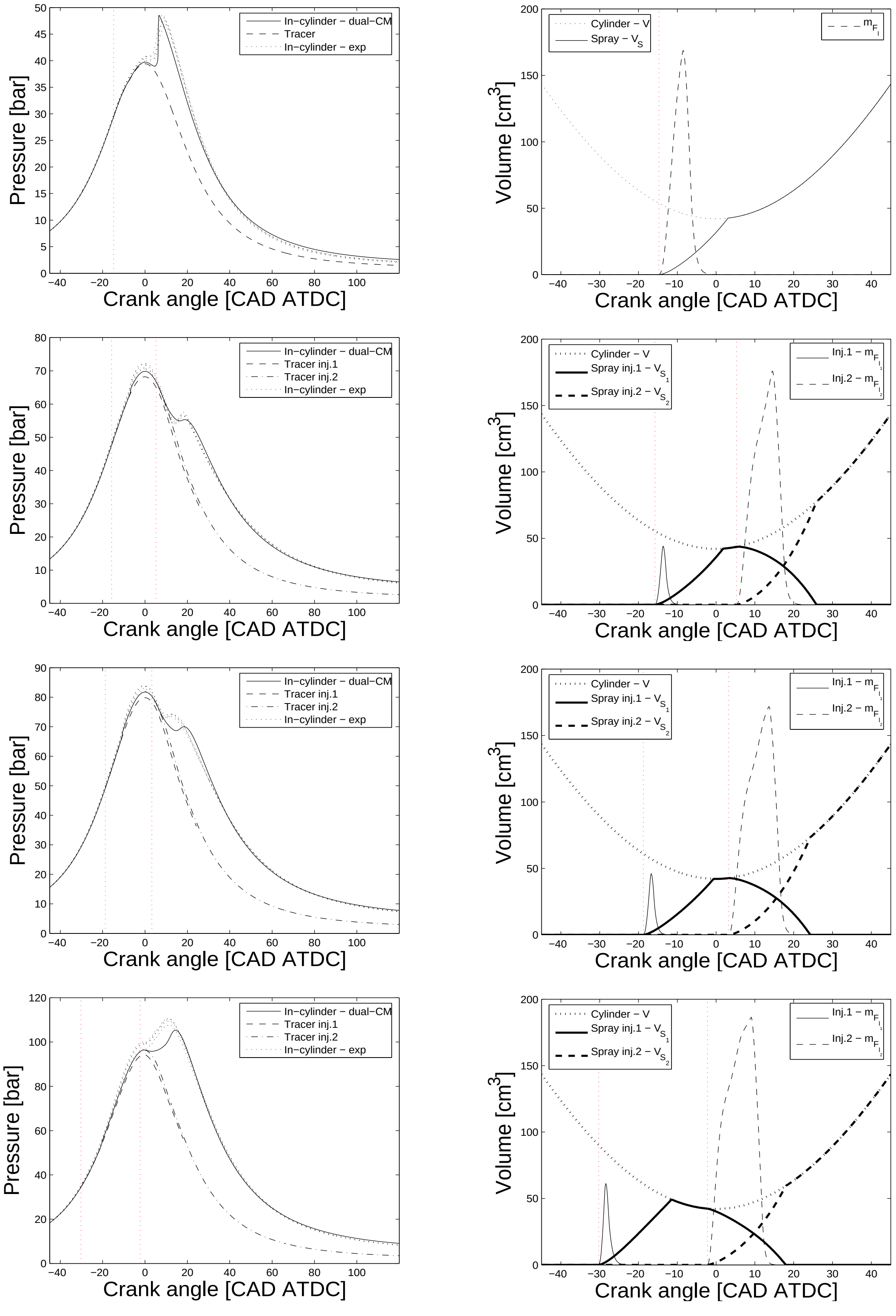

Figure 3.32: Set of engine operating points representing a load variation from 2 up to 12 bar; the engine speed is kept constant to 2500 rpm. From the top, curves correspond to the engine operating points n° 12, 13, 14 and 15 detailed in table 3.5. The figure shows the comparison of the computed pressure curves with experiments (left), and the computed volumes and fuel liquid masses relative to the two sprays (right). The red dotted vertical lines represent the *SOIs*.

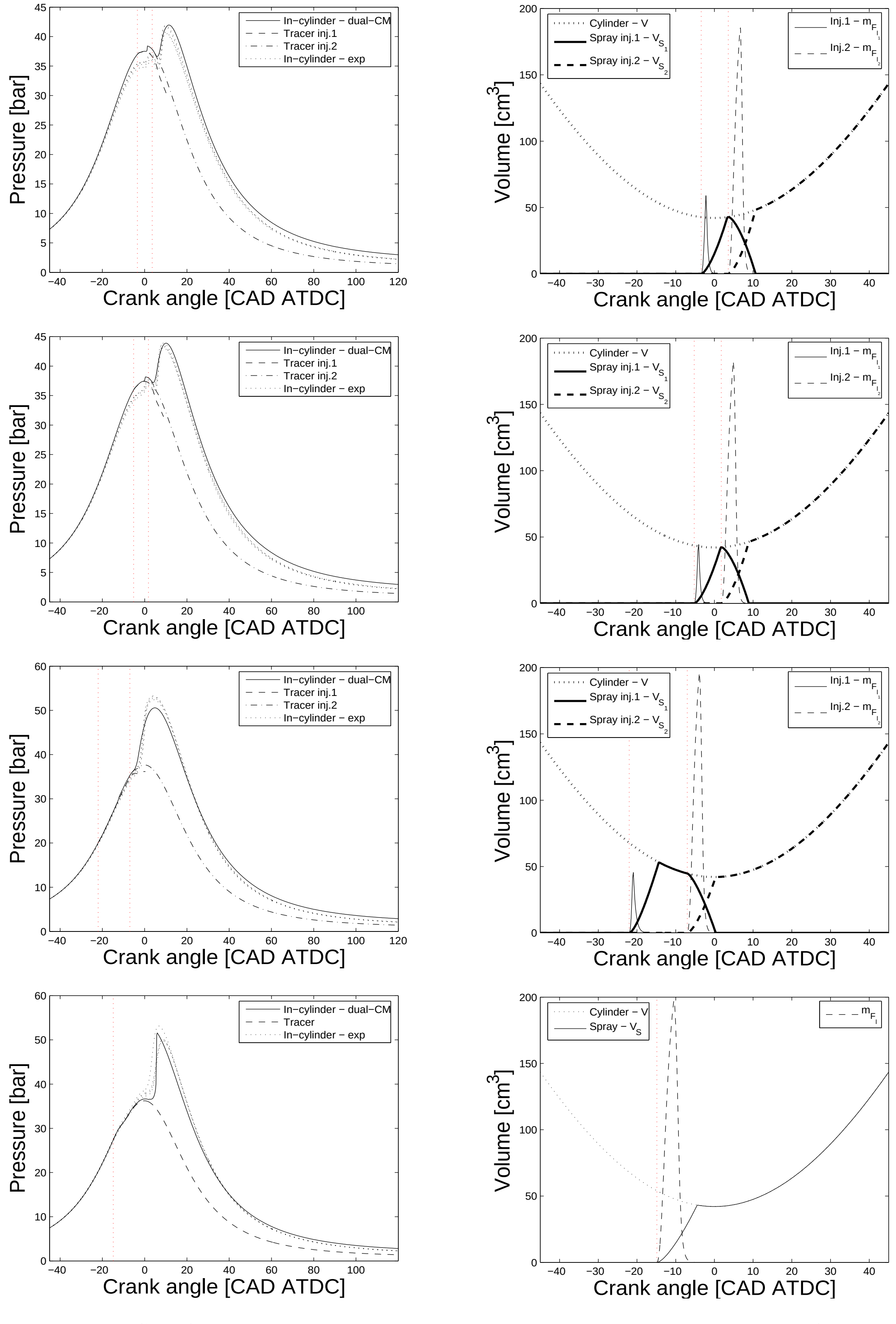

Figure 3.33: Set of engine operating points representing an engine speed variation from 750 up to 1500 rpm; the engine load is kept constant to 3 bar. From the top, curves correspond to the engine operating points n° 3, 5, 6 and 7 detailed in table 3.5. The figure shows the comparison of the computed pressure curves with experiments (left), and the computed volumes and fuel liquid masses relative to the two sprays (right). The red dotted vertical lines represent the *SOIs*.

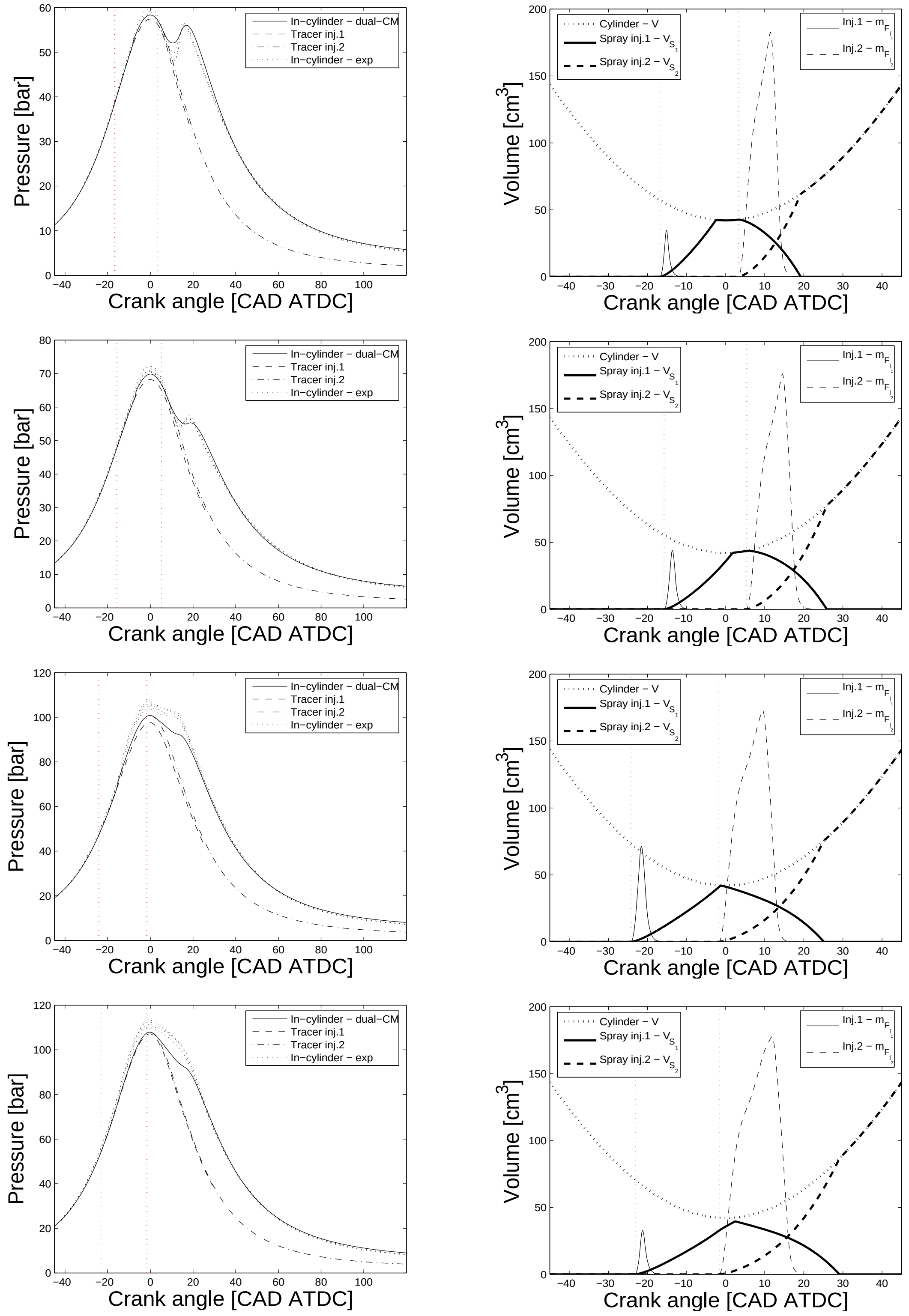

Figure 3.34: Set of engine operating points representing an engine speed variation from 2000 up to 3500 rpm; the engine load is kept constant to 7 bar. From the top, curves correspond to the engine operating points n° 11, 13, 16 and 17 detailed in table 3.5. The figure shows the comparison of the computed pressure curves with experiments (left), and the computed volumes and fuel liquid masses relative to the two sprays (right). The red dotted vertical lines represent the *SOIs*.

Simply looking at the in-cylinder pressure curves, it is not always easy to determine the correct position of the maximum value of pressure due to combustion. As an example, figure 3.35 (top) shows the computed and the mean[13] experimental in-cylinder pressure curves, as well as the computed dual-CM tracer pressure used for reading the complex-chemistry look-up tables, relative to the engine operating point n° 16 in table 3.5.

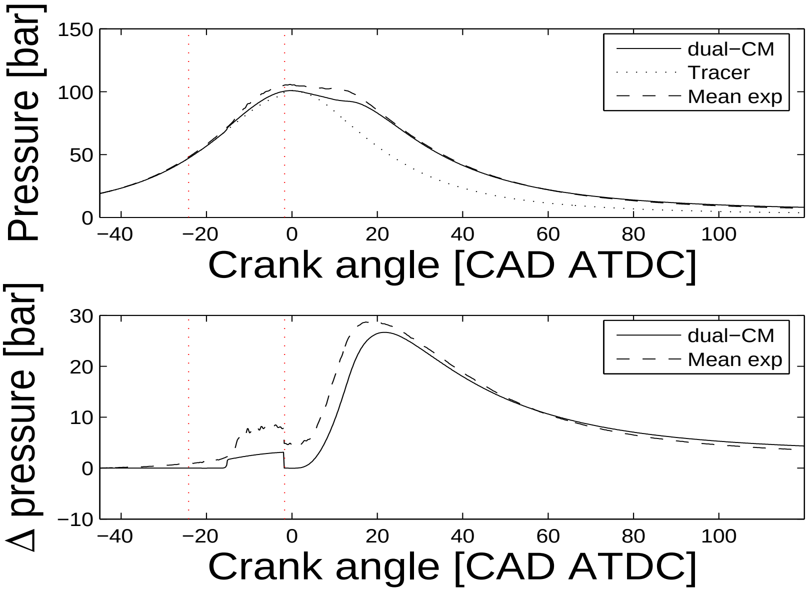

Figure 3.35: Methodology used for determining the maximum in-cylinder pressure value due to combustion and the corresponding crank angle.

The methodology proposed here for the determination of the maximum pressure value due to combustion and its location on the engine cycle is detailed below. The tracer pressure computed by dual-CM represents the pressure relative to the motored engine cycle. Consequently, by subtracting the motored engine-cycle pressure from the fired engine-cycle pressure, the contribution to the pressure value due to combustion, Δ *pressure*, is *isolated*, figure 3.35 (bottom). At this point, it is easy to identify the crank angles corresponding to the maximum values of Δ *pressure* of the computed and experimental curves, figure 3.35 (bottom). The corresponding maximum pressure value is read for the same crank angles directly on the pressure curves, figure 3.35 (top).

On the top of figure 3.36 is shown the correlation between the experimental $IMEP$ values of the 101 tested engine operating points and the $IMEP$ values computed by the dual-CM : a very good correlation is found. By fixing error bands from the experimental values at ± 1 bar, 96% of the computations match with experiments. On the bottom of figure 3.36 are shown the statistics of the absolute errors between experiments and computations. For a given engine operating point k, the $IMEP$ error, $IMEP_{err_k}$, is

---

[13] The mean experimental in-cylinder pressure curve is obtained as the mean of the curves relative to the four cylinders.

computed as :

$$IMEP_{err_k} = IMEP_k^{dual-CM} - IMEP_k^{exp} \tag{3.25}$$

where $IMEP_k^{dual-CM}$ is the $IMEP$ value computed by dual-CM and $IMEP_k^{exp}$ is the one obtained experimentally. As shown, there is a slight tendency to underestimate the $IMEP$. The standard deviation of the distribution is given in the figure.

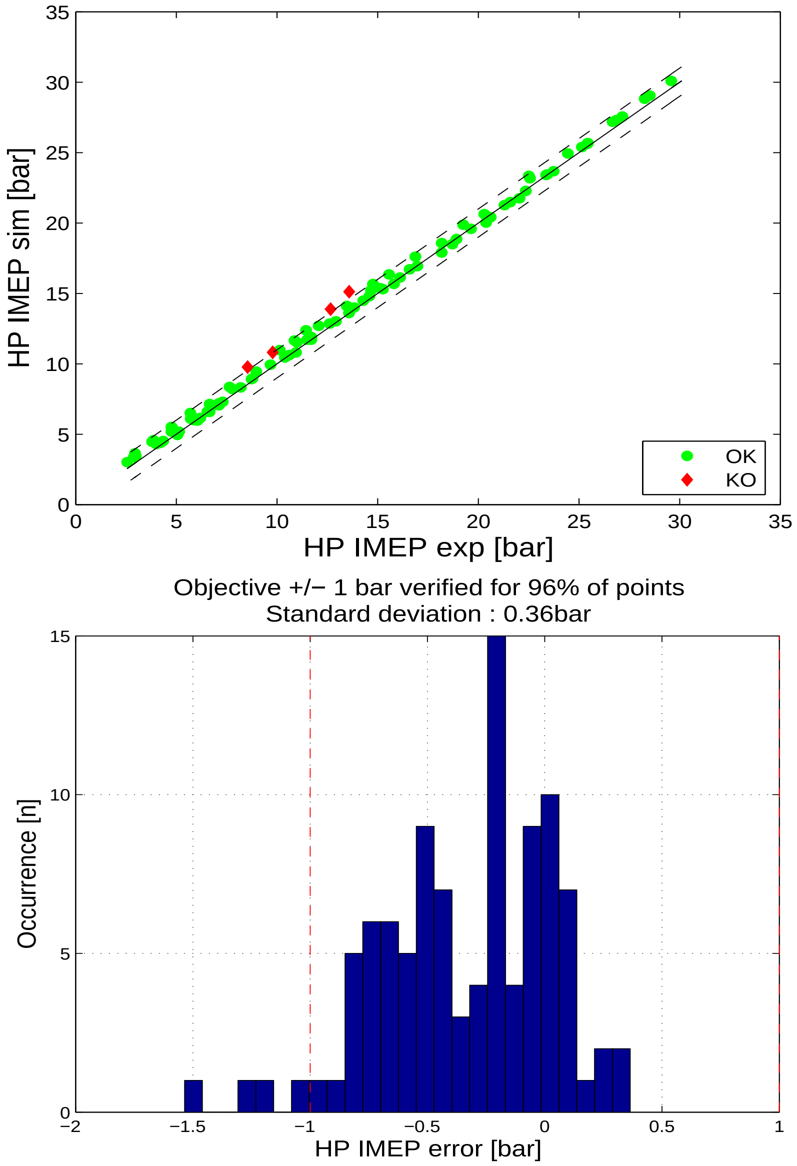

Figure 3.36: On the top, the correlation between the experimental $IMEP$ values and $IMEP$ values computed by using the dual-CM is shown; error bands refer to ± 1 bar of $IMEP$. On the bottom, the bar chart relative to the statistics of the $IMEP$ distribution is presented; more details concerning the distribution are given on the figure.

On the top of figure 3.37 is shown the correlation between the experimental maximum pressure values of the 101 tested engine operating points and the maximum pressure values computed by dual-CM : a satisfactory correlation is found. By fixing error bands from the experimental values at ± 5 bar, 49% of the computations match with experiments. On the bottom of figure 3.37 are shown the statistics of the absolute errors between experiments and computations. For a given engine operating point k, the maximum pressure error, $p_{max_{err_k}}$, is computed as :

$$p_{max_{err_k}} = p_{max_k}^{dual-CM} - p_{max_k}^{exp} \tag{3.26}$$

where $p_{max_k}^{dual-CM}$ is the maximum pressure value computed by dual-CM and $p_{max_k}^{exp}$ is the one obtained experimentally. According to figure 3.36, there is a slight tendency to underestimate the maximum pressure values, which probably induces to an underestimation of the $IMEP$ values. The standard deviation of the distribution is given in the figure.

On the top of figure 3.38 is shown the correlation between the experimental maximum-pressure angles of the 101 tested engine operating points and the maximum-pressure angles computed by dual-CM : a good correlation is found. By fixing error bands from the experimental values at ± 5 CAD, 85% of the computations match with experiments. On the bottom of figure 3.38 are shown the statistics of the absolute errors between experiments and computations. For a given engine operating point k, the maximum pressure angle error, CAD_{err_k}, is computed as :

$$CAD_{err_k} = CAD_k^{dual-CM} - CAD_k^{exp} \tag{3.27}$$

where $CAD_k^{dual-CM}$ is the maximum-pressure angle value computed by dual-CM and CAD_k^{exp} is the one obtained experimentally. As shown, the distribution is centered around the zero, and it presents a longer tail on its right hand side. The standard deviation of the distribution is given in the figure.

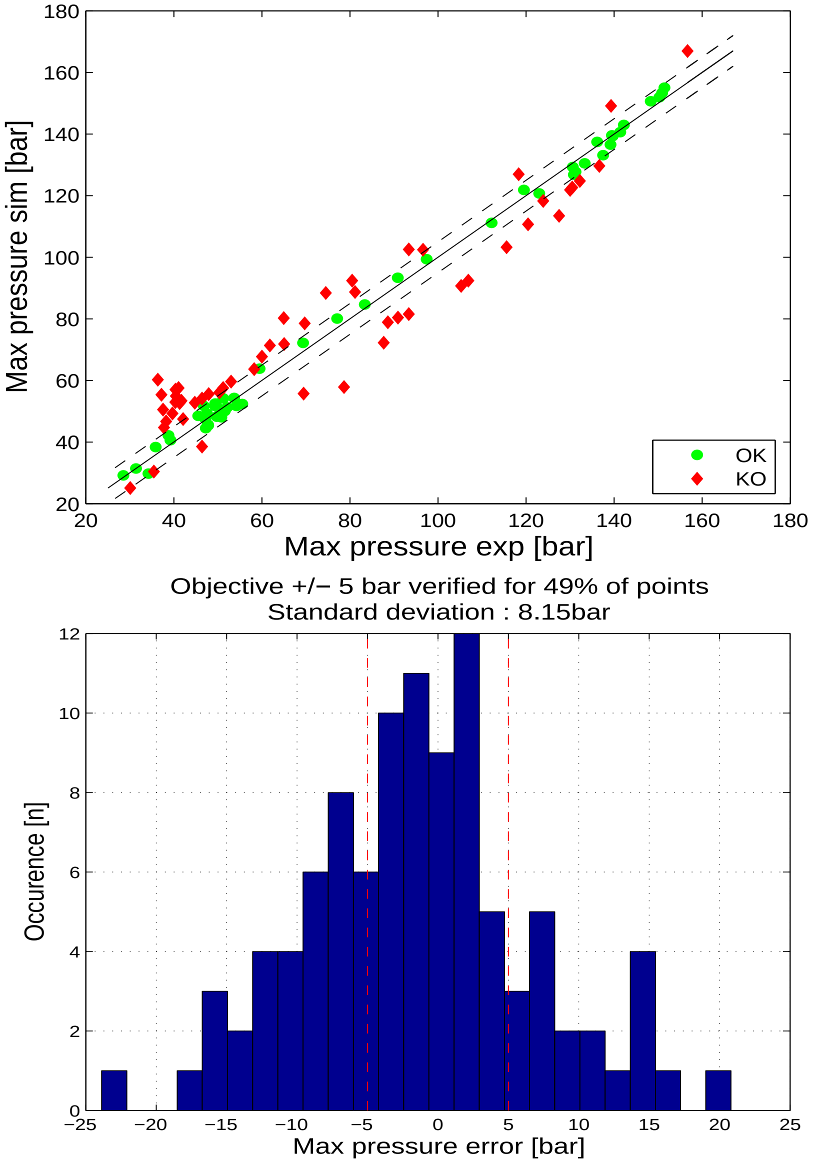

Figure 3.37: On the top, the correlation between the experimental maximum pressure values and maximum pressure values computed by using the dual-CM is shown; error bands refer to ± 5 bar. On the bottom, the bar chart relative to the statistics of the maximum pressure distribution is presented; more details concerning the distribution are given on the figure.

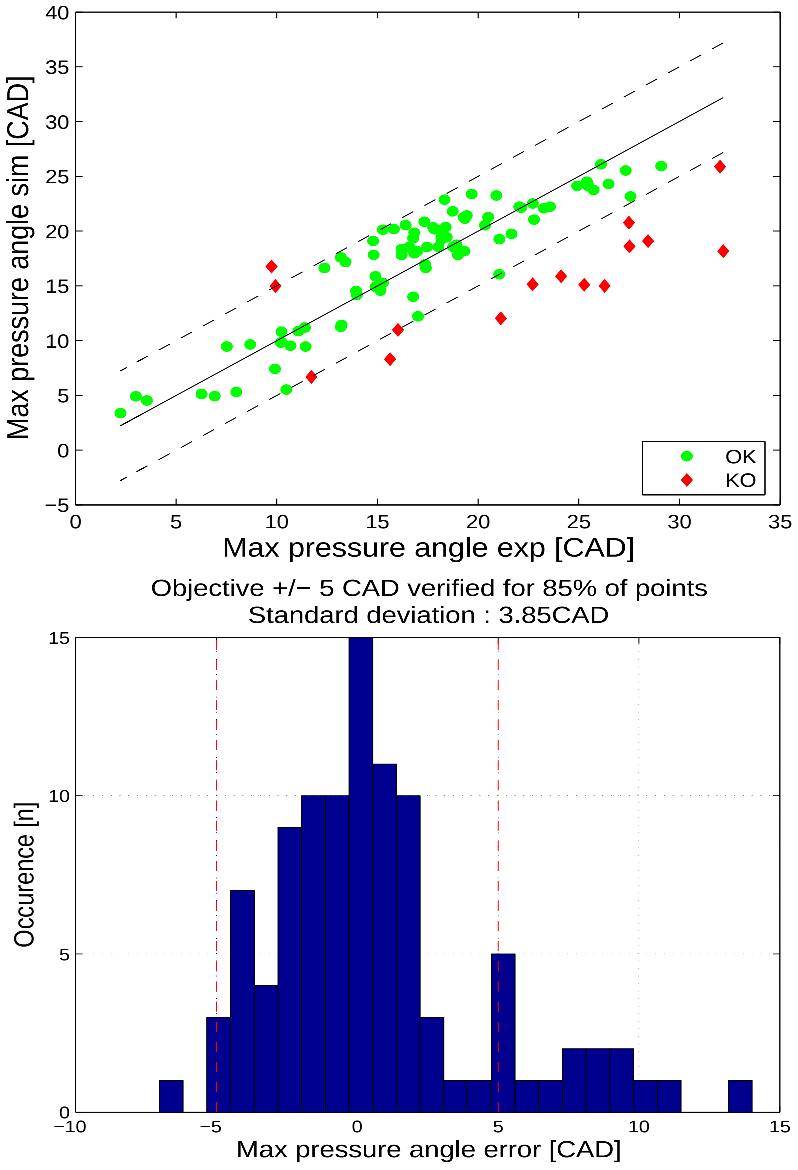

Figure 3.38: On the top, the correlation between the experimental maximum-pressure angles and maximum-pressure angles computed by using the dual-CM is shown; error bands refer to ± 5 CAD. On the bottom, the bar chart relative to the statistics of the maximum-pressure angle distribution is presented; more details concerning the distribution are given on the figure.

Chapter 4

Limits and analysis of precision of dual-CM : investigation making a comparison with a 3D solver

The aim of this chapter is to evidence the limitations associated with the formalism used in developing the dual-CM. In particular, two major axes will be investigated :

- the influence of the combustion chamber shape on mixture formation, section 4.1,
- the influence of adopting a combustion model based on the first order PCM approach [87], section 4.2.

Investigations will be carried out by using as a support the results obtained with the 3D CFD solver IFP-C3D [73]. Experimental results refers to a turbo-charged Renault G9T NADI™ concept engine [93]. The specifications of the engine are given in table 3.1. In order to evidence the influence of the piston geometry on mixture formation process, a different bowl profile was used, figure 4.1. The difference between the two bowls is clearly visible in figure 3.3 : in particular, the new bowl has a greater curvature in its lower part. The fact of using the new piston bowl changes the compression ratio of the engine from 14 to 14.7; the other engine specifications remain unchanged.

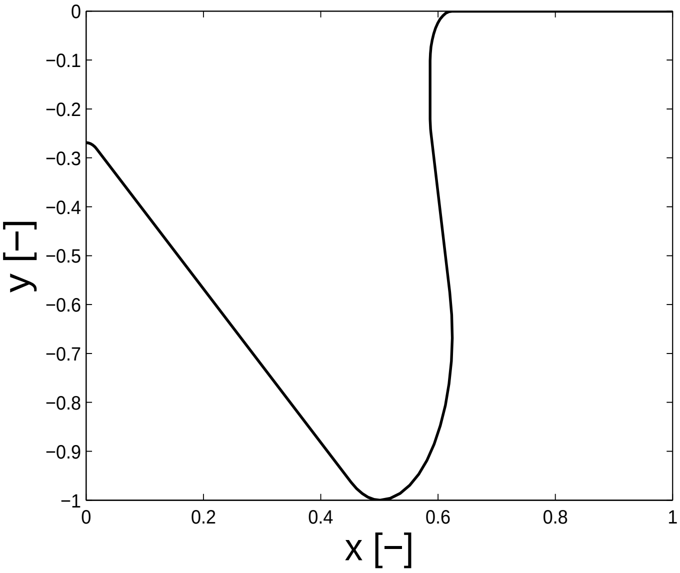

Figure 4.1: Modified bowl for Renault G9T NADI™ concept engine.

Two engine operating points adopting multiple injection strategies were investigated, table 4.1.

Point [-]	Ω_{eng} [rpm]	$IMEP$ [bar]	$EGR\ rate$ [%]	AVI_1 [CAD BTDC]	AVI_2 [CAD BTDC]	Φ [-]	p_{inj} [bar]
1	2500	9.5	11	22.9	4.9	0.76	1200
2	2500	9.5	11	16.9	-1.1	0.72	1200

Table 4.1: Specification of the experimental engine operating points obtained by using the new bowl geometry, figure 4.1.

The two engine operating points were computed by both dual-CM and IFP-C3D. Because of the change of geometry, the dual-CM adjustment parameters were varied in order to fit at best the experimental pressure curves, table 4.2.

Orifice area contraction coeff.	C_a	0.82	$\longrightarrow$	0.82
Orifice velocity coeff.	C_v	0.93	$\longrightarrow$	0.93
Liquid penetration coeff. (inj. 1)	b_1	0.41	$\longrightarrow$	0.55
Liquid penetration coeff. (inj. 2)	b_2	0.41	$\longrightarrow$	0.41
Gaseous penetration coeff. (inj. 1)	C_{S_1}	1.3	$\longrightarrow$	1.09
Gaseous penetration coeff. (inj. 2)	C_{S_2}	1.3	$\longrightarrow$	1.3
Mean kinetic energy dissipation (pre-exponential coeff.)	C_K	15	$\longrightarrow$	15
Mean kinetic energy dissipation (exponential coeff.)	N_K	1.9	$\longrightarrow$	1.9
Turbulent kinetic energy dissipation (pre-exponential coeff.)	C_κ	15	$\longrightarrow$	15
Turbulent kinetic energy dissipation (exponential coeff.)	N_κ	1.9	$\longrightarrow$	1.9
Mixture fraction variance dissipation coeff. (inj. 1)	C_{ds_1}	0.67	$\longrightarrow$	1
Mixture fraction variance dissipation coeff. (inj. 2)	C_{ds_2}	0.67	$\longrightarrow$	0.74

Table 4.2: Variations of the dual-CM adjustment parameters consequently to the change of the piston bowl shape.

Figures 4.2 and 4.3 refer respectively to the engine operating points 1 and 2, table 4.1, and show the comparison between the dual-CM and IFP-C3D computed in-cylinder pressure curves with experiments.

As seen in both figures 4.2 and 4.3, the dual-CM combustion process seems to be *slower* than the two others. In the following of this chapter, a deeper investigation of the physics within the cylinder will be performed by using the 3D CFD solver IFP-C3D, to understand the nature of the differences between the in-cylinder pressure curves.

4.1 Influence of the combustion chamber shape on mixture formation

The first step in order to understand the reasons of the difference between the dual-CM in-cylinder pressure curves, and the IFP-C3D and experimental curves, figures 4.2 and 4.3, is to investigate the mixture formation processes taking place in the cylinder. In the following, the investigation will be focused on the engine operating point n° 1 detailed in table 4.1.

This engine operating point uses a multiple injection strategy : in order to be coherent

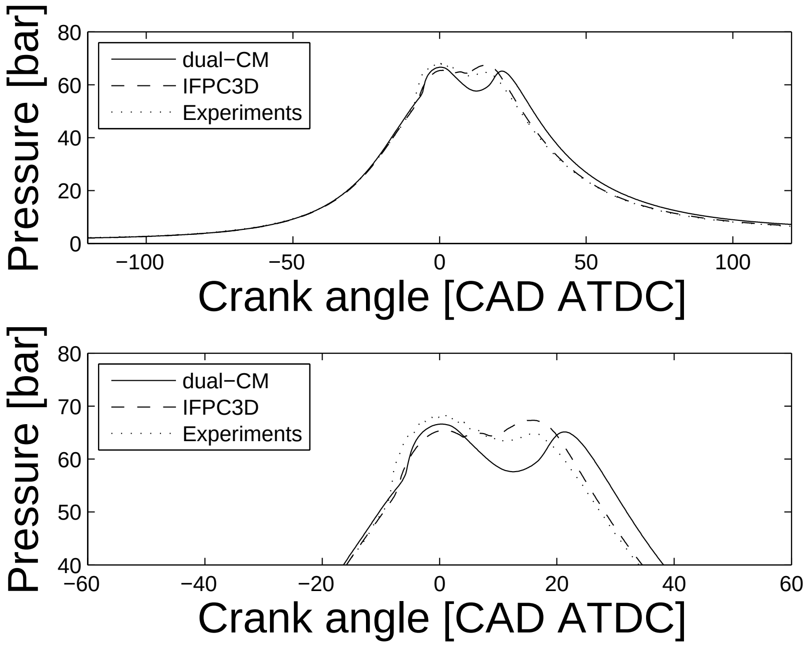

Figure 4.2: Comparison between the dual-CM and IFP-C3D computed in-cylinder pressure curves with experimental data, relatively to the engine operating point n° 1, table 4.1 : a view of the entire high pressure engine cycle (top), and a zoom of the pressure peaks (bottom).

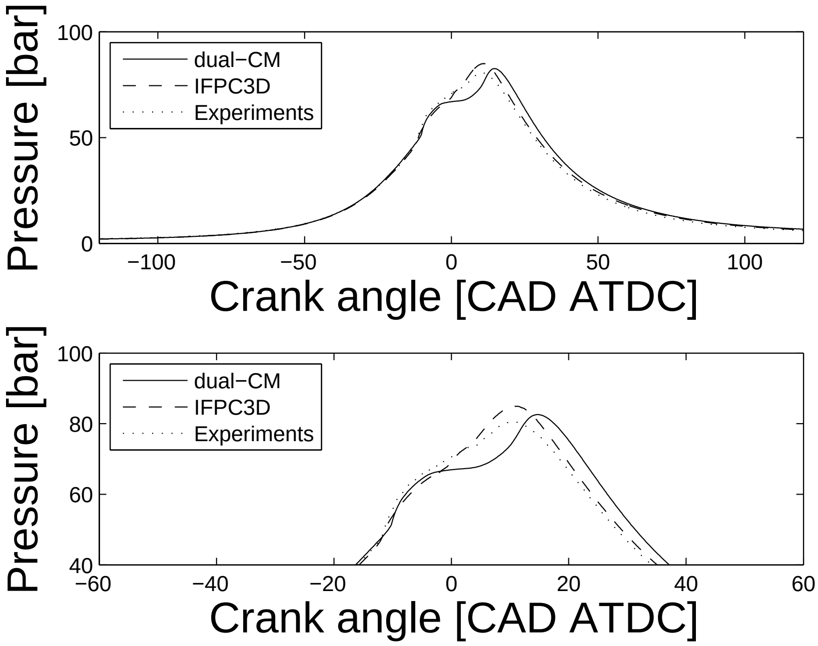

Figure 4.3: Comparison between the dual-CM and IFP-C3D computed in-cylinder pressure curves with experimental data, relatively to the engine operating point n° 2, table 4.1 : a view of the entire high pressure engine cycle (top), and a zoom of the pressure peaks (bottom).

in the comparison between the dual-CM and IFP-C3D computed variables, the IFP-C3D results must be postprocessed in order to be able to distinguish between the spray mixture zones associated to the different injections, by using the same formalism as the one adopted in the dual-CM.

For the sake of clarity, in dual-CM a given mixture is considered to belong to the i^{th} injection spray, where the index i indicates the number of the injection, if among its chemical species exists gaseous fuel injected during the i^{th} liquid fuel injection. As locally fuels could coexist belonging to more than one injection, i is defined as being referred to fuel that was injected the last. For instance, if locally gaseous fuels belonging to the i^{th} and $(i-1)^{th}$ injections coexist, that region is said to belong to the i^{th} spray.

The same definition was used for distinguishing the spray zones in IFP-C3D. In fact, the solver IFP-C3D is able to manage multi-component fuels. As a consequence it was possible to *duplicate* the injected fuel into fuels with different IDs depending on the injection number, but the same physical properties. Accordingly, for each cell k, an array of integers was created, I_k, mapped by the index j varying between 1 and NI, where NI is the number of injections, depending on the injection number. Each element of I_k was computed as :

$$I_k(j) = \begin{cases} j, & \text{if } Y_{F_{\tau_{j_k}}} \geq 1 \cdot 10^{-5} \\ 0, & \text{otherwise} \end{cases} \tag{4.1}$$

where $Y_{F_{\tau_{j_k}}}$ is the tracer fuel mass fraction value associated with the j^{th} injection in the cell k, defined as :

$$Y_{F_{\tau_{j_k}}} = \frac{\rho_{F_{\tau_{j_k}}}}{\rho_k} \tag{4.2}$$

in which $\rho_{F_{\tau_{j_k}}}$ is the partial density of the tracer fuel associated with the j^{th} injection in the cell k, and ρ_k is the density of the cell k. Then a function Ind_S mapped by the index k varying between 1 and NC, where NC is the total number of cells, was defined. For each cell k, $Ind_S\,(k)$ gives the spray number to which the cell belongs. Accordingly, $Ind_S\,(k)$ was computed as :

$$Ind_S\,(k) = \max_{j=1,NI} \left(I_k\,(j)\right) \tag{4.3}$$

Figure 4.4 describes the mixing processes associated with the combustions for which in-cylinder pressure curves are shown in figure 4.2. In the figure are shown the evolutions of the spray volumes, V_{S_i}, liquid fuel masses, $m_{F_{l_i}}$, and total spray masses, m_{S_i}. In IFP-C3D, for the i^{th} injection, these variables were computed respectively as :

$$V_{S_i}^{IFP-C3D} = \sum_{k=1}^{NSC_i} V_k \tag{4.4}$$

$$m_{F_{l_i}}^{IFP-C3D} = m_{F_{l_i}} \tag{4.5}$$

$$m_{S_i}^{IFP-C3D} = \sum_{k=1}^{NSC_i} \rho_k \cdot V_k \tag{4.6}$$

where NSC_i is the number of cells belonging to the i^{th} spray and $m_{F_{l_i}}$ is the instantaneous liquid fuel mass injected during the i^{th} injection.

Observing figure 4.4 different aspects can be put in evidence :

- the spray volumes have a strong interaction : in fact before the first spray completely fulfils the cylinder volume, the second injection starts, and there is competition between the spray volume growths (top of figure 4.4),
- the spray volumes evolutions computed by the two solvers are different (top of figure 4.4),
- the results concerning the liquid fuel masses are in correct agreement between dual-CM and IFP-C3D results (middle of figure 4.4),
- the dual-CM and IFP-C3D computed total gaseous masses in the spray regions, and in particular the curves associated with the first injection sprays, are different (bottom of figure 4.4).

The differences in the mixing process observed in figure 4.4 are essentially due to the fact that the growth of the first injection spray volume, and consequently the entrained ambient air in the spray region, does not follow a classical exponential law as was observed in figure 3.13, but there is a sort of break point at around -6 CAD ATDC. Once again, the answer to this phenomenon can be found by observing the spray dynamics computed by the 3D solver IFP-C3D. Figure 4.5 shows the evolution of sprays volumes for the engine operating point n° 1 of table 4.1.

As seen in figure 4.5, after the start of the first injection, figure 4.5 (a), the spray volume grows, figure 4.5 (b), guided by the bowl surface. At around -5 CAD ATDC, the spray impacts the vertical wall of the bowl, figure 4.5 (c), and its growth rate is abruptly reduced, figures 4.5 (c-e) and 4.4. The discontinuity on the spray volume growth due to the impact against the vertical wall of the bowl was almost imperceptible when the other bowl shape was used. In fact, in that case, the spray was wall-guided by the bowl profile and because of the mild curvature, the spray was simply folded on itself without impact, figure 3.16.

As a consequence, it is possible to affirm that the formalism used in the dual-CM for computing the ambient-air entrainment in the spray region is not sensitive to particular bowl geometries that impose spray growth laws which strongly differ from the ones of free jets.

Figure 4.5 also gives important information concerning the interaction between the two injections. When the second fuel injection starts, the first spray volume is still growing, figure 4.5 (e). As shown, the volume of the second spray is completely contained

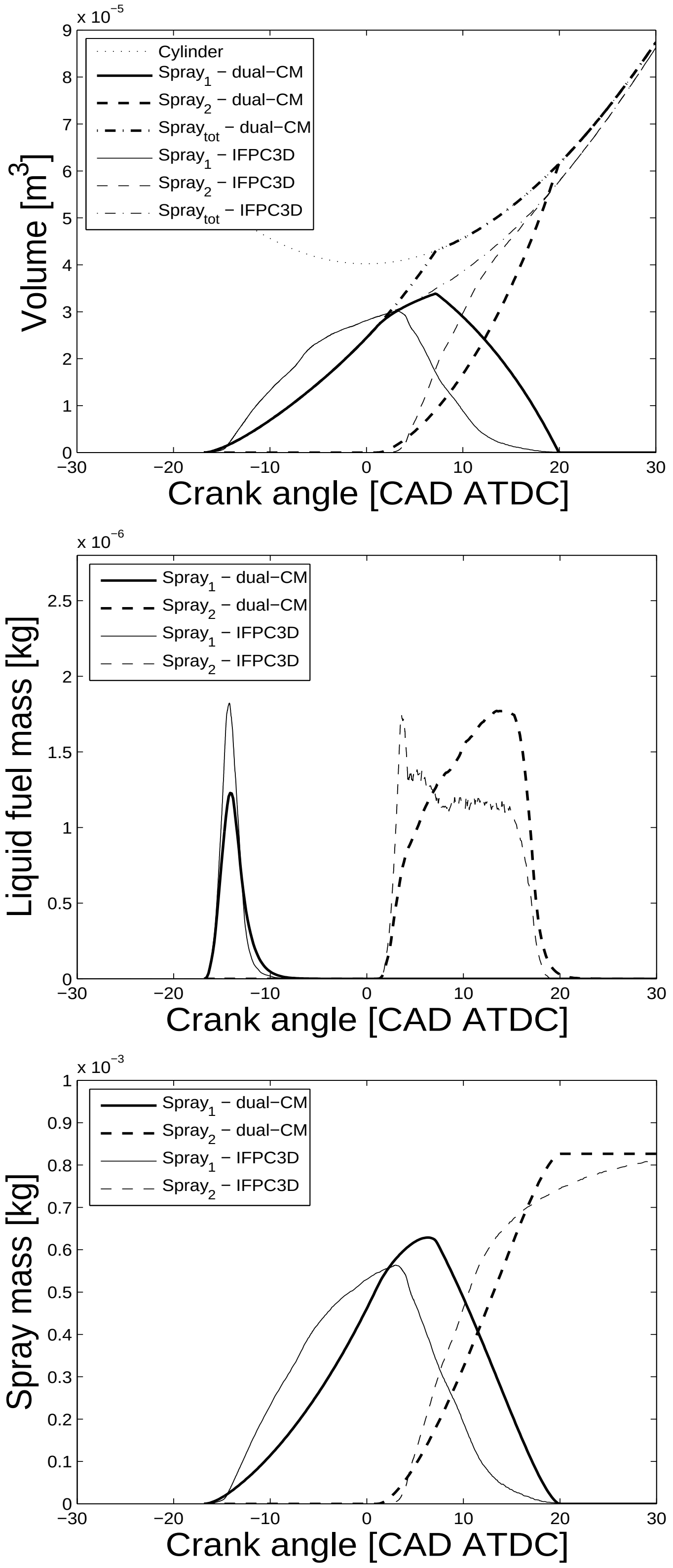

Figure 4.4: Comparison between dual-CM and IFP-C3D results concerning the formation of the spray zones, associated to the engine operating point n° 1 of table 4.1. The evolutions of the spray volumes (top), liquid masses (middle) and total spray masses (bottom) are shown. The described mixing process refers to the in-cylinder pressure curves showed in figure 4.2.

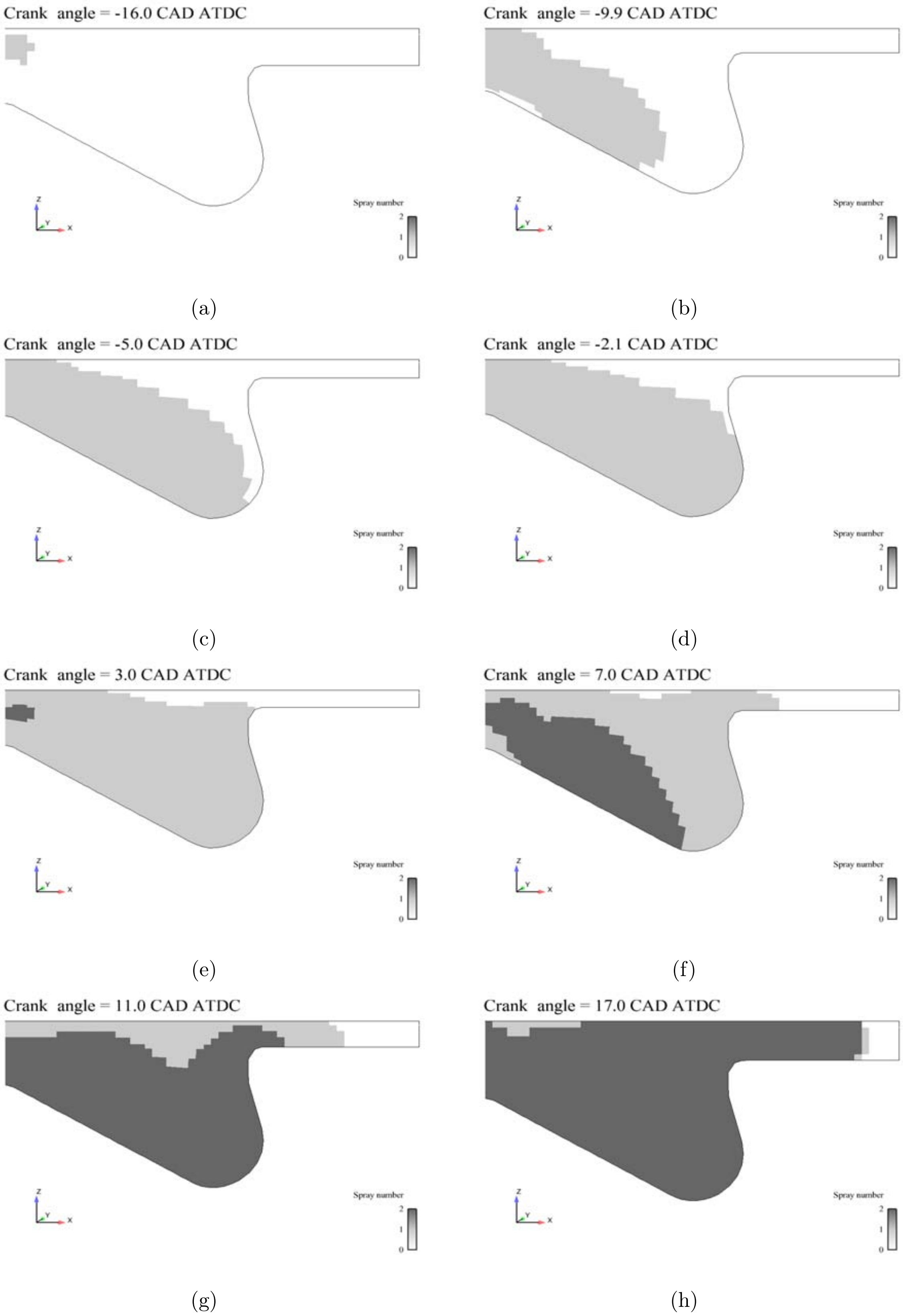

(a) (b) (c) (d) (e) (f) (g) (h)

Figure 4.5: Dynamics of the spray volumes computed by IFP-C3D relative to the engine operating point n° 1 of table 4.1. In the figure no smoothing technique has been used, in order to clearly show the interfaces between the different zones within the cylinder.

within the volume of the first spray. The same spray dynamics related to multiple injections was observed for different engine operating conditions. This validates the hypothesis concerning the spray interactions, section 2.4.2.3.

According to the aim of this chapter (to evidence the limitations of the dual-CM), it is worthwhile to continue the investigation of the combustion dynamics by comparing the dual-CM results with the ones given by the IFP-C3D code. But, in order to do that, it is essential to guarantee that the mixtures characteristics within the spray regions are the same for the two models. Consequently, an ad hoc law for the entrainment of ambient-air was implemented in dual-CM, for this particular engine operating point. This modification, permits us to further extend the investigation of dual-CM.

Figure 4.6 shows the results concerning the formation of the spray zones after the ad hoc modification of the dual-CM ambient-air entrainment law. As seen in figure 4.6, after the change of this law, the volumes and the total spray masses in the sprays computed by dual-CM and IFP-C3D agree.

Figure 4.7 shows the comparison of the mean values and the variances of the fuel mixture fraction distributions computed by the two solvers. In the IFP-C3D code, the mean value and variance of the fuel mixture fraction distribution associated with the i^{th} injection where computed respectively as :

$$\widetilde{Z}_i^{IFP-C3D} = \frac{\sum_{k=1}^{NSC_i} \sum_{m=1}^{NI} Y_{F_{\tau m_k}} \cdot \rho_k \cdot V_k}{\sum_{k=1}^{NSC_i} \rho_k \cdot V_k} \tag{4.7}$$

and :

$$\widetilde{Z"^2}_i^{IFP-C3D} = \frac{\sum_{k=1}^{NSC_i} \left(\sum_{m=1}^{NI} Y_{F_{\tau m_k}} - \widetilde{Z}_i^{IFP-C3D} \right)^2 \cdot \rho_k \cdot V_k}{\sum_{k=1}^{NSC_i} \rho_k \cdot V_k} \tag{4.8}$$

Note that equation 4.8 does not represent the total fuel mixture fraction distribution variance associated with the spray. In fact for each cell, there is a further contribution to the spray mixture fraction variance associated with subgrid-scale mixture-fraction fluctuations. In fact, as shown in section 3.2, the ECFM3Z fuel mixture fraction PDF is represented by three Dirac functions : one corresponding to the pure air region, $Z = 0$, one corresponding to the mean fuel mixture fraction value of the mixing region, figure 3.5, and the last corresponding to the pure fuel region, $Z = 1$. Here, as a first approximation, the subgrid scale variance contributions were neglected.

As seen in figure 4.7, the computed mean fuel mixture fraction values are in good agreement between the two models. On the other hand, as was already observed in figure 3.20, the variances of the sprays are overestimated.

Certainly, part of the variance overestimation is due to the fact that in equation 4.8 the variance contributions associated with the subgrid scale mixture fraction fluctuations

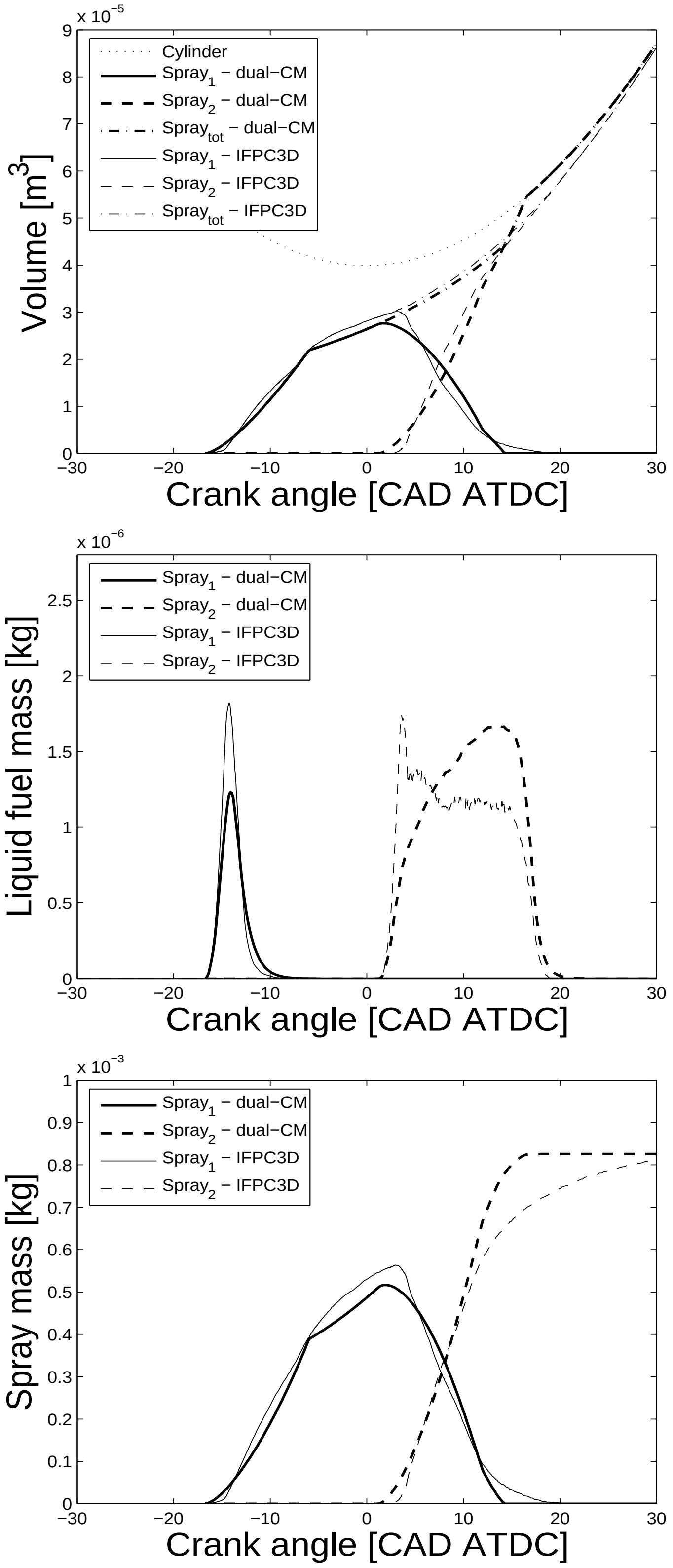

Figure 4.6: Comparison between dual-CM and IFP-C3D results concerning the formation of the spray zones after the ad hoc modification of the dual-CM ambient-air entrainment law. The curves refer to the engine operating point n° 1 of table 4.1. The evolutions of the spray volumes (top), liquid masses (middle) and total spray masses (bottom) are shown.

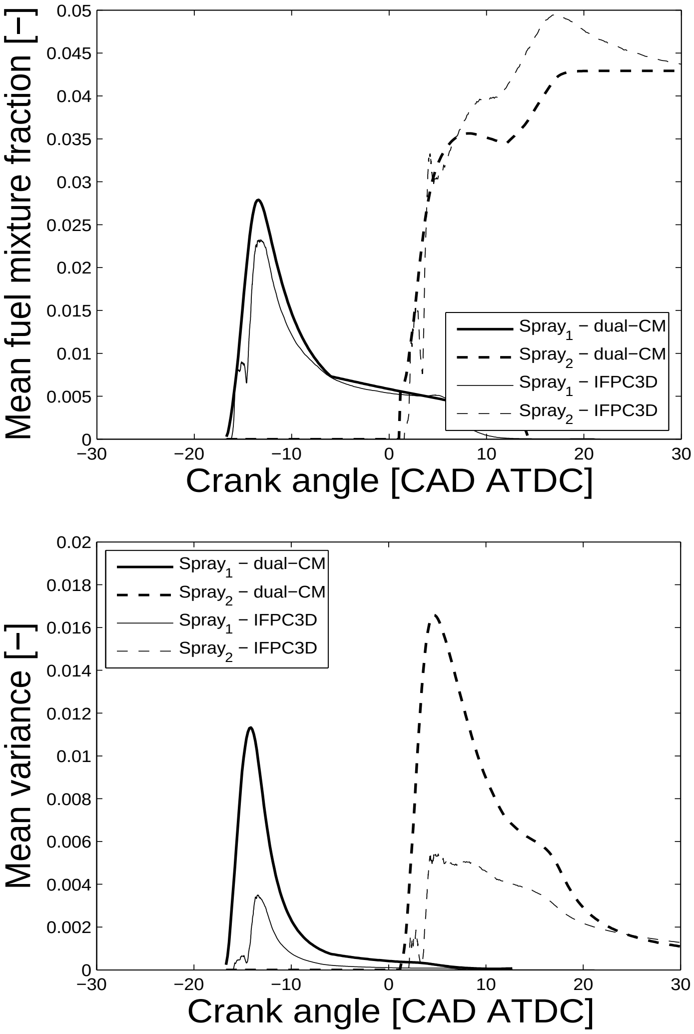

Figure 4.7: Comparison between dual-CM and IFP-C3D results concerning the formation of the spray zones after the ad hoc modification of the dual-CM ambient-air entrainment law. The curves refer to the engine operating point n° 1 of table 4.1. The evolutions of the fuel mixture fractions (top) and the variances (bottom) are shown.

were neglected. However, at this stage, it is not possible to quantify the global contribution to the spray mixture fraction variance associated with the subgrid scale mixture fraction fluctuations.

Nevertheless, there is good agreement between the overall shapes of the curves, this aspect will be discussed more in details in section 4.2.

To conclude, figure 4.8 shows the comparison of the dual-CM, IFP-C3D and experimental in-cylinder pressure curves, after the modification of the ambient-air entrainment law in the dual-CM code. The comparison of the figures 4.2 and 4.8 shows that the strong difference between the dual-CM and experimental in-cylinder pressure curve, figure 4.2, was essentially due to the error in the description of the ambient-air entrainment within the spray region.

As a conclusion of this section, a perspective of development of the dual-CM concerns the improving of the ambient-air entrainment law, in order to be able to account for bowl geometries which strongly impact the ambient-air entrainment within the spray region. For instance, once the system geometry is known, the instant of time at which the spray impacts against the bowl wall (determining the discontinuity in the ambient-air entrainment law) can be estimated with reasonable accuracy.

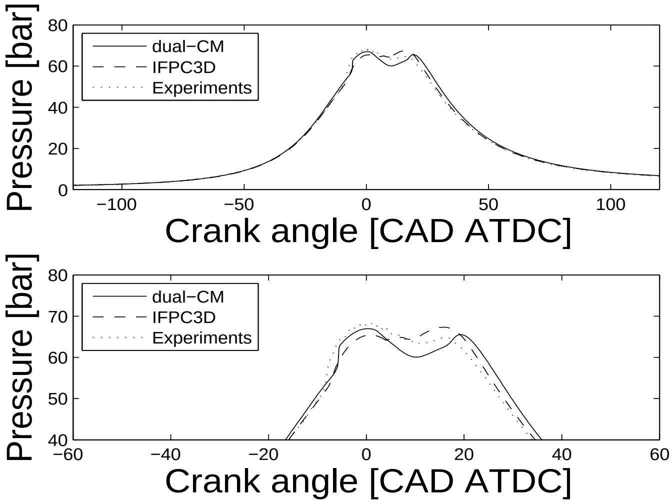

Figure 4.8: Comparison between the IFP-C3D and the modified dual-CM in-cylinder pressure curves with experimental data, relatively to the engine operating point n° 1, table 4.1 : a view of the entire high pressure engine cycle (top), and a zoom of the pressure peaks (bottom).

4.2 The progress variable variance modeling

In section 4.1, it was shown that the strong difference between the dual-CM in-cylinder pressure curve, and the IFP-C3D and experimental curves, figure 4.2, was essentially due to an error in the estimation of the entrained ambient-air mass within the spray region. In fact, the difference was highly reduced once changed the ambient-air entrainment law in the dual-CM code with another one ad hoc for the studied engine operating point, figure 4.8. Nevertheless, a small difference between the dual-CM in cylinder pressure curve and the two others continue to exist : in dual-CM, the combustion process of the second injection seems to be *delayed* with respect to the two others. In this section, the possible reasons of this phenomenon will be investigated.

Figure 4.9 shows the comparison of the IFP-C3D and dual-CM combustion progress variables associated with the second spray mixture, as a function of the fuel mixture fraction, at four crank angle values (given in the figure). As seen, the computed IFP-C3D progress variable varies with fuel mixture fraction, while the dual-CM progress variable is independent of the local value of fuel mixture fraction (hypothesis associated with the first order PCM combustion model, section 2.5).

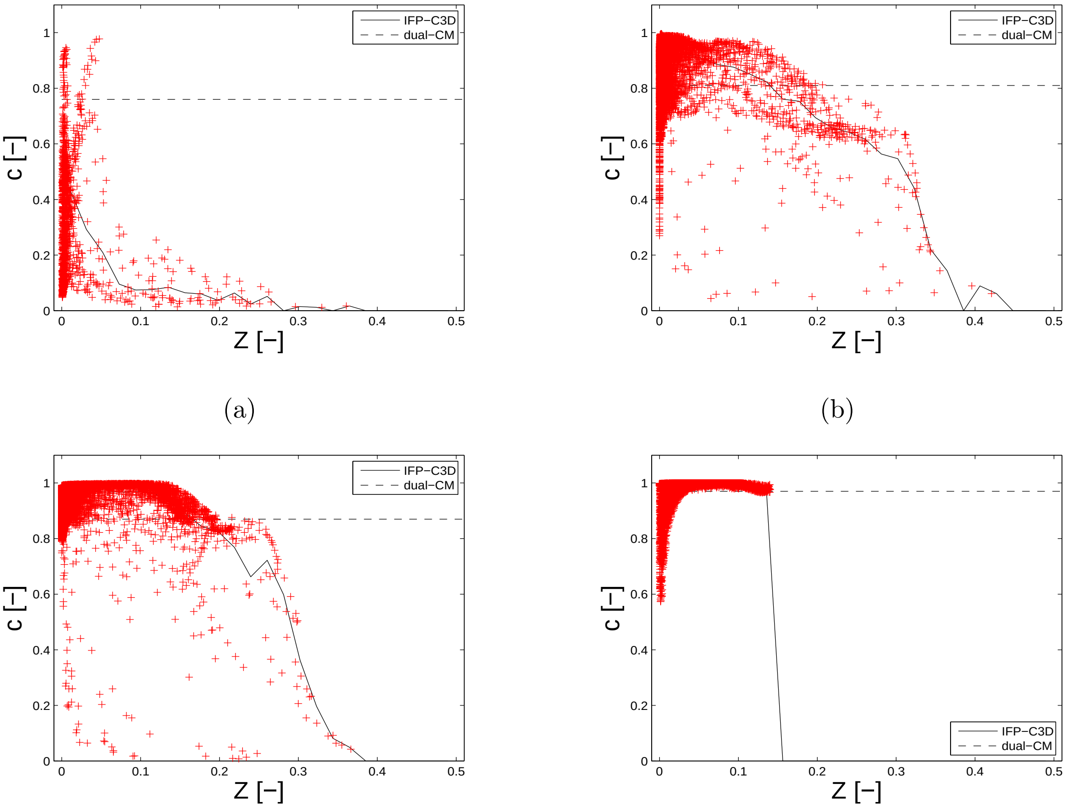

(a) (b)

(c) (d)

Figure 4.9: Comparison of the combustion progresses computed by the dual-CM and IFP-C3D, as a function of the local fuel mixture fraction, Z, for the cells belonging to the second injection spray. Symbols represents the combustion progress values computed by IFP-C3D for each cell, the solid and the dashed lines represents the IFP-C3D and dual-CM mean progress variable as a function of the fuel mixture fraction. Results are shown for four different crank angle values : 4 (a), 9 (b), 14 (c) and 24 (d) CAD ATDC.

Moreover, by discretizing the fuel mixture fraction space in a given number of points (here fifty), it is possible to define classes in the Z-space and sort the computational cells per classes, according with their mean fuel mixture fraction values. In this way it is possible to show that, even for a given class in the Z-space a fluctuation of the progress variable is observed, figure 4.10. As seen in figure 4.10, the progress variable Probability Density Function varies with the mean fuel mixture fraction value representing the class. In particular, the probability to have high values of progress variables is much higher for mixture fractions corresponding to poor mixtures $Z \approx 0.03$, rather than for mixture fractions corresponding to rich mixtures $Z \approx 0.3$. This results is in agreement with observations done when dealing with diffusion flames (high mixture stratifications) showing the existence of most reactive mixture fractions (located at low values of Z) at which the combustion processes are faster. As shown in figure 4.10, this aspect is not taken into account in the dual-CM : its PDFs correspond to Dirac functions located at

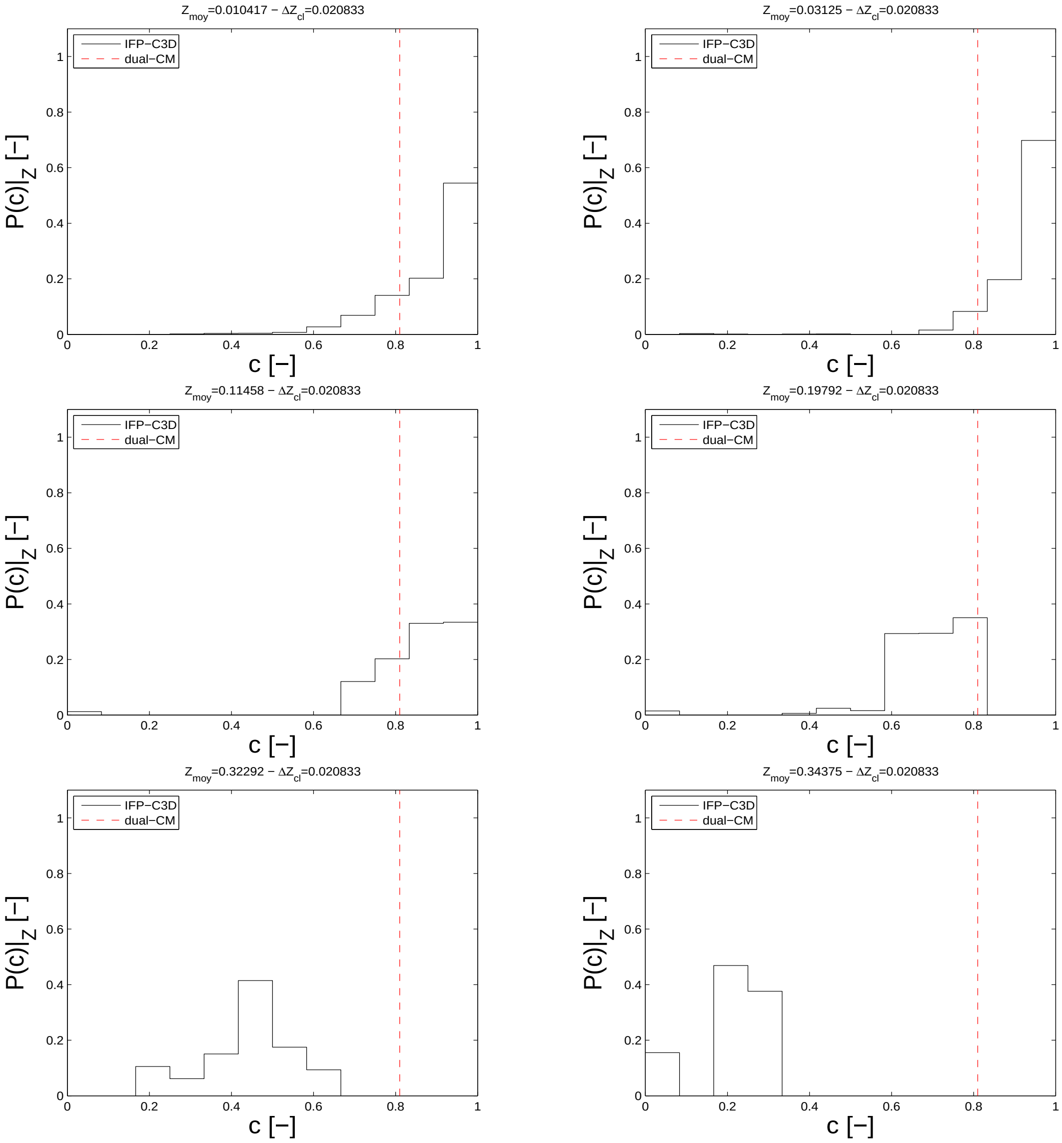

Figure 4.10: Comparison of the progress variable PDFs conditioned to Z computed by IFP-C3D (solid line) and dual-CM (dashed line), for different values fuel mixture fractions (given on the figure), and a crank angle value equal to 9 CAD ATDC, figure 4.9 (b).

the mean combustion progress variable value associated with the spray. It is worthwhile to note that the hypothesis of a mean progress variable independent of the fuel mixture fraction (first order PCM approach) is particularly inaccurate at the beginning of combustion, figure 4.9 (a-b), but becomes less restrictive towards the end of combustion, figure 4.9 (c-d).

Consequently, the impact of the first order PCM approach on the combustion dynamics could be a possible reason for the difference between the IFP-C3D and dual-CM combustions.

To conclude this section, it is worthwhile to spend some more words about the impact that an error in the estimation of the fuel mixture fraction variance can have on the combustion process. In fact, the fuel mixture fraction variance is the only variable associated with the overall spray description which was not completely validated by the comparison between the dual-CM and IFP-C3D curves, as in computing the IFP-C3D mixture fraction distribution variance, the subgrid scale variance contribution was neglected, equation 4.8.

As was seen in section 4.1, the dual-CM probably overestimates the fuel mixture fraction variance, figure 4.7. According to the parametric study of the dual-CM, section 2.7, an overestimation of the mixture fraction distribution variance leads to a decrease of the gaseous mixture reactivity, figure 2.71. Hence, in order to test the impact on the combustion dynamics of a reduction of the dual-CM mixture fraction variance, the parameter representing the maximum saturated fuel mixture fraction value within the distribution, $Z_{s_{max}}$, which was arbitrarily fixed at the value $Z_{s_{max}} = 0.8$, is here changed to $Z_{s_{max}} = 0.5$. In fact, the value of $Z_{s_{max}}$ is directly related to the source term of the fuel mixture fraction distribution variance, equation 2.120 : the lower the $Z_{s_{max}}$ is, the lower the variance production rate is.

Accordingly, the same engine operating point (n° 1 of table 4.1) was computed by fixing in the dual-CM $Z_{s_{max}} = 0.5$.

Figures 4.11 and 4.12 show the results concerning the in-cylinder pressure curves and the spray variances of the computation done by assuming $Z_{s_{max}} = 0.5$, in the dual-CM code.

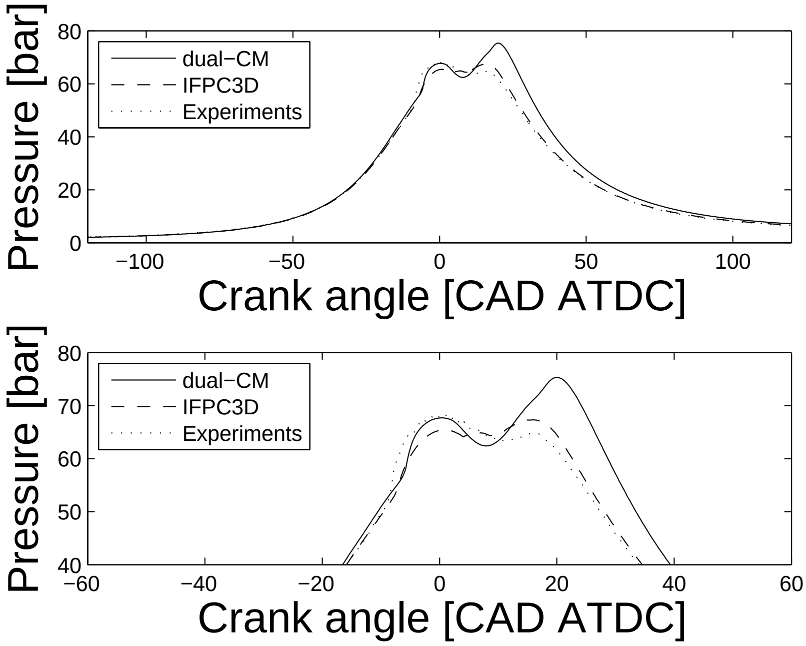

Figure 4.11: Comparison between the IFP-C3D and the dual-CM in-cylinder pressure curves with experimental data, relatively to the engine operating point n° 1, table 4.1 : a view of the entire high pressure engine cycle (top), and a zoom of the pressure peaks (bottom). The dual-CM results refers to a computation done by assuming $Z_{s_{max}} = 0.5$.

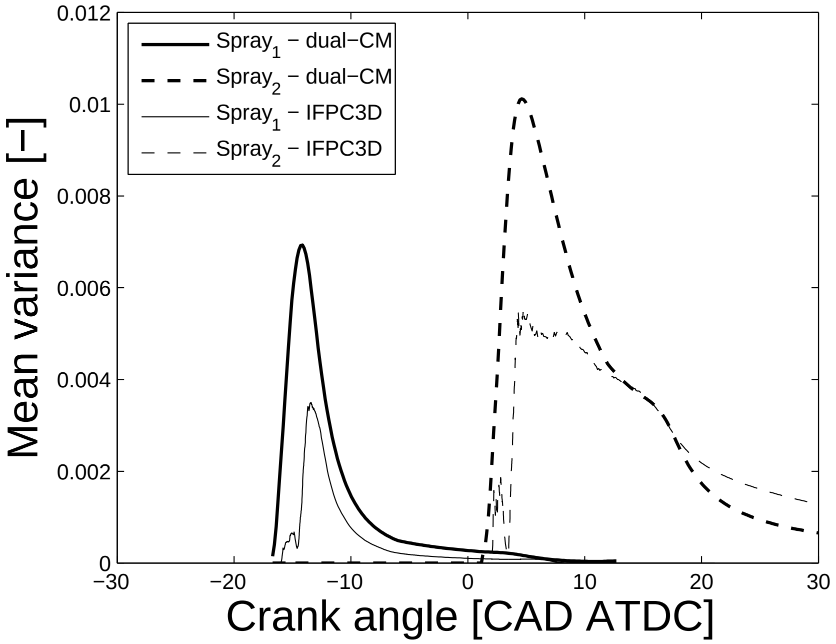

Figure 4.12: Comparison between dual-CM and IFP results concerning the formation of the spray zones. The curves refer to the engine operating point n° 1 of table 4.1. The evolutions of the variances are shown. The dual-CM results refers to a computation done by assuming $Z_{s_{max}} = 0.5$.

As seen in figure 4.12, the variance computed by the dual-CM solver is much smaller than before, figure 4.7. On the other hand, as shown in figure 4.11, the combustion process computed by dual-CM is now too fast and, as a consequence, the peak of pressure is too high.

To summarize, there are two factors that have a major impact on the gaseous mixture combustion process dynamics, which apparently compensate with one another :

- the first order PCM approach hypothesis, which tends to over-predict the in-cylinder gaseous mixture reactivity once the combustion process has begun,
- the overestimation of the fuel mixture fraction distribution variance, which tends to delay the gaseous mixture combustion process.

This aspect of compensation is evident by comparing figures 4.8 and 4.7 (bottom) with figures 4.11 and 4.12.

To conclude, the fact of using a combustion modeling approach based on the first order PCM theory is a strong constraint for the dual-CM model. In fact, in order to limit the high reactivity associated with the fact of considering a homogeneous progress variable in the fuel mixture fraction space, a modification of other modeling parameters (for instance $Z_{s_{max}}$) is required in order to optimize the dual-CM computation results.

Hence, the fact of taking into account different progress variables within the spray region depending on the local fuel mixture fraction values is a key point for the improvement of the dual-CM.

Chapter 5

Conclusions and perspectives

A combustion model for global engine system simulation applications has been developed : the dual-CM.

The dual-CM has been developed for the simulation of the combustion processes taking place within the cylinders of the more recent engine architectures, integrating technologies such as turbo-chargers, EGR loops and high pressure direct injection systems, which allow engines running under different combustion regimes, such as conventional Diesel and Diesel HCCI regimes.

5.1 General conclusions

The dual-CM consists of two main parts : the spray model and the combustion model. The spray model is a multi-zone model which allows us to define control volumes, one for each fuel injection, in which the combustion takes place, and characterize the fuel mixture fraction stratification of each spray by using a PDF approach. The evolution of every single spray is based on the approach proposed by Naber and Siebers [55]. On the other hand, the combustion model is based on a complex chemistry tabulation method inspired by the FPI approach [87, 85, 103, 88], which has been coupled with fuel-mixture fraction PDFs. The chemical kinetics mechanism used for generating the dual-CM FPI table is the one proposed by Anderlohr et al. [86] for n-heptane.

An original spray model able to manage multiple-injection strategies

The major advantages and novelties as well as the drawbacks and limits of the spray model are presented in the following.

Advantages and novelties

- The evolutions of the spray zones are based on geometrical considerations, which are simple to set up and to compute. Nevertheless, the distinction between the spray regions allows us to have a first macroscopic description of the fuel distribution within the cylinder,

- the physical model used for computing the thermochemical properties of the evaporating fuel gives a deep insight on the liquid-gas interface characteristics. This information is necessary to correctly describe the local properties of the mixture in terms of equivalence ratio and temperature, which are fundamental for a correct computation of the combustion kinetics,

- the phenomenological approach used for computing the overall liquid fuel evaporation rate gives sufficiently accurate results using few CPU resources, when compared to more complex evaporation models using a liquid fuel mass discretization,
- the model of liquid fuel penetration gives information about the possibilities of the liquid fuel of impinging the combustion chamber walls. The wall impingement must be avoided, because it would bring a strong increase of engine soot and HC emissions,
- for each spray region, an accurate description of the fuel mixture fraction distribution and of its evolution is given by using presumed PDFs. This kind of detail in the description of the fuel mixture fraction distribution is fundamental to capture the right combustion kinetics,
- thanks to the high level of physical phenomena description, the interpretation of the results is straightforward and the computed results can easily be compared and validated with experimental data and 3D CFD results.

Drawbacks and limits

- The geometrical approach used for the description of the spray region evolutions becomes less accurate when the geometry of the combustion chamber strongly influences the spray dynamics,
- the temperature stratification within the gaseous mixture due to the thermal losses through the cylinder walls and, consequently, its impact on the combustion kinetics have been neglected. This kind of thermal stratification has been shown to have an impact on the mixture auto-ignition delay in pure HCCI combustions,
- the blow-by phenomenon was neglected,
- the evaporation model is not adapted for the computation of cold-start engine operating points, for which the mass and thermal fluxes through the fuel liquid-gas interface are the factors limiting evaporation. In fact, while for warm-engine conditions the hypothesis made in [53] of considering a steady-state fuel evaporation regime is valid (the fuel droplets have small diameters, the combustion chamber walls and the in-cylinder gases are hot), for cold-engine conditions this hypothesis is no more valid. This is due to the fact that in cold-start engine operating points,

large masses of fuel are injected at low pressure and temperature, in an ambient gas which is, in turn, at low temperatures and pressure. Consequently, droplets having relatively large diameters heat-up and vaporize at the same time.

A combustion model for all Diesel combustion regimes

The major advantages and novelties as well as the drawbacks and limits of the combustion model are presented in the following.

Advantages and novelties

- Using an approach based on complex chemistry for computing chemical kinetics permits us to reproduce the specificities of the different Diesel combustion regimes. Accordingly, the set up tabulation method has been shown to be able to :
  - capture the influence of the local thermochemical properties of the mixture (equivalence ratio, pressure and temperature) on the mixture auto-ignition delay and combustion,
  - represent the highly non-linear combustion Heat Releases associated with variations of the dilution rate,
- tabulating the complex chemistry mechanism, and consequently not using it directly for chemical kinetics computations, permits us to highly increase the dual-CM computational speed with only a minor loss in results accuracy,
- species of interest, such as CO, CO_2 and H_2O, can be tabulated and their evolution be followed along with the combustion process.

Drawbacks and limits

- The dual-CM table concerns the combustion of pure n-heptane. Even if the n-heptane has auto-ignition delays similar to those of a commercial Diesel, the latter is far from being a pure hydrocarbon; it is a blend of many different ones, among which aromatic species. In the future, more refined surrogate Diesel fuels should be considered. For instance, α-methylnaphthalene/decane mixtures could be considered,
- the dual-CM table was generated by post-processing computation results, obtained by using the complex chemistry solver CHEMKIN, relative to homogeneous, adiabatic constant volume reactors. In ICE applications, the constant volume hypothesis is acceptable for computing the chemical kinetics around TDC, but is not valid during the expansion stroke. As a consequence differences in the final composition

of the exhaust gaseous mixture can be observed when comparing computed results with experiments. In the future, variable volume tables will need to be considered as initiated at IFP in 3D combustion modeling studies,

- the computation of the chemical kinetics in the dual-CM strictly depends on the mixture properties, and it does not have any adjustment parameters. This is a strong constraint for a 0D model because the uncertainties linked to such a level of modeling need to be considered by adjustment parameters.

Results

The dual-CM transports $(13 + 23 \cdot NI)$ variables, where NI is the number of injections for a given engine cycle. The model computes the evolutions of a reduced number of chemical species, which were considered as the most important species according to mass and energetic criteria : C_7H_{16}, C_7H_{14}, H_2O, CO_2, CO, O_2, H, H_2 and N_2. The dual-CM belongs to the class of the multi-zone models : NI zones corresponding to the spray volumes associated with the different fuel injections, plus a zone corresponding to the gases which do not belong to any spray.

The dual-CM combustion model was tested on academic configurations showing the potential of the modeling approach in capturing the mixture auto-ignition delays, and describing the major species evolutions along the combustion process. Moreover, the use of the model for engine applications confirmed the potential of this kind of approach.

In particular, it has been shown that for the tested engine (Renault G9T NADI™ concept engine [93]), the dual-CM gives good results on the entire engine operating domain, which includes engine operating points adopting both single and multiple-injection strategies. Investigations on the accuracy of the dual-CM results were done by comparing them with experimental data, and with results obtained by using the 3D CFD solver IFP-C3D.

Concerning the computational time, it has been shown that, for a given engine operating point, it can vary from 10^2 to 10^3 times the real time, depending on which choices were done when choosing the numerical method used for solving the system (fixed or variable time step), and the value of the maximum time step.

5.2 Perspectives

At this stage of development, the dual-CM has been shown to give satisfactory results on the entire engine operating domain in what concerns the prediction of the mixing, Heat Release and major species evolutions. However, during this study several possible axes of progress have been detected. These axes are now presented.

Spray model

- As shown, the spray model fails when the bowl geometry strongly interferes with the growth of the spray region. In fact, in this case, the hypothesis of considering the spray as a free gaseous jet is no more valid. A first step for improving the spray model could be to give the dual-CM more information concerning the injector and bowl geometries. In such a way it is possible to compute the instant at which the spray impacts the combustion chamber walls, and, accordingly, to change the spray volume growth law with a more adapt one,

- in order to compute the liquid fuel evaporation rate for engine cold-start conditions, an evaporation model based on the D^2 *law* approach accounting for liquid fuel heating transitory should be used. In order to do that, additional models for liquid fuel atomization, and droplet size and velocity distributions must be introduced in the dual-CM as well.

Combustion model

- In the dual-CM, the hypothesis was that for each spray, a unique progress variable, equal to the value of the mean progress within the spray, is sufficient to describe the dynamics of the combustion process (first order PCM approach). In this study, it was shown that this hypothesis has a non-negligible impact on the combustion dynamics, when dealing with highly stratified mixture regions. A possible solution to take into account the existence of a progress variable distribution in the fuel mixture fraction space consists in discretizing the fuel mixture fraction PDF in a given number of classes, and computing for each class the corresponding progress variable, corresponding to a Conditional Moment Closure (CMC) approach [104]. The drawback of this kind of approach is the enormous number of variables needed : a complete set of mass variables for each fuel mixture fraction class. Another solution could be to directly include in the table the progress variable stratification as done in the Approximated Diffusion Flame - PCM ($ADF - PCM$) [105],

- in order to have an estimate of the $\mathrm{NO_x}$ and soot emissions, approaches based on simple phenomenological laws giving production/destruction characteristic times as a function of the in-cylinder thermochemical state of the mixture computed by the dual-CM can be easily introduced,

- the present dual-CM FPI table should be replaced by a new one generated by using the new tabulation approach developed at IFP taking into account the effects of the combustion chamber expansion on the chemical kinetic. This would permit us to have a better estimate of the mixture final composition.

Computational time

The main limiting factor of the dual-CM computational speed is associated with the use of the FPI table :

- the size of the table will grow if more refined discretizations of the table axes are chosen, or if additional table inputs are necessary (as it is the case for the new tabulation method accounting for the combustion chamber expansion effects on chemical kinetics),
- the AMESim numerical scheme adopting a variable time step is not optimized to manage FPI tables storing species mass fractions. In fact, as the FPI trajectories are supposed to be piecewise linear, their first derivatives are discontinuous. These discontinuities greatly slow down the solver computational speed.

A possible solution could consist in generating the FPI table and then learning it by using an adapted neural network. In such a way, a multi-dimensional polynomial surface containing all the information stored in the table is generated. The polynomial surface, compared to the FPI table, has the advantages of having a very small size and continuous derivatives.

Appendix A

The environment of simulation

The software LMS Imagine.Lab AMESim is a development platform for global system simulations. AMESim uses libraries of models which are associated with the different engineering domains : hydraulics, mechanics, signals, pneumatics, electromagnetism, etc. Among them, the IFP-Engine library is dedicated to Internal Combustion Engine global system modeling.

The IFP-Engine library allows to build very quickly an engine simulator taking into account thermal, mechanical, hydraulic and thermodynamic aspects. Figure A.1 shows the basic elements that belong to the IFP-Engine library.

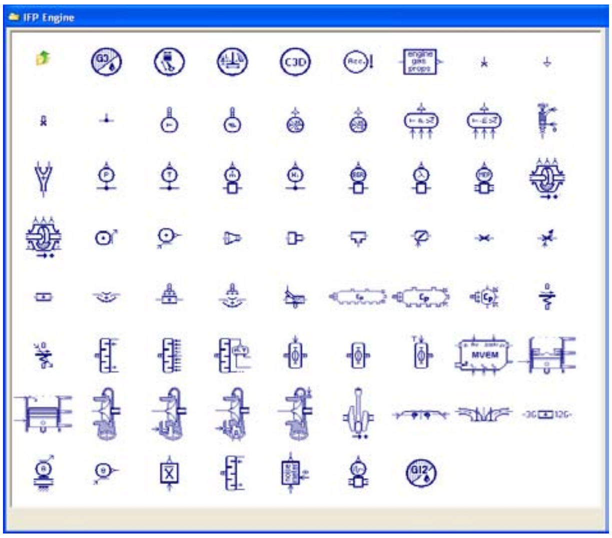

Figure A.1: IFP-Engine library.

Figure A.2 shows a four cylinder turbocharged Direct Injection Diesel engine simulator built using AMESim.

Figure A.3 gives an overview of the results computed by using the engine simulator shown in figure A.2.

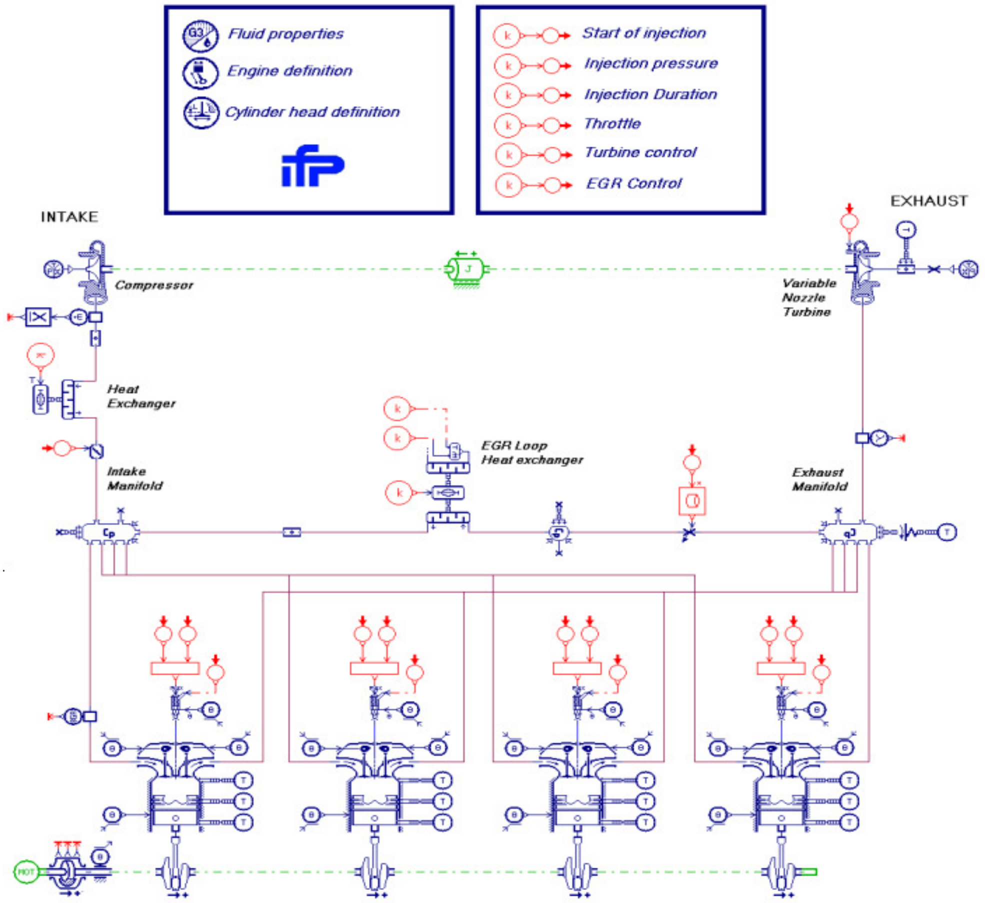

Figure A.2: Four cylinder turbocharged Direct Injection Diesel engine simulator built using AMESim.

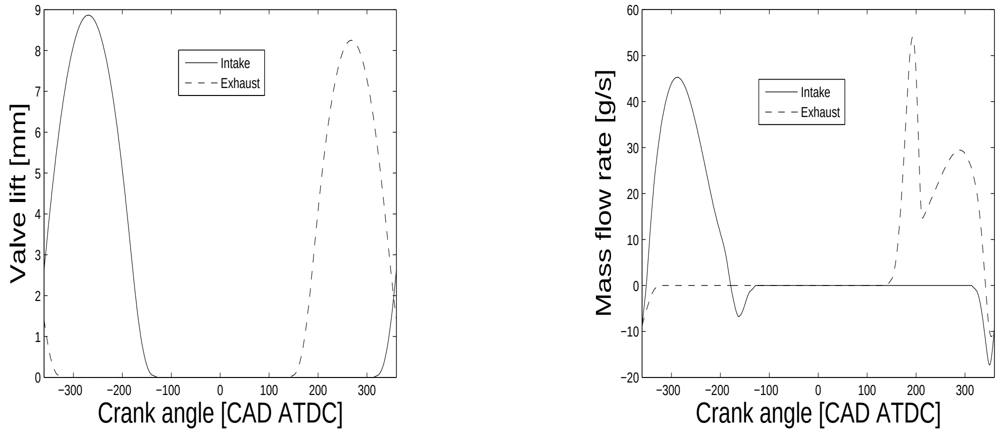

Intake and exhaust valve lift evolutions (Mechanical).

Mass flow rates through the intake and exhaust valves (Fluid-dynamics).

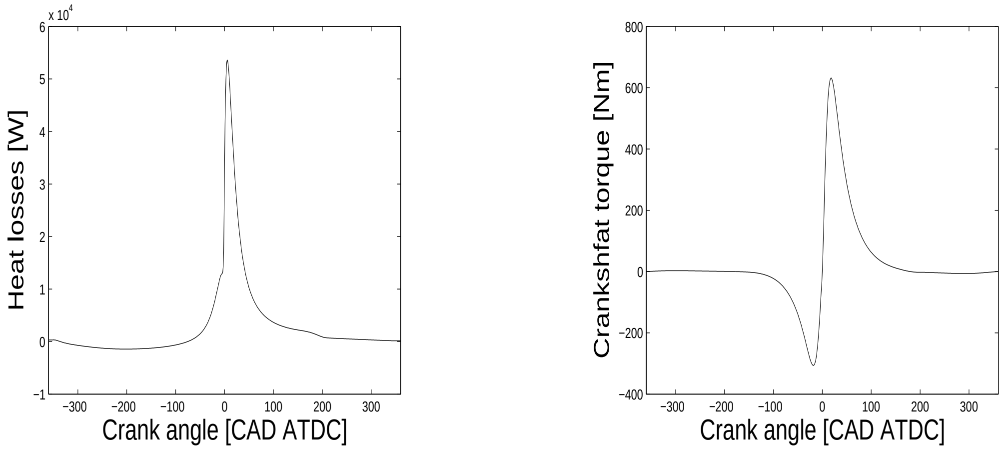

Thermal losses through the combustion chamber walls (Thermal).

Crankshaft torque due to a single cylinder (Mechanical).

Figure A.3: Results computed by using the engine simulator shown in figure A.2.

Appendix B

ECFM3Z equations

In this appendix, the main equations constituting the ECFM3Z sub-grid scale model are briefly presented [34].

Species balance equations

Equations for the unburned and burned gases distribution :

$$\frac{\partial \bar{\rho}\cdot\widetilde{Y}_F^u}{\partial t}+\frac{\partial \bar{\rho}\cdot\widetilde{u}_i\cdot\widetilde{Y}_F^u}{\partial x_i}=\frac{\partial}{\partial x_i}\left[\left(\frac{\mu}{Sc}+\frac{\mu_t}{Sc_t}\right)\cdot\frac{\partial\widetilde{Y}_F^u}{\partial x_i}\right]+\bar{\rho}\cdot\widetilde{\dot{S}}_F^u+\bar{\dot{\omega}}_F^u-\bar{\dot{\omega}}_F^{u\to b} \tag{B.1}$$

$$\frac{\partial \bar{\rho}\cdot\widetilde{Y}_F^b}{\partial t}+\frac{\partial \bar{\rho}\cdot\widetilde{u}_i\cdot\widetilde{Y}_F^b}{\partial x_i}=\frac{\partial}{\partial x_i}\left[\left(\frac{\mu}{Sc}+\frac{\mu_t}{Sc_t}\right)\cdot\frac{\partial\widetilde{Y}_F^b}{\partial x_i}\right]+\bar{\rho}\cdot\widetilde{\dot{S}}_F^b+\bar{\dot{\omega}}_F^b+\bar{\dot{\omega}}_F^{u\to b} \tag{B.2}$$

Equations for the mixing process :

$$\frac{\partial \bar{\rho}\cdot\widetilde{Y}_F^F}{\partial t}+\frac{\partial \bar{\rho}\cdot\widetilde{u}_i\cdot\widetilde{Y}_F^F}{\partial x_i}=\frac{\partial}{\partial x_i}\left[\left(\frac{\mu}{Sc}+\frac{\mu_t}{Sc_t}\right)\cdot\frac{\partial\widetilde{Y}_F^F}{\partial x_i}\right]+\bar{\rho}\cdot\widetilde{\dot{S}}_F+\bar{\rho}\cdot\widetilde{\dot{E}}_F^{F\to M} \tag{B.3}$$

$$\frac{\partial \bar{\rho}\cdot\widetilde{Y}_{O_2}^A}{\partial t}+\frac{\partial \bar{\rho}\cdot\widetilde{u}_i\cdot\widetilde{Y}_{O_2}^A}{\partial x_i}=\frac{\partial}{\partial x_i}\left[\left(\frac{\mu}{Sc}+\frac{\mu_t}{Sc_t}\right)\cdot\frac{\partial\widetilde{Y}_{O_2}^A}{\partial x_i}\right]+\bar{\rho}\cdot\widetilde{\dot{E}}_{O_2}^{A\to M} \tag{B.4}$$

Momentum balance equations

$$\begin{aligned}\frac{\partial \bar{\rho}\cdot\widetilde{u}_i}{\partial t}+\frac{\partial \bar{\rho}\cdot\widetilde{u}_i\cdot\widetilde{u}_j}{\partial x_i} &= \frac{\partial}{\partial x_i}\left[-\widetilde{p}\cdot\delta_{ij}+C_\mu\cdot\bar{\rho}\cdot\widetilde{\kappa}\cdot\frac{\widetilde{\kappa}}{\widetilde{\epsilon}}\cdot\left(\frac{\widetilde{u}_i}{x_j}+\frac{\widetilde{u}_j}{x_i}\right)\right]+\\ &\quad -\frac{2}{3}\cdot\frac{\partial}{\partial x_j}\left(C_\mu\cdot\bar{\rho}\cdot\widetilde{\kappa}\cdot\frac{\widetilde{\kappa}}{\widetilde{\epsilon}}\cdot\frac{\partial u_k}{\partial x_k}+\bar{\rho}\cdot\widetilde{\kappa}\right)\cdot\delta_{ij}+\Pi\end{aligned} \tag{B.5}$$

where Π represents the diphasic coupling term.

Energy balance equation

Concerning the energy, for this kind of approach, it is necessary to transport two enthalpies :

- the total enthalpy [91],
- the sensible enthalpy of the fresh gases, which permits us to reconstruct the thermochemical state of the unburned gases [33].

Total enthalpy balance equation :

$$\frac{\partial \bar{\rho} \cdot \widetilde{h}}{\partial t} + \frac{\partial \bar{\rho} \cdot \widetilde{u}_i \cdot \widetilde{h}}{\partial x_i} = -\frac{\partial}{\partial x_i} \left[\bar{\rho} \cdot \left(\widetilde{u_i h} - \widetilde{u}_i \widetilde{h} \right) \right] + \frac{\partial \widetilde{p}}{\partial t} + \frac{\partial}{\partial x_i} \left(\bar{J}_i^h + \overline{u_j \tau_{ij}} \right) + \overline{u_i F_i} \tag{B.6}$$

Unburned mixture sensible enthalpy balance equation :

$$\frac{\partial \bar{\rho} \cdot \widetilde{h}_s^u}{\partial t} + \frac{\partial \bar{\rho} \cdot \widetilde{u}_i \cdot \widetilde{h}_s^u}{\partial x_i} = \frac{\partial}{\partial x_i} \left[\left(\frac{\mu}{Sc} + \frac{\mu_t}{Sc_t} \right) \cdot \frac{\partial \widetilde{h}_s^u}{\partial x_i} \right] + Dissip + \bar{W} + \frac{\bar{\rho}}{\bar{\rho}^u} \cdot \frac{\partial \widetilde{p}}{\partial t} + \bar{\rho} \cdot \widetilde{\dot{S}}_{h_s}^u \tag{B.7}$$

Mixing modeling

The creation and growth of the mixing zone is described by the terms $\widetilde{\dot{E}}_F^{F \to M}$ and $\widetilde{\dot{E}}_{O_2}^{A \to M}$:

$$\widetilde{\dot{E}}_F^{F \to M} = -\frac{1}{\tau_m} \cdot \widetilde{Y}_F^F \cdot \left(1 - \widetilde{Y}_F^F \cdot \frac{\bar{\rho} \cdot \mathcal{M}^M}{\bar{\rho}^u|_u \cdot \mathcal{M}_F} \right) \tag{B.8}$$

$$\widetilde{\dot{E}}_{O_2}^{A \to M} = -\frac{1}{\tau_m} \cdot \widetilde{Y}_{O_2}^A \cdot \left(1 - \frac{\widetilde{Y}_{O_2}^A}{\widetilde{Y}_{O_2}^\infty} \cdot \frac{\bar{\rho} \cdot \mathcal{M}^M}{\bar{\rho}^u|_u \cdot \mathcal{M}_{pa+EGR}} \right) \tag{B.9}$$

where the mixing characteristing time, τ_m, and $\widetilde{Y}_{O_2}^\infty$ are computed as :

$$\tau_m^{-1} = \beta_m \cdot \frac{\epsilon}{\kappa} \tag{B.10}$$

$$\widetilde{Y}_{O_2}^\infty = \frac{\widetilde{Y}_{O_{2\tau}}}{1 - \widetilde{Y}_{F_\tau}} \tag{B.11}$$

in which β_m is equal to unity. A standard $\kappa - \epsilon$ model must be used for closing the equation system.

Auto-ignition modeling

The mean combustion progress variable, $\widetilde{c}$, is defined as the ratio of mass fractions :

$$\widetilde{c} = 1 - \frac{\widetilde{Y}_F^u}{\widetilde{Y}_{F_\tau}} \tag{B.12}$$

The term $\widetilde{Y}_{F_\tau}$ is computed as :

$$\frac{\partial \bar{\rho} \cdot \widetilde{Y}_{F_\tau}}{\partial t} + \frac{\partial \bar{\rho} \cdot \widetilde{u}_i \cdot \widetilde{Y}_{F_\tau}}{\partial x_i} = \frac{\partial}{\partial x_i} \left[\left(\frac{\mu}{Sc} + \frac{\mu_t}{Sc_t} \right) \cdot \frac{\partial \widetilde{Y}_{F_\tau}}{\partial x_i} \right] + \bar{\rho} \cdot \widetilde{\dot{S}}_F \tag{B.13}$$

In equation B.1, the term $\bar{\dot{\omega}}_F^u$, associated with the auto ignition reaction rate, has been modeled by using the tabulation approach proposed in [33, 45]. According to this approach, the auto-ignition delay, the heat released during auto-ignition and the progress variable reaction rate, $d\widetilde{c}/dt$, are stored in a look-up table as a function of the thermo-chemical properties of the mixture. Then the source term is computed as :

$$\bar{\dot{\omega}}_F^u = \bar{\rho} \cdot \widetilde{Y}_{F_\tau} \cdot \frac{d\widetilde{c}}{dt} \tag{B.14}$$

Diffusion flame modeling

This source term, associated to the diffusion flame reaction rate taking place into the mixing zone of the burned gases, M^b, is computed by using a six steps CO reduced kinetics approach [94].

Appendix C

The D^2 *law*

In this appendix, the evaporation model based on the D^2 *law* approach, applying to steady-state evaporation conditions, is derived and investigated.

According to Kuo [58], for the vaporizing droplet, the total fuel mass flow rate leaving the droplet surface must be equal to the sum of the fuel mass flow rates due to the convective motion of the gaseous mixture at the surface and the mass diffusion rate of the fuel vapor in the radial direction. Diffusion is computed assuming that the only driving force for species diffusion is a concentration gradient in the direction of the diffusion path (Fick's law). Consequently, the fuel balance equation at droplet surface can be written as :

$$\dot{\widehat{m}}_F = \rho_g \cdot u_r = \rho_g \cdot Y_{F_I} \cdot u_r + \rho_g \cdot Y_{F_I} \cdot v_r \tag{C.1}$$

where $\dot{\widehat{m}}_F$ is the specific fuel mass flow rate per unit of surface, ρ_g is the density of the mixture of gases, u_r is the radial component of the convective velocity, Y_{F_I} is the fuel mass fraction at the drop surface and v_r is the radial component of the diffusion velocity. For the species x, the Fick's law can be defined as :

$$J_x = -\mathcal{D}_x \cdot \nabla \mathcal{C}_x \tag{C.2}$$

where J is the diffusion flux, $\mathcal{D}$ is the diffusion coefficient and $\mathcal{C}$ is the molar concentration. Equation C.2 can be rewritten for the fuel in terms of mass fraction and so it is possible to explicite the diffusion velocity in the radial direction, r, at the drop surface as :

$$v_r = -\frac{\mathcal{D}_F}{Y_{F_I}} \cdot \left(\frac{\partial Y_F}{\partial r}\right)_I \tag{C.3}$$

Combining equations C.1 and C.3 the mass fuel evaporation rate results as :

$$\dot{\widehat{m}}_F = \rho_g \cdot u_r = \rho_g \cdot Y_{F_I} \cdot u_r - \rho_g \cdot \mathcal{D}_F \cdot \left(\frac{\partial Y_F}{\partial r}\right)_I \tag{C.4}$$

The state equation of perfect gases can be expressed as :

$$p = \rho_g \cdot R \cdot T \tag{C.5}$$

Combining and rearranging equations C.4 and C.5, the following expression is obtained [49] :

$$\left(\frac{dY_F}{dr}\right)_I = -\frac{R \cdot T}{\mathcal{D}_F \cdot p} \cdot \left(\dot{\widehat{m}}_F \cdot Y_a\right) \tag{C.6}$$

where Y_a is the surrounding air mass fraction, p is the gas pressure, R is the gas constant of the gaseous mixture, r is the radius ($r = 0$ at center of the drop, $r = r_I$ at drop surface) and T is the temperature.

From the continuity condition, the fuel mass rate of diffusion at the drop surface is given by :

$$\dot{\widehat{m}}_{F_I} \cdot 4 \cdot \pi \cdot r_I^2 = \dot{\widehat{m}}_F \cdot 4 \cdot \pi \cdot r^2 \qquad \text{for } r \geq r_I \tag{C.7}$$

$$\frac{dY_F}{dr} = -\frac{R \cdot T}{\mathcal{D}_F \cdot p} \cdot \dot{\widehat{m}}_{F_I} \cdot Y_a \cdot \left(\frac{r_I^2}{r^2}\right) \tag{C.8}$$

or, since $Y_a = 1 - Y_F$:

$$\frac{dY_F}{dr} = -\frac{R \cdot T}{\mathcal{D}_F \cdot p} \cdot \dot{\widehat{m}}_{F_I} \cdot (1 - Y_F) \cdot \left(\frac{r_I^2}{r^2}\right) \tag{C.9}$$

rearranging the formula, it gives :

$$\frac{dY_F}{1 - Y_F} = -\frac{R \cdot T}{\mathcal{D}_F \cdot p} \cdot \dot{\widehat{m}}_{F_I} \cdot r_I^2 \cdot \frac{dr}{r^2} \tag{C.10}$$

The boundary conditions are :

$$\begin{aligned} r &= r_I; & T &= T_I; & Y_F &= Y_{F_I} \\ r &= \infty; & T &= T_\infty; & Y_F &= Y_{F_\infty} = 0 \end{aligned}$$

Integrating equation C.10 between $r = 0$ and $r = \infty$ yields :

$$[\ln(1 - Y_F)]_{Y_{F_I}}^{0} = \left[\frac{R \cdot T}{\mathcal{D}_F \cdot p} \cdot \dot{\widehat{m}}_{F_I} \cdot r_I^2 \cdot \left(-\frac{1}{r}\right)\right]_{r_I}^{\infty} \tag{C.11}$$

it follows :

$$0 - \ln(1 - Y_{F_I}) = \frac{R \cdot T}{\mathcal{D}_F \cdot p} \cdot \dot{\widehat{m}}_{F_I} \cdot r_I \tag{C.12}$$

hence :

$$\dot{\widehat{m}}_{F_I} = -\frac{\mathcal{D}_F \cdot p}{R \cdot T} \cdot \frac{\ln(1 - Y_{F_I})}{r_I} = -\frac{\mathcal{D}_F \cdot \rho_g \cdot \ln(1 - Y_{F_I})}{r_I} \tag{C.13}$$

$$\dot{m}_{F_I} = \dot{m}_F = 4 \cdot \pi \cdot r_I^2 \cdot \dot{\widehat{m}}_{F_I} = -4 \cdot \pi \cdot r_I \cdot \mathcal{D}_F \cdot \rho_g \cdot \ln(1 - Y_{F_I}) \tag{C.14}$$

The state equation yields :

$$p = \rho_g \cdot R \cdot T \tag{C.15}$$

where ρ_g is the density of the gaseous mixture. If we now define the mass transfer number at liquid/gas interface as :

$$B_M = \frac{Y_{F_I}}{1 - Y_{F_I}} \tag{C.16}$$

then :

$$\ln(1 - Y_{F_I}) = -\ln(1 + B_M) \tag{C.17}$$

and, since $D_d = 2 \cdot r_I$, from equations C.14 and C.17 gives :

$$\dot{m}_F = 2 \cdot \pi \cdot D_d \cdot \mathcal{D}_F \cdot \rho_g \cdot \ln(1 + B_M) \tag{C.18}$$

This is the basic equation for the rate of evaporation of a fuel drop of diameter D_d. Introducing the Lewis number :

$$Le = \frac{\left(\frac{k}{c_p}\right)_g}{\rho_g \cdot \mathcal{D}_F} \tag{C.19}$$

where k_g is the mean thermal conductivity of the gas and c_{p_g} is the specific heat at constant pressure of the gas, equation C.18 can be rewritten as :

$$\dot{m}_F = 2 \cdot \pi \cdot \frac{D_d}{Le} \cdot \left(\frac{k}{c_p}\right)_g \cdot \ln(1 + B_M) \tag{C.20}$$

The accuracy of equation C.20 is very dependent on the choice of values for k_g and c_{p_g}. According to Hubbard [49], best results are obtained using the the one-third rule of Sparrow and Gregg [49], where average properties are evaluated at the following reference temperature and composition :

$$T_r = T_I + \frac{T_\infty - T_I}{3} \tag{C.21}$$

$$Y_{F_r} = Y_{F_I} + \frac{Y_{F_\infty} - Y_{F_I}}{3} \tag{C.22}$$

where subscript r identifies the Sparrow's reference conditions, subscript I is relative to interface surface conditions and subscript ∞ is relative to ambient conditions, figure 2.8. If the fuel concentration at an infinite distance from the drop is assumed to be zero, equation C.22 becomes :

$$Y_{F_r} = \frac{2}{3} \cdot Y_{F_I} \tag{C.23}$$

and consequently the air mass fraction is :

$$Y_{a_r} = 1 - Y_{F_r} = 1 - \frac{2}{3} \cdot Y_{F_I} \tag{C.24}$$

Equations C.21 to C.24 are used to calculate the reference values of the relevant physical properties of the vapor-air mixture that constitutes the environment of an evaporating drop. The specific heat at constant pressure and the mean thermal conductivity coefficient are therefore obtained as follows :

$$c_{p_g} = Y_{a_r} \cdot c_{p_a}\left(T_r\right) + Y_{F_r} \cdot c_{p_F}\left(T_r\right) \tag{C.25}$$

$$k_g = Y_{a_r} \cdot k_a\left(T_r\right) + Y_{F_r} \cdot k_F\left(T_r\right) \tag{C.26}$$

where c_{p_a} and c_{p_F} are the heat capacities at constant pressure respectively of the air and of the gaseous fuel and k_a and k_F are the thermal conductivity respectively of the air and of the gaseous fuel. The air gas representative of the environment gas is supposed to be constituted by 21% of oxygen and 79% of nitrogen in molar fractions. The enthalpies of the different gases are tabulated as function of the temperature [73] and are directly inserted in the source code of the different models. The specific heat capacities at constant pressure are evaluated considering the following relation :

$$c_{p_x} = \left(\frac{dh_x}{dT}\right)_{p=const} \tag{C.27}$$

where h is the enthalpy and the subscript x identifies the generic species.

Values of thermal conductivity coefficient have been evaluated in two different ways during the validation phase of the steady-state model. The first one consists in calculating directly the values of the coefficients k ; different relations are proposed in the literature ; the formula used for air [73] (Suttherland's formula) and fuel [49] gases in the following are respectively reported in equation C.28 and C.29.

$$k_a = \frac{A \cdot T_a^{\frac{3}{2}}}{B + T_a} \tag{C.28}$$

where $A = 252 \cdot 10^{-5}$, $B = 200$ are constants values and T_a is the temperature of the air.

$$k_F = 10^{-3} \cdot [13.2 - 0.0313 \cdot (T_{bn} - 273)] \cdot \left(\frac{T}{273}\right)^n \tag{C.29}$$

where :

$$n = 2 - 0.0372 \cdot \left(\frac{T}{T_{bn}}\right)^2 \tag{C.30}$$

where T_{bn} is the boiling temperature at ambient pressure of the fuel.

The second way to compute the thermal conductivity coefficient consists in calculating the dynamic viscosity of the gas, first. A formula with a good level of accuracy relating the gas properties to the viscosity is [50] :

$$\mu = 40.785 \cdot \frac{F_c \cdot (\mathcal{M}_g \cdot T)^{\frac{1}{2}}}{V_{cr}^{\frac{2}{3}} \cdot \Omega_v} \tag{C.31}$$

$$F_c = 1 - 0.2756 \cdot \zeta + 0.059035 \cdot \eta_R^{\frac{4}{}} + K \tag{C.32}$$

$$\eta_R = 131.3 \cdot \frac{\eta}{(V_{cr} \cdot T_{cr})^{\frac{3}{2}}} \tag{C.33}$$

$$\Omega_v = A \cdot (T^*)^{-B} + C \cdot e^{-D \cdot T^*} + E \cdot e^{-F \cdot T^*} \tag{C.34}$$

$$T^* = 1.2593 \cdot T_R \tag{C.35}$$

$$T_R = \frac{T}{T_{cr}} \tag{C.36}$$

where μ is the dynamic viscosity, F_c is the correction factor, $\mathcal{M}_g$ is the molar mass, V_{cr} is the critical volume, Ω_v is the collision integral, ζ is the Pitzer's acentric factor, η_R is the relative dipole momentum, K is the experimental polarity coefficient, η is the dipole momentum, T_{cr} is the critical temperature, T^* is the corrected temperature and

T_R is the relative temperature. The value of the global dynamic viscosity of the gaseous mixture, μ_g, is obtained by using the well known relation of Wilke [50] :

$$\mu_g = \sum_{x=1}^{N} \frac{X_x \mu_x}{\sum\limits_{j=1}^{N} X_j \cdot \Gamma_{xj}}$$

where X_x is the mole fraction of the species x in the mixture and Γ_{xj} is computed as :

$$\Gamma_{xj} = \frac{\left[1 + \left(\frac{\mu_x}{\mu_j}\right)^{\frac{1}{2}} \cdot \left(\frac{\mathcal{M}_j}{\mathcal{M}_x}\right)^{\frac{1}{4}}\right]^2}{\left[8 \cdot \left(1 + \frac{\mathcal{M}_x}{\mathcal{M}_j}\right)\right]^{\frac{1}{2}}}$$

where N is the number of species composing the mixture. All the intrinsical fluid properties are easily available in literature [50,72]. Once the dynamic viscosity of the mixture is known, introducing the Prandtl number defined as :

$$Pr = \frac{\mu}{\frac{k}{c_p}} \tag{C.37}$$

provides a value for the thermal conductivity k_g :

$$k_g = \frac{\mu_g \cdot c_{p_g}}{Pr} \tag{C.38}$$

A constant Prandtl number[1] is imposed in the different models that will be presented later on.

Arguments similar to those employed above, but based on considerations of conductive and convective heat fluxes across a thin shell surrounding the evaporating drop, lead to the following expression for the heat transfer number at steady-state conditions :

$$B_T = \frac{c_{p_g} \cdot (T_\infty - T_I)}{l_I} \tag{C.39}$$

where l_I is the latent heat of fuel vaporization corresponding to the fuel interface surface temperature, T_I.

The heat transfer number B_T denotes the ratio of the available enthalpy in the surrounding gas to the heat required to evaporate the fuel. As such, it represents the driving force for the evaporation process. Where evaporation is controlled by heat transfer rates, the rate of fuel evaporation is obtained as :

$$\dot{m}_F = 2 \cdot \pi \cdot \frac{D_d}{Le} \cdot \left(\frac{k}{c_p}\right)_g \cdot \ln(1 + B_T) \tag{C.40}$$

Expressions to calculate the latent heat are available in the literature; for example by Watson [49] :

$$l_I = l_{bn} \cdot \left(\frac{T_{cr} - T_I}{T_{cr} - T_{bn}}\right)^{-0.38} \tag{C.41}$$

---

[1] A Prandtl number = 0.669 has been chosen to fit the results of the two procedures; that value is very close to values that are available in literature.

where l_{bn} is the fuel latent heat at the normal boiling temperature. In the model developed later on, the latent heat as function of the temperature is tabulated [73].
Under steady conditions $B_M = B_T$ either equation C.20 or C.40 may be used to calculate the rate of fuel evaporation. The term steady-state is used to describe the phase in the drop evaporation process where the drop surface has attained its wet bulb temperature and all the heat reaching the drop surface is used in providing the latent heat of vaporization. At an established temperature at the surface of the drop, T_I, the vapor pressure is readily estimated from the Clausius-Clapeyron equation[2] [50] as :

$$\ln\left(p_{vp_R}\right) = W \cdot \left(1 - \frac{1}{T_R}\right) \tag{C.42}$$

$$W = T_{bn_R} \cdot \frac{\ln\left(\frac{p_{cr}}{101325}\right)}{1 - T_{bn_R}} \tag{C.43}$$

$$p_{vp_R} = \frac{p_{vp_I}}{p_{cr}} \tag{C.44}$$

$$T_{bn_R} = \frac{T_{bn}}{T_{cr}} \tag{C.45}$$

$$T_R = \frac{T_I}{T_{cr}} \tag{C.46}$$

where p_{vp_I} is the fuel saturation pressure at a given interface surface temperature and p_{cr} is the critical pressure of the gas.
Now :

$$Y_{F_I} = \frac{p_{vp_I} \cdot \mathcal{M}_F}{p_{vp_I} \cdot \mathcal{M}_F + (p - p_{vp_I}) \cdot \mathcal{M}_a} = \left[1 + \left(\frac{p}{p_{vp_I}} - 1\right) \cdot \frac{\mathcal{M}_a}{\mathcal{M}_F}\right]^{-1} \tag{C.47}$$

where subscript a refers to air and subscript F refers to the gaseous fuel. It is now possible to compute the steady-state evaporation rate of a fuel droplet once fixed the thermodynamic conditions of the surrounding ambient gas. Using C.16 and knowing that under steady-state conditions the following identity is valid :

$$B_M = B_T = B \tag{C.48}$$

the mass flow rate of fuel is given by :

$$\dot{m}_F = 2 \cdot \pi \cdot \frac{D_d}{Le} \cdot \left(\frac{k}{c_p}\right)_g \cdot \ln(1 + B) \tag{C.49}$$

The values of T_I, Y_{F_I} and B are obtained from equations C.16, C.39 and C.42 to C.48 by using an iterative method[3]. From equation 2.8, rewritten here for the sake of clarity :

$$D_{d0}^2 - D_d^2 = \lambda_{st} \cdot t$$

---

[2] The Clausius-Clapeyron equation is usually expressed in the form $\ln\left(p_{vp_R}\right) = A - \frac{B}{T}$ where A and B are constants relative to gas, and T is the temperature. The form used in the study uses generalized constant values depending on intrinsical properties of the fluid.

[3] At each iteration all the properties of the fluids are reevaluated.

it is now possible to explicit the value of the constant of evaporation in steady conditions (λ_{st}). For this purpose equation 2.8 can be rewritten as :

$$\lambda_{st} = -\frac{d(D_d^2)}{dt} \tag{C.50}$$

The mass of fuel constituting the drop, m_{F_l}, is :

$$m_{F_l} = \frac{\pi}{6} \cdot \rho_{F_l} \cdot D_d^3 \tag{C.51}$$

where ρ_{F_l} is the density of the liquid fuel at the temperature T_I.
Differentiating equation C.51, knowing that to a decrease of the liquid fuel mass, m_{F_l}, corresponds an increase of the gaseous fuel mass, m_F, leads to :

$$\frac{dm_F}{dt} = \dot{m}_F = \frac{\pi}{4} \cdot \rho_{F_l} \cdot \lambda_{st} \cdot D_d \tag{C.52}$$

from equations C.49 - C.52 follows :

$$\lambda_{st} = \frac{8 \cdot k_g \cdot \ln(1+B)}{Le \cdot c_{p_g} \cdot \rho_{F_l}} \tag{C.53}$$

In stationary conditions the Lewis number can be supposed equal to one [49]. The variations of the density of liquid fuel, ρ_{F_l}, as function of the temperature can be estimated from the Hankinson-Brobst-Thompson (HBT) relation [50] :

$$\rho_{F_l} = \frac{\mathcal{M}_F}{V_s} \tag{C.54}$$

$$\frac{V_s}{V^*} = V_R^{(0)} \cdot \left[1 - \zeta_{SRK} \cdot V_R^{(\delta)}\right] \tag{C.55}$$

where :

$$V^* = \frac{R \cdot T_{cr}}{p_{cr}} \cdot \left(A + B \cdot \zeta_{SRK} + C \cdot \zeta_{SRK}^2\right) \tag{C.56}$$

$$V_R^{(0)} = 1 + a \cdot (1-T_R)^{\frac{1}{3}} + b \cdot (1-T_R)^{\frac{2}{3}} + c \cdot (1-T_R) + d \cdot (1-T_R)^{\frac{4}{3}}; \quad 0.25 < T_R < 0.95 \tag{C.57}$$

$$V_R^{(\delta)} = \frac{\left[e + f \cdot T_R + g \cdot T_R^2 + h \cdot T_R^3\right]}{T_R - 1.00001}; \quad 0.25 < T_R < 1.0 \tag{C.58}$$

and the acentric factor, ζ_{SRK}, is a parameter for HBT correlation. V_s is the saturated molar volume of the liquid at the temperature $T_I = T_R \cdot T_{cr}$. Moreover, the constants (that are valid for all hydrocarbons) assume the following values :

$A = 0.2851686$
$B = -0.06379110$
$C = 0.01379173$
$a = -1.52816$
$b = 1.43907$
$c = -0.81446$
$d = 0.190454$
$e = -0.296123$
$f = 0.386914$
$g = -0.0427258$
$h = -0.0480645$

In the following, the equations that constitute the mathematical model for the determination of the thermodynamic properties of the fluid at liquid-gas interface, are reported :

Set of equations used for determining the mixture thermodynamic properties at interface

$$B_M = \frac{Y_{F_I}}{1-Y_{F_I}}$$

$$B_T = \frac{c_{pg} \cdot (T_\infty - T_I)}{l_I}$$

$$B = B_M = B_T$$

$$\ln\left(\frac{p_{vp_I}}{p_{cr}}\right) = \frac{T_{bn}}{T_{cr}} \cdot \frac{\ln\left(\frac{p_{cr}}{101325}\right)}{1-\frac{T_{bn}}{T_{cr}}} \cdot \left(1 - \frac{1}{\frac{T_I}{T_{cr}}}\right)$$

$$Y_{F_I} = \left[1 + \left(\frac{p}{p_{vp_I}} - 1\right) \cdot \frac{\mathcal{M}_a}{\mathcal{M}_F}\right]^{-1}$$

For completeness, below are reported the additional equations used for computing the characteristic D^2 *law* variables :

Set of equations used in the D^2 *law* steady-state model

$$\dot{m}_F = 2 \cdot \pi \cdot \frac{D_d}{Le} \cdot \left(\frac{k}{c_p}\right)_g \cdot \ln(1+B)$$

$$\lambda_{st} = \frac{8 \cdot k_g \cdot \ln(1+B)}{Le \cdot c_{pg} \cdot \rho_{F_l}}$$

$$\frac{dD_d}{dt} = -\frac{1}{2} \cdot \frac{\lambda_{st}}{D_d}$$

$$\frac{dT_I}{dt} = 0$$

The validation results of the steady-state model are reported in section 2.4.1.1 and will not be repeated here.

A parametric study of the model has then been performed to present the influence on the evaporation process of the different parameters of the model. The parameters changed for the parametric study are : the initial droplet diameter, D_{d_0}, the surrounding gas temperature, T_∞, and the surrounding gas pressure, p. The parameters used in the simulations are summarized in table C.1.

Figures C.1 and C.2 show the evolutions of the drop during the evaporation processes for the different initial conditions. The influences of these parameters are the following :

	D_{d_0} [μm]	T_∞ [K]	p [Pa]
Set 1	200	750	100000
Set 2	200	500	100000
Set 3	200	750	1000000
Set 4	300	750	100000

Table C.1: Parameter sets for steady-state parametric study of droplet evaporation.

- the initial diameter of the drop D_{d_0} has no influence neither on the constant of evaporation λ_{st} nor on the steady temperature at surface T_I,
- increasing the surrounding temperature T_∞ leads to an increase of the drop surface temperature T_I, and consequently to an increase of the constant of evaporation λ_{st},
- increasing the surrounding pressure p, the drop surface temperature T_I increases too and the constant of evaporation λ_{st} follows the same trend,
- table C.2 shows that the temperature of the surrounding air, T_∞, has a great influence on the value of the evaporation constant λ_{st} hence on the drop lifetime; whereas the pressure of the surrounding air, p, has a great influence on the value of the drop temperature T_I,
- at a given D_{d_0}, a change in ambient thermodynamic conditions induces a variation of T_I. Because of the density temperature dependence, a variation of T_I causes a variation of the droplet mass, m_{F_l}. In particular, to an increase of T_I, corresponds a decrease of m_{F_l},

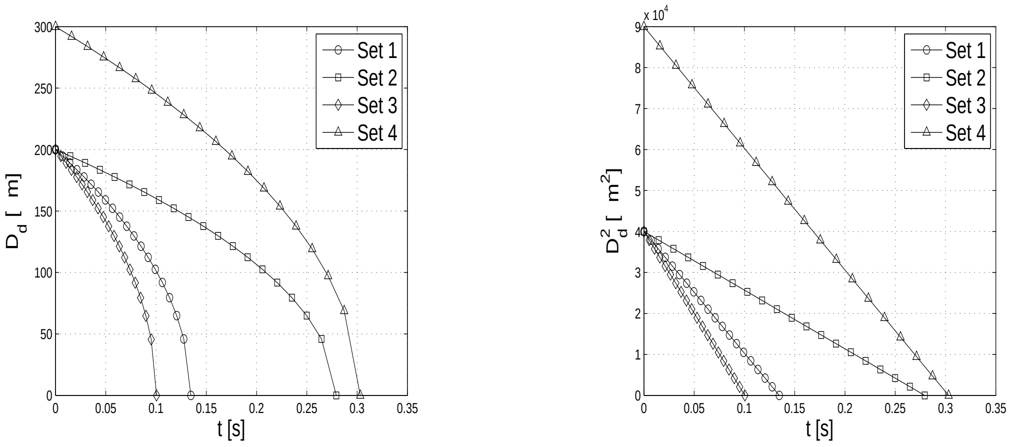

(a) (b)

Figure C.1: Parametric study of the steady-state model : evolutions of droplet diameters, (a), and squared diameters, (b), for different ambient-gas thermodynamic conditions, and droplet sizes.

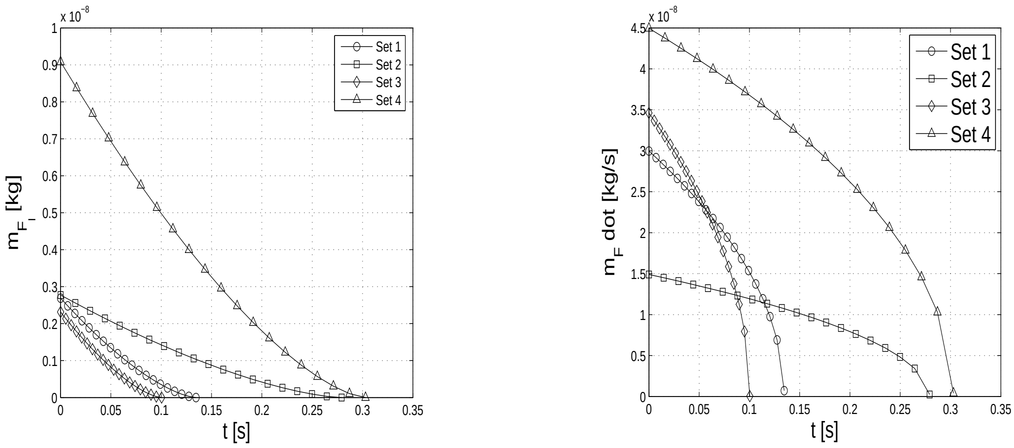

(a) (b)

Figure C.2: Parametric study of the steady-state model : evolutions of droplet masses, (a), and mass evaporation rates, (b), for different ambient-gas thermodynamic conditions, and droplet sizes.

For the test cases listed in table C.1, the values of the evaporation constants and of the temperatures at the droplet surface are given in table C.2.

	λ_{st} [m^2/s]	T_I [K]
Set 1	$2.970e-7$	338.5
Set 2	$1.432e-7$	316.1
Set 3	$3.984e-7$	425.7
Set 4	$2.970e-7$	338.5

Table C.2: Values of the evaporation constants and of the temperatures at the droplet surface relative to the tested cas listed in table C.1.

Appendix D

Variance equation proof

In this appendix, the mathematical proof of equation 2.120 is given. In particular, the validity of equation 2.120 is proved by using two different approaches :

- a Probability Density Function approach and
- a 3D CFD approach.

Proof 1 : a PDF approach

The fuel mass-fraction distribution variance is defined as :

$$\widetilde{Z"^2} = \frac{1}{m_S} \cdot \int_{m_S} Z"^2 \cdot dm = \frac{1}{m_S} \cdot \int_{m_S} \left(Z - \widetilde{Z}\right)^2 \cdot dm \tag{D.1}$$

hence, by introducing the PDF associated with the mixture fraction distribution :

$$\widetilde{Z"^2} = \int_0^{Z_s} \left(Z^* - \widetilde{Z}\right)^2 \cdot \mathcal{P}\left(Z^*\right) \cdot dZ^* \tag{D.2}$$

Differentiating equation D.2 :

$$\begin{aligned} \frac{d\widetilde{Z"^2}}{dt} &= \underbrace{\int_0^{Z_s} \frac{d\left(Z^* - \widetilde{Z}\right)^2}{dt} \cdot \mathcal{P}\left(Z^*\right) \cdot dZ^*}_{(a)} + \\ &\quad + \underbrace{\int_0^{Z_s} \left(Z^* - \widetilde{Z}\right)^2 \cdot \frac{d\mathcal{P}\left(Z^*\right)}{dt} \cdot dZ^*}_{(b)} \end{aligned} \tag{D.3}$$

Developing the term (a) of equation D.3 :

$$\begin{gathered} \int_0^{Z_s} \frac{d\left(Z^* - \widetilde{Z}\right)^2}{dt} \cdot \mathcal{P}\left(Z^*\right) \cdot dZ^* = \\ \int_0^{Z_s} \left(\frac{d\widetilde{Z}^2}{dt} - 2 \cdot Z^* \cdot \frac{d\widetilde{Z}}{dt}\right) \cdot \mathcal{P}\left(Z^*\right) \cdot dZ^* = \\ \frac{d\widetilde{Z}^2}{dt} \cdot \int_0^{Z_s} \mathcal{P}\left(Z^*\right) \cdot dZ^* - 2 \cdot \frac{d\widetilde{Z}}{dt} \cdot \int_0^{Z_s} Z^* \cdot \mathcal{P}\left(Z^*\right) \cdot dZ^* = \\ \frac{d\widetilde{Z}^2}{dt} - 2 \cdot \widetilde{Z} \cdot \frac{d\widetilde{Z}}{dt} = \frac{d\widetilde{Z}^2}{dt} - \frac{d\widetilde{Z}^2}{dt} = 0 \end{gathered} \tag{D.4}$$

As shown, the term (a) does not contribute to the variance variation.

Concerning the term (b) of equation D.3, it represents the variation of the PDF shape in time. In order to correctly describe the PDF evolution, the different contributions to the variance variation will be determined. More precisely, the impacts of the mixture-zone inputs, namely the entrained gaseous mixture and the evaporated fuel, of the mixture zone outputs, namely the outgoing mixture, and of turbulence will be presented in detail. Henceforth, global PDF will be subdivided into five contributions :

- $\mathcal{P}_{in}$, the probability to have a local mixture-fraction in the spray at $Z = Z_{in}$; that is, the composition of the entrained-gas in the spray,
- $\mathcal{P}_s$, the probability to have a local mixture-fraction in the spray at $Z = Z_s$; that is, the mixture composition at liquid-gas interface during evaporation process,
- $\mathcal{P}_0$, the probability to have a local mixture in the spray at $Z = Z_0 = 0$; that is the composition of the pure-air (in the most general case pure-air represents an homogeneous mixture of air and EGR),
- $\mathcal{P}_m$, the probability to have a local mixture in the spray at $Z = \widetilde{Z}$; that is the mean composition of the spray,
- $\mathcal{P}_c$, the probability to have a local mixture-fraction in the spray at a composition different from Z_{in}, Z_s, Z_0 and $\widetilde{Z}$. Henceforth, it will be called the complementary mixture-fraction probability.

$\mathcal{P}_{in}$, $\mathcal{P}_s$, $\mathcal{P}_0$ and $\mathcal{P}_m$ at each instant of time have a well-known composition. Consequently, in the composition space, they can be represented using a Dirac function, ψ.

On the other hand, turbulence acts on the overall mixture-fraction distribution and contributes to dissipate the distribution variance. Physically, its action represents the mixture homogenization caused by turbulent-mixing process.

In the following, the different term contributions to the variance variation will be detailed individually.

Entrained-mass contribution

At a given time, t_0, the probability to have in the spray a local mixture-composition at $Z = Z_{in}$ is :

$$\mathcal{P}\left(Z_{in}, t_0\right) = \mathcal{P}_{in_0} \tag{D.5}$$

after a short interval of time, δt, the spray entrains a certain amount of mass, δm_{in}. Hence :

$$\mathcal{P}\left(Z_{in}, t_0 + \delta t\right) = \mathcal{P}_{in_0} \cdot \frac{m_S}{m_S + \delta m_{in}} + \frac{\delta m_{in}}{m_S + \delta m_{in}} \tag{D.6}$$

Computing the derivative of $\mathcal{P}\left(Z_{in}\right)$ as the limit of the incremental ratio gives :

$$\frac{d\mathcal{P}\left(Z_{in}\right)}{dt}=\lim_{\delta t\to 0}\frac{\mathcal{P}\left(Z_{in},t_0+\delta t\right)-\mathcal{P}\left(Z_{in},t_0\right)}{\delta t}=\frac{1}{m_S}\cdot\frac{dm_{in}}{dt} \tag{D.7}$$

Hence, its contribution to the variance is :

$$\int_0^{Z_s}\left(Z^*-\widetilde{Z}\right)^2\cdot\left(\frac{1}{m_S}\cdot\frac{dm_{in}}{dt}\right)\cdot\psi\left(Z^*-Z_{in}\right)\cdot dZ^*=$$

$$\left(Z_{in}-\widetilde{Z}\right)^2\cdot\frac{1}{m_S}\cdot\frac{dm_{in}}{dt} \tag{D.8}$$

Evaporation-process contribution

Adopting the same method used for entrained gas, the evaporation-process impact on the PDF holds :

$$\frac{d\mathcal{P}\left(Z_{s}\right)}{dt}=\lim_{\delta t\to 0}\frac{\mathcal{P}\left(Z_{s},t_0+\delta t\right)-\mathcal{P}\left(Z_{s},t_0\right)}{\delta t}=\frac{1}{m_S}\cdot\frac{dm_{s}}{dt} \tag{D.9}$$

hence, its contribution to variance is :

$$\int_0^{Z_s}\left(Z^*-\widetilde{Z}\right)^2\cdot\left(\frac{1}{m_S}\cdot\frac{dm_{s}}{dt}\right)\cdot\psi\left(Z^*-Z_{s}\right)\cdot dZ^*=$$

$$\frac{1}{m_S}\cdot\left(Z_{s}-\widetilde{Z}\right)^2\cdot\frac{dm_{s}}{dt} \tag{D.10}$$

Fuel evaporating at saturated conditions implies to introduce in the spray homogeneous mixture of pure ambient-air and pure fuel in the proportions established by the value of Z_s. As the necessary ambient-air mass is already contained in the spray, its transfer from one value of mixture fraction to another represents a further contribution to the variance variation. In the present approach it is assumed that the liquid fuel evaporates in pure ambient-air. Locally, by definition :

$$Z=\frac{m_F}{m_F+m_a} \tag{D.11}$$

where m_a is the mass of pure ambient-air in the spray. Hence, for a given fuel evaporation-rate (evaporating at saturated conditions), dm_F/dt, the total mass at saturated composition introduced in the spray is :

$$\frac{dm_s}{dt}=\frac{\left(dm_F+dm_a\right)_s}{dt}=\frac{1}{Z_s}\cdot\frac{dm_F}{dt} \tag{D.12}$$

According to the assumption that liquid fuel evaporates in pure ambient-air, it is necessary to take into account the impact on the variance variation of the ambient-air mass associated with evaporation process. The withdrawn ambient-air mass, dm_{a_w}, is :

$$\frac{dm_{a_w}}{dt}=\left(1-\frac{1}{Z_s}\right)\cdot\frac{dm_F}{dt} \tag{D.13}$$

It follows that the impact on the PDF is :

$$\frac{d\mathcal{P}\left(Z_0\right)}{dt} = \lim_{\delta t \to 0} \frac{\mathcal{P}\left(Z_0, t_0 + \delta t\right) - \mathcal{P}\left(Z_0, t_0\right)}{\delta t} = \frac{1}{m_S} \cdot \frac{dm_{a_w}}{dt} \tag{D.14}$$

and the impact on the variance variation is :

$$\int_0^{Z_s} \left(Z^* - \widetilde{Z}\right)^2 \cdot \left(\frac{1}{m_S} \cdot \frac{dm_{a_w}}{dt}\right) \cdot \psi\left(Z^* - Z_0\right) \cdot dZ^* =$$

$$\left(Z_0 - \widetilde{Z}\right)^2 \cdot \frac{1}{m_S} \cdot \frac{dm_{a_w}}{dt} = \widetilde{Z}^2 \cdot \frac{1}{m_S} \cdot \frac{dm_{a_w}}{dt} \tag{D.15}$$

as $Z_0 = 0$.

Outgoing mass contribution

According to the stated hypothesis, the outgoing gaseous mixture has a composition equal to the mean value of the distribution. Following the same way of proceeding as before, the outgoing-mass impact on the PDF is :

$$\frac{d\mathcal{P}\left(\widetilde{Z}\right)}{dt} = \lim_{\delta t \to 0} \frac{\mathcal{P}\left(\widetilde{Z}, t_0 + \delta t\right) - \mathcal{P}\left(\widetilde{Z}, t_0\right)}{\delta t} = -\frac{1}{m_S} \cdot \frac{|dm_{out}|}{dt} \tag{D.16}$$

hence, its contribution to variance is :

$$\int_0^{Z_s} \left(Z^* - \widetilde{Z}\right)^2 \cdot \left(-\frac{1}{m_S} \cdot \frac{|dm_{out}|}{dt}\right) \cdot \psi\left(Z^* - \widetilde{Z}\right) \cdot dZ^* =$$

$$-\left(\widetilde{Z} - \widetilde{Z}\right)^2 \cdot \frac{1}{m_S} \cdot \frac{|dm_{out}|}{dt} = 0 \tag{D.17}$$

Complementary mixture-fraction contribution

The used β-PDF is a normalized statistical-tool. Consequently, the following relation must always be verified :

$$\int_0^{Z_s} \mathcal{P}\left(Z^*\right) \cdot dZ^* = 1 \tag{D.18}$$

Taking advantage of equation D.18, at every time, t, it is possible to know the probability to have in the spray a local composition $Z = Z_c$:

$$\begin{aligned} \mathcal{P}\left(Z_c, t\right) &= \int_0^{Z_s} \mathcal{P}\left(Z^*\right) \cdot dZ^* - \mathcal{P}_{in} - \mathcal{P}_s - \mathcal{P}_0 - \mathcal{P}_{out} \\ &= 1 - \mathcal{P}_{in} - \mathcal{P}_s - \mathcal{P}_0 - \mathcal{P}_{out} \end{aligned} \tag{D.19}$$

Differentiating equation D.19 :

$$\frac{d\mathcal{P}\left(Z_c, t\right)}{dt} = -\frac{d\mathcal{P}_{in}}{dt} - \frac{d\mathcal{P}_s}{dt} - \frac{d\mathcal{P}_0}{dt} - \frac{d\mathcal{P}_{out}}{dt} \tag{D.20}$$

The contribution of the complementary mixture-fraction to the variance variation is then computed as :

$$\int_0^{Z_s} \left(Z^* - \widetilde{Z}\right)^2 \cdot \frac{d\mathcal{P}\left(Z_c\right)}{dt} \cdot dZ^* =$$

$$-\int_0^{Z_s}\left(Z^*-\widetilde{Z}\right)^2\cdot\frac{1}{m_S}\cdot\left(\frac{dm_{in}}{dt}+\frac{dm_s}{dt}+\frac{dm_{a_w}}{dt}-\frac{|dm_{out}|}{dt}\right)\cdot dZ^*=$$

$$\frac{\widetilde{Z"^2}}{m_S}\cdot\left(-\frac{dm_{in}}{dt}-\frac{dm_s}{dt}-\frac{dm_{a_w}}{dt}+\frac{|dm_{out}|}{dt}\right) \tag{D.21}$$

Turbulence contribution

Turbulence contributes to reduce the variance of the mixture making it more homogeneous. The dissipation of the mixture-fraction variance is representative of the turbulent mixing-process. This contribution is modeled by using an empirical closure term :

$$\int_0^{Z_s}\left(Z^*-\widetilde{Z}\right)^2\cdot\left.\frac{d\mathcal{P}\left(Z^*\right)}{dt}\right|_{ds}\cdot dZ^*=-2\cdot C_{ds}\cdot\frac{\widetilde{\epsilon}}{\widetilde{\kappa}}\cdot\widetilde{Z"^2} \tag{D.22}$$

Global variance equation

Equation D.3 because of equation D.4 reduces to :

$$\frac{d\widetilde{Z"^2}}{dt}=\int_0^{Z_s}\left(Z^*-\widetilde{Z}\right)^2\cdot\frac{d\mathcal{P}\left(Z^*\right)}{dt}\cdot dZ^* \tag{D.23}$$

Taking advantage of equations D.8, D.10, D.15, D.17, D.21 and D.22, the right-hand side of equation D.23 can be expressed as :

$$\frac{d\widetilde{Z"^2}}{dt}=\frac{1}{m_S}\cdot\left[\left(Z_{in}-\widetilde{Z}\right)^2\cdot\frac{dm_{in}}{dt}+\left(Z_s-\widetilde{Z}\right)^2\cdot\frac{dm_s}{dt}+\right.$$

$$\left.+\widetilde{Z}^2\cdot\frac{dm_{a_w}}{dt}+\left(-\frac{dm_{in}}{dt}-\frac{dm_s}{dt}-\frac{dm_{a_w}}{dt}+\frac{|dm_{out}|}{dt}\right)\cdot\widetilde{Z"^2}\right]+$$

$$-2\cdot C_{ds}\cdot\frac{\widetilde{\epsilon}}{\widetilde{\kappa}}\cdot\widetilde{Z"^2} \tag{D.24}$$

Equation 2.120 is directly obtained by substituting in equation D.24 the results of equations D.12 and D.13.

Proof 2 : a 3D CFD approach

For a given spray[1] the continuity and fuel mixture fraction balance equations can be written, respectively, as :

$$\frac{D\rho}{Dt}=\rho\sum_{j=1}^{NST}\dot{S}_j \tag{D.25}$$

and :

$$\frac{D\rho Z}{Dt}=\rho\sum_{j=1}^{NST}Z_j\dot{S}_j+\nabla\left(\frac{\mu_t}{Sc_t}\nabla Z\right) \tag{D.26}$$

---

[1] The subscript identifying the spray is here omitted in order to facilitate the reading.

where $\dot{S}_j$ is the total mass rate of source j, Z_j is the fuel mass fraction associated with this source, and NST is the Number of Source Terms[2].

Using the equations D.25 and D.26, the transport equation of the fuel mixture fraction variance, $v = \widetilde{Z"^2}$, can be written as :

$$\frac{D\bar{\rho}v}{Dt} = \sum_{j=1}^{NST} \bar{\rho}\left[\left(2\widetilde{ZZ_j - Z^2}\right)\dot{S}_j + \widetilde{Z}^2\widetilde{\dot{S}_j} - 2\widetilde{Z}\widetilde{Z_j\dot{S}_j}\right] + \nabla\left(\frac{\mu_t}{Sc_t}\nabla v\right) + 2\frac{\mu_t}{Sc_t}\left(\nabla\widetilde{Z}\right)^2 - \chi \tag{D.27}$$

where $\bar{\rho}$ is the density mean value of the gaseous mixture, Z is the local fuel mixture fraction value, Z_j is mixture fraction value associated with the source term and χ is the scalar dissipation.

In the following, the contributions to the variance variation associated with each source terms are detailed. The variance source terms associated with diffusion through the volume boundaries are supposed to be accounted for in the volumetric source terms.

Entrained gas contribution

According to equation D.27, the entrained gas contribution to the variance variation can be written as :

$$\left.\frac{D\bar{\rho}v}{Dt}\right|_{in} = \bar{\rho}\left[\left(2\widetilde{ZZ_{in} - Z^2}\right)\ \dot{S}_{in} + \widetilde{Z}^2\widetilde{\dot{S}}_{in} - 2\widetilde{Z}\widetilde{Z_{in}\ \dot{S}_{in}}\right] \tag{D.28}$$

Supposing that the incoming mass is introduced in the fuel mixture fraction distribution at $Z = Z_{in}$, equation D.28 becomes :

$$\left.\frac{D\bar{\rho}v}{Dt}\right|_{in} = \bar{\rho}\left[\left(2\widetilde{Z_{in}^2 - Z_{in}^2}\right)\ \dot{S}_{in} + \widetilde{Z}^2\widetilde{\dot{S}}_{in} - 2\widetilde{Z}\widetilde{Z_{in}\ \dot{S}_{in}}\right] \tag{D.29}$$

Finally, adding the hypothesis that $Z_{in} = constant$, equation D.29 reduces to :

$$\begin{aligned} \left.\frac{D\bar{\rho}v}{Dt}\right|_{in} &= \bar{\rho}\left(Z_{in}^2\widetilde{\dot{S}}_{in} + \widetilde{Z}^2\widetilde{\dot{S}}_{in} - 2Z_{in}\widetilde{Z}\widetilde{\dot{S}}_{in}\right) \\ &= \bar{\rho}\left(Z_{in} - \widetilde{Z}\right)^2\widetilde{\dot{S}}_{in} \end{aligned} \tag{D.30}$$

Outging gas contribution

According to equation D.27, the outgoing gas contribution to the variance variation can be written as :

$$\left.\frac{D\bar{\rho}v}{Dt}\right|_{out} = \bar{\rho}\left[\left(2\widetilde{ZZ_{out} - Z^2}\right)\ \ \dot{S}_{out} + \widetilde{Z}^2\widetilde{\dot{S}}_{out} - 2\widetilde{Z}\widetilde{Z_{out}\ \ \dot{S}_{out}}\right] \tag{D.31}$$

---

[2] Here three source terms are retained : the first associated with the entrained gas, the second associated with the outgoing gas and the third associated with the fuel evaporation.

Supposing that the outgoing mass has no variance, $Z_{out} = \widetilde{Z}$, and the mass is taken out from the fuel mixture fraction distribution at $Z = \widetilde{Z}$, equation D.31 reduces to :

$$\left.\frac{D\bar{\rho}v}{Dt}\right|_{out} = \bar{\rho}\left[\widetilde{\left(2\widetilde{Z}^2 - \widetilde{Z}^2\right)\ \dot{S}_{out}} + \widetilde{Z}^2\widetilde{\dot{S}_{out}} - 2\widetilde{Z}\widetilde{\widetilde{Z}\ \dot{S}_{out}}\right]$$
$$= \bar{\rho}\left(\widetilde{Z}^2\widetilde{\dot{S}_{out}} + \widetilde{Z}^2\widetilde{\dot{S}_{out}} - 2\widetilde{Z}^2\widetilde{\dot{S}_{out}}\right)$$
$$= 0 \tag{D.32}$$

The hypothesis of considering the outgoing mass as homogeneous is a technical choice. In fact, as the mass coming out from the i^{th} spray is entrained in the $(i+1)^{th}$ spray, this hypothesis allows to write the variance source term for the $(i+1)^{th}$ spray according to equation D.30.

Fuel evaporation contribution

According to the spray model, section 2.4.1.1, the liquid fuel evaporating at saturated conditions implies the introduction of fuel at $Z = Z_s$. As the necessary ambient-air mass is already contained in the spray, its transfer from one value of mixture fraction to another represents a further contribution to the variance variation. In the present approach it is assumed that the liquid fuel evaporates in pure ambient-air : the droplets of fuel are supposed to be surrounded by pure air ($Z = 0$), and fuel evaporates at saturated conditions ($Z = Z_s$), figure D.1.

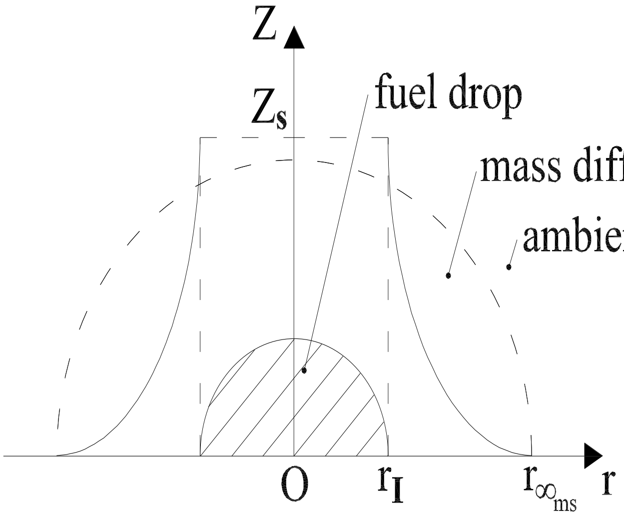

Figure D.1: Scheme of a fuel droplet evaporating at steady state in pure ambient gas. In this figure, the fuel mixture fraction profile along the droplet radial coordinate is shown.

Hence, according to equation D.11, for a given fuel evaporation-rate (evaporating at saturated conditions), $\dot{S}_F$, the total mass flow rate at saturated composition introduced in the spray is :

$$\dot{S}_s = \frac{\dot{S}_F}{Z_s} \tag{D.33}$$

According to the assumption that liquid fuel evaporates in pure ambient-air, it is necessary to take into account the impact on the variance variation of the ambient-air mass associated with evaporation process. The withdrawn ambient-air mass flow rate, $\dot{S}_{a_w}$, is :

$$\dot{S}_{a_w} = \left(1 - \frac{1}{Z_s}\right)\dot{S}_F \tag{D.34}$$

Consequently, the total contribution of liquid fuel evaporation to the fuel mixture fraction distribution variance variation is computed as the sum of the two contributions associated to the gaseous mass introduced at $Z = Z_s$ and to the ambient air withdrawn at $Z = 0$.

According to equation D.27, the contribution of the gaseous mass introduced at $Z = Z_s$ is computed as :

$$\left.\frac{D\bar{\rho}v}{Dt}\right|_s = \bar{\rho}\left[\widetilde{\left(2ZZ_s - Z^2\right)\ \dot{S}_s} + \widetilde{Z}^2\widetilde{\dot{S}}_s - 2\widetilde{Z}\widetilde{Z_s\ \dot{S}_s}\right] \tag{D.35}$$

Supposing that the gaseous mass is introduced in the fuel mixture fraction distribution at $Z = Z_s$, equation D.35 becomes :

$$\left.\frac{D\bar{\rho}v}{Dt}\right|_s = \bar{\rho}\left[\widetilde{\left(2Z_s^2 - Z_s^2\right)\ \dot{S}_s} + \widetilde{Z}^2\widetilde{\dot{S}}_{ev} - 2\widetilde{Z}\widetilde{Z_s\ \dot{S}_s}\right] \tag{D.36}$$

Finally, adding the hypothesis that $Z_s = constant$, equation D.36 reduces to :

$$\begin{aligned}\left.\frac{D\bar{\rho}v}{Dt}\right|_s &= \bar{\rho}\left(Z_s^2\widetilde{\dot{S}}_s + \widetilde{Z}^2\widetilde{\dot{S}}_s - 2Z_s\widetilde{Z}\widetilde{\dot{S}}_s\right) \\ &= \bar{\rho}\left[\left(Z_s - \widetilde{Z}\right)^2\widetilde{\dot{S}}_s\right] \end{aligned} \tag{D.37}$$

In the same manner, according to equation D.27, the contribution of the withdrawn ambient air ($Z = 0$) is computed as :

$$\left.\frac{D\bar{\rho}v}{Dt}\right|_{a_w} = \bar{\rho}\left(-\widetilde{Z^2\ \dot{S}_{a_w}} + \widetilde{Z}^2\widetilde{\dot{S}}_{a_w}\right) \tag{D.38}$$

Supposing that the gaseous mass is withdrawn from the fuel mixture fraction distribution at $Z = 0$, equation D.38 reduces to :

$$\left.\frac{D\bar{\rho}v}{Dt}\right|_{a_w} = \bar{\rho}\widetilde{Z}^2\widetilde{\dot{S}}_{a_w} \tag{D.39}$$

Hence, using the definitions given in equations D.33 and D.34, the total contribution to the variance variation of liquid fuel evaporation rate, obtained by the sum of equations D.37 and D.39, is written as :

$$\left.\frac{D\bar{\rho}v}{Dt}\right|_F = \bar{\rho}\left[\left(Z_s - \widetilde{Z}\right)^2\frac{1}{Z_s} + \widetilde{Z}^2\left(1 - \frac{1}{Z_s}\right)\right]\widetilde{\dot{S}}_F \tag{D.40}$$

Turbulence contribution

Turbulence contributes to reduce the variance of the mixture making it more homogeneous. The dissipation of the mixture-fraction variance is representative of the turbulent mixing-process.

In the dual-CM, an empirical approach has been used for modeling the variance dissipation term, χ, together with the source term associated with mixture fraction mean value gradients, $2\mu_t/Sc_t\left(\nabla\widetilde{Z}\right)^2$, the latter being difficult to *visualize* in a 0D context :

$$2\frac{\mu_t}{Sc_t}\left(\nabla\widetilde{Z}\right)^2-\chi=2C_{ds}\bar{\rho}\frac{\widetilde{\epsilon}}{\widetilde{\kappa}}v \tag{D.41}$$

in which C_{ds} is an adjustment coefficient of the model.

Global variance variation equation

Equation D.27 can be rewritten as :

$$\frac{D\bar{\rho}v}{Dt}=\bar{\rho}\dot{S}_v \tag{D.42}$$

where $\dot{S}_v$ represents the right hand side of equation D.27.

According to the mass variation theorem for a material volume, V_m, equations D.25 and D.42 give respectively :

$$\frac{Dm}{Dt}=\int_{V_m}\frac{D\bar{\rho}}{Dt}dV=\int_{V_m}\bar{\rho}\left(\sum_{j=1}^{NST}\dot{S}_j\right)dV \tag{D.43}$$

and :

$$\frac{Dm<v>}{Dt}=\int_{V_m}\frac{D\bar{\rho}v}{Dt}dV=\int_{V_m}\bar{\rho}\dot{S}_v dV \tag{D.44}$$

where m is the mass in the volume and $<v>$ is the mean value of the fuel mixture fraction variance.

From the left hand side of equation D.44 :

$$\frac{D<v>}{Dt}=\frac{1}{m}\left(\frac{Dm<v>}{Dt}-<v>\frac{Dm}{Dt}\right) \tag{D.45}$$

Using the relations given in equations D.43 and D.44, equation D.45 becomes :

$$\frac{D<v>}{Dt}=\frac{1}{m}\left[\int_{V_m}\bar{\rho}\dot{S}_v dV-<v>\int_{V_m}\bar{\rho}\left(\sum_{j=1}^{NST}\dot{S}_j\right)dV\right]=\dot{S}_v-<v>\sum_{j=1}^{NST}\dot{S}_j \tag{D.46}$$

which is exactly the same expression given in equation 2.120.

Appendix E

FPI trajectories in the phase space

Presented in this appendix is the phenomenon associated with local mixture fraction variations (due to mixing or liquid fuel evaporation) taking place during the combustion process, which can bring to FPI trajectory inconsistencies in the phase space, and how the species mass fraction tabulation approach permits to overcome it. Figure E.1 illustrates the phenomenon. In figure E.1, the tabulated manifolds are plotted in the phase space of the species Y_a and Y_b. In particular, attention must be focused on the two manifolds representing two combustion processes having initial conditions differing only for the equivalence ratio values, indicated with Φ_1 and $\Phi_2 = \Phi_1 + d\Phi$. Suppose, that at a given instant of time, the combustion process is located in A, and mixing is going on. After an infinitesimal interval of time dt, because of a change of equivalence ratio, i.e. due to the fuel evaporation process within the reactor, the combustion physical trajectory will switch to the Φ_2 manifold. Computing the species reaction rates by using the data stored in the look-up table and integrating can locate the combustion state at the point C, rather than at the correct point B. These sorts of errors can be introduced at every single computational step and cumulated errors may give rise to trajectory divergence.

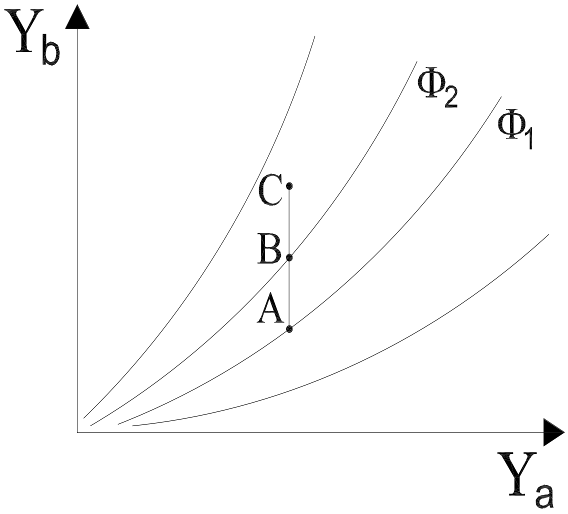

Figure E.1: The computed combustion process trajectory in the phase-space may diverge from the tabulated manifold trajectory. Here a trajectory divergence generated by a variation of the mixture mean equivalence-ratio is represented.

The species concentration approach overcomes this problem and permits us to follow the FPI trajectory even when variations of equivalence ratio, EGR rate and thermodynamic conditions occur. In fact, the species reaction rates are always computed taking into account the correct values of species concentrations, equation 2.141.

Equation 2.141 is repeated here for the sake of clarity :

$$\dot{\omega}_x^{cb} = \frac{\partial Y_x^{cb}}{\partial t} = \frac{Y_x^{TAB}\left(c\left(t+\tau\right)\right) - Y_x^{cb}\left(t\right)}{\tau}$$

As seen, equation 2.141 allows the in-cylinder species composition to relax towards the tabulated manifolds. The relaxation towards the tabulated manifolds constitutes the main advantage of the species mass/molar concentration tabulation approach and permits us to correct the problem of divergence highlighted in figure E.1. Figure E.2 illustrates schematically the impact of the relaxation time, τ, on the combustion trajectory in the phase space. Accordingly in figure E.2, point C localizes the combustion process in the phase space for a mixture characterized by an equivalence ratio equal to Φ_2. As can be seen, C does not lie on the trajectory because a mixing process varying the equivalence ratio of the mixture is in progress, figure E.1. Because of equation 2.141, the computed reaction rates tend to relax the thermochemical state at point C towards the manifold composition. The relaxation time is function of the value given to τ. In particular for $\tau \equiv dt$, C converges to the manifold in an interval of time equal to dt (point B). Otherwise, for $\tau > dt$, the time necessary for the relax is longer. For instance if $dt < \tau' < \tau''$, the complete convergence to the manifold will take place at B' and B'' for τ' and τ'', respectively.

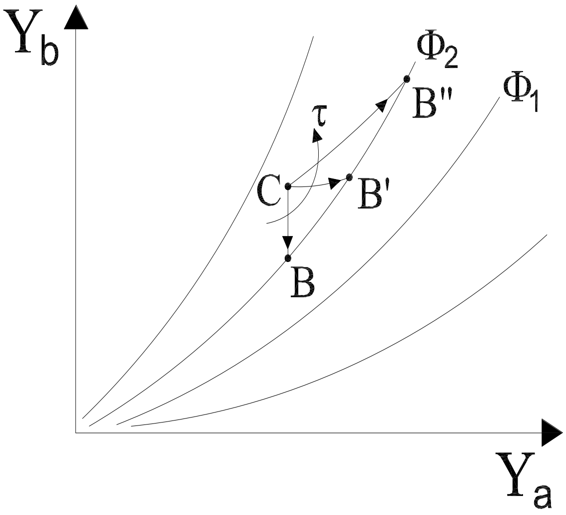

Figure E.2: Trajectory evolutions in the phase space. The state A evolves towards the manifold trajectory, Φ_2. The influence of the parameter τ on the convergence characteristic-time is illustrated. As can be seen, the higher the value of τ, the longer it takes to converge to the manifold trajectory.

Appendix F

Oil & Gas Science and Technology

Oil & Gas Science and Technology – Rev. IFP, Vol. 64 (2009), No. 3, pp. 259-284

DOI: 10.2516/ogst/2008051

Dossier

Simulation Tools for Powertrain Design and Control
Outils de simulation pour la conception et le contrôle du groupe motopropulseur

A New 0D Diesel HCCI Combustion Model Derived from a 3D CFD Approach with Detailed Tabulated Chemistry

A. Dulbecco[1]*, F.-A. Lafossas[1], G. Mauviot[1] and T.J. Poinsot[2]

1 Institut français du pétrole, IFP, 1-4 avenue de Bois-Préau, 92852 Rueil-Malmaison Cedex - France
2 CERFACS, 42 avenue G. Coriolis, 31057 Toulouse Cedex 1 - France
e-mail: alessio.dulbecco@ifp.fr - francois-a.lafossas@toyota-europe.com - gilles.mauviot@ifp.fr - thierry.poinsot@cerfacs.fr

* Corresponding author

Résumé — Un nouveau modèle 0D pour la simulation de la combustion Diesel HCCI obtenu par réduction d'un code CFD 3D utilisant une méthode de chimie complexe tabulée — Cet article présente une nouvelle approche phénoménologique 0D à la modélisation numérique de la combustion Diesel HCCI. Le modèle a été obtenu par réduction du modèle CFD 3D TKI-PDF (*Cinétique Chimique Tabulée pour la détection de l'auto-allumage couplée avec une Fonction à Densité de Probabilité présumée*) développé à l'IFP ; sa formulation est basée sur des considérations de type physique afin de prendre en compte les différents phénomènes qui interviennent dans le cylindre pendant le processus de combustion et leurs interactions. Les aspects relatifs à l'évaporation du carburant, à la pénétration du spray, à la turbulence, à la formation du mélange et à la cinétique chimique ont été étudiés en détail. L'apport original de ce travail concerne la description du mécanisme de formation et d'évolution du mélange air/carburant (au sein de la zone de mélange) et de son couplage avec la cinétique de combustion. Afin de s'affranchir des limitations liées au formalisme 0D (manque de notion d'espace), différents outils couramment adoptés en modélisation 3D ont été utilisés. La théorie relative aux PDF présumées a été adaptée au formalisme 0D pour la description de la distribution de la fraction de mélange dans la zone de mélange. Cette distribution est couplée avec la théorie relative à l'évaporation d'une goutte qui définit les états thermodynamiques caractérisant la composition locale du mélange. L'évolution temporelle du spray, en terme de volume et de masse de gaz entraîné, est déduite à partir des lois de conservation de la masse, de quantité de mouvement et d'énergie. Un modèle $\kappa - \epsilon$ adapté a été utilisé pour prendre en compte les effets de la turbulence dans le cylindre qui, dans les Moteurs à Combustion Interne (*ICE*), joue un rôle très important principalement en ce qui concerne le processus de mélange. La cinétique chimique, qui induit le taux de dégagement d'énergie, est déterminée en utilisant une méthode de tabulation de la chimie complexe inspirée de la méthode FPI (*Prolongation aux Flammes de la méthode ILDM Intrinsic Low Dimensional Manifold)*). Cette méthode permet de simuler une grande plage de régimes de combustion prenant en compte la présence de Gaz Brûlés Recirculés (*EGR*) dans le mélange de gaz. Les résultats du modèle 0D sont comparés avec les résultats du modèle 3D équivalent. Finalement, le modèle 0D est validé sur une large base de données expérimentales.

Abstract — A New 0D Diesel HCCI Combustion Model Derived from a 3D CFD Approach with Detailed Tabulated Chemistry — *This paper presents a new 0D phenomenological approach to the numerical modelling of Diesel HCCI combustion. The model is obtained through the reduction of*

TKI-PDF (Tabulated Kinetics for Ignition, coupled with presumed Probability Density Function) 3D CFD model developed at the IFP. Its formulation is based on physical considerations, to take into account the main phenomena and their mutual interactions that take place in the cylinder during the combustion process. Aspects relating to spray penetration, fuel evaporation, turbulence, mixture formation and chemical kinetics have been studied in detail. The original contribution of this work concerns the modelling of the formation and evolution of the equivalence ratio stratification around the spray, and of its connection to combustion kinetics. In order to achieve this, different tools commonly adopted in 3D modelling have been adapted to 0D modelling. Presumed PDF theory has been extended to a 0D formalism in order to characterize the mixture-fraction distribution. This approach has then been coupled with droplet-evaporation theory in order to have access to the thermodynamic conditions characterizing the mixture. The temporal evolution of the spray is computed in terms of volume and the entrained mass of gases, starting from conservation laws for mass, momentum and energy. An adapted $\kappa - \epsilon$ *model is used to take into account the turbulence in the cylinder, which is very important, in an ICE (Internal Combustion Engine), especially during the mixing process. Further, combustion heat-release is computed using an adapted detailed tabulated chemistry method inspired by the FPI (Flame Prolongation of ILDM (Intrinsic Low Dimensional Manifold)) theory. This look-up table allows the simulation of a large range of combustion regimes, since it takes into account the presence of EGR (Exhaust Gas Recirculation) in the mixture. The results of the 0D model are compared in an initial step to the 3D CFD results. Finally, the OD model is validated against a wide experimental database.*

NOMENCLATURE

Latin abbreviations

a	[–]	constant coefficient (a = 0.66)
b	[–]	constant coefficient (b = 0.41)
B	[–]	transfer number at steady-state
B_m	[–]	mass transfer number
B_t	[–]	thermal transfer number
c	[–]	progress variable
C_a	[–]	orifice area-contraction coefficient
C_d	[–]	orifice discharge coefficient
C_{diss}	[–]	$\widetilde{Z"^2}$ dissipation-term coefficient
C_{ev}	[–]	evaporation-rate coefficient
C_K	[–]	$\tilde{K}$ dissipation-term coefficient
C_p	[J/kg/K]	constant pressure specific heat
C_v	[J/kg/K]	constant volume specific heat
C_θ	[–]	spray opening-angle coefficient
C_κ	[–]	$\tilde{\kappa}$ dissipation-term coefficient
d_h	[m]	injector hole diameter
D	[m]	droplet diameter
E_c	[J]	kinetic energy
h	[J/kg]	enthalpy
k	[J/m/s/K]	thermal conductivity
$\tilde{K}$	[J/kg]	mean specific kinetic energy
L	[m]	liquid-phase fuel penetration
L_v	[J/kg]	latent heat of vaporization
Le	[–]	Lewis number
m	[kg]	mass
m_a	[kg]	stoichiometric mass of air
m_{cyl}	[kg]	total in-cylinder gaseous mass
M	[kg/mol]	molar mass
n	[mol]	mole number
n_h	[m]	number of injector holes
N_K	[–]	$\tilde{K}$ dissipation-term exponent
N_κ	[–]	$\tilde{\kappa}$ dissipation-term exponent
p	[Pa]	pressure
p_{cr}	[Pa]	critical pressure
p_v	[Pa]	fuel vapor pressure
$\mathcal{P}$	[–]	probability function
$\mathcal{P}_{co}$	[–]	coupled probability function
q	[–]	constant coefficient (q = 2.2)
Q_{ev}	[J/s]	fuel evaporation thermal flux
Q_{hu}	[J/s]	fuel heat up thermal flux
Q_{th}	[J/s]	exchanged thermal flux
Q_{tot}	[J/s]	total thermal flux
r	[m]	radius
$\mathcal{R}$	[J/mol/K]	universal gas constant
s	[–]	mass stoichiometric coefficient
S	[m]	spray penetration
t^+	[s]	spray characteristic time-scale
t_{inj}	[s]	relative injection time
T	[K]	temperature
T_b	[K]	normal boiling temperature
T_{cr}	[K]	critical temperature
U_{F_l}	[m/s]	fuel injection velocity
v	[m^3/mol]	molar volume
V	[m^3]	cylinder volume
V_S	[m^3]	spray volume
x^+	[m]	spray characteristic length-scale
x_0	[m]	removed cone height
X	[–]	molar fraction
Y	[–]	mass fraction
Y_{lc}	[–]	mass fraction linear combination
Z	[–]	mixture fraction
$\widetilde{Z"^2}$	[–]	mixture fraction variance

Greek abbreviations

δ	[−]	segregation factor
$\tilde{\epsilon}$	[J/kg/s]	$\tilde{\kappa}$ dissipation rate
θ	[rad]	spray opening angle
$\tilde{\kappa}$	[J/kg]	specific turbulent kinetic energy
λ	[m^2/s]	evaporation constant
ν	[mol]	stoichiometric molar coefficient
ρ	[kg/m^3]	density
σ	[−]	weighting coefficient
τ_{ev}	[s]	characteristic time of evaporation
τ_t	[s]	turbulence characteristic time
φ	[−]	Schwab-Zeldovitch variable
Φ	[−]	equivalence ratio
ψ	[−]	Dirac function
ω	[kg/s]	reaction rate
Ω_{SRK}	[−]	acentric factor

Superscripts

S/I	higher/lower Φ tabulated values
0	Φ reference value

Subscripts

A	ambient gas
c	complementary mixture-fraction
ds	dissipation term
eq	chemical equilibrium conditions
esp	species
F	gaseous fuel
F_{inj}	injected fuel
F_l	liquid fuel
g	equivalent mixture
i/o	inlet/outlet
m	mass diffusion boundary layer
max	maximum value
mix	mixture
O	oxidizer
pr	production term
r	EGR
s	liquid-gas interface
S	spray
S/I	higher/lower X_r tabulated values
t	thermal diffusion boundary layer
w	withdrawn ambient gas
$\beta - PDF$	normalized $\beta - PDF$ variables
τ	tracer (non reactive) conditions
0	reference value
1/3	1/3 *law* reference variable
∞	condition at infinity

INTRODUCTION

Numerical simulation plays an increasingly important role in engine development processes; its most important advantage being due to the fact that, it is possible to perform a great number of numerical tests, at costs that are much lower than those associated with experiments. This becomes particularly important with future generations of ICE. In fact, in order to obtain best performance, engines are increasingly composed of complex system-layouts involving a great number of devices such as an EGR system, a CR (*Common Rail*) Direct Injection System, etc. Such systems need to be optimized [1-4].

In this context, a numerical engine simulator must be able to give an accurate estimate of the main values characterizing the performance of the engine, such as combustion heat release, combustion efficiency, and pollutant formation.

In the literature concerning both conventional Diesel and HCCI (*Homogeneous Charge Compression Ignition*) combustion, it is possible to distinguish two main classes of models, according to their purpose. The first class includes models adapted to global system simulation. Models in this class give access to fewer details of the combustion process, but lesser CPU times are required. Usually in this domain tabulated-base, empirical or phenomenological approaches are used [5-20]. The second class includes models adapted for research purposes. Models in this class give access to greater detail in the combustion process, but much more CPU time is required. Usually in this domain physical approaches are used [21-38].

This paper presents a new 0D approach to the modelling of Diesel HCCI combustion derived from the reduction of a 3D CFD model. The new model is able to accurately predict the combustion process, while requiring low CPU resources. These two aspects outline a model profile adapted to global-system simulation applications. In the following, a global overview of the model is given first. The two main parts of the model are subsequently presented and detailed: the spray and the combustion modelling. Partial validations of these models have been performed using 3D results and experimental data. Finally, validation of the global combustion model is done by comparison with experimental results. The paper ends with a discussion of the model improvements and perspectives.

1 GLOBAL OVERVIEW OF THE MODEL

Conventional Diesel and HCCI combustion modes are governed by different physical mechanisms.

In conventional Diesel combustion, the mixture inside the cylinder is characterized by a high fuel mass fraction stratification. The first site of auto-ignition appears inside the spray, where chemical and thermodynamic conditions are the most favourable. The most important challenge concerning auto-ignition phase description is to capture the shortest ignition delay. Heat release, due to combustion at the first site, subsequently favors the multiplication of auto-ignition sites. This chain reaction leads to the sharp heat release process typical of the premixed Diesel combustion phase. The remaining fuel burns in a diffusion flame and the heat release is governed by the mixing process. In this phase, turbulence plays the most important role.

In HCCI combustion, the mixture inside the cylinder can be considered as homogeneous. Hence chemical kinetics plays the most important role in the combustion process. Because of the homogeneity of the mixture, all of the gas auto-ignites simultaneously. As a consequence, HCCI combustion is characterized by a stiff heat release process. For these reasons, a deep understanding of the spray formation mechanic is necessary [39-44].

In a general situation, the two combustion regimes are not so well distinguished. A modelling challenge, therefore, is to be able to manage all of the different scenarios. Moreover, the presence of EGR in the cylinder modifies the chemical kinetics, and phenomena, such as cold flames, could appear at the beginning of the fuel oxidation process.

The original modelling solution proposed in this work is derived from a reduction of the TKI-PDF 3D CFD model [33, 34, 45]. It has the potential to take into account all of the different phenomena, taking advantage of the common tools used in sub-grid 3D modelling. The first of these is the use of a presumed PDF [12, 13, 46] in order to describe the distribution of fuel inside the spray region. The second is the use of a look-up table in order to take chemical kinetics into account This technique has been inspired by the FPI theory [47]. The third tool is the use of an adapted $\kappa - \epsilon$ model to simulate the impact of turbulence on the mixing and combustion processes.

The synoptical diagram of the complete Diesel HCCI combustion model is presented in Figure 1. As shown, the model is composed mainly of two parts, namely spray modelling and combustion modelling (these will be described in further detail in Sect. 2 and 3 respectively).

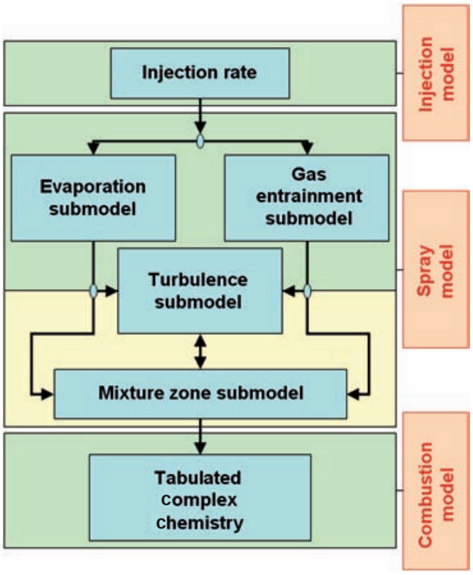

Figure 1

Synoptical diagram of the complete Diesel HCCI combustion model.

The purpose of spray modelling is to represent the formation and the temporal evolution of the spray volume (mixture zone), and to give constant access to the total spray mass and fuel mass-fraction distribution inside the spray. As shown in Figure 1, this model has only one input variable: the fuel injection-rate. The mixture zone has two mass sources: one is the evaporation from liquid fuel injected into the cylinder, and the other is the entrained fresh gas (in the most general case, it is a perfectly stirred mixture of air and EGR). The mixing process of gaseous fuel and fresh gas takes place in the spray volume and is controlled by turbulence. As shown in the diagram, the turbulence submodel has two inputs: one is the kinetic energy contribution associated with the injected mass of fuel and the other is the kinetic energy contribution associated with the entrained fresh gas. The mixture stratification within the spray volume is represented by a presumed PDF. The temporal evolution of the PDF shape is governed by the mass flow-rates concerning the mixture zone and the turbulence intensity. The output of the spray model is the complete spray description. It consists of quantifying the total gaseous mass contained in the mixing zone, and characterizing the fuel mass-fraction distribution inside it as well as the associated temperature field.

The goal of the combustion model is to describe the chemical composition of the mixture and the oxidation process as a function of the in-cylinder thermodynamic conditions. As shown in Figure 1, the only input required for the combustion model is the spray characterization given by the spray model. The outputs of the combustion model are the heat release and the temporal evolution of the species masses during combustion.

2 SPRAY MODELLING

As shown in Figure 1, the spray model contains four submodels (directional arrows indicate the different interactions):

- The *evaporation submodel (Sect. 2.1)*: this model computes the thermodynamic conditions at the liquid-gas interface during the evaporation process, and quantifies the liquid-fuel-mass evaporation-rate. It also gives qualitative information regarding the penetration length of the liquid fuel jet.
- The *gas entrainment submodel (Sect. 2.2)*: this model computes the entrainment of fresh air in the mixture zone. It also gives quantitative information regarding the penetration length and the volume growth of the spray.
- The *turbulence submodel (Sect. 2.3)*: the goal of this model is to compute the characteristic frequency of the turbulence, which is directly connected with the turbulent mixing process of gaseous fuel and fresh gas (air

and eventually EGR). As well known in ICE combustion, molecular diffusion of species is negligible compared to the turbulent one: for this reason molecular diffusion will not be considered [48].

- The *mixture submodel (Sect. 2.4)*: the role of this model is to quantify the total mass in the mixture zone and to characterize the temporal evolution of the fuel mass fraction distribution.

2.1 Evaporation Submodel

The evaporation submodel has two main purposes: firstly, to compute the thermodynamic states of the fluids at the liquid-gas interface, and secondly to quantify the mass evaporation rate of the injected liquid fuel. The evaporation of droplets in a spray simultaneously involves heat and mass transfer processes. The overall rate of evaporation depends on many factors, such as pressure, temperature and transport properties of fluids, drop geometry and relative velocity of drops respective to the ambient gas. In the case of a droplet immersed in a gas at a higher temperature, part of the heat flux increases the droplet temperature, Q_{hu}, and the rest evaporates it. At steady-state, the droplet temperature reaches its *wet-bulb* value and all the heat is used for the evaporation process. When steady state conditions are established, the drop diameter, D, diminishes with time according to the well-established D^2 *law*:

$$\frac{dD^2}{dt} = -\lambda \tag{1}$$

where λ is the evaporation constant.

The thermodynamic interfacial conditions are determined using the approach proposed in [49]. It describes the evaporation process, in steady-state conditions, of a single spherical liquid drop of pure fuel at rest in a gaseous mixture with a given composition, Figure 2. In such conditions, it is possible to define a mass transfer number, B_m, and a thermal transfer number, B_t, characterizing the mass and thermal boundary layers respectively, as follows:

$$B_m = \frac{Y_{F_s} - Y_{F_\infty}}{1 - Y_{F_s}} \quad \text{and} \quad B_t = \frac{C_{p_g} \cdot (T_\infty - T_s)}{L_{v_s}} \tag{2}$$

where Y_{F_s} and Y_{F_∞} are the fuel mass fractions of the mixture at the interface and ambient gas conditions respectively. T_s and T_∞ are the temperature of the mixture at the interface and ambient gas conditions respectively, and L_{v_s} is the latent vaporization heat of the liquid at the interface temperature, computed using the Watson relation [50]. C_{p_g} is the equivalent gas mixture heat-capacity at constant pressure computed using the $1/3$ *law* proposed by Sparrow and Gregg [49]. According to this law, average properties of the mixture are evaluated at reference temperature and composition defined as:

$$T_{1/3} = T_s + \frac{T_\infty - T_s}{3} \quad \text{and} \quad Y_{F_{1/3}} = Y_{F_s} + \frac{Y_{F_\infty} - Y_{F_s}}{3} \tag{3}$$

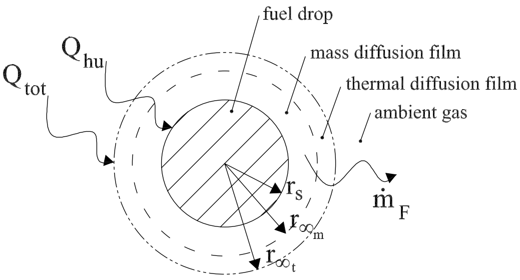

Figure 2

Evaporation model of a liquid fuel drop.

Consequently, the reference ambient-gas mass-fraction, $Y_{A_{1/3}}$, is given by the relation:

$$Y_{A_{1/3}} = 1 - Y_{F_{1/3}} \tag{4}$$

At infinite distance from the drop, fuel concentration is assumed to be zero. C_{p_g} is then obtained as:

$$C_{p_g} = Y_{A_{1/3}} \cdot \left(C_{pA}\left(T_{1/3}\right)\right) + Y_{F_{1/3}} \cdot \left(C_{pF}\left(T_{1/3}\right)\right) \tag{5}$$

where C_{p_A} and C_{p_F} are the heat-capacities of the ambient gas and of the gaseous fuel respectively.

According to [49], steady-state conditions hold:

$$B_m = B_t = B \tag{6}$$

The system is solved iteratively varying the value of T_s in order to verify Equation (6). With a maximum absolute error of $1e^{-5}$, the number of iterations necessary to satisfy Equation (6) varies around 18. The link between the two transfer numbers is detailed as follows. At a given fuel saturation temperature at the liquid-gas interface, T_s, the fuel vapor pressure, p_{v_s}, is estimated from the Clausius-Clapeyron equation as:

$$\ln(p_{v_R}) = h \cdot \left(1 - \frac{1}{T_R}\right) \quad \text{where} \quad h = T_{b_R} \cdot \frac{\ln\left(\frac{p_{cr}}{101325}\right)}{1 - T_{b_R}} \tag{7}$$

in which:

$$p_{v_R} = \frac{p_{v_s}}{p_{cr}}, \quad T_R = \frac{T_s}{T_{cr}} \quad \text{and} \quad T_{b_R} = \frac{T_b}{T_{cr}} \tag{8}$$

where T_b is the normal boiling temperature of the fuel, and p_{cr} and T_{cr} represent its critical pressure and temperature respectively. Fuel mass fraction at the interface can now be expressed as:

$$Y_{F_s} = \left[1 + \left(\frac{p_\infty}{p_{v_s}} - 1\right) \cdot \frac{M_A}{M_F}\right]^{-1} \tag{9}$$

where p_∞ is the ambient pressure and, M_A and M_F are molar masses of ambient gas and fuel respectively.

According to [49], the fuel mass flow rate, $\dot{m}_F$, can be computed as:

$$\dot{m}_F = 2 \cdot \pi \cdot \frac{D}{Le} \cdot \frac{k_g}{C_{p_g}} \cdot \ln(1 + B) \tag{10}$$

and the mass of fuel, m_F, constituting a drop of given diameter is:

$$m_F = \frac{\pi}{6} \cdot \rho_{F_l} \cdot D^3 \tag{11}$$

where k_g is the mixture thermal conductivity, computed using the $1/3$ *law*, Le is the Lewis number (here supposed equal to unity) and ρ_{F_l} is the density of the liquid fuel estimated using the Hankinson-Brobst-Thomson (HBT) relation [50]. HBT relation holds to:

$$\rho_{F_l} = \frac{M_F}{\upsilon_s} \tag{12}$$

in which υ_s is the molar volume of the liquid at the liquid-gas interface temperature, that can be computed as:

$$\upsilon_s = \upsilon_R^{(0)} \cdot \left[1 - \Omega_{SRK} \cdot \upsilon_R^{(\delta)}\right] \cdot \upsilon^* \tag{13}$$

where:

$$\upsilon^* = \frac{\mathcal{R} \cdot T_{cr}}{p_{cr}} \left(A + B \cdot \Omega_{SRK} + C \cdot \Omega_{SRK}^2\right) \tag{14}$$

$$\upsilon_R^{(0)} = 1 + a \cdot (1 - T_R)^{\frac{1}{3}} + b \cdot (1 - T_R)^{\frac{2}{3}} + c \cdot (1 - T_R) + d \cdot (1 - T_R)^{\frac{4}{3}} \tag{15}$$

$$\upsilon_R^{(\delta)} = \frac{\left[e + f \cdot T_R + g \cdot T_R^2 + h \cdot T_R^3\right]}{T_R - 1.00001} \tag{16}$$

and Ω_{SRK} is the acentric factor of the fuel. Moreover, the constant coefficients (that are valid for all hydrocarbons) assume the following values:

$$\begin{array}{lll} A = 0.2851686 & B = -0.0637911 & C = 0.0137917 \\ a = -1.52816 & b = 1.43907 & c = -0.81446 \\ d = 0.190454 & e = -0.296123 & f = 0.386914 \\ g = -0.0427258 & h = -0.0480645 & \end{array}$$

HBT correlation is valid in a temperature domain defined as:

$$0.25 < T_R < 1.0 \tag{17}$$

By differentiating Equation (11) and combining it with (1) and (10), it is possible to express the evaporation constant as:

$$\lambda = \frac{8 \cdot k_g \cdot \ln(1 + B)}{Le \cdot C_{p_g} \cdot \rho_{F_l}} \tag{18}$$

Figure 3 shows the dependence of the evaporation constant on the ambient pressure and temperature conditions for n-heptane. As shown, there is good agreement between the values computed by the model and experimental data [51].

Figure 4 shows the influence of ambient thermodynamic conditions on the mixture temperature at the liquid-gas interface. The computed thermochemical properties of the mixture at liquid-gas interface, such as Y_{F_s} and T_s, will be used in the mixture characterization model and in the combustion model. These models will be presented in Sections 2.4 and 3.3 respectively. In particular, T_s is a very important variable in the spray modelling, as it permits an estimate of the local temperature of the mixture. In what concerns the computation of the global fuel-mass evaporation-rate, several aspects must be highlighted. Equation (10) refers to single-drop evaporation. The real spray scenario is very different as droplet size distribution, ligaments and the undefined geometry of the liquid phase make it much more complicated. Consequently, because of its CPU cost, it can not be solved in a global-system simulation approach.

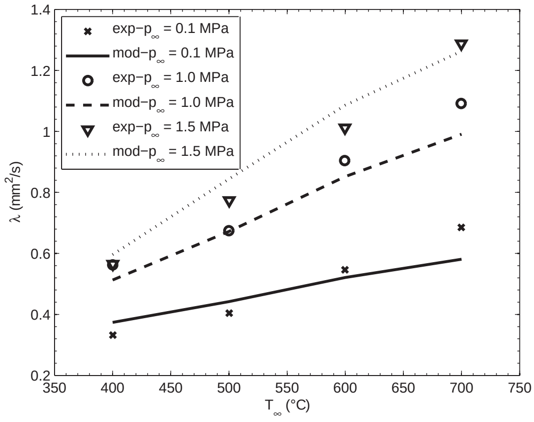

Figure 3

Dependence of the evaporation constant on the ambient conditions.

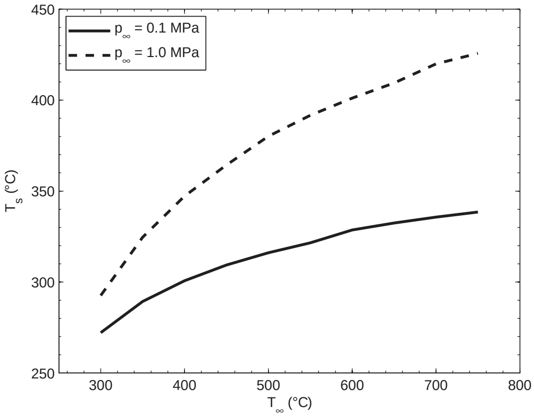

Figure 4

Dependence of the temperature at the liquid-gas interface on the ambient conditions.

For that reason, the global liquid-mass evaporation-rate has been estimated using a simpler approach, based on a characteristic time of evaporation, τ_{ev}:

$$\dot{m}_F = C_{ev}\cdot\frac{m_{F_l}}{\tau_{ev}} \tag{19}$$

where C_{ev} is a dimensionless coefficient and m_{F_l} is the liquid mass of fuel. In Section 4.1 the results of this model are compared with those of the 3D CFD code. The original method used to estimate the evaporation characteristic-time is an approach based on the theory proposed in [52, 53].

This theory permits an estimate to be made of the liquid penetration length in a pressurized vessel as a function of the injector geometry, and of the compositions of the fluids and their thermodynamic states. In this approach, the spatial, x^+, and temporal, t^+, scales are defined as:

$$x^+ = \frac{\sqrt{C_a}\cdot d_h\cdot\sqrt{\frac{\rho_{F_l}}{\rho_A}}}{a\cdot\tan\left(\frac{\theta}{2}\right)} \quad\text{and}\quad t^+ = \frac{x^+}{U_{F_l}} \tag{20}$$

where C_a is the orifice coefficient of area-contraction, d_h is the injector hole diameter, ρ_A is the ambient gas density, a is a dimensionless coefficient (authors recommend $a = 0.66$), θ is the opening angle of the spray (its definition will be given in Sect. 2.2), and U_{F_l} is the fuel velocity in the injector nozzle. The theoretical expression for the maximum liquid penetration, L, is given as:

$$L = \left(b\cdot\sqrt{\left(\frac{2}{B}+1\right)^2 - 1}\right)\cdot x^+ \tag{21}$$

where b is a dimensionless coefficient (authors recommend $b = 0.41$) and B is the transfer number computed using Equation (6).

τ_{ev} is computed by inverting the equation for the jet penetration length as a function of time and imposing a penetration length equal to L [13]. That means that τ_{ev} represents the time necessary to fully evaporate a droplet whose lifetime corresponds to a penetration equal to L, once the velocity law is known. The expression of τ_{ev} is:

$$\tau_{ev} = \tilde{\tau}_{ev}\cdot t^+ \tag{22}$$

where:

$$\begin{aligned}\tilde{\tau}_{ev} = {} & \frac{\tilde{L}}{2} + \frac{\tilde{L}}{4}\cdot\sqrt{1+16\cdot\tilde{L}^2} + \\ & + \frac{1}{16}\cdot\ln\left(4\cdot\tilde{L} + \sqrt{1+16\cdot\tilde{L}^2}\right)\end{aligned} \tag{23}$$

in which:

$$\tilde{L} = \frac{L}{x^+} \tag{24}$$

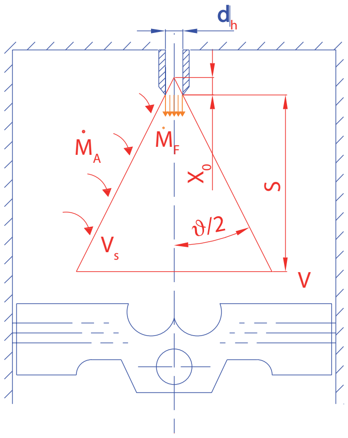

Figure 5

Spray volume description. Although the presence of two distinct volumes, the fresh-air and the spray volumes, the model is a one-zone approach. Hence, only one energy balance-equation is computed for all the in-cylinder gases.

2.2 Gas Entrainment Submodel

This submodel is based on the well known theory developed in [54] for estimating spray penetration and dispersion. The spray region is supposed to be a perfect truncated cone, Figure 5. Its volume, V_S, is completely defined by the height (spray penetration, S), and the angle (spray angle, θ).

These two variables depend on the nozzle geometry, the injection pressure, and the injected and ambient fluid thermodynamic states. They are determined from the following semi-empirical correlations:

$$S = \left[\left(\frac{1}{\frac{t_{inj}}{t^+}}\right)^q + \left(\frac{1}{\left(\frac{t_{inj}}{t^+}\right)^{\frac{1}{2}}}\right)^q\right]^{-\frac{1}{q}}\cdot x^+ \tag{25}$$

and:

$$\tan\left(\frac{\theta}{2}\right) = C_\theta\cdot\left[\left(\frac{\rho_A}{\rho_{F_l}}\right)^{0.19} - 0.0043\cdot\sqrt{\frac{\rho_{F_l}}{\rho_A}}\right] \tag{26}$$

where q is a dimensionless coefficient (authors recommend $q = 2.2$), t_{inj} is the relative time coordinate, with origin at the beginning of the injection, and C_θ is a constant coefficient. Hence:

$$V_S = \frac{\pi}{3}\cdot\tan^2\left(\frac{\theta}{2}\right)\cdot\left[(S+x_0)^3 - x_0^3\right] \tag{27}$$

with x_0 defined in Figure 5.

Through experimentation of injection in a constant volume vessel containing a gas at a given pressure and temperature, these correlations have been widely validated. Results are reported in various works by different authors [20, 42, 54, 55].

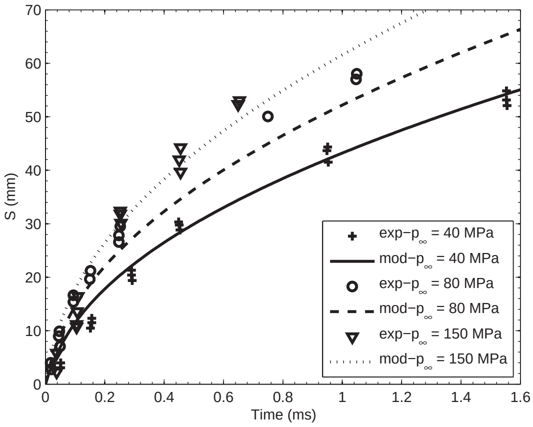

Figure 6

Vapor phase penetration.
n-heptane, $T_\infty = 387$ K, $\rho_A = 25$ kg/m^3.

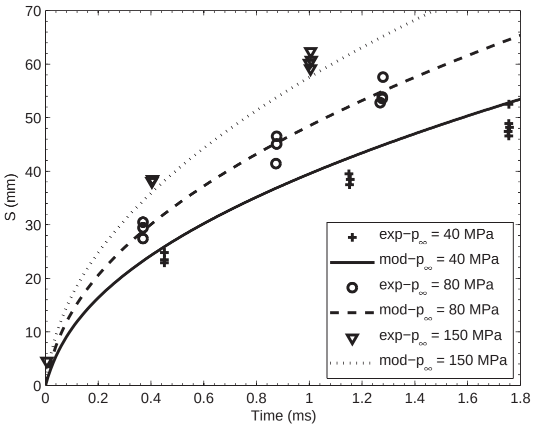

Figure 7

Vapor phase penetration.
n-heptane, $T_\infty = 800$ K, $\rho_A = 30$ kg/m^3.

Figures 6 and 7 compare the computed spray penetrations with experimental data obtained in a high pressure vessel [42]. The results are in good agreement with experiments. As can be seen, the model is sensitive to the variation of parameters such as injection pressure, nozzle geometry and the thermodynamic state of the ambient gas.

In ICE conditions, in-cylinder thermodynamic conditions vary in time because of the piston motion, thermal exchanges and combustion process. In order to take into account the time history of spray penetration, the differential form of Equation (27) has been implemented in the model. Consequently, the spray volume is computed as:

$$V_S = \int \dot{V}_S \cdot dt \tag{28}$$

The mass of entrained gas in the spray volume is deduced from geometrical considerations:

$$\frac{dm_A}{dt} = \rho_A \cdot \frac{dV_S}{dt} \tag{29}$$

where dm_A/dt is the entrained mass-flow-rate and ρ_A is the density of the gas still outside the spray region.

2.3 Turbulence Submodel

In ICE, turbulence plays a very important role, increasing mass, momentum and energy transfer-rates. The dynamics of turbulent motion can be described as follows. At first, kinetic energy associated with the mean flow is transferred to the large scales of the fluctuating motion (integral scale). After that, kinetic energy is transferred isentropically from large to small scales of turbulence (Kolmogorov scale). Finally, the kinetic energy is dissipated by viscous forces and is transformed into thermal energy. The aim of the turbulence submodel is to obtain an estimate of the turbulence characteristic time, τ_t, which is very important in the mixing process modelling.

The proposed approach is based on the well-known $\kappa - \epsilon$ turbulence-model theory. According to this theory, the kinetic energy is decomposed into two contributions:

- the mean kinetic energy, associated to the big structures of the mixture flow,
- the turbulent kinetic energy, associated to the local mixture velocity-fluctuations respect to the mean value.

The procedure to estimate τ_t is detailed in the following.

The turbulence submodel constitutes of two state variables: the spray global kinetic-energy, E_c, and the mean specific kinetic-energy, $\tilde{K}^{(1)}$.

2.3.1 Spray Global Kinetic-Energy

The spray global kinetic-energy rate can be most generally expressed as the sum of a production and a dissipation term:

$$\frac{dE_c}{dt} = \left.\frac{dE_c}{dt}\right|_{pr} + \left.\frac{dE_c}{dt}\right|_{ds} \tag{30}$$

The production term in an ICE application can be detailed as follows:

$$\left.\frac{dE_c}{dt}\right|_{pr} = \frac{dE_{c_{swirl}}}{dt} + \frac{dE_{c_{tumble}}}{dt} + \frac{dE_{c_{squish}}}{dt} + \frac{dE_{c_S}}{dt} \tag{31}$$

The spray energy, E_{c_S}, represents 98% of the total kinetic energy, according to [20]. For that reason, with good approximation, it is possible to affirm that:

$$\left.\frac{dE_c}{dt}\right|_{pr} \approx \frac{dE_{c_S}}{dt} = \frac{U_{F_l}^2}{2} \cdot \frac{dm_{F_{inj}}}{dt} \tag{32}$$

---

(1) The symbol *tilde* means that the mean kinetic energy value has been computed using the Favre mean operator.

in which:

$$U_{F_l} = \frac{1}{C_d \cdot n_h \cdot \rho_{F_l} \cdot \left(\frac{\pi}{4} \cdot d_h^2\right)} \cdot \frac{dm_{F_{inj}}}{dt} \tag{33}$$

where $m_{F_{inj}}$ is the mass of injected fuel, C_d is the discharge coefficient of the orifice and n_h is the number of holes of the nozzle.

The spray global kinetic-energy dissipation-term, mainly due to flow viscous forces, has been modeled by using empirical closure terms [13].

Equation (30) can now be rewritten as:

$$\frac{dE_c}{dt} = \frac{U_{F_l}^2}{2} \cdot \frac{dm_{F_{inj}}}{dt} - m_S \cdot \left(C_K \cdot \tilde{K}^{N_K} + C_\kappa \cdot \tilde{\kappa}^{N_\kappa}\right) \tag{34}$$

where m_S is the total mass of the spray, C_K and N_K are empirical dissipation-term constant-coefficients associated to the mean specific kinetic-energy, $\tilde{K}$, and C_κ and N_κ are empirical dissipation-term constant-coefficients associated to the mean specific turbulent kinetic-energy, $\tilde{\kappa}$.

2.3.2 Mean Specific Kinetic-Energy

Similarly to $\kappa - \epsilon$ theory, by spatially filtering the 3D momentum balance-equation, it is possible to obtain an expression for the temporal evolution of the mean specific kinetic-energy [13]:

$$\begin{aligned} \frac{d\tilde{K}}{dt} = \frac{\sqrt{2 \cdot \tilde{K}}}{m_S} \cdot \Bigg[U_{F_l} \cdot \frac{dm_{F_{inj}}}{dt} - \sqrt{2 \cdot \tilde{K}} \cdot \\ \cdot \left(\frac{dm_A}{dt} + \frac{dm_{F_{inj}}}{dt} \right) \Bigg] - C_K \cdot \tilde{K}^{N_K} \end{aligned} \tag{35}$$

where, as can be seen, the last right-hand-side term represents the mean specific kinetic-energy dissipation-term, already present in Equation (34). The filter size used to obtain Equation (35) is the spray volume, V_S.

2.3.3 Characteristic time of turbulence

It is now possible to compute the mean specific turbulent kinetic-energy value as:

$$\tilde{\kappa} = \frac{E_c}{m_S} - \tilde{K} \tag{36}$$

The term indicating the mean specific turbulent-kinetic-energy dissipation-rate, $\tilde{\epsilon}$, is supposed to have an expression similar to the one used to represent the dissipation rate of the mean specific kinetic-energy:

$$\tilde{\epsilon} = C_\kappa \cdot \tilde{\kappa}^{N_\kappa} \tag{37}$$

as shown in Equation (34).

According to the $\kappa - \epsilon$ turbulent model theory, the characteristic time associated to turbulence is defined as:

$$\tau_t = \frac{\tilde{\kappa}}{\tilde{\epsilon}} \tag{38}$$

The proposed 0D turbulence model, derived from the 3D approach, has the advantage of describing well the mechanism involving the transfer of kinetic energy in the frequency domain from large to small scales of turbulence due to the shear forces. Results concerning the turbulence submodel will be discussed in Section 4.1.

2.4 Mixture Submodel

One of the main issues in Diesel HCCI combustion modelling is that auto-ignition and combustion processes take place in stratified-mixture conditions. In order to define a model able to predict both these phenomena, the modelling of the mixture stratification is of primary importance. To improve this aspect in the model, one solution is to use a presumed PDF approach, commonly used in 3D codes, which describes the mixture stratification using a statistical tool. A PDF is then used to estimate several local variables, such as mixture composition, temperature or reaction rates. Moreover, using the PDF approach implies the addition of only one more state variable and, as a results, a minimum impact on the differential equation system size and consequently on the CPU time cost.

2.4.1 Mixture Fraction Variable

According to the theory developed to study the laminar diffusion flame [48], combining the transport equations of fuel mass fraction, Y_F, and oxidizer mass fraction, Y_O, it is possible to define a combustion-independent scalar (Schwab-Zeldovitch variable), φ, as:

$$\varphi = Y_F - \frac{Y_O}{s} \tag{39}$$

where s, the mass stoichiometric coefficient, is defined as:

$$s = \frac{\nu_O}{\nu_F} \cdot \frac{M_O}{M_F} \tag{40}$$

Here, ν_i represents the molar coefficient of the stoichiometric combustion reaction and M_i is the species molar weight.

The normalization of the variable φ with the mass fractions relative to the fuel and oxidizer streams gives the mixture fraction variable, Z, whose values through the diffusive layer vary between 0, in pure oxidizer, and 1, in pure fuel. Z can be expressed as:

$$Z = \frac{\Phi \cdot \frac{Y_F}{Y_{F_0}} - \frac{Y_O}{Y_{O_0}} + 1}{\Phi + 1} \tag{41}$$

where Y_{F_0} is the fuel mass fraction in the fuel feeding stream and Y_{O_0} is the oxydizer mass fraction in the oxydizer stream. Φ is the equivalence ratio of the nonpremixed flame defined as:

$$\Phi = \frac{Y_{F_0}}{Y_{O_0}} \cdot s \tag{42}$$

It is possible to demonstrate that:

$$Z = Y_{F_\tau} \tag{43}$$

where Y_{F_τ} is the fuel-tracer mass-fraction, that is the local fuel mass-fraction in the case of a non-reactive mixture.

2.4.2 Presumed PDF

Different kinds of PDF are available in the literature. In order to simulate the mixing process taking place in diffusion flames, the PDF described by a β-function has been judged the best adapted [56]. A β-PDF function is a normalized statistical tool representing the probability, $\mathcal{P}(X^*)$, of a generic variable X, defined in its own domain of existence $(0 \leq X \leq 1)$.

A β-PDF is completely described by two parameters. The first one is the mean value of the distribution, $\overline{X}$, defined as:

$$\overline{X} = \int_0^1 X^* \cdot \mathcal{P}(X^*) \cdot dX^* \tag{44}$$

and the second is the segregation factor of the distribution, δ, defined as:

$$\delta = \frac{\overline{X'^2}}{\overline{X'^2}_{max}} \tag{45}$$

where $\overline{X'^2}$ is the value of the variance of the distribution computed as:

$$\overline{X'^2} = \int_0^1 (X^* - \overline{X})^2 \cdot \mathcal{P}(X^*) \cdot dX^* \tag{46}$$

and $\overline{X'^2}_{max}$ is the maximum value of the variance defined as:

$$\overline{X'^2}_{max} = \overline{X} \cdot (1 - \overline{X}) \tag{47}$$

The mathematical expression of $\mathcal{P}(X)$ is:

$$\mathcal{P}(X^*) = \frac{\Gamma(\alpha + \beta)}{\Gamma(\alpha) \cdot \Gamma(\beta)} \cdot X^{*^{\alpha-1}} \cdot (1 - X^*)^{\beta-1} \tag{48}$$

with:

$$\Gamma(a) = \int_0^{+\infty} e^{-t} \cdot t^{a-1} \cdot dt \tag{49}$$

and the coefficients α and β are defined as:

$$\alpha = \overline{X} \cdot \left[\frac{1}{\delta} - 1\right] \quad \text{and} \quad \beta = \frac{1}{\overline{X}} - \alpha \tag{50}$$

Figure 8 shows the typical evolution of the β-PDF.

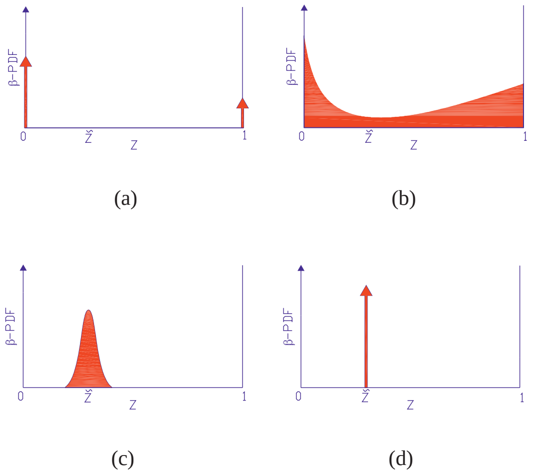

(a) (b)

(c) (d)

Figure 8

Representation of $\beta - PDF$ evolution. At the beginning representing a perfectly unmixed mixture (a); at an intermediary stage still presenting two peaks of mixture fraction (b); at an intermediary stage presenting one peak of mixture fraction (c); and at the end of the mixing process a perfectly stirred mixture (d).

The studied configuration is representative of the mixing process taking place in a closed constant volume initially containing pure fuel and oxidizer. The value of $\tilde{Z}$ is constant in time once the mass proportion of the two gases is fixed. $\tilde{Z}$ can be computed as:

$$\tilde{Z} = \frac{m_F}{m_F + m_O} \tag{51}$$

At $t = 0$, the oxidizer and fuel are perfectly unmixed ($\delta = 1$). In this case, β-PDF presents two peaks: one representing the pure oxidizer (at $Z = 0$), and the other representing the pure fuel (at $Z = 1$). At times t_1 and t_2, two intermediary configurations are presented. The mixing process is going on so consequently δ decreases; β-PDF is a continuous curve. At $t = t_{end}$, the mixture is perfectly stirred, and in this case, β-PDF presents one peak centered at $\tilde{Z}$.

2.4.3 Application of the Submodel to ICE

As shown in the previous paragraph, β-PDF is a tool potentially adapted to reproduce the mixture stratification evolution during a mixing process. The last step in completing the mixture model is to determine the equations giving the temporal evolution of these two parameters defining the PDF (and so of the mixture stratification). For the sake of clarity, it is important to remember that the mixture submodel details the gas mixture composition inside the spray volume.

Compared with the previous example, referred to two perfectly-unmixed gases in a closed constant-volume, the ICE application is much more complicated:

- both volume and total mass grow in time,
- the upper limit of the mixture-fraction existence-domain, Z_s, that corresponds to the value Y_{F_s} computed by the evaporation submodel, evolves in time as a function of the in-cylinder thermodynamic conditions,
- the fuel/ambient gas ratio, and so likewise the mean value of the mixture fraction, varies in time.

Distribution Mean Value Equation

The mean value is computed as the ratio of the total fuel-evaporated mass, m_F, and the total mass of gas in the spray volume, m_S:

$$\tilde{Z} = \frac{m_F}{m_S} = \frac{m_F}{m_F + m_A} \tag{52}$$

m_F and m_A are obtained by integration of the evaporation and entrainment gas submodel-outputs respectively, Figure 1.

Distribution Variance Equation

By definition, the variance of the distribution of Z in the spray is:

$$\widetilde{Z''^2} = \frac{1}{m_S} \cdot \int_{m_S} \left(Z|_{dm} - \tilde{Z}\right)^2 \cdot dm \tag{53}$$

Differentiating this expression (2) [13]:

$$\frac{d\widetilde{Z''^2}}{dt} = \underbrace{-2 \cdot C_{diss} \cdot \frac{\widetilde{Z''^2}}{\frac{\tilde{k}}{\tilde{\epsilon}}}}_{I} + \underbrace{\frac{1}{m_S} \cdot \left(\tilde{Z}^2 - \widetilde{Z''^2}\right) \cdot \frac{dm_A}{dt}}_{II} + \underbrace{\frac{1}{m_S} \cdot \left(\tilde{Z}^2 \cdot \left(1 - \frac{1}{Z_s}\right) + \left(Z_s - \tilde{Z}\right)^2 \cdot \frac{1}{Z_s} - \widetilde{Z''^2}\right) \cdot \frac{dm_F}{dt}}_{III} \tag{54}$$

The use of the β-function to represent the PDF, as already seen, brings several positive aspects, but also imposes some limitations on the mixture-distribution description. For example, Figure 9 shows a situation that cannot be represented by a β-function. To reduce the impact of these limitations on modelling, in the following the upper limit of the distribution domain will be considered as constant and equal to the maximum value reached during the evaporation process, $Z_{s_{max}}$.

In Equation (54), it is possible to distinguish three contributions. The first term, I, corresponds to the mixing-process contribution (term of dissipation of the variance). It is only thought to depend on turbulence and it is proportional to the turbulence characteristic-frequency via the C_{diss} coefficient.

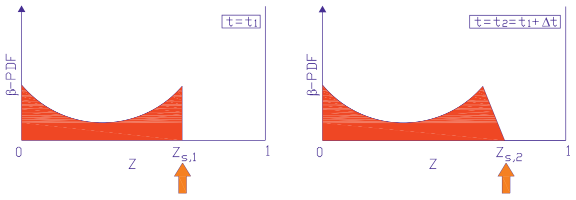

(a) (b)

Figure 9

Representation of $\beta - PDF$ limitation: mixture fraction distribution at the instant $t = t_1$ (a), mixture fraction distribution at the instant $t = t_2 = t_1 + \Delta t$ (b). During Δt temperature increases and liquid fuel evaporates at $Z = Z_{s,2}$.

The second term, II, corresponds to the entrained ambient-gas contribution. The last term, III, corresponds to the fuel-evaporation contribution. In this term, it has been done on the assumption that liquid fuel evaporates at saturated thermodynamic conditions in pure ambient gas.

β-PDF Parameters

Once the mean value and the variance of the mass fraction distribution have been computed, they have to be normalized in order to be adapted for use with a presumed PDF.

The proposed normalization takes into account the fact that $Z_{s_{max}}$ can be smaller than unity. Mean value and variance are respectively normalized as follows:

$$\tilde{Z}_{\beta-PDF} = \frac{\tilde{Z}}{Z_{s_{max}}} \tag{55}$$

and:

$$\delta_{\beta-PDF} = \frac{\widetilde{Z''^2}}{\widetilde{Z''^2}_{max}} = \frac{\widetilde{Z''^2}}{\tilde{Z} \cdot \left(Z_{s_{max}} - \tilde{Z}\right)} \tag{56}$$

The evaporation of the liquid fuel in the cylinder, especially during combustion, takes place under transcritical or supercritical conditions [57, 58]. The evaporation approach proposed in this work is not adapted to describe the evaporation process under these conditions, for the following reasons:

- the perfect gas hypothesis is no longer valid,
- Clapeyron's law is not valid,
- the ambient-gas dissolution in liquid is no longer negligible,
- the concept of a liquid-gas interface vanishes.

According to [57, 59], using a subcritical evaporation model instead of a tran/super-critical one leads to an underestimation of the value of the maximum fuel mass-fraction. For these reasons the maximum value of fuel mass-fraction

---

(2) Complete proof of Equation (54) is given in Appendix.

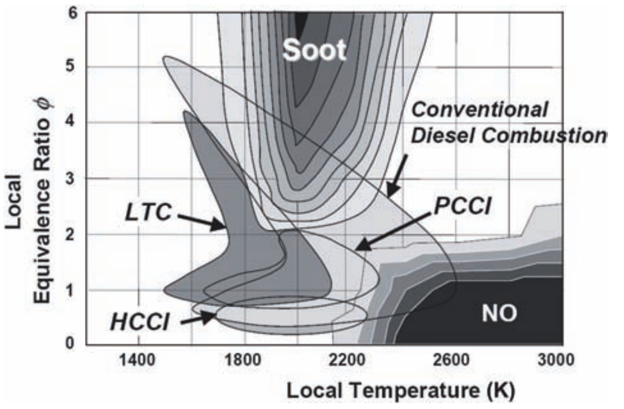

Figure 10

PCCI, LTC and HCCI concept on a $\Phi - T$ map [60].

has been arbitrarily imposed as equal to unity. This assumption will be partially justified in the following by showing the good agreement between the evolutions of the fuel mixture-fraction distributions computed by the 0D and 3D models, Section 4.1.

3 COMBUSTION MODELLING

3.1 Complex Chemistry Approach Motivation

The second part of the Diesel HCCI combustion model, Figure 1, concerns the modelling of the combustion process. Due to the limitations on pollutant emissions, a deeper understanding on the pollutant formation mechanisms must be achieved. The introduction of non-conventional combustion regimes is seen as a possible key point.

This is the case for PCCI (*Premixed Controlled Compression Ignition*), LTC (*Low Temperature Combustion*) and HCCI combustions, Figure 10 [60]. As shown, the tendency is to obtain a combustion process characterized by lower temperatures and a higher level of local air-excess ratio, in order to get off the region relative to NO_x and *soot* emissions. Nowadays, to reduce the combustion temperatures, it is usual to dilute the fuel-air mixture with EGR because of its high specific heat-capacity and immediate availability. The EGR dilution effect has a direct impact on the chemical kinetics of combustion. In particular, it slows the formation process of active radicals of combustion and reduces their local concentration. It is common, by using high EGR rates, to split the heat release process into two stages: the first, called cold flame, associated to the fuel decomposition in intermediary species; and the second, called main flame, associated to the oxidation process.

To predict all of these scenarios, a complex chemistry approach is required. Figure 11 shows the temperature evolutions relative to two examples of combustion processes performed with SENKIN from CHEMKIN [61]. Both configurations are relative to the combustion of a homogeneous fuel/air mixture in an adiabatic constant-volume reactor. Initial conditions do not change between the two configurations, except for the EGR dilution rate. Nevertheless, in the configuration with a higher EGR rate, it is possible to clearly distinguish the two-step auto-ignition process and the reduction of the final combustion temperature.

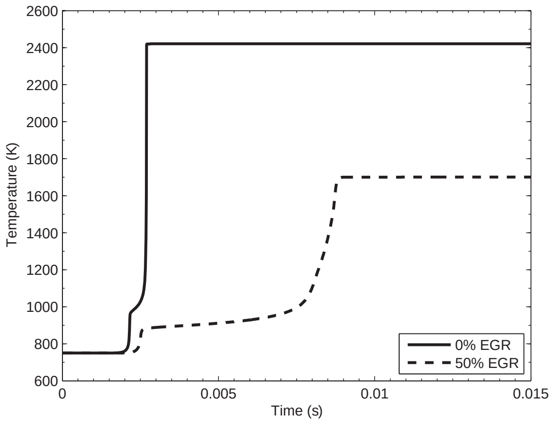

Figure 11

Results from SENKIN for EGR rate influence on auto-ignition of a perfectly stirred mixture of $n\text{-}heptane/air/EGR$ in a constant volume reactor. Initial states: $T_0 = 750$ K, $p_0 = 25$ bar, $\Phi = 0.6$, and $X_r = 0\%$ and 50% for solid and dashed lines respectively.

3.2 Tabulation Methodology

Commercial Diesel fuel is not a pure hydrocarbon but a mixture of many different ones; moreover, a univocal definition of Diesel fuel does not exist. Nevertheless the mixture, in order to be commercialized as Diesel fuel, must respect rigorous specifications.

A Diesel fuel-surrogate is often adopted in combustion modelling. It is usually a pure fuel that presents the same auto-ignition properties as the real fuel. For this paper n-heptane has been chosen as the Diesel fuel substitute.

In literature several complex chemical kinetics schemes exist for n-heptane. Here, the complete scheme proposed in [62] involving 544 species and 2446 reactions has been chosen. In a 0D model dedicated to a global-system simulation context, in which the CPU computation-cost is a first order evaluation parameter, it is an unreasonable choice to solve the complete chemical scheme. Hence a tabulated chemistry method, inspired by 3D approaches [45], has been set up.

In 1992, [63, 64] have demonstrated the existence of attractive trajectories, in the chemical phase space. Based on this, they proposed a theory to simplify the chemical kinetics description, namely the ILDM method. In 2000,

[47] proposed to extend this theory by prolonging trajectories with premixed laminar-flame computations: the FPI method. In 2004, [65] replaced premixed laminar flames with auto-ignition flames, and obtained good results on auto-ignition prediction.

To establish the look-up table, it is necessary to define the main species involved in the chemical scheme. The choice of these species is crucial, because their evolutions have to be sufficient to represent the whole chemical scheme. Here, 8 major species have been identified from mass and energy considerations: C_7H_{16}, N_2, O_2, H_2O, CO_2, CO, H_2 and H [20].

The thermochemical state of the gaseous mixture of fuel, air and EGR can be completely described with the following four parameters:

- p_0: pressure,
- T_0: temperature,
- Φ: equivalence ratio,
- X_r: molar EGR rate in ambient gas. It is defined as:

$$X_r = 1 - \frac{4.76 \cdot X_{O_2}}{1 - X_F} \tag{57}$$

where X_{O_2} and X_F are the oxygen and fuel molar-fractions respectively.

They constitute an orthogonal base in the phase space, and they have been chosen as inputs of the table. In order to describe the progress of the combustion process, a fifth parameter representing the progress variable, c, is necessary.

The progress variable must satisfy the following properties:

- c varies in a closed interval between 0 and 1: 0 in the fresh gases and 1 in the burnt gases,
- c must be monotonic with the progress of combustion,
- c must be representative of all main reactions.

The generic definition of c used in a FPI approach is:

$$c = \frac{Y_{lc}(t) - Y_{lc}(t=0)}{Y_{lc}(t_{eq}) - Y_{lc}(t=0)} \tag{58}$$

with the mass fraction linear combination, Y_{lc}, expressed as:

$$Y_{lc} = \sum_{esp=1}^{N} \sigma_{esp} \cdot Y_{esp} \tag{59}$$

where t_{eq} stands for the time necessary to reach the chemical equilibrium, σ_{esp} is a coefficient depending on the species and N is the number of species.

According to [13], in the model, Y has been defined as:

$$Y_{lc}(t) = -Y_{O_2}(t) + Y_{CO}(t) + Y_{CO_2}(t) \tag{60}$$

The reaction rate associated with a given species is expressed as:

$$\omega_{esp} = \omega_{esp}\left(p_0, T_0, \Phi, X_r, c\right) \tag{61}$$

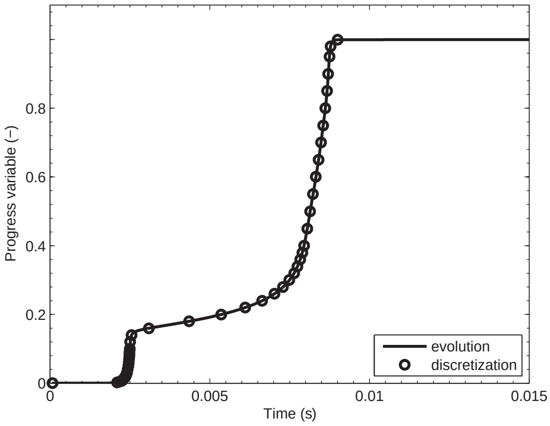

Figure 12

Progress variable discretization. The curve refers to the combustion process of a perfectly stirred mixture of *n-heptane*/*air*/*EGR* in a constant volume reactor. Initial state: $T_0 = 750$ K, $p_0 = 25$ bar, $\Phi = 0.6$, and $X_r = 50\%$.

All the criteria necessary to set up the table are now defined. It remains to define the limits and the discretization of the look-up table domain. They are chosen in order to obtain the best compromise between accuracy and table size. In the model, the following choices have been made:

- 8 initial pressure values chosen in the interval between 10 bar and 90 bar,
- 54 initial temperature values chosen in the interval between 600 K and 1600 K,
- 6 equivalence ratio values chosen in the interval between 0.3 and 3,
- 5 molar EGR rate values chosen in the interval between 0% and 90%,

These correspond to an initial condition map of 12960 operating points. The combustion process computation using SENKIN is then performed at each operating point, considering a perfectly stirred constant-volume reactor and adopting the complete chemical kinetics scheme. From each simulation the evolution of the progress variable is determined and discretized in 44 points (fifth table input). Finally, the table is filled up with the reaction rates of each tabulated species. Figure 12 shows the discretization of the temporal progress variable evolution.

Among the eight major species retained, only four have been tabulated: O_2, CO, CO_2 and H. The others are determined using C, O, H and N atomic balance equations. For example the carbon atomic balance equation is:

$$\frac{d}{dt}\left(7 \cdot X_{C_7H_{16}} + X_{CO_2} + X_{CO}\right) = 0 \tag{62}$$

This tabulation method for n-heptane has been validated and widely discussed [13].

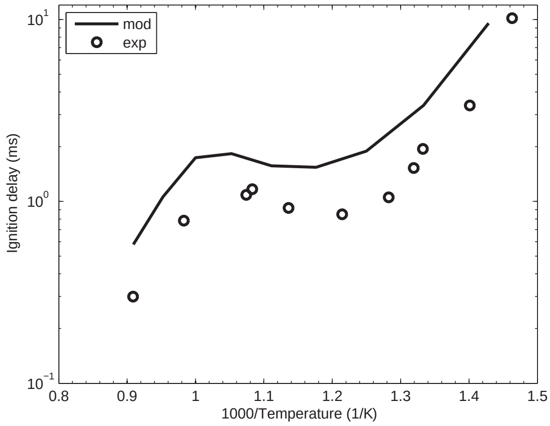

Figure 13

Dependence of the main ignition-delay on the temperature for a perfectly stirred mixture of *n-heptane*/*air* in a constant pressure reactor. SENKIN results are compared with experimental data. Initial state: $p_0 = 42$ bar, $\Phi = 0.5$.

For the sake of clarity, and in order to show the potential of using a complex chemistry approach, some results are reported below.

Figure 13 shows the evolution of the main combustion ignition-delay for a given mixture at a given initial pressure as a function of initial temperature. Values computed using SENKIN are plotted against experimental data [66]. The ignition delays are determined from the maximum temperature gradient. It is interesting to note the NTC (*Negative Temperature Coefficient*) zone in the interval of temperature from 850 K to 950 K. In that interval, an augmentation of the initial temperature corresponds to an augmentation of the ignition delay. Figure 14 shows the evolutions of four major species (C_7H_{16}, O_2, CO_2 and CO) during the combustion process. Results computed using the tabulated chemistry and the complete chemical scheme (SENKIN) are compared. It concerns an homogeneous lean-mixture with 50% of EGR. It is worth pointing out two aspects:

- the species evolution is well predicted if the species is a tabulated one (*e.g.* CO_2). This is not the case for n-heptane as it is a reconstructed species that includes all carbonate species other than CO_2 and CO,
- potentially, the tabulated-chemistry method allows for the description of any species evolution during combustion. Concerning the study of pollutant emissions, this is a very interesting aspect (*e.g.* it allows for the determination of thermochemical conditions that favor pollutant formation).

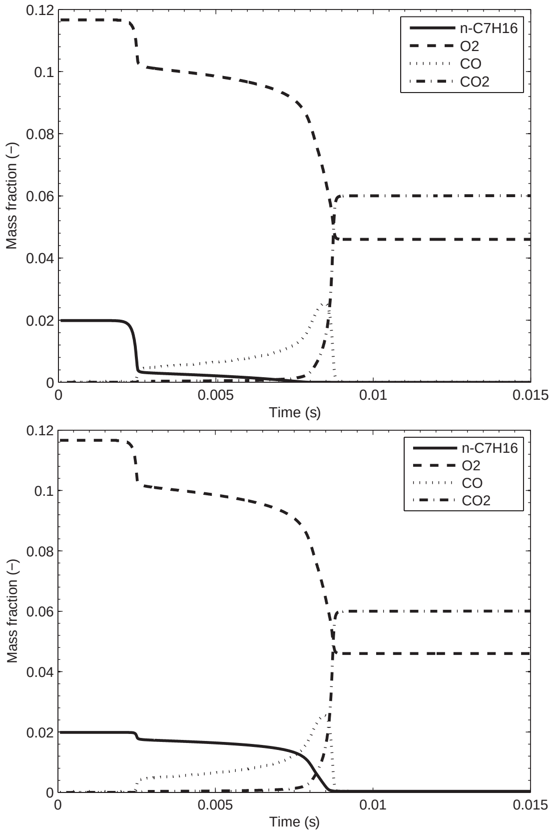

Figure 14

Evolution of several species during combustion. Comparison between complete chemical scheme (top) and tabulated chemical scheme (bottom). The difference between reconstructed (tabulation method) and computed (complex chemistry method) evolutions concerning the *n-heptane* is put in evidence. Curves refer to the combustion process of a perfectly stirred mixture of *n-heptane*/*air*/*EGR* in a constant volume reactor. Initial state: $T_0 = 750$ K, $p_0 = 25$ bar, $\Phi = 0.6$, and $X_r = 50\%$.

3.3 Matching of Spray and Combustion Models

The last step in obtaining the global Diesel HCCI combustion model, Figure 1, consists of matching the spray model with the combustion model.

First of all, it is important to define the relation between the fuel mass-fraction, Z, used to characterize the mixture stratification in β-PDF and the equivalence ratio, ϕ, representing an input variable of the look-up table:

$$Z = \frac{\Phi}{PCO} \cdot \left(1 - X_r \cdot \frac{M_r}{M_{mix}}\right) \cdot \frac{1}{\frac{\Phi}{PCO} + 1} \tag{63}$$

with:

$$\Phi = \frac{Y_F}{Y_{O_2}} \cdot s \quad \text{and} \quad PCO = \frac{m_a}{m_F} \tag{64}$$

where M_r and M_{mix} are the molar masses of the EGR and of the mixture respectively, and m_a is the mass of air necessary to burn the fuel in stoichiometric conditions. As shown in Equation (63), Z is a function of two look-up table inputs. Therefore particular attention must be paid in interpolating the table values. In the presented ICE application, the initial values of pressure and temperature, p_0 and T_0 respectively, correspond to the in-cylinder pressure and temperature conditions associated with the non-reactive engine-cycle simulation:

$$p_0 = p_\tau \quad \text{and} \quad T_0 = T_\tau \tag{65}$$

The most general form of the equation used to compute the mean reaction rate in a stratified mixture associated to a tabulated species is:

$$\bar{\omega}_{esp} = \int \omega \cdot \mathcal{P}_{co} \cdot dp_\tau^* \cdot dT_\tau^* \cdot dZ^* \cdot dX_r^* \cdot dc^* \tag{66}$$

with:

$$\omega = \omega\left(p_\tau^*, T_\tau^*, Z^*, X_r^*, c^*\right) \tag{67}$$

and:

$$\mathcal{P}_{co} = \mathcal{P}_{co}\left(p_\tau^*, T_\tau^*, Z^*, X_r^*, c^*\right) \tag{68}$$

where $\mathcal{P}_{co}$ is the coupled PDF. Equation (66) is very difficult to solve because of the complex interactions between the different variables.

For that reason, in order to compute the mean reaction rate, several assumptions have to be made:

- p_τ and X_r are constant in the domain,
- T_τ depends only on the fuel mass fraction, Z,
- c is considered as homogeneous in the domain during combustion:

  $$c(Z) = \tilde{c} \quad \text{valid} \quad \forall\ Z \tag{69}$$

  This assumption, certainly the strongest one, probably has an impact on the combustion process. However, it is worth noting that it does not impact the computation of the start of combustion [13].

According to these assumptions, the coupled PDF reduces to a simple single-variable PDF:

$$\mathcal{P}_{co} = \mathcal{P}\left(Z^*\right) \tag{70}$$

Now, the mean reaction-rate can be expressed as:

$$\tilde{\omega}_{esp} = \int \omega\left(p_\tau, T_\tau(Z^*), Z^*, X_r, \bar{c}\right) \cdot \mathcal{P}(Z^*) \cdot dZ^* \tag{71}$$

The equation defining the local initial temperature of the mixture, T_τ, as a function of the mixture fraction is:

$$T_\tau = T_\tau(Z) = \tilde{T}_\tau + \left(\frac{T_s - \tilde{T}_\tau}{Z_s}\right) \cdot Z \tag{72}$$

where Z_s and T_s are the values of the mixture fraction and the temperature at the liquid-gas interface under evaporating conditions respectively, and $\tilde{T}_\tau$ is the value of the mean tracer temperature, the definition of which is given below.

The mean progress variable is computed as:

$$\tilde{c} = \frac{\int \left(Y(t, Z^*) - Y(t = 0, Z^*)\right) \cdot \mathcal{P}(Z^*) \cdot dZ^*}{\int \left(Y\left(t_{eq}, Z^*\right) - Y(t = 0, Z^*)\right) \cdot \mathcal{P}(Z^*) \cdot dZ^*} \tag{73}$$

The equilibrium data are tabulated as a function of p_τ, T_τ, Φ and X_r, too. To complete the look-up table set of inputs, the specification of the values of p_τ and T_τ remains. These variables evolve in time because of the thermal losses and the cylinder volume variation. In order to compute p_τ, an energy balance-equation, independent of combustion, has been set up:

$$\begin{aligned}\frac{dp_\tau}{dt} = {} & \frac{p_\tau}{m_{cyl} \cdot C_{v_\tau} \cdot \tilde{T}_\tau} \cdot \left[Q_{th} - Q_{ev} + \sum h_{i/o} \cdot \frac{dm_{i/o}}{dt} + \right. \\ & \left. - \sum_{esp_\tau} h_{esp_\tau} \cdot \frac{dm_{esp_\tau}}{dt}\right] + \\ & p_\tau \cdot \frac{C_{p_\tau}}{C_{v_\tau}} \cdot \left[\sum_{esp_\tau} \frac{1}{n_{esp_\tau}} \cdot \frac{dn_{esp_\tau}}{dt} - \frac{1}{V} \cdot \frac{dV}{dt}\right]\end{aligned} \tag{74}$$

where m_{cyl} is the total mass contained in the cylinder, C_v is the constant volume specific heat, Q_{th} represents the thermal loss flux, Q_{ev} represents the thermal flux to evaporate the liquid fuel, h is the enthalpy, n is the mole number and V is the cylinder volume. The subscript τ indicates the variables associated with the thermochemical conditions without combustion (tracer conditions), and the subscript i/o refers to inlet/outlet variables. Enthalpies and specific heats depend on the thermodynamic state of the system:

$$h_{esp_\tau} = h_{esp_\tau}(\tilde{T}_\tau);\ C_{p_\tau} = C_{p_\tau}(\tilde{T}_\tau) \text{ and } C_{v_\tau} = C_{v_\tau}(\tilde{T}_\tau) \tag{75}$$

Finally, $\tilde{T}_\tau$ is computed using the ideal-gas state equation:

$$\tilde{T}_\tau = \frac{p_\tau \cdot M_{mix_\tau}}{\rho_{mix_\tau} \cdot \mathcal{R}} \tag{76}$$

where ρ_{mix_τ} and $\mathcal{R}$ are respectively the density of the mixture in tracer conditions and the universal gas constant. Thermal losses have been estimated by using the well established theory proposed in [67].

The reaction rates computed using the look-up table are exact only if the set of inputs refers to a table definition node. For all the other conditions, reaction rates are computed using extrapolation and linear interpolation techniques. It is worth investigating both these aspects. In the model, because of the highly non-linear behavior of the chemical kinetics, all kinds of extrapolation have been avoided; that is, in reading the look-up table, the species reaction rate is set to zero if initial conditions do not belong to the definition domain of the table. Concerning interpolation, equivalence ratio and molar fractions (table coordinates) do not linearly depend on fuel mass fraction (PDF coordinate); consequently an adapted interpolation method is necessary.

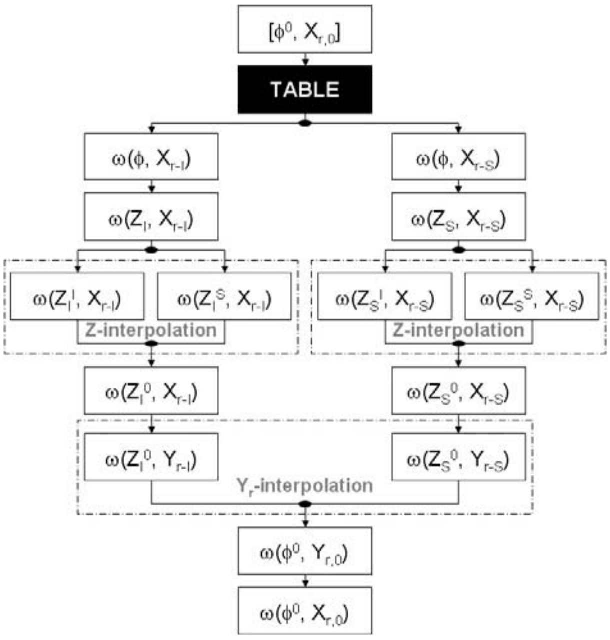

Figure 15

Interpolation method.

The method, presented in Figure 15, is detailed below. The subscripts/superscripts S, I and 0 are relative to the higher and lower tabulated values (with respect to the reference value), and the reference value respectively. If subscripts, they are associated to the EGR rate, otherwise, if superscripts, they are associated to the equivalence ratio. The interpolation method, used to find the reaction rate associated to Φ^0 and X_{r_0}, is resumed in the following steps:

- determining of the upper and lower tabulated values of X_r with respect to X_{r_0},
- once the value of the variable X_r is fixed as $X_{r_{S/I}}$, using Equation (63), reaction rates $\omega\left(\Phi, X_{r_{S/I}}\right)$ can be expressed as $\omega\left(Z_{S/I}, X_{r_{S/I}}\right)$,
- determining the upper and lower values of $Z_{S/I}$ with respect to $Z^0_{S/I}$,
- linear interpolation in $Z_{S/I}$,
- to express the reaction rates $\omega\left(Z^0_{S/I}, X_{r_{S/I}}\right)$ as a function of $\omega\left(Z^0_{S/I}, Y_{r_{S/I}}\right)$, where Y_r indicates the EGR mass fraction in the ambient gas,
- linear interpolation in Y_r,
- to express the resulting reaction rate $\omega\left(\Phi^0, Y_{r_0}\right)$ as a function of $\omega\left(\Phi^0, X_{r_0}\right)$.

4 MODEL VALIDATION

Validation of the global Diesel HCCI combustion model has been carried out by comparing the computed in-cylinder pressures with engine test-bench experimental data (3). The engine used is the four cylinder turbo-charged G9T-NADI™ (*Narrow Angle Direct Injection*). More details concerning the engine can be found in [2].

The model has been validated on a set of eight steady-state operating points that are representative of the engine operating domain, Table 1. The operating point No. 1 has been chosen as the reference operating point. In order to take into account the cylinder-to-cylinder variations, both the minimum and maximum mean cylinder pressures obtained from experimentation are plotted.

TABLE 1

Set of experimental engine operating points.

Point (–)	Crank speed (rpm)	IMEP (bar)	EGR rate (%)	SOI (°)	Φ (–)
1	**1497**	**6.0**	**9.3**	**6**	**0.489**
2	1497	6.1	19.8	6	0.613
3	1497	6.1	36.3	6	0.885
4	3491	6.1	0.2	15	0.356
5	3494	10.1	0.3	18	0.465
6	3491	20.2	0.3	27	0.674
7	1497	6.3	36.8	10	0.888
8	1497	6.2	36.7	8	0.886

Two aspects concerning the simulations are noteworthy:

- the coefficients of the 0D model are tuned only so as to obtain best results at the reference operating point; they are not modified for the other points,
- the initial values of the simulations, such as pressure, temperature and gas mass-fractions, are obtained directly from the engine test-bench. Consequently, their values can not be adjusted to optimize the simulation results. This aspect is an additional challenge for the model.

The reference point has been studied in detail in order to have a deeper understanding of the combustion process.

4.1 Analysis of the 0D and the 3D Model Results

In order to validate the different aspects correlated to the Diesel HCCI combustion model in an ICE application, such as liquid-fuel evaporation, spray formation, mixing process and chemical kinetics, the reference engine-operating-point, Table 1, was simulated using both the Diesel HCCI 0D combustion model and the TKI-PDF 3D CFD model. The results were then compared, Figures 16-23.

---

(3) The presented experimental data represent the mean value of hundreds of acquired cycle pressure signals.

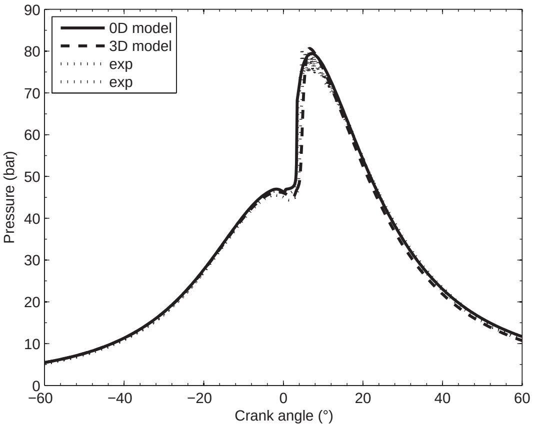

Figure 16

Pressure in the cylinder at the operating point No. 1. Comparison of 0D and 3D modelling results with experimental data.

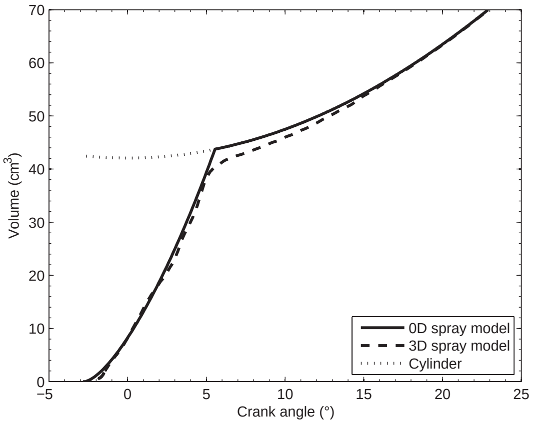

Figure 17

Spray volume at the operating point No. 1. Comparison of 0D with 3D modelling results.

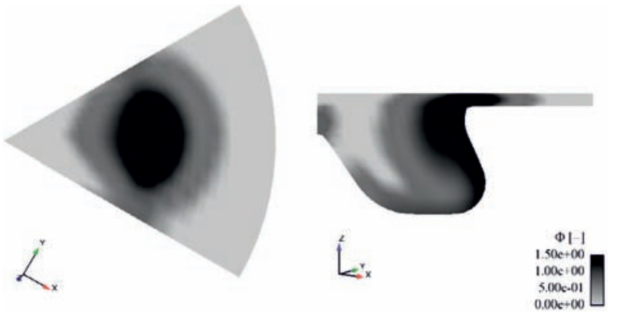

Figure 18

Equivalence ratio field in the cylinder at 5° crankshaft angle. A cross view on a transverse plane close to the TDC (left), and a cross view on a longitudinal plane containg the injection axis (right).

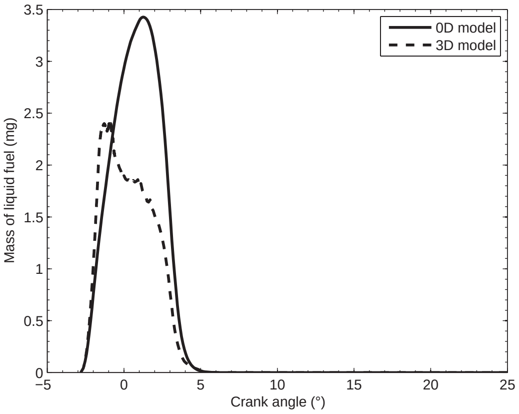

Figure 19

Liquid mass of fuel at the operating point No. 1. Comparison of 0D with 3D modelling results.

Figure 16 shows the evolution of the computed in-cylinder pressures plotted against the experimental pressure-curve envelope. As shown, the simulations are in good agreement with the experiments.

Figure 17 compares the evolution of the spray volumes$^{(4)}$. As shown, near 5° crankshaft angle, the spray-growth rate, as obtained from the 3D model, decreases. This is for two major reasons, both depending on geometry:

– the first, due to the fact that the spray can hardly penetrate the interstitial volumes (*e.g.* the volume between the piston squish-area and the cylinder head, when the piston is close to the TDC (*Top Dead Center*),

– the second, associated with the toroidal coherent turbulent-structure, which is generated by the impact of the spray on the piston bowl.

Figure 18 shows two views of the in-cylinder equivalence ratio field at 5° crankshaft angle.

Figure 19 compares the two total liquid-fuel masses in the cylinder. As shown, the crankshaft-angle intervals necessary to complete liquid-fuel evaporation are very close for both models. The masses of liquid fuel in the cylinder are comparable even though the 0D model underestimates the liquid-fuel evaporation rate.

Figure 20 compares the total masses of gases contained in the sprays. The two curves match each other well. The slight variation is mainly due to the geometrical reasons mentioned above.

Figure 21 compares the specific turbulent kinetic-energies associated to the sprays computed by the 0D and the 3D models. The comparison of the two curves shows

---

(4) Concerning the 3D CFD model, spray volume has been defined as the total volume of the cells containing gaseous fuel.

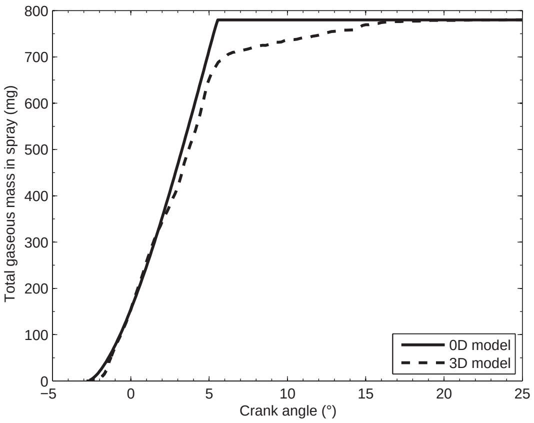

Figure 20

Spray mass at the operating point No. 1. Comparison of 0D with 3D modelling results.

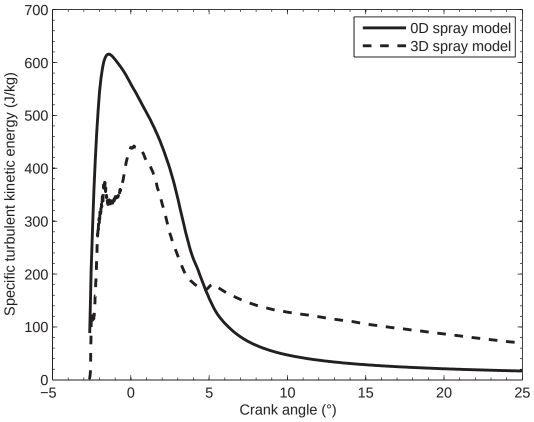

Figure 21

Spray specific turbulent kinetic-energy at the operating point No. 1. Comparison of 0D with 3D modelling results.

that the OD model well represents the first-order magnitude variations of the specific turbulent kinetic-energy.

Figure 22 shows the evolution of the fuel mixture-fraction PDF inside the sprays for different crankshaft-angle values. The crankshaft angle interval considered extends from the SOI (*Start of injection*) proximity to the EOC (*End Of Combustion*). As can be seen all along the interval, the 0D spray mixture model reproduces the air/fuel ratio stratification in the spray well.

Finally, Figure 23 compares the two heat release curves. The two heat-releases are in good agreement, and show that the 0D Diesel HCCI model is able to predict auto-ignition delays (see also *Fig. 16*) and the chemical reaction kinetics. The sharp shape of the curves shows that the heat release process is more representative of conventional Diesel combustion.

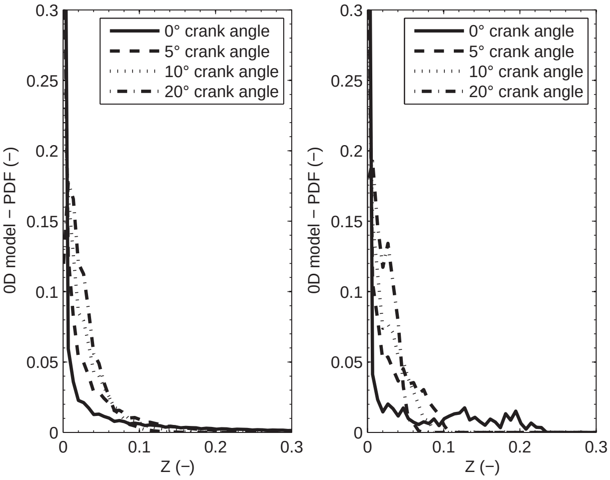

Figure 22

Evolution of the mixture fraction distribution at the operating point No. 1. Comparison of 0D (left) with 3D (right) modelling results at different crank angle values.

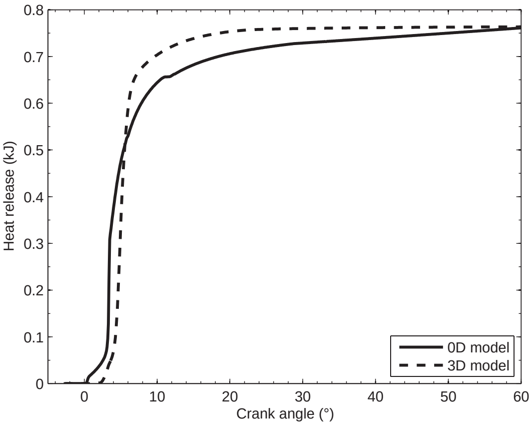

Figure 23

Heat release at the operating point No. 1. Comparison of 0D with 3D modelling results.

4.2 Comparison with Experimental Data

The major challenge for the Diesel HCCI combustion model is to be able to adapt itself to all of the different engine operating-points. An engine operating point is completely defined once initial and boundary conditions are fixed. It follows without saying that model behavior must be sensitive to initial and boundary conditions.

Figures 24-26 show the in-cylinder pressures relative to eight different engine operating points. Computed results are plotted against experimental data.

Figure 24 shows the model's sensitivity to a variation of the IMEP value (points Nos. 4, 5 and 6). Computed pressure evolutions agree with the experimental curves. The most important aspects in combustion prediction, such as SOC

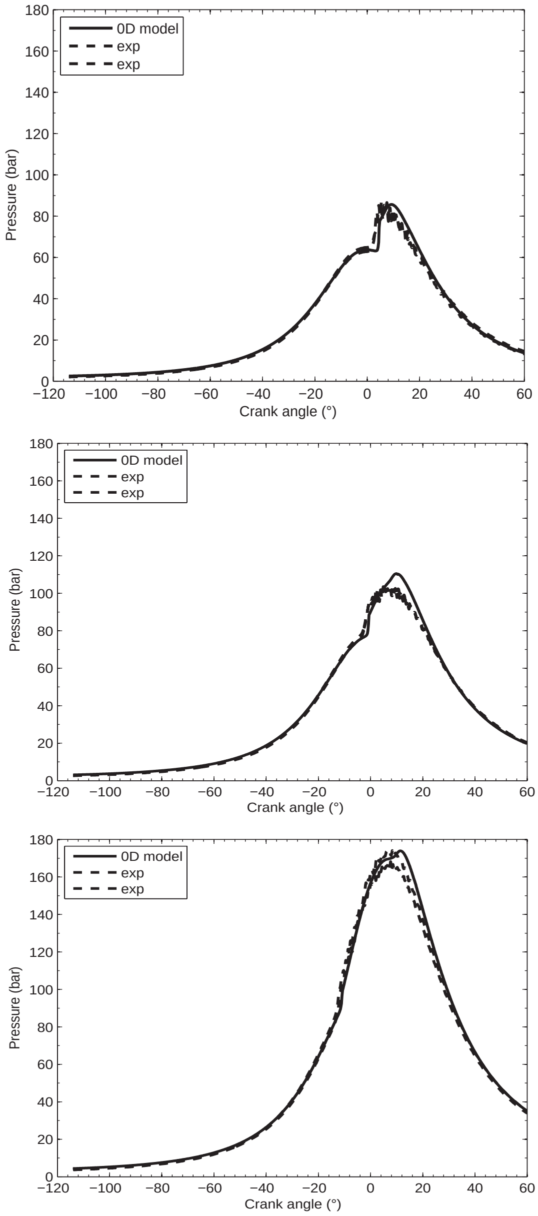

Figure 24

Sensitivity of the 0D model to IMEP variations. Comparison of 0D modelling with experimental data. Curves of pressure refer to the operating points Nos. 4 (top), 5 (middle), 6 (bottom).

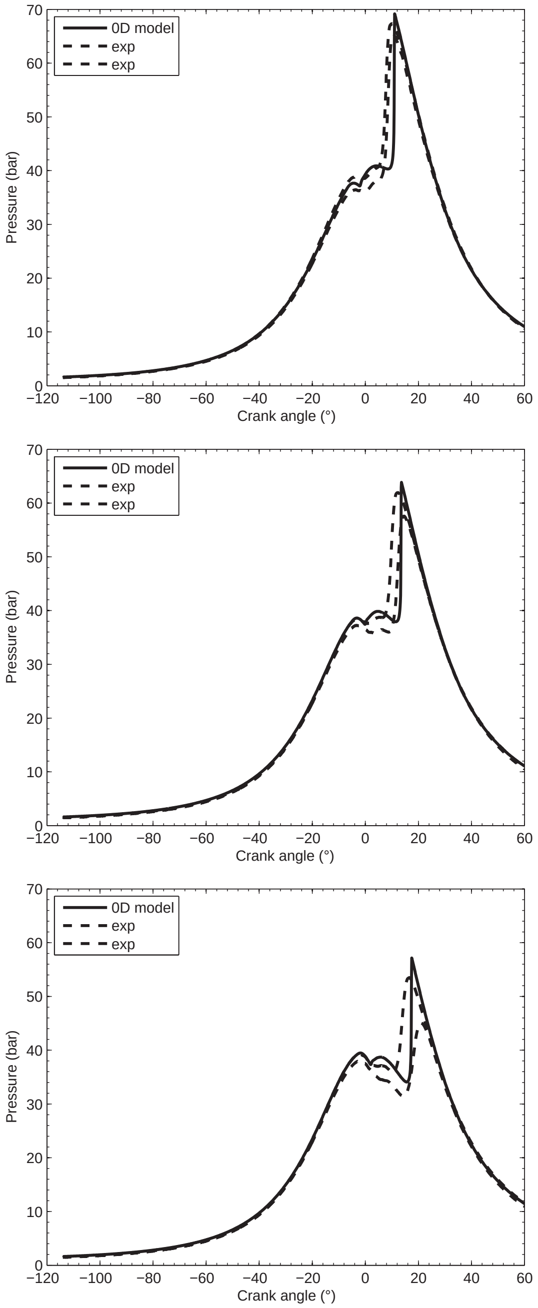

Figure 25

Sensitivity of the 0D model to SOI variations. Comparison of 0D modelling with experimental data. Curves of pressure refer to the operating points Nos. 7 (top), 8 (middle), 3 (bottom).

(*Start Of Combustion*), pressure peak value, and pressure peak position, are well reproduced. All three combustion processes are representative of conventional Diesel combustion.

Figure 25 shows the model's sensitivity to a variation of the SOI value while the other parameters stay constant (points Nos. 7, 8 and 3). The computed pressures follow the experimental results well. In particular, the main ignition-delay growth and the reduction of the pressure peaks, with a reduction in the SOI, are well reproduced. All three operating points concern high EGR rates that, as already seen, favor cold-flame phenomena. Thus, the combustion processes are representative of HCCI combustion. This aspect is clearly put in evidence by the presence of two peaks in

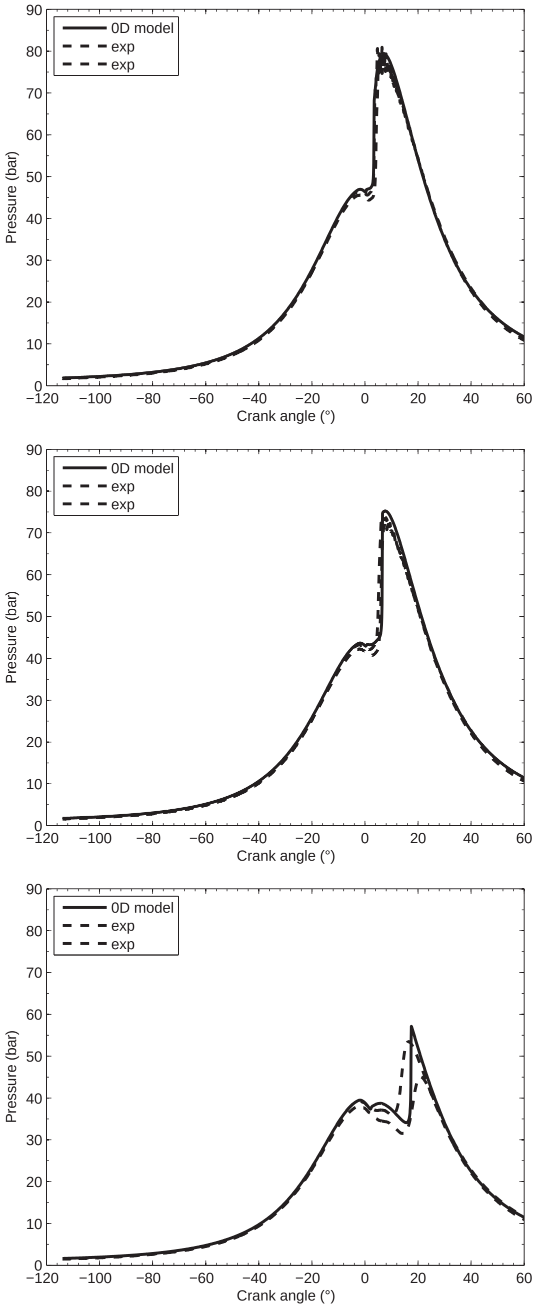

Figure 26

Sensitivity of the 0D model to EGR rate variations. Comparison of 0D modelling with experimental data. Curves of pressure refer to the operating points Nos. 1 (top), 2 (middle), 3 (bottom).

the pressure curves: the first associated with the cold-flame heat-release, and the second associated with the main heat-release.

Finally, Figure 26 shows the model's sensitivity to a variation of the EGR rate value (points No. 1, 2 and 3). This series of operating points considered highlights the potential of the model to predict the combustion process. In fact, with the growth of the EGR rate, the combustion process changes from conventional Diesel to HCCI.

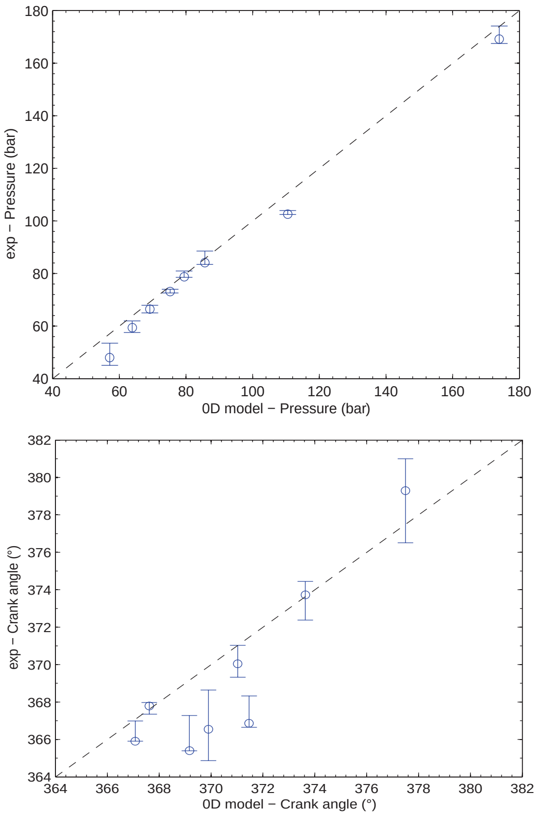

Figure 27

Correlation graphs relative to computed results and experimental data, for the engine operating points listed in Table 1. The circles represent the values referred to the mean experimental curves, cylinder to cyinder variations are pointed out by using error bars. Curves refer to the maximum in-cylinder pressure values (top) and the corresponding crank angle values (bottom).

In order to have a more detailed comparison of the 0D Diesel HCCI combustion-model results with experimental data, some characteristic variables of the combustion process are discussed in the following.

Figures 27-29 show some correlation graphs between computed results and experimental data (5).

Figure 27 shows the correlation graphs relative to the maximum values of the in-cylinder pressure obtained for the different engine operating points and the corresponding crank angle values. As can be seen there is a good correlation between computations and experimental data.

---

(5) Information concerning the combustion progress are obtained by analyzing experimental in-cylinder pressure signals.

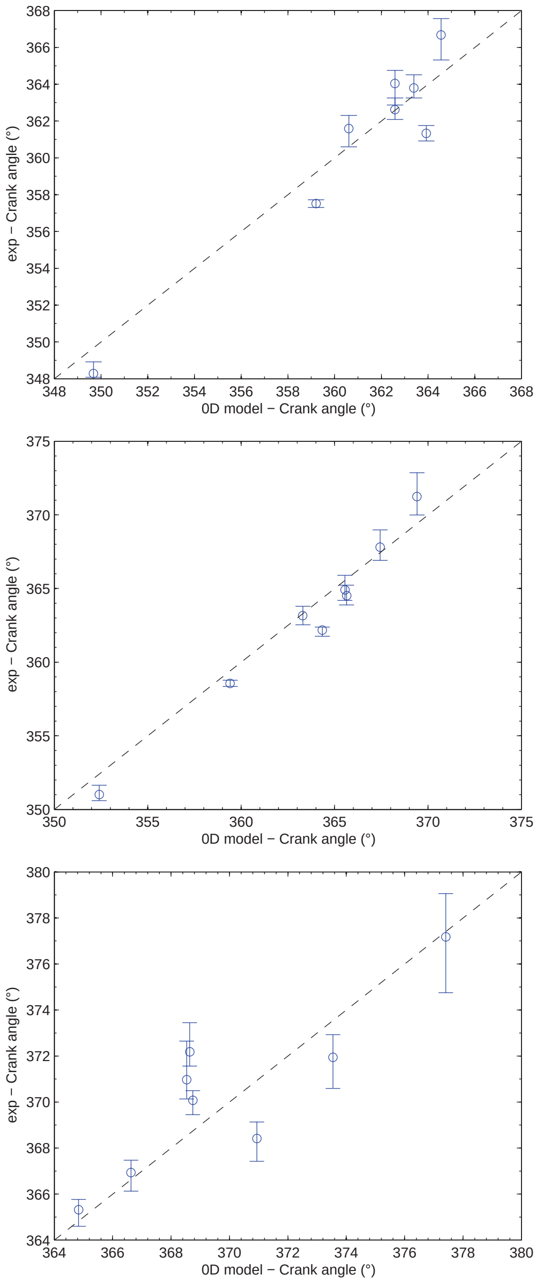

Figure 28

Correlation graphs relative to computed results and experimental data, for the engine operating points listed in Table 1. The circles represent the values referred to the mean experimental curves, cylinder to cyinder variations are pointed out by using error bars. Curves refer to the crank angle values at which the 5% (top), 10% (middle) and 50% (bottom) of the global injected energy is released.

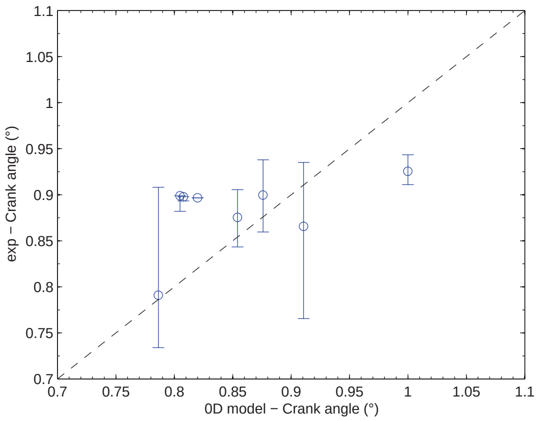

Figure 29

Correlation graphs relative to computed results and experimental data, for the engine operating points listed in Table 1. The circles represent the values referred to the mean experimental curves, cylinder to cyinder variations are pointed out by using error bars. Curve refer to the final values of the burned-mass fractions of injected-fuel.

Figure 28 shows the correlation graphs relative to the combustion progress for the different engine operating points. The crank angle values at which the 5%, 10% and 50% of the global injected-energy are released have been pointed out. Correlation graphs referred to crank angle values relative to the end of combustion (*e.g.* corresponding to the 90% of the global injected-energy) are here omitted as these values, in reason of the very particular adopted engine-control strategies, are not often reached, Figure 29. As shown, the model well predict the mixture auto-ignition angular position (top), which is the most important variable to catch in conventional Diesel and HCCI combustion modelling. The evolution of the combustion process (middle and bottom) is quite well predicted by the model, at least up to the release of half of the injected energy.

Figure 29 refers to the final values of the burned-mass fractions of injected-fuel. As can be seen, the combustion processes are often incomplete and the experimental data present wide intervals of variation. These two aspects, if occurring at the same time, are symptomatic of unstable combustion processes. For that reason computed results are considered as satisfactory.

CONCLUSION

This paper presents an original approach to Diesel HCCI combustion modelling. The main contribution of the model concerns the detailed description of the spray using a 0D formalism. In order to carry this out, tools hitherto commonly adopted in 3D CFD models (such as PDF and $\kappa - \epsilon$ turbulence model) have been modified and integrated in an innovative 0D model. As a consequence, it is possible to have access to a statistical local description of the air/fuel mixture. It consists of an estimate of the local temperature and local composition values. The spray model has then been coupled to a complex-chemistry tabulation method that computes reaction rates associated with the local thermochemical-conditions. The spray model has been widely discussed and validated with results obtained with the TKI-PDF 3D CFD model developed at the IFP. Finally the global Diesel HCCI combustion model has been validated with experimental data on a wide range of engine operating conditions.

This approach is seen to be very promising, mainly for the following reasons:

– it is essentially based on physical considerations (this allows a direct comparison of the computed results with experimental data),
– it gives a detailed description of the dynamics of spray formation and the combustion process, and can therefore be a useful tool in engine control strategy development,
– the detailed chemistry tabulation method gives potential access to all species playing a role in the combustion process; this aspect is very interesting in expanding the study to include pollutant formation mechanisms,
– the model is able to predict both conventional Diesel and HCCI combustion,
– the model is sensitive to both boundary and initial conditions,
– the CPU time required to perform a complete engine-cycle simulation is of the order of 10^2 of real time.

Below are some short-term actions envisaged to further improve the existing model:

– extending the spray model to the multi-injection strategy management,
– investigating the impact on the oxidation process of a combustion progress-variable variance in the reactive mixture,
– defining a new complex-chemistry tabulation more orientated towards prediction of pollutant emissions. Main changes shall concern the surrogate fuel choice and the tabulation method. In particular, a species mass-fraction tabulation approach, instead of a species reaction-rate one, seems to be more promising in ICE modelling.

Further investigations of these topics will be undertaken by the authors in their future works.

REFERENCES

1 Lafossas F.A., Marbaix M., Menegazzi P. (2007) Development and application of a 0D D.I. Diesel combustion model for emissions prediction, *SAE Technical Paper* No. 2007-01-1841.

2 Albrecht A., Corde G., Knop V., Boie H., Castagne M. (2005) 1D simulation of turbocharged gasoline direct injection engine for transient strategy optimization, *SAE Technical Paper* No. 2005-01-0693.

3 Albrecht A., Chauvin J., Lafossas F.A., Potteau S., Corde G. (2006) Development of highly premixed combustion Diesel engine model: from simulation to control design. *SAE Technical Paper* No. 2006-01-1072.

4 Tao F., Liu Y., Rempelewert H., Foster D.E., Reitz R.D. (2005) Modeling the effects of EGR and injection pressure on the soot formation in a High-Speed Direct-Injection (HSDI) Diesel engine using a multi-step phenomenological soot model, *SAE Technical Paper* No. 2005-01-0121.

5 Vibe I.I. (1970) *Brennverlauf und Kreisprozess von Verbrennungsmotoren*, VEB Verlag Technik.

6 Heywood J.B. (1988) Combustion in Compression-Ignition engines, in *Internal combustion engine fundamentals*, McGraw-Hill, New York.

7 Cesario N., Muscio C., Farina M., Amato P., Lavorgna M. (2004) Modelling the rate of heat release in common rail Diesel engines: a soft computing approach, *SAE Technical Paper* No. 2004-01-2967.

8 Arsie I., Di Genova F., Pianese C., Rizzo G., Sorrentino M., Caraceni A., Cioffi P., Flauti G. (2003) A single-zone model for combustion and NOx simulation in common-rail multi-jet Diesel engines, *SAE Technical Paper* No. 2003-01-79.

9 Hiroyasu H., Kadota T., Arai M. (1983) Development and use of a spray combustion modeling to predict Diesel engine efficiency and pollutant emissions, *Bull. JSME* **26**, 214, 569-583.

10 Asay R.J., Svensson K.I., Tree D.R. (2004) An empirical, mixing-limited, zero-dimensional model for Diesel combustion, *SAE Technical Paper* No. 2004-01-0924.

11 Dec J.E. (1997) A conceptual model of DI Diesel combustion based on laser-sheet imaging, *SAE Technical Paper* No. 970873.

12 Mauviot G., Albrecht A., Poinsot T. (2006) A new 0D approach for Diesel combustion modeling coupling probability density function with complex chemistry, *SAE Technical Paper* No. 2006-01-3332.

13 Mauviot G. (2007) Développement d'une modélisation phénoménologique de chambres de combustion de moteurs à piston par réduction de modèle physique 3-D dans la perspective d'une intégration dans un outil de simulation système, *PhD Thesis*, UPMC.

14 Barba C., Burkhardt C., Boulouchos K., Bargende M. (1999) An empirical model for precalculating the combustion rate of the Common Rail Diesel engine for passenger cars, *Motortechnische Z.* **60**, 4, 262-270.

15 Barba C., Burkhardt C., Boulouchos K., Bargende M. (2000) A phenomenological combustion model for heat release rate prediction in high speed DI Diesel engines with common-rail injection, *SAE Technical Paper* No. 2000-01-2933.

16 Chmela F., Orthaber G. (1999) Rate of heat release prediction for direct injection Diesel engines based on purely mixing controlled combustion, *SAE Technical Paper* No. 1999-01-0186.

17 Chmela F., Engelmayer M., Pirker G., Wimmer A. (2004) Prediction of turbulence controlled combustion in Diesel engines, *THIESEL conference on thermo and fluid dynamic processes in Diesel engines*, Valence - Spain, 2004.

18 Schihl P., Tasdemir J., Schwarz E., Bryzik W. (2002) Development of a zero-dimensional heat release model for application to small bore Diesel engines, *SAE Technical Paper* No. 2002-01-0073.

19 Kouremenos D.A., Rakopoulos C.D., Hountalas D.T. (1997) Multi-zone combustion modelling for the prediction of pollutants emissions and performance of DI Diesel engines, *SAE Technical Paper* No. 970635.

20 Jaine T. (2004) Simulation zérodimensionnelle de la combustion dans un moteur Diesel à Injection Directe, *PhD Thesis*, Université d'Orléans.

21 Kong S.C., Ayoub N., Reitz D. (1992) Modeling combustion in compression ignition homogeneous charge engine. *SAE Technical Paper* No. 920512.

22 Kong S.C., Marriot C.D., Reitz C.D., Christensen M. (2001) Modeling and experiments of HCCI engine combustion using detailed chemical kinetics with multidimensional CFD, *SAE Technical Paper* No. 2001-01-1026.

23 Kong S.C., Han Z., Reitz D. (2002) The development and application of a diesel ignition and combustion model for multidimensional engine simulation, *SAE Technical Paper* No. 950278.

24 Kong S.C., Marriot C.D., Rutland C.J., Reitz D. (2002) Experiments and CFD modeling of direct injection gasoline HCCI engine combustion, *SAE Technical Paper* No. 2002-01-1925.

25 Patel A., Kong S.C., Reitz R.D. (2004) Development and validation of a reduced reaction mechanism for HCCI engine simulation, *SAE Technical Paper* No. 2004-01-0558.

26 Nishida K., Hiroyasu H. (1989) Simplified three-dimensional modeling of mixture formation and combustion in a Diesel engine, *SAE Technical Paper* No. 890269.

27 Hasse C., Barths H., Peters N. (1999) Modeling the effects of split-injections in Diesel engines using representative interactive flamelets, *SAE Technical Paper* No. 1999-01-3574.

28 Hasse C., Bikas G., Peters N. (2000) Modeling diesel combustion using the eulerian particle flamelet model (epfm), *SAE Technical Paper* No. 2000-01-2934.

29 Barths H., Pitsch H., Peters N. (1999) 3D simulation of DI diesel combustion and pollutant formation using a two-component reference fuel, *Oil Gas Sci. Technol.* **54**, 2, 233-244.

30 Michel J.B., Colin O., Veynante D. (2008) Modeling ignition and chemical structure of partially premixed turbulent flames using tabulated chemistry, *Combust. Flame* **152**, 1-2, 80-99.

31 Peters N., Rogg B. (1993) *Reduced kinetic mechanisms for applications in combustion systems*, Springer Verlag, Heidelberg.

32 Peters N. (2000) Nonpremixed turbulent combustion, in *Turbulent combustion*, Cambridge University Press, Cambridge.

33 Colin O., Benkenida A., Angelberger C. (2003) 3D Modeling of Mixing, ignition and combustion phenomena in highly stratified gasoline engine, *Oil Gas Sci. Technol.* **58**, 1, 47-52.

34 Colin O., Benkenida A. (2004) The 3-zones extended coherent flame model (ECFM3Z) for computing premixed/diffusion combustion, *Oil Gas Sci. Technol.* **59**, 6, 593-609.

35 Wang Z., Wang J., Shuai S. (2004) Numerical simulation of HCCI engine with multistage gasoline Direct Injection using 3d-cfd with detailed chemistry, *SAE Technical Paper* No. 2004-01-0563.

36 Wang Z., Shuai S., Wang J., Tian G., An X. (2006) Modeling of HCCI combustion from 0D to 3D, *SAE Technical Paper* No. 2006-01-1364.

37 Knop V., Jay S. (2006) Latest developments in gasoline Auto-Ignition modelling applied to an optical CAI™ engine, *Oil Gas Sci. Technol.* **61**, 1, 121-137.

38 Pires-da-Cruz A., Baritaud T., Poinsot T.J. (2001) Self-ignition and combustion modeling of initially nonpremixed turbulent systems, *Combust. Flame* **124**, 1-2, 65-81.

39 Bruneaux G. (2001) Liquid and vapor spray structure in high pressure Common Rail Diesel injector, *Atomization Spray.* **11**, 5, 533-556.

40 Bruneaux G., Augé M., Lemenand C. (2004) A study of Combustion structure in high pressure single hole Common Rail Direct Diesel Injection using laser induced fluorescence of radicals, *COMODIA Congress*, Yokohama - Japan, 2004.

41 Bruneaux G. (2005) Mixing process in high pressure Diesel jets by normalized laser induced exciplex fluorescence. Part I: free jet, *SAE Technical Paper* No. 2005-01-2100.

42 Verhoeven D., Vanhemelryck J.-L., Baritaud T. (1998) Macroscopic and ignition characteristics of high-pressure sprays of single-component fuels, *SAE Technical Paper* No. 981069.

43 Hiroyasu H., Arai M. (1990) Structures of fuel sprays in Diesel engines, *SAE Technical Paper* No. 900475.

44 Jaine T., Benkenida A., Menegazzi P., Higelin P. (2003) Zero dimensional computation of Diesel spray - comparison with experiments and 3D model, *6th International Conference on Engines for Automobile*, Capri - Italy, 2003.

45 Subramanian G. (2005) Modélisation de l'auto-inflammation : analyse des effets de la dilution par les gaz brûlés et des interactions avec la turbulence dédiée aux moteurs Diesel à charge homogène, *PhD Thesis*, INSA Rouen.

46 Pope S.B. (1985) PDF methods for turbulent reactive flows, *Prog. Energ. Combust.* **19**, 11, 119-192.

47 Gicquel O., Darabiha N., Thévenin D. (2000) Laminar premixed hydrogen/air counterflow flame simulations using flame prolongation of ILDM with differential diffusion, *Proc. Combust. Inst.* **28**, 1901-1908.

48 Veynante D., Vervisch L. (2002) Turbulent combustion modeling, *Prog. Energ. Combust.* **28**, 3, 193-266.

49 Lefebvre A.H. (1989) Drop evaporation, in *Atomization and sprays*, Hemisphere Publishing Corporation, United States of America.

50 Reid R.C., Prausnitz J.M., Poling B.E. (1987) *The properties of gases & liquids*, McGraw-Hill, United States of America.

51 Ghassemi H., Baek S.W., Khan S.Q. (2006) Experimental study on binary droplet evaporation at elevated pressures and temperatures, *Combust. Sci. Technol.* **178**, 6, 1031-1053.

52 Siebers D.L. (1998) Liquid-phase fuel penetration in Diesel sprays, *SAE Technical Paper* No. 980809.

53 Siebers D. (1999) Scaling liquid-phase fuel penetration in diesel sprays based on mixing-limited vaporization, *SAE Technical Paper* No. 1999-01-0528.

54 Naber J.D., Siebers D. (1996) Effects of gas density and vaporization on penetration and dispersion of diesel sprays, *SAE Technical Paper* No. 960034.

55 Desantes J.M., Payri R., Salvador F.J., Gil A. (2005) Development and validation of a theoretical model for diesel spray penetration, *Fuel* **85**, 7-8, 910-917.

56 Girimaji S.S. (1991) Assumed β-PDF Model for Turbulent Mixing: Validation and Extension to Multiple Scalar Mixing, *Combust. Sci. Technol.* **78**, 177-196.

57 Kuo K.K. (2005) Gaseous diffusion flames and combustion of a single liquid fuel droplet, in *Principles of combustion*, Wiley J. (ed.), John Wiley & Sons, Hoboken - New Jersey.

58 Givler S.D., Abraham J. (1996) Supercritical droplet vaporization and combustion studies, *Prog. Energ. Combust.* **22**, 4, 1-28.

59 Sirignano W.A. (2004) Droplet behavior at near-critical, transcritical, and supercritical conditions, in *Fluid dynamics and transport of droplets and sprays*, Cambridge University Press, Irvine.

60 Neely G.D., Sasaky S., Huang Y., Leet J.A., Stewart D.W. (2005) New Diesel emission control strategies to meet US Tier 2 emissions regulations, *SAE Technical Paper* No. 2005-01-1091.

61 Kee R.J., Rupley F.M., Miller J.A. (1989) CHEMKIN-II: a fortran chemical kinetics package for the analysis of gas-phase chemical kinetics, *Sandia National Laboratories report* No. SNL-89-8009.

62 Curran H.J., Gaffuri P., Pitz W.J., Westbrook C.K. (1998) A comprehensive modeling study of n-heptane oxidation, *Combust. Flame* **114**, 1-2, 149-177.

63 Maas U., Pope S.B. (1992) Implementation of simplified chemical kinetics based on low-dimensional manifolds, *Proc. Combust. Inst.* **24**, 1, 103-112.

64 Maas U., Pope S.B. (1992) Simplifying chemical kinetics: intrinsic low-dimensional manifolds in composition space, *Combust. Flame* **88**, 3-4, 239-264.

65 Embouazza M. (2005) Étude de l'auto-allumage par réduction des schémas cinétiques chimiques. Application à la combustion homogène Diesel, *PhD Thesis*, École Centrale de Paris.

66 Gauthier B.M., Davidson D.F., Hanson R.K. (2004) Shock tube determination of ignition delay times in full-blend and surrogate fuel mixtures, *Combust. Flame* **139**, 4, 300-311.

67 Sihling K., Woschni G. (1979) Experimental investigation of the instantaneous heat transfer in the cylinder of a high speed Diesel engine, *SAE Technical Paper* No. 790833.

APPENDIX: $\beta - PDF$ VARIANCE FORMULA PROOF

Mathematical proof of Equation (54) holds as follows. The fuel mass-fraction distribution variance is defined as:

$$\widetilde{Z''^2} = \frac{1}{m_S} \cdot \int_{m_S} Z''^2 \cdot dm = \frac{1}{m_S} \cdot \int_{m_S} \left(Z|_{dm} - \tilde{Z} \right)^2 \cdot dm \quad (77)$$

hence, expliciting the PDF of the fuel mass-fraction:

$$\widetilde{Z''^2} = \int_0^{Z_s} \left(Z^* - \tilde{Z} \right)^2 \cdot \mathcal{P}(Z^*) \cdot dZ^* \quad (78)$$

Differentiating Equation (78):

$$\frac{d\widetilde{Z''^2}}{dt} = \underbrace{\int_0^{Z_s} \frac{d\left(Z^* - \tilde{Z} \right)^2}{dt} \cdot \mathcal{P}(Z^*) \cdot dZ^* +}_{(a)} \\ + \underbrace{\int_0^{Z_s} \left(Z^* - \tilde{Z} \right)^2 \cdot \frac{d\mathcal{P}(Z^*)}{dt} \cdot dZ^*}_{(b)} \quad (79)$$

Developping the term (*a*) of Equation (79):

$$\int_0^{Z_s} \frac{d\left(Z^* - \tilde{Z} \right)^2}{dt} \cdot \mathcal{P}(Z^*) \cdot dZ^* = \\ \int_0^{Z_s} \left(\frac{d\tilde{Z}^2}{dt} - 2 \cdot Z^* \cdot \frac{d\tilde{Z}}{dt} \right) \cdot \mathcal{P}(Z^*) \cdot dZ^* = \\ \frac{d\tilde{Z}^2}{dt} \cdot \int_0^{Z_s} \mathcal{P}(Z^*) \cdot dZ^* - 2 \cdot \frac{d\tilde{Z}}{dt} \cdot \int_0^{Z_s} Z^* \cdot \mathcal{P}(Z^*) \cdot dZ^* = \\ \frac{d\tilde{Z}^2}{dt} - 2 \cdot \tilde{Z} \cdot \frac{d\tilde{Z}}{dt} = \frac{d\tilde{Z}^2}{dt} - \frac{d\tilde{Z}^2}{dt} = 0 \quad (80)$$

As shown, the term (*a*) does not contribute to the variance variation.

Concerning the term (*b*) of Equation (79), it represents the variation of the PDF shape in time. In order to correctly describe the PDF evolution, the different contributions to the variance variation will be determined. More precisely, the impacts of the mixture-zone inputs, namely the entrained ambient-gas and the evaporated fuel, and of turbulence will be presented in detail. Henceforth, global PDF will be subdivided into three contributions:

- $\mathcal{P}_A$, the probability to have a local mixture-fraction in the spray at $Z = Z_A = 0$; that is, the composition of pure ambient-gas (a perfectly stirred mixture of air and eventually EGR) entrained in the spray,
- $\mathcal{P}_s$, the probability to have a local mixture-fraction in the spray at $Z = Z_s$; that is, the mixture composition at liquid-gas interface during evaporation process,
- $\mathcal{P}_c$, the probability to have a local mixture-fraction in the spray different from Z_A and Z_s. Henceforth, it will be called the complementary mixture-fraction probability.

$\mathcal{P}_A$ and $\mathcal{P}_s$ at each instant of time have a well-known composition. Consequently, in the composition space, they can be represented using a Dirac function, ψ.

On the other hand, turbulence acts on the overall mixture-fraction distribution and contributes to dissipate the distribution variance. Physically, its action represents the mixture homogenization caused by turbulent-mixing process.

In the following, the different term contributions to the variance variation will be detailed.

Entrained-mass Contribution

At a given time, t_0, the probability to have in the spray a local mixture-composition at $Z = Z_A$ is:

$$\mathcal{P}(Z_A, t_0) = \mathcal{P}_{A_0} \quad (81)$$

after a short interval of time, δt, the spray entrains a certain amount of mass, δm_A. Hence:

$$\mathcal{P}(Z_A, t_0 + \delta t) = \mathcal{P}_{A_0} \cdot \frac{m_S}{m_S + \delta m_A} + \frac{\delta m_A}{m_S + \delta m_A} \quad (82)$$

Computing the derivative of $\mathcal{P}(Z_A)$ as the limit of the incremental ratio gives:

$$\frac{d\mathcal{P}(Z_A)}{dt} = \lim_{\delta t \to 0} \frac{\mathcal{P}(Z_A, t_0 + \delta t) - \mathcal{P}(Z_A, t_0)}{\delta t} = \frac{1}{m_S} \cdot \frac{dm_A}{dt} \quad (83)$$

Hence, its contribution to the variance is:

$$\int_0^{Z_s} \left(Z^* - \tilde{Z} \right)^2 \cdot \left(\frac{1}{m_S} \cdot \frac{dm_A}{dt} \right) \cdot \psi(Z^* - Z_A) \cdot dZ^* = \\ \left(Z_A - \tilde{Z} \right)^2 \cdot \frac{1}{m_S} \cdot \frac{dm_A}{dt} = \frac{\tilde{Z}^2}{m_S} \cdot \frac{dm_A}{dt} \quad (84)$$

Evaporation-process Contribution

Adopting the same way of proceeding, the evaporation-process impact on the PDF holds:

$$\frac{d\mathcal{P}(Z_s)}{dt} = \lim_{\delta t \to 0} \frac{\mathcal{P}(Z_s, t_0 + \delta t) - \mathcal{P}(Z_s, t_0)}{\delta t} = \frac{1}{m_S} \cdot \frac{dm_s}{dt} \quad (85)$$

hence, its contribution to variance is:

$$\int_0^{Z_s} \left(Z^* - \tilde{Z} \right)^2 \cdot \left(\frac{1}{m_S} \cdot \frac{dm_s}{dt} \right) \cdot \psi(Z^* - Z_s) \cdot dZ^* = \\ \frac{1}{m_S} \cdot \left(Z_s - \tilde{Z} \right)^2 \cdot \frac{dm_s}{dt} \quad (86)$$

Fuel evaporation process at liquid-gas interface at saturated conditions implies to introduce in the spray an homogeneous mixture of pure ambient-air and pure fuel in proportions established by the value of Z_s. As the necessary ambient-air mass is already contained in the spray, its transfer from one value of mixture fraction to another represents a further contribution to the variance variation. In the presented approach, it has been done the hypothesis that liquid fuel evaporates in pure ambient-air. Locally, by definition:

$$Z = \frac{m_F}{m_F + m_A} \tag{87}$$

where m_A is the mass of pure ambient-air in the spray. Hence, for a given fuel evaporation-rate (evaporating at saturated conditions), dm_F/dt, the total mass at saturated composition introduced in the spray is:

$$\frac{dm_s}{dt} = \frac{(dm_F + dm_A)_s}{dt} = \frac{1}{Z_s} \cdot \frac{dm_F}{dt} \tag{88}$$

Consequently, the corresponding withdrawn ambient-air mass, dm_{A_w}, is:

$$\frac{dm_{A_w}}{dt} = \left(1 - \frac{1}{Z_s}\right) \cdot \frac{dm_F}{dt} \tag{89}$$

It follows that the impact on the PDF is:

$$\frac{d\mathcal{P}(Z_A)}{dt} = \lim_{\delta t \to 0} \frac{\mathcal{P}(Z_A, t_0 + \delta t) - \mathcal{P}(Z_A, t_0)}{\delta t} = \frac{1}{m_S} \cdot \frac{dm_{A_w}}{dt} \tag{90}$$

and the impact on the variance variation is:

$$\int_0^{Z_s} \left(Z^* - \tilde{Z}\right)^2 \cdot \left(\frac{1}{m_S} \cdot \frac{dm_{A_w}}{dt}\right) \cdot \psi\left(Z^* - Z_A\right) \cdot dZ^* =$$

$$\left(Z_A - \tilde{Z}\right)^2 \cdot \frac{1}{m_S} \cdot \frac{dm_{A_w}}{dt} = \tilde{Z}^2 \cdot \frac{1}{m_S} \cdot \frac{dm_{A_w}}{dt} \tag{91}$$

as $Z_A = 0$.

Complementary Mixture-fraction Contribution

The used β-PDF is a normalized statistical-tool. Consequently, the following relation must always be verified:

$$\int_0^{Z_s} \mathcal{P}(Z^*) \cdot dZ^* = 1 \tag{92}$$

Taking advantage of Equation (92), at every time, t, it is possible to know the probability to have in the spray a local composition $Z = Z_c$:

$$\mathcal{P}(Z_c) = \int_0^{Z_s} \mathcal{P}(Z^*) \cdot dZ^* - \mathcal{P}(Z_A) - \mathcal{P}(Z_s) \tag{93}$$

Differentiating Equation (93):

$$\frac{d\mathcal{P}(Z_c)}{dt} = -\frac{d\mathcal{P}(Z_A)}{dt} - \frac{d\mathcal{P}(Z_s)}{dt} \tag{94}$$

being the first right-hand term of Equation (93) identically equal to unity.

The contribution of the complementary mixture-fraction to the variance variation is then computed as:

$$\int_0^{Z_s} \left(Z^* - \tilde{Z}\right)^2 \cdot \frac{d\mathcal{P}(Z_c)}{dt} \cdot dZ^* =$$

$$-\int_0^{Z_s} \left(Z^* - \tilde{Z}\right)^2 \cdot \frac{1}{m_S} \cdot \left(\frac{dm_A}{dt} + \frac{dm_s}{dt} + \frac{dm_{A_w}}{dt}\right) \cdot dZ^* =$$

$$-\frac{\widetilde{Z''^2}}{m_S} \cdot \left(\frac{dm_A}{dt} + \frac{dm_s}{dt} + \frac{dm_{A_w}}{dt}\right) \tag{95}$$

Turbulence Contribution

Turbulence action contributes to reduce the variance of the mixture making it more homogeneous. The dissipation of the mixture-fraction variance is representative of the turbulent mixing-process. This contribution is modeled by using an empirical closure term:

$$\int_0^{Z_s} \left(Z^* - \tilde{Z}\right)^2 \cdot \left.\frac{d\mathcal{P}(Z^*)}{dt}\right|_{ds} \cdot dZ^* = -2 \cdot C_{diss} \cdot \frac{\tilde{\epsilon}}{\tilde{\kappa}} \cdot \widetilde{Z''^2} \tag{96}$$

Global Variance Equation

Equation (79) because of Equation (80) is reduced to:

$$\frac{d\widetilde{Z''^2}}{dt} = \int_0^{Z_s} \left(Z^* - \tilde{Z}\right)^2 \cdot \frac{d\mathcal{P}(Z^*)}{dt} \cdot dZ^* \tag{97}$$

Taking advantage of Equations (84, 86, 91, 95) and (96), the right-hand side of Equation (97) can be expressed as:

$$\frac{d\widetilde{Z''^2}}{dt} = \frac{1}{m_S} \cdot \left[\tilde{Z}^2 \cdot \left(\frac{dm_A}{dt} + \frac{dm_{A_w}}{dt}\right) + \right.$$

$$\left. + \left(Z_s - \tilde{Z}\right)^2 \cdot \frac{dm_s}{dt} - \widetilde{Z''^2} \cdot \left(\frac{dm_A}{dt} + \frac{dm_{A_w}}{dt} + \frac{dm_s}{dt}\right)\right] +$$

$$-2 \cdot C_{diss} \cdot \frac{\tilde{\epsilon}}{\tilde{\kappa}} \cdot \widetilde{Z''^2} \tag{98}$$

Equation (54) is directly obtained by substituting in Equation (98) the results of Equations (88, 89).

Final manuscript received in October 2008
Published online in June 2009

Appendix G

SAE 2009-01-0678

2009-01-0678

A 0D Phenomenological Approach to Model Diesel HCCI Combustion with Multi-Injection Strategies Using Probability Density Functions and Detailed Tabulated Chemistry

A. Dulbecco and F. A. Lafossas
IFP

T. J. Poinsot
IMFT

ABSTRACT

More and more stringent restrictions concerning the pollutant emissions of ICE (*Internal Combustion Engines*) constitute a major challenge for the automotive industry. New combustion strategies such as LTC (*Low Temperature Combustion*), PCCI (*Premixed Controlled Compression Ignition*) or HCCI (*Homogeneous Charge Compression Ignition*) are promising solutions to achieve the imposed emission standards. They permit low NO_x and soot emissions via a lean and highly diluted combustion regime, thus assuring low combustion temperatures.

In next generation of ICE, new technologies allow the implementation of complex injection strategies in order to optimize the combustion process. This requires the creation of numerical tools adapted to these new challenges.

This paper presents a 0D Diesel HCCI combustion model based on a physical 3D CFD (*Computational Fluid Dynamics*) approach. The purpose of the model is to correctly predict the characteristics of auto-ignition and heat release for all Diesel combustion modes. A new formalism based on PDFs (*Probability Density Functions*) is proposed to describe the mixture formation process in a multi-injection strategy context. This formalism has been coupled with detailed tabulated chemistry to account for the impact of the EGR (*Exhaust Gas Recirculation*) on the kinetics of combustion. The model is finally validated against experimental data. Considering the good agreement with the experiments and the low CPU costs, the presented approach is revealed to be promising for global-system simulations.

INTRODUCTION

Because of increasing strict limitations on pollutant emissions, car manufacturers are constantly investing more money into the R&D (*Research and Development*) sector in order to improve engine performance. Concerning CI (*Compression Ignition*) engines, the most retained idea, in order to contain pollutant emissions, is to shift from conventional Diesel combustion towards new types of combustion regimes.

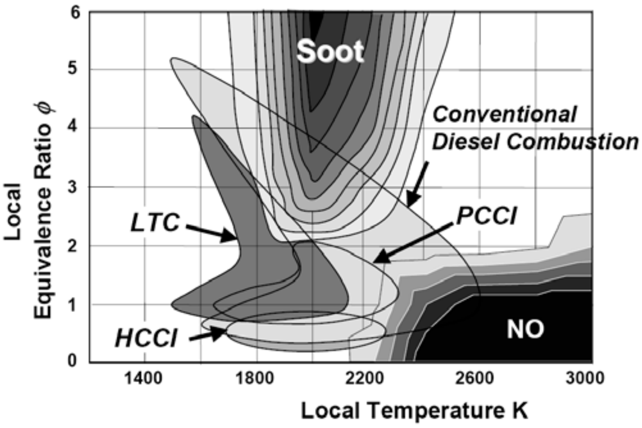

Figure 1 - PCCI, LTC and HCCI concept on a ϕ-*T* map [1].

ISSN 0148-7191

SAE Customer Service: Tel: 877-606-7323 (inside USA and Canada)
Tel: 724-776-4970 (outside USA)
Fax: 724-776-0790
Email: CustomerService@sae.org
SAE Web Address: http://www.sae.org

Printed in USA

9-2009-01-0678

As shown in Fig. 1, combustion regimes such as LTC, PCCI and HCCI are associated with combustion processes characterized by lower temperatures and higher local excess air ratio. In such a way, it is possible to remain clear from the region of NO_x and soot production.

The objective is to extend the operating range of non-conventional combustion processes as far as possible on the engine operating domain. The difficulty to manage these kinds of combustions, especially in the high engine speed and high load operating domains, is mainly due to two reasons: from one side, they need an homogeneous mixture whose preparation requires a certain interval of time, and to the other side, as the oxidation process is mostly controlled by chemical kinetics, the combustion control requires the ability to reproduce the most favorable thermodynamic conditions in the cylinder.

In this perspective, new generations of ICE are equipped with different devices, such as EGR loop or CR (*Common Rail*) DI (*Direct Injection*) systems, to perform more flexible engine-system control-strategies. In particular, recent CR injection devices permit the execution of several injections per engine cycle. Consequently, nowadays engine systems present a large number of parameters to set in order to obtain the optimal performances in terms of BSFC (*Brake Specific Fuel Consumption*) and pollutant emissions.

In this context, numerical modeling is becoming a very important tool in industry and academic R&D programs [1-5]. In fact, it permits a large number of numerical tests to be performed in a short interval of time and at reduced costs compared to those associated with experiments. Because of the trade-off between result detail level and CPU cost of computation, in literature it is possible to find different approaches to Diesel combustion modeling. According to the purpose they have, numerical tools can be classified in global-system-simulation adapted-models, requiring a CPU time close to 10^2 the real time, and physical models, most adapted to research purposes, running in about 10^6 the real time. The first class usually includes tabulated-base, empirical and phenomenological models [6-15] while the second includes CFD models [16-23]. In both cases, it is necessary that numerical tool developments follow the technological ones, in order to account for all the phenomena implied.

In the current global system simulation domain, two approaches for direct-injection combustion modeling are predominant in commercial numerical tools (e.g. GT-POWER [24]). On one hand, empirical mathematical models, usually based on the well known Vibe equation [6], are able to greatly reduce the computation time, but prediction accuracy is limited. On the other hand, phenomenological multi-zone approaches, mostly based on the Hiroyasu et al. approach [15], give a more accurate description of the mixing and the combustion processes; however, in order to have a realistic description of the combustion, the number of zones to be used is often quite large, leading to a significant increase of the CPU time.

The model presented below represents a 0D approach to model Diesel HCCI combustion derived from the reduction of a TKI –PDF (*Tabulated Kinetics for Ignition coupled with PDF*) 3D CFD model developed at the IFP [21,25]. In the following sections, a global overview of the model is given first. Subsequently, the two main parts of the model, the spray and combustion models, are detailed. In the paper, particular attention is paid to the description of the multi-injection modeling. It reveals to be an original approach based on the use of PDFs coupled with tabulated complex-chemistry. Finally, validation of the global combustion model is done by comparing computed results with experimental data. The paper ends with a discussion on model improvements and perspectives.

GLOBAL-MODEL DESCRIPTION

Conventional Diesel and HCCI combustion regimes are governed by different physical mechanisms.

In conventional Diesel combustion, the mixture inside the cylinder is characterized by a high fuel mass fraction stratification. The first site of auto-ignition appears inside the spray, where chemical and thermodynamic conditions are at their most favourable. The most important challenge concerning auto-ignition phase description is to capture the shortest ignition delay. Heat release, due to combustion at the first site, subsequently favours the multiplication of auto-ignition sites. This chain reaction leads to the sharp heat release process typical of the premixed Diesel combustion phase. The remaining fuel burns in a diffusion flame and the heat release is governed by the mixing process. In this phase, turbulence plays the most important role.

In HCCI combustion, the mixture inside the cylinder can be considered as homogeneous. Hence, chemical kinetics plays the most important role in the combustion process. Because of the homogeneity of the mixture, all of the gas auto-ignites simultaneously. As a consequence, HCCI combustion is characterized by a stiff heat release process.

For these reasons, a deep understanding of the spray-formation mechanism is necessary [26-37]. In a general situation, the two combustion regimes are not so well distinguished. Therefore, a modeling challenge is to be able to manage all of the different scenarios. Moreover, the presence of EGR in the cylinder modifies the chemical kinetics, and phenomena, such as cold flames, could appear at the beginning of the fuel oxidation process. This explains the importance of using a detailed chemical-mechanism. Finally, in the case of multi-injection, all these phenomena must be generalised and integrated into a wider context, in which additional phenomena such as interaction of sprays characterised by different equivalence-ratios and chemical compositions (modified by combustion process) could appear.

In the following approach, in order to overtake the lack of spatial-dimension intrinsic to 0D models, several tools commonly used in 3D modeling have been adapted to a 0D formalism. In particular, the following have been used:

- PDF, to describe the fuel-mass distribution inside the spray,
- tabulated chemistry, to take into account the complex-chemical kinetics,
- $\kappa-\varepsilon$ model, to represent the turbulence influence on the mixing process.

Figure 2 shows the synoptical diagram of the global-combustion model in the case of double injection. Directional arrows represent the interactions of the different submodels.

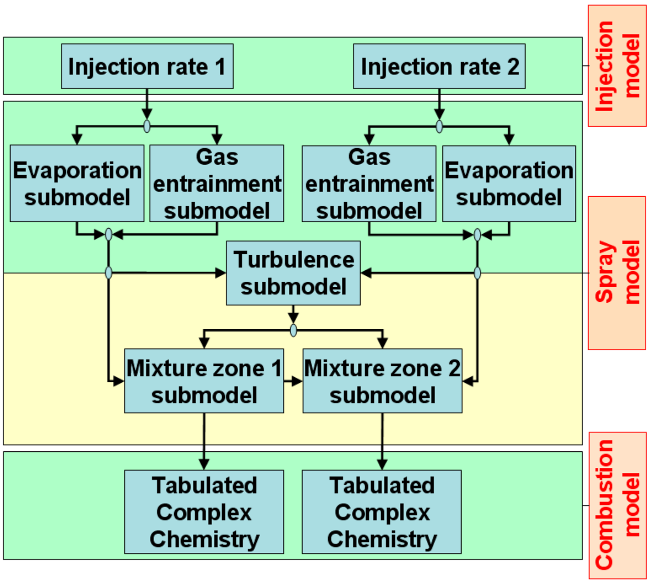

Figure 2 - Synoptical diagram of the complete Diesel HCCI combustion model.

As shown, the global combustion model is made of two main parts:

- the spray model, whose purpose is to represent the formation and the temporal evolution of the spray volume (mixture zone),
- the combustion model, whose role is to compute the heat release and the evolution of the different species characterizing the mixture.

The spray model consists of four different submodels:

- the evaporation submodel, giving the fuel-mass source-term in the spray volume,
- the gas entrainment submodel, giving the ambient-gas (in the most general case considered to be a perfectly stirred mixture of air and EGR) mass source-term,
- the turbulence submodel, computing the turbulence inside the spray; the source terms of the turbulence submodel depend on the fuel and entrained-gas source terms,
- the mixture submodel, describing the fuel-mass distribution inside the spray volume; its source terms are the fuel and entrained-gas mass flow rate inside the spray and the turbulence submodel output, which is directly correlated to the mixing law of the two source terms.

The combustion model consists of a tabulated complex-chemistry inspired by the FPI (*Flame Prolongation of* ILDM (*Intrinsic Low Dimensional Manifold*)) theory [38-40]. Here, injection rates are supposed to be an input of the model.

In the following, a short description of the different submodels will be given in order to explain the impact they have on the global-combustion model. More attention will be paid in the description of the mixing model, as it represents the major contribution of the paper to the state of the art. Thermal losses have been taken into account by using the well-established theory proposed in [41].

SPRAY MODELING

As shown in Fig. 2, spray model can be decomposed into four submodels that interact with each other.

- The evaporation submodel: it computes the thermodynamic conditions at the liquid-gas interface during the evaporation process, and quantifies the fuel-mass evaporation-rate. It also gives qualitative information concerning the penetration length of the liquid jet of fuel.
- The gas entrainment submodel: it computes the mass of gas entrained in the spray volume. It also gives qualitative information regarding the penetration length of the gaseous spray and an estimate of the spray volume.
- The turbulence submodel: it computes the characteristic frequency associated with the turbulent movement of the gas within the spray.

Turbulent frequency is very important in turbulent combustion, as it is the case in ICE, because it is directly connected to the mixing process of evaporated fuel and entrained gas in the spray volume.

- The mixture submodel: it quantifies the total spray gaseous-mass, and describes the fuel-mass distribution within the spray volume.

EVAPORATION SUBMODEL

The evaporation submodel has two main purposes:

- to compute the thermo-chemical properties, in terms of temperature and composition, of the gaseous mixture at the liquid-gas interface during the liquid-fuel evaporation-process,
- to estimate the overall fuel-mass evaporation-rate within the spray.

Methodology to determine the interfacial properties at the liquid-gas interface has been set up according to the theory proposed in [42]. The theory deals with the steady evaporation-process of a single droplet of liquid, which is supposed to be at rest in a gaseous mixture with given composition, Fig. 3.

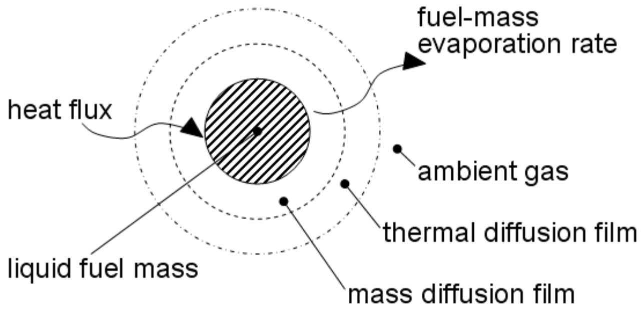

Figure 3 - Evaporation model of a liquid droplet.

Liquid-fuel mass is supposed to have reached its wet-bulb temperature, T_s. Hence, all the heat flux from ambient gas to liquid is used to evaporate the droplet. Moreover, mixture at interface is supposed to be at thermodynamic equilibrium. In such a system, the mass and thermal transfer-processes are respectively characterized by the mass transfer-number, B_m, defined as:

$$B_m = \frac{Y_{F,s} - Y_{F,\infty}}{1 - Y_{F,s}} \tag{1}$$

where $Y_{F,s}$ and $Y_{F,\infty}$ are respectively the mixture fuel mass-fraction at the interface and ambient-gas conditions, and the thermal transfer-number, B_t, defined as:

$$B_t = \frac{C_{p,g} \cdot \left(T_\infty - T_s\right)}{L_{v,s}} \tag{2}$$

where $C_{p,g}$ is the constant-pressure heat-capacity of the mixture at the reference temperature and composition computed using the Sparrow and Gregg 1/3 law according to [42], T_s and T_∞ correspond respectively to the interface and ambient-gas temperature, and $L_{v,s}$ is the fuel latent-heat of vaporization at the interface temperature.

Under the aforesaid hypotheses, the following relation must be verified:

$$B_m = B_t = B \tag{3}$$

The associated equation system is solved iteratively varying the T_s value. More details about the evaporation submodel can be found in [14]. The evaporation submodel allows for the determination of the evaporating liquid-fuel thermo-chemical properties as a function of the pressure, p_∞, and temperature of the surrounding gas, Fig. 4.

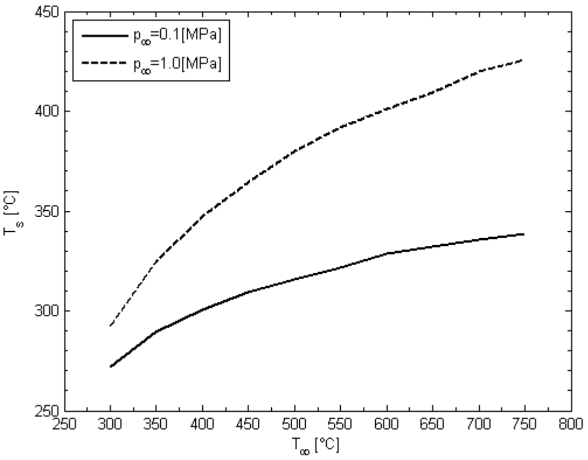

Figure 4 – Influence of the surrounding gas thermodynamic state on the liquid-gas interface temperature for n-heptane [14].

The computed properties at the liquid-gas interface will be used in the mixture characterization submodel and in the combustion submodel presented below. In particular, T_s is very important in spray modeling as it permits an estimate of the local temperature of the mixture.

Concerning the computation of the fuel-mass evaporation-rate, it is worth mentioning that the liquid-fuel mass-distribution within the spray is very complex. In fact, the real scenario consists of droplet-size distribution, ligaments, and undefined geometry of the liquid phase. In a global-system-simulation approach, to solve the associated system of differential equations is not possible because of the CPU cost. For that reason, a more global approach based on the computation of a global characteristic evaporation-time, τ_{ev}, has been preferred.

The overall fuel-mass evaporation-rate, $\dot{m}_F$, is then computed as:

$$\dot{m}_F = C_{ev} \cdot \frac{m_{F,l}}{\tau_{ev}} \tag{4}$$

where C_{ev} is an adjustment constant coefficient of the model, m_F is the mass of gaseous fuel and $m_{F,l}$ represents the liquid-fuel mass.

Characteristic evaporation-time is computed starting from the theory proposed in [29]. This theory permits to estimate the liquid-jet penetration-length, L_0, as a function of the geometry of the injector, the composition of the fluids and their thermodynamic state. τ_{ev} is then computed inverting the equation giving the temporal evolution of the liquid-jet penetration-length, and imposing a liquid penetration equal to L_0. Quantitative results of the model, compared to 3D simulation results relative to ICE application, can be found in [14].

GAS ENTRAINMENT SUBMODEL

This submodel describes the temporal evolution of the spray volumes inside the cylinder and computes the mass transfers between sprays.

Figure 5 shows a 3D computation of the spray-volume evolution in an ICE equipped with a piston bowl with NADI^{TM} (*Narrow Angle Direct Injection*)[1] concept specifications. As can be seen, the narrow angle of injection (angle between the spray penetration and cylinder axes) favours deep penetrations of the spray in the cylinder, (a). Once the tip of the spray impacts the piston, the spray is outward-guided by the bowl shape, (b). Then, the shape of the bowl confers a coherent toroidal movement to the spray, (c)(d). As can be seen, the spray tip reaches the proximity of the injection point before the spray fills up the whole cylinder.

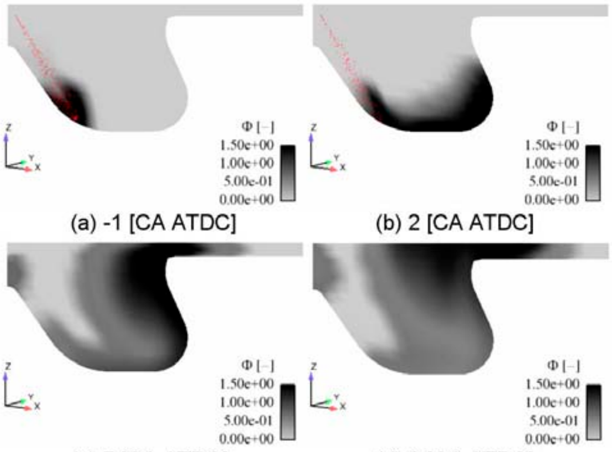

(a) -1 [CA ATDC] (b) 2 [CA ATDC]

(c) 5 [CA ATDC] (d) 8 [CA ATDC]

Figure 5 - Typical spray evolution in an ICE equipped with the NADI^{TM} concept specifications. Equivalence-ratio distribution at different crank angle values: -1, 2, 5 and 8 CA ATDC. Engine speed: 1500 rpm.

Here, spray regions are supposed to be perfect truncated cones, Fig. 6. Spray volumes are completely defined once all the penetration lengths, S_i, and the spray angles, θ_i, are known (subscript *i* indicating the injection number). The hypothesis that the injection *i+1* is performed in the spray region of injection *i* will be retained in the following discussion. This assumption, partially justified by Fig. 5, will be further supported by the good agreement between simulation results and experimental data.

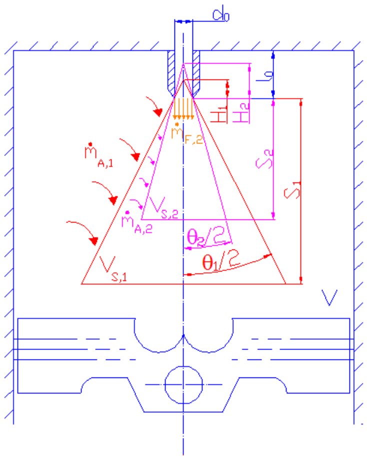

Figure 6 - Description of spray volumes for two injections.

The penetration length of each spray is computed using the well-known semi-empirical correlation given in [26]. According to this theory, once defined the spatial, x_i^+, and temporal, t_i^+, scales as:

---

[1] All the experimental results presented below refer to an ICE equipped with a piston bowl with NADI^{TM} concept specifications.

$$x_i^+ = \frac{\sqrt{C_a} \cdot d_h \cdot \sqrt{\dfrac{\rho_{F,l}}{\rho_{A,i}}}}{a \cdot \tan\left(\dfrac{\vartheta_i}{2}\right)} \quad \text{and} \quad t_i^+ = \frac{x_i^+}{U_{F,l,i}} \tag{5}$$

where C_a is the orifice coefficient of area-contraction, d_h is the injector hole diameter, ρ_A is the ambient-gas density, $\rho_{F,l}$ is the liquid-fuel density, a is a dimensionless coefficient (authors recommend a = 0.66) and $U_{F,l}$ is the fuel velocity in the injector nozzle, penetration length of the *i-th* spray can be expressed as:

$$S_i = \left[\left(\frac{1}{\dfrac{t_{inj,i}}{t_i^+}}\right)^q + \left(\frac{1}{\left(\dfrac{t_{inj,i}}{t_i^+}\right)^{\frac{1}{2}}}\right)^q\right]^{-\frac{1}{q}} \cdot x_i^+ \tag{6}$$

and the relative spray opening-angle as:

$$\tan\left(\frac{\vartheta_i}{2}\right) = C_{\vartheta,i} \cdot \left[\left(\frac{\rho_{A,i}}{\rho_{F,l}}\right)^{0.19} - 0.0043 \cdot \sqrt{\frac{\rho_{F,l}}{\rho_{A,i}}}\right] \tag{7}$$

where q is a dimensionless coefficient (author recommend q = 2.2), $t_{inj,i}$ is the relative-time coordinate referred to injection i with its origin at the SOI (*Start Of the Injection*), and $C_{\theta,i}$ is an adjustment constant-coefficient relative to injection *i*.

Hence, by using geometrical considerations, the volume of the *i-th* injection, $V_{S,i}$, is:

$$V_{S,i} = \hat{V}_{S,i} - \hat{V}_{S,(i-1)} \cdot (i > 1) \tag{8}$$

where:

$$\hat{V}_{S,i} = \frac{\pi}{3} \cdot \tan^2\left(\frac{\vartheta_i}{2}\right) \cdot \left[(S_i + H_i)^3 - H_i^3\right] \tag{9}$$

is the truncated cone relative to the vapor penetration length of the *i-th* injection. Definition of H_i can be found in Fig. 6.

This model, relative to a non-reactive single-injection in a constant-volume vessel, has been widely discussed and validated with experimental data [26,27,36]. The model has been shown to be sensitive to variations of parameters such as injection pressure, nozzle geometry and thermodynamic state of vessel ambient-gas. In ICE applications, in-cylinder thermodynamic-conditions vary in time because of the piston motion, thermal fluxes and combustion process. For that reason, in order to take into account the time history of the spray penetrations, the differential form of Eq. (8) has been implemented in the model. As a consequence, spray volume is computed as:

$$V_{S,i} = \int_0^{t_{inj,i}} \dot{V}_{S,i} \cdot dt_{inj,i} \tag{10}$$

This model has been validated for ICE application through comparison of 0D model results with 3D CFD model results in the case of single injection [14].

Spray-volume evolutions determines the entrainment of ambient gas, m_A, in the spray. Hence, for the injection *i*, the entrained-gas-mass flow-rate is:

$$\frac{dm_{A,i}}{dt} = \rho_{A,(i-1)} \cdot \frac{dV_{S,i}}{dt} \tag{11}$$

In the case of *i=1*, $\rho_{A,0}$ must be considered to be referred to the ambient-gas mixture initially contained in the cylinder.

Figure 7 represents a general case of triple-injection spray evolutions in non-reactive conditions. As shown, although the liquid-fuel injection-rates are all the same for the three injections, (a), the evolutions of the spray volumes are very different from each other because of thermodynamic conditions of the ambient gas and the piston movement, (b). Figure 7 (c) shows the oxygen mass-transfers from one spray to another. As shown, because of the non-reactive conditions, the total initial mass of oxygen is conserved. Finally, the gaseous-fuel mass in the different sprays as well as its global value, are plotted and compared to the liquid-fuel injected-mass, (d).

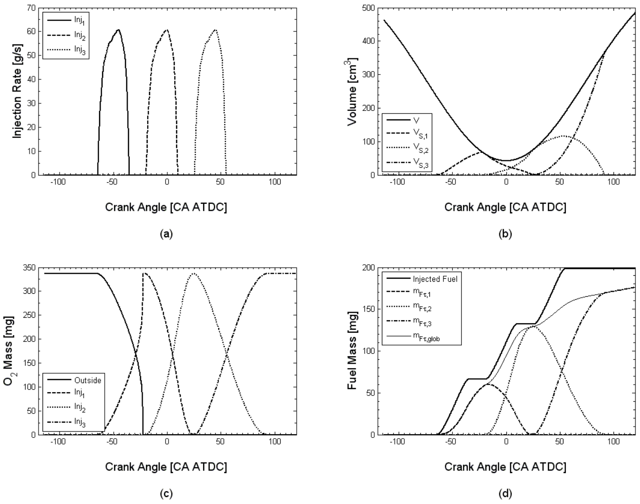

Figure 7 - Triple-injection spray evolutions in non-reactive conditions. Injection rates (a), spray volume evolutions (b), oxygen mass-transfer between sprays (c) and fuel-tracer mass transfer between sprays (d). Global liquid-fuel injected-mass is compared to the global fuel-tracer mass (d).

TURBULENCE SUBMODEL

Turbulence has an enormous impact on the Diesel HCCI combustion process. More particularly, it plays a very important role in the mixture formation process, as it enhances mass, momentum and energy transfer-rates. The goal of the turbulence submodel is to estimate the characteristic turbulent time, τ_t.

The following model is obtained by reduction of the 3D κ–ε turbulence-modeling approach. In the most general way, the balance-equation relative to a closed volume for global kinetic-energy, E_c, can be expressed as the sum of production and dissipation terms:

$$\frac{dE_C}{dt} = \left.\frac{dE_C}{dt}\right|_{pr} + \left.\frac{dE_C}{dt}\right|_{ds} \qquad (12)$$

According to [43], the spray-associated kinetic-energy represents 98% of the total kinetic energy of the mixture. For that reason all different contributions (e.g. swirl, tumble and squish kinetic energies) will be neglected in what follows.

Hence, the E_c production term can be expressed as:

$$\left.\frac{dE_C}{dt}\right|_{pr} \cong \left.\frac{dE_C}{dt}\right|_{spray} = \frac{U_{F,l}^2}{2} \cdot \frac{dm_{F,inj}}{dt} \qquad (13)$$

in which:

$$U_{F,l} = \frac{1}{C_d \cdot n_h \cdot \rho_{F,l} \cdot \left(\frac{\pi}{4} \cdot d_h^2\right)} \cdot \frac{dm_{F,inj}}{dt} \qquad (14)$$

where $m_{F,inj}$ is the injected mass of fuel, C_d is the discharge coefficient of the orifice and n_h is the number of injector holes.

By spatially filtering the 3D momentum balance-equation, it is possible to compute the mean specific kinetic-energy, $\widetilde{K}$[2]:

$$\frac{d\widetilde{K}}{dt} = \frac{\sqrt{2 \cdot \widetilde{K}}}{m_S} \cdot \left[U_{F,l} \cdot \frac{dm_{F,inj}}{dt} - \sqrt{2 \cdot \widetilde{K}} \cdot \right.$$

$$\left. \cdot \left(\frac{dm_A}{dt} + \frac{dm_{F,inj}}{dt} \right) \right] - C_K \cdot \widetilde{K}^{N_K} \qquad (15)$$

where the last term is an empirical expression representing the closure term relative to the dissipation rate. Here, m_S being the global mass of gases in the spray, and C_K and N_K are two constant coefficients of the model. More details on the derivation of Eq. (15) can be found in [44].

Consequently, the mean specific turbulent-kinetic-energy, $\widetilde{\kappa}$, can be computed as:

$$\widetilde{\kappa} = \frac{E_c}{m_S} - \widetilde{K} \qquad (16)$$

The mean specific turbulent-kinetic-energy dissipation-rate, $\widetilde{\varepsilon}$, is supposed to have a similar expression to the dissipation-rate term of $\widetilde{K}$:

$$\widetilde{\varepsilon} = C_\kappa \cdot \widetilde{\kappa}^{N_\kappa} \qquad (17)$$

where $C\kappa$ and $N\kappa$ are two constant coefficients of the model.

Equation (12) can now be rewritten as:

$$\frac{dE_C}{dt} = \frac{U_{F,l}^2}{2} \cdot \frac{dm_{F,inj}}{dt} - m_S \cdot \left(C_K \cdot \widetilde{K}^{N_K} + C_\kappa \cdot \widetilde{\kappa}^{N_\kappa} \right) \qquad (18)$$

---

[2] The symbol tilde means that the variable has been computed using the Favre mean-operator.

According to the well-established κ–ε theory of turbulence, the characteristic turbulent time is computed as:

$$\tau_t = \frac{\widetilde{\kappa}}{\widetilde{\varepsilon}} \tag{19}$$

MIXTURE SUBMODEL

In Diesel HCCI combustion computations, one of the major challenges is to be able to well describe fuel-mass distribution inside the mixture zone. The reason being that both auto-ignition and oxidation processes take place, in the most general case, in a stratified mixture. In a previous work [14], a 0D PDF-based model for the description of the mixture of a single-injection spray, has been exhaustively detailed and validated by comparison with 3D CFD simulations and experimental data.

Here, the same modeling approach has been used and generalised to the computation of multi-injection sprays. As shown in the *Gas Entrainment Submodel* section, each injection generates its own mixture region. Mixture description submodel attributes to each mixture zone a PDF describing the fuel mixture-fraction distribution. Fuel mixture-fraction, Z, is a combustion-independent variable, [45], here defined as:

$$Z = Y_{F\tau} \tag{20}$$

where $Y_{F,\tau}$ is the fuel-tracer mass-fraction, which is the local fuel mass-fraction in the case of a non-reactive mixture. PDFs are then used to estimate several local variables such as temperature and composition of the mixture and species reaction rates.

Presumed PDF

Different kinds of PDF are available in literature. In order to simulate the mixing process taking place in diffusion flames, PDFs described by β-functions have been judged the best adapted [46]. β-PDF shape (here representing the probability to have in the spray a mixture at a given Z, $P(Z)$), is completely described once fixed the values of two parameters. These parameters are the mean value of the distribution, $\tilde{Z}$, and its variance, $\widetilde{Z''^2}$, defined as:

$$\tilde{Z} = \frac{1}{m_S}\int_{m_S} Z\big|_{dm}\cdot dm \tag{21}$$

and:

$$\widetilde{Z''^2} = \frac{1}{m_S}\cdot\int_{m_S}\left(Z\big|_{dm} - \tilde{Z}\right)^2\cdot dm \tag{22}$$

Application to ICE

An ICE is a very complex system to study. A short overview of the difficulties that can be encountered in modeling a spray region relative to ICE applications, can be summarized as follows:

- both volume and mass of the mixture zone grow in time,
- the upper limit of the mixture-fraction existence-domain, $Z_{s,max}$, that corresponds to the maximum value of $Y_{F,s}$ computed by the evaporation submodel, evolves in time as function of the in-cylinder thermodynamic conditions,
- fuel/ambient-gas ratio varies in time.

It is worth to this end to cite some results concerning the use of β-PDF, [14]. The fact of using a β-PDF to represent the Z distribution gives the undeniable advantage (especially in a global-system-simulation approach) to access different necessary information concerning the mixture by only adding one equation (relative to the distribution variance variable) to the system of differential equations built considering averaged quantities. On the other hand, as the β-PDF shape is defined by only two parameters, limitations in mixture characterization could appear, Fig. 8.

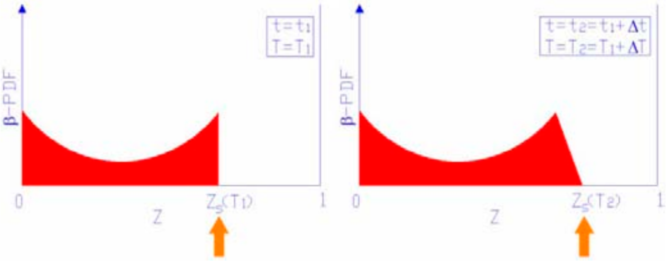

Figure 8 - Representation of β-PDF limitation: mixture fraction distribution at two different instants of time. During *Δt*, temperature increases and liquid-fuel evaporates at $Z = Z_s(T_2) > Z_s(T_1)$. The right-hand distribution shape cannot be represented by a β-PDF [14].

To reduce the impact of these limitations on modeling, in the following, the upper limit of the distribution domain will be considered as constant and equal to the maximum value reached during the evaporation process, $Z_{s,max}$, arbitrarily fixed equal to unity. Nevertheless, in what follows, the notation Z_s will be maintained in order to conserve the generality of the β-PDF parameter equations.

Mean-value equation

In the model, the mean value of the *i-th* spray is computed as:

$$\tilde{Z}_i = \frac{m_{F\tau,i}}{m_{S,i}} \tag{23}$$

where $m_{F\tau,i}$ is the mass of fuel tracer in the spray region.

Variance equation

The differential equation for variance is obtained by differentiating Eq. (22) with respect to time[3]. For the *i-th* spray, it holds:

$$\frac{d\widetilde{Z''^2_i}}{dt} = \left[\underbrace{\left(\tilde{Z}_i^2 \cdot \left(1 - \frac{1}{Z_{s,i}} \right) + \left(\left(Z_{s,i} - \tilde{Z}_i \right)^2 \cdot \frac{1}{Z_{s,i}} - \widetilde{Z''^2_i} \right) \right) \cdot \frac{dm_{F,i}}{dt}}_{I} + \right.$$
$$\left. + \underbrace{\left(\left(Z_{in,(i-1)} - \tilde{Z}_i \right)^2 - \widetilde{Z''^2_i} \right) \cdot \frac{dm_{in,i}}{dt}}_{II} + \underbrace{\widetilde{Z''^2_i} \cdot \frac{\left| dm_{out,i} \right|}{dt}}_{III} \right] \cdot \frac{1}{m_{S,i}} +$$
$$\underbrace{-2 \cdot C_{ds,i} \cdot \frac{\tilde{\varepsilon}}{\tilde{\kappa}} \cdot \widetilde{Z''^2_i}}_{IV} \tag{24}$$

On the right-hand side of Eq. (24), it is possible to distinguish four terms. The first term, *I*, corresponds to the fuel-evaporation contribution. The second term, *II*, corresponds to the contribution of the entrained-gas in the spray region. In the case of *i>1*, entrained-gas is considered to have the mean composition of the spray *(i-1)*. The third term, *III*, is relative to the outgoing gaseous-mass (entrained by the spray *(i+1)*) contribution. The outgoing mass of gas is supposed to have the mean composition of the mixture. This explains its positive contribution to variance. The fourth term, *IV*, represents the mixing-phenomenon contribution to variance. It represents the dissipation of the variance and it has been modeled by using an empirical closure-term [44]. C_{ds} is an adjustment coefficient of the model.

In Eq. (24), the hypothesis that liquid-fuel evaporates at saturated thermodynamic-conditions in pure ambient-gas ($Z=0=Z_0$), is implicit. Equation (24) represents the link between the different mixture zones, Fig. 2.

β-PDF parameters

β-PDF is a normalized statistical tool whose parameters are the mean-value of the distribution, $\tilde{Z}_{\beta-PDF}$, and its variance, $\widetilde{Z''^2_{\beta-PDF}}$, varying between 0 and 1. Hence, once computed the distribution mean-value, $\tilde{Z}$, and its variance, $\widetilde{Z''^2}$, they need to be normalized in order to be associated with the β-PDF. The proposed normalizations, taking into account the fact that the maximum value of Z corresponds to the saturation condition of evaporation, are:

$$\tilde{Z}_{\beta-PDF} = \frac{\tilde{Z}}{Z_s} \tag{25}$$

and:

$$\widetilde{Z''^2_{\beta-PDF}} = \frac{\widetilde{Z''^2}}{\widetilde{Z''^2_{\max}}} = \frac{\widetilde{Z''^2}}{\tilde{Z} \cdot \left(Z_s - \tilde{Z} \right)} \tag{26}$$

COMBUSTION MODELING

Here is presented the second part of the global Diesel HCCI combustion-model: the combustion model, Fig. 2. The choice to use a complex-chemistry approach is mainly due to the following two reasons:

- in an ICE context, the pollutant formation-mechanisms, highly dependent on chemical kinetics, need to be investigated to have a deeper understanding of the engine pollutant emissions,
- it allows the prediction of the chemical kinetics for both conventional and non-conventional combustion-regimes.

Detailed description of the tabulation methodology can be found in [25]. In the following, only the key points of the combustion model necessary for a complete understanding of the paper will be discussed.

n-heptane has been chosen as Diesel-fuel surrogate. The chemical tables, referred to the chemical-kinetics scheme proposed in [47], give the reaction rates of the tabulated species (namely, O_2, CO_2, CO and H) as function of the local thermo-chemical state of the mixture and of the combustion-progress variable, *c*. Four independent thermo-chemical coordinates have been chosen to completely characterize the initial mixture of gases:

---

[3] Complete proof of the equation derivation is given in Appendix.

- p_0: pressure,
- T_0: temperature,
- ϕ: equivalence ratio (definition given below),
- X_r: molar fraction of EGR in the ambient gas, initially contained in the cylinder.

Progress variable, c, varies from 0, in unburned gases, to 1, in fully burned gases, and is computed starting from the local mass-concentrations of O_2, CO_2 and CO, as proposed in [44].

Complex-chemistry computations, performed to generate the chemical tabulation, have been done by using SENKIN, from CHEMKIN package, [48], considering a constant-volume PSR (*Perfectly Stirred Reactor*). Hence, in a multi-injection context, the reaction rate for a given tabulated species, $\varpi_{esp,i}$, relative to the *i-th* injection, can be expressed as:

$$\omega_{esp,i} = \omega_{esp,i}\left(p_{0,i}, T_{0,i}, \phi_i, X_r, c_i\right) \tag{27}$$

By using the computed tabulated-species reaction-rates and the C, O, H and N atomic balance-equations, reaction rates for C_7H_{16}, H_2O, H_2 and N_2 (reconstructed species) can be determined.

MATCHING OF SPRAY AND COMBUSTION MODELS

It is worth detailing how spray and combustion models interact each other. First of all it is important to detail the relation between the fuel mass-fraction, Z, whose distribution is described by using the β-PDF, and the equivalence ratio, ϕ, representing an input to compute $\varpi_{esp,i}$:

$$Z = \frac{\phi}{PCO} \cdot \left(1 - X_r \cdot \frac{M_r}{M_{mix}}\right) \cdot \frac{1}{\frac{\phi}{PCO} + 1} \tag{28}$$

with:

$$\phi = \frac{Y_F}{Y_{O_2}} \cdot \left(\frac{Y_{O_2}}{Y_F}\right)_{st} \quad \text{and} \quad PCO = \left(\frac{m_a}{m_F}\right)_{st} \tag{29}$$

where M_r and M_{mix} are the molar masses of EGR and spray mixture respectively, Y_F and Y_{O2} are the mass fractions of the fuel and oxygen respectively, and m_a is the mass of air. Subscript *st* indicates the stoichiometric conditions of the mixture.

As can be seen in Eq. (28), mixture fraction is a function of two look-up table inputs: the equivalence ratio and the EGR molar-fraction. As the relation between these two inputs and the mixture fraction is not linear, particular attention must be paid in interpolating table values [14].

Concerning the determination of p_0 and T_0 look-up table inputs, in ICE applications, several considerations must be made. Combustion process associated with the *i-th* injection does not take place in a constant-volume reactor. In particular, volume can vary because of:

- piston motion,
- expansion of the volume of the *j-th* spray (where *j•i*) due to its own combustion process.

Hence, for the *i-th* spray, the $p_{0,i}$ and $T_{0,i}$ look-up table inputs are determined as the values of pressure and temperature associated with the spray considered as non-reactive, but sensitive to the aforesaid effects. Consequently, it is necessary to solve for each spray an additional energy-balance equation considering the spray as non-reactive. Values of pressure and temperature associated with the non-reactive spray will be identified henceforth by using the subscript τ, to indicate that they refer to the spray tracer-conditions. Hence:

$$p_{0,i} = p_{\tau,i} \quad \text{and} \quad T_{0,i} = T_{\tau,i} \tag{30}$$

Under the following hypotheses:

- $p_{\tau,i}$ and X_r are constant in the domain,
- $T_{\tau,i}$ only depends on the fuel mass-fraction, Z,
- c_i is homogeneous in the domain and equal to the mean progress-variable value of the spray, $\overline{c}_i$,

the mean reaction-rate for a given species associated with the *i-th* spray can be computed as:

$$\overline{\varpi}_{esp,i} = \int \omega\left(p_{\tau,i}, T_{\tau,i}\left(Z^*\right), Z^*, X_r, \overline{c}_i\right) \cdot P\left(Z^*\right) \cdot dZ^* \tag{31}$$

The equation defining the local initial-temperature of the mixture as function of the mixture fraction is:

$$T_{\tau,i} = T_{\tau,i}\left(Z\right) = \tilde{T}_{\tau,i} + \left(\frac{T_{s,i} - \tilde{T}_{\tau,i}}{Z_{s,i}}\right) \cdot Z \tag{32}$$

where $Z_{s,i}$ and $T_{s,i}$ are respectively the values of the mixture fraction and the temperature at the liquid-gas interface under evaporating conditions, and $\tilde{T}_{\tau,i}$ is the value of the mean tracer-temperature in the *i-th* spray, obtained, once computed the corresponding $p_{\tau,i}$ value, by using the ideal-gas state-equation.

Moreover, starting from the progress variable values associated with each spray and their chemical composition, it is possible to compute a global progress-variable, c_{glob}, representative of the overall combustion process. More details about its behavior in a multi-injection context will be presented in the section below.

MODEL VALIDATION

The validation of the global Diesel HCCI combustion-model has been carried out by comparing the computed results with experimental data. At a given engine operating-point, for each cylinder, the experimental mean-pressure curve is obtained by averaging hundreds of engine-cycle pressure-signals recorded at the test bench. To account for cylinder-to-cylinder variations, both the mean-pressure curve of the cylinder with the lowest peak pressure and that of the cylinder with the highest peak pressure have been plotted.

The model has been tested on a complete engine-map, constituting of 101 steady-state operating-points, giving satisfactory results. The map refers to a four-cylinder turbo-charged G9T-NADI^{TM} engine, Table 1.

Table 1 - Engine Characteristics.

Engine Type	in-line 4 cylinder
Stroke [mm]	92
Bore [mm]	87
Rod Length [mm]	149.9
Compression Ratio [-]	14
Injection System	Bosch CRI 2.2

More details concerning the engine can be found in [2].

It is important to point out two aspects that constitute an additional challenge for the model:

- model parameter setting has been done once and for all,
- simulation initial and boundary conditions, such as injected mass and in-cylinder pressure, temperature and mixture composition, have been obtained directly from engine test-bench measurements. Consequently, they do not represent adjustment parameters of the model.

The engine operating points presented in this paper, Table 2, have been extracted from the computed-experimental database of engine operating points. In particular, the combustion process of the point n° 1 will be studied in detail. This point has been chosen because it presents a strong interaction between the spray volumes. It will be shown that the hypothesis of the *(i+1)-th* spray growing in the *i-th* one is not limiting for modeling. On the other hand, points n° 2 - 6 have been chosen because they are important for the Diesel-engine performance validation.

Table 2 - Set of experimental engine operating points.

Operating Point [-]	**1**	**2**	**3**	**4**	**5**	**6**
Engine Speed [rpm]	3500	950	1501	1499	1499	2000
IMEP [bar]	14.08	1.07	1.08	12.08	16.2	24.2
EGR Rate [%]	0	54.4	53.1	0	0	0
SOI Pilot [CA ATDC]	-41.5	-23		-28	-20	
SOI Main [CA ATDC]	-16	-5	-20	-3	-9	-8
ϕ [-]	0.485	0.319	0.321	0.675	0.794	0.743
Injection Pressure [bar]	1594	448	697	1396	1562	1473

The operating points listed in Table 2 represent a big challenge for the model. In fact they present:

- strong variations of engine speed,
- strong variations of IMEP (*Indicated Mean Effective Pressure*),
- strong variations of dilution,
- very different injection strategies,
- strong variation of injection pressure,

and all these taking place in a context of single and multiple injection.

DETAILED ANALYSIS OF AN OPERATING POINT

In the following, the operating point n° 1, Table 2, will be studied in detail. Figure 9 shows the in-cylinder pressure and temperature evolutions as well as their tracer values used for chemical-table reading (tracer curves referring to the first injection stop to be computed once first spray-volume disappears). In-cylinder pressure is compared to experimental results. As can be seen, the curves match very well.

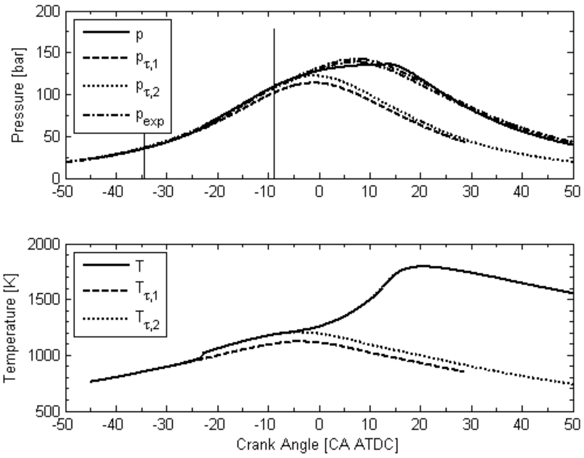

Figure 9 - Operating point n° 1. Top: comparison of computed in-cylinder pressure (solid) with experimental data and spray tracer-pressures; vertical lines indicate the SOIs. Bottom: computed in-cylinder temperature and spray tracer-temperatures.

Figure 10 displays the injected liquid-fuel mass flow-rate (input of the model), and the current liquid-fuel mass contained in the pilot and main spray-volumes. As can be seen, even if the injection rate relative to main injection is higher than the one relative to pilot injection, its current liquid-fuel mass is lower. This is due to the fact that evaporation-rate during main-injection is amplified by the more severe thermodynamic conditions of the liquid surrounding-gases.

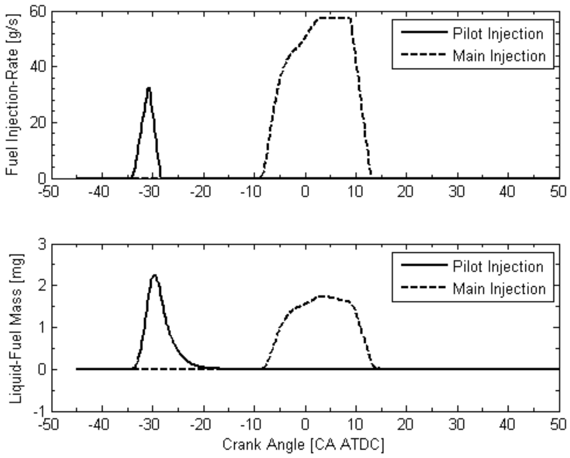

Figure 10 - Operating point n° 1. Top: fuel injection-rates relative to pilot and main injection. Bottom: computed current liquid-mass of fuel relative to pilot and main injection.

Figure 11 refers to the temporal evolution of the spray volumes. Concerning this particular operating point, it is possible to observe that the pilot-injection spray-volume, $V_{S,1}$, does not have the time to completely fill the cylinder volume, V, before the main injection begins. As shown, the evolution of the main-injection spray-volume, $V_{S,2}$, contrasts the growth of the pilot-injection region. During this phase, mass transfer between the two sprays takes place. The evolution of the global-spray volume, $V_{S,glob}$, points out the instant at which sprays completely fill the cylinder volume.

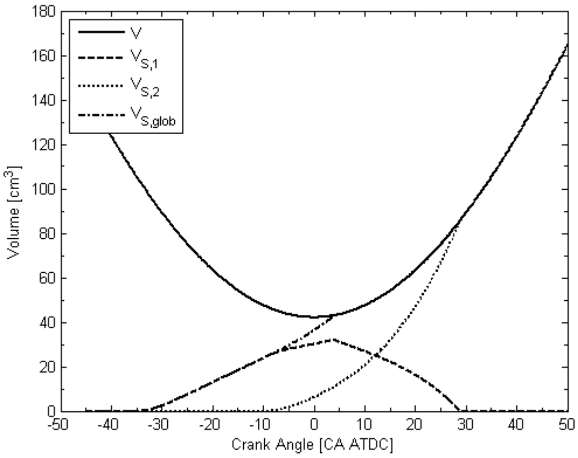

Figure 11 - Operating point n° 1. Evolution of cylinder and computed spray volumes.

Figure 12 shows the global kinetic-energy and mean global turbulent-kinetic-energy associated with the sprays.

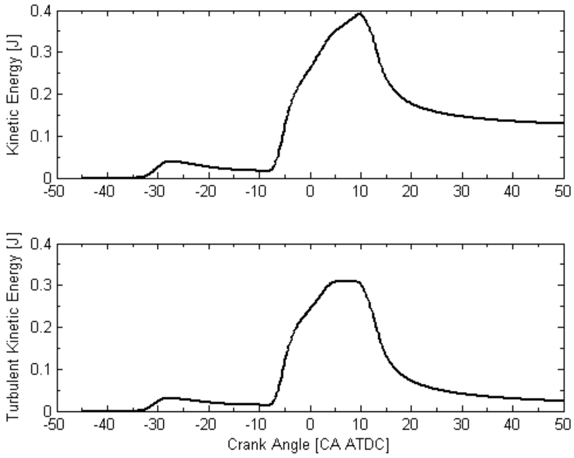

Figure 12 - Operating point n° 1. Top: computed kinetic energy in the sprays. Bottom: computed mean specific turbulent-kinetic-energy in the sprays.

Figure 13 shows the mean equivalence ratios and the mixture-fraction variances associated with the pilot and main injections. It is noteworthy to remember that, under the hypothesis of a β-PDF mixture-fraction distribution, these two variables completely define the fuel-mixture-fraction stratification in the spray.

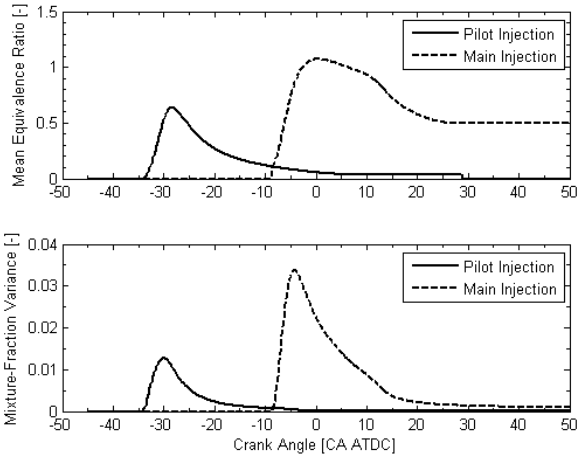

Figure 13 - Operating point n° 1. Top: computed spray equivalence-ratio evolutions. Bottom: computed spray variance evolutions.

Figure 14 shows the HR (*Heat Release*) and the HRR (*Heat release Rate*) associated with the combustion process. As can be observed looking at the HRR curve, the fuel of the pilot injection burns essentially in premixed-flame conditions (peak of HRR), while the fuel of the main injection burns in diffusion-flame conditions. The model tends to overestimate the first peak of the HRR. This is probably due to the hypothesis that the combustion process for each spray can be described at each instant of time using a unique progress variable, which is independent of the equivalence-ratio. Hence only the HR curves are shown in what follows.

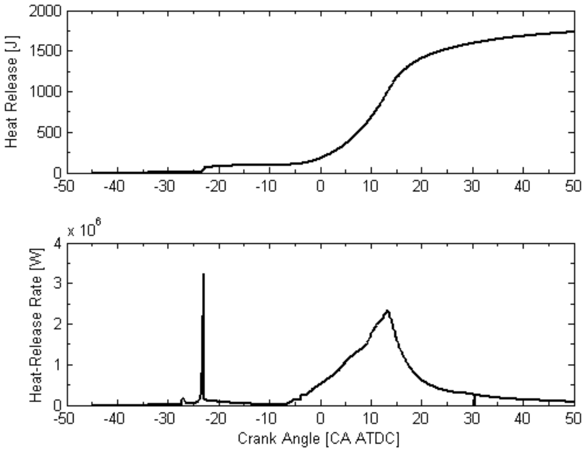

Figure 14 - Operating point n° 1. Top: computed global heat-release. Bottom: computed global heat-release rate.

Figure 15 refers to progress-variable evolutions. As shown, the progress variable relative to the pilot-injection spray, C_1, presents a sharp evolution that is well representative of a premixed-flame combustion. In the main-injection spray, a gas mixture that potentially has already begun its oxidation process is entrained. Thus, at the beginning, its progress variable, C_2, is not stringently equal to zero. It is noteworthy that the global progress-variable, C_{glob}, decreases when main injection begins. This behavior, that at first sight could seem to be unexpected, is explained by the fact that chemical equilibrium of the mixture vary with the variation of the composition of the spray.

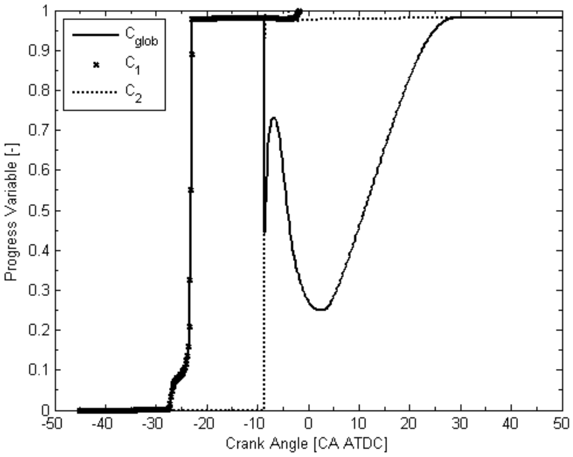

Figure 15 - Operating point n° 1. Evolution of global and spray progress-variables.

COMPARISON WITH EXPERIMENTAL DATA

A major challenge for the Diesel HCCI combustion-model is to be able to reproduce the engine performances in the whole engine operating-domain. Figures 16 - 21 refer to the engine operating-points listed in Table 2. On the top of each figure, the computed in-cylinder pressure is compared to experimental traces; on the bottom part, computed heat release is plotted.

Figure 16, added for completeness, refers to the engine operating-point n°1 which has been widely discussed in the previous section.

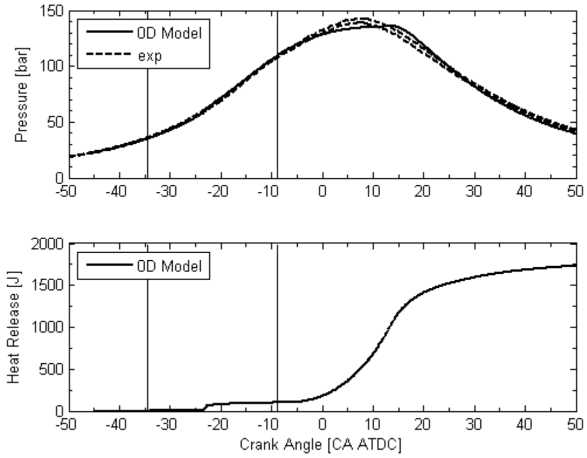

Figure 16 - Operating point n° 1. Top: comparison of computed in-cylinder pressure with experimental data. Bottom: global heat-release. Vertical lines indicate the SOIs.

Figure 17 refers to an idling engine operating-point and, consequently, it is characterized by low load and low engine speed. High EGR rate has been used and a multi-injection strategy has been set up. As shown, pilot-injection presents a long ignition-delay because of the combustion-non-favorable conditions in the cylinder and the high dilution-rate of the oxidant. Subsequently, the oxidation of the pilot-injection contributes to increased pressure and temperature in the combustion chamber. Consequently, the presence of the pilot injection favors the main-injection oxidation-process.

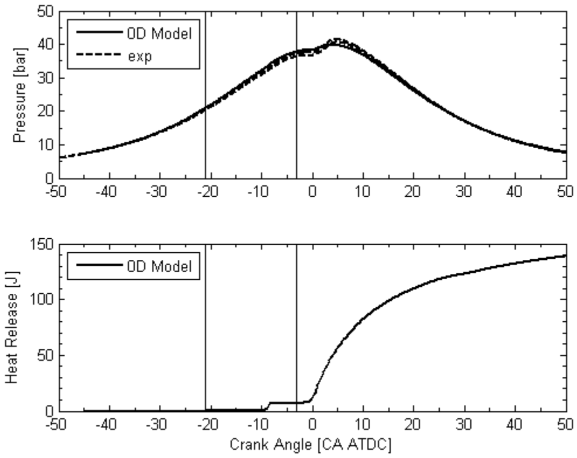

Figure 17 - Operating point n° 2. Top: comparison of computed in-cylinder pressure with experimental data. Bottom: global heat-release. Vertical lines indicate the SOIs.

Figure 18 refers to low-load and medium engine-speed operation-point. High EGR rate has been used and a single-injection strategy has been set up. Because of the high dilution rate of the oxidant, long ignition-delay is observed. Hence, at the beginning of the combustion process, mixture inside the cylinder is relatively homogeneous and, consequently, the whole mixture auto-ignites at the same time. This aspect, which can be noted by observing the sharp shape of the heat-release curve, is typical of HCCI combustion processes. As can be seen, the Diesel HCCI combustion model well predicts this phenomenon.

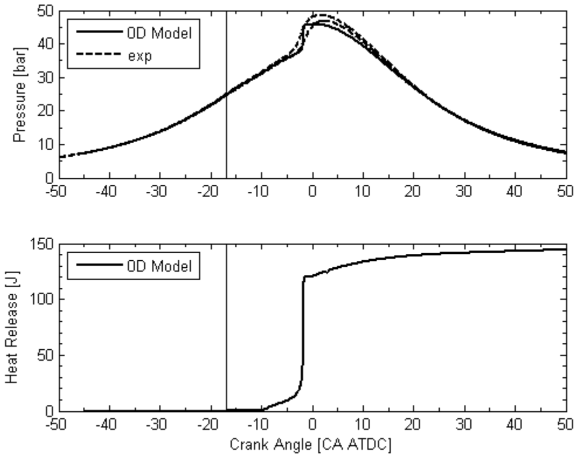

Figure 18 - Operating point n° 3. Top: comparison of computed in-cylinder pressure with experimental data. Bottom: global heat-release. Vertical lines indicate the SOI.

Figures 19 - 20 refer to medium and full load engine operating-points respectively, both at medium engine-speed. No oxidant dilutions by using EGR have been performed and multi-injection strategies have been set up. For the two points, combustion processes are quite similar. As shown, even if the two pressure peaks are slightly overestimated, their angular positions are well captured and the overall shapes of the pressure curves are well predicted.

It is worth noting that Fig. 18 - 20 represent a series of engine operating-points, in which IMEP increases from 1 to 16 bar at constant engine speed. As shown, the model correctly reproduces the combustion-process evolution with load.

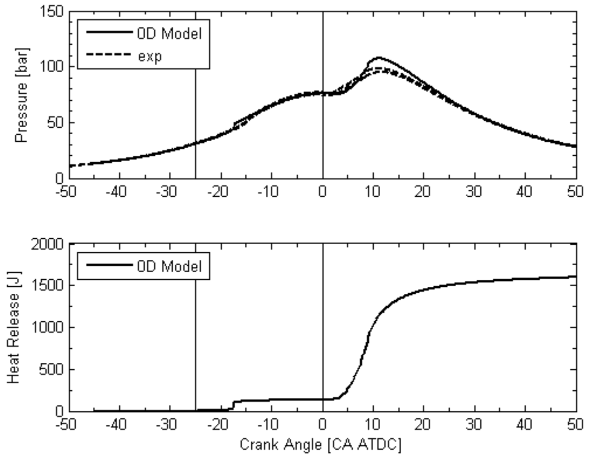

Figure 19 - Operating point n° 4. Top: comparison of computed in-cylinder pressure with experimental data. Bottom: global heat-release. Vertical lines indicate the SOIs.

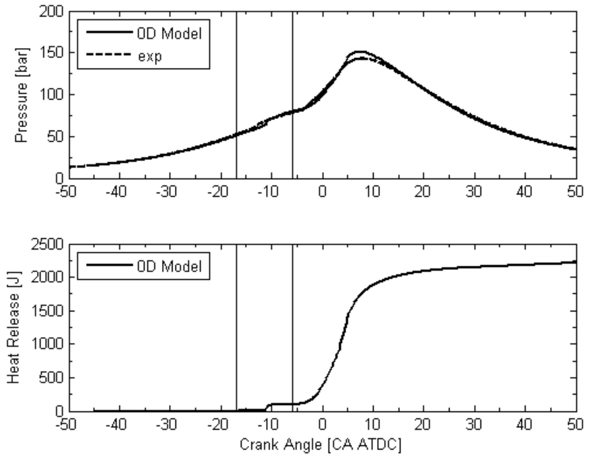

Figure 20 - Operating point n° 5. Top: comparison of computed in-cylinder pressure with experimental data. Bottom: global heat-release. Vertical lines indicate the SOIs.

Figure 21 refers to a full-load and medium engine-speed operating-point, and more precisely to the peak torque output operating-point. No oxidant dilution by using EGR has been performed and a single-injection strategy has been set up. Compared to the experimental curves, computed pressure presents two mismatches. The first one is associated with a model-overestimate of the ignition delay and premixed-flame combustion. This is probably due to the adopted complex-chemistry equivalence-ratio tabulation-limits. In fact, in the model, only a mixture having an equivalence ratio belonging to the interval [0.3 ÷ 3.0] is considered as reactive [14]. This implies that a longer time is needed to obtain a reactive mixture. Authors envisage to investigate this aspect in more detail in their future work. The second mismatch seems to be associated with an underestimate of the mixing frequency, but it could be premature to exclude it as being a consequence of the first one. Nevertheless, the overall shape of the experimental curve is quite well reproduced by the model.

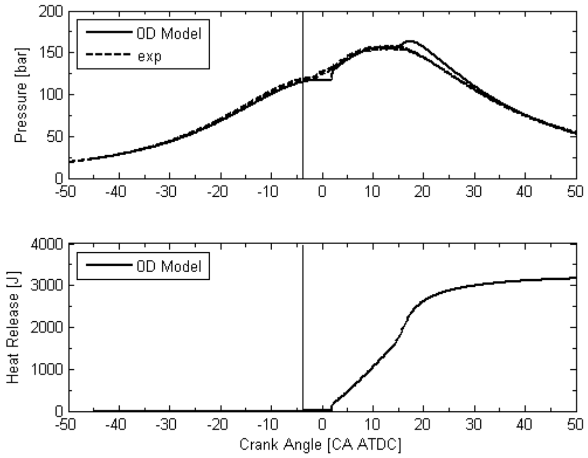

Figure 21 - Operating point n° 6. Top: comparison of computed in-cylinder pressure with experimental data. Bottom: global heat-release. Vertical lines indicate the SOI.

CONCLUSION

A new 0D PDF-based approach to multi-injection Diesel HCCI combustion modeling has been developed and tested on the whole engine operating-domain of an ICE equipped with NADI™ concept specifications. The model has shown the capability to well reproduce the in-cylinder combustion process over a wide range of engine operating-conditions. The principal results are summarized as follows:

- the combustion characteristics are well predicted over a wide range of engine speeds, IMEP, EGR rate, injection strategies and injection pressures,
- the use of PDFs to describe the mixture-fraction distribution inside the sprays allows to have a good description of the mixture process between the gaseous fuel and the ambient gas as well as to take into account the spray interactions in a multi-injection context,
- the complex-chemistry tabulation method reveals to match up with the challenge to simulate both conventional Diesel and HCCI combustion. Moreover, it allows to take into account the impact of the EGR rate on the chemical kinetics of the oxidation process,
- the short computation time, being of the order of 10^2 of real time for multi-injection cases when the simulation is running on a standard PC, allows the model to be used for global-system simulation applications.

In order to improve the existing model, a short-term action envisaged by authors is to set up a new complex-chemistry tabulation with a wider definition domain, especially in terms of the equivalence-ratio coordinate. This new tabulation will be oriented toward the description of the pollutant formation. In particular, a species mass-fraction tabulation approach, instead of a species reaction-rate one, seems to be more promising in ICE modeling.

REFERENCES

1. G.D., Neely, S. Sasaky, Y. Huang, J.A. Leet, D.W. Stewart, "New Diesel emission control strategies to meet US Tier 2 emissions regulations", 2005-01-1091, SAE Technical Paper, 2005.
2. A. Albrecht, G. Corde, V. Knop, H. Boie, M. Castagne, "1D Simulation of turbocharged gasoline direct injection engine for transient strategy optimization", 2005-01-0693, SAE Technical Paper, 2005.
3. A. Albrecht, J. Chauvin, F.A. Lafossas, S. Potteau, G. Corde, "Development of highly premixed combustion Diesel engine model: from simulation to control design", 2006-01-1072, SAE Technical Paper, 2006.
4. F.A. Lafossas, M. Marbaix, P. Menegazzi, "Development and application of a 0D D.I. Diesel combustion model for emissions prediction", 2007-07-1841, SAE Technical Paper, 2007.
5. F. Millo, E. Pautasso, P. Pasero, S. Barbero, N. Vennettilli, "An Experimental and Numerical Study of an Advanced EGR Control System for Automotive Diesel Engine", 2008-01-0208, SAE Technical Paper, 2008.
6. I.I. Vibe, "Brennverlauf und Kreisprozess von Verbrennungsmotoren", *VEB Verlag Technik*, 1970.
7. J.B. Heywood, Internal combustion engine fundamentals, McGraw-Hill, New York, 1988.
8. J.E. Dec, "A conceptual model of DI Diesel combustion based on laser-sheet imaging", 970873, SAE Technical Paper, 1997.
9. F. Chmela, G. Orthaber, "Rate of heat release prediction for direct injection Diesel engines based on purely mixing controlled combustion", 1999-01-0186, SAE Technical Paper, 1999.
10. C. Barba, C. Burkhardt, K. Boulouchos, M. Bargende, "A phenomenological combustion model for heat release rate prediction in high speed DI Diesel engines with common-rail injection", 2000-01-2933, SAE Technical Paper, 2000.
11. N. Cesario, C. Muscio, M. Farina, P. Amato, M. Lavorgna, "Modelling the rate of heat release in common rail Diesel engines: a soft computing approach", 2004-01-2967, SAE Technical Paper, 2004.
12. G. Mauviot, A. Albrecht, T.J. Poinsot, "A new 0D approach for Diesel combustion modeling coupling probability density function with complex chemistry", 2006-01-3332, SAE Technical Paper, 2006.
13. K. Inagaki, M. Ueda, J. Mizuta, K. Nakakita, S. Nakayama, "Universal Diesel Engine Simulator (UniDES): 1st Report: Phenomenological Multi-Zone PDF Model for Predicting the Transient Behavior of Diesel Engine Combustion", 2008-01-0843, SAE Technical Paper, 2008.
14. A. Dulbecco, F.A. Lafossas, G. Mauviot, T.J. Poinsot, "A new 0D Diesel HCCI combustion model derived from a 3D CFD approach with detailed tabulated chemistry", *Oil & Gas Science and Technology*, in press, 2009.
15. H. Hiroyasu, T. Kadota, M. Arai, "Development and use of a spray combustion modelling to predict Diesel engine efficiency and pollutant emissions", Bulletin of the JSME, 26, 214, 569-575, 1983.
16. K. Nishida, H. Hiroyasu, "Simplified three-dimensional modeling of mixture formation and combustion in a Diesel engine", 890269, SAE Technical Paper, 1989.
17. C. Hasse, H. Barths, N. Peters, "Modeling the effects of split-injections in Diesel engines using representative interactive flamelets", 1999-01-3574, SAE Technical Paper, 1999.
18. A. Pires-da-Cruz, T. Baritaud, T.J. Poinsot, "Self-ignition and combustion modeling of initially non-premixed turbulent systems", *Combustion & Flame*, 124, 1-2, 65-81, 2001.
19. Z. Wang, J. Wang, S. Shuai, "Numerical simulation of HCCI engine with multistage gasoline Direct Injection using 3d-cfd with detailed chemistry", 2004-01-0563, SAE Technical Paper, 2004.
20. A. Patel, S.C. Kong, R.D. Reitz, "Development and validation of a reduced reaction mechanism for HCCI engine simulation", 2004-01-0558, SAE Technical Paper, 2004.
21. O. Colin, A. Benkenida, "The 3-zones extended coherent flame model (ECFM3Z) for computing premixed/diffusion combustion", *Oil & Gas Science and Technology*, 59, 6, 593-609, 2004.
22. Z. Wang, S. Shuai, J. Wang, G. Tian, X. An, "Modeling of HCCI combustion from 0D to 3D", 2006-01-1364, SAE Technical Paper, 2006.
23. J.B. Michel, O. Colin, D. Veynante, "Modeling ignition and chemical structure of partially premixed turbulent flames using tabulated chemistry", *Combustion & Flame*, 152, 1-2, 80-99, 2008.
24. Gamma Technologies, User's Manual for GT-POWER, www.gtisoft.com.
25. G. Subramanian, "Modélisation de l'auto-inflammation: analyse des effets de la dilution pas les gaz brûlés et des interactions avec la turbulence dédiée aux moteurs Diesel à charge homogène", PhD Thesis, INSA, Rouen, France, 2005.

26. J.D. Naber, D. Siebers, "Effects of gas density and vaporization on penetration and dispersion of Diesel sprays", 960034, SAE Technical Paper, 1996.
27. D. Verhoeven, J-L. Vanhemelryck, T. Baritaud, "Macroscopic and ignition characteristics of high-pressure sprays of single-component fuel", 981069, SAE Technical Paper, 1998.
28. D.L. Siebers, "Liquid-phase fuel penetration in Diesel sprays", 980809, SAE Technical Paper, 1998.
29. D. Siebers, "Scaling liquid-phase fuel penetration in Diesel sprays based on mixing-limited vaporization", 1999-01-0528, SAE Technical Paper, 1999.
30. J.S. Han, T.C. Wang, X.B. Xie, M.C. Lai, N.A. Henein, D.L. Harrington, J. Pinson, P. Miles, “Dynamics of Multiple-Injection Fuel Sprays in a Small-bore HSDI Diesel Engine”, 2000-01-1256, SAE Technical Paper, 2000.
31. G. Bruneaux, "Liquid and vapor spray structure in high pressure Common Rail Diesel injector", *Atomization and Sprays*, 11, 5, 533-556, 2001.
32. Y. Zhang, K. Nishida, “Effect of injection temporal splitting on the characteristics of fuel-air mixture formation in a common rail Diesel spray”, *Proceeding of the institution of mechanical engineers. Part D, Journal of automobile engineering*, 218, 3, 323-331, 2004.
33. Y. Zhang, K. Nishida, “Imaging of vapour/liquid distributions of split-injected Diesel sprays in a two-dimensional model combustion chamber”, *Combustion Science and Technology*, 176, 1465-1491, 2004.
34. S. Alfuso, L. Allocca, G. Caputo, F.E. Corcione, A. Montanaro, G. Valentino, “Experimental Investigation of a Spray from a Multi-jet Common Rail Injection System for Small Engines”, 2005-24-090, SAE Technical Paper, 2005.
35. G. Bruneaux, "Mixing process in high pressure Diesel jets by normalized laser induced exciplex fluorescence. Part I: free jet", 2005-01-2100, SAE Technical Paper, 2005.
36. J.M. Desantes, R. Payri, F.J. Salvador, A. Gil, "Development and validation of a theoretical model for Diesel spray penetration", *Fuel*, 85, 7-8, 910-917, 2005.
37. C.S. Lee, K.H. Lee, R.D. Reitz, S.W. Park, “Effect of split injection on the macroscopic development and atomization characteristics of a Diesel spray injected through a common-rail system”, *Atomization and Sprays*, 16, 543-562, 2006.
38. U. Maas, S.B. Pope, "Simplifying chemical kinetics: intrinsic low-dimensional manifolds in composition space", *Combustion & Flame*, 88, 3-4, 239-264, 1992.
39. O. Gicquel, N. Darabiha, D. Thévenin, "Laminar premixed hydrogen/air counterflow flame simulations using flame prolongation of ILDM with differential diffusion", *Proceeding of the Combustion Institute*, 28, 1901-1908, 2000.
40. M. Embouazza, "Étude de l'auto-allumage par réduction des schémas cinétiques chimiques. Application à la combustion homogène Diesel", PhD Thesis, École Centrale de Paris, Paris, France, 2005.
41. K. Sihling, G. Woschni, "Experimental investigation of the instantaneous heat transfer in the cylinder of a high speed Diesel engine", 790833, SAE Technical Paper, 1979.
42. A.H. Lefebvre, Atomization and sprays, Hemisphere Publishing Corporation, United States of America, 1989.
43. T. Jaine, "Simulation zérodimensionnelle de la combustion dans un moteur Diesel à Injection Directe", PhD Thesis, Université d'Orléans, Orléans, France, 2004.
44. G. Mauviot, "Développement d'une modélisation phénoménologique de chambres de combustion de moteurs à piston par réduction de modèle physique 3-D dans la perspective d'une intégration dans un outil de simulation système", PhD Thesis, UPMC, Paris, France, 2007.
45. D. Veynante, L. Vervisch, "Turbulent combustion modeling", *Progress in Energy and Combustion Science*, 28, 3, 193-266, 2002.
46. S.S. Girimaji, "Assumed β-pdf Model for Turbulent Mixing: Validation and Extension to Multiple Scalar Mixing", *Combustion Science and Technology*, 78, 177-196, 1991.
47. H.J. Curran, P. Gaffuri, W.J. Pitz, C.K. Westbrook, "A comprehensive modeling study of n-heptane oxidation", *Combustion & Flame*, 114, 1-2, 149-177, 1998.
48. R.J. Kee, F.M. Rupley, J.A. Miller, "CHEMKIN-II: a fortran chemical kinetics package for the analysis of gas-phase chemical kinetics", SNL-89-8009, Sandia National Laboratories report.

CONTACT

Alessio DULBECCO

e-mail: alessio.dulbecco@ifp.fr

NOMENCLATURE

LATIN ABBREVIATIONS

B : transfer number at steady state [-]

B_m : mass transfer number [-]

B_t : thermal transfer number [-]

$\mathbf{c}$: progress variable [-]

$\mathbf{C_a}$: orifice area-contraction coefficient [-]

$\mathbf{C_d}$: orifice discharge coefficient [-]

$\mathbf{C_{ds}}$: variance dissipation coefficient [-]

$\mathbf{C_{ev}}$: evaporation-rate coefficient [-]

$\mathbf{C_K}$: mean-kinetic energy dissipation coefficient [-]

$\mathbf{C_p}$: constant-pressure specific heat [J/kg/K]

$\mathbf{C_\theta}$: spray opening-angle coefficient [-]

$\mathbf{C_\kappa}$: turbulent-kinetic energy dissipation coefficient [-]

$\mathbf{d_h}$: injector hole diameter [m]

$\mathbf{E_c}$: kinetic energy [J]

$\mathbf{H}$: removed cone height [m]

$\mathbf{K}$: mean specific kinetic energy [J/kg]

$\mathbf{L_v}$: latent-heat of vaporization [J/kg]

$\mathbf{L_0}$: liquid-phase fuel penetration [m]

$\mathbf{m}$: mass [kg]

$\mathbf{M}$: molar mass [kg/mol]

$\mathbf{n_h}$: number of injector holes [-]

$\mathbf{N_K}$: mean-kinetic energy dissipation exponent [-]

$\mathbf{N_\kappa}$: turbulent-kinetic energy dissipation exponent [-]

$\mathbf{p}$: pressure [Pa]

$\mathbf{P}$: probability function [-]

$\mathbf{S}$: spray penetration [m]

$\mathbf{t}$: time [s]

$\mathbf{t_{inj}}$: injection time [s]

$\mathbf{t^+}$: characteristic spray time-scale [s]

$\mathbf{T}$: temperature [K]

$\mathbf{U_{F,l}}$: fuel injection velocity [m/s]

$\mathbf{V}$: cylinder volume [m^3]

$\mathbf{V_s}$: spray volume [m^3]

$\mathbf{x^+}$: characteristic spray length-scale [m]

$\mathbf{X}$: molar fraction [-]

$\mathbf{Y}$: mass fraction [-]

$\mathbf{Z}$: mixture fraction [-]

GREEK ABBREVIATIONS

ε : κ dissipation rate [J/kg/s]

θ : spray opening-angle [rad]

κ : specific turbulent kinetic energy [J/kg]

ρ : density [kg/m^3]

τ_{ev} : characteristic time of evaporation [s]

τ_t : characteristic time of turbulence [s]

ϕ : equivalence-ratio [-]

ψ : Dirac function [-]

ω : reaction rate [kg/s]

SUBSCRIPTS

a : homogeneous mixture of pure-air and eventually EGR

A : ambient gas

c : complementary

ds : dissipation term

esp : species

F : gaseous fuel

F,inj : injected fuel

F,l : liquid fuel

g : equivalent mixture

glob : global

i : *i-th* spray

in : incoming

j : *j-th* spray

m : mean composition

max : maximum value

mix : mixture

out : outgoing

pr : production term

r : EGR

s : liquid-gas interface

st : stoichiometric

S : spray

β-PDF : normalized β-PDF variable

τ : tracer (non reactive) conditions

0 : reference value / pure ambient-gas

1 : relative to pilot-injection

2 : relative to main-injection

• : condition at infinity

APPENDIX: VARIANCE-EQUATION PROOF

Mathematical proof of Eq. 24 holds as follows. The variance of the fuel mass-fraction distribution is defined as:

$$\widetilde{Z''^2} = \frac{1}{m_S}\cdot\int_{m_S}\left(Z^*-\tilde{Z}\right)^2\cdot dm \qquad \text{(A1)}$$

hence, by introducing the PDF associated with the mixture-fraction distribution:

$$\widetilde{Z''^2} = \int_0^{Z_s}\left(Z^*-\tilde{Z}\right)^2\cdot P\left(Z^*\right)\cdot dZ^* \qquad \text{(A2)}$$

By differentiating Eq. (A2) with respect to time :

$$\frac{d\widetilde{Z''^2}}{dt} = \underbrace{\int_0^{Z_s}\frac{d\left(Z^*-\tilde{Z}\right)^2}{dt}\cdot P\left(Z^*\right)\cdot dZ^*}_{I} + \underbrace{\int_0^{Z_s}\left(Z^*-\tilde{Z}\right)^2\cdot\frac{dP\left(Z^*\right)}{dt}\cdot dZ^*}_{II} \qquad \text{(A3)}$$

Solving for the first term, *I*, gives:

$$\int_0^{Z_s}\frac{d\left(Z^*-\tilde{Z}\right)^2}{dt}\cdot P\left(Z^*\right)\cdot dZ^* =$$

$$\int_0^{Z_s}\left(\frac{d\tilde{Z}^2}{dt}-2\cdot Z^*\cdot\frac{d\tilde{Z}}{dt}\right)\cdot P\left(Z^*\right)\cdot dZ^* = \frac{d\tilde{Z}^2}{dt}-2\cdot\tilde{Z}\cdot\frac{d\tilde{Z}}{dt}=0 \qquad \text{(A4)}$$

As shown, the term *I* does not contribute to the variance variation of the mixture-fraction distribution.

Concerning the second term in Eq. (A3), *II*, it is associated with the variation of the PDF in time. For this purpose, it is important to well describe how spray inputs, namely entrained air and evaporating fuel, spray outputs, namely the outgoing mixture, and turbulence act on the PDF.

Henceforth, global PDF will be subdivided into five contributions:

- P_{in}, the probability to have a local mixture in the spray at $Z=Z_{in}$; that is the composition of the entrained gas in the spray,
- P_s, the probability to have a local mixture in the spray at $Z=Z_s$; that is the mixture composition at the liquid-gas interface during the evaporation process,
- P_0, the probability to have a local mixture in the spray at $Z=0=Z_0$; that is the composition of the pure-air (in the most general case pure-air represents an homogeneous mixture of air and EGR),
- P_m, the probability to have a local mixture in the spray at $Z=\tilde{Z}$; that is the mean composition of the spray,
- P_c, the probability to have a local mixture in the spray at a composition different from Z_{in}, Z_s, Z_0 and $\tilde{Z}$.

P_{in}, P_s, P_0 and P_m at each instant of time have a well-known composition. It implies that in the composition-space, they can be represented by using a Dirac function, ψ.

On the other hand, turbulence acts on the overall mixture-fraction distribution and its impact is representative of variance dissipation. The physical meaning of that dissipation is related to the turbulent mixing-process.

In the following, the different-term contributions to the variance variation will be presented individually.

ENTRAINED-MASS CONTRIBUTION

At a given time, t_0, the probability to have in the spray a composition at $Z=Z_{in}$ is:

$$P\left(Z_{in},t_0\right)=P_{in0} \qquad \text{(A5)}$$

after a short interval of time, δt, the spray entrains a certain amount of mass, δm_{in}. Hence:

$$P\left(Z_{in},t_0+\delta t\right)=P_{in0}\cdot\frac{m_S}{m_S+\delta m_{in}}+\frac{\delta m_{in}}{m_S+\delta m_{in}} \qquad \text{(A6)}$$

computing the derivative of $P(Z_{in})$ as the limit of the incremental ratio gives:

$$\frac{dP\left(Z_{in}\right)}{dt}=\lim_{\delta t\to 0}\frac{P(Z_{in},t_0+\delta t)-P(Z_{in},t_0)}{\delta t}=\frac{1}{m_S}\cdot\frac{dm_{in}}{dt} \qquad \text{(A7)}$$

Hence, its contribution to the variance is:

$$\int_0^{Z_s}\left(Z^*-\tilde{Z}\right)^2\cdot\left(\frac{1}{m_S}\cdot\frac{dm_{in}}{dt}\right)\cdot\psi(Z^*-Z_{in})\cdot dZ^*=\left(Z_{in}-\tilde{Z}\right)^2\frac{1}{m_S}\cdot\frac{dm_{in}}{dt} \qquad \text{(A8)}$$

EVAPORATION-PROCESS CONTRIBUTION

Following the same way of proceeding as the one used for entrained gas, the evaporation-process impact on the PDF can be expressed as:

$$\frac{dP\left(Z_s\right)}{dt}=\lim_{\delta t\to 0}\frac{P(Z_s,t_0+\delta t)-P(Z_s,t_0)}{\delta t}=\frac{1}{m_S}\cdot\frac{dm_s}{dt} \qquad \text{(A9)}$$

Hence, its contribution to the variance variation is:

$$\int_0^{Z_s}\left(Z^*-\tilde{Z}\right)^2\cdot\left(\frac{1}{m_S}\cdot\frac{dm_s}{dt}\right)\cdot\psi(Z^*-Z_s)\cdot dZ^*=\left(Z_s-\tilde{Z}\right)^2\frac{1}{m_S}\cdot\frac{dm_s}{dt} \qquad \text{(A10)}$$

Fuel evaporation-process at liquid-gas interface at saturated conditions implies to introduce in the spray an homogeneous mixture of pure air and pure fuel in the mutual proportion established by the value of Z_s. As the necessary air mass is already contained in the spray, its transfer from one value of mixture fraction to another represents a further contribution to the variance variation. In the presented approach, the hypothesis that pure air is used to form the saturated mixture, has been adopted. By definition:

$$Z=\frac{m_F}{m_F+m_a} \qquad \text{(A11)}$$

where m_a is the mass of pure air. It follows that for a given fuel evaporation-rate (evaporating at saturation conditions), dm_F/dt, the total mass at saturated composition introduced in the spray is:

$$\frac{dm_s}{dt}=\frac{\left(dm_F+dm_a\right)_s}{dt}=\frac{1}{Z_s}\cdot\frac{dm_F}{dt} \qquad \text{(A12)}$$

According to the foresaid assumption, it is necessary to take into account the impact on the variance variation of the pure-air mass associated with evaporation process. The withdrawn air-mass is:

$$\frac{dm_a}{dt}=\left(1-\frac{1}{Z_s}\right)\cdot\frac{dm_F}{dt} \qquad \text{(A13)}$$

Hence, its impact on the PDF is:

$$\frac{dP\left(Z_0\right)}{dt}=\lim_{\delta t\to 0}\frac{P(Z_0,t_0+\delta t)-P(Z_0,t_0)}{\delta t}=\frac{1}{m_S}\cdot\frac{dm_a}{dt} \qquad \text{(A14)}$$

and its impact on the variance variation is:

$$\int_0^{Z_s}\left(Z^*-\tilde{Z}\right)^2\cdot\left(\frac{1}{m_S}\cdot\frac{dm_a}{dt}\right)\cdot\psi(Z^*-0)\cdot dZ^*=\tilde{Z}^2\cdot\frac{1}{m_S}\cdot\frac{dm_a}{dt} \qquad \text{(A15)}$$

OUTGOING MASS CONTRIBUTION

According to the stated hypothesis, the outgoing gaseous mixture has a composition equal to the mean value of the distribution. Following the same way of proceeding as before, the outgoing-mass impact on the PDF is:

$$\frac{dP\left(\tilde{Z}\right)}{dt}=\lim_{\delta t\to 0}\frac{P(\tilde{Z},t_0+\delta t)-P(\tilde{Z},t_0)}{\delta t}=-\frac{1}{m_S}\cdot\frac{\left|dm_{out}\right|}{dt} \qquad \text{(A16)}$$

Hence, its contribution to the variance is:

$$\int_0^{Z_s}\left(Z^*-\tilde{Z}\right)^2\cdot\left(-\frac{1}{m_S}\cdot\frac{\left|dm_{out}\right|}{dt}\right)\cdot\psi\left(Z^*-\tilde{Z}\right)\cdot dZ^*=-\left(\tilde{Z}-\tilde{Z}\right)^2\frac{1}{m_S}\cdot\frac{\left|dm_{out}\right|}{dt}=0 \tag{A17}$$

CONTRIBUTION OF THE COMPLEMENTARY MIXTURE-FRACTIONS

The used PDF is a normalized statistical-tool. It follows that the following relation must always be verified:

$$\int_0^{Z_s} P\left(Z^*\right)\cdot dZ^*=1 \tag{A18}$$

Taking advantage of Eq. (A18), at a general instant of time, t, the probability to have in the spray a composition at $Z=Z_c$ is:

$$P\left(Z_c,t\right)=\int_0^{Z_s} P\left(Z^*\right)\cdot dZ^*-P_{in}-P_s-P_0-P_{out} \tag{A19}$$

Hence, its derivative holds:

$$\frac{dP\left(Z_c,t\right)}{dt}=-\frac{dP_{in}}{dt}-\frac{dP_s}{dt}-\frac{dP_0}{dt}-\frac{dP_{out}}{dt} \tag{A20}$$

in fact, being the first term on the right-hand side of Eq. (A19) identically equal to unity, its derivative is zero. Thus, the contribution to the mixture-fraction distribution of the complementary mixture-fraction can be computed as:

$$\int_0^{Z_s}\left(Z^*-\tilde{Z}\right)^2\cdot\frac{dP\left(Z_c\right)}{dt}\cdot dZ^*=$$

$$-\int_0^{Z_s}\left(Z^*-\tilde{Z}\right)^2\cdot\frac{1}{m_S}\cdot\left(\frac{dm_{in}}{dt}+\frac{dm_s}{dt}+\frac{dm_a}{dt}-\frac{\left|dm_{out}\right|}{dt}\right)\cdot dZ^*=$$

$$\frac{\widetilde{Z''^2}}{m_S}\cdot\left(-\frac{dm_{in}}{dt}-\frac{dm_s}{dt}-\frac{dm_a}{dt}+\frac{\left|dm_{out}\right|}{dt}\right) \tag{A21}$$

TURBULENCE CONTRIBUTION

Turbulence contributes to make the mixture more homogeneous. Hence, its impact on the distribution represents a dissipation of the variance. This contribution will be modeled by using an empirical closure term, according to [44]. Hence:

$$\int_0^{Z_s}\left(Z^*-\tilde{Z}\right)^2\cdot\left.\frac{dP\left(Z^*\right)}{dt}\right|_{ds}\cdot dZ^*=-2\cdot C_{ds}\cdot\frac{\tilde{\varepsilon}}{\tilde{\kappa}}\cdot\widetilde{Z''^2} \tag{A22}$$

GLOBAL VARIANCE EQUATION

Assembling all the different aforesaid considerations, the global variance-distribution derivative, Eq. (A3), holds:

$$\frac{d\widetilde{Z''^2}}{dt}=\int_0^{Z_s}\left(Z^*-\tilde{Z}\right)^2\cdot\frac{dP\left(Z^*\right)}{dt}\cdot dZ^*=$$

$$\frac{1}{m_S}\cdot\left[\left(Z_{in}-\tilde{Z}\right)^2\cdot\frac{dm_{in}}{dt}+\left(Z_s-\tilde{Z}\right)^2\cdot\frac{dm_s}{dt}+\tilde{Z}^2\cdot\frac{dm_a}{dt}+\right.$$

$$\left.+\left(-\frac{dm_{in}}{dt}-\frac{dm_s}{dt}-\frac{dm_a}{dt}+\frac{\left|dm_{out}\right|}{dt}\right)\cdot\widetilde{Z''^2}\right]-2\cdot C_{ds}\cdot\frac{\tilde{\varepsilon}}{\tilde{\kappa}}\cdot\widetilde{Z''^2} \tag{A23}$$

Equation (24) is straightforward, obtained by substituting in Eq. (A23) the results of Eq. (A12) and (A13). This completes the proof.

Bibliography

[1] Lafossas, F.A., Marbaix, M. and Menegazzi, P. (2007) Development and application of a 0D D.I. Diesel combustion model for emissions prediction. *SAE Technical Paper*, n° 2007-01-1841.

[2] Albrecht, A., Corde, G., Knop, V., Boie, H. and Castagne, M. (2005) 1D simulation of turbocharged gasoline direct injection engine for transient strategy optimization. *SAE Technical Paper*, n° 2005-01-0693.

[3] Albrecht, A., Chauvin, J., Lafossas, F.A., Potteau, S. and Corde, G. (2006) Development of highly premixed combustion Diesel engine model: from simulation to control design. *SAE Technical Paper*, n° 2006-01-1072.

[4] Tao, F., Liu, Y., Rempelewert, H., Foster, D.E. and Reitz, R.D. (2005) Modeling the effects of EGR and injection pressure on the soot formation in a High-Speed Direct-Injection (HSDI) Diesel engine using a multi-step phenomenological soot model. *SAE Technical Paper*, n° 2005-01-0121.

[5] Vibe, I.I. (1970) Brennverlauf und Kreisprozess von Verbrennungsmotoren. *VEB Verlag Technik.*

[6] Heywood, J.B. (1988) Combustion in Compression-Ignition engines, in *Internal combustion engine fundamentals*, McGraw-Hill, New York.

[7] Cesario, N., Muscio, C., Farina, M., Amato, P. and Lavorgna, M. (2004) Modelling the rate of heat release in common rail Diesel engines: a soft computing approach. *SAE Technical Paper*, n° 2004-01-2967.

[8] Arsie, I., Di Genova, F., Pianese, C., Rizzo, G. and Sorrentino M., Caraceni, A., Cioffi, P. and Flauti, G. (2003) A single-zone model for combustion and NOx simulation in common-rail multi-jet Diesel engines. *SAE Technical Paper*, n° 2003-01-79.

[9] Hiroyasu, H., Kadota, T. and Arai, M. (1983) Development and use of a spray combustion modeling to predict Diesel engine efficiency and pollutant emissions. *Bulletin of the JSME*, **26**, 214, 569-583.

[10] Asay, R.J., Svensson, K.I. and Tree, D.R. (2004) An empirical, mixing-limited, zero-dimensional model for Diesel combustion. *SAE Technical Paper*, n° 2004-01-0924.

[11] Dec, J.E. (1997) A conceptual model of DI Diesel combustion based on laser-sheet imaging. *SAE Technical Paper*, n° 970873.

[12] Mauviot, G., Albrecht, A. and Poinsot, T. (2006) A new 0D approach for Diesel combustion modeling coupling probability density function with complex chemistry. *SAE Technical Paper*, n° 2006-01-3332.

[13] Mauviot, G. (2007) Développement d'une modélisation phénoménologique de chambres de combustion de moteurs à piston par réduction de modèle physique 3-D dans la perspective d'une intégration dans un outil de simulation système. *PhD Thesis*, UPMC.

[14] Barba, C., Burkhardt, C., Boulouchos, K. and Bargende, M. (1999) An empirical model for precalculating the combustion rate of the Common Rail Diesel engine for passenger cars. *Motortechnische Zeitschrift*, **60**, 4, 262-270.

[15] Barba, C., Burkhardt, C., Boulouchos, K. and Bargende, M. (2000) A phenomenological combustion model for heat release rate prediction in high speed DI Diesel engines with common-rail injection. *SAE Technical Paper*, n° 2000-01-2933.

[16] Chmela, F. and Orthaber, G. (1999) Rate of heat release prediction for direct injection Diesel engines based on purely mixing controlled combustion. *SAE Technical Paper*, n° 1999-01-0186.

[17] Chmela, F., Engelmayer, M., Pirker, G. and Wimmer, A. (2004) Prediction of turbulence controlled combustion in Diesel engines. *THIESEL conference on thermo and fluid dynamic processes in Diesel engines*, Valence - Spain, 2004.

[18] Schihl, P., Tasdemir, J., Schwarz, E. and Bryzik, W. (2002) Development of a zero-dimensional heat release model for application to small bore Diesel engines. *SAE Technical Paper*, n° 2002-01-0073.

[19] Kouremenos, D.A., Rakopoulos, C.D. and Hountalas, D.T. (1997) Multi-zone combustion modelling for the prediction of pollutants emissions and performance of DI Diesel engines. *SAE Technical Paper*, n° 970635.

[20] Jaine, T. (2004) Simulation zérodimensionnelle de la combustion dans un moteur Diesel à Injection Directe. *PhD Thesis*, Université d'Orléans.

[21] Kong, S.C., Ayoub, N., and Reitz, D. (1992) Modeling combustion in compression ignition homogeneous charge engine. *SAE Technical Paper*, n° 920512.

[22] Kong, S.C., Marriot, C.D., Reitz, C.D. and Christensen, M. (2001) Modeling and experiments of HCCI engine combustion using detailed chemical kinetics with multidimensional CFD. *SAE Technical Paper*, n° 2001-01-1026.

[23] Kong, S.C., Han, Z. and Reitz, D. (2002) The development and application of a diesel ignition and combustion model for multidimensional engine simulation. *SAE Technical Paper*, n° 950278.

[24] Kong, S.C., Marriot, C.D., Rutland, C.J. and Reitz, D. (2002) Experiments and CFD modeling of direct injection gasoline HCCI engine combustion. *SAE Technical Paper*, n° 2002-01-1925.

[25] Patel, A., Kong, S.C. and Reitz, R.D. (2004) Development and validation of a reduced reaction mechanism for HCCI engine simulation. *SAE Technical Paper*, n° 2004-01-0558.

[26] Nishida, K. and Hiroyasu, H. (1989) Simplified three-dimensional modeling of mixture formation and combustion in a Diesel engine. *SAE Technical Paper*, n° 890269.

[27] Hasse, C., Barths, H. and Peters, N. (1999) Modeling the effects of split-injections in Diesel engines using representative interactive flamelets. *SAE Technical Paper*, n° 1999-01-3574.

[28] Hasse, C., Bikas, G. and Peters, N. (2000) Modeling diesel combustion using the eulerian particle flamelet model (epfm). *SAE Technical Paper*, n° 2000-01-2934.

[29] Barths, H., Pitsch, H. and Peters, N. (1999) 3D simulation of DI diesel combustion and pollutant formation using a two-component reference fuel. *Oil & Gas Science and Technology*, **54**, 2, 233-244.

[30] Michel, J.B., Colin, O. and Veynante, D. (2008) Modeling ignition and chemical structure of partially premixed turbulent flames using tabulated chemistry. *Combustion & Flame*, **152**, 1-2, 80-99.

[31] Peters, N. and Rogg, B. (1993) *Reduced kinetic mechanisms for applications in combustion systems*, Springer Verlag, Heidelberg.

[32] Peters, N. (2000) Nonpremixed turbulent combustion, in *Turbulent combustion*, Cambridge University Press, Cambridge.

[33] Colin, O., Benkenida, A. and Angelberger, C. (2003) 3D Modeling of Mixing, ignition and combustion phenomena in highly stratified gasoline engine. *Oil & Gas Science and Technology*, **58**, 1, 47-52.

[34] Colin, O. and Benkenida, A. (2004) The 3-zones extended coherent flame model (ECFM3Z) for computing premixed/diffusion combustion. *Oil & Gas Science and Technology*, **59**, 6, 593-609.

[35] Wang, Z., Wang, J. and Shuai, S. (2004) Numerical simulation of HCCI engine with multistage gasoline Direct Injection using 3d-cfd with detailed chemistry. *SAE Technical Paper*, n° 2004-01-0563.

[36] Wang, Z., Shuai, S., Wang, J., Tian, G. and An, X. (2006) Modeling of HCCI combustion from 0D to 3D. *SAE Technical Paper*, n° 2006-01-1364.

[37] Knop, V. and Jay, S. (2006) Latest developments in gasoline Auto-Ignition modelling applied to an optical CAI™ engine. *Oil & Gas Science and Technology*, **61**, 1, 121-137.

[38] Pires-da-Cruz, A., Baritaud, T. and Poinsot, T.J. (2001) Self-ignition and combustion modeling of initially nonpremixed turbulent systems. *Combustion & Flame*, **124**, 1-2, 65-81.

[39] Bruneaux, G. (2001) Liquid and vapor spray structure in high pressure Common Rail Diesel injector. *Atomization and Sprays*, **11**, 5, 533-556.

[40] Bruneaux, G., Augé, M. and Lemenand, C. (2004) A study of Combustion structure in high pressure single hole Common Rail Direct Diesel Injection using laser induced fluorescence of radicals. *COMODIA Congress*, Yokohama - Japan, 2004.

[41] Bruneaux, G. (2005) Mixing process in high pressure Diesel jets by normalized laser induced exciplex fluorescence. Part I : free jet. *SAE Technical Paper*, n° 2005-01-2100.

[42] Verhoeven, D., Vanhemelryck J-L. and Baritaud, T. (1998) Macroscopic and ignition characteristics of high-pressure sprays of single-component fuels. *SAE Technical Paper*, n° 981069.

[43] Hiroyasu, H. and Arai, M. (1990) Structures of fuel sprays in Diesel engines. *SAE Technical Paper*, n° 900475.

[44] Jaine, T., Benkenida, A., Menegazzi, P. and Higelin, P. (2003) Zero dimensional computation of Diesel spray - comparison with experiments and 3D model. *6°Internation Conference on Engines for automobile*, Capri - Italy, 2003.

[45] Subramanian, G. (2005) Modélisation de l'auto-inflammation : analyse des effets de la dilution par les gaz brûlés et des interactions avec la turbulence dédiée aux moteurs Diesel à charge homogène. *PhD Thesis*, INSA Rouen.

[46] Pope, S.B. (1985) PDF methods for turbulent reactive flows. *Progress in Energy and Combustion Science*, **19**, 11, 119-192.

[47] Gicquel, O., Darabiha, N. and Thévenin, D. (2000) Laminar premixed hydrogen/air counterflow flame simulations using flame prolongation of ILDM with differential diffusion. *Proceedings of the Combustion Institute*, **28**, 1901-1908.

[48] Veynante, D. and Vervisch, L. (2002) Turbulent combustion modeling. *Progress in Energy and Combustion Science*, **28**, 3, 193-266.

[49] Lefebvre, A.H. (1989) Drop evaporation, in *Atomization and sprays*, Hemisphere Publishing Corporation, United States of America.

[50] Reid, R.C., Prausnitz, J.M. and Poling, B.E. (1987) *The properties of gases & liquids*, McGraw-Hill, United States of America.

[51] Ghassemi, H., Baek, S.W. and Khan, S.Q. (2006) Experimental study on binary droplet evaporation at elevated pressures and temperatures. *Combustion Science and Technology*, **178**, 6, 1031-1053.

[52] Siebers, D.L. (1998) Liquid-phase fuel penetration in Diesel sprays. *SAE Technical Paper*, n° 980809.

[53] Siebers, D. (1999) Scaling liquid-phase fuel penetration in diesel sprays based on mixing-limited vaporization. *SAE Technical Paper*, n° 1999-01-0528.

[54] Higgins, B.S., Mueller, C.J. and Siebers, D.L. (1999) Measurements of fuel effects on liquid-phase penetration in DI sprays. *SAE Technical Paper*, n° 1999-01-0519.

[55] Naber, J.D. and Siebers, D. (1996) Effects of gas density and vaporization on penetration and dispersion of diesel sprays. *SAE Technical Paper*, n° 960034.

[56] Desantes, J.M., Payri, R., Salvador, F.J. and Gil, A. (2005) Development and validation of a theoretical model for diesel spray penetration. *Fuel*, **85**, 7-8, 910-917.

[57] Girimaji, S.S. (1991) Assumed β-PDF Model for Turbulent Mixing: Validation and Extension to Multiple Scalar Mixing. *Combustion Science and Technology*, **78**, 177-196.

[58] Kuo, K.K. (2005) Gaseous diffusion flames and combustion of a single liquid fuel droplet, in *Principles of combustion*, Wiley, J. (ed.), John Wiley & Sons, Hoboken - New Jersey.

[59] Givler, S.D. and Abraham, J. (1996) Supercritical droplet vaporization and combustion studies. *Progress in Energy and Combustion Science*, **22**, 4, 1-28.

[60] Sirignano, W.A. (2004) Droplet behavior at near-critical, transcritical, and supercritical conditions, in *Fluid dynamics and transport of droplets and sprays*, Cambridge University Press, Irvine.

[61] Sirignano, W.A. (2004) *Fluid dynamics and transport of droplets and sprays*, Cambridge University Press, Irvine.

[62] Neely, G.D., Sasaky, S., Huang, Y., Leet, J.A. and Stewart, D.W. (2005) New Diesel emission control strategies to meet US Tier 2 emissions regulations. *SAE Technical Paper*, n° 2005-01-1091.

[63] Kee, R.J., Rupley, F.M. and Miller, J.A. (1989) CHEMKIN-II: a fortran chemical kinetics package for the analysis of gas-phase chemical kinetics. *Sandia National Laboratories report*, n° SNL-89-8009.

[64] Curran, H.J., Gaffuri, P., Pitz W.J. and Westbrook, C.K. (1998) A comprehensive modeling study of n-heptane oxidation. *Combustion & Flame*, **114**, 1-2, 149-177.

[65] Maas, U. and Pope, S.B. (1992) Implementation of simplified chemical kinetics based on low-dimensional manifolds. *Proceedings of the Combustion Institute*, **24**, 1, 103-112.

[66] Maas, U. and Pope, S.B. (1992) Simplifying chemical kinetics: intrinsic low-dimensional manifolds in composition space. *Combustion & Flame*, **88**, 3-4, 239-264.

[67] Embouazza, M. (2005) Etude de l'auto-allumage par réduction des schémas cinétiques chimiques. Application à la combustion homogène Diesel. *PhD Thesis*, Ecole Centrale de Paris.

[68] Gauthier, B.M., Davidson, D.F. and Hanson, R.K. (2004) Shock tube determination of ignition delay times in full-blend and surrogate fuel mixtures. *Combustion & Flame*, **139**, 4, 300-311.

[69] Sihling, K. and Woschni, G. (1979) Experimental investigation of the instantaneous heat transfer in the cylinder of a high speed Diesel engine. *SAE Technical Paper*, n° 790833.

[70] Massol, A. (2004) Simulation numérique d'écoulements à travers des réseaux fixes de sphères monodisperses et bidisperses pour nombres de Reynolds modérés. *PhD Thesis*, Institut National Polytechnique de Toulouse.

[71] Lafossas, F.A. and Habchi, C. (2000) Influence des propriétés du carburant sur la préparation du mélange dans les moteurs à injection directe essence. *IFP internal report.*

[72] FLUIDAT, (2007) www.fluidat.com, *Internet Website*

[73] IFP, (2006) IFP-C3D Source Code. *IFP internal files.*

[74] Faeth, G.M. (1983) Evaporation and combustion of sprays. *Progress in Energy and Combustion Science*, **9**, 1-76.

[75] Browne, K.R., Partridge, I.M. and Greeves, G. (1986) Fuel Property effects on fuel/air mixing in an experimental Diesel engine. *SAE Technical Paper*, n° 860223.

[76] Kamimoto, T., Yokota, H. and Kobayashi, H. (1987) Effect of high pressure injection on soot formation processes in a rapid compression machine to simulate Diesel flames. *Transactions of the SAE*, **96**, 4, 4783-4791.

[77] Espey, C. and Dec, J.E. (1995) The effect of TDC temperature and density on the liquid-phase fuel penetration in a DI Diesel engine. *Transactions of the SAE*, **104**, 4, 1400-1414.

[78] Canaan, R.E., Dec, J.E., Green, R.M. and Daly, D.T. (1998) The influence of fuel volatility on the liquid-phase fuel penetration in a heavy-duty DI Diesel engine. *SAE Technical Paper*, n° 980510.

[79] Arai, M., Tabata, M., Hiroyasu, H. and Shimizu, M. (1984) Disintegrating process and spray characterization of fuel jet injected by a Diesel nozzle. *Transactions of the SAE*, **93**, 2, 358-371.

[80] Kadota, T. and Hiroyasu, H. (1976) Evaporation of a single droplet at elevated pressures and temperatures (2^{nd} report, theoretical study). *Bulletin of the JSME*, **138**, 19, 1515-1521.

[81] Park, S.W., Suh, H.K. and Lee, C.S. (2005) Effect of a split injection on spray characteristic for a Common-Rail type Diesel injection system. *International Journal of Automotive Technology*, **6**, 4, 315-322.

[82] Zhang, Y., Nishida, K. and Yoshizaki, T. (2003) Characterization of droplets and vapor concentration distributions in split-injection Diesel sprays by processing UV and visible images. *JSME International Journal*, Series B, **46**, 1, 100-108.

[83] Li, T., Nishida, K., Zhang, Y., Onoe, T. and Hiroyau, H. (2005) Enhancement of stratified charge for DISI engines through split injection (Effect and its mechanism). *JSME International Journal*, Series B, **48**, 4, 687-694.

[84] Spalding, D.B. (1952) The combustion of liquid fuels. *Proceedings* 4^{th} *International Symposium*, **4**, 847-864.

[85] Pera, C., Colin, O. and Jay, S. (2009) Development of a FPI detailed chemistry tabulation methodology for internal combustion engines. *Oil & Gas Science and Technology*, **64**, 3, 243-258.

[86] Anderlohr, J.M., Bounaceur, R., Pires Da Cruz, A. and Battin-Leclerc, F. (2009) Modelling of auto-ignition and NO sensitization for the oxidation of IC-engine surrogate fuels. *Combustion & Flame*, **156**, 2, 505-521.

[87] Vervisch, L., Hauguel, R., Domingo, P. and Rullaud, M. (2004) Three facets of turbulent combustion modelling : DNS of premixed V-flame, LES of lifted non-premixed flame and RANS of jet-flame. *Journal Of Turbulence*, **5**, 1, 4-4(1).

[88] Michel, J.B., Colin, O. and Angelberger, C. (2009) Tabulation methods in the PCM-FPI context in non premixed or partially premixed configurations. *Submitted to Combustion & Flame.*

[89] Dulbecco, A., Lafossas, F.A., Mauviot, G. and Poinsot T.J. (2009) A new 0D Diesel HCCI combustion model derived from a 3D CFD approach with detailed tabulated chemistry. *Oil & Gas Science and Technology*, **64**, 3, 259-284.

[90] Dulbecco, A., Lafossas, F.A. and Poinsot T.J. (2009) A 0D phenomenological approach to model Diesel HCCI combustion with multi-injection strategies using Probability Density Functions and detailed tabulated chemistry. *SAE Technical Paper*, n° 2009-01-0678.

[91] Poinsot, T. and Veynante, D. (2005) *Theoretical and numerical combustion, Second edition*, Edwards (ed.), Philadelphia - USA.

[92] Elgobashi, S. (1994) On Predicting Particle-Laden Turbulent Flows. *Applied Scientific Research*, **52**, 4, 309-329.

[93] Walter, B. and Gatellier, B. (2002) Development of the high power NADI™ concept using dual mode Diesel combustion to achieve zero NO_x and particulate emissions. *SAE Technical Paper*, n° 2002-01-1744.

[94] Jay, S., Béard, P. and Pires da Cruz, A. (2007) Modeling coupled processes of CO and Soot formation and oxidation for conventional and HCCI Diesel combustion. *SAE Technical Paper*, n° 2007-01-0162.

[95] Magand, S., Watel, E., Castagné, M., Soleri, D., Grondin, O., Devismes, S. and Moroz, S. (2008) Optimisation of a Low NOx emission HCCI Diesel prototype vehicle. *THIESEL conference*, Spain, September 9-12, 2008.

[96] European Environment Agency (2008) Annual European Community LRATP Convention emission inventory report 1990-2006. *EEA Technical report*, n° 7/2008.

[97] European Union (2008) European Union emission standards for light duty vehicles (Directive 70/220/EEC). *http://www.dieselnet.com/standards/eu/ld.php*, 2009.

[98] Dronniou, N. (2008) Etude théorique et expérimentale des stratégies de combustion homogène. Application aux moteurs Diesel pour véhicules industriels. *PhD Thesis*, Université d'Orléans.

[99] FIAT (2003) Photothèque moteurs 3 et 4 cylindres Diesel. *http://www.auto-innovations.com*, 2009.

[100] Francois Dovat (2008) L'injection Diesel par Rampe Commune - Dossier. *http://www.auto-innovations.com*, 2009.

[101] Bockhorn, H. (1995) Introduction, in *Soot formation in combustion : mechanisms and models*, Springer Verlag.

[102] Takeda, Y. and Keiichi, N. (1996) Emission characteristics of premixed lean Diesel combustion with extremely early staged fuel injection. *SAE Technical Paper*, n° 961163.

[103] Galpin, J., Naudin, A., Vervisch, L., Angelberger, C., Colin, O. and Domingo, P. (2008) Large-Eddy Simulation of a fuel-lean premixed turbulent swirl-burner. *Combustion & Flame*, **155**, 1-2, 247-266.

[104] Klimenko, A.K. and Bilger, R.W. (1999) Conditional Moment Closure for turbulent combustion. *Progress in Energy and Combustion Science*, **25**, 595-687.

[105] Michel, J.B., Colin, O., Angelberger, C. and Veynante, D. (2009) Using the tabulated diffusion flamelet model ADF-PCM to simulate a lifted methane?air jet flame. *Combustion & Flame*, **156**, 7, 1318-1331.